UNIVERSITAT POLITÈCNICA DE CATALUNYA BARCELONATECH

Contribution to the hydrogeological knowledge of the high mountain karst aquifer of the Port del Comte (SE, Pyrenees)

- article-based thesis -

Joan Ignasi Herms Canellas

UNIVERSITAT POLITÈCNICA DE CATALUNYA
BARCELONATECH
Escola Politècnica Superior d'Enginyeria
de Manresa

"Contribution to the hydrogeological knowledge of the high mountain karst aquifer of the Port del Comte (SE, Pyrenees)"

Joan Ignasi Herms Canellas

A thesis submitted in fulfilment of the requirements for the degree of
Doctor of Philosophy

at the
Universitat Politècnica de Catalunya (UPC)

Doctoral Programme in Natural Resources and Environment

Advisors:
Dr. Albert Soler i Gil (UB) and Dr. Joan Jorge Sánchez (ex-UPC)

Article-based thesis

Manresa (Barcelona), 2022

This thesis includes the four postprints version of the following 4 published scientific papers:

I. Herms, J. Jódar, A. Soler, I. Vadillo, L.J. Lambán, S. Martos-Rosillo, J.A. Núñez, G. Arnó, J. Jorge. (2019). 'Contribution of isotopic research techniques to characterize high- mountain-Mediterranean karst aquifers: The Port del Comte (Eastern Pyrenees) aquifer' Science of the Total Environment 656 (2019) 209–230 https://doi.org/10.1016/j.scitotenv.2018.11.188.

I.Herms, J. Jódar, A. Soler, L.J. Lambán, E. Custodio, J.A. Núñez, G. Arnó, M.I. Ortego, D. Parcerisa, J. Jorge. (2021) Evaluation of natural background levels of high mountain karst aquifers in complex hydrogeological settings. A Gaussian mixture model approach in the Port del Comte (SE, Pyrenees) case study'. Science of the Total Environment 756 (2021) 143864. https://doi.org/10.1016/j.scitotenv.2020.143864

J.Jódar, **I.Herms**, L.J. Lambán, S. Martos-Rosillo, C.Herrera-Lameli, J. Urrutia, A. Soler and E.Custodio.(2021) 'Isotopic content in high mountain karst aquifers as a proxy for climate change impact in Mediterranean zones: The Port del Comte karst aquifer (SE Pyrenees, Catalonia, Spain). Science of the Total Environment Available online 29 May 2021, 148036 https://doi.org/10.1016/j.scitotenv.2021.148036

I.Herms, J. Jódar, A. Soler, L.J. Lambán, E. Custodio, J.A. Núñez, G. Arnó, D. Parcerisa, J. Jorge. (2021). Identification of Natural and Anthropogenic Geochemical Processes Determining the Groundwater Quality in Port del Comte High Mountain Karst Aquifer (SE, Pyrenees). Water 2021, 13, 2891. https://doi.org/10.3390/w13202891

3 Papers published in the Science of the Total Environment journal (editorial Elsevier)
Q1 JCR Impact Factor: 6.551 for the period 2019-2020 'ENVIRONMENTAL SCIENCES' according to the 'Web of Knowledge' website.

1 Paper published in the open-access journal WATER (editorial MDPI)
Q2 JCR Impact Factor: 2.714 for the period 2019-2020 'WATER RESOURCES' according to the 'Web of Knowledge' website.

In addition, the thesis also includes a list of other 10 author's contributions in national and international workshops and congress

Authors: **I.Herms**; A.Soler; J.Jorge; L.Daniele; I.Vadillo

Title of contribution: *Caracterización hidrogeoquímica de las aguas de recarga y descarga del acuífero kárstico del macizo del Port del Comte (Solsonès, Lleida)*

Congress/Workshop: II CONGRESO IBÉRICO DE LAS AGUAS SUBTERRÁNEAS

Format: poster

Location / Country: València, Espanya

Date: 8 to 10 September 2014

Authors: J.Jorge; **I.Herms**

Title of contribution: Mapas de fusión de la nieve en el Pre-Pirineo catalán a partir de datos MODIS/Terra

Congress/Workshop: XVI CONGRESO DE LA ASOCIACIÓN ESPAÑOL DE TELEDETECCIÓN

Format: comunicació

Location / Country: Sevilla, Espanya

Date: 21 - 23 October 2015

Authors: **I.Herms**; A.Soler; J.Jorge; I.Vadillo

Title of contribution: *Isotopical and hydrogeochemical characterization of karst aquifer in the Port del Comte (Solsonès, Lleida)*

Congress/Workshop: KG@B 2015 – INTERNATIONAL CONFERENCE ON GROUNDWATER IN KARST

Format: pòster- comunicació

Location / Country: Birmingham - UK – United Kingdom

Date: 20 - 26 June 2015

Autors: **I.Herms**; A.Soler; J.Jorge; I.Vadillo

Title of contribution: *Aplicación de la geoquímica isotòpica del agua a la comprensión del modelo conceptual del acuífero carbonatado kárstico del macizo del Port del Comte (Lleida, Spain)*

Congress/Workshop: II CONGRESO NACIONAL DE GEOQUÍMICA

Format: comunicació

Location / Country: Jaén, Espanya

Date: 25 - 28 September 2017

Autors: **I.Herms**; J.Jodar, J.Lambán, S.Martos, J.Jorge, I.Vadillo, A.Soler, E.Custodio

Title of contribution: *Estimación de tiempos de tránsito en sistemes hidrogeológicos de alta montaña del Pirineo Central y Oriental mediante isótopos ambientales*

Congress/Workshop: II CONGRESO IBÉRICO SOBRE AGUAS SUBTERRÁNEAS, MEDIO AMBIENTE, SALUD Y PATRIMONIO

Format: poster

Location / Country: Salamanca, Espanya

Date: 12 - 15 November 2018

Autors: **I.Herms**, J.A.Nuñez, M.Colomer, G.Arnó1, J.Jodar, A.Soler, A.Griera.

Title of contribution: *3D geological modeling as a tool for supporting spring catchment delineation in high-mountain karst aquifers: the case study of the Port del Comte (Eastern Pyrenees) aquifer.*

Congress/Workshop: 5th European Meeting on Geological 3D Modelling

Format: poster

Location / Country: Berna, Switzerland

Date: 21 - 24 May 2019

Autors: J-C. Marechal; J-B. Charlier; B. Ladouche; V. Bailly-Comte; V. Hakoun,; E. Krystofova; J. Nikolić; F. Skopljak; G. Schubert; D. Elster; J. Urbanc; C. Hickey; A. Stroj; G. Arno; V. Camps; **I. Herms;** E. Pardo-Igúzquiza; J. de Dios-Gómez; J. Heredia-Diaz; P.A. Robledo; J.A. Luque-Espinar; D. Persa; N. Gal; A. Kovacs; L. Maurice; R. Vernes; M. Van-Vliet; L. Zini; C. Calligaris.

Title of contribution: *Typology of karst aquifers and recommendations for their management – GeoERA RESOURCE project, CHAKA work Package*

Congress/Workshop: 46t IKS 2019 - 27th International Karstological School “Classical Karst”

Format: poster

Location / Country: Málaga, Spain

Date: 17 - 20 June 2019

Autors: **I.Herms**; J.Jodar, J.Lambán, S.Martos, J.Jorge, I.Vadillo, A.Soler, E.Custodio

Title of contribution: *Baseline hydrogeochemical characteristion of a vulnerable pristine high-mountain karst aquifer in the southeastern Pyrenees. The Port del Comte massif (Topic 7 - Karst Hydrogeology)*

Congress/Workshop: 46th International Association of Hydrogeologist AIH Congress - Málaga, Spain 2019

Format: poster

Location / Country: Málaga, Espanya

Date: del 22 al 27 de setembre de 2019

Authors: E. Ardo-Iguzquiza; J-C. Marechal; J-B. Charlier; B. Ladouche; V. Bailly-Comte; V. Hakoun; E. Krystofova; J. Nikolić; G. Schubert; D. Elster; J. Urbanc; C. Hickey; T. Hunter-Williams; A. Stroj; G. Arnó; V. Camps; **I.Herms**; J. De Dios-Gómez; J. Heredia-Díaz; P.A. Robledo; J.A. Luque-Espinar; D. Persa; N. Gal; A. Kovacs; L. Maurice; R. Vernes; M. Van-Vliet; L. Zini; C. Calligaris.

Title of contribution: *Typology of karst aquifers in Europe: a review – GeoERA RESOURCE project, CHAKA work package (Topic 7 - Karst Hydrogeology)*

Congress/Workshop: 46th International Association of Hydrogeologist AIH Congress - Málaga, Spain 2019

Format: poster

Location / Country: Málaga, Spain

Date: 22 - 27 September 2019

Authors: **I.Herms**; J.Jodar, J.Lambán, S.Martos, A.Soler, E.Custodio

Title of contribution: *Impacto potencial del cambio climático en sistemas hidrogeológicos del Pirineo. El caso de estudio del macizo del Port del Comte (Lérida))*

Congress/Workshop: Congreso Ibérico de las Aguas Subterráneas 2021 (auspiciado por el Grupo Español de la Asociación Internacional de Hidrogeólogos)

Format: poster

Location / Country: Universitat Politècnica de València, Espanya

Date: 17 - 19 November 2021

ABSTRACT

This thesis has aimed to improve the hydrogeological knowledge of the Port del Comte Massif (PCM), a karstic aquifer system located in the south-eastern sector of the Pyrenees that plays a strategic role in the provision of water resources in the basins of the Llobregat and Segre river basins. The specific objectives have been aimed at deepening the knowledge of the geological structure of its reservoirs, the hydrodynamic and geochemical behaviour, the establishment of a conceptual model; and the study of climate change (CC) scenarios. A data acquisition work has been carried out followed by its processing and modeling. The results have been published in 4 peer-reviewed scientific papers. The work has been complemented by participation in the EU GeoERA RESOURCE project, where through this thesis, the PCM has been one of the case studies, contributing to the development and testing of new methods for classifying karstic aquifers.

The main aquifer is located in the lower Eocene limestones and dolomites. This aquifer presents in the highest parts of the massif an important karstic development. The overlying materials from the Upper Eocene-Oligocene and the underlying Cretaceous and Triassic constitute relevant aquifers for local supply. More than 100 springs have been inventoried in the study area, of which 43 were selected for monitoring tasks. Of the total, 4 correspond to the main discharge points of the system: the “Cardener” spring that discharges to the East into the Cardener River, “Sant Quintí” that discharges to the SE in the Fred River basin; “Aiguaneix” that discharges towards the NW in the Alinyà River; and “Can Sala” that discharges towards the SE. In addition, there is also a diffuse groundwater flow in a northerly direction towards the La Vansa river basin, and discharge through multiple local springs spread throughout the massif. The use of hydrological models has made it possible to estimate the recharge time-series and the mean transit times in the main karst springs. The recession analysis focused on the "Cardener" spring suggests that it is in the domain of "complex karst systems" similar to the behaviour of other karst springs in the Pyrenees. The new evaluation systems KGWRAI-V and RC-V show that the "Cardener and Sant Quintí" springs can be classified with "medium to high vulnerability" and with "moderate regulatory capacity”. Among the various results obtained from the simulations of the climate change emission scenarios RCP 4.5 and 8.5 for the "Cardener" spring, on average it is observed that the temperature in a horizon of 35 years could increase by about 1.3 ºC and the snow cover could be reduced by 50%. From the geochemical point of view, the underground water is predominantly of the calcium-bicarbonate

type, although up to 6 different facies types have been identified. The multivariate statistical approach using a clustering method based on Gaussian mixture models allowed to classify the 43 springs into 4 groups. These new associations made it possible to better determine natural background levels at aquifer scale for sulfate, nitrate, and chloride. Several points present sulfate concentrations above the potability limit, being the main source of geogenic origin. The nitrate concentration is generally low except in specific points related to agricultural and livestock practices. The results obtained have meant an important advance in the knowledge of the karstic aquifer system of the MPC. The methodology could be replicated in the rest of the strategic karstic aquifers of the Pyrenees, providing valuable information for their sustainable management and for establishing adaptation strategies to the CC.

Keywords: Port del Comte Massif; High-Mountain Karst Aquifer System, isotopes**.**

RESUM

Aquesta tesi ha tingut com a objectiu principal millorar el coneixement hidrogeològic del Massís del Port del Comte (MPC), un sistema aqüífer càrstic ubicat al sector sud-est del Pirineus que té un paper estratègic en la provisió de recursos hídrics a les conques dels rius Llobregat i Segre. Els objectius específics s'han orientat a aprofundir en el coneixement de l'estructura geològica dels seus reservoris, el comportament hidrodinàmic i geoquímic, l'establiment d'un model conceptual; i l'estudi d'escenaris de canvi climàtic (CC). S'ha efectuat un treball d'adquisició de dades seguit del seu processament i modelatge. Els resultats s'han publicat a 4 articles científics revisats per parells. Els treballs s'han complementat amb la participació en el projecte europeu GeoERA RESOURCE, on a través de la present tesi, el MPC ha estat un dels casos d'estudi, contribuint al desenvolupament i test de nous mètodes de classificació d'aqüífers càrstics.

L'aqüífer principal del MPC es localitza a les calcàries i dolomies de la base de l'Eocè. Aquest aqüífer presenta a les parts més altes del massís un desenvolupat càrstic important. Els materials suprajacents de l'Eocè-Oligocè superior i del Cretaci i Triàsic subjacents constitueixen aqüífers rellevants per l'abastament local. S'han inventariat més de 100 fonts a l'àrea d'estudi, de les quals se'n van seleccionar 43 per les tasques de monitoratge. Del total, 4 corresponen als principals punts de descàrrega del sistema: les fonts "del Cardener" que descarrega cap a l'Est al riu Cardener, la de "Sant Quintí" que descarrega cap al SE a la conca del Riu Fred; la "d'Aiguaneix" que descarrega cap al NW al Riu d'Alinyà; i la "de Can Sala" que descarrega vers al SE. A banda, també existeix un flux difús d'aigua subterrània en sentit nord cap a la conca del riu La Vansa, i la descàrrega a través de múltiples fonts locals repartides pel massís. L'ús de models hidrològics ha permès estimar les series de recàrrega i els temps mitjans de trànsit en les fonts principals. L'anàlisi de recessió centrada a les fonts del "Cardener", suggereix que aquesta es troba en el domini de "sistemes càrstics complexos" similar al comportament d'altres fonts càrstiques dels Pirineus. Els nous sistemes d'avaluació KGWRAI-V i RC-V mostren que les fonts "Cardener i Sant Quintí" poden classificar-se amb "vulnerabilitat mitjana a alta" i amb "capacitat reguladora moderada". Entre els diversos resultats obtinguts a partir de les simulacions dels escenaris d'emissions de canvi climàtic RCP 4.5 i 8.5 per les fonts del "Cardener", de mitjana s'observa que la temperatura en un horitzó de 35 anys podria augmentar uns 1.3 ºC i el mantell nival podria reduir-se un 50%. Des del punt de vista geoquímic, l'aigua subterrània és predominantment del tipus bicarbonatada-càlcica, encara que s'han identificat fins a 6 tipus de fàcies diferents. L'enfocament estadístic multivariant utilitzant

un mètode d'agrupament basat en models de mescla gaussiana va permetre classificar les 43 fonts estudiades en 4 grups. Aquestes noves associacions van permetre determinar millor els nivells naturals de fons a escala d'aqüífer per a sulfat, nitrat i clorur. Diversos punts monitoritzats presenten concentracions de sulfat per sobre del límit de potabilitat, essent la principal font d'origen geogènic. La concentració de nitrat és generalment baixa excepte en punts específics relacionats amb pràctiques agrícoles i ramaderes. Els resultats obtinguts han suposat un avenç important en el coneixement del sistema aqüífer càrstic del MPC. La metodologia emprada podria replicar-se a la resta d'aqüífers càrstics estratègics dels Pirineus aportant informació valuosa per a la seva gestió sostenible i per establir estratègies d'adaptació al CC.

Paraules clau: Massís del Port del Comte; Sistema Aqüífer Càrstic d'Alta Muntanya, isòtops.

RESUMEN

Esta tesis ha tenido como objetivo principal mejorar el conocimiento hidrogeológico del Macizo del Port del Comte (MPC), un sistema acuífero kárstico ubicado en el sector sureste del Pirineo que presenta un rol estratégico en la provisión de recursos hídricos en las cuencas de los ríos Llobregat y Segre. Los objetivos específicos se han orientado a profundizar en el conocimiento de la estructura geológica de sus reservorios, el comportamiento hidrodinámico y geoquímico, el establecimiento de un modelo conceptual; y el estudio de escenarios de cambio climático (CC). Se ha realizado un trabajo de adquisición de datos y un procesamiento y modelado. Los resultados se han publicado en 4 artículos científicos revisados por pares. El trabajo se ha complementado con la participación en el proyecto EU GeoERA RESOURCE, donde a través de la presente tesis, el MPC ha sido uno de los casos de estudio, contribuyendo al desarrollo y test de nuevos métodos de clasificación de acuíferos kársticos.

El acuífero principal del MPC se localiza en las calizas y dolomías de la base del Eoceno. Este acuífero presenta en las partes más altas del macizo un desarrollado kárstico importante. Los materiales suprayacentes del Eoceno-Oligoceno superior y del Cretáceo y Triásico subyacentes constituyen acuíferos relevantes para el abastecimiento local. Se han inventariado más de 100 manantiales en el área de estudio, de los que se seleccionaron 43 por las tareas de monitorización. Del total, 4 corresponden a los principales puntos de descarga del sistema: el manantial “del Cardener” que descarga hacia el Este en el río Cardener, “Sant Quintí” que descarga hacia el SE en la cuenca del Río Fred; “Aiguaneix” que descarga hacia el NW en el Río de Alinyà; y “Can Sala” que descarga hacia el SE. Además, también existe un flujo difuso de agua subterránea en sentido norte hacia la cuenca del río La Vansa, y la descarga a través de múltiples manantiales locales repartidos por el macizo. El uso de modelos hidrológicos ha permitido estimar las series de recarga y los tiempos medios de tránsito en los principales manantiales. El análisis de recesión centrado en el manantial del “Cardener", sugiere que este se encuentra en el dominio de "sistemas kársticos complejos" similar al comportamiento de otros manantiales kársticos de los Pirineos. Los nuevos sistemas de evaluación KGWRAI-V y RC-V muestran que los manantiales “Cardener y Sant Quintí” pueden clasificarse con “vulnerabilidad media a alta” y “capacidad reguladora moderada”. Entre los diversos resultados obtenidos a partir de las simulaciones de los escenarios de cambio climático RCP 4.5 y 8.5 para el manantial “Cardener”, de media se observa que la temperatura en un horizonte de 35 años podría aumentar unos 1.3 ºC y el manto nival podría reducirse un 50%.

Desde el punto de vista geoquímico, el agua subterránea es predominantemente del tipo bicarbonatada-cálcica, aunque se han identificado hasta 6 tipos de facies diferentes. El enfoque estadístico multivariante mediante un método de agrupamiento basado en modelos de mezcla gaussiana permitió clasificar los 43 manantiales en 4 grupos. Estas nuevas asociaciones permitieron determinar mejor los niveles naturales de fondo a escala de acuífero para sulfato, nitrato y cloruro. Varios puntos presentan concentraciones de sulfato por encima del límite de potabilidad, siendo la principal fuente de origen geogénico. La concentración de nitrato es generalmente baja, salvo en puntos específicos relacionados con prácticas agrícolas y ganaderas. Los resultados obtenidos han supuesto un importante avance en el conocimiento del sistema acuífero kárstico del MPC. La metodología podría replicarse en el resto de los acuíferos kársticos estratégicos de los Pirineos aportando información valiosa para su gestión sostenible y para establecer estrategias de adaptación al CC.

Palabras clave: Macizo del Port del Comte; Sistema Acuífero Kárstico de Alta Montaña, isótopos

ACKNOWLEDGMENTS

First of all, I would like to express my deepest gratitude to my Thesis Directors and friends Dr. Albert Soler and Dr. Joan Jorge (ex-UPC, now retired) and my tutor and friend Dr. David Parcerisa (UPC) for his confidence, time and support during the duration of my thesis. In particular, I also want to thank immensely the help of Jorge Jódar, Dr. (IGME), a big friend who has given me many advice, ideas, tools, which has been vital and key to be able to carry out the articles presented in the thesis and with whom we have had numerous very interesting talks and scientific discussion meetings either face2face and virtually during the covid pandemic. This work would not be possible without all their support.

Also, I have to thank the rest of people that has been help me and contribute to my work like my boss Dr. Joan Palau (ICGC) to make me easy the work, my friends Joan Agustí Núñez, MSc. (ACA, ex-ICGC), Guillem Piris (Doctorate student, UAB), Rosa Maria Palau (doctorate student at UPC and now already a Doctor) and Carla Pérez (UB) for all the field-work support, and also specially Toni and Clara from the Refugi Bages of the Port del Comte for the logistics and where I stayed a lot of time during the different field campaigns; el Dr. J.L. Lambán (IGME), el Dr J.Martos-Rosillo (IGME), el Dr. E.Custodio (UPC) and the Dr. Iñaki Vadillo Dr. (UdM), and others. I am particularly grateful to the Team of the Hydrogeology and Geothermal Unit of the ICGC (Georgina Arnó / Montse Colomer and Víctor Camps) and the CCiT of the University of Barcelona (UB) for their technical assistance, and especially to Dr. Raul Carrey and Dr. Raúl Carrey of the MAiMA group of the University of Barcelona for the help in the laboratory analyses. We thank the Ebro Hydrographic Confederation (CHE) and the Catalan Agència de l'Aigua (ACA) for providing data and other background information.

Finally, it is time to thank and give a thousand thanks to my dear and beloved wife (and geological engineer) Mª Lluïsa Rodríguez Lázaro and my daughter Aina Herms Rodríguez, who have also helped me immensely to be able to carry out all the field work week after week, and therefore are the people who have suffered the most over the years with my doctorate. Without them, without doubt, I would not have been able to move forward. Also thank the rest of the family, my brother Josep Mª and especially my mother who gave me the studies to reach this final goal. I love you!

FUNDING

This research has been financed in part with my own resources and in part through the help of various projects managed by the University of Barcelona (UB), Universitat Politècnica de Catalunya (UPC) and Universitat de Málaga (UdM) as well as contributions of other organizations such as the Instituto Geológico y Minero de España (IGME) and the Institut Cartogràfic i Geològic de Catalunya (ICGC). The supervision and contributions in this research by the different co-authors of the papers presented, as well as all the laboratory costs for the geochemical and isotope analysis for all the samples (a total of 371 -water samples - 8 – rocks samples-) have been assumed through the projects of the Agencia Estatal de Investigación (AEI) of the Government of Spain and the European Regional Development Fund (ERDF) of the EU, REMEDIATION (CGL2014-57215-C4-1-R), and PACE-ISOTEC (CGL2017- 87216-C4-1-R), of the PIRAGUA project (EFA210 / 16 / PIRAGUA) co-financed by the European Regional Development Fund (ERDF) through the Interreg Program V Spain-France-Andorra (POCTEFA 2014-2020) of projects of the European Union, the aid of the Generalitat de Catalunya to support the consolidated research groups MAG (Mineralogia Aplicada, Geoquímica i Geomicrobiologia, 2017SGR-1733) of the University of Barcelona (UB) and GREM (Grup de Research on Sustainable Mining) of the University s Universitat Politècnica de Catalunya (UPC), the Ministry of Science, Innovation and through the project METhods for COpositional analysis of DAta (CODAMET) (Ref: RTI2018-095518-B-C22, 2019-2021), the research group of the Junta de Andalucía RNM-308 (Hydrogeology Group) and own resources of the ICGC. We thank to the Centres Científic i Tecnològics of Universitat de Barcelona CCiT-UB for the isotopic analysis. The access to the meteorological data used by the Spanish Meteorological Agency (AEMET) entailed a cost that was paid with my own resources, whereas the data used by the Meteorological Service of Catalonia (SMC) were provided free of charge. To carry out the four general field campaigns in October 2013, April 2014, October 2014 and April 2015, I had the support of geology students from the University of Barcelona, whose expenses were covered by the projects managed by the UPC and UB universities. The rest of the associated costs to carry out this research, i.e. including the personal logistics costs to carry out all the field campaigns for water sampling, periodic campaigns to monitor spring discharges and to monitor physical-chemical parameters, other visits of field required for the geological, hydrogeological reconnaissance of the study area (that is, the travel costs, stays and diets), as well as the cost associated to the implementation of the rain gauge network (design, implementation, monitoring and dismantling), part of the field material for measure and sampling and the tuition fees for the doctoral program long all years have been financed entirely from my own resources.

THESIS BREAKDOWN

The structure of the dissertation is the following:

Chapter 1. It includes the general introductory aspects of the thesis, the general framework and that of the case study, as well as the objectives and a review of the previous state of the art

Chapter 2. Field implementation for data collection and post-processing This chapter provides complementary information in relation to the implementation of field work, the acquisition of data, as well as the post-processing of the information necessary to address the thesis.

Chapter 3. It presents the post-print of published PAPER 1. "CONTRIBUTION OF ISOTOPIC RESEARCH TECHNIQUES TO CHARACTERIZE HIGH- MOUNTAIN-MEDITERRANEAN KARST AQUIFERS: THE PORT DEL COMTE (EASTERN PYRENEES) AQUIFER" (Herms et al, 2019), Science of Total Environment. Elsevier. (Q1, JRC)

Chapter 4. It presents the post-print of published PAPER 2. "EVALUATION OF NATURAL BACKGROUND LEVELS OF HIGH MOUNTAIN KARST AQUIFERS IN COMPLEX HYDROGEOLOGICAL SETTINGS. A GAUSSIAN MIXTURE MODEL APPROACH IN THE PORT DEL COMTE (SE, PYRENEES) CASE STUDY" (Herms et al, 2021), Science of Total Environment. Elsevier. (Q1, JRC)

Chapter 5. It presents the post-print of published PAPER 3. ISOTOPIC CONTENT IN HIGH MOUNTAIN KARST AQUIFERS AS A PROXY FOR CLIMATE CHANGE IMPACT IN MEDITERRANEAN ZONES: THE PORT DEL COMTE KARST AQUIFER (SE PYRENEES, CATALONIA, SPAIN) (Jodar et al, 2021), Science of Total Environment. Elsevier. (Q1, JRC)

Chapter 6. It presents the post-print of published PAPER 4. "IDENTIFICATION OF NATURAL AND ANTHROPOGENIC GEOCHEMICAL PROCESSES CONTROLLING GROUNDWATER QUALITY IN PORT DEL COMTE HIGH MOUNTAIN KARST AQUIFER (SE, PYRENEES)" (Herms et al, 2021b), WATER. MDPI. (Q2, JRC)

Chapter 7. It presents the summary of the contribution to the CHAlk and KArst Aquifer (CHAKA) Working Package 5 of the European project "Resources of groundwater harmonized at cross-border

and pan- European scale (RESOURCE)" focused on Typology of karst aquifers in Europe, and its application to the Cardener and Sant Quintí karstic springs, in the Port del Comte massif.

Chapter 8. It presents the General Discussion about the results achieved within the thesis frame and the main Conclusions reached within the framework of the thesis.

Chapter 9. Supplementary information published in the 4 scientific articles and in the other chapters is included

CONTENT

LIST OF FIGURES

Chapter 1

Chapter 2

Chapter 3. Paper 1.

Chapter 4. Paper 2.

Chapter 5. Paper 3.

Chapter 6. Paper 4.

Chapter 7

Chapter 8

LIST OF TABLES

Chapter 1.

Chapter 2.

Chapter 3. Paper 1.

Chapter 4. Paper 2.

Chapter 5. Paper 3.

Chapter 6. Paper 4.

Chapter 7.

1 GENERAL INTRODUCTION

1.1 Thematic unit of the thesis

1.1.1 Mountain karst aquifers

High mountain karst deposits are vulnerable and usually strategic systems for the population since they provide a large amount of water resources to ensure the supply for human activity (tap water, agriculture, industry, tourism), whereas at the same time many environmental ecosystems depends on the amount and quality of these resources (Kresic and Stevanović, 2010). An important aspect of the aquifers is that they act as regulating natural reservoirs. Thanks to this storage capacity, the water recharged in these aquifers upstream of the population areas, remains longer in the basin, thus providing a strategic water resource in periods of drought, which is especially important in the Mediterranean area, where more often the availability of water is a challenge. Karstified carbonate aquifers represent more than 15% of the earth's surface, and a very significant part is found in mountainous areas. Besides, approximately 20–25% of the world's population depends directly or indirectly on its resources (Goldscheider et al., 2020; Viviroli et al., 2020). These hydrogeological systems have particular characteristics that must consider. Usually, they are located in geological settings result of complex tectonic processes (e.g. faults, fold-and-thrust belts, wedge pinch out layers), which can often cause a strong compartmentalization and involving different lithologies (i.e. from carbonates to evaporites). This complex aquifer system determines the groundwater flow patterns, the storage capacity of reservoirs, and their hydrogeochemistry. Moreover, they are affected by more or less development of an internal complex network of karstic conduits that facilitates high rates of infiltration and groundwater flow patterns through the cavities and therefore with residence times that can short. These aspects make them much more vulnerable to pollution, but also to the effects of climate change, than other type of aquifers. Pollutants associated with human activity (for example, slurry) can more easily infiltrate and enter into the karst system and spread rapidly through the network of karstic conduits without any natural attenuation of the pollutant taking place, thus putting at risk the water resources of dependent populations and ecosystems. In addition, the progressive increase in temperature and the alteration of the rainfall regime can cause a decrease in recharge and consequently a loss of resource availability. Despite its fragility, in many parts of the world, and especially in developing countries with economic capabilities, even the most strategic high-mountain hydrogeological systems are neither monitored

nor sufficiently understood. In this sense, it is essential to allocate resources with the aim of launching new and oriented research work in order to understand the functioning of these mountain hydrological systems, especially in the Mediterranean area, where their water resources play an important role in the global management.

1.1.2 Hydrological modeling in karstified mountain aquifer systems

The characterization and hydrological modeling of mountain karst systems is a necessary step to understand how they work and thus be able to foresee management scenarios or be able to evaluate impacts related to climate change scenarios. An important aspect is the time series of outputs, i.e. spring discharges, relative to inputs, i.e. precipitation (in the form of rain and/or snow) (Lauber and Goldscheider, 2014). One of the key aspects of understanding and managing alpine groundwater systems and determining the vulnerability of springs is the magnitude of groundwater recharge and the mean transit time in the aquifer (Farlin and Maloszewski, 2013; Malard et al., 2016). The most common approach is the analysis of the discharge flow hydrographs of these systems combined with the use of tracers. This is useful to characterize the aquifer recharge and discharge processes, estimate the altitude of the recharge zone in the system and the transit times, determine the internal drainage model, and calculate the available and renewable water resources. However, obtaining flow data is not trivial, since many aquifers do not have gauging stations, and access can be difficult (Lauber et al., 2014). On the other hand, the use of artificial tracers in high mountain areas may be limited for several reasons: in little-known systems with great exokarst development, often there is no evidence on the surface of the functional systems, the flow path is not known a priori, and above all the thickness of the unsaturated zone can be very important with several hundreds of meters. In this sense, the use of natural tracers such as the stable isotopes of hydrogen and oxygen of water molecule ($\delta\ ^{18}O$ and $\delta\ ^{2}H$) in rainfall and in the water discharge, have proved to be good environmental tracers for investigating the dynamics of such hydrological systems karst systems. They are considered as ideal, not expensive at all, and technically easy solution to implement in the field. In any case, in pristine areas, it will be necessary to obtain a minimum of time series of discharge flows and water samples to determine the isotopic content.

Once this challenge has been overcome, it is desirable that the subsequent analysis go beyond the classical hydrological analysis through empirical and graphical methods used in karst hydrology,

and approach the modeling and numerical simulation of the system's operation, taking into account, among other aspects, the dynamics snow accumulation and melting as an important component of the hydrologic water cycle in mountainous areas, and when a decrease in the snow cover exposes longer the karst system to external pollutants or directly affect economic dependent activities such as sky or tourism in general. In this regard, fully distributed physically based models that normally are used in porous media, are often difficult to apply or directly impossible. On the contrary, the uses of lumped black-box and semi-distributed parameter models are very useful to simulate the behaviour of such complex mountain karst systems, even though they can be poorly characterized as do not require a detailed hydrological knowledge of the physical system. Once calibrated, these models can be used to evaluate multiple climate change scenarios and consequently analyse the hydrological results obtained in order to establish management and preservation measures.

1.1.3 Hydrogeochemistry of karst systems and pollution

The knowledge but also the understanding of the processes that controls the chemistry of the water is important for the management of karstic aquifers in the mountains. The EU Water Framework Directive (EC, 2000) defines the rules for the identification of the different groundwater bodies (GWB), and the criteria for the evaluation of their chemical status by defining the threshold values of pollutants (TV) and the natural background levels (NBL). These provide information on the concentration of a certain element, species or chemical substance present in solution that is derived from natural processes from geological, chemical, biological and atmospheric sources, and therefore are key to quantitatively assess whether groundwater is affected or significantly modified by anthropogenic influences. Nevertheless, in geologically complex environments, such as those that usually affect mountain karstic aquifers, its determination is neither straightforward nor trivial though it may seem so at first. For this reason, the use of multivariate statistical techniques for the analysis of geochemical data is highly recommended in order to identify the processes that take place (Puig et al., 2011) and group and/or separate types of water before addressing the NBL calculation to reach reasoned and plausible conclusions. However, geochemical data are 'compositional' in nature and this means that the concentration of an element is actually expressing a part of a whole, regardless of the dimensions in which the concentration of the component is expressed as for example, mg/L. Consequently, the information provided by the concentration of a solute is actually relative, because it implies that it does not vary independently if other

concentrations of other solutes also do, because the sum of all gives the total. Therefore, the raw geochemical data is not well represented by the usual Euclidean mathematical real structure, as mathematical and statisticians' researchers have demonstrated years ago (Aitchison, 1986, Egozcue et al., 2003, Pawlowsky-Glahn et al., 2015). This can lead to incorrect conclusions if multivariate statistics are used directly for geochemical analysis if the proper transformations are not performed first. In this sense, for years there has been a joint line of research between geochemists and statisticians that aims to apply transformation procedures based on log-ratios and implement them in common computer tools to express compositional raw data sets in real space, and thus make them suitable for use in multivariate statistics.

1.1.4 Climate change challenge in the management of karst aquifers

Mountain karst aquifers are vulnerable to climate change (Hoerling et al., 2012; Chen et al., 2018; Mas-Pla, 2010). The increasing warming trends impacts directly in the snowpack cover formation, the corresponding snowmelt infiltration and hence aquifer recharge. Therefore, after addressing the geological, hydrological and hydrogeochemical characterization of high mountain karst aquifers, it is essential to understand their response to climate change from a water resources perspective. This is even more relevant, especially in the Mediterranean area, where water scarcity is becoming an increasingly recurring problem (Vicente-Serrano et al., 2014). This information will be crucial to design the most appropriate adaptation measures to minimize adverse effects. The climate change projections in the whole Mediterranean region forecast an increase in temperature and a decrease in precipitation at the end of the 21st century, in line with the global diagnosis produced by the Intergovernmental Panel on Climate Change (IPCC). These scenarios may impact Mediterranean high mountain areas, consequently modifying their hydrological regime. Actually, there is already evidence of such changes in the Pyrenees if we look at the evolution of the glaciers in the last decades (OPCC1, 2013; OPCC-CTP, 2018). The Pyrenean glaciers have suffered an intense retreat since the middle of the last century, foreseeing a disappearance in the short term. Apart from the progressive increase in temperature, the average annual precipitation and the number of rainy days show a decreasing trend, which directly affects the area covered and its maintenance during the winter. These effects directly impact the water storage capacity, as well as its associated hydrological response in terms of river discharge flows and the timing of maximum discharges. These changes will have a direct impact on downstream areas by complicating the current situation

of water stress in the Mediterranean area. For all these reasons, it is important to carry out the necessary studies to evaluate the hydrological impacts and anticipate, as far as possible, the effects and thus achieve the most resilient management possible.

1.1.5 The pillars for characterizing and evaluating high-mountain karst aquifers

In summary, karst aquifer and karst springs represents an enormous and very vulnerable natural important resource that sustains the flow of many surface streams and ecosystems and are used to cover water supply needs of hundreds of millions of people in the world. Therefore, the study of the karst is essential to estimate, plan and manage hydraulic resources in an adequate and sustainable manner. In this regard, it is advisable to adopt a multidisciplinary approach to study karst mountain massifs, in the sense of, for example, supporting the analysis of hydrochemical data through other tools such as 3D geological modeling to understand the origin of water, or the isotopes to determine their recharge altitudes, or hydrological modeling to determine transit times to give several examples.

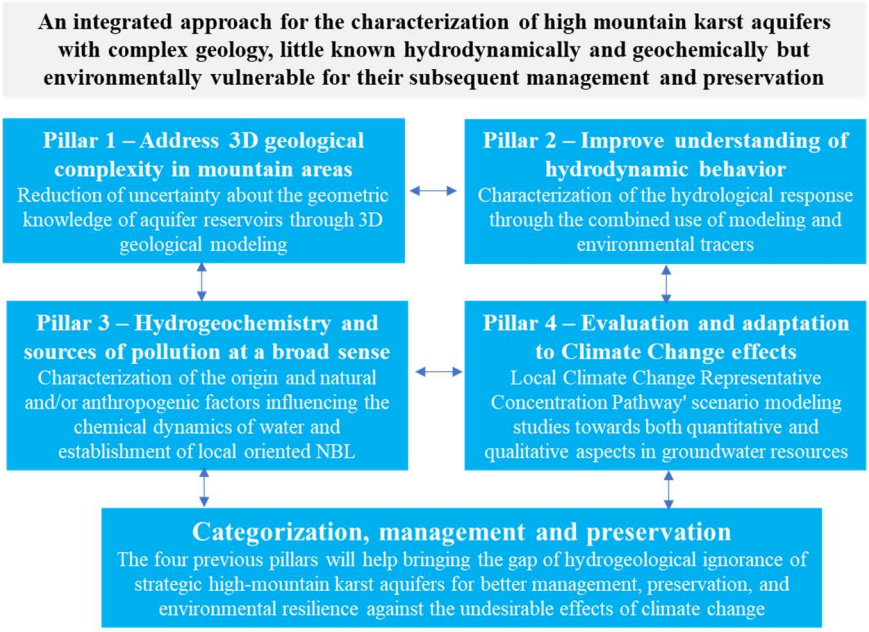

Figure 1. 1 The four pillar-oriented integrated approach to address poor hydrogeological knowledge of strategic high mountain karst aquifers in the context of climate change challenges.

In summary, there is a need to use an approach based on four pillars (**Figure 1. 1**): the first pillar is aimed at addressing the geological complexity of these systems; the second and third to address the lack of hydrological and hydrogeochemical characterization, and the fourth to assess the effects of climate change on these systems. In the end, all of this must allow the ability to categorize the available systems, based on the use of topological classification methods dependent on the availability of resources and the vulnerability of the hydrogeological systems, in order to implement the pertinent management and adaptation measures

1.1.6 Groundwater karst aquifers in Catalonia

A significant part of the territory of Catalonia is covered by karstic aquifers, most of them very important from the point of view of available resources and dependent ecosystems. The **Figure 1. 2** shows a modified version (from ICGC, 2017) of the 'Map of the Nature of the Aquifers based on lithology at a scale of 1:250,000'. This map presents a summary of the hydrogeological macro-units into which the territory of Catalonia can be divided, and includes the classification of the geological units on the Geological Map of Catalonia 1:250,000 into hydrogeological formations, taking into account the nature of their lithological features classified into 8 different types: A1, A2, B1, B2, C1, C2, D1 and D2.

Class B2 corresponds exclusively to consolidated carbonate aquifers with porosity due to fracturing and/or karstification from any geological period (Triassic, Jurassic, Cretaceous and Tertiary), and its entire extension is considered as potentially karstifiable terrain. The Tertiary limestones of the Port del Comte structural unit, which is the main focus of this thesis, are included in this class. On the other hand, class B1 corresponds mainly to conglomerate and sandstones aquifers that may contain potentially karstifiable carbonate clasts while class C1 corresponds to detrital deposits normally of low permeability that locally can also contain karstifiable conglomerates. The entire area occupied by class B2 and the areas of classes C1 and B2 identified with karstifiable potential constitutes the Map of 'Potentially Karstifiable Areas' (ICGC, 2017) also shown in the upper-right corner in the **Figure 1. 2.** These areas cover a total area of 21% of the whole territory of Catalonia, mostly located in the Pyrenees, Pre-Pyrenees, and in the Catalan Coastal Ranges.

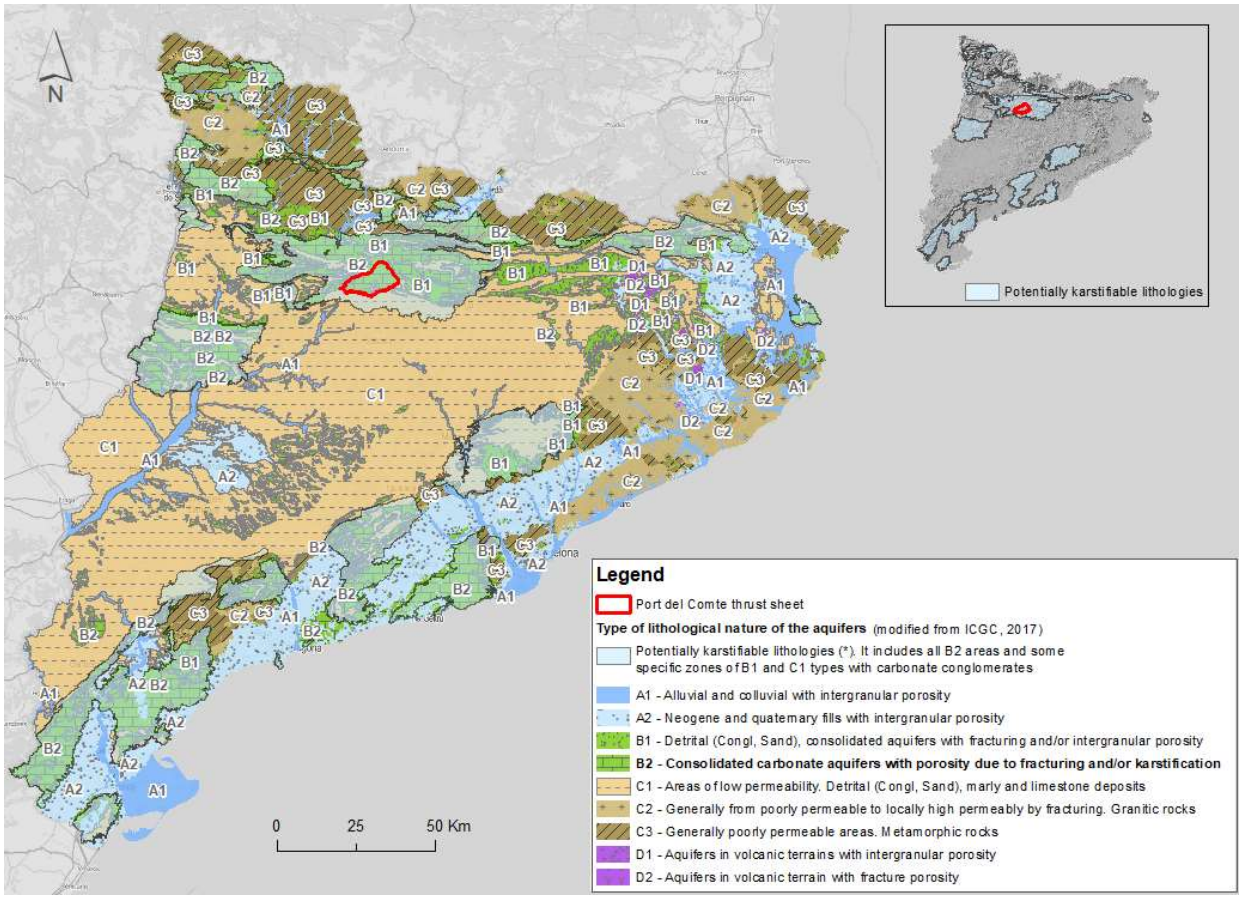

Figure 1. 2 Map of the nature of the aquifers based on the lithology at a scale of 1:250,000 (modified from ICGC, 2017). The situation of the Port del Comte thrust sheet is in the south-eastern part of the Pyrenees

Groundwater from karst aquifers represent a very important and major drinking water resource in Catalonia. In the past, many technical articles have been written related to karstic aquifers, a large part of them, especially located in populated coastal areas of Catalonia such as the Garraf massif (Custodio, et al, 1990, among many others), or for particular karstic Systems such as Banyoles at Girona Province (NE, Catalonia) (Sanz-Perera, 1981; Brusi, et al, 1997, among others) or on the associated karstic systems in conglomeratic alluvial fans of Sant Llorenç del Munt and Montserrat, at central-east of Catalonia (Freixes, 1986; and more recently Anglès, 2013). Without aiming to go into more detail, because the list would be very large, it should be noted that much less research has been done explicitly related to karst aquifers in mountain areas (although they do not come precisely from the Pyrenees or the Pre- Pyrenees). Beyond the work of the IGME (1985) and its antecedents, the few works carried out in the past were done mainly between the 80s and 90s (Pascual, et al, 1996, Ramoneda, et al, 1999; among others).

From an academic point of view, it is worth highlighting the extremely important work carried out by Freixes (2014) and all his previous work published in many papers related to his doctoral thesis on the karstic aquifers of the Pyrenees in Catalonia (Freixes, et al, 196, among many others). His thesis focuses on the study of the functioning of the hydrogeological system of the most important karstic springs located in the Arán Valley ('Uelhs deth Joeu', 'Fonts de Lastoar'; 'Fonts de Tèrme i Pila'; 'Fonts d'Aigüèira') that drain aquifers in carbonate rocks, especially limestone from the Devonian (and Lower Carboniferous), the Cambro-Ordovician, but also the Upper Ordovician, the Silurian-Devonian and the granites of the Maladeta and Marimanha batholiths; and on the other hand, the 'Alt Llobregat and Alt Segre' area in the Cadí mountains (Fuentes de Bastareny'; 'Fuentes del Llobregat'; 'Fou del Bor') which mainly drain limestone from upper Devonian and lower Carbonifer for the first two, and the Eocene limestones of the Cadi range mountain in the last.

Beyond the reference work carried out by Freixes (2014), there are still many karstic mountain aquifers located further east or south of the Pre-Pyrenees, such as Port del Comte unit, among many others, which have not been addressed in an intensive or particular way from a hydrogeological point of view.

1.2 A case study: The Port del Comte high mountain aquifer system

The study area is located at the Port del Comte Massif (PCM), which is situated in the eastern part of the Pyrenees, NE Spain (Figure 1) between the regions of Solsonès, and Alt Urgell (Lleida), in the southern part of the Eastern Catalan Pyrenees. The elevation of the watershed ranges from approximately 900 m a.s.l., up to 2387 m a.s.l., at the 'Pedró dels Quatre Batlles' peak. With approximately 110 km^2, it contains one of the main mountain karst aquifers of the Catalan Pyrenees. The watershed of the massif divides the river basin of the Cardener River at the E and S and the river basin of the Segre River at the NW and SW. The massif constitutes an independent structural and hydrogeological unit.

1.2.1 Geological setting

1.2.1.1 Regional geological context

The sector represented in the Port del Comte mantle includes the southern limit of the overlying plates of the eastern Pyrenees and its folded foreland (**Figure 1. 3**) (Berastegui, X et al., 2001). Paleogene-aged (Eocene and Oligocene) foreland basins predominate in this area. These materials make up all the outcrops of the deformed foreland and occupy a considerable extent of the non-native units.

The formation of the Pyrenees took place during the Pyrenean orogeny, the result of the subduction of the Iberian plate under the European plate. The South-Eastern Pyrenees is represented, in this area, by the structural unit of the Port del Comte, which is linked to the Cadí unit (**Figure 1. 3**). This constitutes the relative with respect to the South Pyrenees Central Unit (SPCU), formed by the overlapping thrusts of Bóixols, Montsec and Serres Marginals, displaced to the south (located to the west of the study area), and with respect to the unit of the Pedraforca (located to the east and directly related to the SPCU in paleogeographic sense).

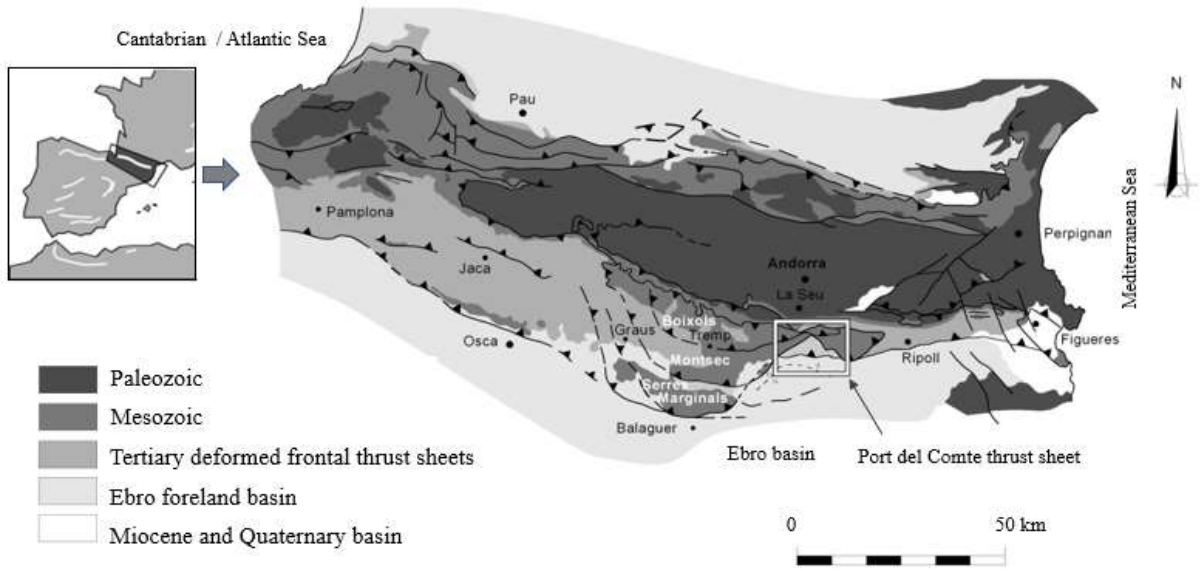

Figure 1. 3 Geological sketch of the Pyrenees (version modified from Magna 291 - Oliana, which was originally modified from Puigdefàbregas and Souquet, 1986). The situation of the Port del Comte mantle is indicated in the south-eastern part of the Pyrenees.

The most representative series of the structural unit of the Port del Comte consists mainly of Paleogene materials and, to a lesser extent, Mesozoic materials, restricted to the Middle and Upper Triassic and Upper Cretaceous.

1.2.1.2 Geological structure

The Pyrenees mountain range originated from the collision of the Iberian and European plates during the Alpine orogeny. They have a general direction E-W and a surface length of 425 km. They are limited to the north by the Aquitaine basin and to the south by the Ebro basin. These are separated, from west to east, into three large geological regions: Western Pyrenees (from the Cantabrian Sea to the Pamplona fault), Central Pyrenees (from the Pamplona fault to the Segre structure) and Eastern Pyrenees (from the structure of the Segre to the Mediterranean Sea). The general structure of the Pyrenees is formed by a complex system of thrusts.

The structure of the Pyrenees was considered by several authors at the beginning of the 20th century to be totally autochthonous, with folds, normal faults and minor thrusts (Ashauer, 1943; Fontboté, 1962). Starting in the 1970s, the work carried out of other authors (Séguret, 1972; Garrido-Megías, 1973; Choukroune, 1976) revealed the existence of a greater number of allochthonous units in the central and eastern Pyrenees, such as the mantles of Pedraforca and Montsec in Catalonia. In the other hand, the data acquired by the geophysical exploration campaigns did by oil companies and the ECORS deep seismic profile (Choukroune P, 1989; Daignières et al, 1994), showed the allochthonous nature of the structures of the Pyrenees (Muñoz 1992; Vergés, 1993., Berastegui, et al. 1993). The division between the Eastern and Central Pyrenees is determined by the Segre structure. On both sides of this structure there are three large units with similar series and locations: i) the upper mantle of Pedraforca, equivalent to the Bóixols mantle; ii) the lower mantle of Pedraforca, equivalent to the mantle of Montsec and Serres Marginals; and iii) the mantle of the Cadí (**Figure 1. 4**).

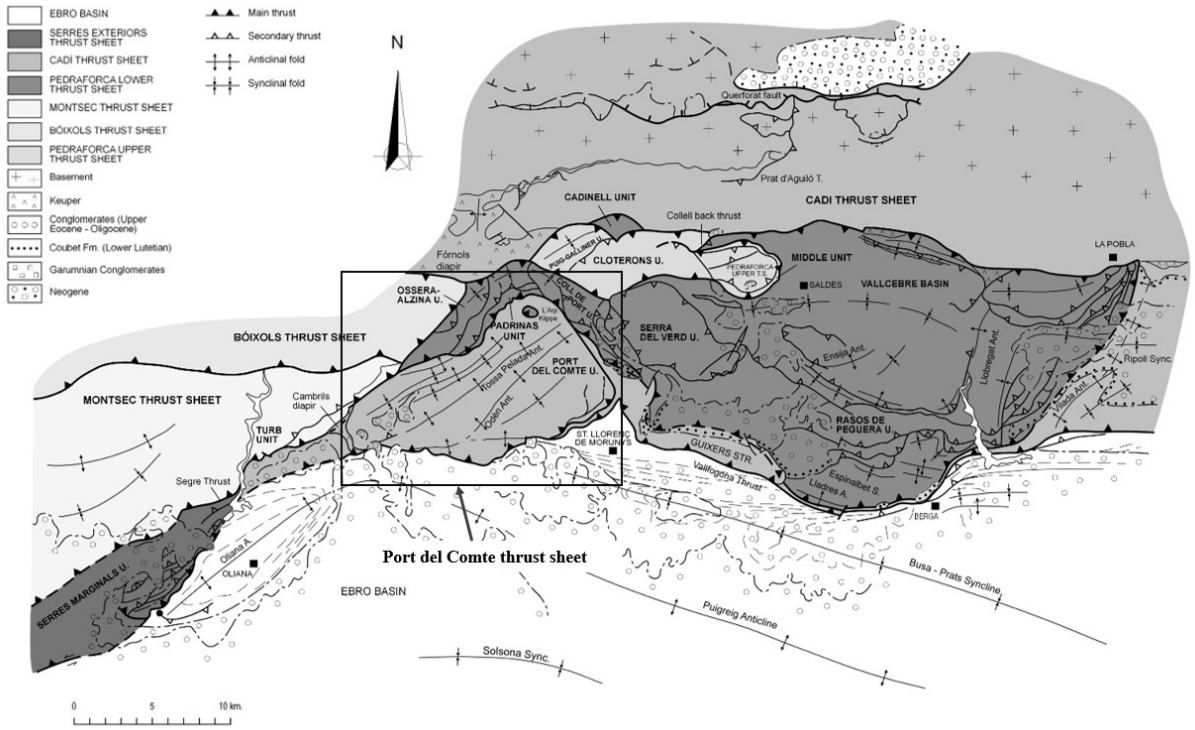

Figure 1. 4 Geological map of the main structural units (version modified from Magna 291 - Oliana, Berastegui, et al 2001). The situation of the Port del Comte mantle is indicated.

As far as the Port del Comte thrust, cartographically it has a triangular shape and is limited, to the east, by the Cardener fault; to the west, it is overlain by units from the Boixols and Montsec thrusts; and to the south limits with the Foreland Ebro basin. The internal structure is formed by a series of folds in a general NE-SW direction with the Keuper acting as basal detachment level (Vergés, 1993), which crops out in the Odèn area (SW of the Port del Comte sheet). In the western area there is a NW-SE fault where Keuper crops out cutting the surrounding structures, interpreted as the Cambrils diapir (see **Figure 1. 4**).

1.2.1.3 General stratigraphy and local geological units.

The materials that outcrop in the study area **Table 1. 1** belong to the Triassic, Jurassic, Cretaceous, Paleogene and Quaternary. In the 1:50,000 geological map (ICGC, 2007), the following geological units are differentiated:

Table 1. 1 Geological units presented in the regional domain of the Port del Comte unit.

Epigraph	Description	Series/Epoch	System/Period
Tm	Limestones and dolomites with intercalations of marls. Muschelkalk facies.	Middle-Upper Triassic	TRIASSIC
Tk	Marls and marly limestones, shale and gypsum. Facies Keuper.	Upper Triassic	
TJb	Breccias and marls.	Upper Triassic Lower Jurassic	TRIASSIC-JURASSIC
TJcd	Limestones and dolomites.	Upper Triassic. – Middle Jurassic	
JLcb	Bioclastic limestones, limestones with algal laminations and oolitic limestones.	Lias / Lower Jurassic	JURASSIC
JLmc	Ocher marls and limestones.		
JLcd	Tabular limestones and laminated dolomites.		
JLcm	Marls with Gripheas, limestones with oolites and dolomitic limestones.		
JDd	Massive brown and gray dolomites and limestones.	Dogger / Middle Jurassic	
CIcc	Massive micritic limestones and / or limestones with carophytes. Prada Formation.	Lower Cretaceous	CRETACEOUS
CIcr	Reef limestones with corals, rudists and orbitolines. Senyús Formation.		
CImmc	Marls and limestones with ammonites and echinoderms. Lluçà Formation.		
CNb	Carbonate breccia		
CKml	Limestone and lignite.	Lower-upper Cretaceous	
Cb	Red lateritic clays with bauxite, sand and gravel.		
KCMma	Blue-gray marls, marly clays and limestones.	Upper Cretaceous	
KCTp	Limestones with prealveolins. Santa Fe Formation.		
KMga	Sandstones. Areny Formation		
KSCc	Nodular limestones and marly limestones. Terradets Formation		
KScm	Limestones and marls with lacazine.		
KScm1	Detrital organic limestones, marls and sandstones. Cava i Bagasses Formation.		
KSCmv	Gray marls. Vallcarga sequence.		
KSCat	Conglomerates, sandstones, limestones and marly limestones. Adraén Formation.		

Epigraph	Description	Series/Epoch	System/Period
KCMca	Bioclastic limestones, calcarenites, sandstones and bioconstructions. Good Formation.		
KMgp	Limestones, shales and marl limestones, traditionally named "Garumnian Facies" also called "Garumnian Red Beds of the Pre-Pyrenees". It corresponds to the most extensive non-marine facies of the latest Cretaceous deposits of the Pyrenees. It represents the first continentalization of the Pyrenean Foreland Basins.		
PPcm1	Micritic limestone. Vallcebre limestones.	Lower Paleocene	PALEOGEN
PPcm	Micritic limestones and red clays.		
PPEc	Limestones with alveolins and dolomites. Cadí Formation.	Paleocene-Lower Eocene	
PEci	Gray marls, sandstones and micritic limestones. Coronas Formation		
PEcp1	Micritic limestones. Lower Penya Formation.	Lower Eocene	
PEcp2	Limestones with macroforaminifers. Upper Penya Formation.	Middle Eocene	
PEgmf	Alternation of sandstones and marls with conglomerates. Vallfogona Formation.		
PEccv	Limestones with milliolides.		
PEcgc2	Bioclastic sandstones. Coubet Formation		
Tm	Limestones and dolomites with intercalations of marls. Muschelkalk facies.	Middle-Upper Triassic	TRIASSIC
Tk	Marls and marly limestones, shale and gypsum. Facies Keuper.	Upper Triassic	
TJb	Breccias and marls.	Upper Triassic Lower Jurassic	TRIASSIC-JURASSIC
TJcd	Limestones and dolomites.	Upper Triassic. – Middle Jurassic	
JLcb	Bioclastic limestones, limestones with algal laminations and oolitic limestones.	Lias / Lower Jurassic	JURASSIC
JLmc	Ocher marls and limestones.		
JLcd	Tabular limestones and laminated dolomites.		
JLcm	Marls with Gripheas, limestones with oolites and dolomitic limestones.		
JDd	Massive brown and gray dolomites and limestones.	Dogger / Middle Jurassic	
CIcc	Massive micritic limestones and / or limestones with carophytes. Prada Formation.	Lower Cretaceous	CRETACEOUS
CIcr	Reef limestones with corals, rudists and orbitolines. Senyús Formation.		

Epigraph	Description	Series/Epoch	System/Period
CImmc	Marls and limestones with ammonites and echinoderms. Lluçà Formation.		
CNb	Carbonate breccia		
CKml	Limestone, limestone and lignite.	Lower-upper Cretaceous	
Cb	Red lateritic clays with bauxite, sand and gravel.		
KCMma	Blue-gray marls, marly clays and limestones.	Upper Cretaceous	
KCTp	Limestones with prealveolins. Santa Fe Formation.		
KMga	Sandstones. Areny Formation		
KSCc	Nodular limestones and marly limestones. Terradets Formation		
KScm	Limestones and marls with lacazine.		
KScm1	Detrital organic limestones, marls and sandstones. Cava i Bagasses Formation.		
KSCmv	Gray marls. Vallcarga sequence.		
KSCat	Conglomerates, sandstones, limestones and marly limestones. Adraén Formation.		
KCMca	Bioclastic limestones, calcarenites, sandstones and bioconstructions. Good Formation.		
KMgp	Limestones, shales and marl limestones. Garumnian Facies.		
PPcm1	Micritic limestone. Vallcebre limestones.	Lower Paleocene	PALEOGEN
PPcm	Micritic limestones and red clays.		
PPEc	Fissured/karstified alveoline limestones and dolostones. Cadí Formation. It has a thickness of up to 1,000 m and from the hydrogeological point of view, it is the most important unit in the study area. It constitutes the main karstic aquifer in the Port del Comte area.	Paleocene-Lower Eocene	
PEci	Gray marls, sandstones and micritic limestones. Coronas Formation		
PEcp1	Micritic limestones. Lower Penya Formation.	Lower Eocene	
PEcp2	Limestones with macroforaminifers. Upper Penya Formation.	Middle Eocene	
PEgmf	Alternation of sandstones and marls with conglomerates. Vallfogona Formation.		
PEccv	Limestones with milliolides.		
PEcgc2	Bioclastic sandstones. Coubet Formation		
PEcgb6	Conglomerates, sandstones and shales.	Middle Eocene	PALEOGEN
PEcgb7	Lutites and conglomerate sandstones.		
PEcgm1	Red sandstones and shales. Puigsacalm Formation.		
PEm1	Gray sandstones, marls and shales. Vic Marls Formation		
PEm2	Limestones.		

Epigraph	Description	Series/Epoch	System/Period
PEm	Fossil blue marls with red limolites. Igualada Marls Formation.		
PEc	Biomicritic limestones and gray marls.		
PEalb	Sandstone and silt. Margues de Vespella Formation.		
PEOcmg	Conglomerates.	Eocene-Oligocene	
PEOcc	Conglomerates.		
PEcgs	Massive conglomerates, sandstones and red shales.	Eocene-Oligocene	
PEOgs	Red shales, sandstones and conglomerates.		
PEOcgs	Conglomerates and breccias.		
PExb	White laminated gypsum and marl. Beuda gypsum Formation.	Eocene undifferentiated	
PEmb	Bluish gray marls and shales and PEmb1: nodular limestones with nummulites and bivalves. Banyoles Marls Formation.		
PEcgb	Sandstones and conglomerates.		
POgac	Sandstones, clays and some conglomerate channels.	Lower Oligocene	
PORb	Breccia		
PObm	Monomictic breccia		
POcp	Polymictic conglomerates.		
POCc	Conglomerates with granitic pebbles and sandy matrix.	Upper Oligocene	
POmlg	Red lutites with sandstone and conglomerate paleochannels.	Undifferentiated Oligocene	
POb	Gaps, conglomerates, sandstones and shales.		
POgs	Sandstones, red shales and conglomerates.		
POcgs	Polymictic conglomerates.		
Nd	Conglomerates, sandstones and shales.	Pliocene / Miocene	NEOGENE
Q	Undifferentiated Quaternary	Holocene/ Pleistocene	QUATERNARY

The previous geological mapping available (ICGC, 2007) has been revised and slightly modified based on certain field observations (see section 2.1). The final result of this review is expressed in the following geological map (**Figure 1. 5**) which is the one used in the thesis.

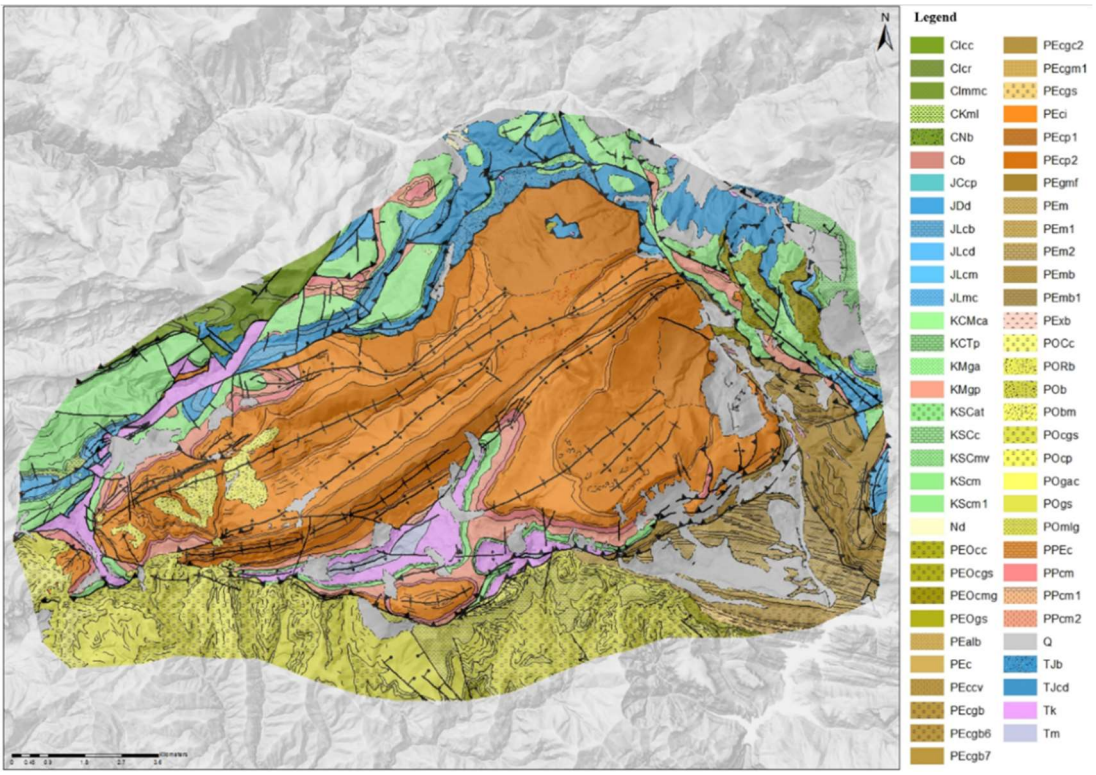

Figure 1. 5 Modified – restyled - geological map at 1:50.000 scale (modified from ICGC, 2007).

1.2.2 Hydrogeological setting

The Port del Comte is an independent morpho-structural and hydrological unit. The whole domain covers approximately 106 km^2, from which, according to IGME (1985) 86 km^2 corresponds to permeable formations (which this corresponds the limestones formations outcropping). The Map of hydrogeological areas of Catalonia MAH250M (ICGC 2017) at scale 1:250.000 include a layer classifying the geological units 1:250.000 as 'hydrogeological formation'. **Figure 1. 6** shows this map in the area of the Port del Comte. Most of the area is covered by karstifiable lithologies, such as limestones and dolomites, conglomerates with carbonate clasts or rocks with evaporites.

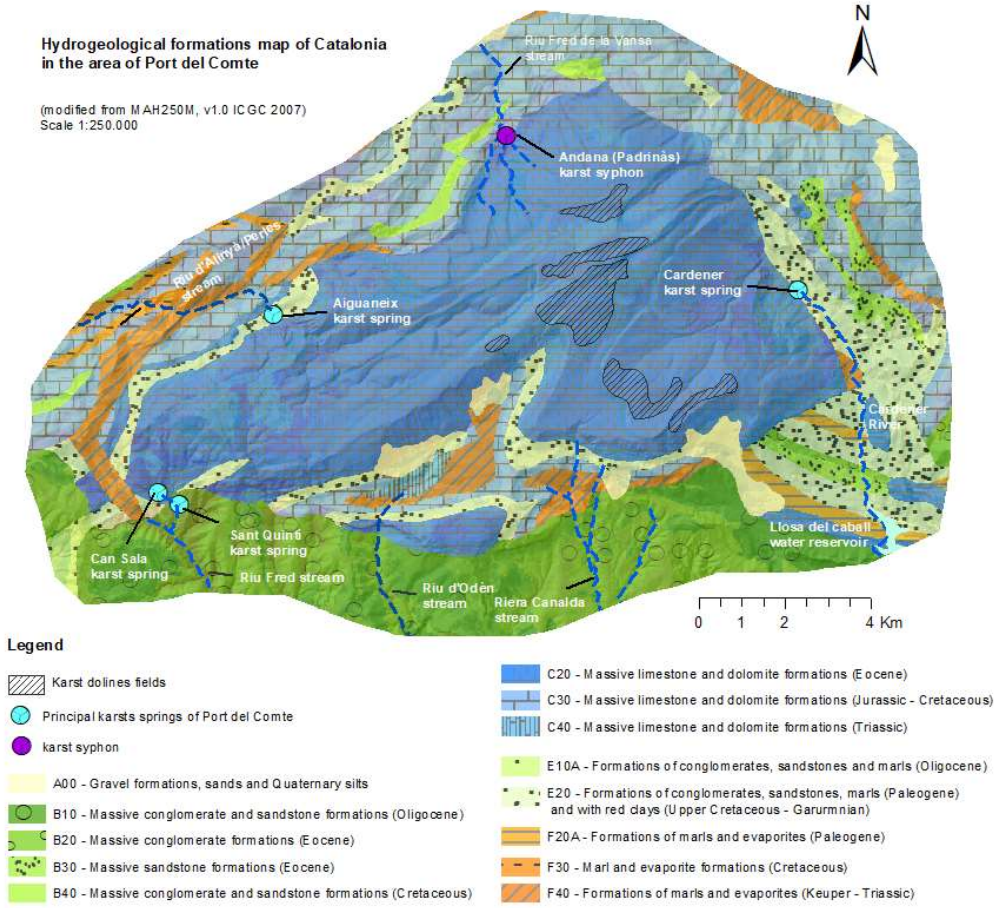

Figure 1. 6 Hydrogeological formations map at scale 1:250.000 in the area of Port Comte (modified version of ICGC, 2017)

The 'C20 hydrogeological formation' corresponds to the domain of the well-known Eocene karst aquifer. The recharge of the Port del Comte massif takes place essentially in a diffuse way in all its outcrop and in a concentrated way through the karst elements, and directly both by the rain and by the melting of the snow. The discharge of the system is made essentially in natural regime through karst sources: towards the East through the spring of the CARDENER (146 L / s; measured in the summer of 2013) towards the Cardener river, affluent of the Llobregat river ; to the SW through the spring of SANT QUINTÍ (153 L/s) and that of CAN SALA (also known as 'El Racó') (23 L/s) to the basin of the Cold River tributary of the Ribera Salada and then from the Segre basin; to the NE through the AIGUANEIX spring (48 L/s) towards the Alinyà - Perles river basin, also a tributary of the Segre basin, and finally with a diffuse drainage to the north of the Port del Comte

massif towards the Fred la Vansa river basin, also a tributary of the Segre river (30 L/s, summer 2013).

The “E20 hydrogeological formation” includes sediments of the upper Cretaceous-lower Paleogene (Cretaceous-Tertiary boundary, according to Rosell (2001) associated to red interbedded clays, and sandstone conglomerates, and occasionally limestone (known locally as Garumnian facies or “Garumnian Red Beds”). Its upper limit acts as the lower limit for the karst aquifer of the Eocene above, and it itself acts as an aquitard. Below, the C30 and C40 Cretaceous and Triassic carbonate formations, and the Keuper F40 facies form a low-permeability aquifer system that is locally recharged by its outcrops and discharged through multiple small springs with low flow discharges, from 5 L/s to 0.001 L/s or some of them directly dry.

Only two water supply wells in operation have been identified in the Port del Comte area within the limits. Both exploit the limestones of the PPEc unit (C20 hydrogeological formation), but the volume discharged it is very limited compared with the total groundwater discharge of the system.

On the other hand, karstic aquifers usually present high to very high levels of vulnerability to contamination due to the ease of infiltration and transport of potential contaminants through the system. The vulnerability mapping of Catalonia was elaborated by Arnó et al. (2020, ICGC), used the DRASTIC method (Aller, 1987) for non-karstified areas and the COP method (Zwalhen, 2003; Vias et al., 2006), for carbonate karstified aquifers. This last is a method developed in the frame of COST 620, “Vulnerability and Risk Mapping for the Protection of Carbonate (Karst) Aquifers” supported by the European Commission, a European Approach for groundwater vulnerability mapping. The results obtained in the area of the Port del Comte massif (**Figure 1. 7**) suggest that 55.8% of the area presents high vulnerability (orange class), 18% moderate vulnerability (yellow class), 14.7% low vulnerability (green), 7.1% high vulnerability (red class) and 4.4% very low vulnerability (green dark class). Therefore, the results confirm that the massif is now dominated by the class of vulnerability, as in fact was expected for an environment where many superficial karst forms, also called exokarst, predominate.

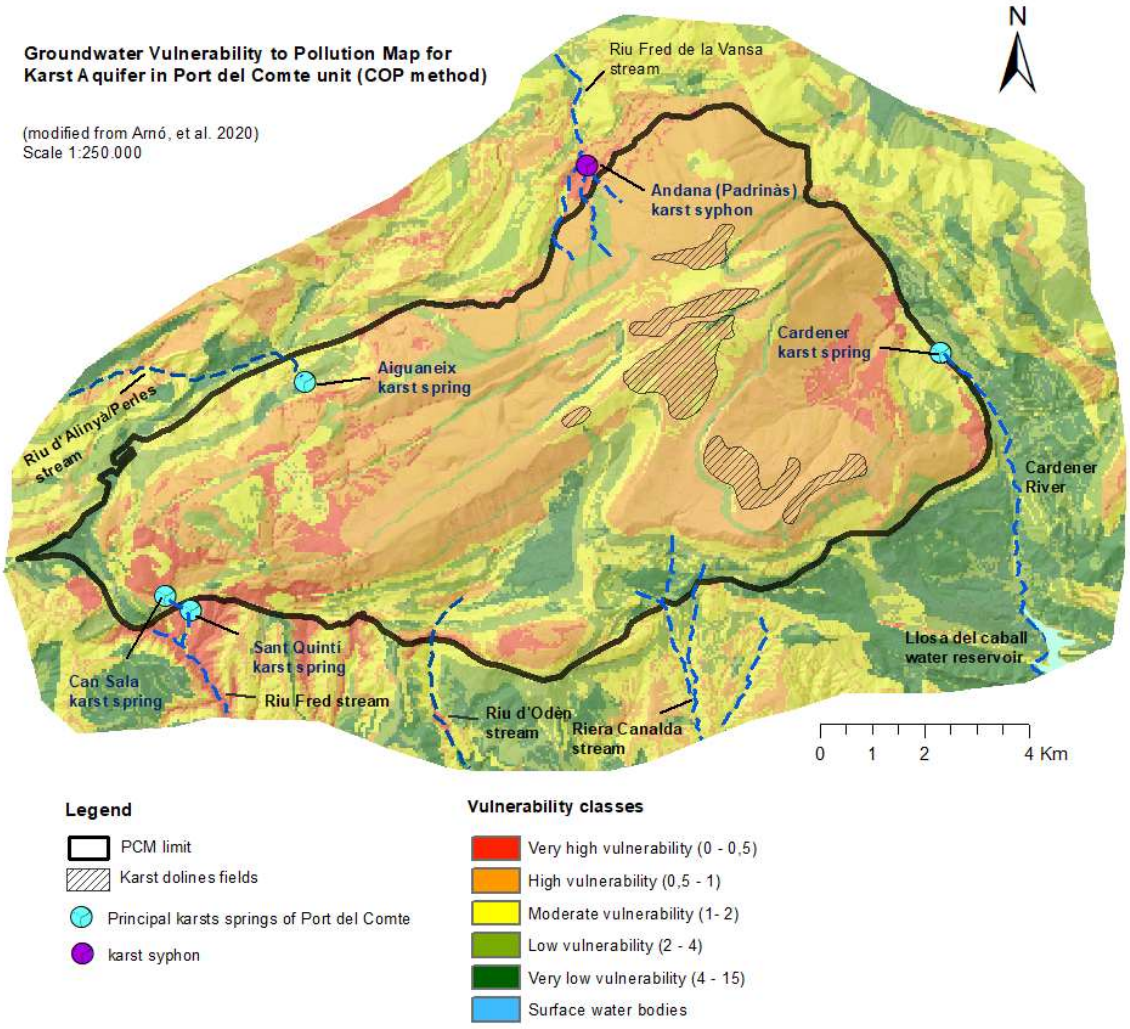

Figure 1. 7. Groundwater vulnerability to pollution map (COP method) in the area of Port del Comte. (modified version from Arnó, et al. 2020, ICGC)

1.2.3 The karst features and karst springs

The Port del Comte massif is a carbonate massif that is characterized by being one of the important karst aquifers in the Catalan Pre-Pyrenees. The karst is formed from the dissolution of soluble rocks such as limestone and dolomite, but it also affects geological units with gypsum content. Despite the high rainfall, greater than the 1000 mm annual average of the meteorological stations (see chapter 1.2.4) most of the extension of the massif is an area where surface runoff is almost nil. Precipitation water quickly infiltrates the karstified rocky outcrops to finally spring up in the lower

part of the massif mainly through a few karst springs, as is the case of the CARDENER SPRING in La Coma and La Pedra town, the SANT QUINTÍ SPRING near Cambrils town; and to a lesser extent the CAN SALA SPRING also near Cambrils town and the AIGUANEIX SPRING in the Alinyà valley on the northwest boundary of the massif. Karst features are normally classified into exokarst, epikarst and endokarst. The epikarst is defined as the uppermost zone of exposed karst rock in which permeability due to the fissuring and karstification is higher (Goldschneider and Drew, 2007).

In the Port del Comte massif, the karstic features are common throughout the massif (**Figure 1. 8**).

Figure 1. 8 Examples of the karst landforms, in the Port del Comte massif. (Upper) Dolines fields in the Serra Querol and Serra Port del Comte / (Bottom left) karren fields / (Bottom right) the "Gran Bòfia feature" cave, in the "Serrat de la Bòfia" – Sub-unit Bòfia - in the southern block of the mantle.

In the area there are at least three fields of sinkholes:

- The first is located to the south in the Serra de Querol – Serra de la Bòfia, in the 'Pla de Bacies' or 'Pla de les Bòfias', with numerous depressions in the form of sinkholes and with the cavity of the "Gran Bòfia" as the most characteristic and representative feature in the Port del Comte, but also karren fields and lot of points that act as water sinks when precipitation occurs and small caves. In this area dolines are surrounded either by karren fields or meadows.

- The second field of sinkholes, located in the upper part of the massif, in the "Serra del Port del Comte" in the area surrounding the top "Padró dels Quatre Batlles" 2.386 m. a.s.l., Tossa Pelada, (2,373 m a.s.l.), Tossa de la Comtessa (2,342 m a.s.l.) and Estivella (2,331 m a.s.l.). In this soil is poorly developed or non-exists and karren fields appear. In this area dolines are also surrounded either by karren fields or meadows.

- The last sinkhole field is in the "PratLlong" sector on the north side of the massif. In this part the dolines are surrounded mainly by meadows.

The karst development mainly affects the Eocene Tertiary units, i.e., the fissured/karstified alveoline limestones and dolostone PPEc unit (the Cadi Formation), which constitutes the main karstic aquifer in the Port del Comte area, and the limestone units PEcp1 and PEcp2 which are situated stratigraphically above the PPEc unit and which in this case act as the unsaturated part of the main karst system of Port del Comte.

The other geological units described in the geological map and that also contain soluble lithologies, also suffer, to a greater or lesser degree, karstification, such as the Oligocene conglomerates that present carbonate clasts: For example, the San Quintí spring discharges in its final part through a karst conduit developed in the conglomerates of the POcgs Unit. Another example of karstification of the conglomerates is the well-known Montserrat Ubach chasm (avenc de Monserrat Ubach) located in the Canalda town, explored for the first time in 1963, and one of the deepest that have been inventoried in Catalonia with 202 meters of vertical drop catalogued and since 2004 with the distinction "Space of Geological Interest of Catalonia", it is still one of the most important caves

developed in conglomerates in the world (Lloret and Ubach, 2017). This also affect the units POcgs and the underling POgs and is located 750m in a straight line from the Port del Comte thrust sheet limit within the Ebro basin.

On the other hand, Keuper materials also show phenomena of dissolution and formation of sinkholes (for example, in the Cambrils town rea, the formation of sinkholes has been documented in the farmland that covers these materials).

Other kind of karst features characteristics of the Port del Comte is the well-known 'trop-plein' syphon systems (from the French, which means 'too full; overflowing') or simply syphon karst functioning system. Trop-plein would be defined as openings or conduits located above the natural discharge point in springs, and which only function as an upper level overflow when the aquifer is too full. In general, they can be activated when enough recharge circumstances occur, such as high precipitation events after very intense summer storms; or in the snow melt periods.

In Port del Comte area, trop-plein functioning system can be identified in the Can Sala spring (SE od the Port del Comte unit), Aiguaneix spring (NE) and the called Font Andana spring (located at the N which discharge towards the 'Riu Fred de la Vansa' riber basin.

Can Sala spring has three trop-pleins (lower, intermediate and upper). The upper one has a small cave accessible up to 8 m in length. The lower aperture or top-plein is approximately activated for events from 100 L/s (**Figure 1. 9**; as it has been observed during the thesis fieldwork did between September 2013 – October 2015 - see chapter 2-).

The Aiguaneix spring, located at the north side of the mantle, and at the southern flank of the 'Alinyà -Roc de la Pena' anticline (**Figure 1. 10**), has a trop-plein located 2m above the natural discharge point, but it cannot be ruled out that there are others above these discharge points. The trop-plein identified in the field has been activated when the discharge 60 L/s in the spring has been exceeded, according to the data measured during the field campaign.

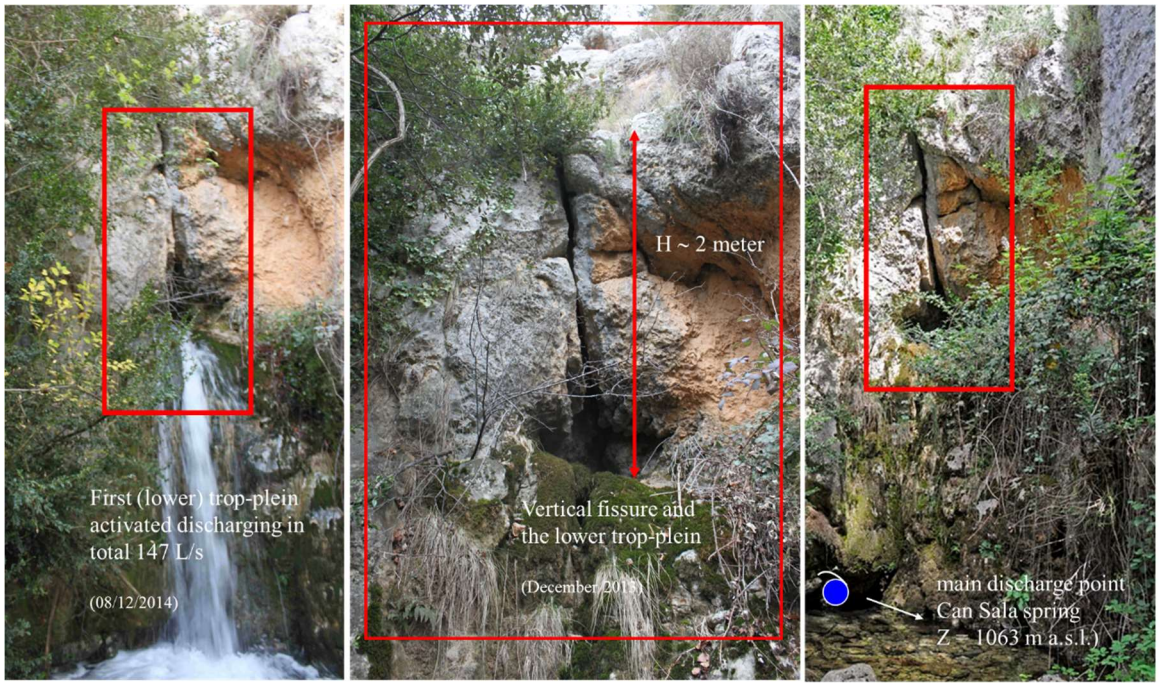

Figure 1. 9 Trop-plein karst System functioning in the Can Sala spring (1063 m a.s.l.) (Right photo: author/source: A. M. http://notesdecamp.blogspot.com/2014/07/les-fonts-de-cal-sala-i-sant-quinti.html)

Figure 1. 10 Landscape view of the Alinyà – Roc de la Pena – anticline, the PPEc unit and the position of the Aiguaneix spring (1098 m a.s.l.)

The Font Andana spring (also known as Padrinàs spring) (**Figure 1. 11**), is located in the municipality of Vansa i Fórnols (Z= 1124 m a.s.l.). It is actually a karstic syphon connected to the natural discharge that occurs towards the Riu Fred de la Vansa. It is found in the Upper Triassic - Lower Jurassic structural mantle (geological unit to the TJb geological unit) located to the north of the massif on the lower Eocene PEcp2 limestone unit of the Port del Comte massif. Since 1998, the point is arranged with a circular tube that has to prevent its collapse. It only goes into discharge in episodes of great discharge. During the thesis it has not been seen with water flowing. It was explored by speleologist and has 137m drop and 679 m of length.

Figure 1. 11 (Left) View of the Fondt Andana cave of the syphon (source: https://espeleoworld.com/ . (Right) view of the spring point in October 2015 (source: Herms, I.)

From the speleological point of view, in 1997 and in 2009 attempts were made to explore into the karstic conduit in conglomerates through which the St. Quintí spring (**Figure 1. 12**) (Montserrat, 2014) (SE, of the Port del Comte) discharges, but only a few meters could be entered. Some other small caves are known but any with groundwater.

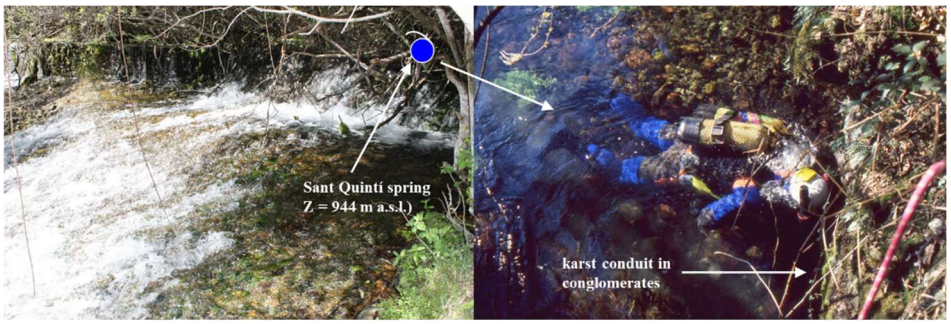

Figure 1. 12 Sant Quintí spring. (Right) view of the spring point in 10/05/2015 (source: Herms, I.). (Left) Scuba diving in 1997 (author/source: Monserrat, 2014).)

1.2.4 Meteorological setting

In the Port del Comte area there are two official weather stations (**Figure 1. 14**). The first, managed by the Weather State Meteorological Agency of the Spanish Government is located on the Alpine Sky resort area of the Port del Comte and has daily data since the 1990s. The second station is located at the almost highest point of the massif at the 'Padró dels Quatre Batlles' peak (2383 m a.s.l.) and is managed by the Meteorological Service of Catalonia (SMC). It has daily precipitation and temperature data as well as snow cover thickness daily data since mid-2004 (**Figure 1. 13**).

Official name	Management	X UTM ETRS89 31 N	X UTM	Elevation (m a.s.l.)	Precipitation (mm)	Tmin, max, avg (mm)
XEMA Port del Comte Z8	SMC	378115	4671098	2315	from 04/08/2004	from 04/10/2002
PORT DEL COMTE - 0127O	AEMET	381456	4669420	1811	from 01/01/1990	from 01/01/1990

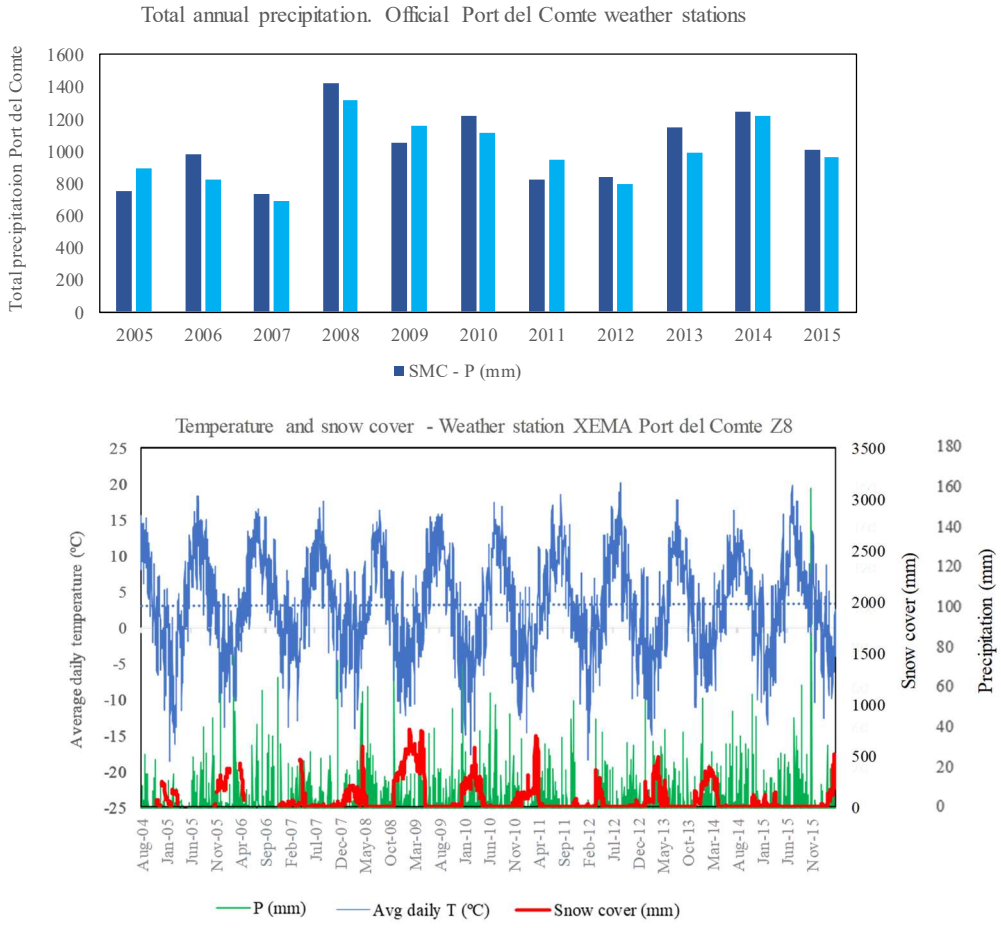

Figure 1. 13 Availability of climatological data in the SMC and AEMET weather stations. (Upper). Total precipitation records between 2005 and 2015). (lower). P, average T and Snow cover at SMC station

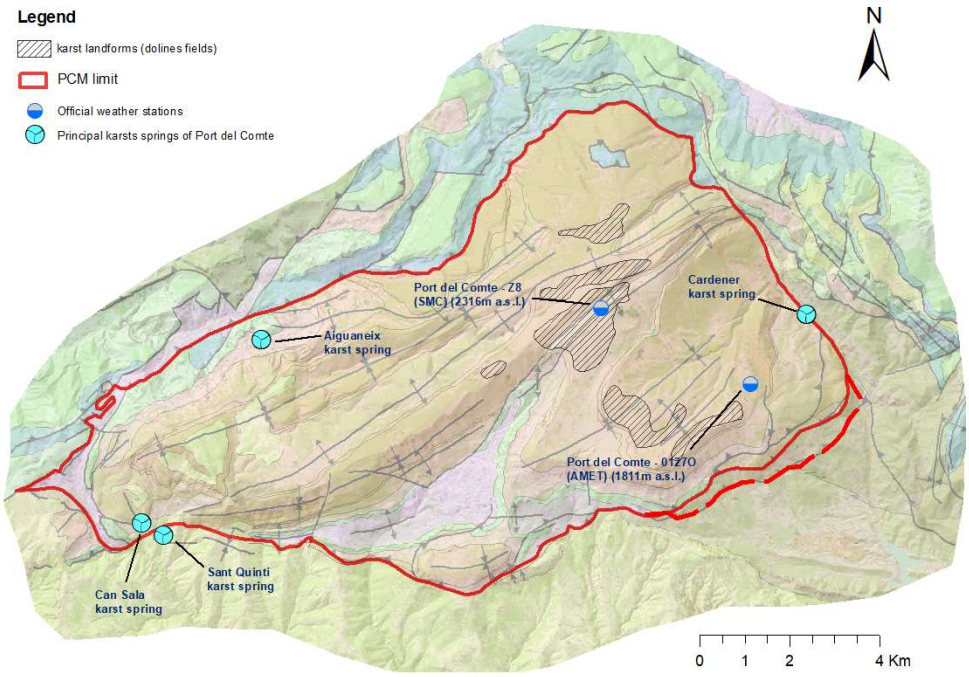

Figure 1. 14 Location of the two official weather stations available in the Port del Comte massif (SMC and AEMET). The figure also shows the location of the main 4 karst spring of the system.

According to the Köppen-Geiger classification (Peel et al., 2007), the study zone has a cold climate without dry season and temperate summer (defined as 'Dfb' type; accordingly, to AEMET and IMA, 2011). At the meteorological station of SMC (**Figure 1. 14**), which is located at 2315 m a.s.l., the average values of precipitation (P), temperature (T) and potential evapotranspiration (ETP) calculated with the Hargreaves and Samani (1982) (see Chapter 3, Paper 1) are estimated in 1055 mm/yr, 3,24 °C and 525 mm/yr, respectively. The measured vertical gradients (lapse rate) of precipitation (∇_zP), atmospheric temperature (∇_zT) and potential evapotranspiration (∇_zETP) are 8,9 mm/yr/100 m, −0,74 °C/100 m and −32,3 mm/yr/100 m, respectively. Precipitation is partly produced as snow at the top of the Port del Comte massif. This occurs on average about 30 days a year only at elevations above 1800m a.s.l., persisting for a few months until April when the snowmelt normally occurs, meaning that precipitation. As has been said before, despite the high average rainfall above 1000 mm/year, in most of the study area the surface runoff is almost non-existent, and it is not observed until reaching lower altitudes.

1.2.5 Land use

From the 1: 250,000 land cover map of Catalonia (CREAF, 2009), the percentage of the distribution of land use types has been quantified. (**Figure 1. 15**).

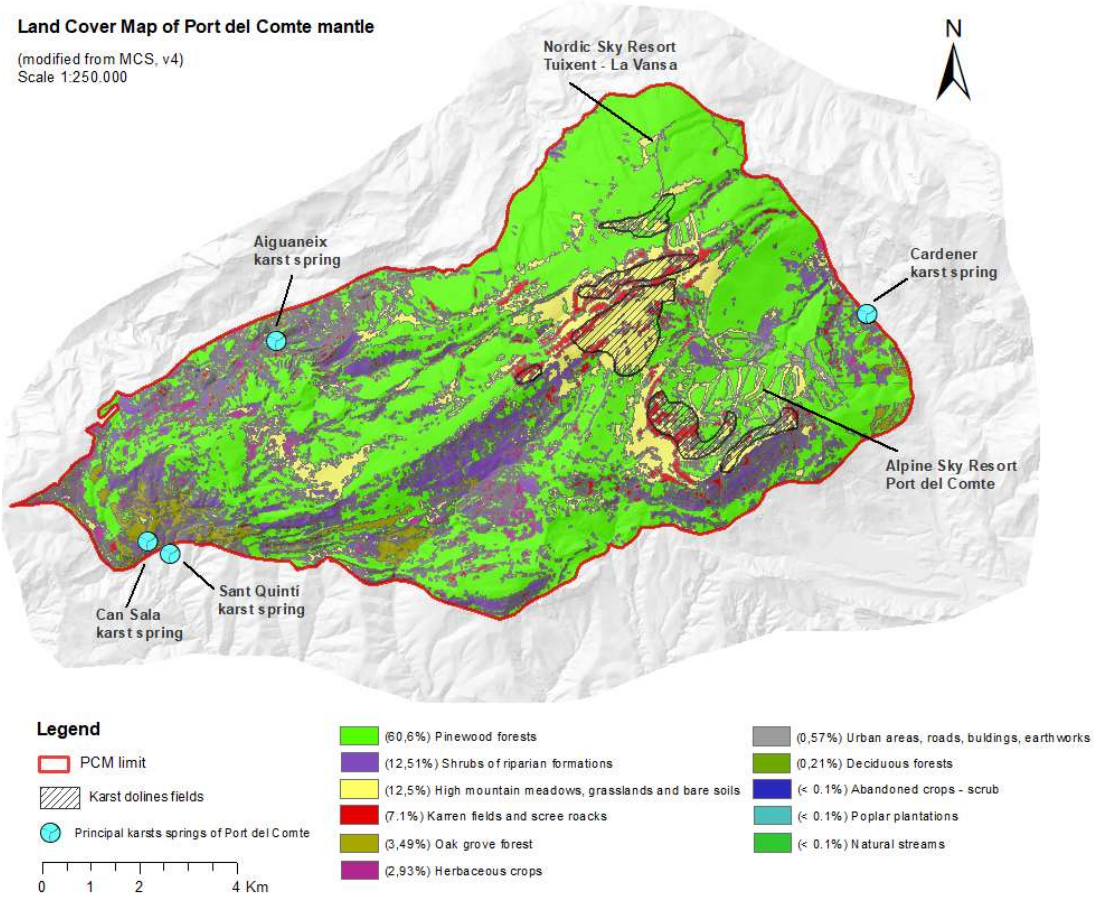

Figure 1. 15 Land cover map of Port del Comte (modified version of MCS, v4, CREAF, 2009)

The Port del Comte massif is a mountainous area where pinewood forests predominate (61%), followed by bushy areas (12.51%), high meadow meadows and bare soils (12.5%) and areas of karren fields and scree rooks (7.1%). The karst sinkholes fields that exist at the top of the massif (striped area indicated in the figure) are scattered in mountain meadows and rocky areas without the development of edaphic soil. This is the main area for the recharge of the karstic system and therefore the most vulnerable. The 'Port del Comte' alpine ski resort is located in the SW area of the massif, while the Tuixent-La Vansa Nordic ski resort is located in the northern part of the massif. The sky areas of the Port del Comte usually use fertilizer to regenerate the grass of the

slopes in summer, an aspect that is intended to be studied in the framework of the thesis if it can have an impact into groundwater quality. These slopes also use artificial snow cannons. However, its future viability is highly conditioned by the effects of climate change on temperature evolution. If it increased substantially, not only would they not have precipitation in the form of snow, but they would also not be able to use artificial snow to put the activity into operation. There is also an urbanized area around the sky resort. In the rest of the massif, some of the mountain meadows are used for potato plantations where fertilizers are used too. In the western part of the massif, meadows are used for cow pasture, and also there is a farm where manure accumulates which can also affect springs. The distributed farmhouses do not have sewers and use septic tanks system.

1.3 Literature review

The Port del Comte is a calcareous massif located in the south eastern part of the Pyrenees (Catalonia, Spain). Despite the high rainfall, over 1000 mm annual average, the entire extensive upper part of the massif is a dry area, without streams, because the water quickly infiltrates to discharge in the lower part of the mantle in form of karstic springs, some of them well-known such as the "Fonts del Cardener" in the municipality of ‘La Coma’ (Solsonès), and others that are not as well known, such as the Aiguaneix spring in the Vall d'Alinyà (Alt Urgell) at the NW side. But the massif is also known for its peculiar karstic landscapes, and a clear example is their fields of sinkholes in the ‘Pla de Bacies’ and the presence of its 'Gran Bòfia', a 30-40 m deep chasm that has been used since time immemorial as ice pit.

From a geological point of view, numerous studies have been published in the past related to specific aspects of the stratigraphy, sedimentology and structural context of the Port del Comte mantle and its framework in the south-east of the Pyrenees (Solé Sugrañes, 1973, Caus et al, 1988; Betzler, C. 1989; Puigdefàbregas and Souquet, 1986, Ullastre and Masriera, 2000 and previous; among many others). Important reference is the PhD thesis Solé Sugrañes (1970) as well as the PhD thesis of Vergés, J. (1993) published later as monography (Vergés, J., 1999). In this last, the author presented a network of 15 perpendicular seismically supported geological cross-sections, some of them balanced and restored, between the eastern and central Pyrenees, from which the named ‘J-5’ (Western end of the Cadí's mantle), the ‘J-6’ (Western end of the Port del Comte’s

mantle) cross both the Port del Comte unit from North to South and finally the 'J-15' (Port del Comte) that cross it from E to W. This last one shows perfectly the high topographical position of the Port del Comte thrust sheet.

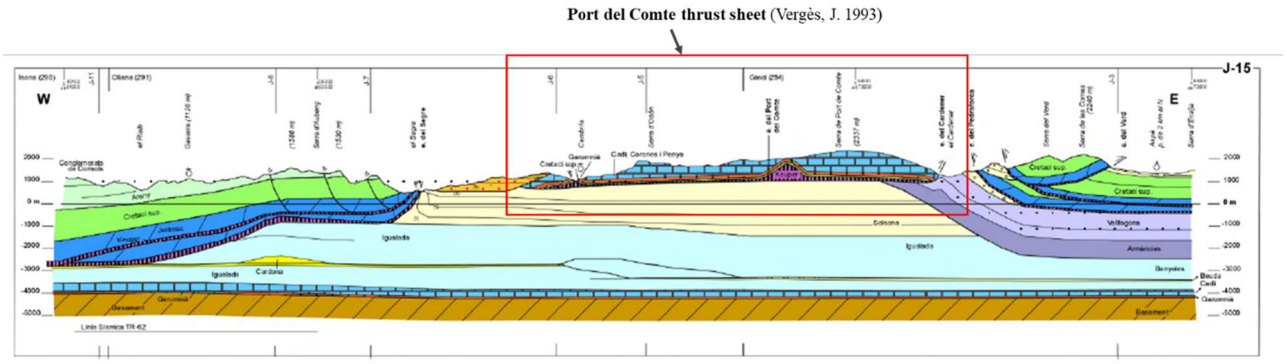

Figure 1. 16 Geological cross-section J-15 'Port del Comte' (Vergés, J. 1999). PhD, UB

The geological framework presented by Vergés, J. (1993) is the reference base considered in the elaboration of the present thesis, together with the geological cartographic information available at a scale of 1:50,000 elaborated by ICGC (2007), which represents a mapping synthesis of the MAGNA serie geological mapping program in Catalonia, together with the particular memories of the MAGNA Oliana Sheet 291 (Berastegui et al., 2001), Sant Llorenç de Morunys Sheet 292 (Ardèvol et al., 2000) and Gòsol Sheet 254 (Ardèvol et al., 2000b) geological maps. The most relevant general conclusion of the previous geological research is that the massif itself constitutes an independent structural unit, as can be appreciated in **Figure 1. 16**. From the hydrogeological point of view, which is the general objective of this thesis, it's expected that geological structure and stratigraphy influence substantially the local hydrogeology in the sense of location and storage capacity of the main karst springs that drain the existing aquifers, but also in the hydrogeochemistry of its groundwater.

From the geomorphological point of view, some other research and local publications exists, among them Chevrier-Magne, S. (1974) and Balasch, et al (2010) that addressed some of the aspects of the karstic morphology of the surface exokarst. From the surface hydrology point of view, some modelling studies has been carried out in the area of Ribera Salada' basin which collect waters from the 'Riu Fred' basin where discharge ones of the main important karst springs of the Port del Comte karst aquifer of the system (Sant Quintí and Can Sala springs) for then draining towards the Segre

Basin (Loaiza 2007), or specifically about the Canalda Basin (Verdú et al., 2020, Estruch, J, 2001; and Loaiza, J.C. and Casamitjana M. 2008), which collect surface waters from the Southern central part of the Port del Comte thrust sheet, another tributary to the Ribera Salada basin.

From the hydrogeological point of view, until now the majority of the karst massif in the south-eastern Pyrenees has really been little investigated, despite the strategic importance of the groundwater resources it drains, and the Port del Comte is one of the examples. Indeed, nowadays the hydrogeological conceptual model of the Port del Comte massif is relatively little known. The study of the Total Hydraulic Resources of the Eastern Pyrenees -known as REPO - Recursos Hidráulicos Totales del Pirineo Oriental - carried out by the extinct Geological Service of Public Works (SGOP), then part of the MOP (Ministry of Public Works of the Government of Spain), and the Water Commission of the Eastern Pyrenees (CAPO), then the authority responsible for the application of the Water Law of the Eastern Pyrenees (PO), and today corresponding to the internal basins of Catalonia, i.e. the Catalan Water Agency (MOPU-CAPO-SGOP (1970-72) during the years 1968-72, it was the first attempt at a very regional level to frame the hydrogeological context of the Pyrenees area. Years later, a most specific hydrogeological report to assesses the groundwater resources dates back to 1985 and was carried out by the Geological and Mining Survey of Spain (IGME, 1985) within the Research Plan of Groundwater of the Project of the Hydrological planning of the eastern Pyrenees. This study focused of characterizing the karstic areas of the Eastern Pyrenees and first area was the named Subsystem 69.1 ALTO LLOBREGAT which included the Oden-Port del Comte mountains ranges – referring the Port del Comte unit -, and had the aim to provide the necessary technical basis to be able to undertake rationalized management of all groundwater resources. In that study, a preliminary inventory of the most important water points, some gauging of springs and rivers, and a hydrological balance of each sub-basin were carried out, among them the Cardener basin, tributary of the Llobregat basin. The work defined the 'Port del Comte Unit (Eocene limestones)' with 86 km^2 of permeable outcropping lithologies, as one of the 16 hydrogeological units of the 'Alto Llobregat' basin. In general terms, it was estimated that the total groundwater resources in the Port del Comte Unit were 26.8 Hm^3/yr (year 1984-85), of which 9.34 Hm^3/yr would discharge into the groundwater basin of the Cardener spring estimated in this study at 32 km^2 (the SE part of the Port del Comte mantle) and the rest 17.5 Hm^3/yr would drain towards the Segre River basin to the N and SW (discharging an area equivalent to 54 km^2) of the Port del Comte mantle. The effective infiltration coefficient calculated in the whole area was 0.29.

Today, these figures on the availability of groundwater resources are considered as reference and are still used systematically in official reports. However, beyond the exact amounts, (IGME, 1985) made an error by attributing the discharge of the 17.5 Hm^3/year to the Segre river either directly by groundwater flow or through the La Vansa river (in the NE of the massif), ignoring completely the existence and therefore the importance of the discharges from the karstic springs that exist in the SW of the massif (to the Riu Fred Basin, tributary of the Ribera Salada basin) and on the NW side (to the Perles river basin).

A few years later, between 1990 and 1993, the Department of Agriculture, Livestock and Fishing of the Generalitat de Catalunya (Gencat 1990; 1991; 1993) in the framework of a project to improve the water supply in the mountain area of Solsonès region (N of Catalonia), carried out several new specific studies in the towns of Odèn (including Lladurs and Cambrils), Sant Llorenç de Morunys, La Pedra i La Coma and Guixers. The objective was to improve the knowledge of groundwater resources availability and determine the most appropriate areas to capture them. A new inventory of water points (springs and dug water wells) were did, followed by a hydrogeological mapping at 1:50.000 scale, the elaboration of hydrogeological conceptual cross-sections, definition of hydrogeological units and its groundwater-flow patterns, determination of the water quality, estimation of a water balance to determine the available interannual groundwater resources, new geophysical exploration works and the establishment the recommendation and execution of five new: 'Sant Quintí', 'Bartolo', 'La Sala', and 'Cambrils' 4 in the SW area of Port del Comte and 'Can Quirse-La Codina' in the E side. The former 'Sant Quintí' currently constitute the water supply well of the Cambrils town. The technical report of the drills carried out provides stratigraphic information and hydraulic well test data. The materials drilled in the Sant Quintí well correspond to carbonate clast breccias from lower Eocene limestone with alveoline. According to Gil & Núñez (2003), the hydraulic transmissivity in the Sant Quintí well would be around 700 m^2/d, a value in fact difficult to interpret considering the local setting. The water demand of town in 2003 was 0.004 Hm^3/year and it was not expected any growth for the 2015 to 2025 (ACA, 2005). This amount, in terms of groundwater resource availability in the balance of the Sant Quintí / Can Sala springs aquifer basin is totally negligible. One of the several conclusions obtained with this work was that the chemistry of the karst springs of Sant Quintí and Can Sala, although they are located very close to each other, suggests a different origin, hypothesis that will be confirmed through this thesis.

Later, in 2003, a specific hydrogeological study was carried out mainly focused on the SW part of the massif in the Riera Salada basin (Gil & Núñez 2003) publishing a summary of the results in the VIII hydrogeological symposium of the AIH held in Zaragoza in 2004 (Núñez et al. 2004). An inventory of water points was carried out with a total of 16 springs and 2 water supply wells in survey located in the municipalities of Cambrils (the previous borehole Sant Quintí did in 1993, and a new in Llinars town). 10 water samples were taken to determine the main ions and in 2 of the points (the Cardener spring, and in borehole Sant Quintí) the stable isotope content of the water was determined concluding that recharge in Cardener springs must be located at 1800 m as.l. This study is considered a very important reference since it provided the basis for the conceptual hydrogeological model presented in the frame of this thesis. Nevertheless Gil & Núñez (2003) only addressed the part of the Port del Comte Thrust sheet that drains towards the SE and E of the system (i.e. they did not consider the existing groundwater karst springs discharging though the Perles river basin to the NW (Alinyà valley) neither the diffuse discharge to the Vansa river basin (Tuixent valley) to the N. Within the Port del Comte karst system they proposed a groundwater flow pattern model explained by two main sub-units (**Figure 1. 17**): The Oden sub-unit 'A1' (that drains to SO mainly through the Sant Quintí and Can Sala karst springs) limited to the north by the Alinyà – Roc de la Pena Anticline with 16.3 Hm^3/year of outputs, and the 'Bòfia Sub-unit 'A2' with 11.1 Hm^3/year of outputs (drained by the Cardener springs). Considering that estimated data corresponds a different period that it was by IGME (1985), the results estimated could be considered consistent.

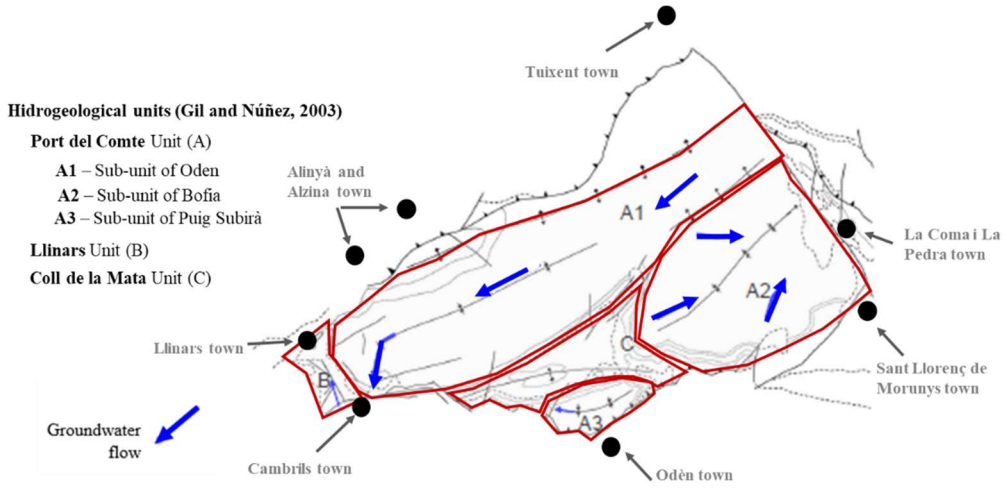

Figure 1. 17 Conceptual groundwater flow pattern model by Gil & Núñez (2003) (modified sketch with respect to the original version to highlight the domains defined in the units and subunits).

They also concluded that the underground boundaries of these systems are probably closed to groundwater flow or that it should be minor. The concept of closed groundwater flow boundaries would confirm in general terms that the Port del Comte Unit can be considered an independent structural but also hydrogeological unit. In any case, the model is incomplete because, for example, it neglected the existence of the spring called Aiguaneix, which also drains thanks to the southern slope of the Alinyà anticline, as it will be commented on in different parts of this thesis (e.g. see chapter 2.2). Another aspect cited by Nuñez, et al (2004) that would not be correct is that among the geological units that would form the "Lower Aquifer" defined in their proposed bi-layer conceptual model mentioned the contribution of the Bona Formation (Upper Cretaceous, Campanian-Maastrichtian) and the Bonansa Formation (Jurassic), but the latter actually disappears due to erosion, and only appears outcropping in a very small area in the northern limit of the mantle in the core of the Alinyà - also called 'Roc de La Pena'- anticline (Vergés, 1993). The proposed hydrogeological model based on a simple bi-layer system must be updated, since the springs existing within the Port del Comte mantle boundary below the defined Aquitard (the Garumnian units, Tremp Formation) correspond to very local aquifers draining either the limestone-sandstone levels of the Upper Cretaceous but also the outcropping Triassic layers (some springs exist within the Keuper facies and very locally in the Muschelkalk).

On the eastern side of the massif in the area of La Pedra i la Coma, at the end of the 1980s, drilling was carried out to locate water to supply the urbanization and its alpine ski resort known as 'Port del Comte'. In 1993 new wells were carried out, one of which called Pou-02 is the one situated within the karst system and that currently continues to supply water to the urbanization and the ski complex. The water demand in 2003 was 0.0135 Hm^3/year (ACA, 2005). Although urban growth was expected, to date it has hardly occurred. This amount, in terms of groundwater resource availability in the balance of the Cardener spring aquifer basin, is almost negligible.

Finally, in 2004 the last research drilling was carried out, according to the available information, to locate complementary resources, with a new 416m deep boreholes from 1850m a.s.l. altitude executed in the area known as 'Rasa de la Bòfia' in the middle of the axis of the syncline that drains towards the Cardener spring, reaching the 1,434 m a.s.l. resulting completely dry so it had to be abandoned.

An important aspect of the high mountain karst system of Port del Comte, which should be noted, is that it is affected by a purely administrative division into two groundwater bodies managed by different hydrological basins, and apart from that, the remaining parts are aggregated with other hydrogeologically unconnected surrounding aquifers without too much sense:

- The Port del Comte mantle is an independent geological and hydrogeological structural unit whose main aquifer is the karstified limestone from the Lower Eocene. However, for management purposes this is hydrologically separated by the surface basins of the Segre and Cardener rivers. This conditions that the high mountain tertiary karst aquifer is left separated in two parts: The first, corresponding to the SE part called 'Sub-unit A2 of Bòfia' (according to Gencat 1991,1992,1993 and Gil & Núñez 2003) which is managed by the Catalan Water Agency (ACA), and the rest of the Port del Comte mantle (which would include the called 'Sub-unit A1 of Oden' plus the part that drains to the NW and NE not considered by Gil & Núñez, 2003) is managed by the Ebro Hydrographic Confederation (CHE).

- This hydrographic division into two different basins by the official management organizations is also reflected in the delimitation of the official Groundwater bodies, as management units, in application of the EU Water Framework Directive 2000/60/EC (WFD).

- The SE part managed by ACA that includes the Cardener spring basin is included in the Groundwater Body (GWB) number 5 named 'CONCA ALTA DELS CARDENER I LLOBREGAT'. This GWB goes beyond the Port del Comte mantle itself and includes other aquifers of different geological ages, such as the Cretaceous units of the 'Serra del Verd' that are hydraulically separated from the mantle of the Port del Comte massif by the Cadí thrust sheet. Indeed, the Port del Comte massif in the Cardener side (SE), is included in the called '*Aqüífer de les calcàries de Pedraforca – Llobregat* 1161C01' that includes that Cretaceous materials without any evidence of hydrogeological connection.

- The rest of the massif of the Port del Comte mantle is management by CHE and is included in Groundwater Body (GWB) 'CADÍ-PORT DEL COMTE' number 039 (according to CHE,

2010) and n.44 (according to ACA, 2005). The Port del Comte is also defined as Hydrogeological Unit N 321 - CADÍ - PORT DEL COMTE by the CHE (**Figure 1. 18**). The whole area covered also includes not only the western and northern part of the Port del Comte mantle, but also other aquifers of different geological ages, mixing different lithologies such as some Mesozoic (Jurassic and Cretaceous) aquifers of the Boixols and Montsec mantles probably also disconnected from the Port del Comte mantle.

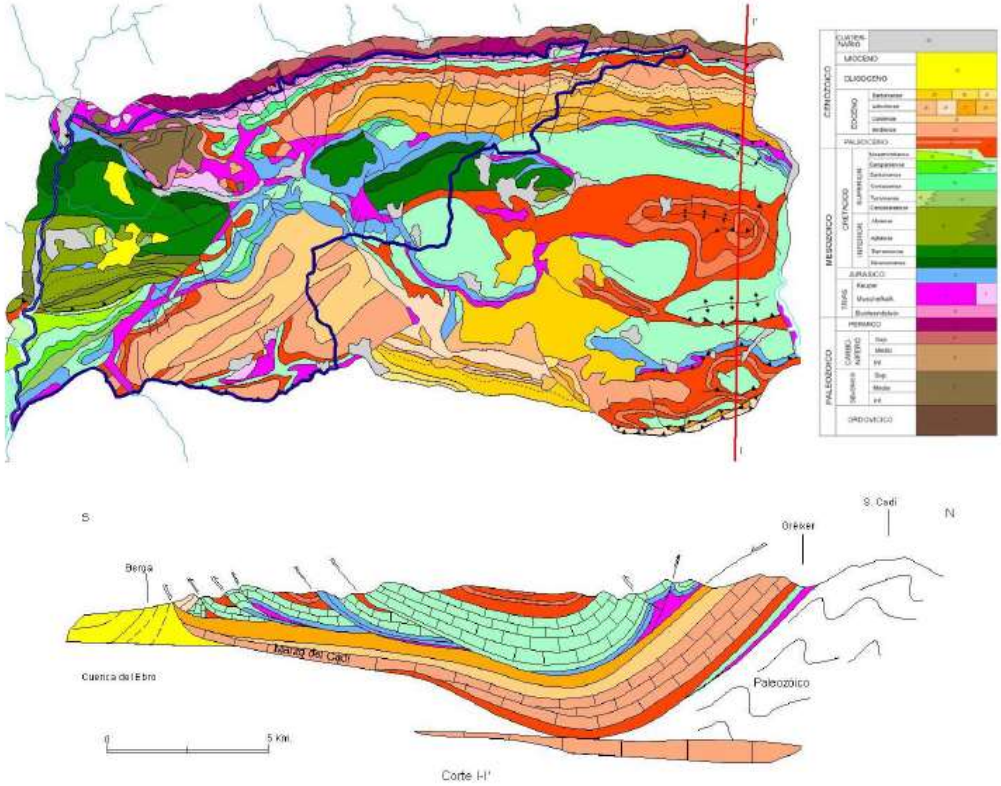

Figure 1. 18 Geological map and cross-section of the GB 091.039 Cadí – Port de Comte (CHE, 2010). The limit is indicated in a dark blue line.

These divisions and then aggregations, imply some erroneous conceptual assumptions and can lead to difficulties for the interpretation and the subsequent reuse of the reports and studies carried out. This happens when, for example, natural background levels are established at the scale of groundwater bodies when aquifers with different ages and lithologies are being mixed (in the Pyrenees the presence of Triassic levels can greatly affect the quality of the water in terms of sulphates and chloride); or for instance when recharge estimates are made (ACA, 2009) by aggregating aquifers with disparate recharge rates if later assessments of the effects of climate

change on specific important springs are to be made. Therefore, to carry out specific and local studies, for example if pollution episodes have to be contrasted with natural background levels, or for example in case of wanting to evaluate the effects of climate change on springs, it will always be necessary to review and redefine the initial criteria taken by the definition of these GWB.

1.4 The strategic importance of the Tertiary karst aquifer of Port del Comte

The Pyrenees are extremely important for the availability of water resources in the territories where they are located, since at its headwaters generates a very important part of the surface flows and groundwater that is used downstream, in this case, in the Ebro and Llobregat basins.

The Port del Comte carbonated karstic aquifer represents one of the most important mountain aquifers in the territory of Catalonia. From the resource availability point of view, if we look at the Cardener spring (which drains the SE part of the Port del Comte mantle or Bòfia sub-unit according to the definition of Gencat 1991,1992,1993) and based on the water resource balance carried out by the IGME (1985) for the hydrological year 1984-85 in which considered data from 5 gauging did between March and July 1985 in the spring with an average Q flow rate of 267 L/s (almost 8 Hm3/y), the contribution of the Cardener spring represents 26% of the total groundwater resources that reach the 'Llosa del Cavall' water reservoir (Navès, Solsonès), which is the most important reservoir of the two existing ones in the Cardener river basin.

On the other hand, high mountain karstic aquifers are important above all for the role of the snow cover and the snowmelt process acting as regulator of aquifer recharge. Climate change projections suggest an important variation in the temperature and precipitation regime in European alpine karst regions during the next decades throughout the 21st century (Chen et al, 2018) and in particular in the Pyrenean region (OPCC-CTP, 2018).

Karstic mountain systems located further south, such as the Port del Comte massif, will be much more vulnerable to these variations. The models predict a clear trend towards increased temperatures that will have a direct impact on the availability in space and time of snow cover, as well as on the dynamics of aquifer recharge. This possible effect on the snow cover, at the same

time, could affect one of the most important economic activities in Port del Comte, such as the existing alpine ski resort.

These forecasted changes in annual and seasonal recharge and groundwater flows can lead in the same time to a decrease in groundwater quality, since they imply a decrease in the dilution effect of polluting natural or anthropogenic substances.

All aspects evidence the importance of first, investigating the hydrological functioning of this mountainous karst system taking into account the snow accumulation and melting and the recharge regime of the massif using a semi-distributed rainfall-runoff modeling approach for then evaluating the potential impacts of climate change, and secondly, to improve knowledge of the geochemical processes that take place in these mountain aquifers, currently still considered almost pristine.

1.5 Objectives, strategies and results

The main objective of this thesis is to improve the general hydrogeological knowledge of the functioning of the high mountain karstic aquifer of the Port del Comte unit (SE, Pyrenees) through the acquisition of new information on the quantity and quality.

The specific objectives to achieve the main goal are to:

- Characterize the general geological structure and geometry of the potential groundwater reservoirs associated with the main karstic springs draining the Port del Comte mantle.
- Characterise the temporal and spatial flow regime of the springs present in the domain
- Characterise the snowmelt and rain contribution to the recharge process of the main karst springs and estimate the mean transit times of the groundwater within the karst system
- Characterize and classify the families of groundwater present in the Port del Comte domain, the chemical processes that determine the characteristics of their groundwater, the influence of geogenic and anthropogenic factors and to establish the background geochemical levels

associated with the most common contaminants in these almost virgin mountainous environments with little human activity, such as chloride, sulphate and nitrate.

- Establish the whole hydrogeological conceptual model of functioning.
- Study the hydrological response of the karstic system to regionalized climate change scenarios

The strategy followed to achieve the established objectives has been divided into:

- **Field work campaigns**: These have been programmed and executed during a period between the summer of 2013 and the end of 2017, with a more intense period between September 2013 and October 2015, in which new geological data have been acquired, it has been implemented and monitored a network of CoCORAH (CoCoRaHS RG202 Official 4 "Long Term Professional Rain and Snow Gauges totalizer collectors imported from the USA for sampling and analysis of the stable isotope content of water in precipitation water; The main karstic groundwater springs have been monitored regularly for two years, taking water samples for chemical characterization with the determination of the content of major ions and stable isotopes of the water, nitrate and sulphate, and subsequently they have been gauged by the method of slug injection with salt in solution. At a general level, global gauging and annual sampling campaigns have been carried out before and after the melting during the two years for the spatial characterization of a spatially distributed set of springs. The sampling works have been complemented by taking samples of natural and artificial snow, and rock samples for the characterization of the sulphate isotopic content in gypsum from different geological formations.

- **Analysis, modelling and processing**. For the geological modelling, the 3DMove software platform (Midland Valley Exploration Ltd.) has been used. To characterize the hydrological response of the system two lumped parameter models has been used: (1) a semi-distributed rainfall-runoff HBV model that simulates the observed hydrodynamical system response while taking into account the elevation dependences of the different hydrometeorological variables (i.e. Precipitation and temperature), land uses and associated processes (e.g. snow accumulation and ablation), and (2) a FlowPC® model that estimates the mean transit time of the hydrological system while simulating the environmental tracer content evolution in

the system discharge. This is done by numerically integrating a convolution integral. The study of the geochemical process has been addressed using hydrogeochemical speciation and inverse modelling PHREEQC® code within the version PhreeqC Interactive (version 3.3.3 10424), and with the phreeqc.dat database

The results achieved have been published in **4 peer-reviewed scientific papers** in the journal Science of the Total Environment (STOTEN) of Elsevier (Q1 JCR Impact Factor: 6.551 for the period 2019-2020 'ENVIRONMENTAL SCIENCES' according to the 'Web of Knowledge' website) and in the open access journal on water science and technology 'WATER' of MDPI (Q2 JCR Impact Factor: 2.714 for the period 2019-2020 'WATER RESOURCES' according to the 'Web of Knowledge' website). The 4 pre-prints are included within this thesis as Chapters numbered in order of publication 3, 4, 5 and 6. The results achieved has been also focus of several contributions in national and international conferences and workshops cited in the first page of this thesis.

In the other hand, the established objectives have been complemented with the participation in the European project "Resources of groundwater harmonized at cross-border and pan- European scale (RESOURCE)" executed between 2018 and 2021, and co-financed under the umbrella of the GeoERA (Establishing the European Geological Surveys Research Area to deliver a Geological Service for Europe, 731166) H2020 Era-Net. Its work package 7 (WP7), called CHAlk and KArst Aquifer (CHAKA), focused in the typology of karst aquifers in Europe, in which several national and regional geological service organizations have contributed with a pilot case study. My contribution was with the study case of Port del Comte as pilot area to test the classification methodologies for karstic aquifers. The result of this work is presented very briefly in chapter 7.

Ultimately, the work constitutes a contribution to the knowledge of the hydrogeological functioning of the carbonate aquifers of the eastern Pyrenees and the work methodology presented, its conclusions, may serve as an approach and starting point for works in aquifers with similar characteristics not yet explicitly explored and that contribute significantly to the global water resources balance within the Pyrenees system.

1.6 Structure of the doctoral thesis

This thesis responds to an article-based thesis. It includes the compilation of 4 scientific articles already published in the journals STOTEN and WATER and is divided in 10 chapters.

Chapter 1 corresponds to the general introduction that describes the framework in which this research is situated and includes a preliminary description of the objective case study: the Port del Comte high-mountain karst aquifer system; then it includes a bibliographic review, a specific part on the strategic importance of this aquifer in the availability of groundwater resources in Catalonia; a section on the objectives of the thesis and the general strategy followed and the results obtained and some references.

Chapter 2 of the thesis focuses on describing some of the methodologies and approaches taken to deploy the field and office work to meet the objectives of the thesis which have not been explicitly included and documented in any of the four scientific papers presented.

Next, the results obtained in the 4 scientific articles are presented in the following Chapters 3, 4, 5 and 6. Considering that they follow the structure of the pre-print, each one of them has its own introduction, methodology, results, discussion, conclusions and references.

These are followed by the complementary chapter number 7 where the main results obtained from the contribution of the doctoral student in the work package 7 called CHAlk and KArst Aquifer (CHAKA) focused on Typology of karst aquifers in Europe of the European project “Resources of groundwater harmonized at cross-border and pan- European scale (RESOURCE)” are presented.

Later in Chapters 8 general discussion and the conclusions of the thesis are presented. Finally, in chapter 9, the supplementary material associated with chapters 2, 3, 4, 5 and 6 is added.

.

1.7 References

ACA (2005). Document IMPRESS. Document de pressions i impactes, i anàlisi del risc d'incompliment dels objectius de la Directiva marc de l'aigua. (link). Fitxa Massa d'iagua subterrània CADÍ-PORT DEL COMTE núm. 44. (Accessed on July 2013)

ACA (2009). Estimació de la recàrrega d'aigua subterrània a les conques de Catalunya. Report pp48.

Agencia Estatal de Meteorología de España (AEMET) and Instituto de Meteorologia – Portugal (IMA). 2011. Iberian climate atlas. Air temperature and precipitation (1971-2000). (link) (Accessed on July 2013)

Aller, L.; Bennett, T.; Lehr, J.; Petty, R.; Hackett, G. (1987). DRASTIC: A standardized system for evaluation ground water pollution potential using hydrogeological settings. National Water Well Association, Dublin, Ohio and Environmental Protection Agency, Ada, Ok. EPA/600/2-85/018. (link).

Anglès, M. (2013). Hidroestratigrafia del ventall deltaic de sant Llorenç del Munt (Eocè mig – superior. Conca de l'Enre). Tesis doctoral. Universitat Autònoma de Barcelona. 196 pp.

Ardèvol, Ll., Solé, X., Escuer, J., Martínez, A., Puig, C. y Samsó, J.Mª (2020). Memoria de la Hoja nº 292 (Sant Llorenç de Morunys). Mapa Geológico de España E. 1:50.000 Segunda Serie (MAGNA). Primera edición. IGME, 100 p.

Ardèvol, Ll., Solé, X., Losantos, M., Martínez, A., Puig, C., Escuer, J. y Casanovas, J. (2020b). Memoria de la Hoja nº 254 (Gósol). Mapa Geológico de España E. 1:50.000. Segunda Serie (MAGNA). Primera edición. IGME, 132 p.

Arnó, G.; Conesa, A.; Carreras, X.; Camps, V.; Fraile, J.; Herms, I.; Iglesias, M. (2020). Mapa de Vulnerabilitat Intrínseca a la contaminació dels Aqüífers de Catalunya (MVIAC) 2020.Institut Cartogràfic i Geològic de Catalunya (ICGC)

Aitchison, J., 1986. The Statistical Analysis of Compositional Data. Monographs on Statistics and Applied Probability Chapman and Hall, London, New York (416 pp.).

Balasch, J.C., Delgado, J., Llorens, P.,Vericat, D., Gallart, F. (2010): Visita geomorfológica al valle del alto Cardener (cuenca del Llobregat), sierra del Port del Comte y valle de la ribera salada (cuenca del Segre). Centre Tecnològic Forestal de Catalunya, Solsona. 44 p. ISBN: 978-84-693-5185-7.

Betzler, C. (1989) A carbonate complex in an active foreland basin: the Paleogene of the Sierra de Port del Comte and the Sierra del Cadi (Southern Pyrenees), Geodinamica Acta, 3:3, 207-

220, https://doi.org/10.1080/09853111.1989.11105187

Berástegui, X., Losantos M., Muñoz J.A. i Puigdefàbregas, C. (1993) Tall geològic del Pirineu central.1:200000. Barcelona: Servei Geològic de Catalunya.

Berastegui, X., Pi, M.E., Escuer, J., Casanovas, J., Smaso, J.M., Arbués, P., Martínez, A., Vilella, L. (2001). Memoria de la Hoja nº 291 (Oliana). Mapa Geológico de España E. 1:50.000 (MAGNA), Primera edición. IGME, 113 pp. Depósito legal: M-24.012-2017. ISBN: 978-84-9138-038-2.

Brusi, D., Pallí, L., Roqué, C., Pujadas, A., Capellà, I. (1997). Zona lacustre de Banyoles. Comunicaciones de la III Reunion Nacional de la Comisión de Patrimonio Geológico, Girona, septiembre 1997. I.S.B.N.: 84-88762-84-4

Caus, E., Rodes, D., Solé Sugrañes, LL. (1988), Bioestratigrafia y estructura del Cretacico superior de la Vall d' Alinya (Pirineo oriental, prov. de Lleida). Acta geològica Hispánica, t.23 núm. 2 pp 107-118

CHE (2010). Masa de agua subterranea. Cadí – Port del Comte 039. (link). (Accessed on July 2013)

Chen, Z., Hartmann, A., Wagener, T., Goldscheider, N (2018). Dynamics of water fluxes and storages in an Alpine karst catchment under current and potential future climate conditions. Hydrol. Earth Syst. Sci., 22, 3807–3823, 2018. https://doi.org/10.5194/hess-22-3807-2018

Chevrier-Magne, S. (1974). Les phénomènes karstiques dans le Massif de Port del Comte (Pyrénées Catalanes Espagnoles). Mémoires et Documents, nouvelle sèrie Vol. 15, Phénomènes karstiques, Tomé II. Clermont Ferrand.

Choukroune P., and ECORS Team, The ECORS Pyrenean deep seismic profil·le reflection data and the overall structure of an orogenic belt, Tectonics,8, 23-39, 1989. https://doi.org/10.1029/TC008i001p00023

Custodio, E.; A. Bayó; M. Pascual y X. Bosch (1990). Results from studies in several karst formations in Southern Catalonia (Spain). Hydrogeologic Processes in Karst Terranes. (Ed. G. Günay, A.I. Jonhson and W. Back). Intern. Assoc. Hydrological Sciences, Publ. 207: 295–326. ISBN 0–947571– 28–0.

CREAF, 2009. Land Cover Map of Catalonia (MCSC) 1:250,000. 4a edition (2009). http://www.creaf.uab.es/mcsc/usa/index.htm

Daignières M., Séguret M., Specht M., ECORS Team (1994) The Arzacq-Western Pyrenees ECORS Deep Seismic Profile. In: Mascle A. (eds) Hydrocarbon and Petroleum Geology of

France. Special Publication of the European Association of Petroleum Geoscientists, vol 4. Springer, Berlin, Heidelberg. https://doi.org/10.1007/978-3-642-78849-9_15

EC (2000). "Directive 2000/60/EC of the European Parliament and of the Council establishing a framework for the Community action in the field of water policy.

Egozcue, J., Pawlowsky-Glahn, V., Mateu-Figueras, F., Barceló-Vidal, C. (2003). Isometric logratio transformations for compositional data analysis. Math Geol; 35:279–300.

Estruch J. (2001). Informació del territori i càlcul de l'escolament superficial mitjançant el model HEC-1. Aplicació al mapa de sòls 1:50.000 de la conca de Canalda (el Solsonès). Butll. Inst. Cat. Hist. Nat., 69: 95-116. 2001 ISSN: 1133-6889

Farlin, J., Maloszewski, P., (2013). On the use of spring baseflow recession for a more accurate parameterization of aquifer transit time distribution functions. Hydrology and Earth System Sciences, 17(5), 1825-1831. https://doi.org/10.5194/hess-17-1825-2013

Freixes, A. (1986). El carst conglomeratic experimental de Rellinars: un enfocament sisttmic i hidrogeologic en la recerca del medi carstic. Tesi de Llicenciatura.Universitat de Barcelona, 157 pag.

Freixes, A., Monterde, M., Ramoneda, M. (1996). Geochemistry of the Surface and groundwaters of the upper basin of the river Llobregat. Pirineos, 147-148; 41 a 59, Jaca, 1996.

Freixes, A. (2014). Els aqüífers càrstics dels Pirineus de Catalunya. Interès estratègic i sostenibilitat. Tesis doctoral. Facultat de Geologia. Universitat de Barcelona, Barcelona, 650 pp.

Gencat (1990). Proyecto de prospección e investigación hidrogeológica en el Solsonès (Lleida). 128 pp. Technical report. Unpublished.

Gencat (1991). Estudio geofísico para la prospección de aguas subterráneas (Solsonès– Lleida). 20pp. Technical report. Unpublished.

Gencat (1993). Informe de los sondeos de investigación en la comarca del Solsonès. 58pp. Technical report. Unpublished.

Gil, R. y Núñez, I. (2003). Estudio hidrogeológico de la sierra de Odén – Port del Comte (Solsonès–Lleida). Trabajo de curso CIHS, 85pp. Informe interno. Inédito.

Goldscheider, N. And Drew, D. (2007). Methods in Karst Hydrogeology. IAH: International Contributions to Hydrogeology. 1st Edition. Taylor & Francis, London. https://doi.org/10.1201/9781482266023

Goldscheider, N.; Chen, Z.; Auler, A.S.; Bakalowicz, M.; Broda, S.; Drew, D.; Hartmann, J.; Jiang,

G.; Moosdorf, N.; Stevanovic, Z.; et al. (2020) Global Distribution of Carbonate Rocks and Karst Water Resources. Hydrogeol. J. 28, 1661–1677, doi:10.1007/s10040-020-02139-5.

Herms, I y Jorge, J. (2012). Variación anual e interanual del manto nivoso en el macizo del Port del Comte (Solsonès– Lleida) a partir de imágenes MODIS. Libro resúmenes XV Congreso Nacional de Tecnologías de la Información Geográfica, pp. 97-105.

Hoerling, M., Eischeid, J., Perlwitz, J., Quan, X., Zhang, T., and Pegion, P. (2012). On the increased frequency of Mediterranean drought. J. Clim. 25 (6), 2146–2161. https://doi.org/10.1175/JCLI-D-11-00296.1

ICGC (2007). Mapa geològic comarcal de Catalunya 1:50 000. Full Alt Urgell (BDGC50M). http://www.icgc.cat/ca/Administracio-i-empresa/Descarregues/Cartografia-geologica-i-geotematica/Cartografia-geologica/Mapa-geologic-comarcal-de-Catalunya-1-50.000/Mapa-geologic-comarcal-de-Catalunya-1-50.000

ICGC (2017). Mapa d'Àrees Hidrogeològiques de Catalunya 1:250.000 (MAH250M v1.0, 2017). (retrieved from https://www.icgc.cat/Administracio-i-empresa/Descarregues/Cartografia-geologica-i-geotematica/Cartografia-hidrogeologica/Mapa-d-arees-hidrogeologiques-de-Catalunya-1-250.000-MAH250M-v1.0-2017) (Last accessed 18/02/2022)

IGME (1985). Estudio hidrogeológico para la integración de los recursos subterráneos de la cuenca del Pirineo Oriental en la planificación hidrológica. Subsistema 69.1. Alto Llobregat. Informe Técnico, 163pp

Kresic, N., Stevanović, Z., (2010). Groundwater hydrology of springs: engineering, theory, management, and sustainability. Butterworth-Heinemann, Oxford

Lauber, U., Goldscheider, N., (2014). Use of artificial and natural tracers to assess groundwater transit-time distribution and flow systems in a high-alpine karst system (Wetterstein Mountains, Germany). Hydrogeology Journal, 22(8), 1807-1824. http://dx.doi.org/10.1007/s10040-014-1173-6

Lloret, J. and Ubach, M. (2017). Ruta geològica de l'Avenc Montserrat Ubach, Odèn Solsonès. 148.pp. ISBN:9788494172595

Loaiza (2007). Soil hydrology in the Ribera Salada Catchment (Catalan Pre Pyrenees) Application of hydrologic models for the estimation of hydrologic transitional regimes. PhD thesis. 117pp. Universitat de Lleida.

Loaiza, J.C. and Casamitjana M. (2008). Caracterización del caudal en dos subcuencas demontaña mediterránea, estudio de aplicabilidad de un modelo hidrológico. Avances en Recursos

Hidraúlicos - Número 18, Octubre de 2008, Medellín - Colombia - ISSN 0121-5701

Malard, A., Sinreich, M., Jeannin, P.Y. (2016). A novel approach for estimating karst groundwater recharge in mountainous regions and its application in Switzerland. Hydrological Processes, 30(13), 2153-2166. https://doi.org/10.1002/hyp.10765

Mas-Pla, J. (2010). "Vulnerabilitat territorial dels recursos hidrològics al canvi climàtic"; in Llebot, J.E: (Eds.) "Segon informe sobre el canvi climàtic a Catalunya" (pp. 309-342). Institut d'Estudis Catalans. Generalitat de Catalunya. Dipòsit Legal: B. 44160-2010 http://cads.gencat.cat/ca/publicacions/informes-sobre-el-canvi-climatic-a-catalunya/segon-informe-sobre-el-canvi-climatic-a-catalunya/

Monserrat, A. (2014). Les fonts de Cal Sala i Sant Quintí (Cambrils-Odèn). http://notesdecamp.blogspot.com/2014/07/les-fonts-de-cal-sala-i-sant-quinti.html (Accessed on 01/11/2021)

MOPU-CAPO-SGOP (1970-72): "estudio de los recursos hidráulicos totales del Pirineo Oriental (REPO)".Empresa consultora : PANTECNIA-HERRING y EDES.

Muñoz, J.A. (1992) "Evolution of a continental collision belt: ECORS-Pyrenees crustal balanced crosssection". In Thrust Tectonics. K.R. McClay (ed.). London: Chapman & Hall: 235-246.

Núñez, I., Gil, R., García M.A, y Vázquez, E. (2004). Estudio hidrogeológico de la cabecera de la Ribera Salada, (Lleida). Libro resúmenes VIII Simposio de Hidrogeología, (AIH - IGME), p. 107-120.

OPCC1 (2013). Interreg POCTEFA Project. (2007-2013) https://www.opcc-ctp.org/en/sector/past-and-present-climate (Accessed on 02/11/2021)

OPCC-CTP (2018). El canvi climàtic als Pirineus: impactes, vulnerabilitats i adaptació. 150pp ISBN: 978-84-09-06268-3

Pascual, J M, Freixes, A., Maslch, J M., Balasch, C , Monterde, M , Ramoneda, J I Remacha, R (1996) "Los acuiferos carbonatados en el Pirineo de Lleida (Pirineo occidental de Catalunya)" Actas de las Jomadas sobre Recursos Hídricos en Regiones Kársticas. Vitória, pp 127-144

Peel, M.C.; Finlayson, B.L.; McMahon, T.A. Updated World Map of the Köppen-Geiger Climate Classification. Hydrol Earth Syst Sci 2007, 12.

Pawlowsky-Glahn, V., Egozcue, J.J., Tolosana-Delgado, R., (2015). Modeling and Analysis of Compositional Data. ed. John Wiley & Sons Ltd, The Atrium, Southern Gate, Chichester, West Sussex, PO19 8SQ, United Kingdom. 272 pages. ISBN: 9781118443064

Puig, R., Tolosana-Delgado, R., Otero, N., Folch, A., (2011). Combining isotopic and

compositional data: a discrimination of regions prone to nitrate pollution. In V. Pawlowsky-Glahn and A. Buccianti (Eds.), Compositional Data Analysis: Theory and Applications 390.

Ramoneda, J.; Freixes, A.; Monterde, M.; Morin, J.P., Gourcy, L., (1999). Los sistemas kársticos del parque del Cadí-Moixeró (Pirineo Oriental, Catalunya). Contribución del estudio científico de las cavidades kársticas al conocimiento geológico. pp. 483-495. Patmnato de la Cuev. de Nerja, 1999, Nerja (Málaga).

Rosell, J., Linares, R., Llompart, C. (2001). : El «Garumniense» prepirenaico. Rev. Soc. Geol. Espafia, 14(1-2): 47-56.

Sanz-Parera, M (1981). El sistema hidrogeologico de banyoles-la garrotxa. Tesis Doct. Univ. Autònoma de Barcelona. 306 pp

Solé Sugrañes, L. (1970). Estudio geológico del Prepirineo Español entre los ríos Segre y Llobregat. Tesis doctoral. Univ. de Barcelona; 495 pp.

Solé Sugrañes, L. (1973). Algunos aspectos de la tectónica del Prepirineo Oriental entre los ríos Segre y Llobregat. Acta Geològica Hispánica VIII (1973), n.o 3, pp. 81-89.

Ullastre, J.; Masriera, A. (2000). Noves dades sobre les relacions paleogeogràfiques del massís del Port del Comte amb les Serres marginals sud-pirinenques (Pirineu català, Espanya). Treballs del Museu de Geologia de Barcelona, 2000, Vol. 9, p. 155-6, https://raco.cat/index.php/TreballsMGB/article/view/72441

Verdú, J.M., Batalla, R.J., Poch, R.M., (2000). Dinámica erosiva y aplicabilidad de modelos físicos de erosión en una cuenca de montaña mediterránea (Ribera Salada, Cuenca del Segre, lleida, España). Pirineos. 155. pp. 37 - 57.

Vergés, J. (1993). Estudi geològic del vessant sud del Pirineu oriental i central. Evolució cinemàtica en 3D. Tesis doctoral. Inédita. Universitat de Barcelona (UB), Facultat de Geologia, 203 pp.

Vergés, J. (1999). Estudi geològic del vessant sud del Pirineu oriental i central. Evolució cinemàtica en 3D (Monografies Tècniques). Institut Cartogràfic de Catalunya., n. 7, 192 pp. ISBN-13 : 978-8439349839

Vías, J.M.; Andreo, B.; Perles, M.J.; Carrasco, F.; Vadillo, I.; Jiménez, P. (2006) Proposed method for groundwater vulnerability mapping in carbonate (karstic) aquifers: The COP method. Hydrogeol., 14, 912–925. https://doi.org/10.1007/s10040-006-0023-6

Vicente-Serrano, S.M., López-Moreno, J.I., Beguería, S., Lorenzo-Lacruz, J., Sanchez-Lorenzo, A., García-Ruiz, J.M., Azorin-Molina, C., Morán-Tejeda, E., Revuelto, J., Trigo, R., Coelho, F., and Espejo, F. (2014). Evidence of increasing drought severity caused by temperature rise

in southern Europe. Environ. Res. Lett. 9 (4), 044001. https://doi.org/10.1088/1748-9326/9/4/044001

Viviroli, D., Kummu, M., Meybeck, M., Kallio, M., Wada, Y., 2020. Increasing dependence of lowland populations on mountain water resources. Nature Sustainability, 1-12. https://doi.org/10.1038/s41893-020-0559-9

Zwalhen (2003). COST Action 620. Vulnerability and Risk Mapping for the Protection of Carbonate (Karst) Aquifers. Final Report (link).

2 IMPLEMENTATION OF DATA COLLECTION AND PROCESSING

In this chapter 2 of the thesis, I have incorporated several sections to describe the methodologies and approaches taken to deploy the field and office work to meet the objectives of the thesis, and which have not been explicitly included and documented in any of the four scientific papers presented (which corresponds to the chapters 3, 4, 5 and 6). Therefore, its inclusion in this previous chapter later helps to supplement the information about the origin of the collected and elaborated data before going into addressing the specific objectives of each of the scientific papers presented in the thesis by compendium.

2.1 Geological and hydrogeological preliminary campaign

The fieldwork done for the thesis began at the end of spring 2013. Between the April until August of that year, preliminary tasks were carried out: Firstly, a field reconnaissance of the geology and a collection of complementary geological information was done. Secondly, the inventory of groundwater points (springs and water wells) was carried out after collecting bibliographic information about their existence, which served to organize and program and hydrogeochemical sampling field campaigns and the laboratory work of the following two years.

2.1.1 Geological field reconnaissance and new data collection

Regarding the geological aspects, in the first place, a field reconnaissance of the geology (structures and geological units of the area) was carried out, according to the information available in the geological map 1:50,000 (ICGC, 2007). At this moment it was started a campaign to acquire new dip /azimuth field data in the outcrops of the different lithologies present in the Port del Comte structural unit. The objective was to be able to build later on a 3D surface-based geological model at a regional scale that would allow, firstly, to elaborate several longitudinal and transversal geological cross-sections in the study area, and secondly, understand the structure in relation to the catchment and discharge sub-basins of the main karst springs of the Tertiary karstic hydrogeological system, corresponding to the PPEc unit as has been described in subchapter 1.2.1.

The structural data measurement field campaign began in July 2013 and was extended with four more campaigns: October 2013, August 2014, August 2015 and November 2017 (Table 1 and Figure 1). The method used for data collection is that of measuring the line of the maximum slope with respect to north (azimuth), and then its inclination with respect to the horizontal (dip): for example 300/17, where 300 would be the angle with respect to north and clockwise, and 17 would be the angle from the horizontal. The measurements were made using a manual Silva compass and a Garmin Etrex GPS to locate the points and with the use of the 'FieldMOVE Clino' App (by Midland Valley) digital compass-clinometer for data capture on an Android smartphone that geolocate the point. FieldMove Clino is a Midland Valley geological field mapping app designed for geologists utilising digital data collection. The datum for the location of the points was the EPSG:25831 - ETRS89 / UTM zone 31N.

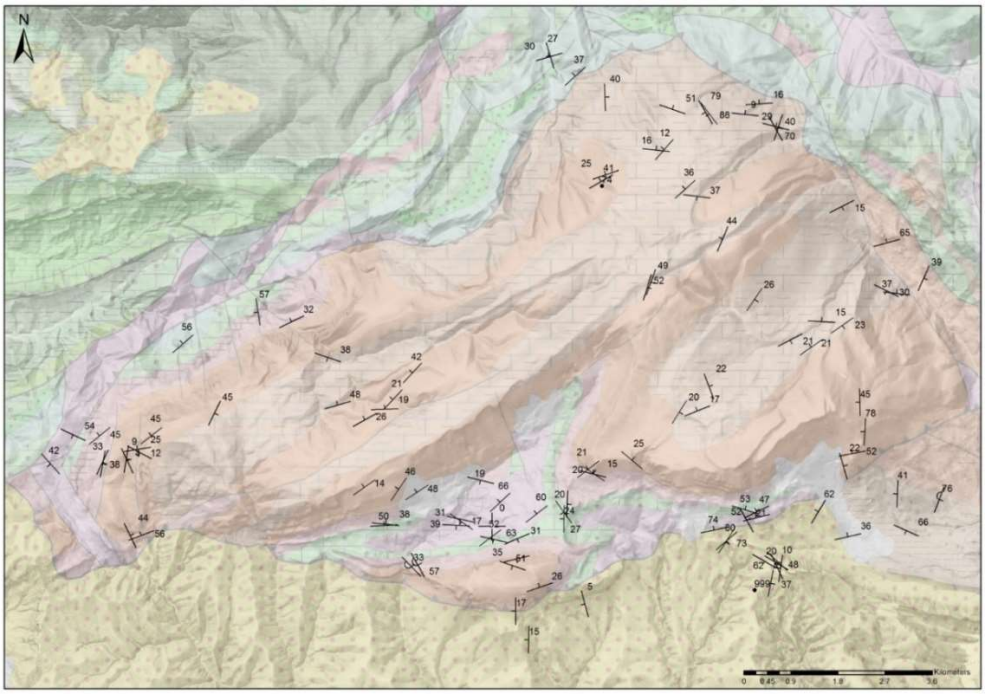

Figure 2. 1 New 107 dip/azimuth measurements collected during the fieldworks

The results of the field campaign are found in Table 11.1.1, in chapter 11. SUPPLEMENTARY MATERIAL. APPENDIXES OF DATA. The new data collected from the field complement the data available from the MAGNA serie sheets of the IGME geological maps of Oliana (Sheet 291), Sant Llorenç de Morunys (Sheet 292) and Gósol (Sheet 254) (Ardèvol, et al 2020, 2020b, Berastegui, et al. 2001).

Review of previously available geological map 1:50.000

The basic geological information of this thesis has been the Geological database 1:50,000 of the ICGC (ICGC, 2007) and the memories of the Oliana (Sheet 291), Sant Llorenç de Morunys (Sheet 292) and Gósol (Sheet 254) MAGNA geological maps (second edition). During the fieldwork, a reconnaissance of the lithologies described in the existing geological map was carried out. The geological mapping work was outside the scope of this work. However, in the various field trips it has been possible to observe certain discrepancies in the cartography such as geological contacts not correctly located, outcropping geological units in larger areas, new outcropping units previously not mapped that could be relevant for the subsequent interpretation of the hydrochemistry of springs. On the other hand, the styles of the map have been modified to offer a better visual understanding of the structure and the different associated lithologies. The different observations made on the field are described below:

- **Figure 2. 2**: Review of the "Alinyà-Roc de la Pena Anticline" (**Figure 2. 3**) cartography: based on the field observations from PK 14 of the C-463 road (before Alinyà town) and from Coll d'Ares, it was interpreted that the "Roc de la Pena Anticline" extends much further to the west (right figure) of what is represented in the cartography (left figure). This agrees with the cartographic trace of the geological units.

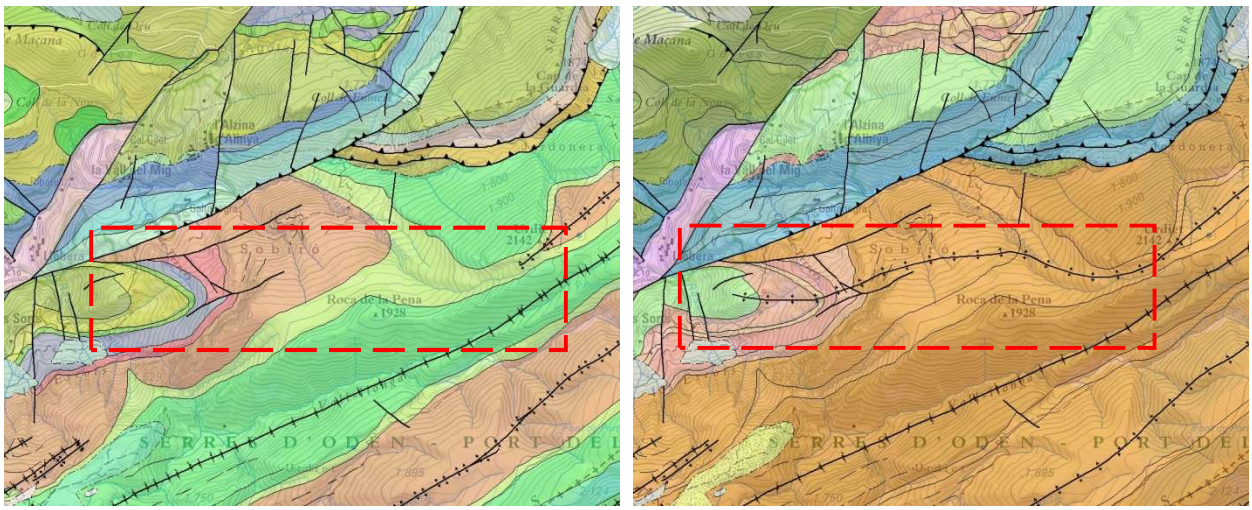

Figure 2. 2 Comparison of the previous map (ICGC, 2007) and the reviewed one in the area of 'Roc de la Pena Anticline'

Figure 2. 3 View of the Alinyà - Roc de la Pena anticline from the hermitage of Santa Pelaia.

- **Figure 2. 4**: Review of the "geological contacts in the 'Coll de la Mata' and the 'Montnou' area: based on the field observations, at this point the traces of the Muschelkalk (Tm) facies have been modified in Montnou (its surface has been extended to the east), whereas the extension of the Garumnian (KMgp) in 'Collada de la Mata' has been modified. The latter totally replaces the Upper Cretaceous facies (KCMca) that were first mapped.

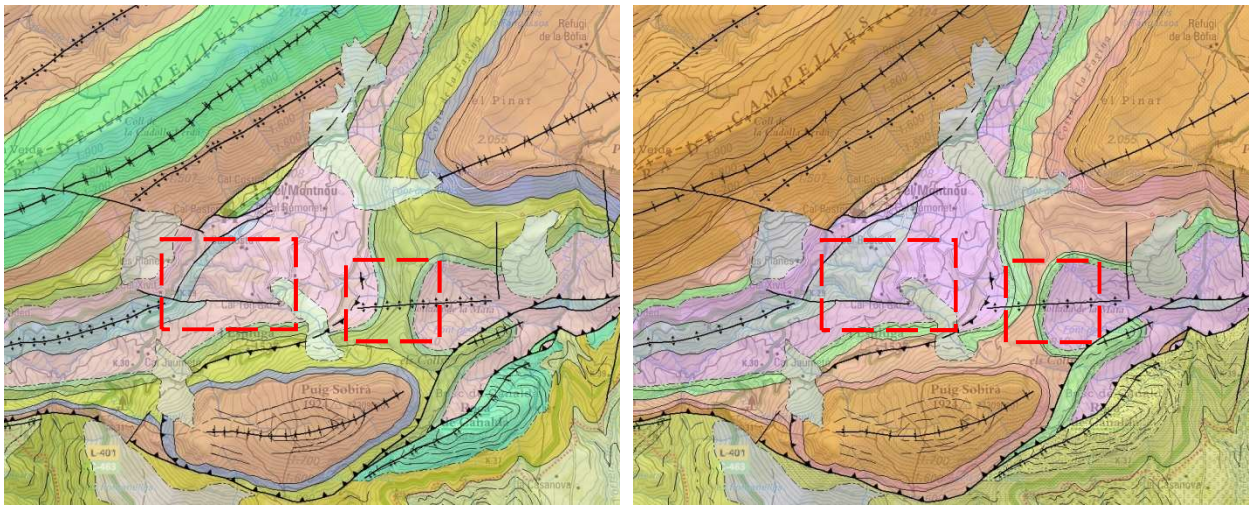

Figure 2. 4 Comparison of the previous map (ICGC, 2007) and the reviewed one in the area of 'Coll de la Mata- Montnou'.

- **Figure 2. 5**: Review of the klippe and geological units of the 'Arp area' and surroundings: based on the field observations, it can be concluded that in the Arp area, in the Nordic ski resort of Tuixén – La Vansa, a small outcrop of red and gray clays has been located that are attributed to the Keuper (Tk) facies under the Triassic-Jurassic facies. This can outcrop has allow later on explained the hydrogeochemical characteristics of some springs. On the other hand, further to the west, in the area of the Sangonelles and Arderic springs, the contact between the PEci, PEcp2 and PPEc units has been redrawn. In the surroundings of the municipality of Padrinàs, the lower contact of the sandstones and shales of the Adraén Formation (KSCat) with the Triassic-Jurassic breccias (TJb) has been reconstructed.

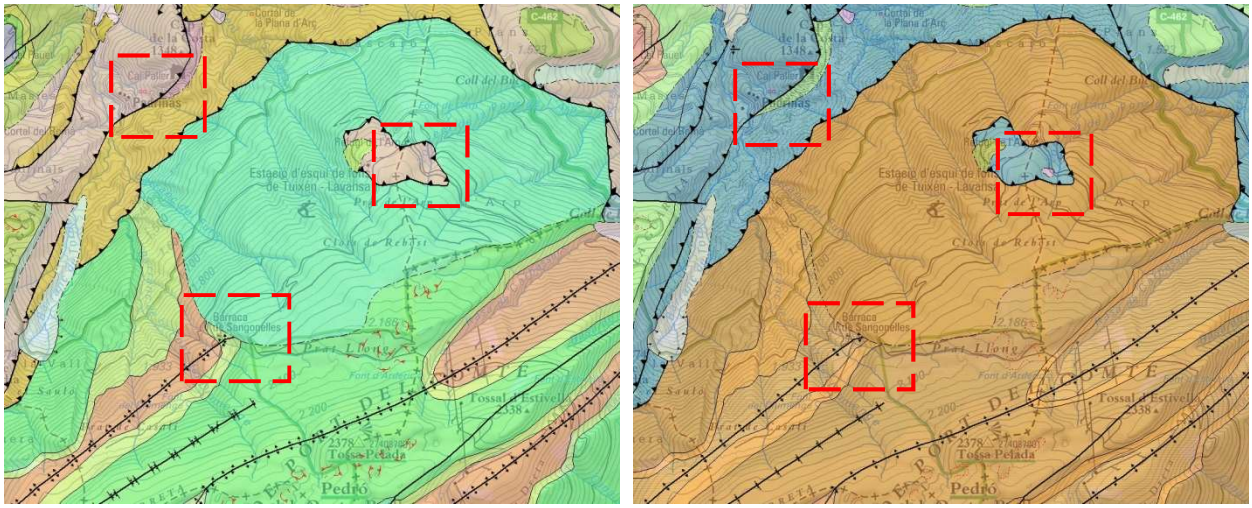

Figure 2. 5 Comparison of previous map (ICGC, 2007) (a) and the reviewed (b) in the area of 'Arp'.

- **Figure 2. 6**: Review of the south area of the 'Serra de Querol' based on the field observations, small modifications were made with the lower contact of the Garumnian (KMgp) with the Upper Cretaceous (KCMca), in the area of Les Costes and the Garganta karst spring, as well as the upper contact of the Garumnian with the alveoline limestones units (PPEc) in the Rock of Querol.

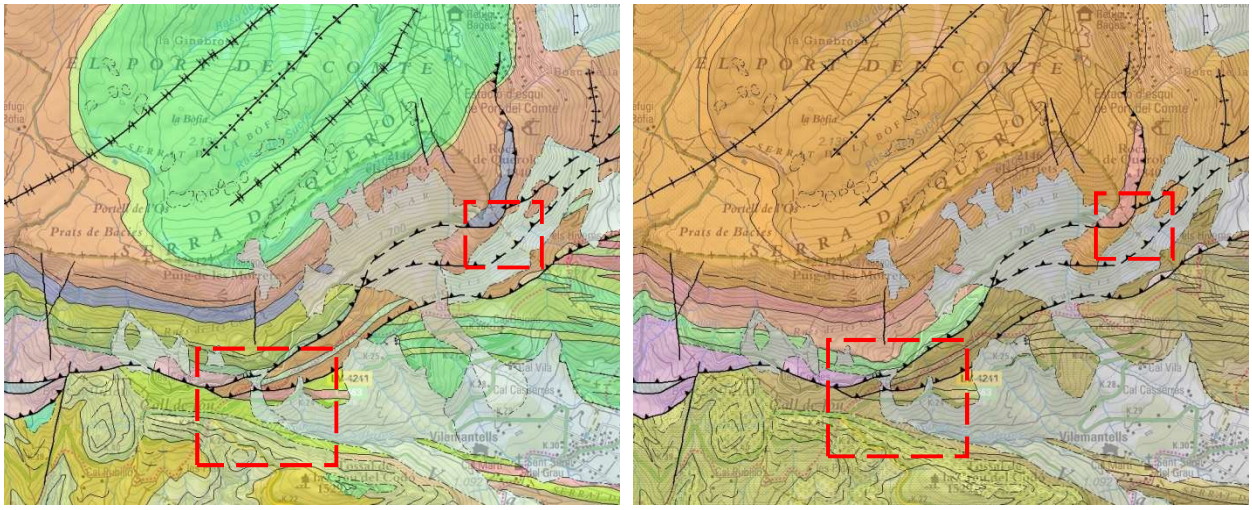

Figure 2. 6 Comparison of previous map (ICGC, 2007) (a) and the reviewed (b) in the area of 'Serra Querol'.

- **Figure 2. 7**: Review of the south area of the 'Cambrils town and Colldemà area': based on the field observations in the town of Cambrils, the PPlgc and PPcm units from the original 1:50,000 map have been merged into a single PPcm unit. In the 'Colldemà area', the upper contact of the Garumnian (PPcm unit in this case) with the limestones (PPEc) has been redrawn.

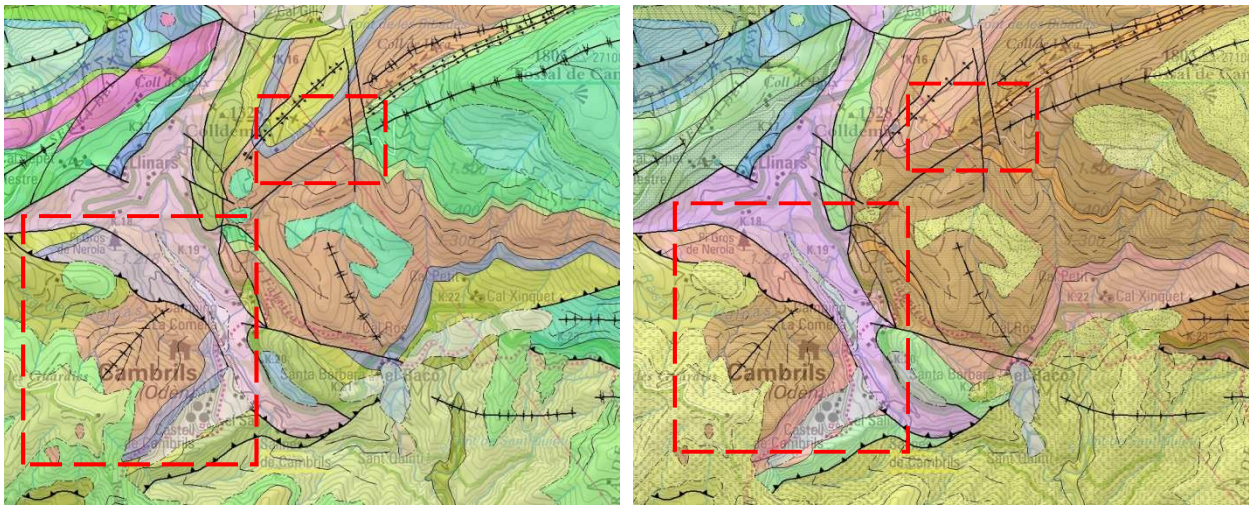

Figure 2. 7 Comparison of previous map (ICGC, 2007) (a) and the reviewed (b) in the areas of 'Cambrils-Colldemà'.

- On the other hand, since it is not the objective of this work, the Quaternary have all been merged into a single unit (Q), which encompasses all the fluvial, slope and karstic deposits. In general, they tend to have little power and quite small extensions.

The geological cartography finally synthesized and used throughout the thesis is shown in the **Figure 2. 8**, where the names of the anticlines and certain local toponyms are indicated.

The simplification made can be summarised as follow:

- Triassic: Tk + Tm
- Jurassic: TJb + TJcd + JLcb + JLmc + JLcd + JLcm + JDd
- Lower Cretaceous: CIcc + CIcr + CImmc + CNb
- Upper Cretaceous: Cb + CKml + KCTp + KSCat + KScm + KScm1 + KSCmv + KSCc + KCMca + KMga
- Garumnià: KMgp + PPcm1 + PPcm
- Lower Eocene (Cadí Formation): PPEc
- Lower Eocene (Coronas Formation): PEci
- Lower Eocene (Roc de la Penya Formation): PEcp1 + PEcp2
- Middle Eocene: PEgmf + PEccv + PExb + PEcgc2 + PEcgb6 + PEcgb7 + PEmb + PEcgm1 + PEm1 + PEm2 + PEm + Pec + PEalb + PEcgb
- Upper Eocene: PEcgs + PEOcc + PEOgs + PEOcgs + PEOcmg
- Neogene: Nd and Quaternary: Q

It should be noted that although the changes described above cannot be depicted at the used map scale, for the interpretation of the conceptual model of hydrogeological and hydrogeochemical functioning of some of the springs in their own local situation (discussed in chapters 4 and 6), had to be considered.

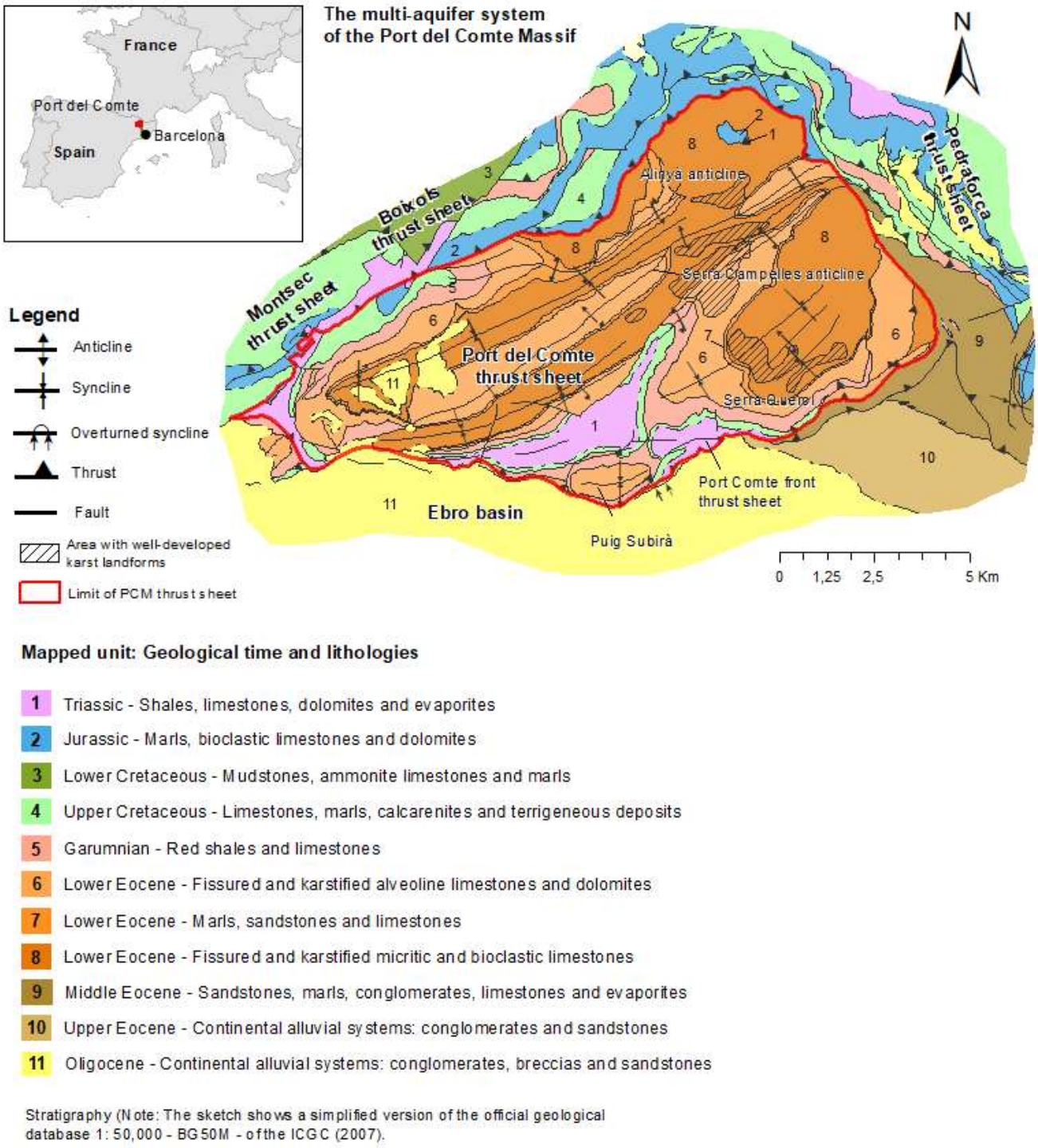

Figure 2. 8 Geological cartography finally synthesized used throughout the thesis.

2.1.2 Fieldwork for conducting the preliminary groundwater point inventory

Between April and May 2013, a compilation of bibliographic information on the existence of water points in the whole area of the Port del Comte high mountain karst area was carried out.

The first consulted source of information was the topographic databases at scales 1:5,000 and 1:25,000 (ICGC and ICGCb, 2013), to which were added the information from several PABCAT reports (ACA, 2005), the information extracted from the BDH hydrogeological data base of Catalan Water Agency (ACA, 2013), the information from the previous hydrological and hydrogeological studies (Gencat 1990, 1991, 1992; Núñez & Gil, 2003), and various dissemination websites among other sources. All points collected were centralized in a GIS database. It is important to emphasize that the starting information was not, as expected, directly usable to plan the field work, but rather required an arduous task of filtering and cleaning by crossing information, taking into account that there are often points in the same location named with different toponyms, points named with the same name located in different locations although within the same area, and points that actually do not have a natural origin. Based on the filtered and cleaned information, the field work and inventory was planned and carried out in July 2013. The objective of the inventory work was to recognize the existence, the precise position, the toponym and the natural state of the points, and as far as possible, the acquisition of first physical-chemical and flow rate data (Q, EC and Tº).

In total more than 120 locations were visited but only 100 water points were located or what remains of some of them, from which 75 springs, 4 dug wells, 3 boreholes water wells in production and 8 boreholes wells that were encountered not equipped, dry, or they found lost. **Figure 2. 9** shows the resulting map where the visited points are indicated as well as the rest of the bibliographic information previously collected on the possible location of water points. As can be seen in the figure, points were visited both within the Port del Comte thrust sheet and through its external boundary. The typology of the springs and their state of conservation is very uneven. There are 4 important karstic springs that have been the basis of the thesis work: they correspond to the points SANT QUINTÍ spring (153 L/s; in summer 2013), CARDENER spring (146 L/s), AIGUANEIX spring (48 L/s) and CAN SALA (also known as ‘El Racó’) spring (23 L/s). The rest of the springs were found with much lower flow discharges, from 5 L/s to 0.001 L/s or some of them directly dry (**Figure 2. 10**).

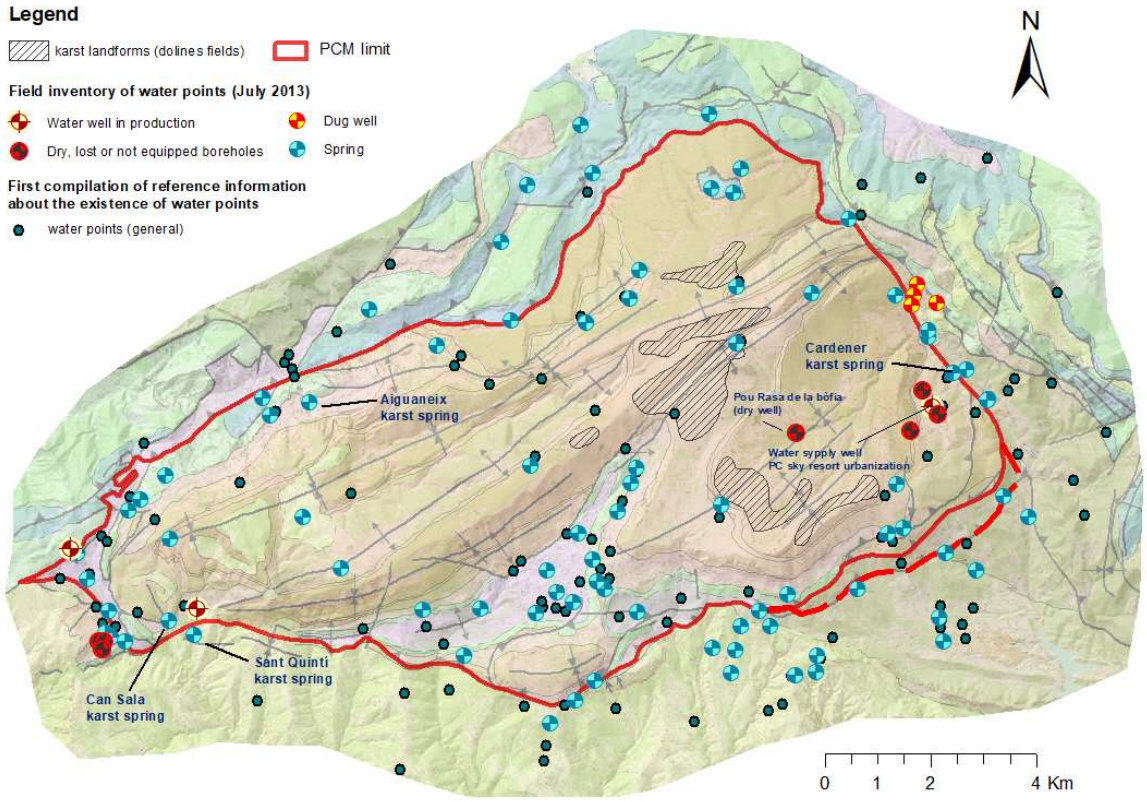

Figure 2. 9 Documented and visited (inventoried) points (July 2013).

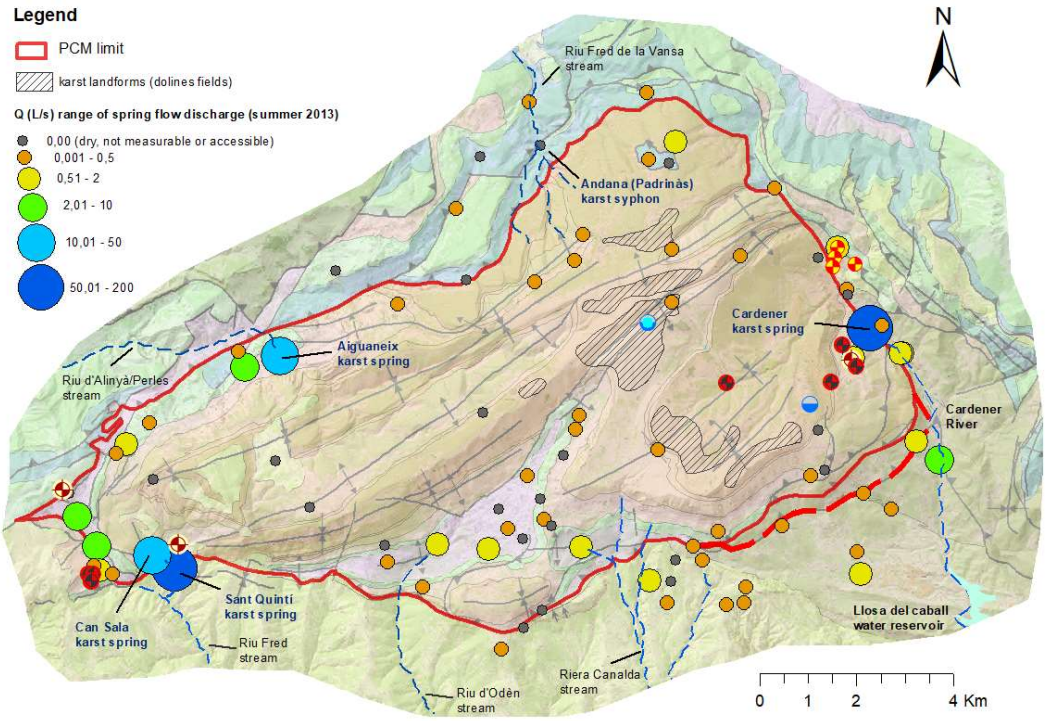

Figure 2. 10 Map of flow discharges measured in summer 2013 of all inventoried points

From the result of the field inventory carried out in July -August 2013, it was decided to select a total of 43 points (all corresponding to springs) to plan the sampling and gauging campaigns for the hydrogeological characterization of the Port del Comte study area along the fieldwork of the thesis. Apart from the 4 main karstic springs (Aiguaneix, Can Sala, Sant Quintí and Cardener), to select the rest of the points, the criterion followed was the representativeness of the geological formations, accessibility, the state of the point, and the drainage flow. **Figure 2. 11** shows the map with the points finally selected. The results of the inventory field campaign is found in Table 9.1.3, subchapter 9.1 of chapter 9. SUPPLEMENTARY MATERIAL. APPENDIXES OF DATA. In this table, the 43 selected springs and its ID used (M-XX) are indicated. In chapter 2.5 'Implementation of hydrogeochemical field campaigns', it is explained how the hydrochemical sampling fieldwork was organized in the following steps of the thesis carried out between September 2013 and October 2015.

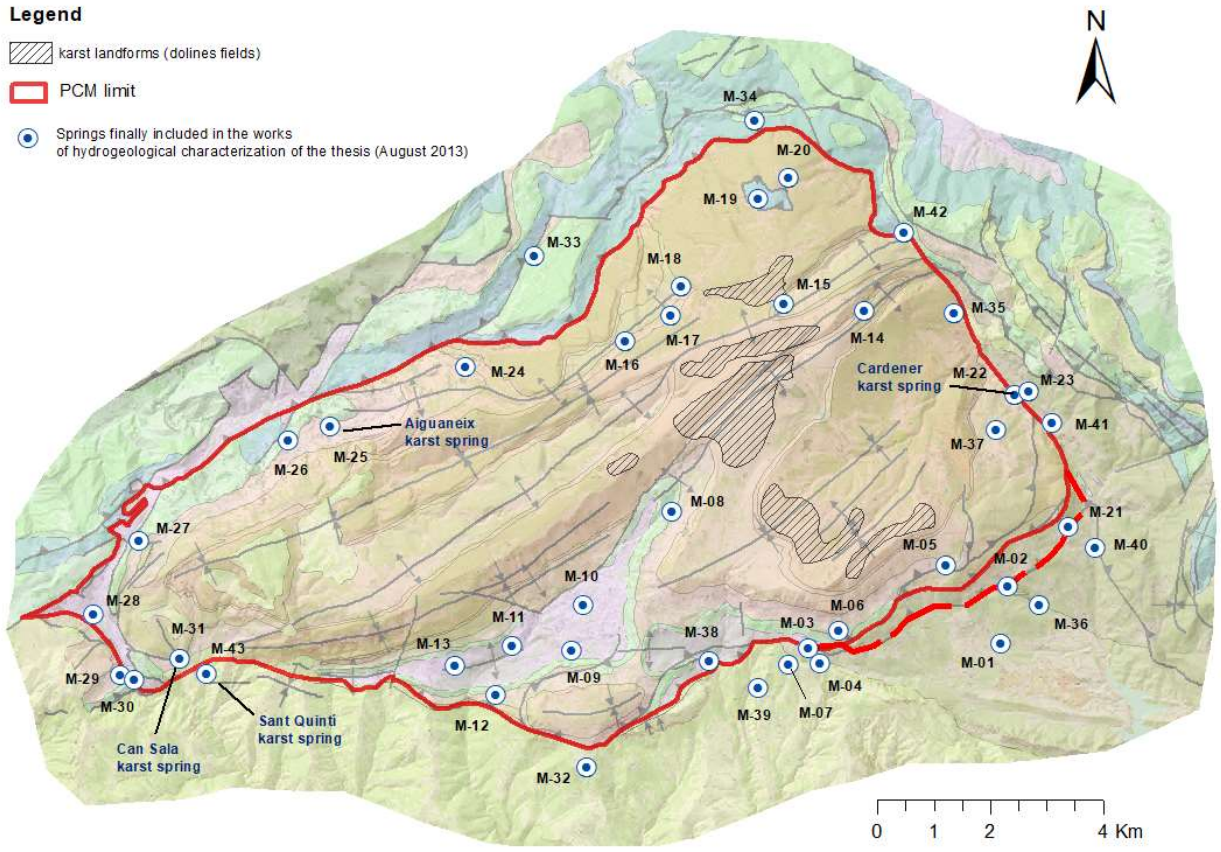

Figure 2. 11 Map of the final springs selected for the hydrogeological characterization of the study area

2.2 2D and 3D geological modelling

2.2.1 2D cross-section preparation

2D and 3D geological modeling has been based on surface structural dip/azimuth data and the existing 1:50.000 geological maps, in a simplified way, from both the ICGC (2007) and the MAGNA serie sheets of the IGME. The dip/azimuth data were acquired in several field campaigns, set out in chapter 2.1 and extracted from the MAGNA Oliana Sheet 291 (Berastegui, et al 2001), Sant Llorenç de Morunys Sheet 292 (Ardèvol et al, 2000) and Gósol Sheet 254 (Ardèvol et al, 2000b) geological maps, being a total of 309 points (108 new collected field dip/azimuth data and 202 acquired from the MAGNA database). The collected dip/azimuth data are shown in the following screenshot of the modeling process (**Figure 2. 12**) on the digital elevation model (topography) with traces used for the geological cross-section construction.

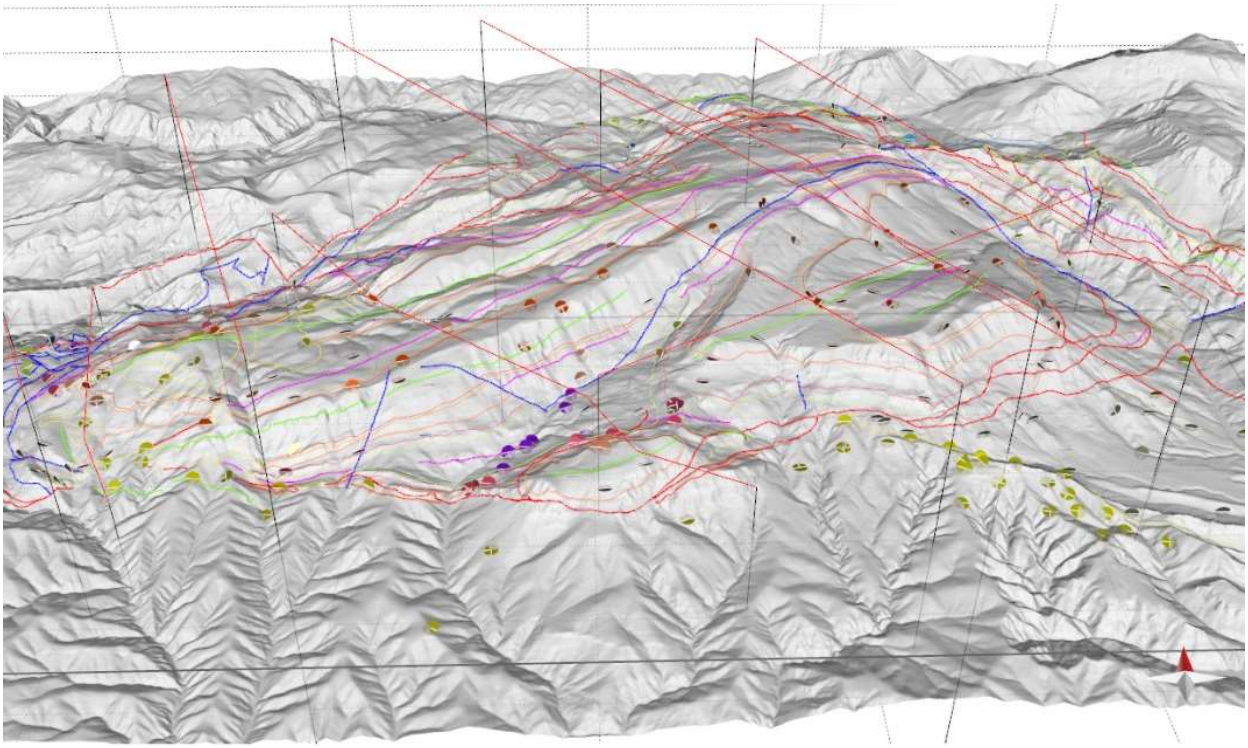

Figure 2. 12 Screenshot of a 3D projected view of the dip/azimuth data and cross-sections prepared with MOVE 3D geological modeling software

Based on the new modified version of the geological map 1:50000 cartography and the collected dip/azimuth data in field campaigns and from the Magna sheets of the IGME, a total of 9 geological

cross-sections have been elaborated, from which 8 are transversal to the main geological structures (anticlines/synclines/faults) and the last parallel to them. These geological cross-sections then have been used to build the surface-based 3D geological model. The cartography has been simplified joining geological units with hydrogeological sense. The final and resulting cartography, is showed here after in **Figure 2. 13** and **Figure 2. 14**.

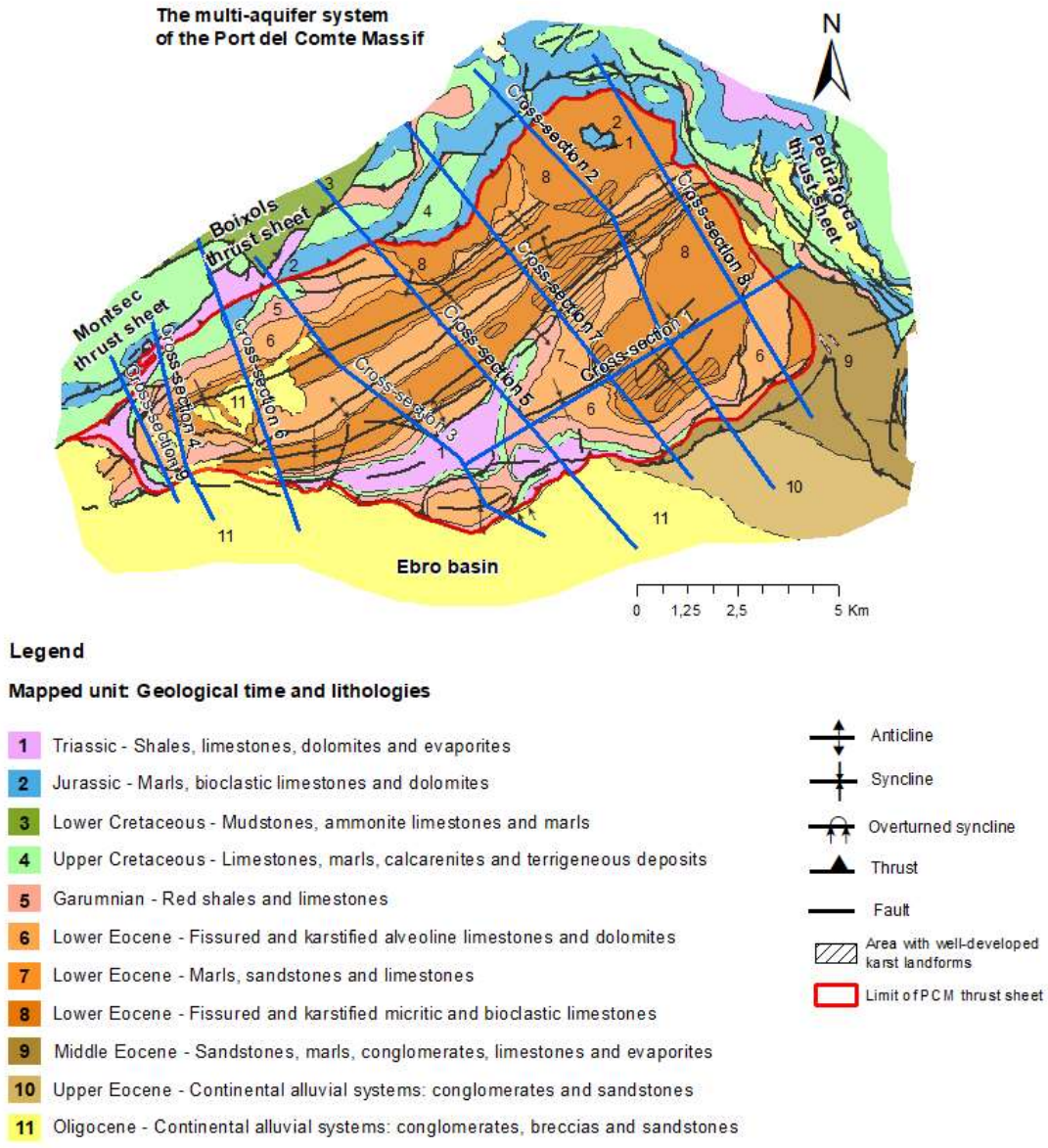

Figure 2. 13 Simplified version of the previous modified geological map and location of the cross-sections

The geological cross-sections have been built using the MOVE® 2017.1 software (Midland Valley Exploration Ltd) which allows import and integrate different data types such as the dip/azimuth

field data, the digital elevation model and the geological map in fully geo-referenced space.

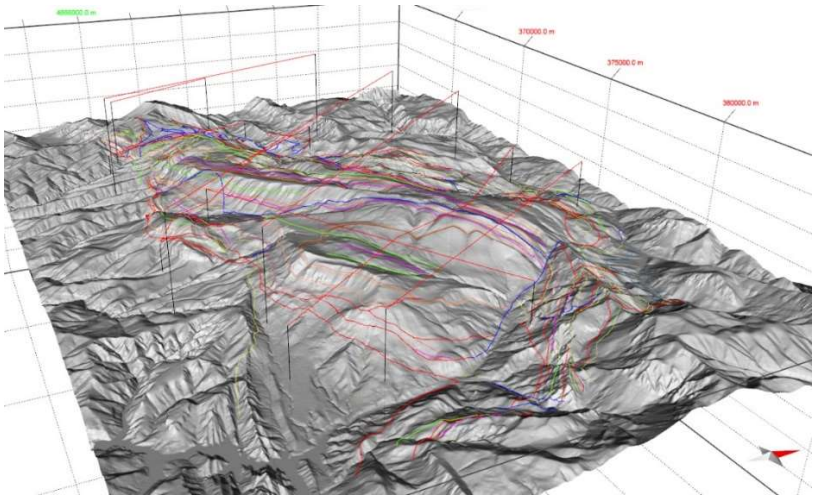

Figure 2. 14 3D representation of the digital elevation model, the simplified geology and the cross-sections.

From these data and a basic stratigraphy (with thickness estimated according to data from the Magna sheets of the IGME) the different cross- sections have been made. The stratigraphy considered 12 layers (**Figure 2. 15**) In total 9 cross-sections have been built by creating the contacts according to specific data and / or known contacts, extrapolating in depth in parallel according to the Kink method which considers each dip measurement to define a zone where the dip is constant and considering constant thickness (**Figure 2. 16** and **Figure 2. 17**). Finally, and manually, they have been adapted to the general structure, to the existing contacts in the cartography and to the topographic surface.

Stratigraphy | Rock Properties | Strat. Column | Compaction Curves

	Horizon	Colour	Rock Type	Age	Thickness	Active
1	Neogen		Default	2.0 Ma		☑
2	Oligocè		Default	23.0 Ma		☑
3	Eocè superior		Default	34.0 Ma		☑
4	Eocè mitjà		Default	38.0 Ma		☑
5	Fm. Penya		Default	41.0 Ma	500.0 m	☑
6	Margue...		Default	48.0 Ma	80.0 m	☑
7	Calcària ...		Default	53.0 Ma	850.0 m	☑
8	Garumnià		Default	61.0 Ma	400.0 m	☑
9	Cretaci superior		Default	65.0 Ma	300.0 m	☑
10	Cretaci inferior		Default	99.6 Ma		☑
11	Juràssic		Default	176.0 Ma		☑
12	Triàsic		Default	245.0 Ma		☑

Figure 2. 15 Stratigraphy used in the modeling of geological sections and the 3D model in Move 2017.

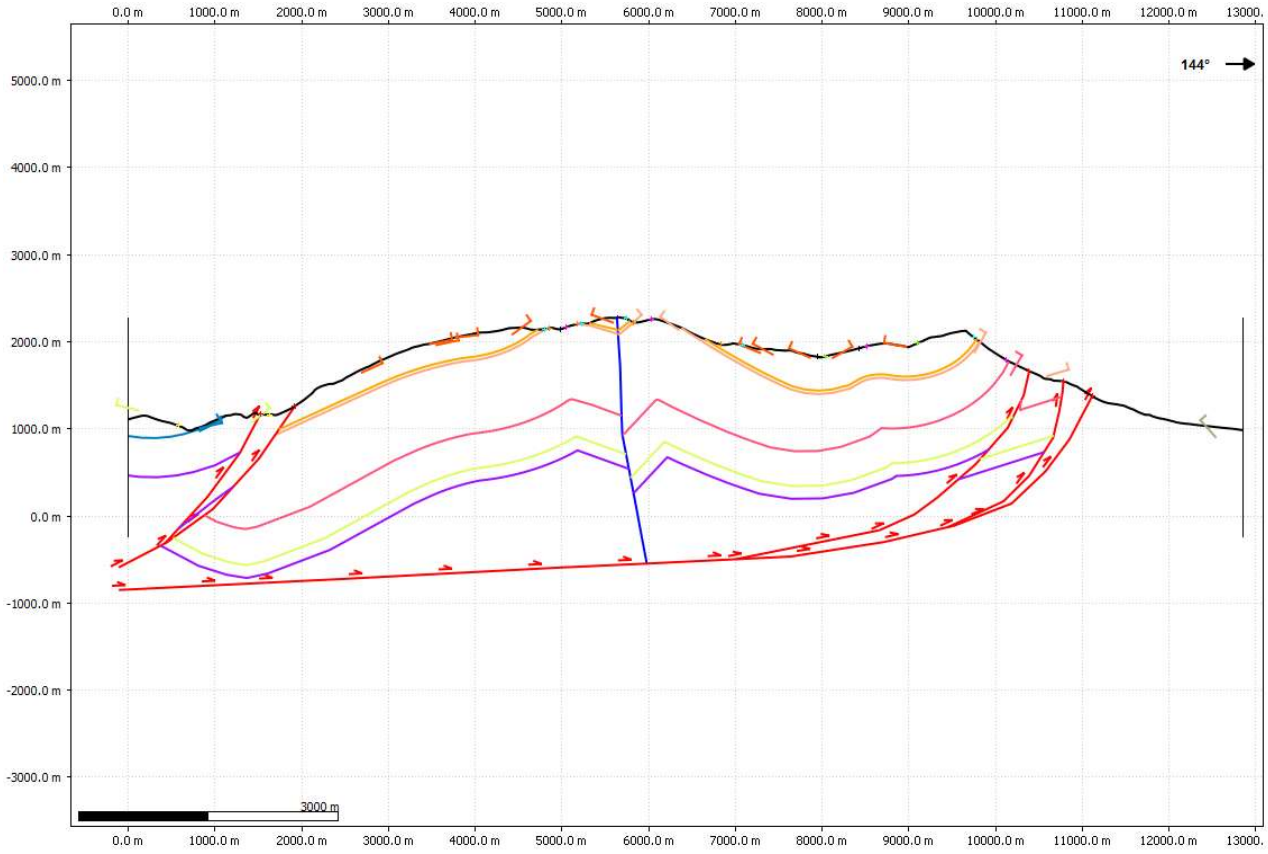

Figure 2. 16 Example of a geological cross-section construction within the Move 2017 suite. Dip / azimuth data and geological contact projections on the topographic line can be observed.

Geological cross-section - 1

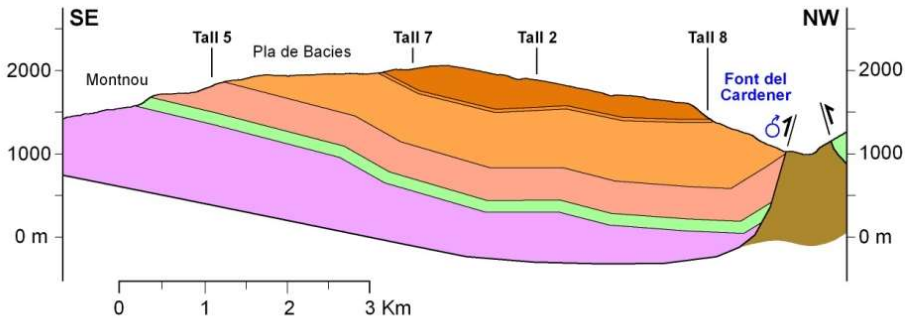

Geological cross-section - 2

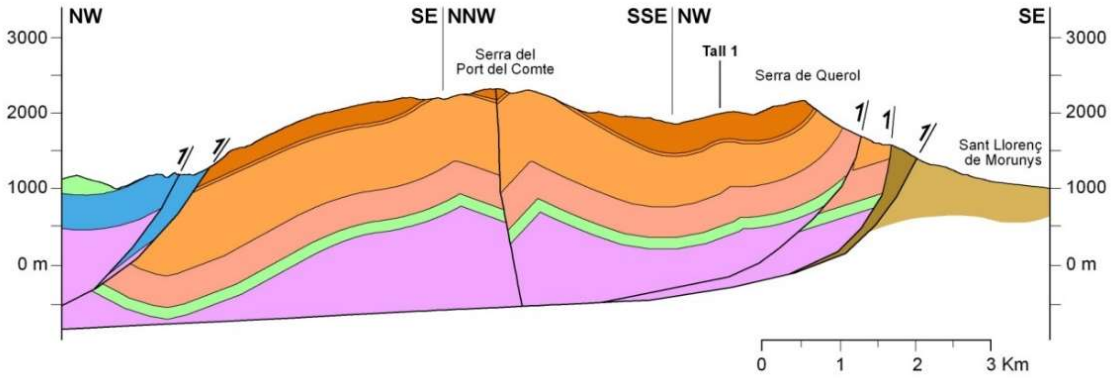

Geological cross-section - 3

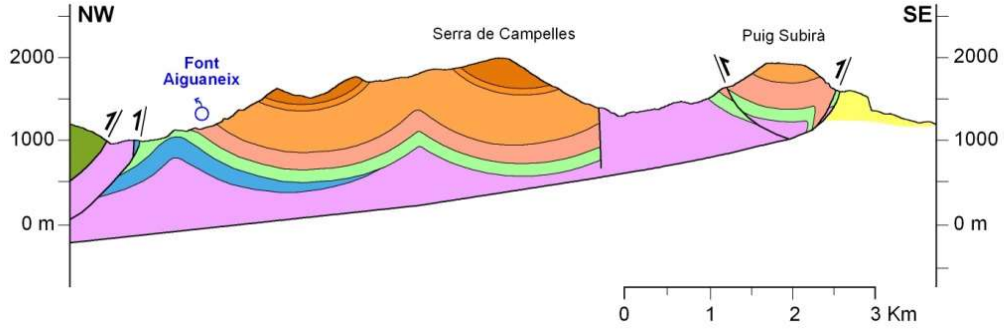

Geological cross-section - 4

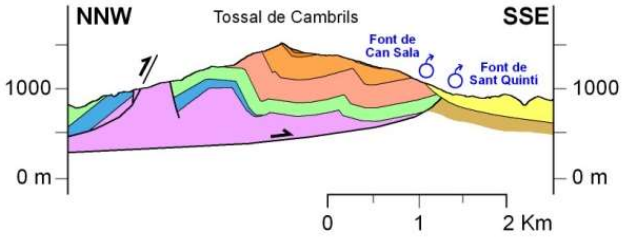

Geological cross-section - 5

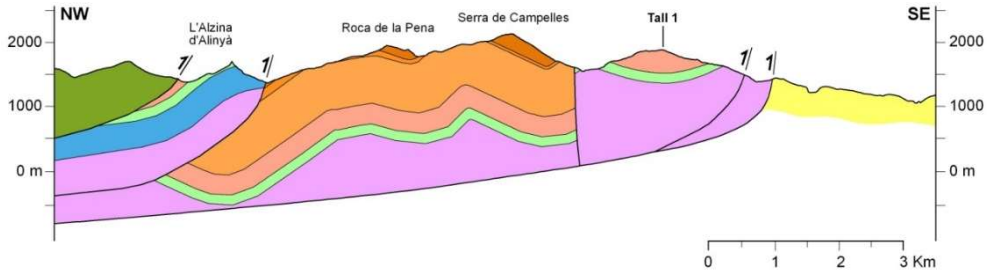

Geological cross-section - 6

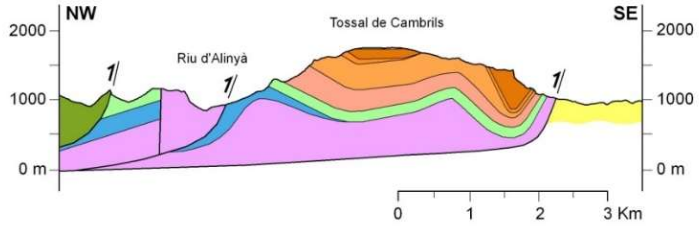

Geological cross-section - 7

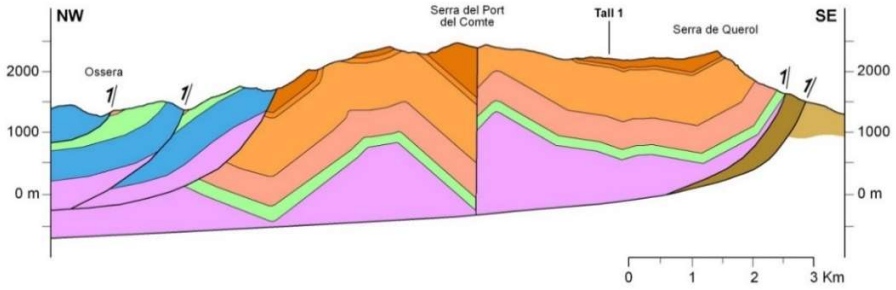

Geological cross-section - 8

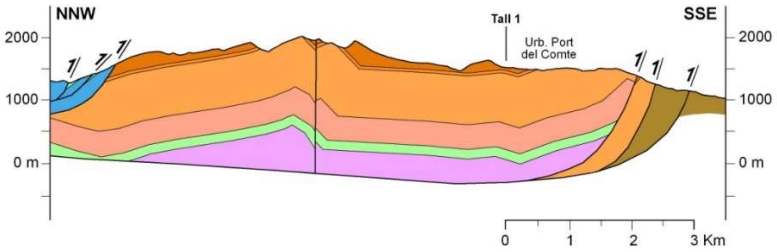

Geological cross-section - 9

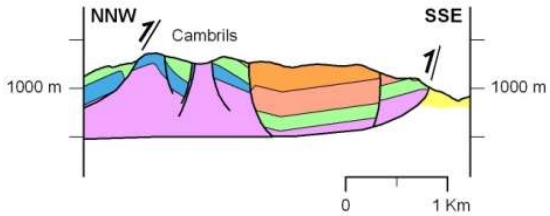

Figure 2. 17 Collection of 9 geological cross-sections

2.2.2 Construction of a 3D surface-based geological model (3DGM)

The Surface-based 3D geological modeling has been built directly using the 8 parallel geological cross-sections (numbers 2 to 9, **Figure 2. 17**). The lithological contacts in these sections have been extended above the topographic surface so that the surfaces contact the digital terrain model and can be drawn correctly and cut through the same topographic surface (**Figure 2. 18**). The model has been greatly simplified from the original cartography in order to better represent the structure of the study area. In this case, a basal sheet (Port del Comte thrust sheet), a western thrust sheet (evolving the Bóixols and Serres Marginals thrust sheets), a fault in the centre of the mantle that divides the structure in two blocks north and south, and a fault to the north-west (**Figure 2. 19**).

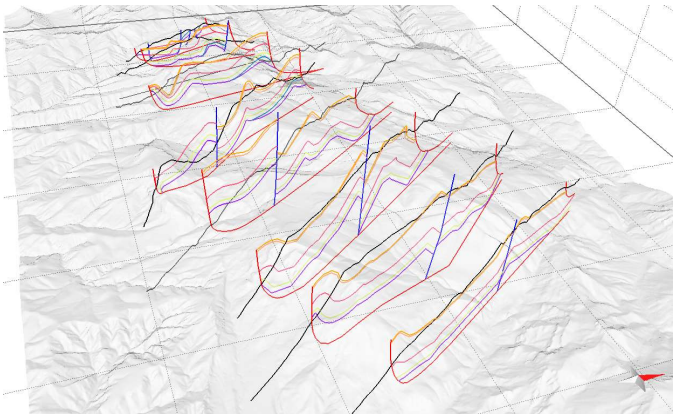

Figure 2. 18 Screenshot of the 3D representation of the geological cross-sections.

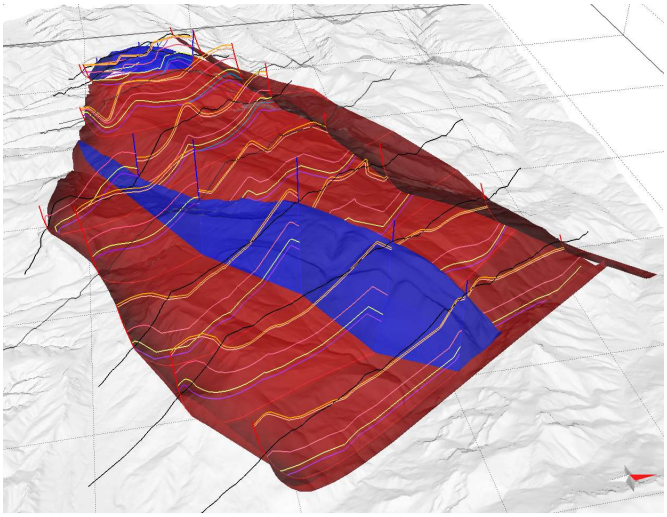

Figure 2. 19 Screenshot of the 3D view of the simplified tectonic structure considered in the Surface-based 3D geological model (tectonic thrust surfaces are represented in red and fault surfaces in blue)

Once the geological structure was defined, different surfaces were constructed according to the previously defined stratigraphy (**Figure 2. 20** and **Figure 2. 21**). The surfaces are finally cut by the topographic surface.

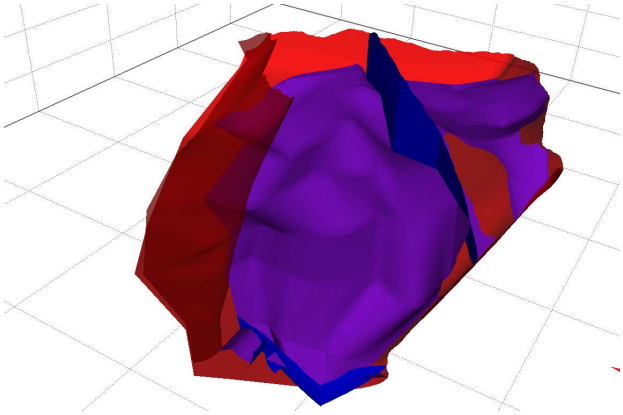

Top of Triassic – base of Jurassic / Upper Cretaceous

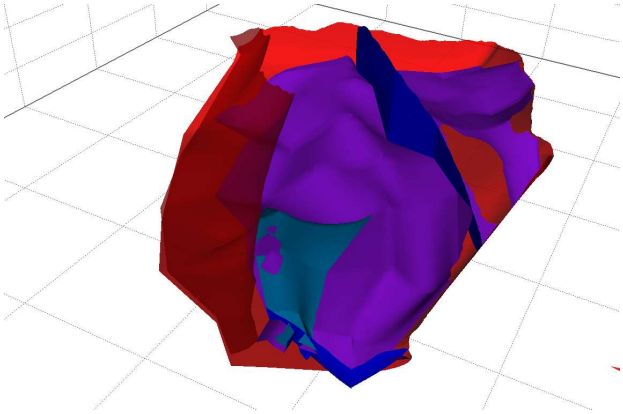

Top of Jurassic – base of Upper Cretaceous

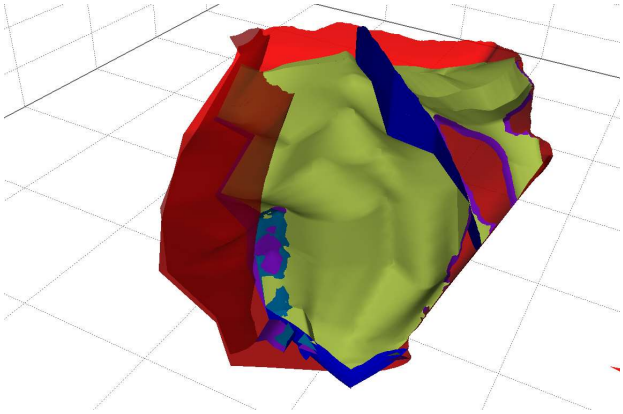

Top Upper Cretaceous – base of Garumnian

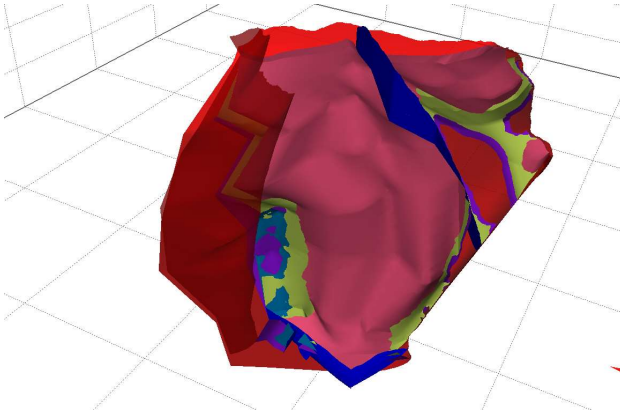

Top of Garumnian – base of Cadí Formation (PPEc)

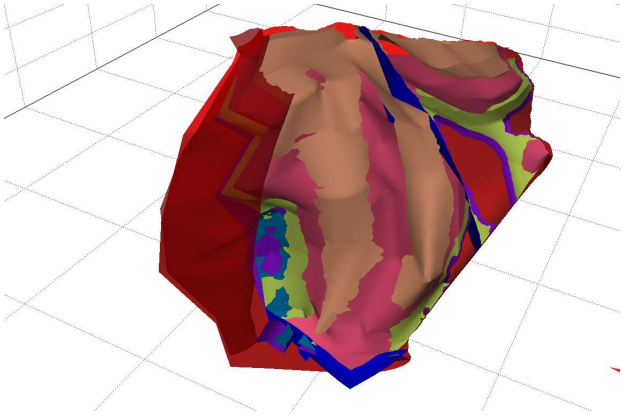

Top of Cadí Formation (PPEc) – base of Coronas Formation (PEci)

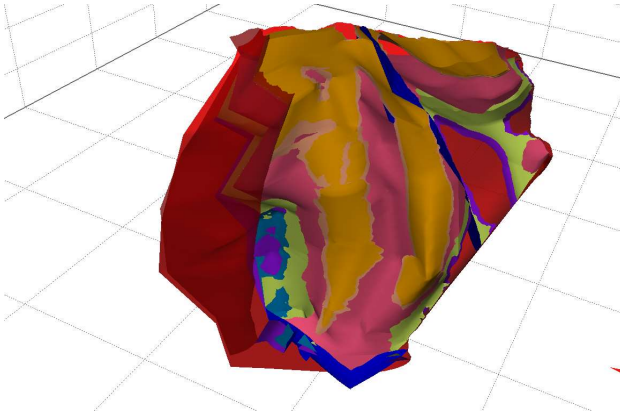

Top of Corones Formation (PEci) – base of Penya Formation (PEcp1 + PEcp2)

Figure 2. 20 Screenshot of the different 3D modelled geological surfaces

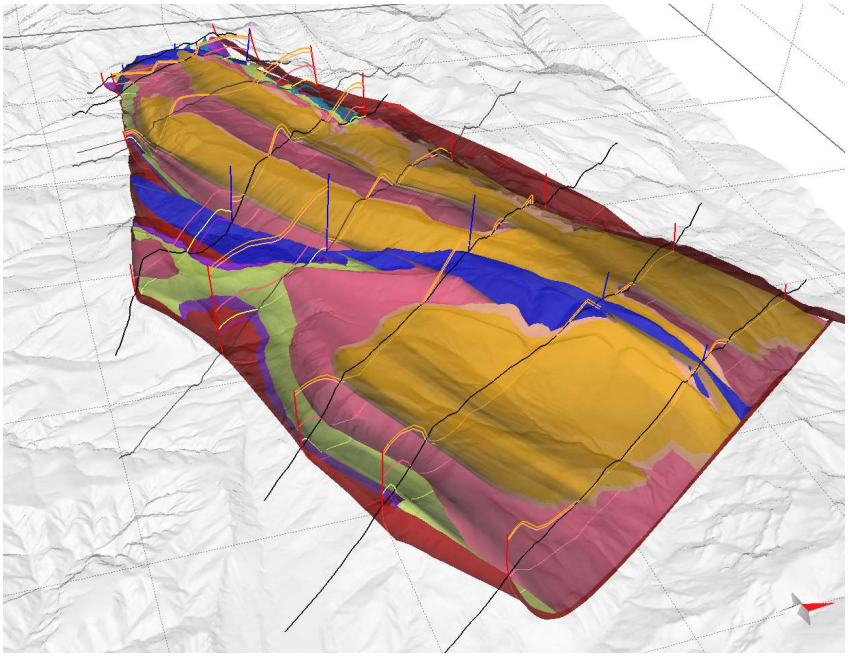

Figure 2. 21 Screenshot of the different final 3D modelled geological surfaces (tectonic thrust surfaces are represented in red and fault surfaces in blue)

Based on the modeling results, it can be concluded that:

- The Port del Comte mantle has pairs of anticline-syncline folds following NE-SW direction.
- The Port del Comte fault, in a NE-SW direction (like the axes of the folds) divides the massif and the structure of the sheet into two blocks. This fault is responsible for the different dip of the fold axes to the north and south of the mantle. This characteristic is very important from the hydrogeological point of view of the karst system of Port del Comte, as it conditions the direction and groundwater flow discharge of the main karst springs, as explained in the hydrogeological conceptual model presented in Chapter 6:
    - south block: the axis of the fold dip to the NEE where Cardener spring (the most important spring in the area) discharge.
    - north block: the axis of the fold dip to the SW where the other main karst springs of the Port del Comte Tertiary karst aquifer (PPEc unit) discharge: the Sant Quintí, Can Sala and Aiguaneix springs.

- The most important geological body / layer in the mantle with 1000m thick and the one with a more developed karst (which conditions all the hydrogeology of the massif), is the

PPEc or Alveoline Limestone (Cadí Formation). This constitutes the main karst aquifer of the Port del Comte system.

2.2.3 The use of the 3DGM to infer the geometries of groundwater reservoirs

A critical aspect of many research work done up to know in the literature for understanding their hydrologic functioning of karst springs is the delineation of the reservoir geometry and their boundaries. The use of 3D structural geological models in hydrogeological studies helps to understand the geometry and to establish the conceptual models of high mountain karst aquifers.

Butscher and Huggenberger (2007) developed the aquifer base gradient (ABG) approach. This method was based mainly on the assumption that in unconfined, mature, karst the development of conduits and the resulting conduit flow are strongly influenced by the geometry of the aquifer bottom. Therefore, this approach includes geometric modeling of karst aquifers. Later, Malard, A. et al (2012) and Jeannin et al (2013) of the Swiss Institute of Speleology and karst-Research (SISKA) developed the KARSYS approach. This method builds an explicit conceptual model of the karst aquifer, assuming that the groundwater flow is predominantly conditioned again by its geometry and the assumed hydraulic gradients. So, this method is based on the use of 3D structural geological models combined with some basic hydraulic principles and assumption considered that are taking place within the karst media to delineate in 3D the subsurface extension of the karst reservoirs.

The main principles of the KARSYS approach are: (i) The 3D geometry (usually the bottom) of the aquifer set the framework in which flow processes take place (ii) Aquifers are flooded or saturated below the level of the main perennial springs (iii) The expansion of the water table upstream of the main springs can be considered lower than 1% (at low water stage).

Different authors have shown the consistency of the results of this method in various alpine aquifers (Turk, J. et al., 2013 and Ballesteros, D. et al., 2015 among others). In the South-Eastern Pyrenees, - in the Catalan territory - up to the date of writing the thesis it has not been used, and the Port del Comte is the first case study.

Implementation of the KARSYS approach to the he specific case of the Port del Comte model:

The results obtained from the surface-based 3D geological model prepared to understand the internal structure of the Port del Comte were used here to infer the potential extension of the saturated underground reservoir of the main four karst springs of the Port del Comte, i.e. the Aiguaneix spring (identified in this case as S-01 in the **Figure 2. 22**, located at the altitude 1098 m a.s.l.), Can Sala spring (S-02, 1063 m a.s.l), Sant Quintí (S-03, 944 m a.s.l) and Cardener (S-05, 1040 m a.s.l). The aim of delimiting these potential extension of the reservoirs, from the geological structure point of view, is to be able to understand if the existence of one or several independent reservoirs can be assumed or if, on the contrary, there can be a certain degree of intercommunication between them, and also explain the existence of a groundwater flow diffusively discharging to the La Vansa river basin to the North of the port del Comte thrust sheet.

The assumptions considered in the modelling were the following:

- On average, the regional level of groundwater discharge related to the high mountain karstic aquifer associated with the PPEc unit (Cadí Formation) is between 940 and 1100 m a.s.l.
- The whole karst system presents 4 main groundwater discharge directions:
    - 1) In the southern block, it drains to the northeast through the Cardener spring (S-05 in Figure 26) following the main syncline of the Serra de Querol – Serra de la Bòfia.
    - 2) The north block (separated to the south by the fault NE-SW) discharges following three main directions:
        - 2.1.) towards the southwest through the Can Sala and Sant Quintí springs (into the Riu Fred basin, affluent of the Ribera Salada and then to the Segre River) following the axis of the main syncline of the Serra de Campelles.
        - 2.2.) Secondly, to the northwest, following the southern slope of the Alinyà anticline axis through the Aiguaneix spring (feeding the Perles River, tributary of the Segre Basin)
        - 2.3.) finally to the Northeast, following the northern slope of the Alinyà anticline axis diffusely towards the basin of the Riu Fred de la Vansa (tributary of the Segre River).

- The bottom of the regional karstic reservoirs associated with the PPEc unit coincides with the top of the Garumnian materials.

- The groundwater flow at the base of the saturated aquifer always is conditioned by the direction and inclination of the synclines axes of the structure, although in the upper unsaturated part, can be perfectly assumed without any doubt that the epikarst developed through conduits, caves, siphons and fractures may favour deviations in the groundwater flow path into horizontal direction and therefore traverse said synclinal and anticlinal axes. This hypothesis implies that the catchment boundary (i.e., the global recharge area of each karst spring) may perfectly cover an area beyond the structural limits of the anticlinal and syncline axes, and therefore, it must be assumed that the resulting extension of the saturated underground reservoirs does not have to coincide with the delimitation of their respective surface extension of the recharge area.

- The highest part of the massif is at 2,386 m a.s.l. (Pedró dels Quatre Batlles peak). The PPEc limestone unit reaches a maximum thickness of 1300m, and an unsaturated zone can average 1000m thickness.

- For the case study, a gradient of up to 1%, -considering similar studies (Turk et al., 2013) - was finally considered to conceptually infer the possible maximum geometries of the reservoirs associated with the main outputs (i.e., the 'regional springs') of the karstic system in low water period. Notwithstanding, the hydraulic gradients upstream of the karstic springs in the ‘very low’ water stage specifically for the Can Sala spring (less important than the Cardener and San Quintí springs) could be close to 0%, since during the monitoring period (see sub-chapter 2.5) has almost dried up in some moments.

    - The only information in the whole area about the possible gradients comes from the following information within the Cardener spring basin:
        - A borehole well (named Pou Rasa de la Bòfia) located in the southern block in the Cardener spring basin (see **Figure 2. 9**), drilled in 2004 at an elevation of 1,832 m a.s.l. reached a height of 1416 m a.s.l. without finding the regional water table, data that would confirm that the gradient cannot exceed 9% in

any case up to the point of discharge (S-05 spring) and that the level must indeed be at a lower level.

- The water supply well named 'PC sky resort urbanization' (see figure 15) drilled in 1993 from 1,348 m a.s.l. encountered the groundwater static level at a depth of 280 m (1,068 m a.s.l.). This point is located 740m away from the discharge point at 1040 m a.s.l. which means that the gradient at the NE boundary of the aquifer can be estimated at 3.7%.

The final modelled underground reservoirs obtained with the Port del Cote structural geological model can be seen in the **Figure 2. 22**. The results have allowed to sketch the discharge domain and inferring the flow-paths directions of the main regional springs.

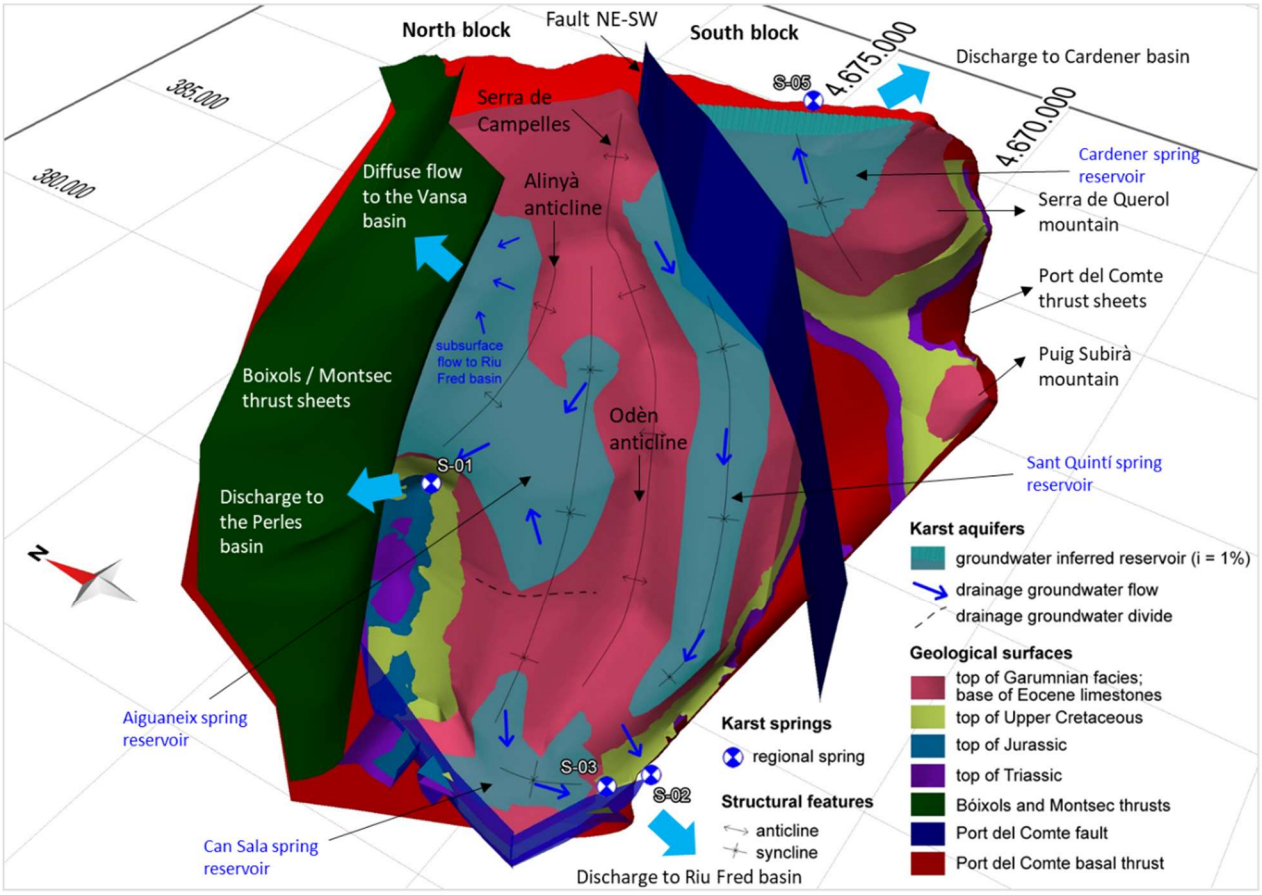

Figure 2. 22 Screenshot of a 3D view of estimated aquifer reservoirs considering a 1% gradient, where S-1 is Aiguaneix spring; S-02 Sant Quintí spring; S-03 Can Sala spring and S-05 Cardener spring.

The results suggest that:

- The Sant Quintí spring has a recharge area that reaches the top of the massif in the Estivella area. The NE-SE fault that separates the north to the south block is assumed that could act as a hydraulic barrier. From this area a groundwater flow is produced in a south-westerly direction, following the syncline until the thrust front is found, where it must connect through a karst conduit developed in the conglomerates of the POcgs unit through which the spring discharge at the end. The geometry of the base of the limestones of the PPEc unit allows delimiting an extension of the reservoir very considerable with just 1% gradient

- The Cardener spring captures the waters of the southern block and drains them following the synclinal towards the NE. Its recharge must also take place from the highest part of the massif, sharing the capture zone with the San Quintí spring, as has been also demonstrated by the isotopes (Chapter 6). Regardless, at the depth where the aquifer level is located, the NE-SW fault can act as a hydraulic barrier.

- The Can Sala spring has a clearly different origin than that of Sant Quintí. Its recharge zone does not extend to the upper parts of the massif as has been also demonstrated by the isotopes (Chapter 6), and the capacity of its reservoir is much lower. For the simulated scenario of 1% of gradient, the reservoirs would be disconnected. This explains why it can dry out at times of little precipitation, as has been observed sometimes along the field work.

- The Aiguaneix spring is conditioned by the axis of the Alinyà anticline (also named 'Roc de La Pena anticline, in Verges, 1993) (see **Figure 1. 10** chapter 1), which separates on its southern flank the waters that drain into the Perles River through this spring, mainly through an underground flow, from another groundwater flow that discharge diffusely towards the basin of the Riu Fred de la Vansa on the north flank of the anticline. Its recharge zone, as in the case of the Can Sala spring, is restricted to medium altitudes.

The results of the 3D model were presented in the "5th European Meeting on 3D Geological Modelling"; Bern, Switzerland, 2019. **Figure 2. 23**

3D GEOLOGICAL MODELLING AS A TOOL FOR SUPPORTING SPRING CATCHMENT DELINEATION IN HIGH-MOUNTAIN KARST AQUIFERS.

The case study of the Port del Comte (Eastern Pyrenees) aquifer.

Ignasi Herms (1,5), J. Agustí Nuñez (1), Montse Colomer (1), Georgina Arnó (1), Jorge Jódar (2), Albert Soler (3), Albert Griera (4)

(1) Institut Cartogràfic i Geològic de Catalunya (ICGC), Barcelona (Spain) / (2) Instituto Geológico y Minero de España (IGME), Zaragoza, (Spain) / (3) Facultat de Ciències de la Terra - Universitat de Barcelona, Barcelona (Spain) / (4) Dept. de Geologia. Facultat de Ciències. Universitat Autònoma de Barcelona (UAB), Bellaterra (Spain) / (5) Universitat Politècnica de Catalunya / Contact e-mail:

ABSTRACT

This study presents the first 3D structural geological model (3DGM) of the Port del Comte (PC) aquifer (Catalan Pyrenees), a high mountain karst aquifer (HMKA) formed by Lower Eocene fissured and karstified limestones and dolomites. The drought prone geographical location of PC along with the short groundwater transit times reveal the high vulnerability of this HMKA. Moreover, the simulations of climate models for latest emission scenarios considered in the 5th report of the IPCC (2013) forecast an increase of temperature and a decrease of precipitation in the PC for the end of the 21st century that threaten the water resources generated in this still vaguely characterized HMKA. The use of a 3DGM helps to understand the aquifer geometry and to conceptualize its hydrogeological functioning, a necessary step to numerically simulate the behavior of such HMKAs.

GENERAL SETTINGS

The elevation of the PC massif ranges between 900 to 2387 m a.s.l., and it has an area of 110 km². The unconfined karst aquifer presents very thick unsaturated zone (~1000 m) in the highest part of the massif, which is the zone where the main recharge areas, mainly associated to surface expressions of epikarst development, are located. The mean groundwater discharge of (~15 hm³/yr) postulates this aquifer as one of the most important HMKA of the eastern Pyrenees.

The massif constitutes an independent structural and regional hydro-geological unit delimited by faults, where apart from the karst development, the geologic structure and stratigraphy influence both the storage capacity of the aquifer and the location of the main springs discharging the system.

Figure 1. geological map (modified from ICGC, 2007)

MATERIALS AND METHODS

The existing structural and conceptual geological model (Vergés, 1999), the available geological maps (ICGC, 2007) and new geological fieldworks (2013-2015) have provided the basis for building the surface-based 3DGM, which is implemented by using the MOVE® 2017.1 software (Midland Valley Exploration Ltd). The balance assessment of the model has not been specifically addressed in this research / Steps: 1) new dip/azimuth data collection and revision of geological contacts and units in fieldwork. 2) construction of 9 geological cross-sections using the Kink Method for parallel folds. 3) construction the 3D geological surfaces (horizons and faults).

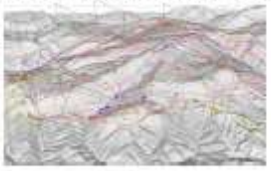

Figure 2. Dip/azimuth data set projected in 3D

Figure 3. View of the projected 9 Geological Cross-Sections (GCS) elaborated to constructed the 3DGM

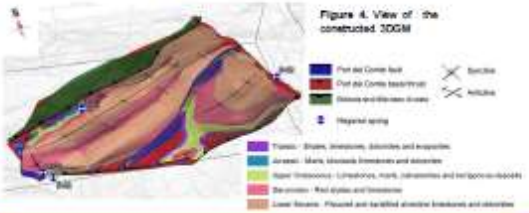

Figure 4. View of the constructed 3DGM

RESULTS AND DISCUSSION

The final subsurface-based 3DGM (Fig. 4), contains 6 geological horizons and the main faults and regional aggregated thrusts (Fig. 5).

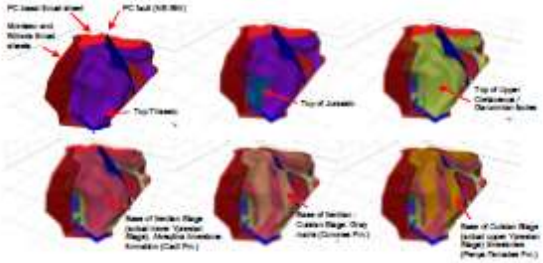

Figure 5. modelled geological surfaces.

The information provided by the 3DGM allows to sketch the discharge domain and inferring the flow-paths of the main regional springs (Fig.7). Although hydraulic gradients upstream from the karst springs at low-water stage could be close to 0%, a gradient up to 1% (Turk et al., 2013) is considered to infer conceptually the possible max reservoirs geometries associated to the main outlets of the karst system (i.e. the 'regional springs').

Figure 6. Final modelled 3D geological volume for the fissured and karstified limestones and dolomites

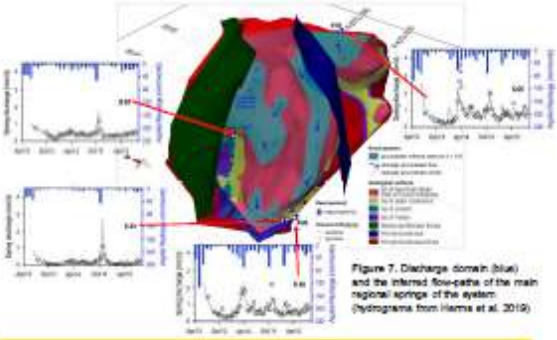

Figure 7. Discharge domain (blue) and the inferred flow-paths of the main regional springs of the system (hydrograms from Herms et al. 2019)

CONCLUSIONS

- The use of 3D geological models (3DGM) in hydrogeological studies (e.g. the KARSYS approach (Malard, A. et al 2012, Jeannin et al 2013, Turk, J., et al 2013 and Ballesteros, D., et al 2015 among others) helps to understand the geometry and conceptualize the functioning of karst systems.
- The combined interpretation of the 3DGM with hydrogeochemical data like ^{18}O and ^{2}H isotopes from precipitation and groundwater improve this understanding of the hydrogeological functioning of the system allowing to better sketch the recharge and discharge domains. The results in this research have been used afterward in a hydrological model to study the main transit time of the system (Herms et al., 2019).

ACKNOWLEDGEMENTS

This work was partially supported by PhD program on Natural Resources and Environment 2013-2019 within the GREM (UPC) and MAiMA (UB) research groups. It has also had the collaboration of IGME, UAB and GH-UMA.

REFERENCES

- Ballesteros, D., et al. (2015). KARSYS hydrogeological 3D modeling of alpine karst aquifers developed in geologically complex areas: Picos de Europa National Park (Spain). Environ Earth Sci DOI 10.1007/s12665-015-4712-0
- ICGC, 2007. Mapa geològic comarcal de Catalunya 1:50 000. Full Alt Urgell (SDGC50M).
- Jeannin, PY., et al., (2013). KARSYS: a pragmatic approach to karst hydrogeological system conceptualization. Assessment of groundwater reserves and resources in Switzerland. Environmental Earth Sciences, 69(3): 999-1013 p.
- Herms I., et al. (2019). Contribution of isotopic research techniques to characterize high-mountain Mediterranean karst aquifers: The Port del Comte (Eastern Pyrenees) aquifer. Science of The Total Environment Vol 656, Pg 209-220. https://doi.org/10.1016/j.scitotenv.2018.11.188
- Malard, A. et al (2012) SWISSKARST Project - how to document the karst aquifers in Switzerland using the KARSYS approach. Geophysical Research Abstracts Vol. 14, EGU2012-2607, 2012
- IPCC (2013). Climate Change 2013: The Physical Science Basis. Cambridge University Press.
- Turk, J., et al (2013). Interpretation of hydrogeological functioning of a high plateau using the karsys approach: The case of Trnovsko-Banjska Planota (Slovenia). Acta carsologica, vol 42, No 1, 14pp
- Vergés, J. (1999). Estudi geològic del vessant sud del Pirineu oriental i central. Evolució cinemàtica en 3D. PhD Thesis. University of Barcelona (UB), Faculty of Geology, 180 pp.

6th European Meeting on 3D Geological Modeling. 21st – 24th May 2018, Bern (Switzerland)

Figure 2. 23 Poster presented to the "5th European Meeting on 3D Geological Modelling"; Bern, Switzerland, 2019. Herms et al.2019

2.3 Design and implementation of a network of rain gauge collectors

2.3.1 Use of H and O isotopic composition of water molecule

One of the tools used in the development of the thesis, are the H and O stable isotopes of water molecule (δ^2H and δ^{18}O). These are natural tracers in the water cycle that have been used either to characterize the mean and seasonal variation of the isotope content of precipitation and in the spring groundwater discharging. Its interpretation has allowed us to determine:

- The Local Meteoric Water Line" (LMWL) of the Port del Comte area (Chapter 3).
- The Mean Transit Times (MTTs) of the main karst springs (Chapter 3).
- The recharging altitudes of the different springs in the area (Chapter 6),
- The impact of climate change under various RCP (*) scenarios of emissions (Chapter 5).
- The hydrogeological conceptual model of functioning of the aquifers (Chapter 6).

where (*) RCP are Representative Concentration Pathway, a greenhouse gas concentration (not emissions) trajectory adopted by the Intergovernmental Panel on Climate Change (IPCC).

2.3.2 Materials used for designing and installing a network of precipitation collectors

In order to characterize the isotopic composition of H and O of water precipitation (snow or direct rain), at the beginning of the field work (during the autumn of 2013), it was designed, built and installed a network of 8 rain gauge collectors (**Figure 2. 24**, **Figure 2. 25** and **Figure 2. 26**). Its sole purpose was to collect precipitation water (rain or snow) at various altitudes from the minimum 800 m. a.s.l to almost 2000 m. a.s.l. throughout the area in order to analyse the isotope content. It was not the objective to monitor the precipitation episodes in terms of quantity, due to two complete meteorological station already exist in the area (as described in subchapter 1.2.3) with daily time series of P – precipitation and T – air temperature.

CoCORAH (CoCoRaHS RG202 Official 4 "Long Term Professional Rain and Snow Gauge) type rain gauges collectors imported from the USA were used for the installation. These were installed on a 2m high wooden masts and were tightened with the original support that comes with the rain

gauge. The rain gauge collector consists of a polycarbonate cylindrical deposit with a diameter of 10,8 cm. The rain gauge collector include a top funnel that captures and guides precipitation into the storing deposit, where according to the technical procedure for the stations of the Global Network of Isotopes in Precipitation (GNIP) of the International Atomic Energy Agency (IAEA), a 0,5 cm paraffin oil floating layer is added to avoid evaporation. These were installed at elevations between 896 and 1935 m a.s.l. (P-01 a P-08; **Figure 2. 24**). taking special care to cover a significant altitudinal variation. Rainfall situation data is shown in **Table 2. 1.**

Table 2. 1 Location and identification of the 8 CoCoRaHS total rain gauges - chemical – installed

ID rain gauge	Name (in Catalan) and location	X	Y	Z (m. a.s.l.)
P-01	Refugi de l'Arp. Tuixen La Vansa	378052	4674452	1935,6
P-02	Bassa Clot de la Vall (tanca perimetral). Direcció Estivella	379262	4670685	1946,1
P-03	Refugi Bages (Port del Comte)	381407	4669713	1767,8
P-04	Casa Xema & Anna (urbanització Port del Comte)	381699	4669935	1657
P-05	Casa Ramonet (Montnou)	375026	4667250	1450,5
P-06	Casa Cavallera Turisme Rural (Odèn)	375322	4663491	1216,5
P-07	Càmping Comella Cambrils Ca l'Agustí (Cambrils)	366768	4666573	1062,2
P-08	Càmping Sant Llorenç Morunys	383770	4666876	896,2

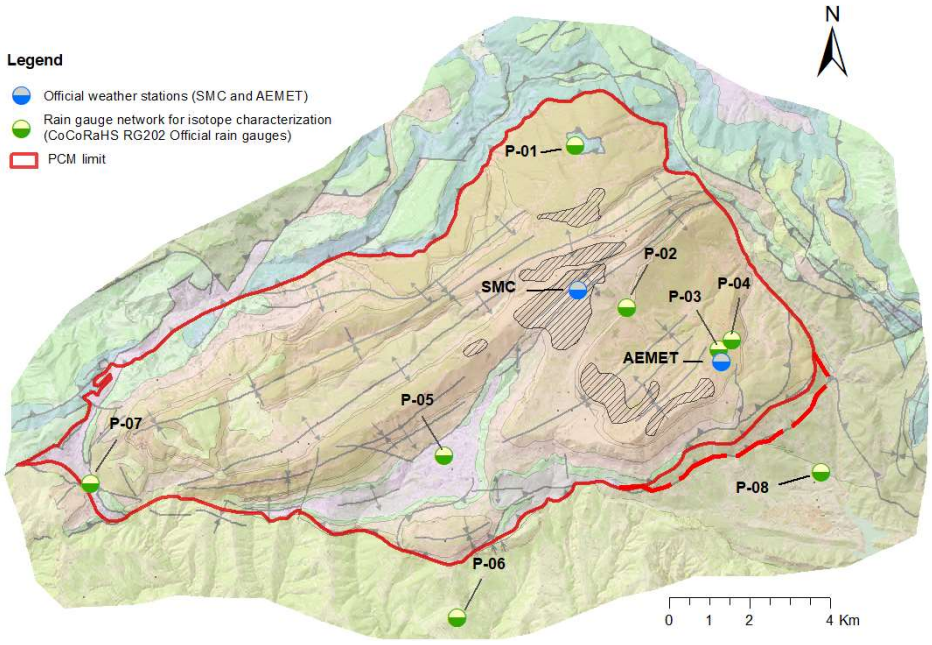

Figure 2. 24 Location of own precipitation water collectors and available official weather stations

Figure 2. 25 Images of the pre-assembly of rain gauge masts, in Port del Comte (December 2013)

Figure 2. 26 Images of the CoCoRaHS RG202 Official rain gauge, assembled and in operation in summer and winter in Port del Comte at 8 different altitudes

The CoCoRaHS total rain gauges were sampled seasonally (except the first winter with two campaigns) from December 2013 to December 2015 with a total of 9 campaigns. Liquid paraffin was used to preserve the precipitation sample by adding it inside the rain gauges. This supernatant sheet prevents the evaporation of water, and therefore the isotopic fractionation of precipitation

water. Given that the samples cover different rain episodes, all the samples collected represents a weighted composition of the period. In total 70 samples were taken.

The results of isotope content for all samples are included in the Table 9.1.2. in CHAPTER 9.2-FIELD WORK of Chapter 9. SUPPLEMENTARY MATERIAL. APPENDIXES OF DATA.

As it is said, the results have been used to determine the Local Meteoric Water Line" (LMWL) of the Port del Comte area (in Chapter 3), quantify the Mean Transit Times (MTTs) of the main karst springs (in Chapter 3) discharging the Port del Comte karst system, quantify the recharging altitudes of the different springs in the area (in Chapter 6), used to simulate the impact of climate change under various RCP scenarios of emissions (in Chapter 5) and used to establish the hydrogeological conceptual model of functioning of the aquifers in the area (in Chapter 6).

2.4 Strategy for monitoring spring discharge

One of the key aspects in hydrogeological studies in karst mountain areas is the determination of the spring discharges. On the other hand, to hydrologically model the system a time series with a minimum of data is required.

The inventory of water points carried out in the Port del Comte massif in the summer of 2013, made it possible to identify the most important karst springs that discharge the system. These are:

- The **Cardener springs** located at the western boundary of the Port del Comte mantle, discharging to the Cardener River, one of the main tributaries of the Llobregat River, with expected Q between 50 and 1000 L/s
- The **Sant Quintí** and **Can Sala springs**, located to the south-western boundary of the system and which discharge to the ‘Riu Fred, a tributary of the ‘Ribera Salada, which is an effluent of the Segre River, with expected Q between 50 and 500 L/s and 5 and 200 L/s respectively

- The **Aiguaneix spring**, located at the northwest limit of the system, which discharge to the 'Aiguaneix rasa' and from here to the Alinyà River, an effluent of the Segre River, with expected Q between 10 and 200 L/s

In the specific case of the Cardener spring, the Catalan Water Agency (ACA) has had in the past a permanent gauging station officially named "EA087 La Coma i La Pedra" equipped with an analogic limnograph and a section controlled with a limnimetric column. At the time of the start of the fieldwork of the thesis, this station was already disused. However, the ACA at the beginning facilitated the H (height) / Q (flow rate) curve, that is, the empirical equation that relates the discharge flow that passes through the station in relation to the height of the water sheet in the controlled stream section. Therefore, during fieldwork campaigns, the value of H could be easily taken to determine its flow discharge. Although there was a historical time-series of Q data available it was not possible to localise and collect them until the second part of the thesis, taken the possibility to re-used them by the paper presented in Chapter 5.

In the case of the Sant Quintí spring, an old disused limnimetric mast was found at the discharge point. During the time that the field work lasted, it was not possible to locate the entity that placed it, nor did the owner of the private land where the spring is located have any more information. In the case of the other two springs (Can Sala and Aiguaneix), no gauging infrastructure was located.

Regarding the availability of previous flow discharge data, for the springs of Sant Quintí, Can Sala and Aiguaneix it has only been possible to locate and consult some specific data from previous academic works. Therefore, one of the main objectives of the study was to apply a methodological approach to discharge measurements to obtain a new dataset.

The option of building some type of permanent gauging station for each of the karst springs was rejected, because it would require the necessary implementation of some type of civil work, having to deal with the cost of acquiring fixed instrumentation, and the need to obtain permits from landowners to fix them in place. Therefore, the method of gauging the springs had to be by means of a punctual measurement technique that was easy to implement in the field and that could be replicated as many times as necessary throughout the two years of scheduled field work. On the other hand, it was necessary to consider that the flow rates could present important variations during

the spring periods coinciding with the snowmelt, since they are karst springs that drain the main aquifer of the Port del Comte.

Streamflow discharge can be measured by various techniques, including the volumetric method, the velocity gauging method with a current meter, the gauging flumes method, or the dilution gauging method (Carter, & Davidian; 2009). The uses of the volumetric method (measurement of the time elapsed in filling a known volume) was not a suitable option in these cases due to the magnitude of their flow rate. The technique of stream gauging by measuring water velocity (using a current meter) and water depth at several points along a cross-section of a stream channel, as well as the gauging flumes were also completely disregarded due to the physical characteristics of the stream channels and the flow velocities. Therefore, the most appropriate option was to use chemical gauging by injecting conservative tracers. Among the different available approaches (instantaneous slug injection vs. constant rate injection), the method selected was the 'slug' injection using a conservative tracer in solution, due to the fact that constant rate would be more appropriate just for small streams (less than about 2 m in wetted width) under low flow rate conditions or less that 100 L/s (Elder & Kattelman, 1990; Moore 2004 and 2005). Dilution gauging is especially used in mountainous streams where the irregular cross-sections and the strong turbulence decrease the accuracy of the other methods.

2.4.1 The use of Salt Slug Injection Method

Dilution gauging has become a common technique for measuring stream discharge in high gradient channels, for years, it has been a common technique used in research work in karst hydrogeology. For instance, Radulovic et al (2008) use the method to calculation discharge of karstic spring Bolje Sestre, Montenegro using sodium chloride (Na Cl) as tracer; Sappa et al 2015, used the slug injection method using NaCl in the karst area of the Upper Valley of Aniene River (Central Italy). Sessinni et al (2019), use it the tracer dilution method applied to the hydrogeological study of karst springs in the Mount Albo area (Sardinia NE). De Luca et al, (2019) used the method to monitor the Montellina Spring located in an Alpine mountain area in NW Italy using either Na Cl and fluorescein as a conservative tracer.

The method consists of injecting a solution with conservative tracer V_o (m^3) into the stream and then the tracer breakthrough curve at a specific cross-section is recorded with a datalogger where

the tracer has been completely mixed across the stream width (Kilpatrick and Cobb, 1985, Moore, 2005). As a conservative tracer, NaCl was used. This has a high solubility in water, if its use is not abused it is environmentally sustainable, it is cheap and easy to obtain and handle in the field, it can be measured directly with a previously calibrated electrical conductivity (EC) meter. The slug injection tests work well in streams with significant gradients and flows in a turbulent regime, as is the case of mountainous streams (Moore, 2005).

The equipment used in the field was:

- Several 1 kg salt bags (several kg)
- HI-9829 waterproof portable logging multiparameter meter to record CE respect time (Hanna Instruments). The elapsed time of measurement was adapted in each test depending on the experience.
- Buckets (between 1 and 3) depending on the expected quantity to be dissolved. Every 10 liters, we dissolved well around 3 kg of salt at the temperature of the spring water
- 2 people (one for injection and the other to control the multiparameter probe), with a pair of walkie talkie, to communicate from the injection point to the sampling point

Then stream discharge can be calculated from the measurements using the following equation:

$$Q = \frac{M}{\int (C - C_b) \cdot dt} \approx \frac{M}{\sum (C - C_b) \cdot dt} = \frac{V_o \cdot C}{\sum (C - C_b) \cdot dt} = \frac{V_o \cdot EC}{k \cdot \sum (EC - EC_b) \cdot dt}$$

where

- M is the mass (kg of NaCl)
- V_o is the volume of the tracer solution injected into the stream
- C_o is the concentration of the tracer solution injected into the stream
- C is the measured concentration (or EC) of the tracer solution at a given time
- C_b is the background concentration level of the stream water
- dt is the integrated time or time between two EC measurements
- Q is the flow rate of the stream in the measured point
- EC – Electrical conductivity

- k – calibration constant to go from EC to concentration of NaCl in water. In this case a calibration curve obtained thanks to the analytical laboratory of the mining company Salinera de Cardona SL was used.

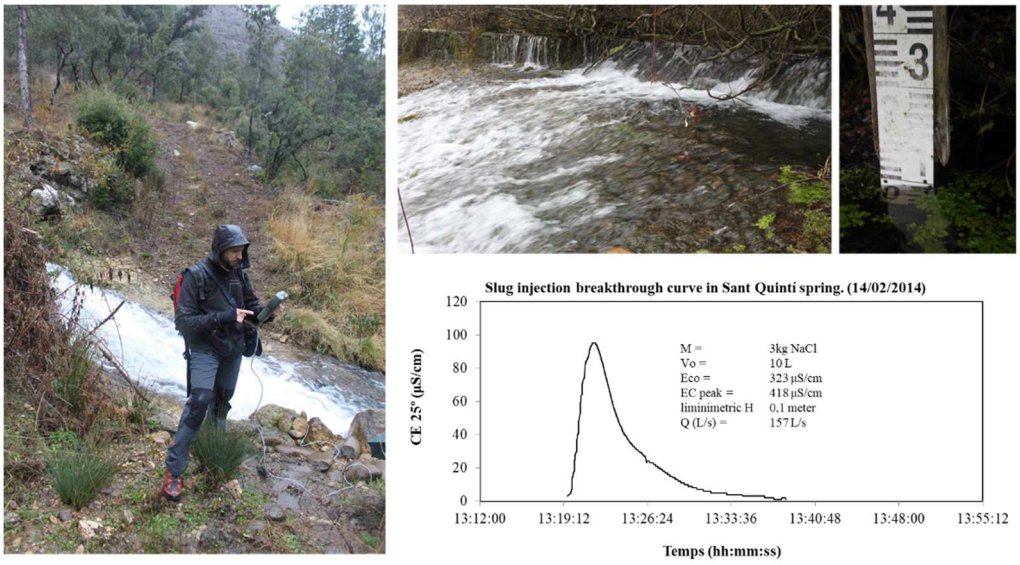

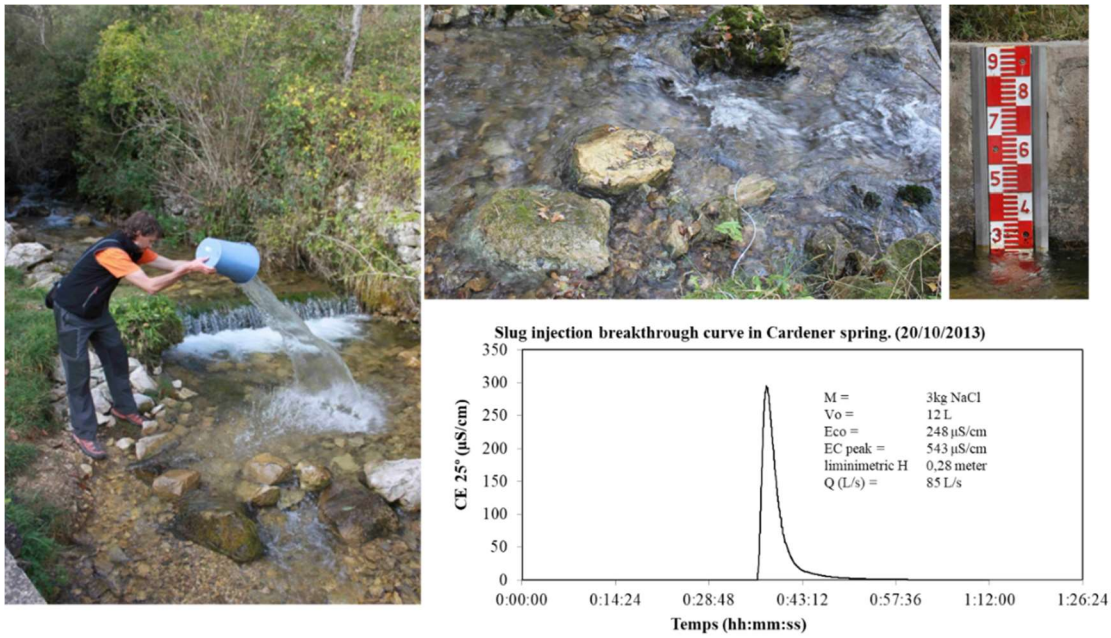

Figure 2. 27 (Upper) Slug injection using salt dilution at Sant Quintí spring on 14/02/2014. (Bottom) Slug injection using salt dilution at Cardener spring on 20/10/2013.

2.4.2 Validation of the technique in the Cardener Spring

The validation of the field experimental procedure was carried out using the H / Q limnograph curve of the gauge station EA087 La Coma and La Pedra (ACA) with the data of the first tests carried out in summer 2013. The average error in the first two test between the value of the estimated flow with the instantaneous slug injection and the value of the flow obtained from the empirical equation of the gauging station was ± 2.13%. These data were considered satisfactory, given that under appropriate conditions, according to Day (1976), slug injection flow measurements may have an error of up to ± 5%. From that, it was decided to extend the use of this methodology to the three remaining karstic springs with the aim of monitoring the evolution of flows rates throughout the entire fieldwork period programmed between September 2014 to October 2015. Throughout the two years, the verification of the discharges in the Cardener springs was repeated. At the end of the work, it has been possible to verify that the average of the errors of all the campaigns is ± 4.32%, although it seems that for high flows, the error increases slightly (**Figure 2. 28**, **a**). In the case of Sant Quintí spring, the slug injection technique was applied simultaneously to the measurement of the height of the old existing limnograph which allow us to obtain after several test an own empirical H/Q curve (**Figure 2. 28**, **b**), from which to rely on in the following campaigns.

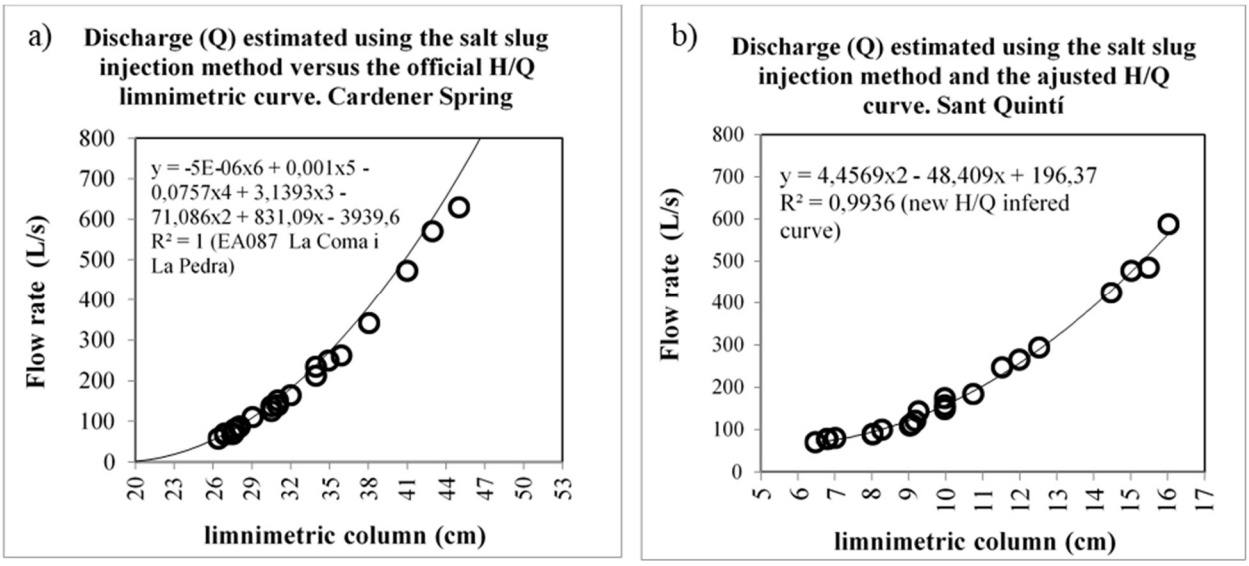

Figure 2. 28 (Left) Discharge (Q) estimated using the salt slug injection method versus the H/Q limnometric curve in the EA087 La Coma i La Pedra gauge station (ACA) in Cardener spring. (Right) H/Q limnometric curve inferred in Sant Quintí spring

The slug injection procedure for gauging using salt in solution is a very simple, fast and easy method to use in the field and particularly in mountainous areas, as it does not require a complicated infrastructure, it is cheap and does not require too much time to carry them out. Its application has given good results in the Port del Comte and its application could easily be extended by monitoring other springs of mountain karst aquifers that are not equipped with permanent gauging stations in the framework of environmental monitoring plans. The campaigns of measurement of the flow of the four regional karst springs (Cardener, Sant Quintí, Can Sala and Aiguaneix) during the field work have allowed to characterize the hydrodynamics of the discharge of the system in relation to the recharge. The data generated using this methodology have been used to hydrologically model the system using the semi-distributed rainfall-runoff hydrological HBV model (Bergström, 1992, 1995 and 2006, Seibert and Vis, 2012). The data and methodology used, and the results obtained from the modeling were the subject of the first of the scientific papers of the thesis (Herms et al, 2019) which are presented in the following Chapter 3.

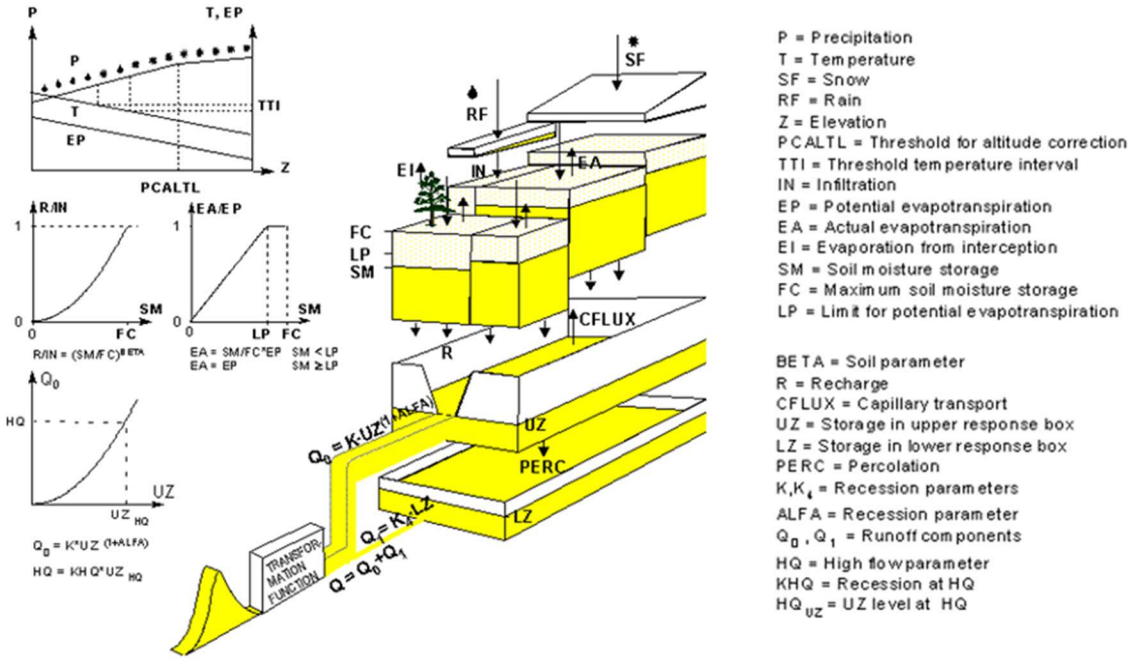

Figure 2. 29 Schematic structure of one sub-basin in the HBV model (Lindström et al., 1997), with routines for snow, soil and the unsaturated and saturated ground (source: SMHI)

2.5 Implementation of hydrogeochemical field campaigns

2.5.1 Strategy followed during fieldwork

In order to achieve the objectives of the thesis, a fieldwork has been carried out that globally covers several periods from April 2013 to November 2017.

- **Period between April 2013 to August 2013 and November 2017**: It was carried out the initial geological reconnaissance work and the inventory of water points (see chapter 2.1). In addition, in November 2017, complementary field trips were made to collect more geological data for the purposes of preparing the surface-based 3D geological modeling, ending all the field work of the thesis on that date.

- **Period October 2013 to December 2015**. The implementation of rain gauges and rainwater collection lasted until the end of December 2015, the date on which the sampling work was completed.

- **Period between September 2013 to October 2015**: This is the period in which all the water sampling campaigns were carried out to characterise spring groundwaters - and for the sampling other specific points such as natural and artificial snow and water ponds samples, and to perform the gauging field work.

On the other hand, with the aim of characterizing the hydrochemistry of the water both spatially and temporally, it was decided to carry out several general campaigns and, on the other hand, to carry out monitoring with a greater frequency of a smaller number of points. The strategy finally applied was the following:

- The spatial characterization: It was carried out through 4 complete characterization campaigns of a total of 43 springs previously selected (see subchapter 2.1) from the total number of springs inventoried in the study area of the Port del Comte area. These campaigns would be carried out before and after the snow melting: in October 2013, April 2014, October 2014 and April 2015. In each campaign and for each spring, the basic physical-chemical parameters (e.g. temperature, electrical conductivity, alkalinity, pH and Redox)

were collected, discharge flows were gauged and water samples were taken for hydrogeochemical characterization in the laboratory (by determining of major ions and cations and stable isotopes of water).

- The temporal characterization of the evolution of chemistry and dynamics: It was carried out specifically in 6 springs of the previous 43 previously selected, 4 of which correspond to the four main karstic springs at the regional level of the system (see chapter 2.1) where the slug injections with salt in solution gauging method was applied (Cardener, Sant Quintí, Aiguaneix and Can Sala), plus two other smaller springs in which the systematic gauging was carried out using the volumetric method ('Carretera Arp' and 'Coll de Jou' springs). In all of them, a fortnightly monitoring of basic physical-chemical parameters (e.g. temperature, electrical conductivity, alkalinity, pH and Redox) and the periodic gauging of the discharge flow was carried out, and then a monthly sampling for the hydrogeochemical characterization in laboratory (with complete sample to determine major ions and cations and stable isotopes of water).

At the end of the thesis fieldwork, a total of 371 samples were taken (**Table 2. 2**) for chemical analysis, mainly springs but also samples from the network of rain gauges, snow samples and water pond samples.

Table 2. 2 Summary of water sample types and analysis done in the research project

Type of sample	number of control points	Total field campaigns	Total number of samples	Number of analysis with major ions	Total number analysis stable isotopes of δ^2H_{H2O}, $\delta^{18}O$	Total number analysis stable isotopes of $\delta^{34}S$, $\delta^{18}O_{SO42-}$	Total number analysis stable isotopes of $\delta^{15}N$, $\delta^{18}O_{NO3-}$
Rain gauge collector (quarterly)	8	9	71	-	71	-	-
Spring samples	-	-	288	**288**	**283**	**209**	**72**
Springs (biannually)	40 / 43	4	-	138	134	88	42
Spring (monthly)	6	25	-	150	149	121	30
Snow samples			10	**10**	**10**	**1**	**-**
Natural snow	10	-	-	7	7	-	-
Artificial snow	3	-	-	3	3	1	-
Water ponds (artificial snow production)	2	-	2	2	-	-	-
		TOTAL	**371**				

The Table 9.1.3. of the Sub-Chapter 9.1. Field work specify the ID general identification number, coordinates and name of all water points used in the thesis. (However, the reader must refer to the tables and maps included in each of the scientific papers included in this thesis by compendium of publications as chapters 3, 4, 5 and 6, in order to know which water points and which nomenclature to identify them has been used at the end in each case).

2.5.2 Monthly hydrogeochemical sampling and hydro-chemographs

Monitoring the temporal evolution of natural physical properties or solutes present in groundwater, commonly known as "environmental tracers", can provide very valuable scientific information on the characteristics of hydrogeological systems. The dynamics of the spring discharge (hydrographs) together with the hydrogeochemical dynamics of water discharge (called "chemographs") reflect the set of processes that take place within the system. Therefore, its monitoring and analysis allows obtaining a better understanding of its hydrogeological functioning. (Gil-Márquez et al., 2019; Stroj et al., 2020, Prieto-Mera et al. 2018). In karstic systems where the dynamic response of the system is very fast, it is advisable to use datalogger-type devices to capture more detailed time series and carry out sampling campaigns with a very short frequency. However, characterization with high precision detail is beyond the scope and possibilities of this thesis. Therefore, temporal characterization was addressed along two years by regularly monitoring discharge flows and physical-chemical parameters (temperature, pH and electrical conductivity, among others) on a fortnightly scale, and water chemistry (major ions and stable isotopes of water) on a monthly scale. The monitoring was carried out in six springs: Cardener, Sant Quintí, Aiguaneix and Can Sala, which correspond to the most important springs in the area, plus the springs of 'Carretera Arp' and 'Coll de Jou', which correspond to representative points of medium and small flows. The data collected has provided very relevant and valuable information that did not exist before the work carried out in the thesis.

Although the particular analysis of the chemographs have not explicitly included in any of the scientific publication in the thesis, although the data collected has been used in all: The temporal evolution of the discharge flows have been used to establish a conceptual precipitation-runoff model and to calibrate a lumped hydrological HBV model (Bergström, 1992, 1995 and 2006) to

simulate the observed response in the discharge flow for each spring and calculate its recharge time-series (chapter 3). After that, subsequently climate change RCP scenarios have been simulated and analysed (chapter 5). The time evolution of the isotopic input isotopic input (rainfall) and output response of the springs has been used to fit a transport model to estimate the mean transit time MTT using the FlowPC model (Chapter 3). The median water chemistry values have been used to establish regional geochemical background levels of three pollutants, sulfate, chloride, and nitrate, (Chapter 4), while chemistry evolution has implicitly been used to globally establish the functioning hydrogeological conceptual model of the karst system (chapter 6).

The following **Figure 2. 30**, **Figure 2. 31** and **Figure 2. 32** show the chemographs with the results obtained for the 6 springs, grouped by its hydrodynamic behaviour and relevance of the springs. The first chemograph (**Figure 2. 30**) presents the results of the two main springs of Port del Comte: The Cardener spring (Q = 50-900 L/s in the monitored period) that drains towards the Llobregat basin in the eastern boundary of the thrust sheet, and the Sant Quintí spring (Q = 70-575 L/s in the monitored period), which drains into the Ribera Salada basin (Segre basin) on the south-west side of the mantle. Their groundwater flow has the largest travel distance (unsaturated zone of 1000m of thickness). Regarding the discharge hydrograph, it is observed that both present approximately the same sinuosity with the same peaks and valleys, an aspect that would demonstrate that both receive recharge from the same altitude, as demonstrated in chapter 6. Another aspect that is observed is the correlation when the snow cover disappears in spring between March and April (snow depth measured at the SMC weather station at 2316 m a.s.l.), and a rapid and sudden increase in discharge flow. and the sharp decrease in electrical conductivity, temperature, isotopic content, and solute content ($Mg^{2+,}$ $Ca^{2+,}$ $SO_4^{2-,}$ Cl^- and $Na^{-)}$. This demonstrates that the two main springs of Port del Comte behave as a complex and mixed drainage system with fissured/karstic conduits that affect the unsaturated zone. When there is an important input, as in the case of the rapid melting of snow cover, these facilitate rapid recharge and dilution of older groundwater already existing in the saturated reservoir.

Figure 2. 31 presents the results of the second most important pair of springs in the Port del Comte aquifer system, the Aiguaneix (Q = 8-75 L/s in the monitored period) and Can Sala (Q = 0-150 L/s in the monitored period) springs. In these two cases, the behaviour between them is quite similar but on the contrary quite different compared to the previous ones.

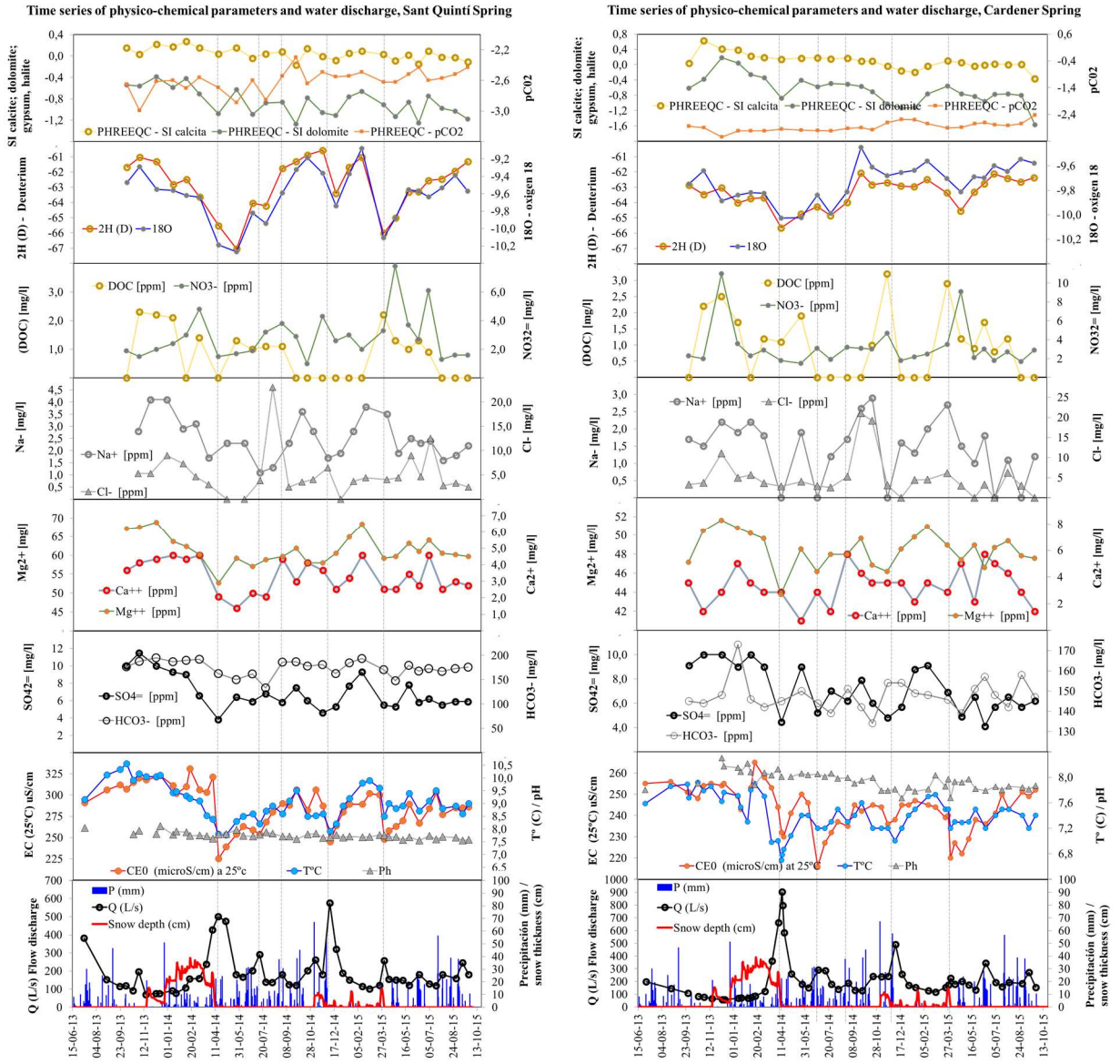

Figure 2. 30 Chemograph and hydrographs of the Sant Quintí and Cardener karst springs

For example, the flow discharge response due to the snow melting process is almost imperceptible, but instead they are quite sensitive to the November 2014 precipitation event. This would confirm, as has also been shown using isotopes (Chapter 6), that the recharge is located at lower altitudes respect where the snow cover is usually stored. Besides, neither a decrease nor any of the natural tracers is observed. For the rest of the period, the behaviour is rather damped, an aspect that could indicate that these are systems in which the diffuse flow has a more relevance than the karstic conduits.

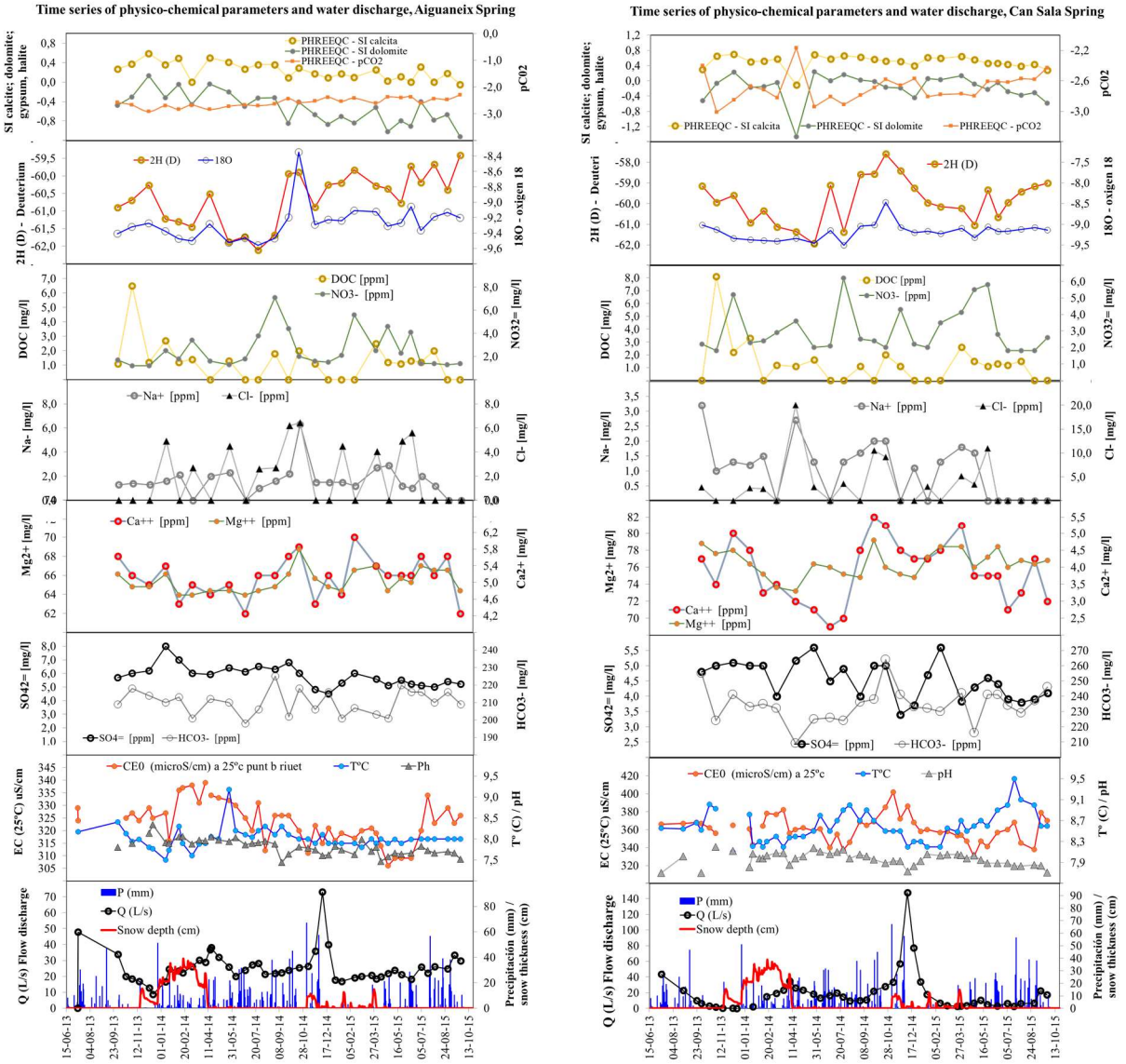

Figure 2. 31 Chemograph and hydrographs of the Aiguaneix and Can Sala karst springs

Finally, **Figure 2. 32** presents the results of two monitored minor springs, 'Carretera Arp' (Q = 0.03-7 L/s in the monitored period) and Coll de Jou" (Q = 0.03-0.6 L/s in the monitored period). These are subsurface springs located hanging from the regional piezometric level (the water temperature shows a seasonal response mostly influenced by air temperature, very pronounced in the case of the Coll de Jou spring). In the case of the "Carretera Arp" spring located at 1856 m a.s.l., like the Cardener and Sant Quintí springs, it also shows a rapid response to melting, with a sudden and very important percentage increase in flow followed by a rapid drop in the EC, and solutes such as Mg^{2+} and Ca^{2+}, but not T. Nevertheless, the travel distance is shorter compared to the previous big springs. Coll de Jou spring, it is not influenced by the snowmelt process, and shows a behaviour

rather influenced by each of the precipitation episodes, symptom that it is about local and very superficial diffuse flow and of little distance from its recharge area.

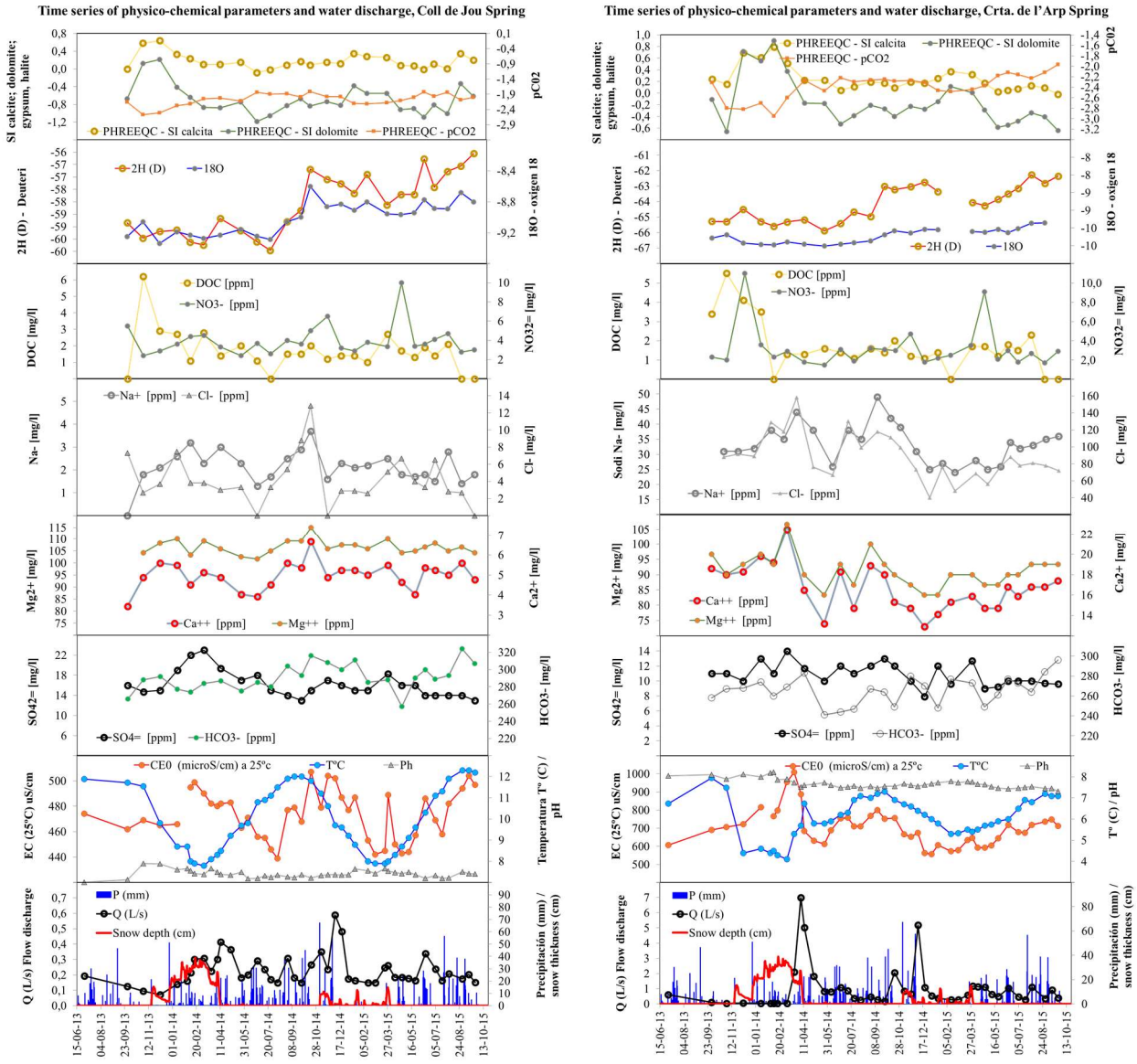

Figure 2. 32 Chemograph and hydrographs of the Coll de Jou and Carretera de l'Arp karst springs

2.6 Data processing for analysis and interpretation

Throughout the thesis, various tools and computer programs have been used. To produce all the maps ArcGIS® desktop mostly v 10.6 from ESRI® under a license from the ICGC has been used.

The reference cartography and the digital elevation models used have been provided by the ICGC. The geological modeling has been carried out with the use of the MOVE® 2017.1 software (Midland Valley Exploration Ltd) for 2D and 3D Structural geology with a license from the ICGC. All the descriptive, bivariate and multivariate statistical treatment (computing and graphics preparation) presented in the scientific papers of chapters 4 and 6 has been carried out with the open-source free R software and its graphical user interface RStudio (version 1.2.15 for Mac OS X systems through Mac OS X 10.5) using a wide variety of R packages. The calculation of saturation indices and the inverse geochemical modeling presented in chapter 6 has been carried out using the free USGS software PHREEQC® (Parkhurst and Appelo, 2013) within the version PhreeqC Interactive® (version 3.3.3 10424), and with the phreeqc.dat database. The semi-distributed rainfall-runoff hydrological model has been prepared using the HBV program with its light version (Bergström, 1976; Seibert, 2005), and the calculation of mean transit times with the FlowPC solute transport model version 3.2. The management of all bibliographic references of the scientific papers has been carried out with the use of the free and open-source reference manager Zotero (for Mac). Finally, MS Excel® has been used for the preparation of tables and MS Word® (office 365 under ICGC licence) for the writing of this thesis report.

2.7 References

ACA (2013). BDH hydrogeological data base of Catalan Water Agency. Base de dades d'inventari de captacions d'aigües subterrànies de Catalunya - Base de Dades Hidrogeològica – BDH. Agència Catalana de l'Aigua (Accessed on 01/05/2013),

ACA (2005). PABCAT (Pla d'ABastament i distribució d'aigua en alta a Catalunya). Informes finals. La Coma i La Pedra; Fígols i Alinyà; Ribera d'Urgellet; Odèn; Sant Llorenç de Morunys; Josa i Tuixen; Guixers; Vansa i Fórnols

ACA. Hydrogeological databse - Base dades Hidrogeològica (BDH). (Accessed April 2013)

Ardèvol, Ll., Solé, X., Escuer, J., Martínez, A., Puig, C. y Samsó, J.Mª (2020). Memoria de la Hoja nº 292 (Sant Llorenç de Morunys). Mapa Geológico de España E. 1:50.000 Segunda Serie (MAGNA). Primera edición. IGME, 100 p.

Ardèvol, Ll., Solé, X., Losantos, M., Martínez, A., Puig, C., Escuer, J. y Casanovas, J. (2020b). Memoria de la Hoja nº 254 (Gósol). Mapa Geológico de España E. 1:50.000. Segunda Serie (MAGNA). Primera edición. IGME, 132 p.

Ballesteros, D., Malard, A., Jeannin, PY. et al. (2015). KARSYS hydrogeological 3D modeling of alpine karst aquifers developed in geologically complex areas: Picos de Europa National Park (Spain). Environ Earth Sci 74, 7699–7714. https://doi.org/10.1007/s12665-015-4712-0

Berastegui, X., Pi, M.E., Escuer, J., Casanovas, J., Smaso, J.M., Arbués, P., Martínez, A., Vilella, L. (2001). Memoria de la Hoja nº 291 (Oliana). Mapa Geológico de España E. 1:50.000 (MAGNA), Primera edición. IGME, 113 pp. Depósito legal: M-24.012-2017. ISBN: 978-84-9138-038-2.

Bergström, S. (1992). The HBV Model – Its Structure and Applications, SMHI Hydrology, RH No. 4, Norrköping (35 pp.).

Bergstrom, S. (1995) The HBV Model. In: Singh, V.P., Ed, Computer Models of Watershed Hydrology. Water Resources Publications, Highlands Ranch, CO, 443-476.

Bergström, S., 2006. Applications of the HBV hydrological model in prediction in ungauged basins. Large Sample Basin Experiments for Hydrological Model Parameterization: Results of the Model Parameter Experiment MOPEX. 307. IAHS Publ., pp. 97–107.

Butscher C, Huggenberger P (2007) Implications for karst hydrology from 3D geological modeling using the aquifer base gradient approach. J Hydrol 342:184–198. https://doi.org/10.1016/j.jhydrol.2007.05.025

Carter, R.W.; Davidian, J. (2009); General procedures for gaging streams. In Techniques of Water Resources Investigations; US Geological Survey: Denver, CO, USA, Book 3, Chapter A-14 https://doi.org/10.3133/twri03A6

Day, T.J. (1976). On the precision of salt dilution gauging. Journal of Hydrology 31:293–306. https://doi.org/10.1016/0022-1694(76)90130-X

Day, T.J. (1977). Field procedures and evaluation of a slig dilution gauging method in mountain streams. Journal of Hydrology (New Zealand) 16, pp. 113-133

De Luca, Domenico A., Elena Cerino Abdin, Maria G. Forno, Marco Gattiglio, Franco Gianotti, and Manuela Lasagna. (2019). "The Montellina Spring as an Example of Water Circulation in an Alpine DSGSD Context (NW Italy)" Water 11, no. 4: 700. https://doi.org/10.3390/w11040700

Elder, K., R. Kattelmann, and R. Ferguson. (1990). Refinements in dilution gauging for mountain streams. In Hydrology in Mountainous Regions. I – Hydrological Measurements; the Water Cycle. International Association for Hydrological Science (Proceedings of two Lausanne symposia, August 1990). IAHS Publication No. 193, pp. 247–254.

Gencat (1990). Proyecto de prospección e investigación hidrogeológica del Solsonès (Lleida). 128 páginas. Technical report. Unpublished.

Gencat (1991). Estudio geofísico para la prospección de aguas subterráneas (Solsonès– Lleida). 20 páginas. Technical report. Unpublished.

Gencat (1993). Informe de los sondeos de investigación en la comarca del Solsonès. 58 pp. Technical report. Unpublished.

Gil, R. y Núñez, I. (2003). Estudio hidrogeológico de la sierra de Odén – Port del Comte (Solsonès–Lleida). Trabajo de curso CIHS, 85pp. Technical report. Unpublished.

Gil-Márquez, J.M.; Andreo, B.; Mudarra, M. (2019). Combining hydrodynamics, hydrochemistry, and environmental isotopes to understand the hydrogeological functioning of evaporite-karst springs. An example from southern Spain J. Hydrol., 576 pp. 299-314, https://doi.org/10.1016/j.jhydrol.2019.06.055

Kilpatrick, F.A., and Cobb, E.D., (1985), Measurement of discharge using tracers: U.S. Geological Survey Techniques of Water-Resources Investigations, book 3, chap. A16, 52 p. (Also available at https://pubs.usgs.gov/twri/twri3-a16/

Herms, I., Jódar, J., Soler, A., Vadillo, I., Lambán, L. J., Martos-Rosillo, S., Núñez, J.A., Arnó, G., Jorge, J., (2019). Contribution of isotopic research techniques to characterize high-mountain-Mediterranean karst aquifers: The Port del Comte (Eastern Pyrenees) aquifer. Science of The Total Environment, 656, 209-230. https://doi.org/10.1016/j.scitotenv.2018.11.188

I.Herms, J.A.Nuñez, M.Colomer, G.Arnó1, J.Jodar, A.Soler, A.Griera (2019). 3D geological modelling as a tool for supporting spring catchment delineation in high-mountain karst aquifers: the case study of the Port del Comte (Eastern Pyrenees) aquifer. 5th European Meeting on 3D Geological Modeling, 21th – 24th May 2019, Bern (Switzerland)

ICGC. Base topogràfica 1:5.000. Institut Cartogràfic i Geològic de Catalunya. (accessed 01/04/2013)

ICGCb. Base topogràfica 1:25.000. Institut Cartogràfic i Geològic de Catalunya. (ccessed 01/04/2013)

Jeannin, P-Y., Eichenberger, U., Sinreich, M., Vouillamoz, J., Malard, A., Weber, E. (2013). KARSYS: a pragmatic approach to karst hydrogeological system conceptualization. Assessment of groundwater reserves and resources in Switzerland. Environmental Earth Sciences, 69(3): 999-1013 p.). https://doi.org/10.1007/s12665-012-1983-6

Malard, A. Vouillamoz, J., Jeannin, P-Y, Weber, E., Eichenberger, U. (2012) SWISSKARST

Project - how to document the karst aquifers in Switzerland using the KARSYS approach. Geophysical Research Abstracts Vol. 14, EGU2012-2637, 2012

Moore, R.D. (2004), Introduction to salt dilution gauging for streamflow measurement: Part I. Streaml. Water. Manage. Bull. 7, 20–23.

Moore, R.D. (2005). Slug Injection Using salt in Solution. Streamline. Wathershed Management Bulletin. Volume 8. Number 2 Spring 2005

Núñez, I., Gil, R., García M.A, y Vázquez, E. (2004). Estudio hidrogeológico de la cabecera de la Ribera Salada, (Lleida). Libro resúmenes VIII Simposio de Hidrogeología, (AIH - IGME), p. 107-120.

Parkhurst, D.L., Appelo, C.A.J., 2013. Description of Input and Examples for PHREEQC Version 3—A Computer Program for Speciation, Batch-Reaction, One-Dimensional Transport, and Inverse Geochemical Calculations: U.S. Geological Survey Techniques and Methods, Book 6, Chap. A43: 1–497. (Available only at https://pubs.usgs.gov/tm/06/a43 Last access 28 August 2020).

Prieto-Mera, J., Andreo, B., Barberá, J.A. (2018). Coupling hydro-geo-chemical and isotopic approaches to assess the main factors controlling karst development in a fissure-dominated carbonate aquifer system (s-Spain). 45th IAH Congress https://hdl.handle.net/10630/16502

Radulović, M.; Radojević, D.; Dević, D.; Blečić, M. (2008) Discharge calculation of the spring using salt dilution method. Application site Bolje Sestre Spring (Montenegro). In Proceedings of the BALWOIS 2008, Ohrid, Republic of Macedonia, 27–31 Ma

Seibert, J., Vis, M.J.P, (2012). Teaching hydrological modelling with a user-friendly catchment-runoff-model software package, Hydrol. Earth Syst. Sci., 16(9), 3315–3325. https://doi.org/10.5194/hess-16-3315-2012

Stroj, Andrej, Maja Briški, and Maja Oštrić. 2020. "Study of Groundwater Flow Properties in a Karst System by Coupled Analysis of Diverse Environmental Tracers and Discharge Dynamics" Water 12, no. 9: 2442. https://doi.org/10.3390/w12092442

Turk, J., Malard.A., Jeannin, P-Y., Vouillamoz, J., Masini, J., Petrič, M., Gabrovšek, F., Ravbar, N., Slabe, T., (2013). Interpretation of hydrogeological functioning of a high plateau using the karsys approach: The case of Trnovsko-Banjska Planota (Slovenia). Acta carsologica, vol 42, No 1, 14pp. https://doi.org/10.3986/ac.v42i1.640

I. Herms, J. Jódar, A. Soler, I. Vadillo, L.J. Lambán, S. Martos-Rosillo, J.A. Núñez, G. Arnó, J. Jorge. 'Contribution of isotopic research techniques to characterize high- mountain-Mediterranean karst aquifers: The Port del Comte (Eastern Pyrenees) aquifer' Science of the Total Environment 656 (2019) 209–230 https://doi.org/10.1016/j.scitotenv.2018.11.188.

Science of The Total Environment

Volume 656, 15 March 2019, Pages 209-230

Contribution of isotopic research techniques to characterize high-mountain-Mediterranean karst aquifers: The Port del Comte (Eastern Pyrenees) aquifer

I. Herms [a], J. Jódar [b], A. Soler [c], I. Vadillo [d], L.J. Lambán [e], S. Martos-Rosillo [e], J.A. Núñez [a], G. Arnó [a], J. Jorge [f]

Show more

+ Add to Mendeley Share Cite

https://doi.org/10.1016/j.scitotenv.2018.11.188

Get rights and content

3 PAPER 1. CONTRIBUTION OF ISOTOPIC RESEARCH TECHNIQUES TO CHARACTERIZE HIGH- MOUNTAIN-MEDITERRANEAN KARST AQUIFERS: THE PORT DEL COMTE (EASTERN PYRENEES) AQUIFER

Authors: **Herms. I**., Jódar, J., Soler, A., Vadillo, I., Lambán, L.J., Martos-Rosillo, S., Núñez, J.A., Arnó, G., Jorge, J.

Abstract

Water resources in high mountain karst aquifers are usually characterized by high rainfall, recharge and discharge that lead to the sustainability of the downstream ecosystems. Nevertheless, these hydrological systems are vulnerable to the global change impact. The mean transit time (MTT) is a key parameter to describe the behavior of these hydrologic systems and also to assess their vulnerability. This work is focused on estimating MTT by using environmental tracers in the framework of high-mountain karst systems with a very thick unsaturated zone (USZ). To this end, it is adapted to alpine zones a methodology that combines a semi-distributed rainfall-runoff model to estimate recharge time series, and a lumped-parameter model to obtain MTT. The methodology has been applied to the Port del Comte Massif (PCM) hydrological system (Southeastern Pyrenees, NE Spain), a karst aquifer system with an overlying 1000 m thick USZ. Six catchment areas corresponding to most important springs of the system are considered. The obtained results show that hydrologically the behavior of the system can be described by an exponential flow model (EM), with MTT ranging between 1.9 and 2.9 years. These MTT values are shorter than those obtained by considering a constant recharge rate along time, which is the easiest and most applied aquifer recharge hypothesis when estimating MTT through lumped-parameter models.

Keywords: Stable isotopes; Seasonal isotopic amplitude; Altitudinal line; Recharge; Mean transit time; Karst.

3.1 Introduction

High mountain zones are known as "water towers" because they generate the main water resources feeding the most important rivers in the world (Viviroli et al., 2007). This phenomenon is especially important in the drought-prone Mediterranean area (Vicente-Serrano et al 2014), where water availability is scarce and greatly dependent on runoff from headwater basins (De Jong et al., 2009). Moreover, water discharge from mountain areas is critical to ensure water supply in the lowland and coastal fringe (Viviroli and Weingartner, 2004; García-Ruiz et al 2011), where human activity

(agriculture, industry, tourism) concentrates.

Future scenarios for climate change in the whole Mediterranean region forecast an increase in temperature and a decrease in precipitation at the end of the 21st century (Giorgi and Lionello, 2008). These effects may well impact the Mediterranean high mountain zones (Nogués-Bravo et al., 2008; Lopez-Moreno et al., 2009; Ribalaygua et al., 2013), modifying the hydrological behavior of their headwater basins (Barnett et al., 2005; García-Ruiz et al. 2011, and references therein). Nevertheless, the first evidence of such changes has already been reported in the Pyrenees, the southernmost European range where glaciers can be found (Grunewald and Scheithauer, 2010). Pyrenean glaciers have undergone an intense retreat since the middle of the last century, causing most of them to face a certain close extinction (Chueca et al., 2007; René 2013; Marti et al., 2015; López-Moreno et al., 2016). In addition, during this period, both mean annual precipitation and number of rainy days have shown a clear decreasing trend in this zone (Lopez-Moreno et al., 2010), along with a lesser snowfall and snow accumulation (López-Moreno, 2005). These effects directly impact the water storage capacity of the associated headwater systems (Seibert et al., 2015), as well as their associated hydrological response in terms of both river discharge flowrates and timing of maximum discharges (López-Moreno and García-Ruiz, 2004; Gremaud et al., 2009). These changes will directly impact the downstream zones by complicating the current water stress situation in the Mediterranean zone (Milano et al., 2013; Hernández-Mora et al., 2014, Molina and Melgarejo, 2016). Because of the hydrological outlook that is not so promising, it is essential to understand the functioning of the mountain hydrological systems of the Mediterranean area, especially those scenarios in which groundwater (GW) plays a major role in the headwater discharge, because mountain aquifers maintain base flows to rivers during the recurrent Mediterranean dry periods (Hoerling et al 2012; Vicente-Serrano et al., 2014).

Despite playing a strategic role, most high mountain hydrogeological systems are still insufficiently understood (Goldscheider, 2011). Conventional hydrogeological investigation techniques (Bakalowicz, 2005; Goldscheider and Drew, 2007) are often difficult to apply in alpine regions because of the difficult access and the harsh working conditions, along with the types of instruments needed for conducting research in high mountain zones (Lauber et al., 2014; Hood and Hayashi, 2010). However, a growing number of publications are focusing on the importance of groundwater in the functioning of high-mountain watershed rivers in different geological settings, including

alluvial/rockfall/talus aquifers (Lauber and Goldscheider, 2014; Kurylyk and Hayashi, 2017), fractured aquifers (Jódar et al., 2017; Barberá et al., 2018a) and karst systems (Wetzel, 2004; Goldscheider, 2005; Gremaud et al., 2009; Mudarra et al., 2014; Allocca et al., 2015; Lambán et al., 2015; Chen, 2017; Barberá et al., 2018b; Kazakis et al., 2018). Determining the magnitude of groundwater recharge and aquifer Mean Transit Time (MTT) are key issues for understanding and managing alpine groundwater systems. Spring hydrograph analysis and environmental tracer methods allow for characterizing aquifer recharge and discharge processes, estimating recharge zone elevation and transit times, determining drainage structures, and assessing spring vulnerability, as well as calculating water resources in headwater aquifers (Wetzel, 2004; Rodgers et al., 2005; Einsiedl, 2005; Farlin and Maloszewski, 2013; Jódar et al., 2016b; Malard et al., 2016; Epting et al., 2018).

In high-altitude alpine karst aquifers, groundwater recharge processes highly depend on temporal and spatial distribution of precipitation and snowmelt (Lauber and Goldscheider, 2014). The estimation of MTT in karst systems is conditioned by the existence of variable flow conditions. These systems normally show triple-porosity and different connected parts: the karstic conduits that allows rapid flow, and the fissured-porous matrix that shows intermediate to slow flow. Artificial tracer test normally injected in preferential flow paths (i.e. the channels) doesn't consider the fissured-porous matrix of the aquifer, which can be important as far as the total karst water volumes (Maloszewski et al., 2002). In this respect, the use of artificial tracers to characterize such hydrological systems is not enough since it doesn't allow characterizing all the components of the flow. Others important factors that govern the suitability of injection test for MTT estimations is the existence of a thick unsaturated zones (USZ): conducting tracer tests by injecting it at the surface of the thick USZ is likely a failing tracer test given the large uncertainties regarding the likelihood of hydraulic connection between the tracer injection point and the sampled system discharge point (Lauber and Goldscheider, 2014). Additionally, the adverse working conditions and the type of material of the instruments necessary to correctly perform the tracer test (Goldscheider et al., 2008) in high-mountain areas make it difficult to execute them.

As a result, the hydrogeological behavior of most of the mountain karst systems with an associated thick USZ remain uncharacterized, despite of being the exploration of these systems on the focus of speleogenetic research since the last decades (Ballesteros et al., 2015a, and references therein).

Lumped parameter models (LPMs) are useful to simulate the behavior of such complex mountain karst systems, even when they are poorly characterized. These models do not require a detailed hydrological knowledge of the physical system. Moreover, LPMs naturally integrate the USZ of the aquifer as a part of the whole hydrological system to be modeled (Turnadge and Smerdon, 2014). Additionally, the stable isotopes of water ($\delta^{18}O$ and $\delta^{2}H$) in rainfall have proved to be good environmental tracers for investigating the dynamics of such hydrological systems karst systems (Andreo et al., 2004). These tracers enter the system as recharge, migrate downgradient exploring the whole hydrological system, and leave the karst aquifer with spring discharge or by lateral mass transfer to other hydrogeologically connected aquifer units. In this line, this work is devoted to estimate MTT of a high-mountain karst aquifer with a thick unsaturated zone by using ^{8}O and ^{2}H as environmental tracers along with LPMs. To this end, it is considered the approach presented by Vitvar et al. (1999) to estimate MTT in a small Swiss pre-alpine aquifer. The original approach is adapted to high mountain zones by considering the existing vertical gradients of precipitation and air temperature along the slope of high mountains, but also the role played by the snow accumulation and ablation processes in the runoff generation. The resulting method combines in series two LPMs: (1) a semi-distributed rainfall-runoff HBV model (Bergström, 1976; Seibert, 2005) that simulates the observed hydrodynamical system response while taking into account the elevation dependences of the different hydrometeorological variables (i.e. Precipitation and temperature) and associated processes (e.g. snow accumulation and ablation), and (2) a FlowPC model (Małoszewski and Zuber, 1996) that estimates the mean transit time of the hydrological system while simulating the environmental tracer content evolution in the system discharge. This is done by numerically integrating a convolution integral (Maloszewski et al., 1983; Jódar et al., 2014). In our case, the FlowPC model uses as input data: a) the recharge time series of the aquifer obtained with the HBV model, and b) the time series isotope content ($\delta^{18}O$ and $\delta^{2}H$) in recharge, which is obtained through a spatiotemporal characterization of the isotope contained of precipitation.

The methodology is applied to the hydrological system of Port del Comte Massif (PCM; NE Spain), a karst aquifer with a 1000 m thick USZ. The hydrological system mainly discharges though the Cardener springs into the homonym river, which is the main tributary of the Llobregat River, the first water resources provider to the city of Barcelona (NE Spain). Despite the strategic role of

Cardener springs the hydrologic behavior of the karst system remains unknown. This study contributes to a better hydrological characterization of PCM hydrological system. Moreover, the proposed methodology can be applied to characterize other high mountain karst aquifers with an overlying thick USZ that are common in many alpine zones elsewhere the globe.

3.2 Study area

The study area is located at the Port del Comte Massif (PCM), which is situated in the eastern part of the Pyrenees, NE Spain (**Figure 3. 1**). The elevation of the watershed ranges from approximately 900 m a.s.l., up to 2387 m a.s.l., at the 'Pedró dels Quatre Batlles' peak. With approximately 110 km^2, it contains one of the main mountain karst aquifers of the Catalan Pyrenees. The watershed of the massif divides the river basin of the Cardener River at the E and S and the river basin of the Segre River at the NW and SW. The massif constitutes an independent structural and hydrogeological unit.

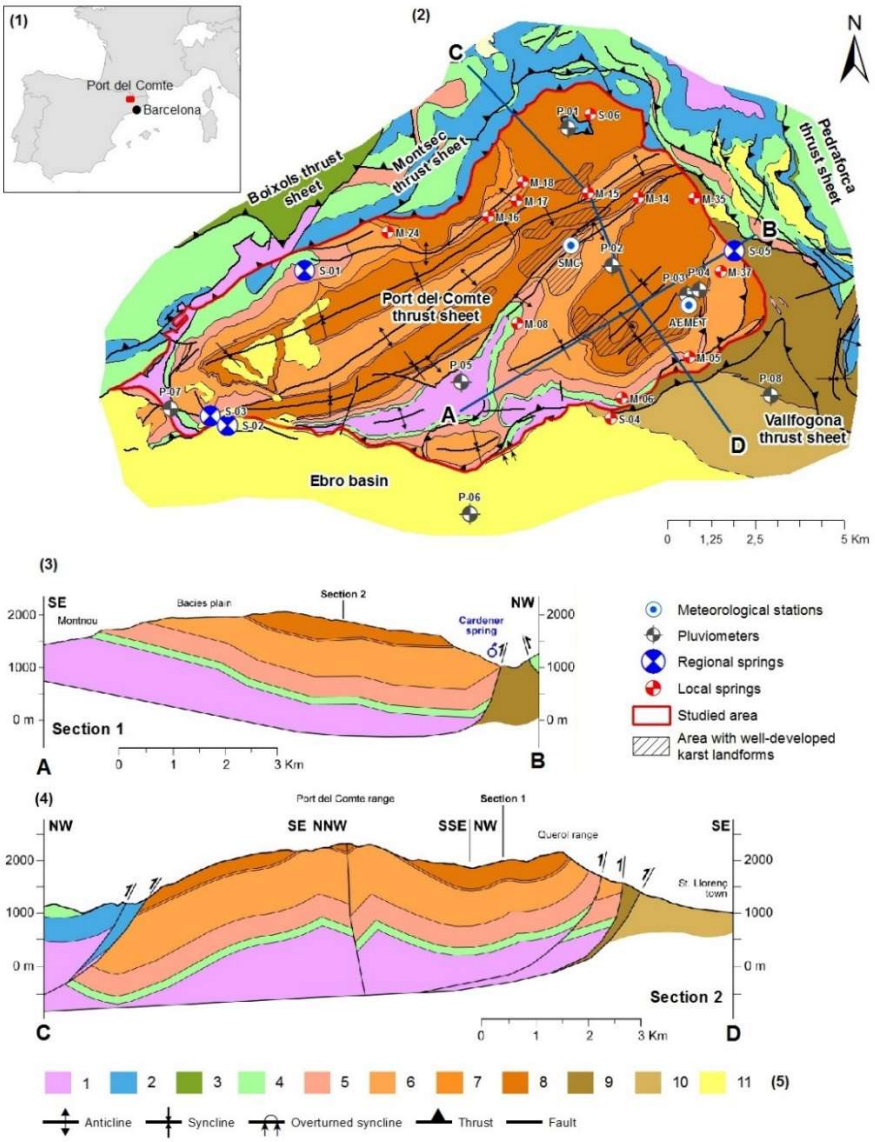

Figure 3. 1. (1) Location map of the study zone. (2) Geological map (modified from ICGC, 2007). (3) Geological cross-section A-B (4) Geological cross-section C-D. (5) Geological legend: [1] Triassic – shales, limestones, dolomites and evaporates; [2] Jurassic – marls, bioclastic limestones and dolomites; [3] Lower Cretaceous – mudstones, ammonite limestones and marl; [4] Upper Cretaceous – limestones, marls, calcarenites and terrigenous deposit; [5] Garumnian – red shales and limestones; [6] Lower Eocene – fissured and karstified alveoline limestones and dolomites; [7] Lower Eocene – marls, sandstones and limestone; [8] Lower Eocene – fissured and karstified micritic and bioclastic limestones; [9] Middle Eocene – sandstones, marls, conglomerates, limestones and evaporates; [10] Upper Eocene – continental alluvial systems: conglomerates and sandstones; [11] Oligocene – continental alluvial systems: conglomerates, breccias and sandstones.

3.2.1 Meteorological setting

From a climatic point of view, and according to the Köppen-Geiger classification (Peel et al., 2007), the study zone has a cold climate without dry season and temperate summer (defined as 'Dfb' type; accordingly, to AEMET and IMA, 2011). At the meteorological station MS-01 (**Figure 3. 1**), which is located at 2315 m a.s.l., the average values of precipitation (P), temperature (T) and potential evapotranspiration (ETP) calculated with the Hargreaves and Samani (1982) equation are 1055 mm/yr, 3,24 °C and 525 mm/yr, respectively. These three variables show a seasonal variation (**Figure 3. 2**) and an elevation dependence. The measured vertical gradients (lapse rate) of precipitation (∇_zP), atmospheric temperature (∇_zT) and potential evapotranspiration (∇_zETP) are 8,9 mm/yr/100 m, −0,74 °C/100 m and −32,3 mm/yr/100 m, respectively. The snow cap is present in the upper zones of the basin in winter and spring, maintained annually for 3 to 4 months since 1800 m a.s.l., meaning that precipitation is partly produced as snow.

Despite the high average rainfall above 1000 mm/year, in most of the study area the surface runoff is almost nonexistent, and it is not observed until reaching lower altitudes.

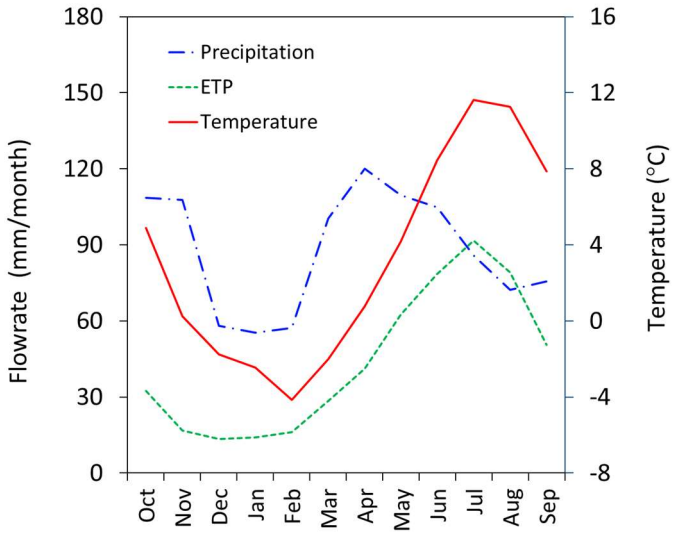

Figure 3. 2. Seasonal variation of precipitation, potential evapotranspiration and temperature measured at the meteorological station MS-01 (see Table 1) located at 2315 m a.s.l. for the period Sep 2005- Apr 2016.

3.2.2 General settings of the study zone

From a geological perspective, the massif belongs to the PCM thrust sheet that presents complex structural relationships in its contours (**Figure 3. 1**). On the E, the PCM mantle borders on the mantle of Cadí, coinciding with the point of origin for the Cardener River (spring S-05; **Figure 3. 1**). To the NE and NW, the PCM is limited by the tectonic plates of the mantles of Sierras Marginales, Montsec and Boixols. To the S, the PCM mantle overlaps with the conglomeratic materials of the Ebro Basin, the southern foreland basin of the Pyrenees. The internal structure of the PCM mantle is formed by a set of folds and thrusts detached above the Triassic. These folds have a constant direction NE-SW parallel to the NW limit of the mantle (Vergés, 1999). The stratigraphic series contains materials from the Triassic, Jurassic, Cretaceous and Paleogene with a total of approximately 1000 m thickness. The main karst aquifer inside PCM massif is in the Paleocene - Eocene carbonate rocks. The geologic structure and stratigraphy of the PCM thrust strongly influence the location of the existing karst springs, their groundwater geochemistry and their hydrologic behavior. The lower Upper Cretaceous/Paleocene (Garumnian facies) substrate materials underlying the Palaeocene aquifer are composed of sandstone, siltstone and shale. These materials constitute an impervious layer for the overlaying aquifer system.

From the geomorphological point of view, the PCM has a characteristic triangular geometry. The PCM has a smooth rounded landscape with a plain in the highest part without vegetation cover and with almost no soil, which corresponds to approximately 10% of the total area. The rest of the massif is covered by mountain meadows (29%) and forest (61%) with scarce soil depth up to medium developed soil cover. Different karstic forms progressively appear from 1950 m a.s.l. upwards, being well developed at 2050 m a.s.l., with sinkholes, dry caves, dolines and karren fields, generating a heterogeneous karstified hydrogeological system.

The hydrogeological conceptual model of the PCM aquifer system considers that recharge is produced by infiltration of precipitation as rainfall and snowmelt. The magnitude and distribution of infiltration is conditioned by the development of the karst landforms. The infiltration is produced (1) in a concentrated way through the local karstic elements such as dolines and (2) in a diffuse way by rain and snowmelt along the whole PCM area. The epikarst unsaturated zone (NSZ) presents a thickness close to 1000 m in the highest zones of the PCM. The infiltrated water flows vertically

through the NSZ towards the saturated zone.

The hydrogeological system naturally discharges through the large number of existing springs. Approximately 100 springs have been found in the PCM showing large discrepancies in their mean discharge flow rate, ranging from values <<1 L/s up to values > 100 L/s. Most of these springs discharge a local subhorizontal interflow characteristic of a small entity (i.e., Local springs, Table 1). However, in terms of groundwater discharge, there are six important springs in the PCM (i.e., Regional springs, **Table 3. 1**). These springs have been monitored regularly for this research, showing that all of them have a highly variable discharge flow rate (**Figure 3. 3**). Four of these regional springs (S-01, S-02, S-03 and S-05) are the principals discharging points of the whole hydrogeological system. The four springs are located at elevations between 944 and 1098 m a.s.l. (see Table 1). Through these main springs, the hydrogeological system discharges at two principal watersheds: the Cardener River watershed to the east and the Segre River watershed to the northwest. Groundwater flow direction is conditioned by the geological structure of PCM. Nevertheless, the exact position of the regional groundwater table is poorly known.

Table 3. 1 Meteorological stations, pluviometers and springs in the study zone sampled during the period July 2013 – October 2015.

Code	Type	Name	Elevation (m a.s.l.)	Num. water samples (-)	Discharge rate (L/s)
MS-01	Met. Station	SMC-Z8	2315	-	-
MS-02	Met. Station	AEMET-0127O	1800	-	-
P-01	Pluviometer	Refugi de l'Arp	1936	7	-
P-02	Pluviometer	Bassa Clot de la Vall	1946	8	-
P-03	Pluviometer	Refugi Bages	1768	8	-
P-04	Pluviometer	Casa X&A	1657	8	-
P-05	Pluviometer	Casa Ramonet	1450	8	-
P-06	Pluviometer	Casa Cavallera	1216	7	-
P-07	Pluviometer	Camp. La Comella	1062	8	-
P-08	Pluviometer	Camp. Morunys	896	9	-
S-01	Regional Spring	Font Aiguaneix	1098	25	8 - 73
S-02	Regional Spring	Font Sant Quintí	944	25	70 – 575
S-03	Regional Spring	Font Can Sala	1062	25	0,25 – 148
S-04	Local Spring	Font Coll de Jou	1464	25	0,07 - 0,59
S-05	Regional Spring	Fonts del Cardener	1032	25	57 – 904

S-06	Local Spring	Font carretera Refugi Arp	1858	25	0,04 – 7
M-05	Local Spring	Font del Ginebró	1730	4	<0,001
M-06	Local Spring	Font de la Garganta	1657	4	0,02-0,49
M-08	Local Spring	Font Orris 02	1871	4	0,1 – 0,7
M-14	Local Spring	Font Estivella	2053	4	0,07 – 5
M-15	Local Spring	Font Arderic	2158	3	0,03 – 2,8
M-16	Local Spring	Font del Casalí	2077	1	<0,001
M-17	Local Spring	Font del Diumenge	1989	2	0,004 – 0,026
M-18	Local Spring	Font barraca Sangonella	1940	1	0,001 - 0,01
M-24	Local Spring	Font dels Acens	1550	4	0,06 – 0,23
M-35	Local Spring	Font Ca l'Arreplagant	1330	4	<0,001 – 0,02
M-37	Local Spring	Font La Part (esllav.)	1315	4	0,5 – 1

3.3 Materials and methods

3.3.1 Field work

To collect precipitation samples, a network of 8 cumulative precipitation gauges (pluviometers) of the type CoCoRaHS RG202 Official-4 was installed at elevations between 896 and 1935 m a.s.l. (P-01 a P-08; **Figure 3. 1**). The pluviometers consist of a polycarbonate cylindrical deposit with a diameter of 10,8 cm. The pluviometers include a top funnel that captures and guides precipitation into the storing deposit, where according to the technical procedure for the stations of the Global Network of Isotopes in Precipitation (GNIP) of the International Atomic Energy Agency (IAEA), a 0,5 cm paraffin oil floating layer is added to avoid evaporation. The pluviometers were sampled seasonally (except the first winter with two campaigns), a total of 9 campaigns from Dec. 2013 to Dec. 2015. Additionally, one snow sampling survey was conducted in December 2003. The snow samples were obtained by drilling through the entire snow depth (Lambán et al., 2015) and were taken at different locations with elevations ranging from 1935 to 2150 m a.s.l.

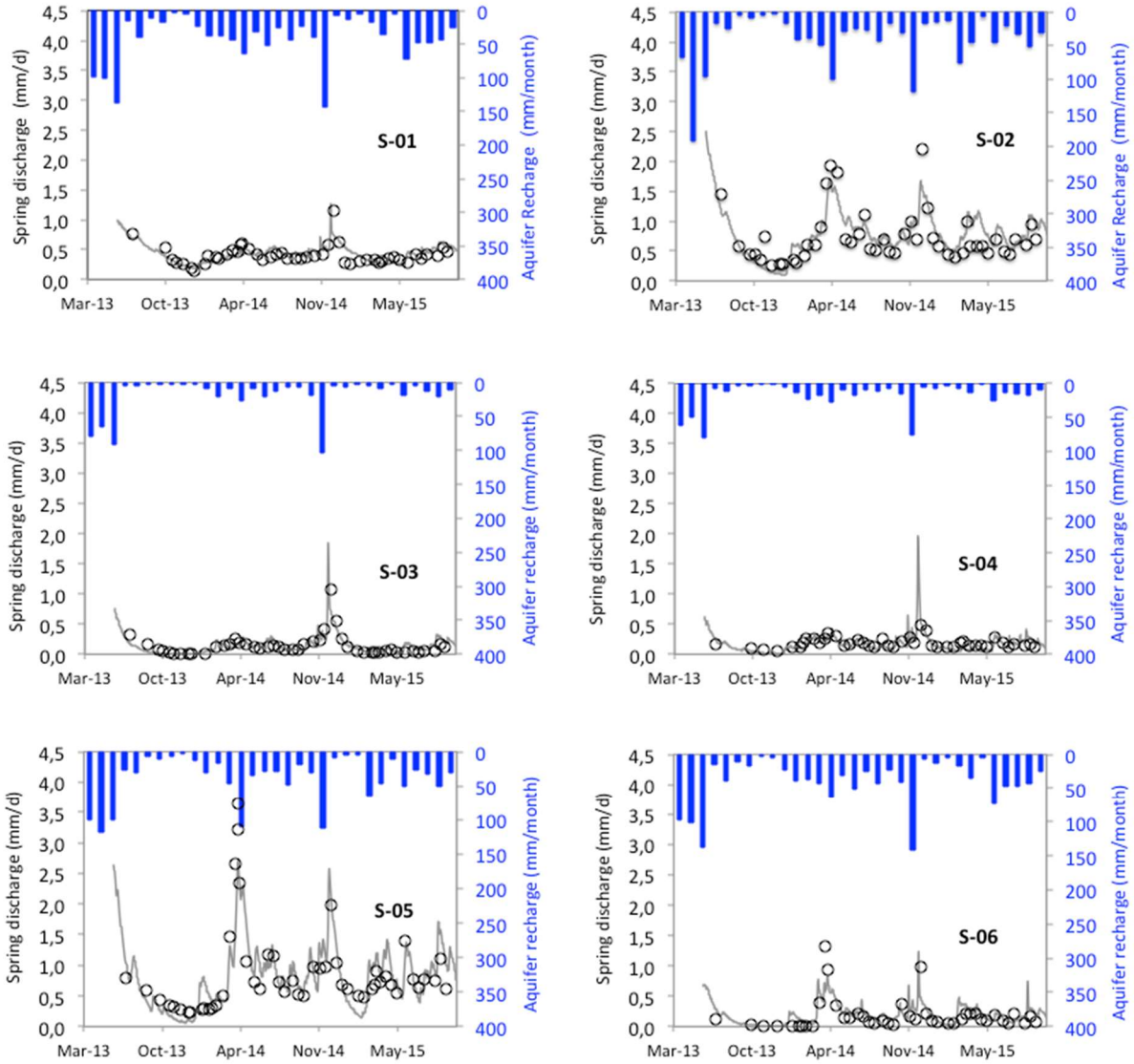

Figure 3. 3. Measured spring discharge (circles) in the six monitored springs (S-01 to S-06, **Table 3. 1**) of the PCM hydrogeological system. Gray lines indicate the spring discharge numerically simulated with the HBV model (Seibert and Vis, 2012). For each spring, blue columns indicate the recharge values time series used as input data to the corresponding HBV model.

Groundwater samples were collected under different hydrodynamic conditions between Oct. 2013 and Dec. 2015. In this period, the springs S-01 to S-06 were sampled approximately monthly, for a total of 25 sampling campaigns. Groundwater samples were taken before the snow arrival in autumn (Oct. 2013 and Oct. 2014), and after the snow-melting season (Apr. 2014 and Apr. 2015). In these springs, groundwater discharge was measured once every two weeks from Jul. 2013 to Oct. 2015

(**Figure 3. 3**). In springs S-01, S-02, S-03 and S-05 the discharge flow rate was measured by conducting slug-injection salt dilution tests (Cervi et al., 2014), whereas the volumetric method was used for the precision discharge measurement in springs S-04 and S-06. The M-## springs (Table 1) showed a tiny and intermittent discharge. Therefore, groundwater samples were only taken with uneven frequency when it was possible.

The isotopic composition (δ^2H and δ^{18}O) of all low salinity water samples was determined in the Center of Hydrogeology of the University of Málaga (CEHIUMA), where a Picarro® "L2130-I" isotopic water analyzer was used. The analytical uncertainties for δ^{18}O and δ^2H are ±0.2 ‰ and ±1.0 ‰, respectively. According to Coplen et al., (2011) several international and laboratory standards have been interspersed for normalization of analyses. The standards used (WICO-13, WICO-14, WICO-15) were calibrated in an interlaboratory comparison (Wassenaar et al., 2012). All results are given relative to the V-SMOW standard.

3.3.2 Approach for spring catchment delineation

A critical aspect to understand the behavior of karst hydrogeological flow systems is the delineation of the spring capture zones (i.e., recharge areas) and their boundaries (Goldscheider and Drew, 2007). Ideally, the delineation should be based on the proven information of connection between recharge areas and the discharge points. In high mountain zones, this connection may be confirmed by conducting tracer tests (Goldscheider et al., 2008; Mudarra et al., 2014; Barberá et al., 2018b). When this information is not available, the spring capture zone can be indirectly inferred by considering inputs from other classical information sources such as geophysics, structural geology and geomorphology data interpretation. However, 3D conceptual modeling techniques are currently being used to delineate the spring capture zones: Malard et al. (2015) analyze spring discharge hydrographs based on geological three-dimensional (3D) conceptual modeling (Butscher and Huggenberger, 2007, 2008; Martos-Rosillo et al., 2014; Ruiz-Costán et al., 2015; Malard et al., 2015; Ballesteros et al., 2015b; Epting et al., 2018).

In this work, a combined 3D conceptual methodology has been used to delineate the catchment areas associated with each spring. The delineating criteria are based on the information provided

by three complementary methods: (1) the interpretation of the geological structure and the subsurface catchments relative to each spring location. To this end, a 3D geological model has been developed in the 3DMove software platform (Midland Valley Exploration Ltd.); (2) the analysis of the disposition and location of the karst landforms over the area, and (3) the analysis through GIS spatial analysis tools of the ground surface structure, including type of soils (CREAF, 2009) and vegetation (Appendix A) at the spring recharge elevation zones. In the case of the regional springs S-01, S-02, S-03 and S-05, the three listed methods have been applied to delineate their catchment zone, whereas in the case of the perched springs S-04 and S-06, only the previous methods (2) and (3) could be applied. Figure A1 (Appendix A) shows the catchment zones (i.e., aquifer units) obtained for the selected springs.

The delineated catchment zones associated with the regional springs divide PCM into two main blocks: (1) a southwestern block that includes only the catchment zone associated with S-05. This catchment zone is characterized by a syncline dipping NW structure (**Figure 3. 1**). From a functional point of view, this zone is hydrodynamically independent of the rest of PCM given the existence of an anticline and a main NE-SW fault that prevents lateral flows. (2) The north-eastern block formed by the catchment zone associated with springs S-01, S-02 and S-03. The geological structure of this block regulates the regional groundwater flows, so as the Alinyà anticline controls the discharge of spring S-01, and the main syncline-anticline system dips SW along with the minor faults and synclines dipping south conditions the discharge of springs S-02 and S-03. Table A1 (Appendix A, Chapter 9 Supplementary material, Part 9.2.) provides the geographical details of the delineated groundwater catchment zones.

3.3.3 Characterizing the seasonal variation of environmental tracers

The evolution of some environmental variables is linked to the atmospheric temperature variation. As a result, these variables often show a similar seasonal pattern that can be characterized with a general sinusoidal function $\delta(t)$ (Jódar et al., 2014). This function consists of two additive terms, a sine-wave function [Eq. 1] plus a temporal linear trend for the mean [Eq. 2].

$$\delta(t) = A\sin(\omega(t - t_0) + \varphi) + \bar{\delta} \quad (1)$$

$$\bar{\delta} = \alpha(t - t_0) + \overline{\delta_0} \quad (2)$$

where A is the amplitude of the sinusoidal function, ω is the angular frequency, φ is the angular initial at time t_0, α is the slope of the linear trend, and $\overline{\delta_0}$ is the linear trend value at time t_0. The parameters A, α and $\overline{\delta_0}$ can be estimated by using the solution of any of the commonly available spreadsheet software's or manually. In this work, the root-mean-squared error (RMSE) is used as the selection criterion for the best fit to the measured isotope content time series. In the case time series with a short amount of data (e.g., associated with the M-## springs in **Table 3. 1**), it is not possible to obtain reliable estimates for, α, A, and $\overline{\delta_0}$ by using the method proposed above. In this case, no linear trend in the mean value is assumed ($\alpha = 0$), and $\overline{\delta_0}$ and A are estimated as:

$$\overline{\delta_0} = \frac{1}{N}\sum_{i=1}^{N}\delta_i \quad (3)$$

$$A = \max\left(\mathrm{Abs}\left(\overline{\delta_0} - \delta_i\right)\right);\ \forall i = 1 \div N \quad (4)$$

where N is the number of the isotopic content value of the time series.

Hydrogeological systems transfer the isotopic input signal of recharge. The tracer input seasonal signal is buffered and delayed as it propagates through the aquifer towards the discharging point (**Figure 3. 4**). This tracer transport process through the hydrological system can be described by the convolution integral that relates the tracer input content in recharge δ_{in} to the tracer input content in the spring discharge δ_{out} as shown below.

$$\delta_{out}(t) = \int_{-\infty}^{t}\delta_{in}(t)g(t - t')dt' \quad (5)$$

where t is the time of tracer entry as recharge, t' is the integration variable and $g(t')$ is a weighting function describing the Transit Time Distribution (TTD) exit of tracer content that entered the aquifer at different times in the past. The differences between the input and the output tracer signals

are related to the aquifer system MTT (τ) which is the first moment of the system TTD and is given by

$$\tau = \int_0^\infty t g(t) dt \tag{6}$$

where V is the volume of mobile water in the system (Małoszewski et al., 1983), and Q is the volumetric flow rate through the system. In the case of natural gradient hydrogeological systems, MTT corresponds to the mean amount of time for groundwater to travel from the recharge zone to the discharging spring. In this situation, MTT is related to the spring discharge flow rate Q, and the aquifer storage Vas follows (Custodio and Llamas, 1976):

$$\tau = \frac{V}{Q} \tag{7}$$

Additionally, in natural gradient hydrogeological systems with a seasonal varying input tracer function, MTT can be estimated as (Małoszewski et al., 1983):

$$\tau = \frac{1}{\omega}\sqrt{\left(\frac{A_{\delta_{\text{in}}}}{A_{\delta_{\text{out}}}}\right)^2 - 1} \tag{8}$$

where $A_{\delta_{\text{in}}}$and $A_{\delta_{\text{out}}}$ are the amplitudes of the seasonal variation of the isotopic content in the aquifer recharge and the spring discharge, respectively. As can be shown, the above equation compares $A_{\delta_{\text{in}}}$with respect to $A_{\delta_{\text{out}}}$, so the larger the amplitude dampening is, the longer the transit time.

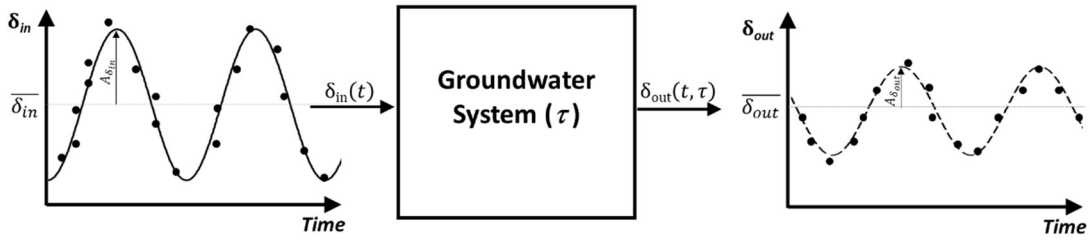

Figure 3. 4. Schematic representation of the groundwater system response $\delta_{out}(t, \tau)$ to a hypothetical input tracer function $\delta_{in}(t)$ (modified from Jódar et al., 2016b), where τ means MTT.

3.3.4 Numerical approach for simulating the aquifer behavior

To reproduce the observed spring discharge flow rates and the associated isotopic content, a two-step methodology has been used:

(1) Simulation of the hydrodynamic behavior of the hydrogeological system. To this end, the freely available version of the semi-distributed conceptual precipitation–runoff model HBV-Light (Seibert and Vis, 2012) is used. HBV is a conceptual rainfall-runoff model for catchment hydrology modeling that solves a general water balance equation. HBV has been used in different alpine mountain hydrologic research studies (Braun and Renner, 1992; Hottelet, et al., 1993; Uhlenbrook et al., 1999; Merz and Blöschl, 2004; Konz and Seibert, 2010; Staudinger et al., 2017; Epting, et al., 2018; Jódar et al., 2018). This model has become a standard tool for simulating high mountain snow-dominated hydrological systems. This code requires as input data some hydroclimatic catchment information such as the relative weight with respect to the total area of the different altitude and associated vegetation zones in the catchment, the vertical lapse rates $\nabla_z P$ and $\nabla_z T$, as well as the time series of daily P, T, and ETP. The hydrological catchment can be separated into numerous elevation zones, depending on the elevation gap between the lowest and the highest points of the catchment. In this work, every zone has been divided into three elevation zones (Table A1 in Appendix A, Chapter 9 Supplementary material, Part 9.2.). Additionally, every elevation zone can be divided into different vegetation zones. Based on the Land Cover Map of Catalonia (CREAF, 2009), three vegetation zones are considered: (1) open areas corresponding to zones of both poor or no soils where karst landforms are very well-developed (karren fields, sinkholes, dolines, etc.), (2) areas with mountain meadows and soil moderately developed, and (3) alpine forest zones with moderate to well-developed soils. A two stacked linear reservoir is used to simulate the hydrological system dynamics. The upper reservoir is used to generate surface and subsurface runoff whereas the lower reservoir generates groundwater runoff. The model considers vegetation zones parameters and catchment zone parameter (Tables C1 and C2 of Appendix C, respectively, Chapter 9 Supplementary material, Part 9.2). They are can be automatically calibrated by minimizing an efficiency objective function (R_{eff}; Table C3, Appendix C, Chapter 9 Supplementary

material, Part 9.2), which is already implemented in HBV. The model output includes the daily time series of aquifer recharge Q_R, which is used in the following step.

(2) Simulation of the transient isotopic content variation in the groundwater discharge. The temporal variation of the isotopic content in the spring discharge is simulated with FlowPC (Małoszewski and Zuber, 1996, 2002), a lumped parameter model typically used to estimate groundwater MTTs with the aid of observed environmental tracer data (Viville et al., 2006; Einsiedl et al., 2009; Katsuyama et al., 2010; Lauber and Goldscheider, 2014; Sánchez-Murillo et al., 2015; Mądrala et al., 2017). The program solves the convolution integral [Eq. 5] and transforms the isotopic input tracer signal $\delta_{in}(t)$ entering the hydrogeological system as recharge into the isotopic output tracer signal $\delta_{out}(t)$ leaving the system through the spring discharge. To this end, FlowPC includes among others two parametric TTDs which are especially well suited for simulating karst aquifer systems: (A) The exponential model (EM), also known as a "good mixing model", is typically applied in systems where the groundwater flow lines tend to converge towards the water sampling points (Zuber, 1986; Amin and Campana, 1996). (B) The Exponential-Piston model (EPM) or "real system model", which combines two parts in line, an unconfined upstream part where recharge enters the system and an exponential distribution of transit times is assumed, and a confined downstream part where the flow scheme is approximated like the piston flow model (Zuber, 1986). The weighting function for EPM is described by the following equation.

$$g(t) = \begin{cases} 0 & t < \tau\left(1 - \frac{1}{\eta}\right) \equiv t_\tau \\ \frac{1}{\tau}\eta e^{-\frac{\eta}{\tau}+\eta-1} & t \geq t_\tau \end{cases} \quad (9)$$

where η is the ratio of total volume of the hydrogeological system to the volume of the system in which the exponential TDD exists, and τ is MTT. [Eq. 9] also describes the EM weighting functions when η =1, which is the lowest bound of this parameter. The model parameters (η and τ) are calibrated by minimizing the RMSE function.

FlowPC requires the time series of (1) monthly aquifer recharge $\widehat{Q_R}$ (hereinafter, a circumflex accent over a flow or an isotopic content variable indicates that the variable is cumulated monthly or averaged, respectively), which is obtained from the HBV model outputs for each simulation, and (2) the corresponding monthly averaged isotopic content of the recharge $\widehat{\delta_R}$. Given the karstic nature of the hydrogeological system, we assume that the isotopic content of local recharge and its seasonal characteristics (i.e., $\overline{\delta}_{\mathrm{in}}, A_{\delta_{in}}$) are the same as the isotopic content and seasonal characteristics of local precipitation ($\overline{\delta}_{\mathrm{P}}, A_{\delta_{\mathrm{P}}}$). Since $\overline{\delta}_{\mathrm{P}}$ and $\mathrm{A}_{\delta_{\mathrm{P}}}$ are known, then $\delta_{\mathrm{P}}(t)$ is analytically obtained through [Eq.1]. As $\delta_{\mathrm{P}}(t)$ is a daily time function, it is necessary to transform it into $\widehat{\delta_{\mathrm{P}}}$. For the j^{th} month, $\widehat{\delta_{\mathrm{P}}}_j$ is obtained by weighting the daily values of recharge isotopic content $\delta_{\mathrm{P}_{ij}}$ by the corresponding daily recharge rate $Q_{\mathrm{P}_{ij}}$ as

$$\widehat{\delta_{\mathrm{R}}}_j \sim \widehat{\delta_{\mathrm{P}}}_j = \frac{\sum_{i=1}^{N} \delta_{\mathrm{P}_{ij}} Q_{\mathrm{R}_{ij}}}{\sum_{i=1}^{N} Q_{\mathrm{R}_{ij}}} \qquad (10)$$

where N is the number of days of the j^{th} month. The Appendix D, Chapter 9 Supplementary material, Part 9.2, includes all the technical details corresponding to the different FlowPC models used in this work.

3.3.5 Statistical analysis of the relationship between the infiltration coefficient and recharge

To analyze the factors that controls the mean calculated infiltration coefficient (ξ) in the PCM, a linear regression model has been built, expressing the dependent variable ξ as a linear function of N explanatory variables Ψ_i as

$$\xi = \lambda_0 + \sum_{i=1}^{N} \lambda_i \Psi_i \qquad (11)$$

where λ_0 is the intercept (constant) term, and λ_i ($i \geq 1 \div N$) are the regression coefficients associated

with the predictors Ψ_i. In this study, the predictor variables of the linear regression model of the [Eq.11] are the elevation of the spring recharge zone Z_R (Table 3), the mean precipitation at the spring recharge zone P_{ZR} (Table 6), and the percentages of open areas, mountain meadows and forest in the spring catchment zones (VZ_1, VZ_2 and VZ_3, respectively; Table A1 in Appendix A, Chapter 9 Supplementary material, Part 9.2). The coefficient of determination of the regression is one, so the model reproduces the whole variance of ξ. **Table 3. 7** shows the intercept value λ_0, the regression coefficients λ_i, and their corresponding standardized value β_i ($i \geq 1 \div N$). The standardized value β_i measures the expected change in ξ, in standard deviation units, for a one standard deviation change in Ψ_i, provided that other explanatory variables in the model (Ψ_j, $\forall i \neq j$) are fixed (Nimon and Oswald, 2013). The larger the absolute value of β_i, the more important the corresponding predictor Ψ_j is.

3.4 Results and discussion

3.4.1 Results from observed data

The isotopic content of the precipitation corresponding to the water samples taken is shown in Figure 5A. The mean isotopic content of precipitation is lighter in winter and autumn than that in spring and summer, as one would expect given the dependence between the isotopic content in rainfall and temperature (Mook and De Vries, 2000). The obtained values are aligned between the Global Meteoric Water Line (GMWL) and the West Mediterranean Meteoric Water Line (WMMWL) (**Figure 3. 5** A). The local water meteoric water line (LMWL) that is obtained by linear regression (N= 76; R^2= 0,97) is defined as $\delta^2H = 8{,}05 \cdot \delta^{18}O + 12{,}74$. From a seasonal point of view, the isotopic content of precipitation in autumn and winter presents a larger variability than the isotopic content of precipitation in spring and summer, as shown in **Figure 3. 5** B by the error bars indicating the standard deviation associated with every seasonal value. The isotopic content in groundwater changes seasonally much less, than the isotopic content in precipitation (**Figure 3. 5** B), pointing out the existence of a good mixing flow process in the discharging points of the aquifer.

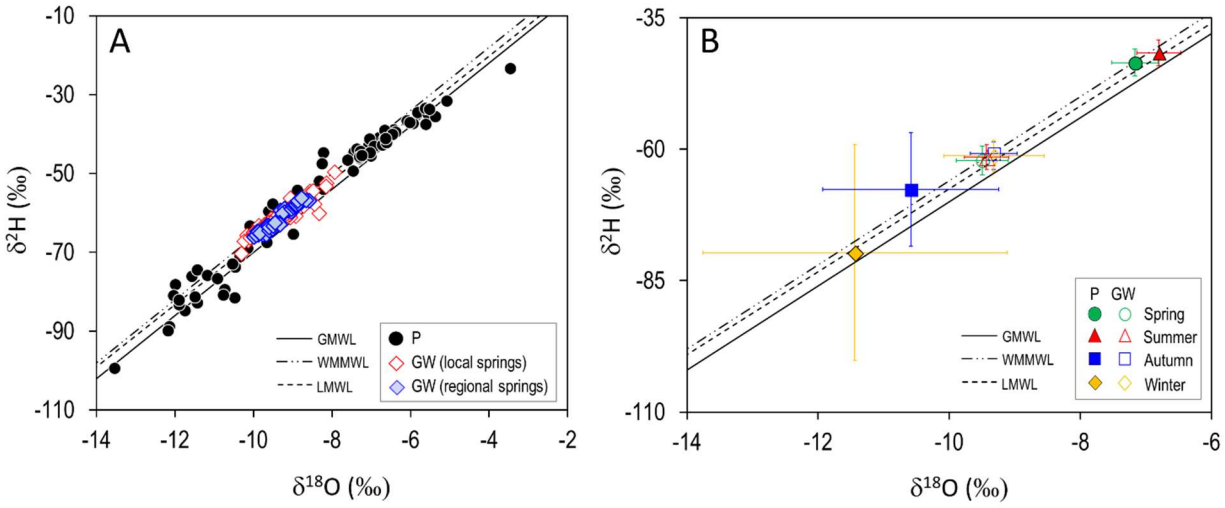

Figure 3. 5. (A) Values of $\delta^{18}O$ and $\delta^{2}H$ in precipitation (P; solid circles) and groundwater (GW) from local springs (empty red diamonds) and from regional springs (solid blue diamonds) for the period Oct. 2013 – Dec. 2015. (B) Seasonal overall averages of $\delta^{18}O$ and $\delta^{2}H$ for precipitation (P; solid symbols) and groundwater (GW; empty symbols). The spring, summer autumn and winter values are indicated by green circles, red triangles, blue squares and orange diamonds, respectively. GMWL (Clarke and Fritz, 1997) is the Global Meteoric Water Line (slope 8 and *dex*=10‰), WMMWL is the Western Mediterranean Meteoric Water Line (slope 8 and *dex*=14‰) and LMWL is the Local Meteoric water Line (slope 8,05 and *dex*=12,74‰).

The geographical location of the study zone postulates the Mediterranean as the most important source of precipitation. This assumption is supported by the overall mean deuterium excess (*dex*= $\delta^{2}H - 8\cdot\delta^{18}O$) value of 12,03 ± 3,37 ‰ obtained for all the precipitation samples analyzed (Celle-Jeanton et al., 2001; Jiménez-Martínez and Custodio, 2008). Nevertheless, the Atlantic fingerprint in rainfall can be observed in the above *dex* value through its variation interval, which provides a minimum *dex* value of 8,66 ‰ (Froehlich et al., 2001; Araguás-Araguás and Díaz-Teijeiro, 2005).

The isotopic composition of precipitation and spring discharge show a seasonal variation, which is not reflected in the deuterium excess. A seasonal variation in *dex* would indicate the existence of different moisture sources generating rainfall in the study zone by following a certain seasonal pattern (Schotterer et al 1993; Liu et al 2008; Froehlich et al 2008). The lack of such seasonal pattern supports the Mediterranean as the main rainfall source.

A sine-wave function [Eq.1] is used to characterize every one of the measured seasonal time series of isotopic content in water from the sampling points (Figure B1 in Appendix B, Chapter 9 Supplementary material, part 9.2). and **Table 3. 2** and **Table 3. 3** show the calibrated mean isotopic content ($\bar{\delta}$) and amplitude (A) corresponding to the time series of isotopic content of precipitation and spring discharge, respectively.

Table 3. 2. Mean value $\bar{\delta}_{in}$ and amplitude $A_{\delta_{in}}$ of the seasonal variation in the isotopic content of precipitation for the sampled pluviometers

	$\bar{\delta}_{in}$ (‰)			$A_{\delta_{in}}$ (‰)	
Pluviometer	$\delta^{18}O$	$\delta^{2}H$	*dex*	$\delta^{18}O$	$\delta^{2}H$
P-01	-9.20	-59.91	14.56	3.34	26.89
P-02	-9.50	-62.29	13.88	2.87	23.23
P-03	-9.20	-60.25	12.94	3.29	27.92
P-04	-8.60	-56.11	12.87	3.02	26.05
P-05	-8.60	-55.65	12.37	3.05	23.31
P-06	-7.80	-51.10	9.53	2.76	23.96
P-07	-7.50	-49.06	10.24	2.59	20.92
P-08	-7.50	-50.22	9.40	2.55	19.53

Table 3. 3. Mean value $\bar{\delta}_{out}$ and amplitude $A_{\delta_{out}}$ of the seasonal variation in the isotopic content of groundwater for the springs sampled. For every spring, the elevation of the corresponding recharge zone Z_R is included. For this elevation, the associated amplitude $A_{\delta_{ZR}}$ of the seasonal variation in isotopic content of precipitation is shown.

	$\bar{\delta}_{out}$ (‰)			$A_{\delta_{out}}$ (‰)		Z_R (m a.s.l)			$A_{\delta_{ZR}}$ (‰)	
Spring	$\delta^{18}O$	$\delta^{2}H$	*dex*	$\delta^{18}O$	$\delta^{2}H$	$\delta^{18}O$	$\delta^{2}H$	dex	$\delta^{18}O$	$\delta^{2}H$
S-01	-9,31	-60,65	13,81	0,12	1,10	1892	1881	1852	3,16	26,23
S-02	-9,61	-62,82	14,06	0,25	1,93	2038	2046	1902	3,24	27,18
S-03	-9,18	-59,85	13,60	0,11	1,07	1830	1819	1702	3,12	25,88
S-04	-9,01	-58,11	13,95	0,10	0,67	1745	1686	1881	3,07	25,12
S-05	-9,73	-63,36	14,50	0,14	0,88	2099	2088	1994	3,28	27,41
S-06	-9,69	-64,03	14,80	0,15	0,90	2078	2140	1798	3,27	27,71
M-05	-9,01	-58,53	13,52	0,44	1,81	1744	1718	1793	3,07	25,31
M-06	-8,70	-54,75	14,88	0,54	2,51	1597	1428	2071	2,98	23,65
M-08	-9,49	-62,22	13,68	0,27	1,84	1979	2001	1826	3,21	26,92
M-14	-9,69	-64,01	13,53	1,08	8,01	2079	2138	1795	3,27	27,70
M-15	-9,73	-63,81	14,05	0,87	6,24	2099	2123	1901	3,28	27,61
M-16	-9,77	-64,13	14,05	0,65	4,00	2118	2147	1902	3,29	27,75

M-17	-9,76	-64,32	13,73	0,49	2,86	2110	2161	1836	3,29	27,83
M-18	-9,59	-63,12	13,64	0,62	4,12	2031	2070	1817	3,24	27,31
M-24	-9,41	-62,26	13,02	0,47	1,64	1941	2004	1690	3,19	26,93
M-35	-8,90	-57,02	14,14	0,94	7,54	1690	1602	1920	3,04	24,65
M-37	-8,44	-54,00	13,53	0,26	0,93	1469	1371	1795	2,90	23,33

The mean isotopic content in rainfall $\bar{\delta}_{in}$ shows a clear-cut linear relationship with elevation (**Figure 3. 6**) that allows defining Isotopic Altitudinal Lines (IAL) for $\delta^{18}O$, $\delta^{2}H$ and *dex*, with slopes (i.e., vertical gradients $\nabla_z\delta^{18}O$, $\nabla_z\delta^{2}H$ and $\nabla_z dex$) of -1,9, -12,1 and 4,7 ‰/km, respectively. Vertical gradients ($\nabla_z\delta$) of mean isotopic content in precipitation are common in mountain zones (see Poage and Chamberlain, 2001, and references therein) and are related to the atmospheric decreasing thermal vertical profile existing along the slope of the mountains. $\nabla_z\delta$ values obtained for the study zone are like those obtained in other alpine areas, especially in the central Pyrenees and the Alps (Table 4).

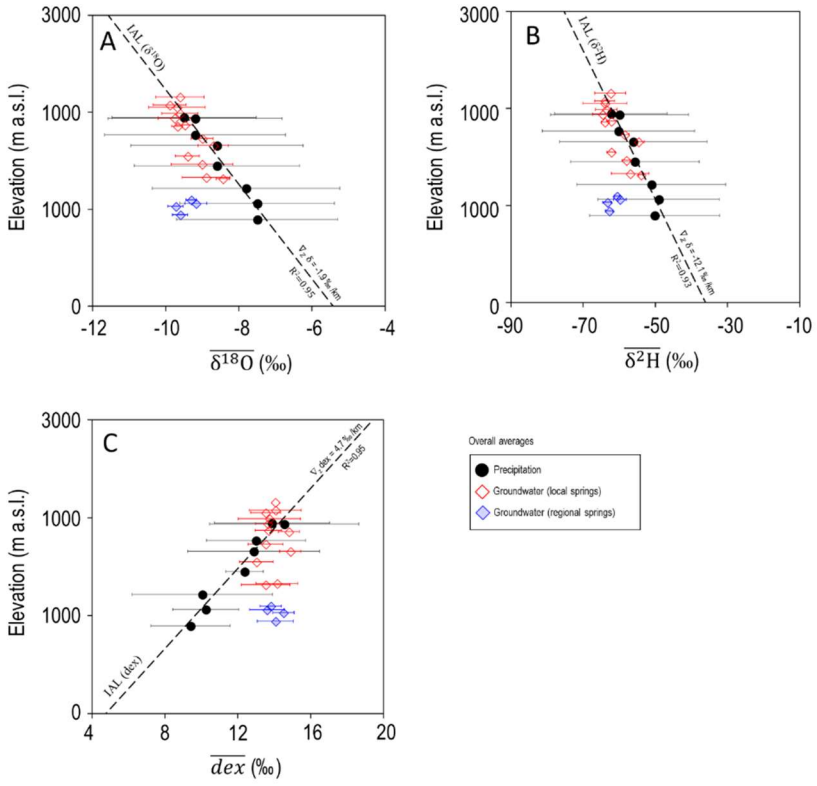

Figure 3. 6. Relationship between elevation and the mean isotopic content in precipitation and springs. (A) $\delta^{18}O$, (B) $\delta^{2}H$, and (C) *dex*. Error bars indicate the standard deviation. Dashed lines indicate the local Isotopic Altitudinal Line (IAL) of precipitation.

The vertical gradients of the mean isotopic content in precipitation depend linearly on the mean seasonal precipitation (**Figure 3. 7**). In the case of $\delta^{18}O$ and $\delta^{2}H$, the higher the seasonal precipitation is, the lower the seasonal gradient is. In the case of *dex*, the relationship is reversed, obtaining a higher $\nabla_z dex$ value as seasonal precipitation increases. In a seasonal framework, recycling moisture evaporated from the land surface to atmosphere may increase *dex* of local precipitation. Soil evaporation is maximum when atmospheric vapor pressure deficit (Δe = e-e_{sat}, e being the atmospheric water pressure and e_{sat} the saturating water pressure at the air parcel temperature) is maximum, if the soil contains water for evaporating. Therefore, to allow soil water to evaporate, it is necessary to have enough (1) soil water content, which is higher in spring and autumn since these are the rainiest seasons, and (2) atmospheric vapor pressure deficits (Δe). Satisfying these two conditions, $\nabla_z dex$ is maximum when the difference in *dex* (i.e., Δe) between the highest and the lowest points of the mountain slope is maximum. Given that e_{sat} is an increasing function of temperature (Gonfiantini et al., 2001), Δe will decrease as temperature declines. During the cold season, despite a thermal difference existing between the highest and lowest points of the mountain, the difference in Δe between these points is minimum. Additionally, the commented Δe difference is minimum as well when there is no thermal difference along the mountain slope, a situation that is favored by the cathabaltic winds in winter (Obleitner, 1994; Gladich et al., 2011) but is also favored by the vertical atmosphere air mixing during the typical summer local low-pressure convective rainfall events.

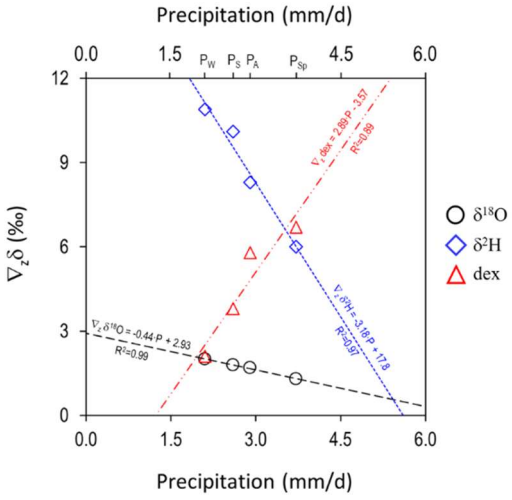

Figure 3. 7. Dependence of the vertical gradient of the mean isotopic content with respect to the mean seasonal precipitation. The subscripts Sp, S, A, and W stand for spring, summer, autumn and winter, respectively.

The amplitude of the seasonal variation in the isotopic content of precipitation $A_{\delta_{in}}$ relates linearly to elevation (**Figure 3. 8**) to allow defining Amplitude Altitudinal Lines (AAL) for $\delta^{18}O$ and $\delta^{2}H$ with slopes (i.e., vertical gradients $\nabla_z A_{\delta^{18}O}$ and $\nabla_z A_{\delta^{2}H}$) of 0,6 and 5,7 ‰/km, respectively. Similar vertical gradients have previously been reported in the central Pyrenees (Jódar el al., 2016b) and the Bernese Alps (Jódar el al., 2016a) (**Table 3. 4**).

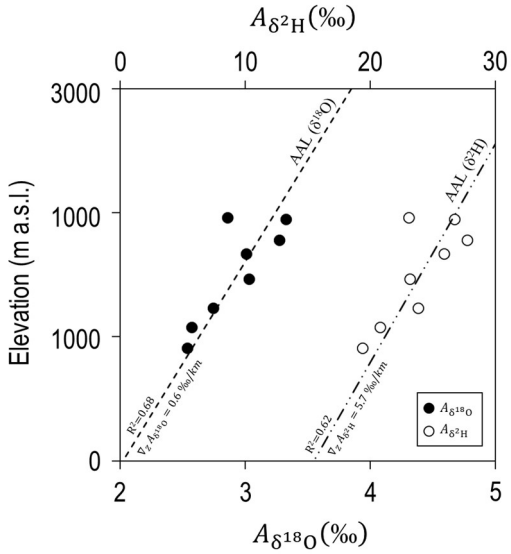

Figure 3. 8. Relationship between elevation and amplitude of the seasonal variation of the isotopic content ($\delta^{18}O$, $\delta^{2}H$) in precipitation. Dashed line and dashed-dotted line indicate the local Amplitude Altitudinal Lines (AALs) of precipitation for $\delta^{18}O$ and $\delta^{2}H$, respectively.

Table 3. 4 Vertical gradients of mean isotopic water content and amplitude of the seasonal variation of the isotopic water content in precipitation.

Zone	Z_{min} - Z_{max} (m a.s.l.)	$\nabla_z \delta^{18}O$ (‰/km)	$\nabla_z \delta^{2}H$ (‰/km)	$\nabla_z dex$ (‰/km)	$\nabla_z A_{\delta^{18}O}$ (‰/km)	$\nabla_z A_{\delta^{2}H}$ (‰/km)	Reference
Eastern Pyrenees (PCM[a])	896-1936	-1,9	-15,2	4,7	0,6	6,1	This study
Central Pyrenees (PNOMP[b])	772-2200	-2,2	-17,4	2,2	0,9	4,4	Jódar et al. (2016a)
Bernese Alps	874-2023	-3,0	-19,7	3,7	1,6	14,6	Jódar et al. (2016b)

Austrian Alps	580-2245	-1,9	-12,0	2,7	-	-	Froehlich et al. (2008)
Austrian Alps	469-1598	-1,3	-8,0	3,4	-	-	Froehlich et al. (2008)
Central Andes (western flank)	2380-4250	-4,7	-42,5	2,2	-	-	Aravena et al. (1989)
Central Andes (eastern flank)	2380-4250	-1,9	-14,3	1,1	-	-	Fiorella et al. (2015)
Central Andes (eastern flank)	200-4080	-1,7	-11,7	2,0	-	-	Gonfiantini et al. (2001)
Western Carpathians	104-2008	-2,1	-	-	-	-	Holko et al. (2012)
Mount Cameroon	10-4050	-1,16	-11,4	1,4	-	-	Gonfiantini et al. (2001)

(a): Port del Comte Massif; (b): Ordesa and Monte Perdido National Park

The mean isotopic content of groundwater corresponding to local (perched) springs shows a relationship with elevation dependence with a vertical gradient larger than that of precipitation (Figure 6), indicating the existence of aquifer recharge along the mountain slope, a process also known as slope effect (Custodio and Jódar, 2016). Additionally, the evolution of the isotopic content in the spring discharge shows a seasonal dependence like precipitation but showing smaller amplitudes (Figure B1 in Appendix B, Chapter 9 Supplementary material, part 9.2). Even being lumped, the seasonal pattern of recharge is observed in the spring discharge, indicating that MTT should not be longer than 5 or 6 years (DeWalle et al., 1997).

The isotopic altitudinal line (IAL, Figure 6) allows estimation of the elevation of the recharge zone (Z_R) corresponding to every spring by projecting their mean isotopic content on IAL. Table 3 shows Z_R for all the springs, with their mean Z_R value ranging between 1420 m a.s.l. (M-37) and 2136 m a.s.l. (M-17). With a known value for Z_R, it is possible to calculate the amplitude of the variation in the isotopic content in precipitation at the recharge zone elevation ($A_{\delta_{ZR}}$) by projecting Z_R on the amplitude altitudinal line (AAL, Figure 8). Table 2 shows $A_{\delta_{ZR}}$ for every spring. Finally, if both $A_{\delta_{ZR}}$ (i.e., $A_{\delta_{in}}$ at the springs recharge zone) and $A_{\delta_{out}}$ are known, it is possible to obtain a first analytical estimate of MTT through [Eq. 8]. **Table 3. 5** provides the MTT values obtained for all the springs. As can be shown, the obtained MTT values range between 0,5 and 5 yr.

Table 3. 5 MTT values estimated for the springs sampled

Spring	$\delta^{18}O$			$\delta^{2}H$		
	τ^{a}(yr)	τ^{b}(yr)	η(-)	τ^{a}(yr)	τ^{b}(yr)	η(-)
S-01	4,10	2,25	1,02	3,78	3,00	1,01
S-02	2,06	1,42	1,02	2,23	1,96	1,00
S-03	4,67	2,25	1,00	3,83	2,33	1,01
S-04	4,70	2,33	1,01	5,93	2,67	1,00
S-05	3,73	2,88	1,02	4,98	2,83	1,01
S-06	3,47	2,58	1,02	4,90	2,75	1,02
M-05	1,10	-	1,00	2,22	-	1,00
M-06	0,86	-	1,00	1,49	-	1,00
M-08	1,89	-	1,00	2,32	-	1,00
M-14	0,45	-	1,00	0,53	-	1,00
M-15	0,58	-	1,00	0,69	-	1,00
M-16	0,79	-	1,00	1,09	-	1,00
M-17	1,06	-	1,00	1,54	-	1,00
M-18	0,82	-	1,00	1,04	-	1,00
M-24	1,07	-	1,00	2,61	-	1,00
M-35	0,49	-	1,00	0,5	-	1,00
M-37	1,77	-	1,00	3,99	--	1,00

(a) Analytical MTT value obtained by [Eq. 8]. (b) Numerical MTT value obtained by FlowPC.

3.4.2 Aquifer recharge evaluation through HBV

The HBV semi-distributed conceptual rainfall–runoff model has been used to simulate the observed groundwater discharge in every spring. The spring discharges were measured every fortnight between July 2013 and October 2015. This period has been used for calibrating the HBV parameters, which are shown in Table C4 (Appendix C, Chapter 9 Supplementary material, part 9.2). The efficiency parameter R_{eff} that describes the goodness of the model fit ranges between 0,55 (S-01) and 0,77 (S-05) (Table C5, Appendix C, Chapter 9 Supplementary material, part 9.2). The computed discharges resemble the observed discharges by reproducing their temporal evolution in all the springs (**Figure 3. 3**).

The results from the HBV model indicated that recharge is especially concentrated in the open areas (VZ_1) and meadow areas (VZ_2). The yearly average effective recharge ranges from 210 mm/yr (S-04) to 637 mm/yr (S-06). The aquifer infiltration capacity ξ (i.e., the ratio between Q_{Re} – the effective recharge of the aquifer, and P_{ZR} - precipitation at the spring recharge zone) ranges as the yearly average ranges from 28,3% (S-03) to almost 62% (S-06) (**Table 3.6.**).

Table 3. 6 Mean annual precipitation P_{ZR}, mean aquifer recharge $\mathbf{Q_R}$, seasonal distribution of recharge, infiltration capacity ξ.

Spring	P_{ZR}	Q_R	$\frac{Q_{R_e\ Spring}}{Q_R}$	$\frac{Q_{R_e\ Summer}}{Q_R}$	$\frac{Q_{R_e\ Autumn}}{Q_R}$	$\frac{Q_{R_e\ Winter}}{Q_R}$	ξ^a
	(mm/yr)	(mm/yr)	(%)	(%)	(%)	(%)	(%)
S-01	954	473	37,5%	15,0%	25,4%	22,1%	49,6%
S-02	1006	433	40,8%	12,3%	23,8%	23,1%	43,0%
S-03	793	227	38,1%	6,7%	27,2%	27,9%	28,6%
S-04	698	210	37,0%	10,2%	25,4%	27,4%	30,1%
S-05	1008	429	42,5%	14,3%	23,0%	20,2%	42,6%
S-06	1030	637	45,9%	8,9%	21,2%	24,0%	61,9%

(a) $\xi = Q_{R_e}/P_{ZR}$

Aquifer recharge follows a linear relationship similar to precipitation, as found by Martos-Rosillo et al. (2015) for the mountain carbonate aquifers in the Betic Cordillera (Southern Spain), where recharge is generally lower (**Figure 3. 9** A). In PCM, recharge is at a maximum in spring, accounting for 40,3% of the total recharge, and this outcome is explained by both rainfall and snow melt infiltration. Recharge is at a minimum (11,2%) in summer, coinciding with the period of minimum seasonal precipitation.

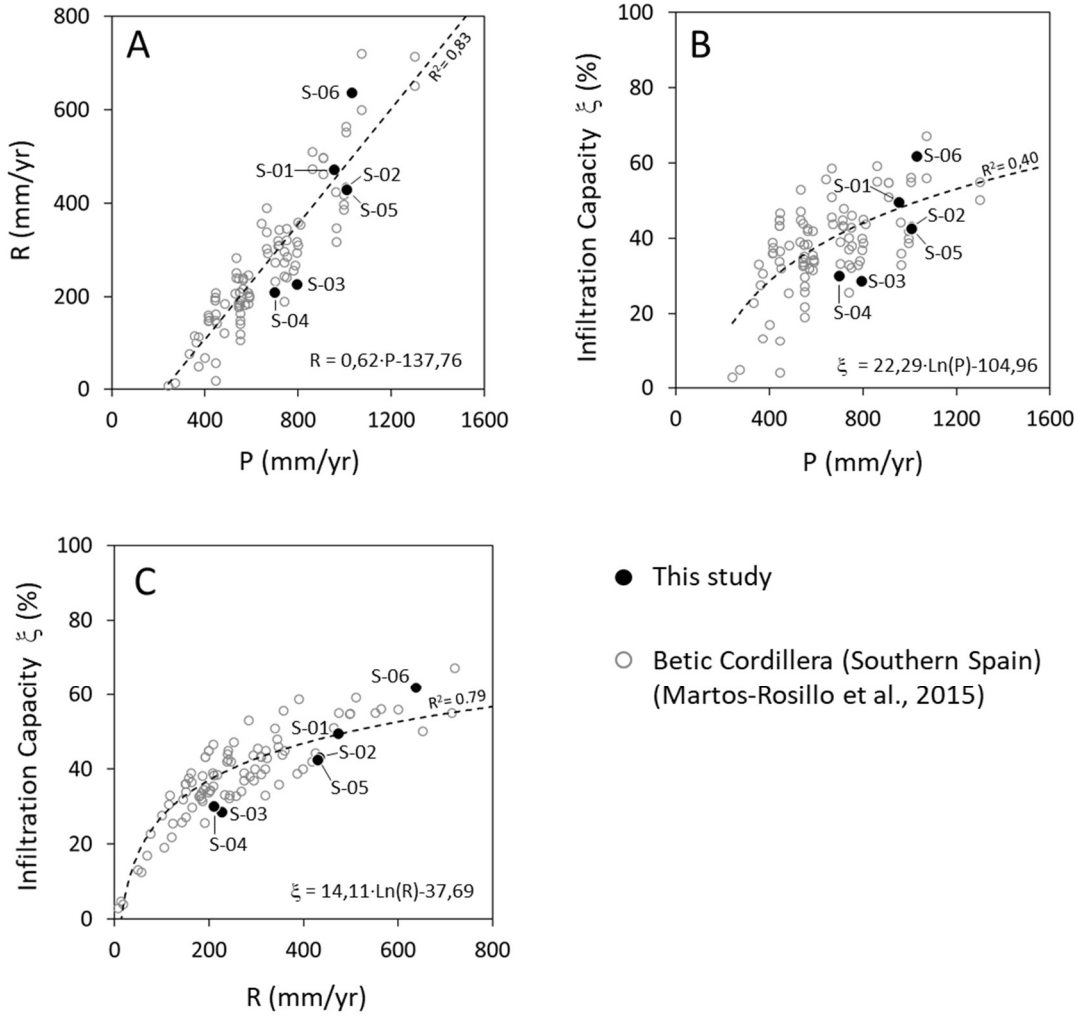

Figure 3. 9. (A) Mean annual rainfall versus mean annual recharge, (B) Mean infiltration coefficient versus mean annual rainfall, and (C) Mean infiltration coefficient versus mean annual recharge.

The relationship between ξ and P (**Figure 3. 9** B) is not as clear as the relationship between ξ and R (**Figure 3. 9** C), indicating that precipitation is a necessary condition for aquifer recharge, but it is not enough. In this respect, the results of the application of the linear regression model between the variables Z_R, $P_{ZR,\ and}$ VZ_1, VZ_2 and VZ_3; shows that the Z_R and is the most important predictor controlling the aquifer infiltration capacity ξ. In addition, VZ_1 (karren fields and sinkholes at the highest parts of the massif) and VZ_3 (forest fields at the lowest of the massif) also play a role regarding ξ. These parameters reflect the differences in both the karstification degree and the vegetation covering the epikarst system in the PCM.

Table 3. 7 No standardized (λ) and standardized (β) regression coefficients associated with the explanatory variables used in the multiple regression method.

Explanatory Variable	λ	β
Intercept (λ_0)	-39,562	--
Z_R	0,047	0,823
P_{ZR}	-0,007	-0,054
VZ_1	6,034	0,133
VZ_2	4,018	0,072
VZ_3	258,518	0,122

3.4.3 Determination of spring discharge mean transit time

To estimate the mean transit time of the spring discharge, the program FlowPC v3.2 (Małoszewski and Zuber, 1996) has been used. According to the hydrogeological setting, it is assumed that the EPM flow model can describe the behavior of the aquifers discharging through the springs of PCM. The lumped model parameters (η and τ) have been calibrated (**Table 3. 5**) by fitting the isotopic contents observed in the spring discharge from December 2013 to December 2015 (**Figure 3. 10**). The goodness of fit is defined in terms of RMSE, ranging between 0,02‰ (S-05) and 0,04‰ (S-02) for $\delta^{18}O$ (Table D1, Appendix D, Chapter 9 Supplementary material, part 9.2), and between 0,17‰ (S-03) and 0,22‰ (S-04) for $\delta^{2}H$ (Table D2, Appendix D).

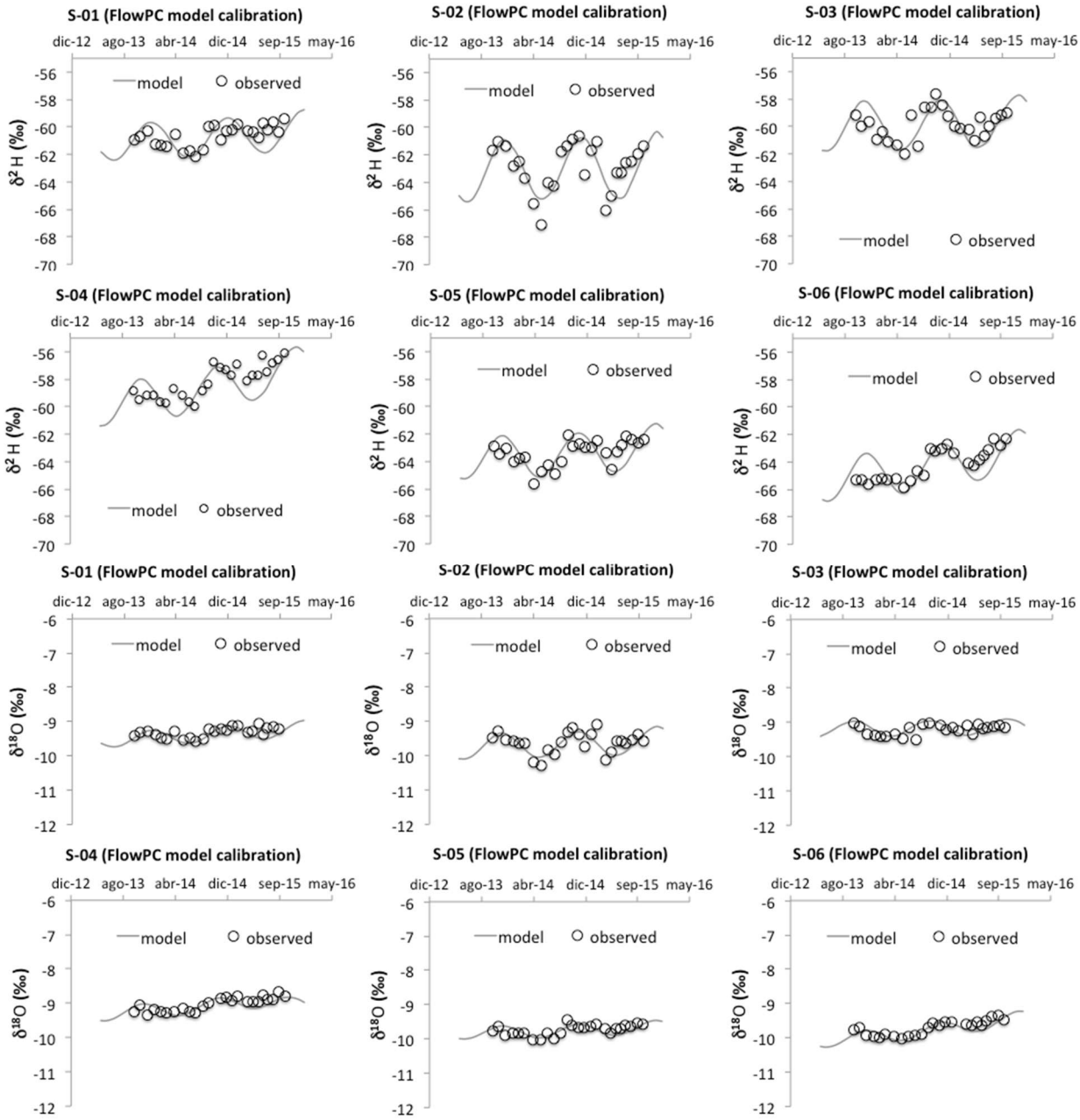

Figure 3. 10. Measured against simulated isotope content evolution with FlowPC and an EPM model. The gray line represents the best fit.

The estimated value of η is very close to 1 regardless of the spring, indicating that the corresponding aquifers behave as almost an exponential flow model in coherence with the behavior of a karst aquifer system discharging through a main spring. The estimated MTT with the applied methodology ranges between 1,69 yr (S-02) and 2,85 yr (S-05), while in the case of the analytical approach MTT ranges between 2,14 yr (S-02) and 5,31 yr (S-04).

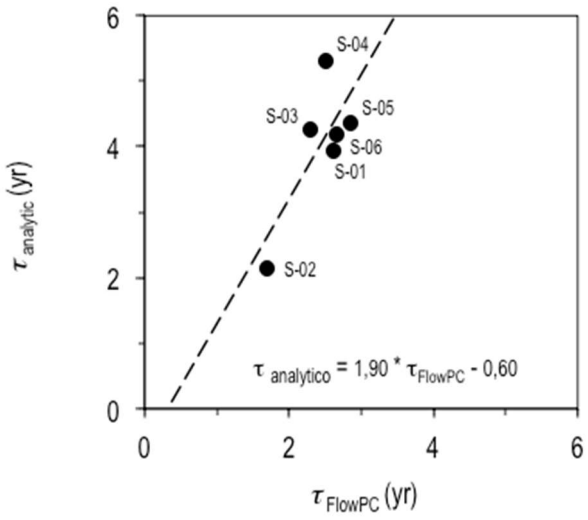

Figure 3. 11. Graph showing the MTT values estimated based on the lumped parameter model FlowPC (Maloszewski, 1996) versus the MTT values estimated based on the analytical model [Eq. 8] (Maloszewski et al., 1983)

The MTT values obtained by this numerical approach are 1,9 times shorter than the MTT values analytically obtained through [Eq. 8] that compares the amplitude of the seasonal isotopic content of recharge with the seasonal isotopic content in the spring discharge (**Figure 3. 11**). In the numerical case, the monthly isotopic content in recharge is weighted by the monthly volumetric recharge rate, whereas in the analytical case, the isotopic content weighting coefficients for the monthly recharge are all equal to 1 because recharge is assumed constant (i.e., steady state) for the whole period covered by the isotopic content time series. This assumption is worth keeping in mind when using [Eq. 8] for estimating groundwater mean transit times. In other words, if aquifer recharge shows a seasonal pattern, then the numerical approach should be used instead of the analytical approach to estimate MTT. The transit time discrepancies between both approaches may be critical when MTT is used as a vulnerability indicator for karst-fissure aquifers (Malík et al, 2016). The results obtained suggest that the numerical approach based explicitly on considering the recharge series in the LPM model provides a more accurate evaluation of hydraulic dynamics throughout the system. This allows better MTT estimations, similar of what concluded Vitvar et al. (1999) in pre-alpine non-karst aquifers. The MTT values obtained in this work are consistent with the conceptual model of the karst system. The aquifer presents specific zones with rapid recharge through surficial karstic

elements (e.g. swallow holes) and slow recharge trough meadows and forest.

In terms of MTT, the results obtained in this study are similar to those obtained in other hydrological karst systems located in mountain zones: (1) In the case of the Ordesa and Monte Perdido karst aquifer system (Central Pyrenees, Spain), which is the highest calcareous massif in Western Europe, Lambán et al. (2015) and Jódar et al. (2016b) estimated MMT for several springs. For each spring the authors fitted a sinusoidal function [Eq. 1] to the measured tracer ($\delta^{18}O$ and $\delta^{2}H$) content time series corresponding to rainfall entering the system as recharge and the spring discharge, obtaining the amplitude of the seasonal variation of both the input and output system tracer function ($A_{\delta_{in}}$ and $A_{\delta_{out}}$, respectively; **Figure 3. 4**). Besides, the authors assumed a constant recharge rate along the year. This hypothesis allowed obtaining an analytical solution to the convolution integral [Eq. 5] (Jódar et al., 2014) but also applying [Eq. 8] to directly estimate MTT, that ranged between 1,12 and 4,48 yr.

(2) In the Wimbach high-alpine karst system (Berchtesgaden Alps) Einsiedl et al. (2009) estimated MTT with FlowPC. To this end, they used as tracer input function the time series of ^{3}H content in rainfall measured in a meteorological station close to the study zone, and as system output the time series of ^{3}H content in groundwater discharge for different springs and also at the outlet of the hydrological catchment. They obtained MTT ranging between 4 and 5 yr for the considered springs, and 5 yr for the whole hydrologic catchment. For the same catchment, Maloszewski et al. (1992) evaluated the MTT by using monthly recharge time series instead of rainfall time series. The aquifer recharge time series was obtained by applying a seasonal infiltration coefficient to the observed monthly precipitation time series. With this approach they estimated a MTT of 4,15 yr. This value is close to that obtained by Einsiedl et al. (2009). Additionally, Garvelmann et al. (2017) expanded the previous studies in the Berchtesgaden Alps for a total of eight springs. For each spring they estimated MTT using two different methods; (A) by numerically solving the convolution integral [Eq. 5], and (B) though [Eq. 8] by previously conducting a sin-wave analysis [Eq. 1] to the input (i.e. rainfall) and output tracer functions. The MTT obtained by both methods did not show large discrepancies for the same spring. In terms of the obtained MTT the sampled springs were be classified in two groups: a first group with relatively short MTTs (0,7 to 1,9 yr) and a second group with longer MTTs (7,3 to 12,5 yr).

(3) In the Schneealpe massif Rank et al. (1992) used the environmental tracers to study the karstic-fissured-porous aquifer system of Schneealpe, The aquifer system that is drained by two principal springs is the main drinking water resource for Vienna (Austria). It is composed of a fissured-porous aquifer with a high storage capacity that partially feds a karst aquifer conformed by a high-conductivity drainage channel network. For each aquifer they estimated MTT by calibrating a LPM with a 8 years long time series of environmental tracer data, using ^{3}H and $\delta^{18}O$ for the fissured-porous and the karst aquifer, respectively. In the former case MTTs ranged between 2,5 and 4,5 yr, whereas in the karst aquifer the estimated MTT was only 2 months. Maloszewski et al. (2002) recalibrated both LPMs by refining and extending up to 20 years the length of the observed time series of ^{3}H and $\delta^{18}O$ measurements. In the case of the fissured-porous aquifer the obtained MTTs ranged between 14 and 26 yr, being significantly larger than those obtained by Rank et al (1992). Nevertheless, in the case of the karst aquifer the obtained MTTs were similar ranging between1,2 and 1,5 months. The large discrepancy between the MTT associated to the Fissured-Porous and karst aquifer indicates that water enters the aquifer system at the surface and flows through it towards the conductive drainage channels until reaching the springs. Nevertheless, the short MTTs associated to the karst aquifer reveal a direct hydraulic connection between the sinkholes at the surface and the drainage channel network.

(4) In the Wetterstein Mountains karst aquifer system Lauber and Goldscheider (2014) used both artificial (uranine) and environmental tracers (^{18}O and ^{2}H) to investigate the hydrological behavior of the system. Despite the low recovery of artificial tracer during the tracer test, the fast tracer arrival observed in all the sampled springs, with peak times between 1,8 and 3,2 days, indicates as in the previous case, the existence of well-developed flow paths through thick (>1000 m) USZ. This result underlines the role that may play the USZ conditioning the hydrologic response of the karst system. The authors estimated the aquifer MTT with FlowPC by using as input tracer content that of precipitation, and assuming a constant (without any seasonality) aquifer recharge rate. The obtained MTT values ranged between 3 and 5 months, being significantly shorter than those MTT presented above for the other karst systems.

The hydrological system MTT reflects the diversity of aquifer flow paths and groundwater mixing from the recharge zone to the discharge point. Considering that the different aquifers constituting the PCM show an exponential flow model (EM) behavior, and provided that MTT (τ; Table 5) and

the aquifer mean recharge flow rate (Q_R; Table 6) are known, it is possible to estimate the aquifer storage (i.e., mixing) volume by using [Eq. 7]. In **Table 3. 8**, the stored dynamic volume ('mobile water volume -V_m'; Małoszewski and Zuber (2002); where: $V_m = Q_R \cdot \tau$) is associated with the catchment areas (Figure A1 of the Appendix A, Chapter 9 Supplementary material, part 9.2) discharging through the springs S-01 to S-06. S-05 and S-02 play a major role in terms of both groundwater discharge and aquifer storage. The springs S-05 and S-02 present a similar area and a similar discharge. Nevertheless, from a geometrical point of view, they are different: S-05 is rounded in shape whereas S-02 is elongated. Considering that aquifer recharge is produced mainly in the highest parts of PCM, it is clear that the distance between the recharge and discharge points is larger in the case of S-02. This difference is interesting if one considers that the mean transit time of S-02 is shorter than the mean transit time of S-05. The shorter transit time would indicate a higher development of the karst water conducting features in the catchment area of S-02. The springs S-04 and S-06 denote their perched character with the associated low discharge flow rates and groundwater reserve volumes.

Table 3. 8 Estimation of dynamic volume V_m stored in the aquifer for the springs analyzed

Spring	V_m (hm^3)
S-01	2,44 + 0,49
S-02	11,54 + 2,61
S-03	1,72 + 0,04
S-04	0,03 + 0,01
S-05	19,39 + 0,20
S-06	0,09 + 0,01

The few available groundwater level depth data from old water wells in the PCM suggest the karst aquifer presents low regional hydraulic gradients in the phreatic zone ranging between 1 - 2%. Nevertheless, while considering the expected mean phreatic level above the horizontal plane from the spring levels (i.e., the groundwater that contributes to each spring discharge), the 3D geological model evaluates the total aquifer formation volume (V_{aq}) associated with the regional springs S-01, S-02, S-03 and S-05. Assuming V_{aq} as known, the mean aquifer interconnected porosity (ϕ) can therefore be estimated as the ratio V_{GW}/V_{aq}. In the PCM, the average ϕ obtained is 3,1%. This result agrees with the value obtained for other carbonate aquifers of the Betic Cordillera (Southern Iberian Peninsula) with an average value of 3% (Pulido-Bosch et al., 2004; Martos- Rosillo et al., 2014).

This work is aimed to characterize the hydrological behavior of a high mountain karst system with an overlaying thick UZS that plays a relevant role along with in the system response. The applied approach allows accounting the effects of the extreme alpine climate conditions on both the aquifer recharge rates and the isotopic composition of recharge. The used approach provides a more reliable assessment of the hydrological behavior of these alpine karst systems than the obtained applying the traditional approaches found in the scarce bibliography. The methodology used in this work for characterizing the hydrological behavior of PCM can be applied in many analogue high mountain karst systems whose hydrologic behavior still remains unknown. In this sense, **Table 3. 9** shows a brief summary of the available bibliography at the pan-European zone focused on high-mountain karst aquifers with a thick USZ in which this methodology could be tested (**Figure 3. 12**).

Table 3. 9 Brief summary of published research studies of groundwater flow karst systems in mountain areas with thick USZ the pan-European zone.

Code	High mountain karst system	NSZ Thickness	Reference
1	Yunquera-Sierra de las Nieves	1000	Andreo et al. (2004); Pardo-Iguzquiza et al. (2015)
2	Alta Cadena	700	Mudarra and Andreo (2011)
3	Sierra Gorda	500	Mudarra and Andreo (2015)
4	Picos de Europa	1500	Ballesteros et al. (2015a); Ruiz and Poblete (2012)
5	Ordesa y Monte Perdido	1500	Lambán et al. (2015); Jódar et al. (2016b)
6	Port del Comte	1000	(This research)
7	Fontaine Vaucluse	800	Fleury et al. (2007)
8	Schlichenden Brünnen -Muotathal	1000	Jeannin (2001)
9	Wetterstein Mountains (Zugspitze)	1000	Lauber and Goldscheider (2014)
10	Wimbachtal catchment	1500	Maloszewski et al. (1992)
11	Totes Gebirge	1000	Laimer (2010)
12	Schneealpe Massif	900	Rank et al 1992; Maloszewski et al. (2002)
13	Cansiglio-Cavallo karst aquifer	800	Filippini et al. (2018)
14	Mount Kanin	2000	Zini et al. (2015); Turk et al. (2015)
15	Gacka	1000	Ozyurt et al. (2014)
16	Gran Sasso aquifer	1500	Falcone et al. (2008); Amuroso et al. (2013)
17	Arabika Massif	2500	Klimchouk (2009)
18	Aladaglar Mountains	2000	Ozyurt and Bayari (2008)

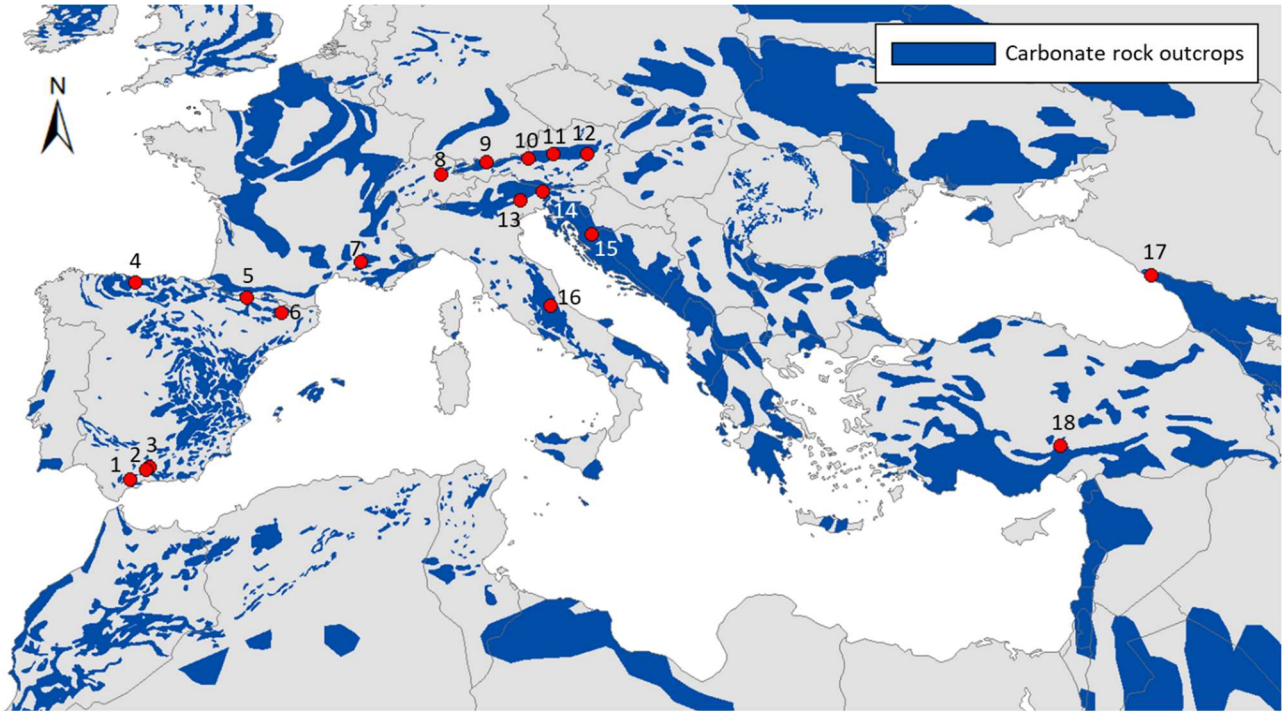

Figure 3. 12. Spatial distribution of carbonate rock outcrops at the pan-Mediterranean zone. Red points indicate the position of those high mountain karst aquifers zones with a thick (<500 m) NSZ referenced in the existing bibliography (map modified from the *World Map of Carbonate Rock Outcrops v.3.0*. Source: http://www.fos.auckland.ac.nz/our_research/karst). Numbers in bullets correspond to the codes shown in **Table 3. 9**.

3.4.4 Evaluation of results for groundwater management purposes

MTT is a corner stone for groundwater management strategies, and many authors have used this variable as a proxy of vulnerability assessment in hydrogeological systems (Einsiedl et al., (2009) and Malik et al., (2016), among others). This work provides the first estimation of the MTT associated with most important springs discharging the PCM karst system. From the perspective of aquifer vulnerability, the intensive cattle grazing conducted in the PCM is the most threading activity to the groundwater resources stored in the underlying aquifer so far. The relatively large MTTs (2,25 yr) along with the exponential flow model describing the hydrologic behavior of PCM, points to groundwater mixing as a natural attenuation/dilution process inside the aquifer system. However, it must be taken in mind that the presence of unnoticed but likely well-developed flow paths through the USZ and also the existence of karst conductive features in the saturated zone of

the PCM may favor fast contaminant migration from the recharge areas to the groundwater discharge points of this aquifer system, but this is investigation is out of the scope of this work.

From the perspective of water resources management, the storage and dynamic volumes associated with the PCM aquifer system are also valuable information obtained in this study. In this line, it is worth to comment that the PCM aquifer system has an integrated groundwater storage capacity (V_{GW}) of 35,2 hm^3, and generates an overall mean annual groundwater discharge of 15,35 hm^3/yr, that represents 15% of the mean annual water consumption in the city of Barcelona (Barcelona City Council, 2018). Moreover, the average discharge of S-05, which is one of the main groundwater springs of the PCM represents 7% of the mean annual water consumption of Barcelona city. This discharge tributes to the Llobregat River Basin, which in turns provides critical water resources to the Barcelona metropolitan area. It is important keeping these numbers in mind to estimate the water resources availability given the increased frequency and severity of the Mediterranean droughts reported by the experts (Hoerling et al., 2012; Vicente-Serrano et al., 2014).

In the Pyrenean range, climate models forecast a precipitation decrease up to 14% with respect to the observed mean precipitation and a temperature increase between 2 and 4 °C that will reduce the amount of solid precipitation and the corresponding snowmelt runoff (López-Moreno et al., 2008, 2009). In addition, the duration of the snowpack will be shorter, shifting the timing of the snowmelt (Adam et al., 2009). The PCM is in the pre-Pyrenean zone to the South of the Pyrenean axial zone. Here, the elevation of the mountains is lower, and the climate conditions are not so severe, accelerating the impact of the forecast temperature increase on snow precipitation, snowmelt runoff generation and the dynamics of the hydrological systems located in this area. Therefore, the geographical and hydrogeological settings of the PCM, along with the groundwater transit times calculated, make the PCM aquifer system an exceptional observatory for anticipating and studying the climate change impact on southern Europe. In this line, it would be extremely important to maintain the observation research program to fully understand the hydrogeological behavior of this aquifer system.

3.4.5 Future works in PCM

This study is the first stage in the full hydrogeological characterization of this aquifer system. The next step is to conduct the hydrogeochemical characterization of recharge and groundwater springs discharge to complement the results obtained in this work by focusing in relevant unsolved questions like (1) the role play by the epikarst zone in the total transit time of groundwater and how this role is reflected in the hydrogeochemical evolution of the springs discharge after important rainfall events and during low-flows and (2) the use of artificial tracers and environmental isotopes (e.g. 34S, 15N) to characterize not only the mean transit time (i.e. the first moment of the transit-time distribution) but also to profile the groundwater transit-time distribution in terms of fast, intermediate and slow groundwater flows. This investigation is crucial to evaluate the aquifer vulnerability.

3.5 Conclusions

A distributed rainfall-runoff model and a lumped-parameter model have been combined to estimate MTT in high-mountain karst systems with an overlying thick unsaturated zone by using the stable isotopes of precipitation as environmental tracers. The presented approach accounts for the effects of the alpine climate conditions on both the aquifer recharge rates and the isotopic composition of recharge. The used approach provides a more reliable assessment of mean transit time compared to traditional methods for such alpine karst systems.

The approach presented in this work has been used to characterize the hydrological behavior of the Port del Comte Massif, a high mountain karst aquifer with a 1000 m thick unsaturated zone located in the south-eastern part of the Pyrenees. The percentage of precipitation that enters into the hydrogeological system as aquifer recharge reaches 61,9% (the highest studied spring in the area). This elevated infiltration capacity is controlled by the presence of karren fields and sinkholes at the highest parts of Port del Comte Massif, at elevations between 2050 and 2300 m a.s.l. The evolution of the isotopic content in the sampled springs shows a sinusoidal pattern that reflects the seasonal variation of the isotopic composition of recharge. This is consistent with the relatively short groundwater transit times (2,25 yr) obtained for the hydrological system, which is in agreement with its karstic nature of the aquifer system, and emphasizes the high vulnerability of the aquifer system to variations in recharge.

The mean annual groundwater discharge and the mean water storage of the Port del Comte Massif hydrogeological system represent 16 and 34% of the mean annual water consumption in the city of Barcelona, underlying the important role as a strategic water resource that the Port del Comte Massif may play for stakeholders and water resources managers when facing the drought episodes that the Mediterranean region iteratively suffers. Moreover, given the geographical position of the study zone, located to the south of the Pyrenean axial zone, and the hydrogeological settings of the associated karst aquifer system, the Port del Comte Massif is an exceptional watchtower for anticipating the impact of climate change in Southern Europe.

3.6 Acknowledgements

This research was supported by Agencia Estatal de Investigación (AEI) from the Spanish Government and the European Regional Development Fund (FEDER) from EU, REMEDIATION (CGL2014-57215-C4-1-R), and PACE-ISOTEC (CGL2017-87216-C4-1-R) projects, the PIRAGUA project (EFA210/16/ PIRAGUA) which is funded by the European Union through the Interreg-POCTEFA territorial cooperation program, the Catalan Government projects to support consolidated research groups MAG (Mineralogia Aplicada, Geoquimica i Geomicrobiologia, 2017SGR-1733) from Universitat de Barcelona (UB) and GREM (Grup de Recerca de Minería Sostenible) from the Universitat Politècnica de Catalunya (UPC), and the Junta de Andalucía research group RNM-308 (Hydrogeology Group). We also thank the Institut Cartogràfic i Geològic de Catalunya (Hydrogeology and Geothermics Team) and CCiT from the Universitat de Barcelona (UB) for their technical assistance, and especially Raul Carrey from the MAiMA group for the help in the laboratory analyses. The Meteorological Service of Catalonia (SMC) has kindly provided the meteorological data. The constructive comments and interesting suggestions from four anonymous reviewers are greatly appreciated since they have led to a substantial improvement of the final article.

3.7 References

Adam, J.C., Hamlet, A.F., & Lettenmaier, D.P., 2009. Implications of global climate change for

snowmelt hydrology in the twenty-first century. Hydrological Processes: An International Journal, 23(7), 962-972. https://doi.org/10.1002/hyp.7201

Agencia Estatal de Meteorología de España (AEMET) and Instituto de Meteorologia – Portugal (IMA). 2011. Iberian climate atlas. Air temperature and precipitation (1971-2000). http://www.aemet.es/documentos/es/divulgacion/publicaciones/Atlas-climatologico/Atlas.pdf

Allocca, V., De Vita, P., Manna, F., Nimmo, J.R. 2015. Groundwater recharge assessment at local and episodic scale in a soil mantled perched karst aquifer in southern Italy. Journal of Hydrology, 529 (2015) 843–853. https://doi.org/10.1016/j.jhydrol.2015.08.032

Amin I.E., Campana, M.E. 1996. A general lumped parameter model for the interpretation of tracer data and transit time calculation in hydrologic systems. J Hydrol; 179 (1–4):1–21 https://doi.org/10.1016/0022-1694(95)02880-3

Andreo, B., Linan, C., Carrasco, F., De Cisneros, C. J., Caballero, F., Mudry, J. 2004. Influence of rainfall quantity on the isotopic composition (18O and 2H) of water in mountainous areas. Application for groundwater research in the Yunquera-Nieves karst aquifers (S Spain). Applied Geochemistry, 19(4), 561-574. https://doi.org/10.1016/j.apgeochem.2003.08.002

Araguás-Araguás, L.J., Díaz-Teijeiro, M.F. 2005. Isotope composition of precipitation and water vapour in the Iberian Peninsula. In "Isotopic Composition of Precipitation in the Mediterranean Basin in Relation to Air Circulation Patterns and Climate" (pp. 173-190). IAEA-TECDOC-1453.

Aravena, R., Peña, H., Grilli, A., Suzuki, O., Mordeckai, M., 1989. Evolución isotópica de las lluvias y origen de las masas de aire en el altiplano chileno. Isotope hydrology investigations in Latín America. IAEA-TECDOC-502. IAEA, Vienna, pp. 129–142.

Bakalowicz, M. (2005). Karst groundwater: a challenge for new resources. Hydrogeology Journal, 13(1), 148-160. https://doi.org/10.1007/s10040-004-0402-9

Ballesteros, D., Jiménez-Sánchez, M., Giralt, S., García-Sansegundo, J., Meléndez-Asensio, M. 2015a. A multi-method approach for speleogenetic research on alpine karst caves. Torca La Texa shaft, Picos de Europa (Spain). Geomorphology, 247, 35-54.

Ballesteros, D., Arnauld Malard., A., Pierre-Yves Jeannin, P-Y., Jimenez-Sanchez M., García-Sansegundo, J., Meléndez-Asensio, M., Sendra, G. 2015b. KARSYS hydrogeological 3D modeling of alpine karst aquifers developed in geologically complex areas: Picos de Europa National Park (Spain). Environ Earth Sci. Volume 74, Issue 12, pp 7699–7714.

https://doi.org/10.1007/s12665-015-4712-0

Barberá, J.A., Jódar, J., Custodio, E., González-Ramón, A., Jiménez-Gavilán, Vadillo, I., Pedrera, A., Martos-Rosillo, S., 2018a. Groundwater dynamics in a hydrologically-modified alpine watershed from an ancient managed recharge system (Sierra Nevada National Park, Southern Spain): insights from hydrogeochemical and isotopic information. Science of the Total Environment 640–641, 874–893, https://doi.org/10.1016/j.scitotenv.2018.05.305

Barberá, J. A., Mudarra, M., Andreo, B., De la Torre, B., 2018b. Regional-scale analysis of karst underground flow deduced from tracing experiments: examples from carbonate aquifers in Màlaga province, southern Spain. Hydrogeology Journal, 26(1), 23-40. https://dx.doi.org/10.1007/s10040-017-1638-5

Barcelona City Council, 2018. Evolution of water consumption in the city of Barcelona. http://www.bcn.cat/estadistica/angles/dades/economia/consum/evoconsum/coev04.htm (last access 08/07/2018).

Barnett, T.P., Adam, J.C., Lettenmaier, D.P., 2005. Potential impacts of a warming climate on water availability in snow-dominated regions. Nature, 438(7066), https://dx.doi.org/10.1038/nature04141

Bergström, S., 1976. Development and Application of a Conceptual Runoff Model For Scandinavian Catchments, SMHI, Report No. RHO 7 (134 pp Norrköping).

Braun, L.N., Renner, C.B., 1992. Application of a conceptual runoff model in different physiographic regions of Switzerland. Hydrological Sciences Journal, 37(3), 217-231. https://doi.org/10.1080/02626669209492583.

Butscher C, Huggenberger P., 2007. Implications for karst hydrology from 3D geological modeling using the aquifer base gradient approach. J Hydrol; 342 (1–2):184–98. https://doi.org/10.1016/j.jhydrol.2007.05.025

Celle-Jeanton,H., Travi, Y., Blavoux, B., 2001. Isotopic typology of the precipitation in the Western Mediterranean region at three different time scales. Geophysical Research Letters, Vol. 28, no. 7, pages 1215-1218

Cervi, F., Marcaccio, M., Petronici, F., Borgatti, L., 2014. Hydrogeological characterization of peculiar Apenninic springs. Proceedings of the International Association of Hydrological Sciences, 364, 333-338.

Chen, Z., 2017. Modeling a geologically complex karst aquifer system, Hochifen-Gottesacker, Alps. PhD. Thesis. Karlsruher Instituts für Technologie, Germany. https://d-

nb.info/1136660852/34

Chueca, J., Julián, A., López-Moreno, J.I., 2007. Recent evolution (1981–2005) of the Maladeta glaciers, Pyrenees, Spain: extent and volume losses and their relation with climatic and topographic factors. Journal of glaciology, 53(183), 547-557. https://doi.org/10.3189/002214307784409342

Clark, I.D., Fritz, P. 1997. Environmental isotopes in hydrogeology. Lewis Publishers, New York.

Coplen 2011. Guidelines and recommended terms for expression of stable-isotope-ratio and gas-ratio measurement results. Rapid Commun. Mass Spectrom. 2011, 25, 2538–2560.

CREAF, 2009. Land Cover Map of Catalonia (MCSC) 1:250,000. 4a edition (2009). http://www.creaf.uab.es/mcsc/usa/index.htm

Custodio, E., Llamas, M.R. (Eds.), 1976. Hidrología subterránea [Groundwater hydrology]. 2 Vols: 1–2350. Ediciones Omega, Barcelona.

Custodio, E., Jódar, J., 2016. Simple solutions for steady–state diffuse recharge evaluation in sloping homogeneous unconfined aquifers by means of atmospheric tracers. J. Hydrol. http://dx.doi.org/10.1016/j.jhydrol.2016.06.035

De Jong, C., Lawler, D., Essery, R., 2009. Mountain hydroclimatology and snow seasonality and hydrological change in mountain environments. Hydrological Processes 23, 955–961. https://doi.org/10.1002/hyp.7193

De Walle, D.R., Edwards, P.J., Swistock, B.R., Aravena, R., Drimmie, R.J., 1997. Seasonal isotope hydrology of three Appalachian forest catchments. Hydrological Processes, 11(15), 1895-1906.b https://doi.org/10.1002/(SICI)1099-1085(199712)11:15<1895::AID-HYP538>3.0.CO;2-#

Einsiedl, F., 2005. Flow system dynamics and water storage of a fissured-porous karst aquifer characterized by artificial and environmental tracers. J Hydrol 312:312–321. https://doi.org/10.1016/j.jhydrol.2005.03.031

Einsiedl, F., Maloszewski, P., Stichler, W., 2009. Multiple isotope approach to the determination of the natural attenuation potential of a high-alpine karst system. Journal of Hydrology 365 (2009) 113–121. https://doi.org/10.1016/j.jhydrol.2008.11.042

Epting, J., M.Page, R., Auckenthaler, A., Huggenberger, P. 2018. Process-based monitoring and modeling of Karst springs – Linking intrinsic to specific vulnerability. Sci. Total Environ. 625, 403-415-https://doi.org/10.1016/j.scitotenv.2017.12.272

Falcone, R.A., Falgiani, A., Parisse, B., Petitta, M., Spizzico, M., Tallini, M. 2008. Chemical and

isotopic ($\delta^{18}O‰$, $\delta^{2}H‰$, $\delta^{13}C‰$, ^{222}Rn) multi-tracing for groundwater conceptual model of carbonate aquifer (Gran Sasso INFN underground laboratory–central Italy). Journal of hydrology, 357(3-4), 368-388.

Farlin, J., Maloszewski, P., 2013. On the use of spring baseflow recession for a more accurate parameterization of aquifer transit time distribution functions. Hydrology and Earth System Sciences, 17(5), 1825-1831. https://doi.org/10.5194/hess-17-1825-2013

Fiorella, R.P., Poulsen, C.J., Pillco Zolá, R.S., Barnes, J.B., Tabor, C.R., Ehlers, T.A., 2015. Spatiotemporal variability of modern precipitation $\delta^{18}O$ in the central Andes and implications for paleoclimate and paleoaltimetry estimates. Journal of Geophysical Research: Atmospheres, 120(10), 4630-4656. https://dx.doi.org/10.1002/2014JD022893

Fleury, P., Plagnes, V., Bakalowicz, M. 2007. Modelling of the functioning of karst aquifers with a reservoir model: Application to Fontaine de Vaucluse (South of France). Journal of Hydrology 345, 38– 49. https://doi.org/10.1016/j.jhydrol.2007.07.014

Filippini,M., Squarzoni, G., De Waele, J., Fiorucci, A., Vigna, B., Grillo, B., Riva, A., Rossetti, S., Zini, L., Casagrande, G., Stumpp, C., Gargini, A. 2018. Differentiated spring behavior under changing hydrological conditions in an alpine karst aquifer. Journal of Hydrology, 556, 572-584. https://doi.org/10.1016/j.jhydrol.2017.11.040

Freixes, A., 2014. Els aqüífers càrstics dels Pirineus de Catalunya. Interès estratègic i sostenibilitat [The karstic aquifers of the Catalonian Pyrenees. Strategic interest and sustainability]. PhD. Thesis. Universitat de Barcelona. http://hdl.handle.net/2445/65187

Froehlich, K., Gibson, J.J., Aggarwal, P., 2001. Deuterium excess in precipitation and its climatological significance. In Study of environmental change using isotope techniques (Vol. 13, pp. 54-66). IAEA.

Froehlich, K., Kralik, M., Papesch, W., Rank, D., Scheifinger, H., Stichler, W., 2008. Deuterium excess in precipitation of Alpine regions–moisture recycling. Isotopes in Environmental and Health Studies, 44(1), 61-70. https://doi.org/10.1080/10256010801887208

García-Ruiz, J.M., López-Moreno, J.I., Vicente-Serrano, S.M., Lasanta–Martínez, T., Beguería, S., 2011. Mediterranean water resources in a global change scenario. Earth-Science Reviews, 105(3-4), 121-139. https://doi.org/10.1016/j.earscirev.2011.01.006

Garvelmann, J., Warscher , M., Leonhardt, G., Franz, H., Lotz. A., Kunstman, H. 2017. Quantification and characterization of the dynamics of spring and stream water systems in the Berchtesgaden Alps with a long-term stable isotope dataset. Environ Earth Sci 76:766

https://doi.org/10.1007/s12665-017-7107-6

Giorgi, F., Lionello, P., 2008. Climate change projections for the Mediterranean region. Global and planetary change, 63(2-3), 90-104. https://doi.org/10.1016/j.gloplacha.2007.09.00 5

Gladich, I., Gallai, I., Giaiotti, D. B., & Stel, F. 2011. On the diurnal cycle of deep moist convection in the southern side of the Alps analysed through cloud-to-ground lightning activity. Atmospheric Research, 100(4), 371-376. https://doi.org/10.1016/j.atmosres.2010.08.026

Goldscheider, N., 2005. Fold structure and underground drainage pattern in the alpine karst system Hochifen-Gottesacker. Eclogae Geologicae Helvetiae, 98(1), 1-17. https://doi.org/10.1007/s00015-005-1143-z

Goldscheider N, Drew D (eds) (2007) Methods in Karst Hydrogeology. International Contributions to Hydrogeology 26, International Association of Hydrogeologists, Taylor & Francis, London, 264 pp. ISBN 978-0-415-42873-6

Goldscheider, N., Meiman, J., Pronk, M., Smart, C., 2008. Tracer tests in karst hydrogeology and speleology. International Journal of Speleology, 37(1), 3. http://dx.doi.org/10.5038/1827-806X.37.1.3

Goldscheider, N., 2011. Alpine Hydrogeologie [Alpine hydrogeology]. Grundwasser 16:1–1. https://doi.org/10.1007/s00767-010-0157-2

Gonfiantini, R., Roche, M.A., Olivry, J.C., Fontes, J.C., Zuppi, G.M., 2001. The altitude effect on the isotopic composition of tropical rains. Chemical Geology, 181(1-4), 147-167. https://doi.org/10.1016/S0009-2541(01)00279-0

Gremaud, V., Goldscheider, N., Savoy, L., Favre, G., Masson, H., 2009. Geological structure, recharge processes and underground drainage of a glacierised karst aquifer system, Tsanfleuron-Sanetsch, Swiss Alps. Hydrogeol. J. 17, 1833–1848. https://doi.org/10.1007/s10040-009-0485-4

Grunewald, K., Scheithauer, J., 2010. Europe's southernmost glaciers: response and adaptation to climate change. Journal of glaciology, 56(195), 129-142. https://doi.org/10.3189/002214310791190947

Hernández-Mora, N., del Moral Ituarte, L., La-Roca, F., La Calle, A., Schmidt, G., 2014. Interbasin water transfers in Spain: Interregional conflicts and governance responses. In Globalized Water (pp. 175-194). Springer, Dordrecht. ISBN 978-94-007-7322-6. https://doi.org/10.1007/978-94-007-7323-3_13

Hargreaves, G.H. and Samani, Z.A. 1982. Estimating potential evapotranspiration. Journal of

Irrigation and Drainage Engineering, 108, 223-230

Hoerling, M., Eischeid, J., Perlwitz, J., Quan, X., Zhang, T., Pegion, P., 2012. On the increased frequency of Mediterranean drought. Journal of Climate, 25(6), 2146-2161. https://doi.org/10.1175/JCLI-D-11-00296.1

Holko, L., Dóša, M., Michalko, J., Šanda, M. 2012. Isotopes of oxygen-18 and deuterium in precipitation in Slovakia. Journal of Hydrology and Hydromechanics, 60(4), 265-276. https://doi.org/10.2478/v10098-012-0023-2

Hood, J.L., Hayashi, M., 2010. Assessing the application of a laser rangefinder for determining snow depth in inaccessible alpine terrain. Hydrology and Earth System Sciences, 14(6), 901. http://dx.doi.org/10.5194/hess-14-901-2010

Hottelet, Ch., Braun, L.N., Leibundgut, Ch., Rieg, A., 1993. Simulation of Snowpack and Discharge in an Alpine Karst Basin. IAHS Publication No. 218, pp. 249–260

ICGC, 2007. Mapa geològic comarcal de Catalunya 1:50 000. Full Alt Urgell (BDGC50M). http://www.icgc.cat/ca/Administracio-i-empresa/Descarregues/Cartografia-geologica-i-geotematica/Cartografia-geologica/Mapa-geologic-comarcal-de-Catalunya-1-50.000/Mapa-geologic-comarcal-de-Catalunya-1-50.000

Jeelani, G., Shah, R.A., Deshpande, R.D., Fryar, A.E., Perrin, J., Mukherjee, A., 2017. Distinguishing and estimating recharge to karst springs in snow and glacier dominated mountainous basins of the western Himalaya, India. Journal of hydrology, 550, 239-252. https://doi.org/10.1016/j.jhydrol.2017.05.001

Jeannin, P-Y. 2001. Modeling flow in phreatic and epiphreatic karst conduits in the Hölloch cave (Muotatal, Switzerland). Water Resources Research. Vol. 37, No. 2, pp 191-200. https://doi.org/10.1029/2000WR900257

Jiménez-Martínez, J. y Custodio, E., 2008. El exceso de deuterio en la lluvia y en la recarga a los acuíferos en el área circum-mediterránea y en la costa mediterránea española. Boletín Geológico y Minero, 119 (1): 21-32.

Jódar, J., Lambán, L.J., Medina, A., Custodio, E., 2014. Exact analytical solution of the convolution integral for classical hydrogeological lumped-parameter models and typical input tracer functions in natural gradient systems. J. Hydrol. 519, 3275–3289. http://dx.doi.org/10.1016/j.jhydrol.2014.10.027

Jódar, J., Custodio, E., Liotta, M., Lambán, L.J., Herrera, C., Martos-Rosillo, S., Sapriza, G., Rigo, T., 2016a. Correlation of the seasonal isotopic amplitude of precipitation with annual

evaporation and altitude in alpine regions. Sci. Total Environ., 550: 27-37. https://dx.doi.org/10.1016/j.scitotenv.2015.12.034

Jódar, J., Custodio, E., Lambán, L.J., Martos-Rosillo, S., Herrera-Lameli, C., Sapriza-Azuri, G., 2016b. Vertical variation in the amplitude of the seasonal isotopic content of rainfall as a tool to jointly estimate the groundwater recharge zone and transit times in the Ordesa and Monte Perdido National Park aquifer system, north-eastern Spain. Sci. Total Environ. 573, 505–517. https://dx.doi.org/10.1016/j.scitotenv.2016.08.117

Jódar, J., Cabrera, J.A., Martos-Rosillo, S., Ruiz-Constan, A., Gonzalez-Ramón, A., Lambán, L.J., Herrera, C., Custodio, E., 2017. Groundwater discharge in high-mountain watersheds: a valuable resource for downstream semi-arid zones. The case of the Bérchules River in Sierra Nevada (Southern Spain). Science of The Total Environment, https://doi.org/10.1016/j.scitotenv.2017.03.190

Jódar, J., Carpintero, E., Martos-Rosillo, S., Ruiz-Constán, A., Marín-Lechado, C., Cabrera-Arrabal, J.A., Navarrete-Mazariego, E., González-Ramón , A., Lambán, L.J., Herrera, C., González-Dugo, M.P. 2018. Combination of lumped hydrological and remote-sensing models to evaluate water resources in a semi-arid high altitude ungauged watershed of Sierra Nevada (Southern Spain). Sci. Total Environ., 625: 285-300. https://doi-org.recursos.biblioteca.upc.edu/10.1016/j.scitotenv.2017.12.300

Katsuyama, M., Tani, M., Nishimoto, S., 2010. Connection between streamwater mean residence time and bedrock groundwater recharge/discharge dynamics in weathered granite catchments. Hydrological Processes, 24(16), 2287-2299. https://doi.org/10.1002/hyp.7741

Kazakis, N., Chalikakis, K., Mazzilli, M., Ollivier, C., Manakos, A., Voudouris, K., 2018. Management and research strategies of karst aquifers in Greece: Literature overview and exemplification based on hydrodynamic modelling and vulnerability assessment of a strategic karst aquifer. Sci. Total Environ., 643: 592–609. https://doi.org/10.1016/j.scitotenv.2018.06.184

Klimchouk, A. Samokhin, G.V., Kasian, Y.M. 2009. The deepest cave in the world in the arabika massif (western caucasus) and its hydrogeological and paleogeographic significance. 2009 ICS Proceedings. 15th International Congress of Speleology

Konz, M., Seibert, J., 2010. On the value of glacier mass balances for hydrological model calibration. Journal of hydrology, 385(1-4), 238-246. https://doi.org/10.1016/j.jhydrol.2010.02.025

Kurylyk, B.L., Hayashi, M., 2017. Inferring hydraulic properties of alpine aquifers from the propagation of diurnal snowmelt signals. Water Resources Research. https://doi.org/10.1002/2016WR019651

Laimer, H.J. 2010. Neue Ergebnisse zur Karsthydrogeologie des westlichen Toten Gebirges (Österreich). (New karst hydrogeological research in the western Totes Gebirge, Austria). Grundwasser. Volume 15, Issue 2, pp 113–122

Lambán, L.J., Jódar, J., Custodio, E., Soler, A., Sapriza, G. and Soto, R., 2015. Isotopic and hydrogeochemical characterization of high-altitude karst aquifers in complex geological settings. The Ordesa and Monte Perdido National Park (Northern Spain) case study. Sci. Total Environ., 506–507: pp 466–479, https://doi.org/10.1016/j.scitotenv.2014.11.030

Lauber, U., Kotyla, P., Morche, D., Goldscheider, N., 2014. Hydrogeology of an Alpine rockfall aquifer system and its role in flood attenuation and maintaining baseflow. Hydrology and Earth System Sciences, 18(11), 4437. http://dx.doi.org/10.5194/hess-18-4437-2014

Lauber, U., Goldscheider, N., 2014. Use of artificial and natural tracers to assess groundwater transit-time distribution and flow systems in a high-alpine karst system (Wetterstein Mountains, Germany). Hydrogeology Journal, 22(8), 1807-1824. http://dx.doi.org/10.1007/s10040-014-1173-6

Liu, Z., Tian, L., Yao, T., & Yu, W. 2008. Seasonal deuterium excess in Nagqu precipitation: influence of moisture transport and recycling in the middle of Tibetan Plateau. Environmental Geology, 55(7), 1501-1506. http://dx.doi.org/10.1007/s00254-007-1100-4

López-Moreno, J.I., García-Ruiz, J.M., 2004. Influence of snow accumulation and snowmelt on streamflow in the central Spanish Pyrenees/Influence de l'accumulation et de la fonte de la neige sur les écoulements dans les Pyrénées centrales espagnoles. Hydrological Sciences Journal, 49(5). https://doi.org/10.1623/hysj.49.5.787.55135

López-Moreno, J. I., Goyette, S., Beniston, M., 2008. Climate change prediction over complex areas: spatial variability of uncertainties and predictions over the Pyrenees from a set of regional climate models. International Journal of Climatology, 28(11), 1535-1550. https://doi.org/10.1002/joc.1645

López-Moreno, J.I., Revuelto, J., Rico, I., Chueca-Cía, J., Julián, A., Serreta, A., Serrano, E., Vicente-Serrano, S.M., Azorin-Molina, C., Alonso-González, E., García-Ruiz, J.M., 2016. Thinning of the Monte Perdido Glacier in the Spanish Pyrenees since 1981. The Cryosphere, 10(2), 681-694. https://doi.org/10.5194/tc-10-681-2016

Mądrala, M., Wąsik, M., Małoszewski, P., 2017. Interpretation of environmental tracer data for conceptual understanding of groundwater flow: an application for fractured aquifer systems in the Kłodzko Basin, Sudetes, Poland. Isotopes in environmental and health studies, 53(5), 466-483. https://dx.doi.org/10.1080/10256016.2017.1330268

Malard, A., Jeannin, PY., Vouillamoz, J. et al 2015. An integrated approach for catchment delineation and conduit-network modeling in karst aquifers: application to a site in the Swiss tabular Jura. Hydrogeol J 23: 1 1341–1357. https://doi.org/10.1007/s10040-015-1287-5

Malard, A., Sinreich, M., Jeannin, P.Y., 2016. A novel approach for estimating karst groundwater recharge in mountainous regions and its application in Switzerland. Hydrological Processes, 30(13), 2153-2166. https://doi.org/10.1002/hyp.10765

Malík, P., Svasta, J., Michalko, J., Gregor, M., 2016. Indicative mean transit time estimation from δ18O values as groundwater vulnerability indicator in karst-fissure aquifers. Environmental Earth Sciences. 75. https://doi.org/10.1007/s12665-016-5791-2

Małoszewski, P., Rauert, W., Stichler, W., Herrmann, A., 1983. Application of flow models in an alpine catchment area using tritium and deuterium data. Journal of Hydrology, 66: 319–330. http://dx.doi.org/10.1016/0022-1694(83)90193-2

Maloszewski, P., Rauert, W., trimborn, P., Herrmann, A., Rau, R. 1992. Isotope hydrological study of mean transit times in an alpine basin (Wimbachtal, Germany). Journal of Hydrology, 140: 343-360. https://doi.org/10.1016/0022-1694(92)90247-S

Małoszewski, P., Zuber, A., 1996. Lumped parameter models for the interpretation of environmental tracer data. Manual on mathematical models in isotope hydrology. IAEA-TECDOC 910. Vienna (Austria): IAEA; 1996

Małoszewski, P., Zuber, A., 2002. Manual on lumped parameter models used for the interpretation of environmental tracer data in groundwaters (IAEA-UIAGS/CD--02-00131). International Atomic Energy Agency (IAEA) (https://inis.iaea.org/search/search.aspx?orig_q=RN:33037906, last access 12/04/2018)

Marti, R., Gascoin, S., Houet, T., Ribière, O., Laffly, D., Condom, T., Monnier, S., Schmutz, M., Camerlynck, C., Tihay, J.P., Soubeyroux, J.M., 2015. Evolution of Ossoue Glacier (French Pyrenees) since the end of the Little Ice Age. The Cryosphere, 9(5), 1773-1795. http://dx.doi.org/10.5194/tc-9-1773-2015.

Martos-Rosillo, S., Marín-Lechado, C., Pedrera, A., Vadillo, I., Motyka, J., Molina, J.L., Ortiz, P., Martín-Ramírez, J.M., 2014. Methodology to evaluate the renewal period of carbonate

aquifers: a key tool for their management in arid and semiarid regions, with the example of Becerrero aquifer, Spain. Hydrogeology Journal, 22(3), 679-689. http://dx.doi.org/10.1007/s10040-013-1086-9

Martos-Rosillo, S., González-Ramón, A., Jiménez-Gavilán, P., Andreo, B., Durán, J.J., Mancera, E., 2015. Review on groundwater recharge in carbonate aquifers from SW Mediterranean (Betic Cordillera, S Spain). Environ Earth Sci. 74: 7571. https://doi.org/10.1007/s12665-015-4673-3

Merz, R., Blöschl, G., 2004. Regionalisation of catchment model parameters. Journal of hydrology, 287(1-4), 95-123. http://dx.doi.org/10.1016/j.jhydrol.2003.09.028

Milano, M., Ruelland, D., Fernandez, S., Dezetter, A., Fabre, J., Servat, E., Fritsch, J.M., Ardoin-Bardin, S., Thivet, G., 2013. Current state of Mediterranean water resources and future trends under climatic and anthropogenic changes. Hydrological Sciences Journal, 58(3), 498-518. http://dx.doi.org/10.1080/02626667.2013.774458

Molina, A., Melgarejo, J., 2016. Water policy in Spain: seeking a balance between transfers, desalination and wastewater reuse. International Journal of Water Resources Development, 32(5), 781-798. http://dx.doi.org/10.1080/07900627.2015.1077103

Mook,W.G., De Vries, J.J., 2000. Volume I, Introduction: theory methods review. Environmental Isotopes in the Hydrological Cycle—Principles and Applications, International Hydrological Programme (IHP-V). Technical Documents in Hydrology (IAEA/UNESCO) No, 39 vol. 1 (http://www-naweb.iaea.org/napc/ih/IHS_publication.html, last access 12/04/2018).

Mudarra, M., Andreo, B. 2011. Relative importance of the saturated and the unsaturated zones in the hydrogeological functioning of karst aquifers: The case of Alta Cadena (Southern Spain). Journal of Hydrology 397, 263–280. https://doi.org/10.1016/j.jhydrol.2010.12.005

Mudarra, M., Andreo, B., Marín, A.I., Vadillo, I., Barberá, J.A., 2014. Combined use of natural and artificial tracers to determine the hydrogeological functioning of a karst aquifer: the Villanueva del Rosario system (Andalusia, southern Spain). Hydrogeology journal, 22(5), 1027-1039. http://dx.doi.org/10.1007/s10040-014-1117-1

Mudarra, M., Andreo, B., 2015. Role of the Soil-Epikarst-Unsaturated Zone in the Hydrogeological Functioning of Karst Aquifers. The Case of the Sierra Gorda de Villanueva del Trabuco Aquifer (Southern Spain). Hydrogeological and Environmental Investigations in Karst Systems. (ed. Andreo, B., Carrasco, F., Durán, J.J., Jiménez, P., LaMoreaux.) Series: Environmental Earth Sciences. Springer. 638 pp.

Nimon, K.F., Oswald, F.L., 2013. Understanding the results of multiple linear regression: Beyond standardized regression coefficients. Organizational Research Methods, 16(4), 650-674.

Nogués-Bravo, D., Araújo, M.B., Lasanta, T., López-Moreno, J.I., 2008. Climate change in Mediterranean mountains during the 21st century. AMBIO: A Journal of the Human Environment, 37(4), 280-285. https://doi.org/10.1579/0044-7447(2008)37[280:CCIMMD]2.0.CO;2

Obleitner, F., 1994. Climatological features of glacier and valley winds at the Hintereisferner (Ötztal Alps, Austria). Theoretical and Applied Climatology, 49(4), 225-239. https://doi.org/10.1007/BF00867462

Ozyurt, N.N., Bayari, C.S. 2008. Temporal variation of chemical and isotopic signals in major discharges of an alpine karst aquifer in Turkey: implications with respect to response of karst aquifers to recharge. Hydrogeology Journal 16: 297–309. http://dx.doi.org/10.1007/s10040-007-0217-6

Ozyurt, N.N., Lutz, H.O., Hunjak, T., Mance, D., Roller-Lutz, Z. 2014. Characterization of the Gacka River basin karst aquifer (Croatia): Hydrochemistry, stable isotopes and tritium-based mean residence times. Sci. Total Environ. 87 245–254. http://dx.doi.org/10.1016/j.scitotenv.2014.04.018

Pardo-Igúzquiza, E., Durán, J.J., Luque-Espinar, J.A., Robledo-Ardila, P.A., Martos-Rosillo, S., Guardiola-Albert, C., Pedrera, A. 2015. Karst massif susceptibility from rock matrix, fracture and conduit porosities: a case study of the Sierra de las Nieves (Málaga, Spain). Environ Earth Sci. 74:7583–7592. http://dx.doi.org/10.1007/s12665-015-4545-x

Peel, M.C., Finlayson, B.L., McMahon, T.A., 2007. Updated world map of the Köppen–Geiger climate classification. Hydrol. Earth Syst. Sci. 11, 1633–1644. http://dx.doi.org/10.5194/hess-11-1633-2007

Poage, M.A., Chamberlain, C.P., 2001. Empirical relationships between elevation and the stable isotope composition of precipitation and surface waters: considerations for studies of paleoelevation change. Am. J. Science 301 (1), 1–15. http://dx.doi.org/10.2475/ajs.301.1.1

René, P., 2013. Glaciers des Pyrénées: le réchauffement climatique en images. Éd. Cairn.

Ribalaygua, J., Pino, M.R., Pórtoles, J., Roldán, E., Gaitán, E., Chinarro, D., Torres, L., 2013. Climate change scenarios for temperature and precipitation in Aragón (Spain). Science of the Total Environment, 463, 1015-1030. https://doi.org/10.1016/j.scitotenv.2013.06.089

Rodgers, P., Soulsby, C., Waldron, S., 2005. Stable isotope tracers as diagnostic tools in upscaling

flow path understanding and residence time estimates in a mountainous mesoscale catchment. Hydrol Process 19(11):2291–2307. http://dx.doi.org/10.1002/hyp.5677

Ruiz-Constán, A., Marín-Lechado, C., Martos-Rosillo, S., Fernández-Leyva, C., García-Lobón, J. L., Pedrera, A., López-Geta, J.A., Hernández-Bravo, J.A., Rodríguez-Hernández, L., 2015. Methodological Procedure for Evaluating Storage Reserves in Carbonate Aquifers Subjected to Groundwater Mining: The Solana Aquifer (Alicante, SE Spain). In Hydrogeological and Environmental Investigations in Karst Systems (pp. 255-262). Springer, Berlin, Heidelberg. http://dx.doi.org/10.1007/978-3-642-17435-3_28

Sánchez-Murillo, R., Brooks, E.S., Elliot, W.J., Boll, J., 2015. Isotope hydrology and baseflow geochemistry in natural and human-altered watersheds in the Inland Pacific Northwest, USA. Isotopes in environmental and health studies, 51(2), 231-254. http://dx.doi.org/10.1080/10256016.2015.1008468

Schotterer, U., Froehlich, K., Stichler, W., Trimborn, P., 1993. Temporal variation of 18O and deuterium excess in precipitation, river and spring waters in Alpine regions of Switzerland. In Isotope Techniques in the study of Past and Current Environmental Changes in the Hydrosphere and the Atmosphere. Edited by IAEA. Proceedings series, ISSN 0074-1884, STI/PUB/908, ISBN 92-0-103293-5 (https://inis.iaea.org/search/search.aspx?orig_q=RN:25027909, last access 12/04/2018).

Seibert, J., 2005. HBV Light Version 2. User's Manual. Uppsala University, Dept. of Earth Science, Hydrology, Uppsala, Sweden.

Seibert, J., Vis, M.J.P, 2012. Teaching hydrological modelling with a user-friendly catchment-runoff-model software package, Hydrol. Earth Syst. Sci., 16(9), 3315–3325. http://dx.doi.org/10.5194/hess-16-3315-2012, 102012

Seibert, J., Jenicek, M., Huss, M., Ewen, T., 2015. Snow and ice in the hydrosphere. In Snow and Ice-Related Hazards, Risks and Disasters (pp. 99-137). ISBN: 978-0-12-394849-6. https://doi.org/10.1016/B978-0-12-394849-6.00004-4

Solder, J.E., Stolp, B.J., Heilweil, V.M., Susong, D.D., 2016. Characterization of mean transit time at large springs in the Upper Colorado River Basin, USA: a tool for assessing groundwater discharge vulnerability. Hydrogeology Journal, Volume 24, Issue 8, pp 2017–2033, https://doi.org/10.1007/s10040-016-1440-9

Staudinger, M., Stoelzle, M., Seeger, S., Seibert, J., Weiler, M., Stahl, K., 2017. Catchment water storage variation with elevation. Hydrological Processes, 31(11), 2000-2015.

https://doi.org/10.1002/hyp.11158

Turnadge, C., Smerdon, B.D. 2014. A review of methods for modelling environmental tracers in groundwater: advantages of tracer concentration simulation. Journal of Hydrology, 519, 3674-3689. https://doi.org/10.1016/j.jhydrol.2014.10.056

Turk, J., Malard, A., Jeannin, P.-Y., Petric M., Gabrovšek, F., Ravbar, N., Vouillamoz, J., Slabe, T., Sordet, V., 2015. Hydrogeological characterization of groundwater storage and drainage in an alpine karst aquifer (the Kanin massif, Julian Alps). Hydrological Processes 29(8), 1986-1998. https://doi.org/10.1002/hyp.10313

Uhlenbrook, S., Seibert, J.A.N., Leibundgut, C., Rodhe, A., 1999. Prediction uncertainty of conceptual rainfall-runoff models caused by problems in identifying model parameters and structure. Hydrological Sciences Journal, 44(5), 779-797. https://doi.org/10.1080/02626669909492273

Vergés, J. 1999. Estudi geològic del vessant sud del Pirineu oriental i central. Evolució cinemàtica en 3D. PhD Thesis. University of Barcelona (UB), Faculty of Geology, 180 pp.

Vicente-Serrano, S.M., Lopez-Moreno, J.I., Beguería, S., Lorenzo-Lacruz, J., Sanchez-Lorenzo, A., García-Ruiz, J.M., Azorin-Molina, C., Morán-Tejeda, E., Revuelto, J., Trigo, R., Coelho, F., Espejo, F., 2014. Evidence of increasing drought severity caused by temperature rise in southern Europe. Environmental Research Letters, 9(4), 044001. https://doi.org/10.1088/1748-9326/9/4/044001

Vitvar, T., Gurtz, O., Lang, H. 1999. Application of GIS-based distributed hydrological modelling for estimation of water residence times in the small Swiss pre-alpine catchment Rietholzbach. Integrated Methods in Catchment Hydrology—Tracer. Remote Sensing and New Hydrometric Techniques (Proceedings of IUGG 99 Symposium HS4, Birmingham, July 1999). IAHS Publ. no. 258, 1999

Viville, D., Ladouche, B. and Bariac, T., 2006. Isotope hydrological study of mean transit time in the granitic Strengbach catchment (Vosges Massif, France). Application of the FlowPC model with modified input function. Hydrol. Process. 20, 1737–1751. https://doi.org/10.1002/hyp.5950

Viviroli, D., Weingartner, R., 2004. The hydrological significance of mountains: from regional to global scale. Hydrology and Earth System Sciences 8, 1016–1029. https://doi.org/10.5194/hess-8-1017-2004

Viviroli, D., Dürr, H.H., Messerli, B., Meybeck, M., Weingartner, R., 2007. Mountains of the

world— water towers for humanity: typology, mapping and global significance. Water Resources Research 43 (7), W07447. https://doi.org/10.1029/2006WR005653

Wassenaar, L. I., Ahmad, M., Aggarwal, P., van Duren, M., Pöltenstein, L., Araguas, L., & Kurttas, T. 2012. Worldwide proficiency test for routine analysis of δ2H and δ18O in water by isotope-ratio mass spectrometry and laser absorption spectroscopy. Rapid Communications in Mass Spectrometry, 26(15), 1641-1648. https://doi.org/10.1002/rcm.6270

Wetzel, K., 2004. On the hydrogeology of the Partnach area in the Wetterstein Mountains (Bavarian Alps). Erdkunde 58:172–186. http://www.jstor.org/stable/25647659

Zini, L., Casagrande, G., Calligaris, C., Cucchi, F., Manca, P., Treu, F., Zavagno, E., Biolchi. S. 2015. The Karst Hydrostructure of the Mount Canin (Julian Alps, Italy and Slovenia). Hydrogeological and Environmental Investigations in Karst Systems. (ed. Andreo, B., Carrasco, F., Durán, J.J., Jiménez, P., LaMoreaux.) Series: Environmental Earth Sciences. Springer. 638 pp. https://doi.org/10.1007/978-3-642-17435-3

I.Herms, J. Jódar, A. Soler, L.J. Lambán, E. Custodio, J.A. Núñez, G. Arnó, M.I. Ortego, D. Parcerisa, J. Jorge. Evaluation of natural background levels of high mountain karst aquifers in complex hydrogeological settings. A Gaussian mixture model approach in the Port del Comte (SE, Pyrenees) case study'. Science of the Total Environment 756 (2021) 143864. https://doi.org/10.1016/j.scitotenv.2020.143864

Science of The Total Environment

Volume 756, 20 February 2021, 143864

Evaluation of natural background levels of high mountain karst aquifers in complex hydrogeological settings. A Gaussian mixture model approach in the Port del Comte (SE, Pyrenees) case study

I. Herms [a], J. Jódar [b], A. Soler [c], L.J. Lambán [b], E. Custodio [d], J.A. Núñez [a], G. Arnó [a], M.I. Ortego [e], D. Parcerisa [f], J. Jorge [f]

Show more

+ Add to Mendeley Share Cite

https://doi.org/10.1016/j.scitotenv.2020.143864

Get rights and content

4 PAPER 2. EVALUATION OF NATURAL BACKGROUND LEVELS OF HIGH MOUNTAIN KARST AQUIFERS IN COMPLEX HYDROGEOLOGICAL SETTINGS. A GAUSSIAN MIXTURE MODEL APPROACH IN THE PORT DEL COMTE (SE, PYRENEES) CASE STUDY'

Authors: **Herms, I.**, Jódar, J., Soler, A., Lambán, L.J., Custodio, E., Núñez, J.A., Arnó, G., Ortego, M.I., Parcerisa, D., Jorge, J.

Abstract

The hydrogeological processes driving the hydrochemical composition of groundwater in the alpine pristine aquifer system of the Port del Comte Massif (PCM) are characterized through the multivariate statistical techniques Principal Component Analysis (PCA) and Gaussian Mixture Models (GMM) in the framework of Compositional Data (CoDa) analysis. Also, the groundwater Natural Background Levels (NBLs) for NO_3 and SO_4 and Cl are evaluated, which are especially important for indicating the occurrence of groundwater contamination derived from the anthropic activities conducted in the PCM.

The different hydrogeochemical facies found in the aquifer system of the PCM comprises low mineralized Ca-HCO_3 water for the main Eocene karst aquifer, and Ca-SO_4 and highly mineralized Na–Cl water types in the minor aquifers discharging from the PCM. The NBL values of SO_4, Cl and NO_3 obtained for the main karst aquifer are 14.33, 4.06 and 6.55 mg/L, respectively. These values are 35, 3 and 1.2 times lower than the respective official NBLs values that were determined by the water administration to be compared with in the case of conducting a pollution assessment characterization in the main karst aquifer. Official overestimation of NBLs can put important groundwater resources in the PCM at risk.

Keywords: High-mountain karst system; Natural background levels; Compositional data; Model-based clustering; Gaussian mixing model.

4.1 Introduction

High mountain zones produce globally essential water resources that feed fresh water to the lowland depending ecosystems and a large portion of the world's population (Viviroli et al., 2020). Mountain aquifers, especially those developed in karstifiable carbonate rocks, store the infiltrated precipitation, thus maintaining important groundwater resources. These resources are typically

released through large springs that regulates the hydro-ecological regime of the downstream rivers (Kresic and Stevanović, 2010), and provide water resources during the dry season in semi-arid regions, where they are often the primary source of drinking water (Stevanović, 2019).

Karst aquifers are much more vulnerable to pollution than other aquifers. Contaminants may easily enter the subsurface into the karst system and rapidly spread in the conduit system without any substantial attenuation (Marín and Andreo, 2015), threatening the water resources of a region, at large scale. These aquifers need special protection (Drew and Hötzl 1999, Zwahlen, 2004). In this line, the European Union enacted the Water Framework Directive (2000/60/EC) (WFD, 2000) as an integrated approach focusing on the monitoring of water bodies. The WFD (2000) also defines the rules for the identification of the different groundwater bodies (GWB), but also the criteria for chemical status assessment through defining pollutants threshold values (TVs) and groundwater natural background values (NBLs). The TVs are quality standards for pollutants in groundwater representative of those groundwater bodies considered to be at risk. The NBLs provide the information regarding the concentration of a given element, species or chemical substance present in solution which is derived by natural processes from geological, chemical, biological and atmospheric sources (Müller et al., 2006). In other words, NBLs are the corner stone to quantitatively evaluate whether groundwater is significantly affected or modified by anthropogenic influences (Nieto et al., 2005; Custodio et al., 2007).

It is not easy to define NBLs in high mountain karst aquifer systems (HMKS). For a given aquifer and a certain component, the corresponding NBL value is obtained by averaging the dissolved content of that component in groundwater discharge for the different springs draining the aquifer. HMKS are usually embedded in geological structures that are the result of complex tectonic processes (e.g. faults, fold-and-thrust belts, wedge pinch out layers). This often causes a strong compartmentalization (Ballesteros et al, 2014) that may involve different lithologies (i.e. from carbonates to evaporites), thus generating a complex aquifer system. The geological variability of such aquifer system influences the hydrogeochemical signature of groundwater along the different flowlines, which typically converge while mixing around springs. As a result, a different hydrochemical composition than the expected may be obtained in the discharge of a spring given its geological setting (Lambán et al., 2015), thus complicating a consistent NBLs characterization for the different aquifers conforming the hydrogeological system.

To correctly define NBLs in HMKS it is fundamental to have both a good hydrogeological characterization and sound conceptual model of the aquifers at local scale, and a good characterization of the relevant hydrogeochemical fingerprints describing the whole picture of the aquifer system. In this framework, multivariate statistical analysis (MSA) techniques/tools have shown a proven track record in characterizing complex hydrogeological systems through the analysis of spatial variations in hydrochemical data.

Geochemical data (and hence also hydrogeochemical data) are compositional by nature. This means that the concentration of a given element is actually expressing a part of a whole, regardless of the dimensions in which the component concentration is expressed, either as weight per cent ratio (e.g., %, mg/kg), or given as component mass per unit of dissolution volume (e.g., mg/L). Consequently, according to Aitchison (1986), they carry only relative information. In geochemistry and statistics, they are known as 'closed data' which implies that they not vary independently. As a consequence, they are not well represented by the usual Euclidean mathematical real structure. This may lead to important drawbacks in the analysis, widely discussed by different authors (Reimann et al., 2012; Buccianti and Grunsky, 2014; Filzmoser et al., 2018; Pawlowsky-Glahn, et al. 2015), which can affect its direct use in MSA if the appropriate transformations are not previously done. To overcome the problem, Aitchison (1986) described mathematically the structure of the Simplex (the sample space for compositional data) and proposed the first log ratio approaches, such as the additive log ratio (alt) and centered log ratio (clr), in order to express the compositional data sets in the usual real space. Later on, Egozcue, et al. (2003) proposed the isometric log-ratio (ilr) coordinates, also known as 'balances'. The latter transformation has better mathematical properties, and most importantly, allows to better interpret intermediate results of the analysis. These sets of methods are usually refered as compositional data (CoDa) analysis and allow to 'open' geochemical data, transforming the raw data before the application of classical MSA tools. The CoDa approach has been widely used in soil geochemistry studies (Buccianti et al., 2018; Carranza, 2011; Reimann et al., 2012, among others) and less often for hydrogeological studies, (Blake et al., 2016; Bondu et al., 2020; Otero et al., 2005; Owen et al., 2016, among others). In some cases this has already been used specifically for NBL studies.

The combination of MSA tools (e.g. principal component analysis and clustering analysis) allow to

investigate the factors controlling the processes taking place in aquifers driving the hydrogeochemical composition of groundwater (Puig et al., 2011; Blake et al., Piña et al., 2018; Shelton et al., 2018). Clustering analysis (CA) methods have been largely used to separate groundwater samples, especially for large and/or complicated datasets, into homogeneous groups to show up different source contributions to groundwater in the sampled springs (see Suk and Lee, 1999; Cloutier et al., 2008; Yidana, 2010; Kim et al., 2014; Yolcubal et al., 2019, among others). This faculty makes CA methods a promising tool to correctly define NBLs in HMKS.

There are two mainstreams in CA, (1) the "hard clustering" methods like hierarchical clustering and partitioning methods (k-means, k-medoids: Partitioning Around Medoids – PAM -, and Clustering Large Applications – CLARA), where each data point (i.e. the sample) is assigned to one and only one cluster (hard assignment), and (2) the "soft clustering" methods, like model-based clustering (e.g. the Gaussian Mixture Models – GMM) and fuzzy clustering where instead of assigning each data point into a unique specific cluster, it is assigned to all the clusters with different probabilities or weights (soft assignment) (Güler and Thyne, 2004).

Soft clustering methods are getting more popular since they provide degrees of membership at different hydrogeochemical clusters, rather than clear-cut distinctions. As a result, they can better reflect the spatial continuity of a hydrological system while providing a more rigorous framework to validate the clustering results (Kim et al., 2014; 2015; Wu et al., 2017; Bondu et al., 2020). Moreover, in the framework of HMKA where the limited number of observations often is a challenge, GMM clustering algorithms are shown to be able to provide valuable insights into hydrochemical processes, delineating the different groundwater sources imprinting the hydrochemical signature of the aquifer system, despite a sparse hydrochemical dataset (Wu et al., 2017). GMM are specially well suited to provide a solid basement for NBLs determination in HMKS. Although GMM have been used for some authors to evaluate NBLs (Kim, et al. 2015), surprisingly, there are no references in the scientific literature using GMM in the framework of CoDa analysis to evaluate NBLs in HMKS.

This work aims at filling this gap. To that end, we characterize the hydrochemical composition of the different aquifers associated to the alpine karst aquifer system of the Port del Comte Massif (PCM) to evaluate in a consistent way the NBLs for the different aquifers integrated in this HMKS.

This is conducted through a MSA approach that combines in a CoDa analysis framework both PCA and GMM clustering analysis.

4.2 The study area

The PCM is located in the South-Central Catalan Pyrenees (north-east of Spain), which constitute an orogenic system that runs along the boundary between the Iberian and European plates. It is of Late Cretaceous to Miocene age (Muñoz, et al 2018). The elevation of the mountainous massif ranges from 900 m a.s.l. to 2390 m a.s.l. The massif constitutes an independent structural and hydrogeological system with a surface area of 110 km^2. The highest peaks of the massif conform a water divide between the upper Segre River basin to the NW and SW (a large tributary in the Ebro basin) and the upper Cardener River basin (a tributary of the Llobregat River) to the SE (Figure 1).

According to the Köppen-Geiger classification (Peel et al., 2007), the study area is characterized by a cold climate without a dry season and with a temperate summer. For the period 2005-2019, the average annual precipitation (P), temperature (T) and potential evapotranspiration (Hargreaves' method) at the SMC meteorological station located at 2315m a.s.l. (**Figure 4. 1**) are 1055 mm, 3.2° C and 525 mm, respectively. At elevations > 1800 m a.s.l. the snow covers the massif from December to March.

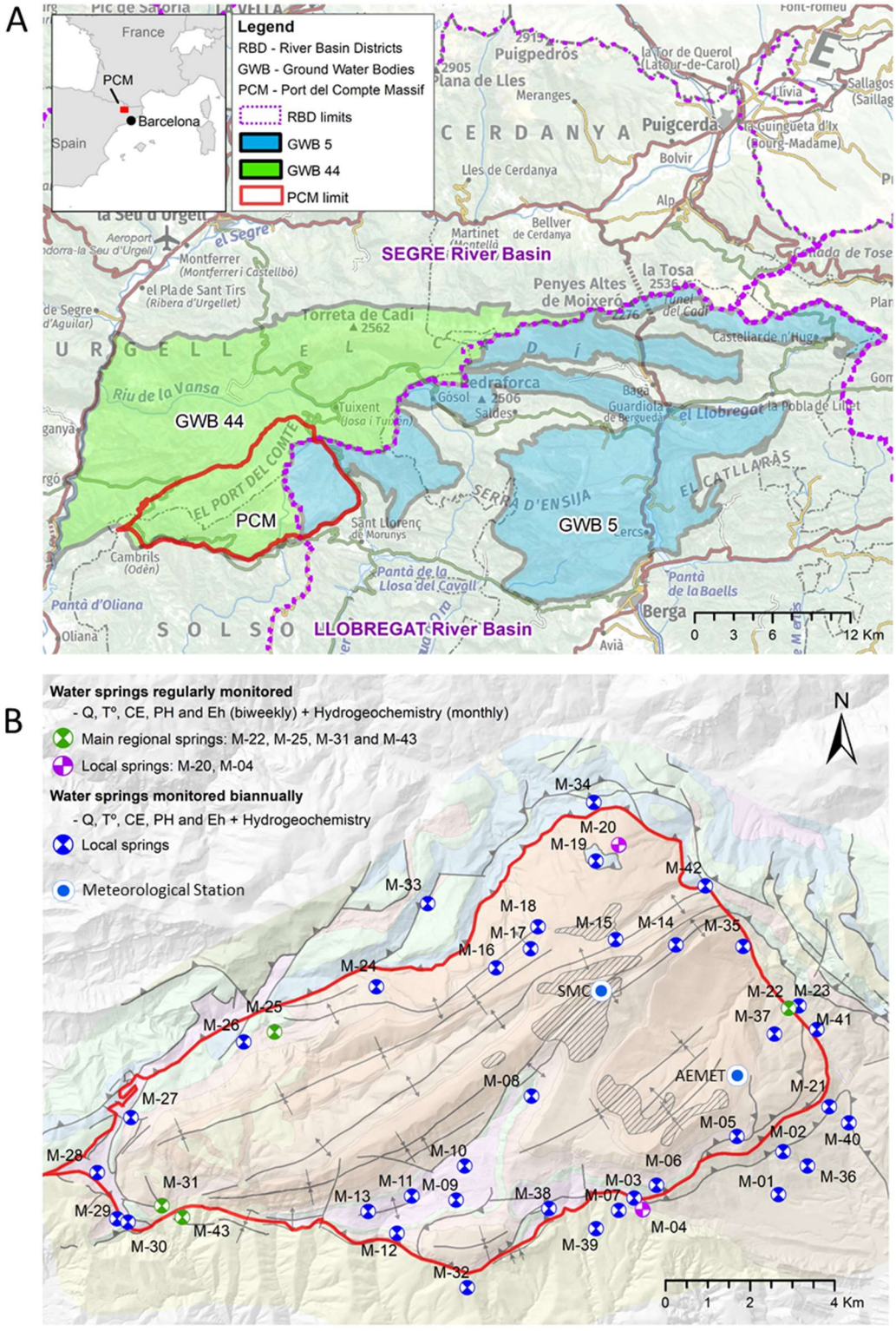

Figure 4. 1. (A) Location map of the study area. (A). Delimitation of the groundwater bodies affecting the PCM; GWB-44 belongs to the Segre river basin, and GWB-5 belongs to the Llobregat river basin. (B) Location of the 43 monitored springs in the PCM

Geologically, the PCM constitutes an independent thrust sheet which presents complex structural shapes in its boundaries (**Figure 4. 2**), with different thrust sheets individualizing the whole domain in one independent structural system. The internal structure of the PCM is formed by a set of folds and thrusts. These folds have a constant direction NE-SW parallel to the NW limit (Vergés, 1999). The stratigraphic series contains limestones and evaporites mainly from the Triassic, Cretaceous limestones, Paleogene calcarenites, and shales, and Eocene-Oligocene limestones, sandstones and marls. The Jurassic marls, limestones and dolomites only outcrops in the NW part of the geological sheet. The limestones have a total thickness greater than 1300 m. From the geomorphological perspective, the PCM presents a rounded-soft landscape in the highest domains with no vegetation cover and almost no soil horizon development. The rest of the massif is covered by mountain meadows and forest, with a shallow soil depth up to medium development ground cover. Many different karst forms appear progressively from 1950 m.a.s.l. upwards, being well developed at 2050m a.s.l. (see **Figure 4. 2**, indicated as 'Area with well-developed karst landforms'), with sinkholes, dolines and karren fields. They underline the heterogeneity of the karst system.

From the hydrogeological point of view, the PCM can be considered an independent unit multi-aquifer system. The main aquifer is formed by Lower Eocene – fissured and karstified limestones and dolomites. It constitutes one of the most important karst aquifers of the Catalan Pyrenees. The other existing aquifers and aquitards in the system are related to the Cretaceous limestones, Triassic limestone and evaporites, other Paleogene conglomerates and sandstones, and to small Quaternary aquifers draining small areas, which can be recharged locally at low or medium elevations. The lower Upper Cretaceous/Paleocene (Garumnian facies) substrate materials, composed by siltstone and shales constitute an impervious layer for the overlaying Lower Eocene karst aquifer. The geometric characteristics of the geologic structure of the system strongly influences the location of the existing karst springs, their groundwater geochemistry and their long-term hydrologic behaviour.

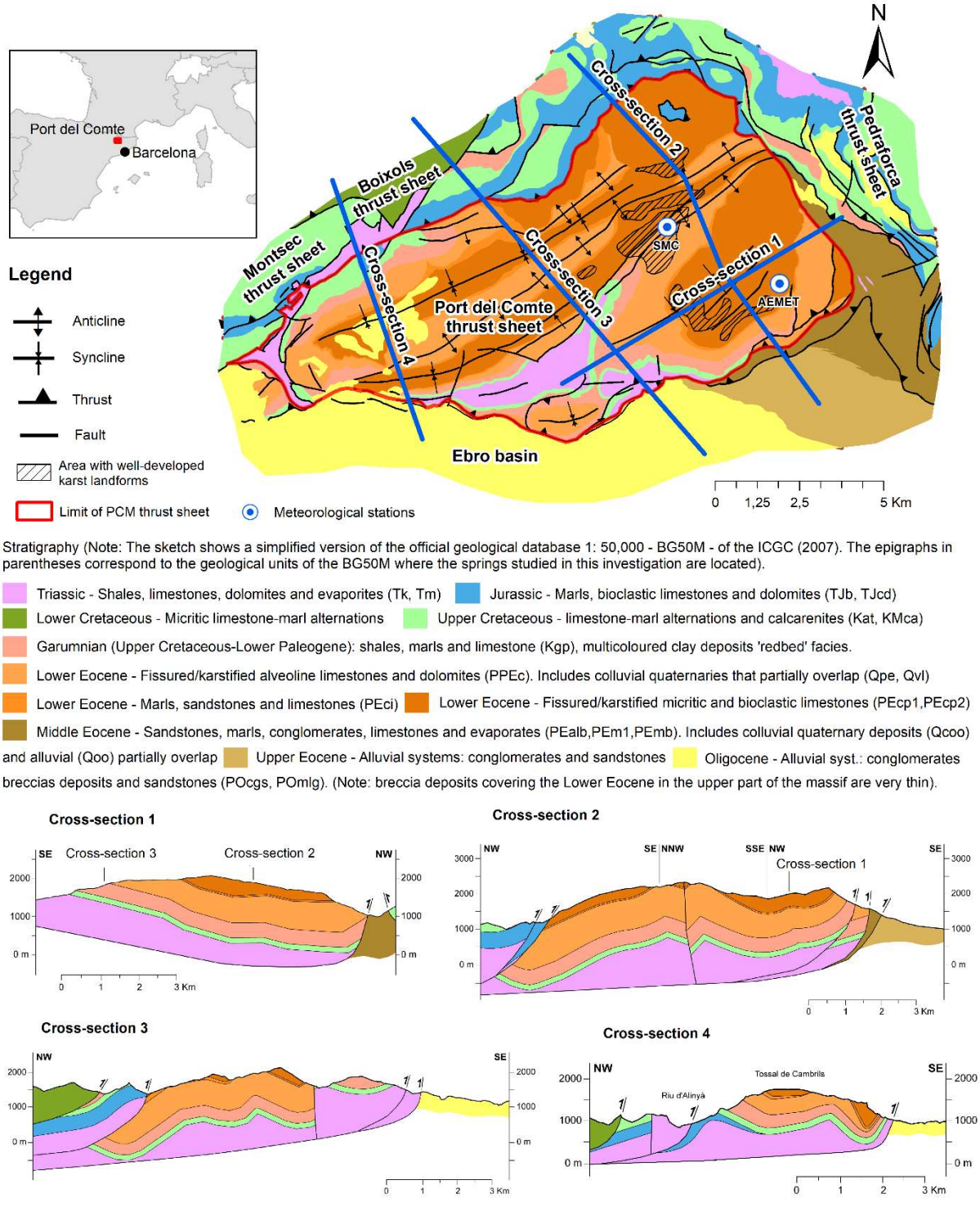

Figure 4. 2. Geological map and geological cross-sections of the PCM (modified from ICGC, 2007)

The hydrogeological conceptual model of the PCM aquifer system, as presented by Herms, et al. (2019), considers that recharge is produced by infiltration of precipitation as rainfall and snowmelt, and occurs both concentrated through the local karst conductive features, mostly situated at the top of the massif, and diffuse through the whole domain. The infiltrated water percolates through the thick unsaturated zone (more than 1000 m at the top of the massif) towards the saturated zone, and discharges through a large number of springs.

More that 100 springs were inventoried in the study zone. Nevertheless, only 43 of them discharge throughout the year (**Figure 4. 1**). These springs were monitored during the period September 2013 – October 2015. Most of them discharge small-scale local sub-surface water flows, with flow rates ranging between 0.1 L/s to 1 L/s. Nevertheless, there are four 'regional' springs (M-22, M-25, M-31 and M-43) with flow rates between 1 L/s and 900 L/s during the monitored period. These regional springs are recharged at medium to high elevations, and drain the system discharging through the limestones outcrops (M-31), Quaternary deposits overlying the limestones (M-25, M-22), and also through well-developed karst conduits in the conglomeratic materials of the Ebro Basin (M-43). These conglomerates conform the southern foreland basin of the Pyrenees, which is located just at the southern border of the PCM. There is also a diffuse groundwater discharge through the 'Riu Fred' sub-basin, to the North. With the exception of two singular groundwater wells on the SW and E edges of the PCM, there are no other water wells within the perimeter of the PCM that exploit the main karst aquifer. It is estimated that the regional water table of the karst system is between 1000 and 1100 m a.s.l. (Herms et al., 2019).

Although the whole PCM massif belongs to the same geomorphological structure, the SE sector has been assigned to GWB-5 ('Conca Alta del Cardener i Llobregat'), whereas the rest of the PCM was assigned to GWB-44 ('Cadí Port del Comte'). summarizes the natural background levels at the 90th percentile values (NBL90), determined through the Pre-selection (PS) method described by the EU research project "BRIDGE" (2007) (Müller et al., 2006) using different control points for each GWB. It is worth noting the high values for SO_4 contents in both GWBs. The NBLs values are assigned to the entire GWBs, and therefore are understood as representative of all units / aquifers included in these bodies. However, when the focus is on particular aquifers such as the pristine waters related to the Eocene karst aquifer included in the PCM, the assigned input value appears high.

Table 4. 1 NBL90 values for Cl, NO_3 and SO_4 in the GWB-5 and GWB-44

	NBL90		
	Cl [mg/L]	SO_4 [mg/L]	NO_3 [mg/L]
GWB-5	12 [a]	485 [a]	-
GWB-44	36[b]	609[b]	8[b]

(a) Data source: Agència Catalana de l'Aigua

(b) Data source: Confederación Hidrográfica del Ebro

In the current Spanish regulation for drinking water (MHCASWS, 2003) the limit of potability for sulfate is 250 mg/L of SO_4. According to this value, the whole GWB5 and 44 would be exceeding the regulatory limit, when groundwater from the Eocene aquifer is actually being used safely for drinking downstream. Therefore, assigning a global NBL value when the GWB integrates a number of aquifers with a different hydrochemical signature is not a minor issue.

4.3 Materials and methods

4.3.1 Sampling and analysis

In this work, 43 springs were sampled twice per year (i.e. before snowfall and after snowmelt seasons) between September 2013 and October 2015. Nevertheless, in six of them (M-04, M-20, M-22, M-25, M-31 and M-43) (**Figure 4. 1**) the groundwater sampling frequency was higher, every three to four weeks, to study the hydrogeochemical evolution of groundwater discharge. The springs M-22, M-25, M-31 and M-43 correspond to regional discharge points of the karst system, whereas springs M-04 and M-20 are considered representative of the local small aquifers of the area (Herms et al., 2019).

A total of 288 groundwater samples were collected. Additionally, 10 snow samples (7 from natural snow and 3 from artificial snow produced in the existing ski resort in the NE zone of the PCM) and two water samples from water ponds used to artificial snow production were collected. In all cases, the in situ physico-chemical parameters Temperature (T), electrical conductivity (EC), pH, Eh and the total dissolved solid (TDS) were measured. The geochemical analysis considered major cations

and anions.

All samples were filtered using a 0.45µm membrane filter and stored in new 200-500 mL polyethylene bottles washed with diluted nitric acid and rinsed with the water to be sampled prior to sampling. Samples for cation analysis were acidified with ultrapure HNO_3, to pH<2 to prevent precipitation. Samples for anion analysis were not acidified. All water samples were preserved at 4 ºC before laboratory measurement. T, CE, pH, Eh and TDS were measured by a portable Hanna meter (Multiparameter Water Quality Meter HI9829). The total alkalinity was determined in situ using the titration method - and later for the rest of campaigns using a photometer colorimetric method with the HI755 alkalinity test checker (Hanna Instruments). The major cations (Ca, Mg, Na, K, NH_4) and anions (Cl, NO_3, HCO_3,CO_3, SO_4, and F) were determined in the Laboratori Ambiental d'Aigües de Terrassa: the cations were analysed by inductively coupled plasma atomic emission spectrometry (ICP-OES Agilent 5100 DV), except the ammonium, which was measured using a ultraviolet-visible (UV-VIS) spectrophotometer, and the anions by ion chromatography (Dionex, DX-120). Ionic balance errors were calculated using the USGS software PHREEQC (Parkhurst and Appelo, 2013) within the version PhreeqC Interactive (version 3.3.3 10424), and with the phreeqc.dat database, except for the most salinized natural waters (M-30 and M-41) related to deep flow through Keuper evaporates. The majority of analyses had ionic balance errors below the recommended standard of ±5% (Appelo and Postma, 2005).

4.3.2 Data transformation using the CoDa approach

Geochemical datasets contain mostly compositional variables, that is, multivariate variables where the individual parts are parts of a whole (Buccianti and Grunsky, 2014). Classical examples refer to constant sum variables, but recent definitions of compositional data include all types of data representing parts of some whole. Ignoring the compositional character of these geochemical variables may lead to misleading results (Pawlowsky-Glahn et al., 2015). In this context, the CoDa analysis methodology is used in this work. In order to avoid the problems derived from the compositional data character, three transformations, all based on log-ratios have been historically proposed, named as: additive log-ratio (alr) transformation, centered log-ratio (clr) transformation (Aitchison, 1986) and isometric log-ratio (ilr) transformation (Egozcue et al., 2003).

In this study, the hydrochemical dataset was transformed using, firstly clr and secondly ilr. If **x** is the compositional vector, $\mathbf{x} = (x_1, \dots, x_n)$, the former transformation is described by

$$\mathrm{clr}(\mathbf{x}) = ln\left(\frac{x_i}{g(x_i)}\right);\ i = 1 \div D, \qquad (1)$$

where $g(\mathbf{x}) = \sqrt[D]{\prod_{i=1}^{D} x_i}$ is the geometric mean of all the considered components (ions), and D is the column matrix dimension.

The ilr transformation allows to express hydrochemical compositions with respect to an orthonormal basis. Their coordinates, called balances, may be easily obtained using a Sequential binary partition (SBP) (Egozcue et al., 2003; Egozcue and Pawlowsky-Glahn, 2005, 2006; Pawlowsky-Glahn et al. 2015). The SBP has been widely used for many authors on water chemistry studies (Engle and Rowan, 2013; Owen et al., 2016; Hee Kim et al., 2019; Bondu et al., 2020). For a D column matrix, i.e. a D-part composition, D-1 balances are calculated from the SBP as

$$\mathrm{ilr}(\mathbf{x}) = \sqrt{\frac{r_{i_+} \cdot r_{i_-}}{r_{i_+} + r_{i_-}}} \ln \frac{g(c_{i_+})}{g(c_{i_-})};\ \ i = 1 \div D - 1\ , \qquad (2)$$

where c_{i_+} and c_{i_-} are the groups of parts separated in the i^{th} step of the SBP; r_{i_+} and r_{i_-} are the numbers of parts included in c_{i_+} and c_{i_-}, respectively.

According to Egozcue and Pawlowsky-Glahn (2005; 2006), two methods for performing SBP can be applied: (1) directly from the PCA, and (2) by experienced judgment, where non-overlapping groups of parts, known as balances, are defined.

There are different software tools that allow to perform these transformations. The called CoDaPack v.2.0. program (Comas-Cufi and Thió-Henestrosa, 2011) is a software developed by the Research Group in Statistics and Compositional Data Analysis at University of Girona (UdG). This software can be freely downloaded from http://ima.udg.edu/codapack. It allows performing the log-

ratio transformations and to prepare different kind of plots to show the results. In this research, all statistical analyses were done using the statistics program R version 3.6.1 (2019-07-05) (R Development Core Team 2004), which is available for free under the GNU-public License and for all platforms from http://www.cran.r-project.org, through the software RStudio, a graphical user interface for R . For multivariate statistical analysis (MSA) using the CoDa analysis approach, the following packages for R software were used: {stats} version 3.6.1. (R-core R-core@R-project.org); {compositions} version 1.40-5 (Van den Boogaart and Tolosana-Delgado, 2008) {zCompositions} version 1.3.4 (Palarea-Albaladejo and Martín-Fernández, 2015).

Water samples with solute dissolved concentrations lower than the detection limit (the so-called 'left-censored values') put an extra challenge when addressing MSA techniques. The censored data can be either removed or replaced or imputed (e.g. values below detection limit are rounded as zeros) (Carranza, 2011). Following the criteria used for several authors (Reimann and Filzmoser, 2000; Farnham et al., 2002), in this work, left-censored values were excluded from the MSA when they represented > 25% of the total number of samples (i.e. when the variable had a 'medium–high' level of nondetects according to Palarea-Albaladejo and Martín-Fernández, 2014). Different algorithms can be applied within the {zCompositions} package for R for imputing these values (like multRepl, multLN, lrEM and lrDA methods).

4.3.3 Univariate exploratory data analysis

In order to explore the internal structure of the datasets, different Exploratory Data Analysis (EDA) plots combining a histogram, density trace, one-dimensional scatterplot and a boxplot (Kürzl, H. 1988) were used. Having this in mind, the ilr coordinates are adapted to the univariate case with the package {StatDa} (Filzmoser et al, 2009, 2009b). The variable of interest x (i.e. Cl, NO_3 and SO_4) is single ilr-transformed (Eq. 3):

$$z = \frac{1}{\sqrt{2}} \cdot ln\left(\frac{x}{1-x}\right) \quad (3)$$

4.3.4 Principal Component Analysis (PCA) and Model-based clustering

The first step to apply any MSA, is to check the presence of left-censored data and the imputation of values. The function 'zPatterns' {zCompostions} is used to find and display patterns of zeros/missing values in the whole dataset (see pattern diagrams at Figure SM.2.1 of Supp. Mat.). In this work, the left-censored detected values were imputed using the 'lrDA' (log ratio Data Argumentation) function. It is based on the log ratio Markov Chain Monte Carlo Data Argumentation algorithm (Palarea-Albaladejo and Martín-Fernández, 2015), and it has been already used by different authors to delineate water types (e.g. Owen et al 2016; Hee Kim et al., 2019). Following the commented procedure two data matrices were prepared:

- Dataset Matrix (300x8), corresponding to 300 water samples (288 groundwater samples and 12 snow and water ponds samples) and 8 variables (HCO_3, Cl, SO_4, NO_3, Ca, Mg, Na, K).

- Dataset Matrix (43x8), corresponding to the median hydrochemical composition of groundwater evaluated for each of the 43 springs and 8 variables (HCO_3, Cl, SO_4, NO_3, Ca, Mg, Na, K) (Table SM.1. Supp. Mat.) The consideration of "median composition" of time series follows the requirements to estimate NBL's using the PS method (see section 4.3.5).

Table SM.3.1 (Supp. Mat.) shows the list of parameters 'included' and 'excluded' for the MSA and their justification.

PCA is a very common method that is based on dimensionality reduction of datasets. It helps deciphering hydrogeochemical patterns and to infer the controlling variables of the water chemistry (Merchán et al., 2015; Moya et al., 2015). In order to perform the PCA it is necessary to calculate the '*variation matrix*' of the dataset (Aitchison, 1986) as a first step to obtain a measure of the dependence of the different variables, that is, the parts of the composition. Each component of the variation matrix, τ_{ij}, describes the log-relationship between two of the composition x_i and x_j (in this case chemical species). It is defined as

$$\tau_{ij} = \mathrm{var}\left(\ln\frac{x_i}{x_j}\right) = \frac{1}{N-1}\sum_{n=1}^{N}\ln^2\left(\frac{x_{ni}}{x_{nj}}\right) - \ln^2\left(\frac{g_i}{g_j}\right) , \quad (4)$$

where N is the number of observations and g_i, g_j are the geometric mean values for the two variables considered. A small value of τ_{ij} (which is equivalent to τ_{ji}) implies a good proportionality between the two variables. The variation matrix, τ_{ij}, is obtained using the R function '*summary.acomp'* of the package {compositions}.

Once the variation matrix is obtained, then the correlation between the variables x_i and x_j is estimated through the '*index of proportionality*' function, ρ_{ij} (Eq. 5) (Aitchison, 1986). The stronger the correlation between x_i and x_j the closer to 1 is the value of ρ_{ij}.

$$\rho_{ij} = \exp\left(\frac{-\tau_{ij}^2}{2}\right) \quad (5)$$

Data transformation following the CoDa analysis approach is applied before using any MSA tool. In this case, the PCA is applied using clr-transformed data (Eq. 1) obtained with the function 'clr' of the {compositions} R package. The method provides a new matrix of standardized coordinates for each sample called 'the scores', and also a new matrix of variable 'loadings' with columns representing the principal components of the (clr-transformed) data.

The graphical representations of the PCA results of clr-transformed data were done using the well-known biplot graphic (Gabriel, 1971) (**Figure 4. 3**), where the individuals are expressed as dots and the variables as rays. However, the interpretation of the clr-biplot differs from the interpretation of the classical biplot. Te clr-biplot interpretation is conducted by following the criteria proposed by Aitchison and Greenacre (2002), which is well suited for analyzing compositional data (Otero et al., 2005; Engle and Rowan, 2013; Blake et al., 2016; Piña et al., 2018). The criteria can be summarized as:

- The length of a link (i.e. black shaded line) between the rays (red arrows) defining clr(x_i) and clr(x_j) is proportional to the variance of ln(x_i/x_j).

- If two rays lay near each other, their quotient might be almost constant, and they might be proportional.
- If two links between four different clr-variables are orthogonal, then the corresponding pairwise quotients may be independent.
- If three or more vectors lie on the same link, the corresponding sub-composition might have one single degree of freedom.
- If two links between four separate clr-variables are orthogonal then the corresponding pairs of variables may vary independently of each other.

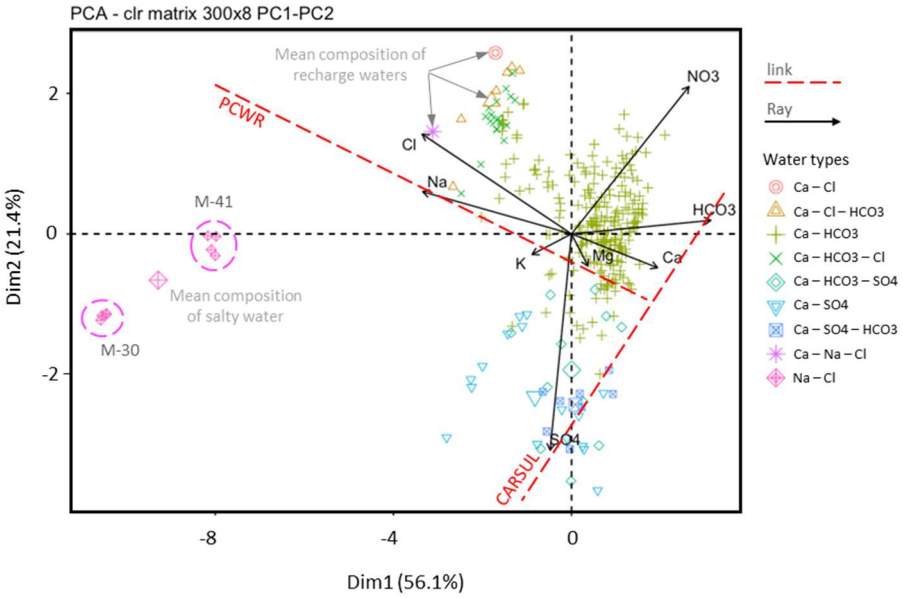

Figure 4. 3. clr-Biplot of the Principal Components PC1 and PC2 for the dataset Matrix (300x8). The label of the axes indicates the percentage of the variance explained by PC1 and PC2, respectively. The PCWR dashed line indicates the link between pristine waters and groundwater with water-rock interaction. The CARSUL dashed line indicates the link between CARbonate and SULphate waters. The smaller circles correspond to the different water samples and their color indicates their corresponding water type, whereas the larger circles represent the average composition of the different water types. To illustrate this, the groundwater samples from springs M-30 and a M-41 are indicated, as well as the corresponding mean composition.

The principal aim of cluster analysis is to split a number of observations into groups that are similar

in their characteristics or behaviour (Reimann et al. 2008). The cluster analysis is applied to group observations into several homogeneous clusters. It is based upon similarities between the observations and provides insights regarding the multivariate geochemistry characteristics (Bondu et al., 2020; Templ et al., 2008).

In this work it is used the 'soft' model-based clustering method. One of the main advantages is that it uses a probability-based approach. Therefore, the obtained partition can be interpreted from a statistical point of view, unlike the classical 'hard' - or heuristic-based - algorithms (k-means, hierarchical clustering, etc.) (Bouveyron and Brunet-Saumard, 2014). The model-based clustering approach used considering the ilr-transformed data was the finite mixtures of multivariate-normal or Gaussian distributions known as Gaussian Mixture Model (GMM), which is included in the {Mclust} R package (Fraley and Raftery, 2002; Fraley et al. 2012; Scrucca et al., 2016), and using the R version: 5.4.6 (Raferty et al., 2020). It assumes that observed data come from a mixture of underlying probability distributions representative of two or more clusters.

The GMM assumes the following probability distribution function (PDF)

$$f(x) = \sum_{k=1}^{K} \omega_k f_k(x|\mu_k, D_k) \ , \qquad (6)$$

where ω_k represents the weight or mixing proportion ($0 \leq \omega_k \leq 1$; $\sum_{k=1}^{K} \omega_k = 1$) or probability that an observation comes from the k_{th} mixture component, K is total number of components (i.e., groups or clusters), and f_k is the PDF of the observations for the k^{th} variable. Each component is usually modeled by a normal distribution (Eq. 7) with mean μ_k and covariance matrix D_k.

$$f_k(x|\mu_k, D_k) = \frac{1}{(2\pi)^{\frac{p}{2}} \cdot |D_k|^{\frac{1}{2}}} \exp\left[-\frac{(x-\mu_k)^2}{2 \cdot D_k}\right] \qquad (7)$$

Considering Eq. 6 the conditional probability of assigning one observation to a given cluster is given by

$$P(cluster\ k|x) = \frac{\omega_k f_k(x|\mu_k, D_k)}{f(x)} \qquad (8)$$

The greater the value of P the closer the association of sample x with the PDF corresponding to the cluster k is. By definition, those samples for which P > 0.5 for PDF *k* constitute a ‘‘cluster’’.

For the different components K, the model parameters ω_k, μ_k, and D_k are estimated using the expectation–maximization (EM) algorithm (Dempster et al., 1977). The covariance matrix D_k describes the geometry of the clusters with its volume, shape and orientation The different combinantions of these parameters allows to define 14 multivariate mixture models grouped in three main families: spherical, diagonal and ellipsoidal, which are included in the version used of {Mclust} package. In the other hand, this package uses the Bayesian Information Criterion (BIC) to find the optimum number of clusters. It identifies from those 14 multivariate mixing models, the one that best characterizes the data while maximizing BIC. More details of the GMM, BIC and EM mathematical approach, can be found on Biernacki and Govaert (1999), Fraley and Raftery (2002, 2012) and Raferty et al. (2020). In this study, model-based clustering has been applied to the dataset Matrix (43x8) of major ion data (HCO_3, Cl, SO_4, NO_3, Ca, Mg, Na, K), represented in this case using ilr-coordinates (Eq. 2).

The use of "hard" clustering methods was also analysed using the {clValid} (Brock et al. 2008), the {factoextra}R package (Kassambara and Mundt, 2016) and the {NbClust} R package (Charrad et al. 2014). Considering the results obtained, it was decided to rule out their use in front of the GMM in order to avoid the degree of subjectivity in the choice of the most suitable options for determining the relevant number of clusters and the best ‘hard’ method with the 43x8 matrix dataset. The results obtained can be consulted in the Supplementary Material in the Chapter 9, Part 9.3.

4.3.5 Determination of Natural Background Levels (NBLs) and Threshold Values (TV)

After identifying the number of underlying clusters in the data set in hand, based on MSA tools, the NBL and TV values for Cl, SO_4 and NO_3 are determined, which are the most common solutes causing specific groundwater pollution issues in HMKS. In this work, the PS-method developed in

the framework of the EU "BRIDGE" (2007) project (Müller et al., 2006) is applied since it has been successfully proven in many studies (Coetsiers et al., 2009; Ducci and Sellerino, 2012; Hinsby et al., 2008; Marandi and Karro, 2008; Parrone et al., 2019; Preziosi et al., 2010; Wendland et al., 2008; Zabala et al., 2016). The PS-method considers the following criteria for data preparation before estimating the NBL's:

- Time series should be replaced by medians (i.e. all sampling sites contribute equally to the NBL estimation).
- Samples with incorrect ion balance (exceeding 10%) and samples with median NO_3 contents >10 mg/L must be rejected.
- Brackish waters (i.e. NaCl) exceeding 1 g/L must not be considered.
- If samples are anaerobic (O_2 < 1 mg/L) or denitrification occurs, the dataset needs to be evaluated for the aerobic and anaerobic samples separately.

To obtain the NBL, the 90th percentile of the data sets is advisable for small datasets (N ≤ 60 sampling points) or when human impact cannot be excluded from the data, which is the case of the case study in this research. For n > 60 the 97.7th percentile is preferred. Once the NBLs are defined then the TVs are obtained following the final methodology suggested by the EU "BRIDGE" project:

$$TV = \begin{cases} \frac{1}{2} \cdot (\mathrm{NBL} + \mathrm{Ref}); & NBL \leq Ref \\ NBL; & NBL > Ref \end{cases}, \qquad (9)$$

where *Ref* is the reference value. In case of the Spanish Royal Decree 140/2003 of 7 February, laying down the health criteria for the quality of water intended for human consumption, the values of *Ref* for SO_4, NO_3 and Cl are 250 mg/L, 50 mg/L and 200 mg/L, respectively.

4.4 Results and discussion

4.4.1 Exploratory analysis of data and general water chemistry

The resulting EDA plots histograms for Cl, NO_3 and SO_4 of the dataset Matrix (43x8) (**Figure 4. 4**) show multi-model shapes in all the cases (i.e. major ions) suggesting that different populations are superimposed. In order to explain the dataset, and considering the geological setting of the area, a hypothetical mixture model with multiple components of different natural geogenic origin (possibly affected with local anthropogenic sources) must be considered, further to that coming from atmospheric deposition and evapo-concentrated in the soil and top rock. Thus, a simply bi-modal distribution composed of natural vs anthropogenic contamination cannot be considered to establish the NBLs without taking into account the multivariate character of the data. Thus, the first step is to separate the chemical groups or clusters.

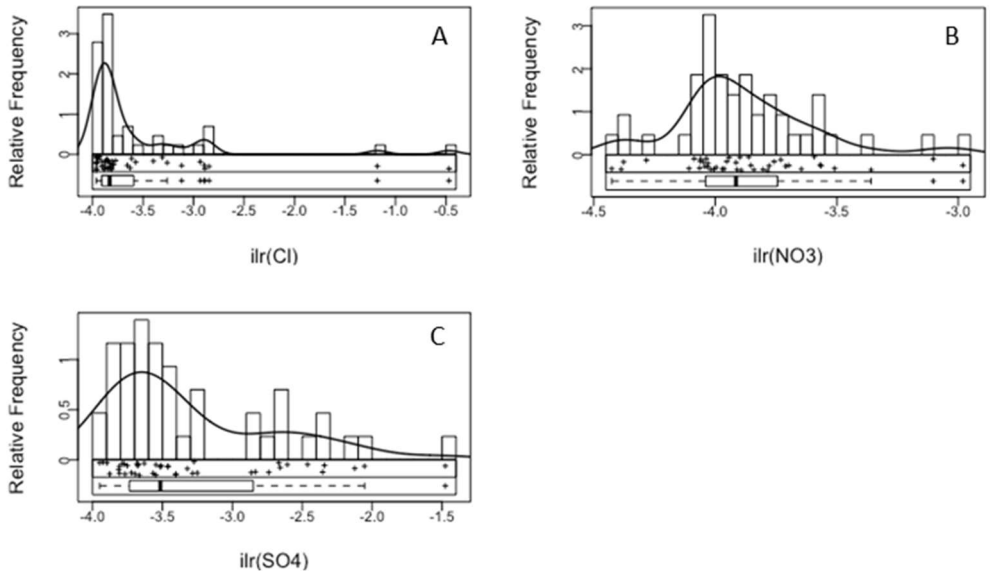

Figure 4. 4. EDA plots of ilr transformed data for Cl (A), NO_3 (B), and SO_4 (C) of the Matrix (43x8).

Classical graphical methods for the classification of water chemistry data, such as Piper and modified Stiff diagrams were used as a first step to analyse the whole dataset (except water samples from pluviometers (i.e. in total 288 samples). **Figure 4. 5** shows a map with the modified Stiff diagrams distribution over the PCM and also the corresponding modified Piper diagram. Based on that information, it is possible to initially aggregate the groundwater discharge from the 43 springs into 6 types of hydrogeochemical facies (**Error! No s'ha trobat l'origen de la referència.**):

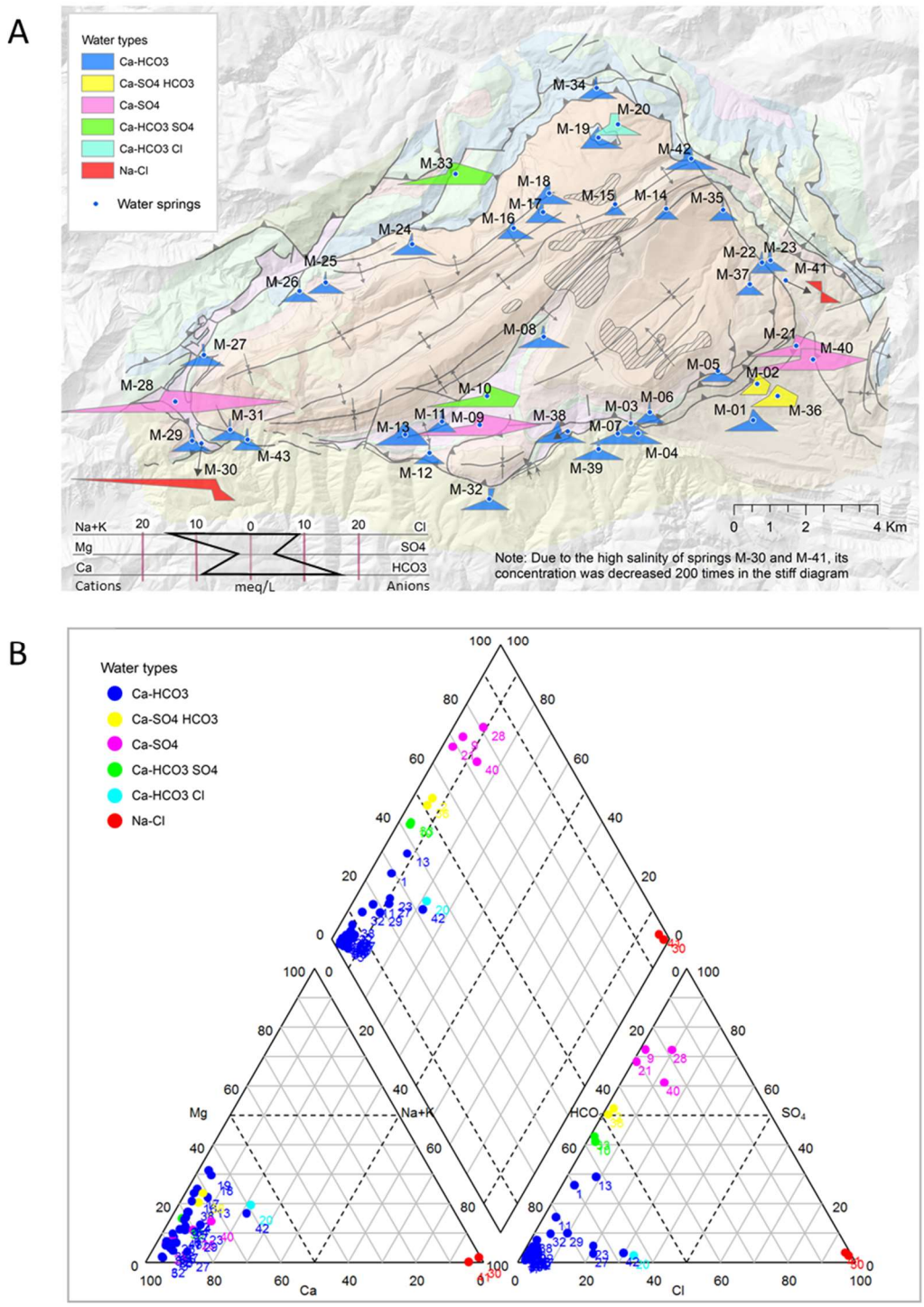

Figure 4. 5. Hydrochemical diagrams. (A) Modified Stiff diagram map and (B) Piper diagram associated to the selected springs in the PCM. In both cases, for every spring the ion content values correspond to the median value associated to all samples taken from that spring. The springs are classified by their hydrochemical facies.

Table 4. 2 Identified water types

Water type	Num. Springs	Geological units[a]
Ca-HCO_3	32	Cretaceous (KMca, Kgp, Kat)
		Paleogene-Eocene (PEab, PEci, PEcp1, PEm1)
		Paleogene-Oligocene (POcgs, POmlg, PPEc)
		Quaternary (Qpe, Qt0, Qvl)
		Triassic-Jurassic (TJb, TJcd)
		Triassic Muschelkalk (Tm)
Ca-HCO_3-Cl	1	Paleogene-Eocene (PEcp2)
Ca-SO_4_	4	Quaternary (Qcoo)
		Triassic-Keuper (Tk)
Ca-HCO_3-SO_4	2	Triassic-Keuper (Tk)
Na-Cl	2	Triassic-Keuper (Tk)
Ca-SO_4-HCO_3	2	Paleogene-Eocene (Pemb)

(a) For a given Water type, the geological units based on ICGC, (2007) ordered by number of springs

At the first glance, the results show that diverse springs outcropping from different geological units (ICGC, 2007) show similar groundwater facies, or also the same facies can be obtained from different points located at different geological units. In this context, these graphical techniques should not be considered determinant alone to discriminate between hydrochemical groups and therefore, their results should be considered preliminary. Table SM.1.1 (Supp. Mat.) shows the summary of the major ions content of the 43 monitored springs (expressed as median values of time series for the period September 2013 – October 2015) and also the water facies associated to them.

4.4.2 PCA and dataset matrix size

The variation matrix for the dataset Matrix (300x8) (**Table 4. 3**) shows strong correlations between different pairs of variables such as Ca and HCO_3, Na and Cl, and Mg and HCO_3. Besides, NO_3 shows a high correlation with Ca and HCO_3, whereas almost no correlation with SO_4. This result indicates that the most groundwater samples affected by nitrate pollution are those from the Eocene karst aquifer with a Ca–HCO_3 hydrochemical composition.

Table 4. 3 The upper triangle over the main diagonal shows the '*index of proportionality'* (Eq. 5) of the dataset Matrix (300x8). The lower triangle over the main diagonal shows in italic the *'index of proportionality'* of the dataset Matrix (43x8). In both cases, the correlation values larger than 0.5 are shaded in blue.

	Ca	Mg	Na	K	HCO_3	Cl	NO_3	SO_4
Ca	--	0.88	0.06	0.51	0.98	0.04	0.57	0.44
Mg	*0.76*	--	0.34	0.69	0.67	0.26	0.27	0.52
Na	*0.01*	*0.10*	--	0.54	0	0.96	0	0.15
K	*0.49*	*0.75*	*0.58*	--	0.15	0.36	0.13	0.43
HCO_3	*0.94*	*0.41*	*0*	*0.07*	--	0	0.56	0.06
Cl	*0.01*	*0.07*	*0.99*	*0.40*	*0*	--	0	0.05
NO_3	*0.55*	*0.07*	*0*	*0.02*	*0.59*	*0*	--	0.01
SO_4	*0.17*	*0.24*	*0.07*	*0.25*	*0*	*0.02*	*0*	--

The PCA is conducted initially with the whole dataset (N=300), including the hydrochemical composition of natural and artificial snow, water from ponds and groundwater samples. The PCA with clr transformed data shows that only with three principal components, the 87.4 % of total variance can be explained (**Figure 4. 6**). The PCA is affected by the presence of natural outliers, in our case from the Na-Cl hydro-facies, that completely distorts the shape of the biplots (Figure 6B, 6C and 6D). The scores are classified according to the singled out nine water types when considering the complete dataset.

From the distribution of the water samples in the clr-biplots several subgroups of waters with clear similarities can be read. The biplot between PC2 and PC3 clearly separates sulfate waters. Moreover, looking closely at the biplot between PC1 and PC2 (**Figure 4. 3**), different hydrochemical spatial trends can be observed, likely associated with changes in terms of bedrock lithology. In fact, it can be inferred that: (1) The highest clr-variances are shown for SO_4, Cl and NO_3, followed by Na and HCO_3. The lowest clr-variances are shown for Ca, K, and Mg; (2) The PCA has emplaced separately the saltiest waters (M-30 and M-41) in the western quadrant of the biplot. Using clr-transformed data allows to correctly separate characteristic points of the domain, which correspond to the deepest drainage from the Keuper materials; (3) The groundwater samples from the remaining springs are located in the north-eastern and southern quadrants: the freshest waters that are more related to the upper Eocene karst aquifer are situated at the north-eastern quadrant and

present some correlation with NO_3. The samples related to Cretaceous and Triassic materials appear to be more disperse, being most of them at the south-eastern part of the biplot with extreme values in springs M-21, M-9, M-33, M-36, among others.

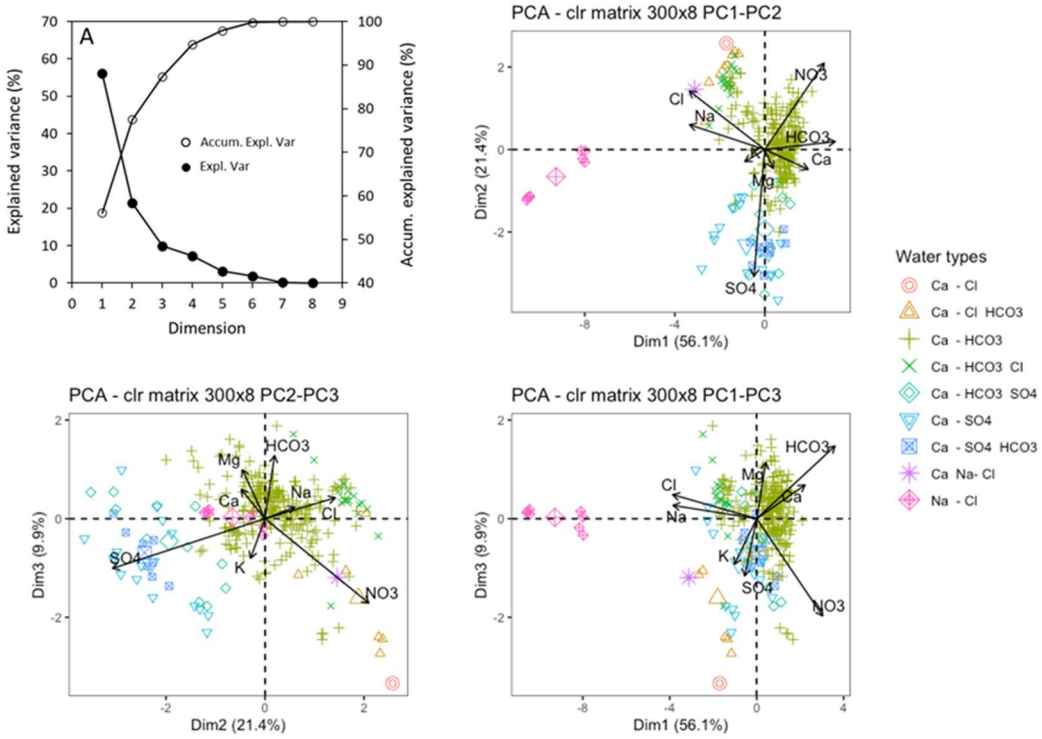

Figure 4. 6. (A) Scree-plot of dataset Matrix (300x8) showing the explained (solid circles) variance associated to every PC of the PCA, and the accumulated explained variance (empty circles) as the different PCs are accounted in the PCA. (B) Compositional biplot PC1 vs PC2 (C) Compositional biplot PC2 vs PC3 and (D) Compositional biplot PC1 vs PC3 showing scores (circles) and loadings (arrows) for clr transformed data. In the biplots, the bigger points represent the mean clr-value for each water type.

Taking into account the specific rules for interpreting clr-biplots, the following aspects can be highlighted:

- It is possible to draw a link between the vertices of Na, K and Mg, indicating that these variables may form a sub-composition with a single degree of freedom.
- The vertices of SO_4, Ca and HCO_3 lie almost on a common link. This link is also almost orthogonal to the link drawn between Na, K and Mg, suggesting that these two sub-compositions may vary independently of each other.

- The two indicated links can be interpreted as two independent set of hydrochemical processes in the springs: (1) The "Pristine Character/Water-Rock interaction" link PCWR [Na, K, Mg] which represents as one end-member, the groundwaters influenced by NaCl contributions derived from Keuper materials but also to recharged waters (Ca–Cl–HCO_3; Ca–Cl, Ca–NaCl) at the upper part of the PCM, which represent the other end members of waters that have interacted longer with the Tertiary karst system materials and more evapo-concentrated . (2) The "CARbonate/SULfate dissolution" link 'CARSUL' [SO_4, Ca, HCO_3] representing the dissolution of different types of carbonate and sulfate rocks (HCO_3 as one end member of the link and SO_4 as the other one).
- Samples in the south-eastern quadrant of the biplot are more disperse and have a stronger association with the SO_4 vertices.

In the case of the dataset Matrix (43x8) the variation matrix (Table 4) is consistent with that of the dataset Matrix (300x8), showing strong correlations between the same pairs of variables, and even with similar correlation values. The PCA with clr transformed data shows that when considering two or three PCs, 87.4% and 91.7% of total variance can be explained, respectively (**Figure 4. 7**). Besides, the resulting clr-biplots are similar in shape to those of Matrix (300x8). As it can be shown, the reduction of the dataset matrices from (300x8) to (43x8) in the PCA does not introduce any relevant change in the final inference regarding the geochemical characteristics of groundwater. This is convenient from the perspective of dimensionality issues.

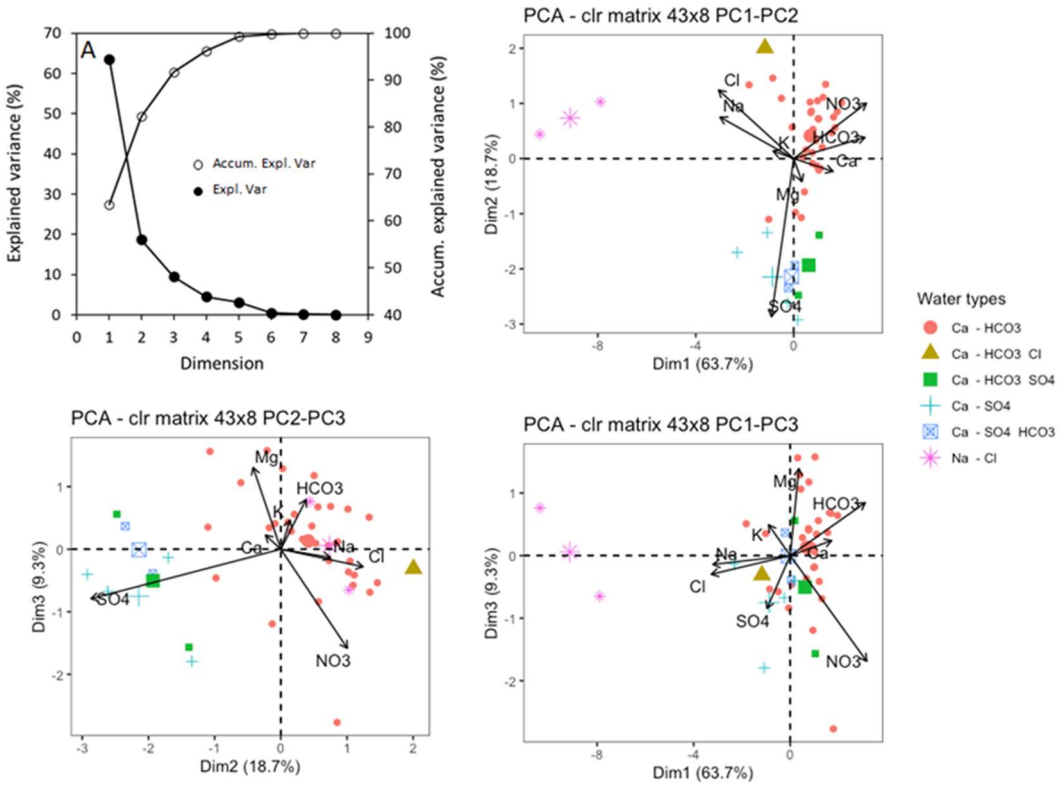

Figure 4. 7. (A) Scree-plot of dataset Matrix (43x8) showing the explained variance (solid circles) associated to every PC of the PCA, and the accumulated explained variance (empty circles) as the different PCs are accounted for in the PCA. (B) Compositional biplot PC1 vs PC2 (C) Compositional biplot PC2 vs PC3 and (D) Compositional biplot PC1 vs PC3 showing scores (circles) and loadings (arrows) for clr transformed data. In the biplots, the bigger points represent the mean value for each water type.

4.4.3 Clustering analysis

The GMM clustering analysis was applied to the Matrix (43,8) dataset. Before conducting the ilr transformation, an intuitive sequential binary partition (SBP) was used to characterize the hydrochemical variability within the domain. In this case the partition is based on knowledge of the groundwater chemistry in the study area and on the resulting compositional biplot (**Figure 4. 7**). As a result, seven groundwater partitions are considered (**Table 4. 4**): the ilr_1 balance separates the Ca-HCO_3 waters (mostly affected by NO_3) from the rest; the ilr_2 separates those waters affected/non-affected by NO_3 pollution; the ilr_3 separates the contribution of calcite and dolomite

to groundwater; the ilr_4 separates Ca from HCO_3; the ilr_5 separates SO_4 waters from most salty waters; the ilr_6 separates K from Na/Cl; and finally the ilr_7 separates Na and Cl.

Table 4. 4 SBP of a 7-part composition (ilr_1, ilr_2, …, ilr_7) for describing isometric log ratio (ilr) coordinates based on the separation of anions and cations related to the hydrochemical composition of natural groundwaters for the clustering analysis.

ilr	Ca^{2+}	Mg^{2+}	Na^{+}	K^{+}	HCO_3^{-}	Cl^{-}	NO_3^{-}	SO_4^{2-}
ilr_1	+1	+1	-1	-1	+1	-1	+1	-1
ilr_2	+1	+1	0	0	+1	0	-1	0
ilr_3	+1	-1	0	0	+1	0	0	0
ilr_4	+1	0	0	0	-1	0	0	0
ilr_5	0	0	+1	+1	0	+1	0	-1
ilr_6	0	0	+1	-1	0	+1	0	0
ilr_7	0	0	+1	0	0	-1	0	0

The results obtained from the GMM, suggest that the best multivariate clustering option is obtained applying the 'EEI' model (see Scrucca et al., 2016 for the geometric characteristics of the model) while considering a total of 4 clusters (see Figure SM.4.1 in Suppl. Mat.).

The scatterplot matrix obtained with the model-based clustering process using the seven ilr coordinates, being *D* the previous dimension of the original dataset matrix (43x8), *D*-1 coordinates can be shown in Figure SM.4.2 (Suppl. Mat.). In order to visualize the clusters in a most suitable way, the dimension reduction function 'MclustDR' (Scrucca, L. 2010) for visualizing the classification structure obtained from the finite mixture of Gaussian densities of the {Mclust} package is used to reduce the dimensionality of the ilr matrix and estimate the principal components. Table. SM.4.1 and Figure SM.4.3 (Suppl. Mat.) provide the scores of the reduced ilr-matrix and their representation in a scatterplot, respectively. The two main principal components explain 86,42% of the total variance. As a result, with only a glance at the scatterplot of PC1 and PC2 (**Figure 4. 8**A) the cluster division for the different springs shows up clearly, and each cluster can be described by the corresponding PDFs (**Figure 4. 8**B). It is worth to point out the similarity between the distributions of samples in the 2D space (albeit in a symmetric plane). The **Figure 4. 8**C presents the mean hydrochemical composition of each cluster (Table SM.4.2 in Suppl. Mat.)

after the modified Stiff diagrams, and **Figure 4. 8**D shows in a Piper diagram how the mean hydrochemical composition of the clusters is representative of the composition of the corresponding springs.

The probabilistic GMM framework estimates the optimal number of clusters and provides for every spring the probability of belonging to these clusters (soft assignment). This approach is more interesting that the classical clustering approaches, in which the number of clusters is assumed fixed, and every spring is assigned to one and only one of the previously assumed clusters (hard assignment) (Kim et al., 2014). From an hydrochemical point of view, the soft assignment often provides the more interesting interpretation because the method reveals if one observation is influenced by several factors (Templ et al., 2008). Moreover, Wu et al., (2017) show how the probabilistic GMM clustering provides insights into hydrochemical processes affecting groundwater, even with a limited number of observations, which is a common situation in high mountain kart aquifers such as the PCM.

The conditional probabilities (P) of assigning one observation to a given cluster (Eq. 7) are given in Table SM.4.3 (Suppl. Mat.). In all cases, springs are assigned to one cluster with a probability > 0.95, and more than 83% of the springs reach the probability of '1'. The smaller probabilities occur in M-01 (P = 0.911 cluster A) and M-13 (P = 0.969 cluster B). Spring M-01 discharges from the Eocene karstic limestones. Nevertheless, this discharge might be affected by weak contributions of Tertiary sulfates (which are related to the formation locally known as 'Beuda gypsum Formation'). The discharge in M-13 shows a Ca-HCO_3 hydrogeochemical composition despite discharging from the Triassic (Muschelkalk) limestone aquifer. In this case, the groundwater discharge is weakly affected by the underlying Keuper materials.

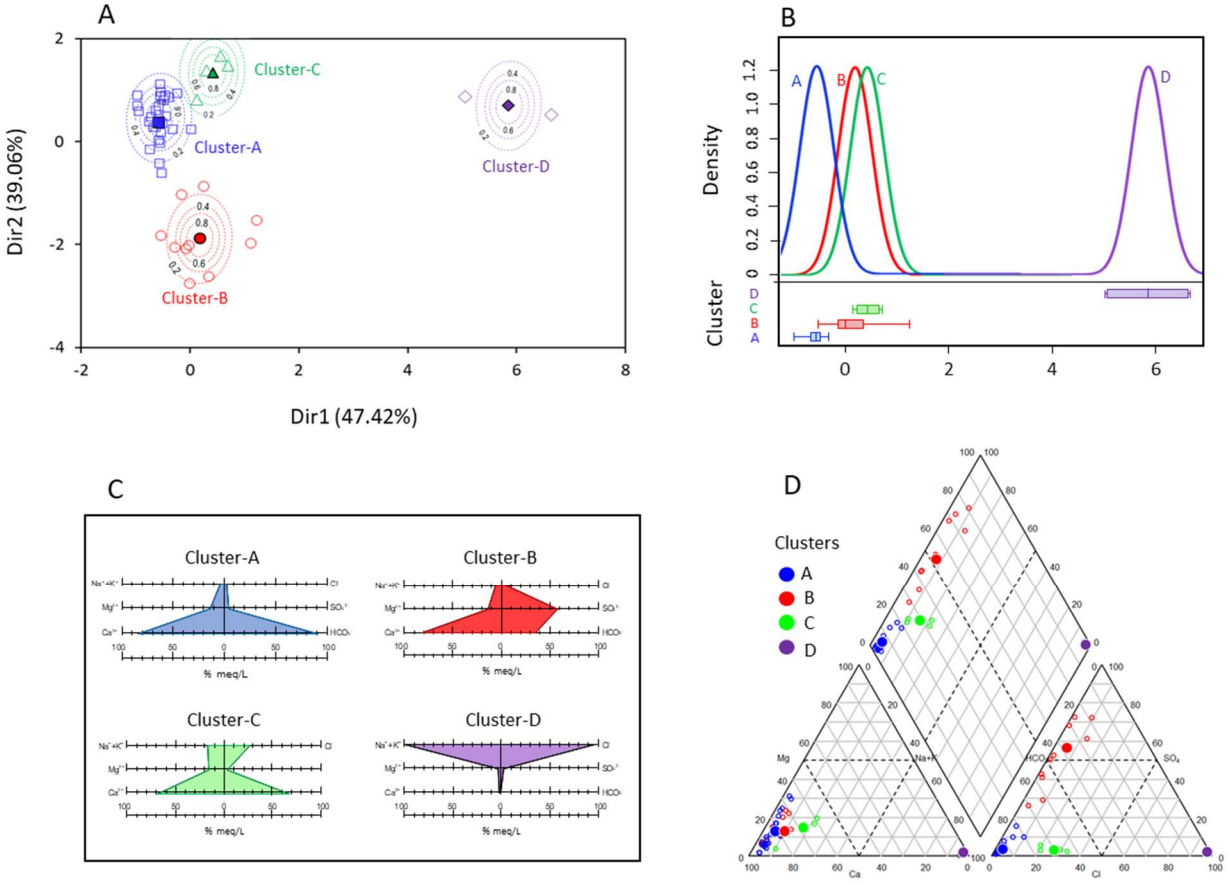

Figure 4. 8. (A) Density biplot for PC1 vs PC2 components obtained from GMM for the Matrix (43x8) of ilr-transformed data after dimension reduction. The dashed lines correspond to the probability zones of belonging a certain cluster in the subspace PC1-PC2. Solid symbols correspond to the mean hydrochemical composition of the clusters. (B) PDF's of the resulting 4 clusters in PC1 (47.42%). (C) Modified Stiff diagram associated to the mean hydrochemical composition of the clusters. (D) Piper diagram associated to the selected springs in the PCM classified by their corresponding cluster to which they belong. Solid symbols correspond to the mean hydrochemical composition of the clusters.

The hydrogeochemical description of each groundwater cluster can be summarized as:

- **Cluster A** is characterized by low mineralization and dominated by slightly alkaline Ca–HCO_3 water type. In total 27 springs are grouped in this cluster which correspond to 203 groundwater samples collected in the study from the total of 288. All the springs drain directly or indirectly (i.e. covered by local Quaternary deposits) the Tertiary Eocene upper karst aquifer of the PCM (**Figure 4. 9**) and from the higher parts of the mountain (944 - 2144 m a.s.l.). They are mainly found inside the structural limits of the PCM sheet and at

its boundaries except some of them localized in Quaternary deposits or discharging karstic conduits trough the Oligocene carbonate karstic conglomerates situated just in the front of the thrust sheet (e.g. M-03, M-04, M-07, M-39, M-32 and M-43, which is one of the most important karst springs of the system). Another special case is the spring M-06 which lies over Garumnian shales, marls and limestones (Kgp) outcropping materials. In this zone, a fault affecting the stratigraphy might allow the hydrological connection between the lower Eocene limestones (PPEc) and Kgp formations. This connection would explain the Ca–HCO_3 water type associated to spring M-06, and also its classification in the cluster A, thus pointing the groundwater discharge origin as the Eocene Tertiary aquifer. Finally, spring M-29 actually drains an Eocene limestone level situated at the west of the PCM boundary.

Cluster A presents the lower EC values, which ranges between 186 and 486 µS/cm and has the minimum values of groundwater temperatures. The concentrations of Cl and SO_4 are very low, ranging between 2.5 and 15 mg/L and between 2.6 and 25.3 mg/L respectively. In 13 samples, the concentration of NO_3 is above 10 mg/L, and in one specific spring (M-32) it exceeds in all samples the legal limit for potable water (50 mg/L). The average Saturation Indices (SI) estimated with the Phreeqc program (Parkhurst and Appelo, 2013) for calcite, gypsum and halite are 0.23, -2.67 and -9.68, respectively. The groundwaters are representative of the recharge of the karst system in the highest altitudes of the massif, where the dissolution of carbonates is the dominant geochemical process controlling groundwater chemistry.

- **Cluster B** encompasses water types from Ca–HCO_3 to Ca–HCO_3–SO_4, Ca–SO_4-HCO_3 and Ca–SO_4, which are characterized by slightly alkaline moderate mineralization. This group includes 10 springs. A total of 40 groundwater samples collected in the study would correspond to this cluster. The springs related to Cluster B are situated either inside or outside the internal structural limits of the PCM thrust sheet. The springs situated inside (M-9, M-10 and M-13) occur mostly in (1) Cretaceous and Triassic (Keuper) materials outcropping in the area. These materials underly the principal aquifer of the massif (the Eocene carbonate karstic system), and (2) local shallow granular aquifers. The springs M-01, M-02, M-21 and M-36 are related to sediments with high content of Tertiary gypsum from the Beuda Formation, which outcrops in small pinched out belts located in front of the southeastern part of the PCM thrust sheet. Springs are located at the lowest parts of massif

(altitudes ranging between 867 and 1456 m a.s.l.). The EC varies between 493 and 2102 µS/cm. The SO_4 concentration is quite high and ranges between 88 and 989 mg/L, exceeding in most cases the legal limit for potable water (250 mg/L). The concentration of Cl ranges between 3.8 and 94.5 mg/L. The average SI for calcite, gypsum and halite are 0.32, -0.99 and - 8.61 respectively.

- **Cluster C** includes water types from Ca–HCO3 and Ca–HCO3-Cl water types. This group includes 4 springs and a total of 37 groundwater samples from which 26 of them correspond to the spring M-20 (located at 1858m a.s.l.). Except the spring M-20, the rest (M-23, M-27, M-42) are located at the boundaries of the PCM geological sheet. The EC varies between 332 and 747 µS/cm. Although they have SO_4 concentration similar to cluster A, with 9.7-15.3 mg/L, the content of Cl is much higher, ranging between 24 and 82 mg/L. These higher values compared to cluster A are interpreted as related with groundwater flow through areas with the presence of relict halite or salty water in closed pores in the Keuper materials, or that may receive the solutes through diffusion. In the case of M-20 (which is located inside the PCM sheet) the salt is related to a klippe of Jurassic delineated into the geological map. Besides, in the catchment area of this spring, there are small outcrops of Keuper materials detected during the fieldwork. The average SI for calcite, gypsum and halite are 0.24, -2.32 and -7.42 respectively.

- **Cluster D** contains the most evident and special waters correspondings to Na–Cl type facies **Figure 4. 8**. This group is composed of 2 salty springs (M-41 and M-30) located at the 993 and 1023 m a.s.l. at the East and West boundaries of the PCM sheet respectively. They are characterized by very high mineralization and saturated in gypsum, discharging from Keuper confined bedrocks and interpreted as the contribution of deep groundwater flow with elevated transit times that allows a significant solute diffusion. The waters are slightly acidic to near-neutral. The M-41 and M-30 samples presents EC values of 57.2 and 247.1 mS/cm, Cl concentrations of 21 and 178.2 g/L, and SO_4 concentrations of 1.2 and 8.1 g/L respectively. The M-30 spring can currently be considered the saltiest spring of natural origin in Catalonia as those in the Cardona salt diapire of Oligocene age, not far away, disappeared due to potash mining activities. Due to the presence of Middle Eocene evaporates at the East boundary of PCM, the M-41 spring can also be affected by an interaction with Tertiary gypsium.

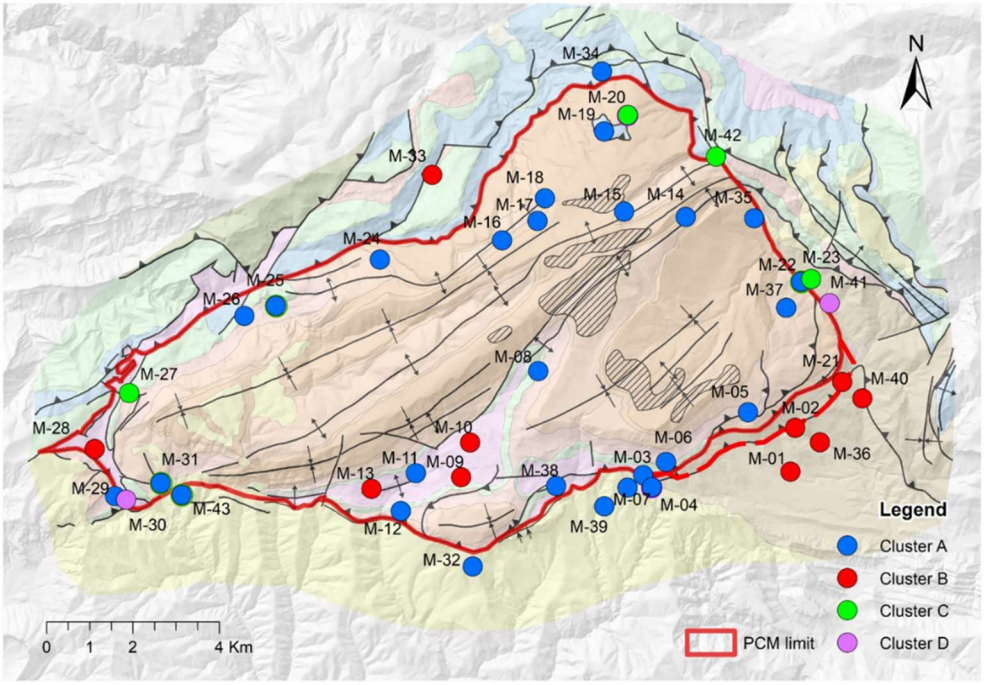

Figure 4. 9. Spatial distributions of the 43 clustered springs over the geological map of the PCM based on the GMM. The description of the different geological materials is the same presented in Figure 2.

In the framework of multivariate statistics data analysis (e.g. PCA and data clustering), specially dealing with compositional data (i.e. data that carry only information about the relative abundance of each component on the whole, such as the hydrogeochemical data sets), it is important to suitably transform the dataset using the CoDa analysis approach (e.g., Eq.1 or Eq.2) before conducting any analysis. Otherwise it is very likely to obtain wrong results (Otero et al., 2005). Moreover, uninterpretable results are also obtained when applying the classical standardization methodology known as "z-score" on compositional data, which considers logarithms and then subtracts the mean and divides it by the standard deviation to scale them (Blake et al., 2016). To illustrate the importance of using correct CoDa transformations, the dataset Matrix (43x8) is used to apply the same MSA analysis techniques (PCA and the model-based clustering GMM) but using the classical standardization approach (or z-score normalization). If the effect of the closed nature of the geochemical data is not accounted for, and therefore the CoDa approach is not applyed, then the distribution of loadings (variables) and scores (samples) in the biplots, as well as their

interpretation, may be critically affected. In this line, the biplot shown in Figure SM.5.1. (Suppl. Material) strongly suggests the existence of a negative relationship between all Ca - HCO_3 water samples respect all variables, which does not make any hydrogeological sense given the carbonatic nature of the aquifer and the hydrogeological knowledge supporting the existing conceptual model (Herms et al., 2019). Additionally, the clustering results obtained through GMM may have no hydrogeological sense. To illustrate this, **Figure 4. 10** presents the PDF's of the best GMM obtained for PC1 with the dataset Matrix (43x8) from the z-score approach after dimension reduction. Unlike in the case of considering the CoDa approach (**Figure 4. 8**B), now the PDFs corresponding to the six clustes identified can not be clearly separated, thus making clustering results uninterpretable.

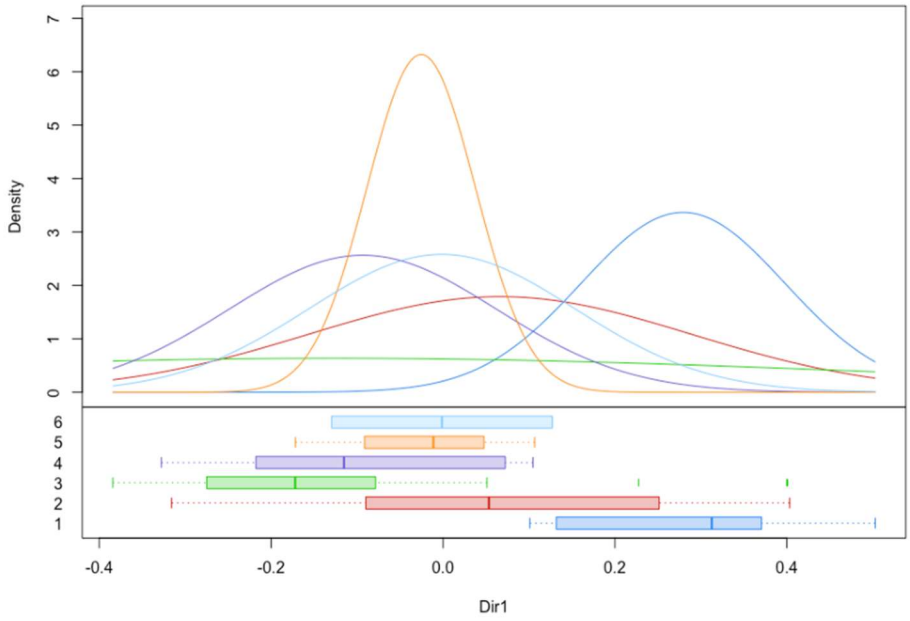

Figure 4. 10. Separated PDF's after dimension reduction with the best GMM with the transformed data using the classical standardization z-score approach.

4.4.4 NBLs and TVs values.

Once the groundwater clusters are defined for the PCM, the NBL and TV's for NO_3, SO_4 and Cl have been obtained applying the PS-method (Müller et al., 2006). Taking into account the criteria required for data to be accounted when estimating the NBLs with this method, the following

observations apply:

- The groundwater samples from M-30 and M-41 (the whole cluster D) present Cl concentrations of geogenic origin above the drinking water limit (>200 mg/L). Therefore, these samples are not considered in the NBL determination.
- NO_3 concentrations above the drinking water limit (>50 mg/L) are mostly observed in M-32 spring (cluster A). Besides, the springs M-32, M-10, M-11 and M-28 present NO_3 concentrations > 10 mg/L. Following the PS-method criteria, these springs have been excluded of the NBL determination.

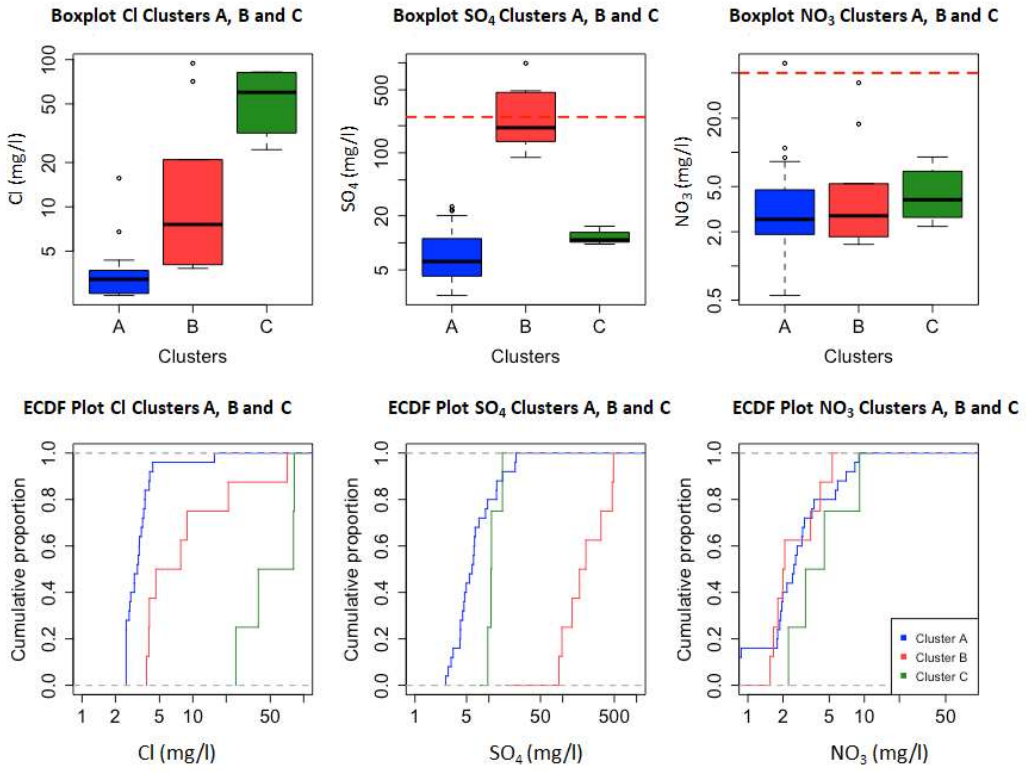

Figure 4. 11. (**A**) boxplots of the clusters A, B and C for SO_4, Cl and NO_3. The dashed red lines indicate the reference limits established in the Spanish Royal Decree 140/2003 (**B**) ECDF plots.

The NBLs for the remaining groundwater samples belonging to the clusters A, B and C are obtained considering the 90th percentiles (P90) of the corresponding cluster ECDF plots (**Figure 4. 11**B). The obtained NBL90 and TVs are presented in **Table 4. 5**. The results indicate that Tertiary Eocene karst aquifer (cluster A), which is the principal aquifer inside the PCM, presents the lowest NBL90 values

for Cl, SO_4 and NO_3. Cluster B, which is related to the aquifers on the Cretaceous and specially the Triassic Keuper materials, presents the highest NBL90 value for SO_4, and Cluster C, which is generally related to local small aquifers located at the boundaries of the PCM, presents the highest values of NBL90 for both Cl and NO_3.

Comparing the obtained NBL90 values with those officially assigned to GWB-5 and GWB-44 (), it looks that the NBL official values of SO_4 assigned to both GWBs (485 and 609 mg/L, respectively) are likely conditioned by the interaction between fresh groundwater and most probably evaporites of the Upper Triassic (Keuper facies), directly or through diffusion. These evaporites appear very often at the boundaries of many thrust sheets throughout the Southern Pyrenean zone. Additionally, the official NBL90 value of Cl assigned to GWB-44 is similar to that obtained for cluster B, which is related to the Keuper deposits. Likewise, the obtained NBL90 value of NO_3 for the Cluster C is similar to the official one for GWB-44. As can be shown, none of the official NBL90 values defined for GWB-5 and GWB-44 correspond to those values obtained for the Lower Eocene limestones and dolomites, which constitute by large the main aquifer of the PCM.

Table 4. 5 Summary results of the NBL and TV's values derived from the PS-method (BRIDGE, 2007) for clusters A, B and C for the solutes Cl, SO_4 and NO_3.

	Cl [mg/L]		**SO_4 [mg/L]**		**NO_3 [mg/L]**	
Clusters	**$NBL_{90\%}$**	**TVs**	**$NBL_{90\%}$**	**TVs**	**$NBL_{90\%}$**	**TVs**
A	4.06 ± 2	8.12 ± 2	14.33 ± 2	29.66 ± 2	6.55 ± 2	13.1 ± 2
B	35.98 ± 2	71.96 ± 2	471.71 ± 2	471.71 ± 2	4.51 ± 2	9.02 ± 2
C	81.92 ± 2	140.96 ± 2	13.96 ± 2	27.92 ± 2	7.73 ± 2	15.46 ± 2

It is well known that high mountain karst aquifers generate highly valuable water resources for the downstream water depending ecosystems. Their protection and rational management are of utmost importance to sustain such ecosystems and satisfying their water demands (Kazakis et al., 2018). In this framework, NBLs provide an objective scale to compare with when the quality status of the aquifer is assessed. Nevertheless, these aquifers are often immersed in deformed and faulted geological structures, as happens in other axial zones of the Central Pyrenees (Lambán et al., 2015),

in the Picos de Europa massif (Ballesteros et al., 2015), in the Jura Mountains (Luetscher and Perrin, 2005) and the Hochifen–Gottesacker Alps (Goldscheider, 2005), among others. The NBLs are obtained as a function of the hydrochemical content measured in the different springs discharging the system. Nevertheless, in geological complex zones it is difficult to assert if one certain spring is discharging groundwater from the aquifer of interest or not, because the geographical location of the spring may suggest an origin for the sampled groundwater while hiding mixing relations between groundwater flow lines from other local aquifers with different hydrogeochemical fingerprint (Lambán et al., 2015; Barbieri et al., 2017; Sánchez et al., 2017).

The European Union Water Framework Directive (WFD, 2000) defines a general framework for integrated river basin management in Europe to ensure their "good water status". Nevertheless, the river basin is often an entity hard to manage because the larger the size of the basin the larger is (1) the number of water bodies enclosed and (2) the likelihood of political-administrative boundaries issues to appear. To avoid such problems, instead of looking at river basins, the WFD refocussed on the smaller scale "river basin districts", for which administrative structures were defined to correctly manage the corresponding bodies, thus ensuring -hopefully- the right management of whole river basin (Boeuf and Fritsch, 2016). In this line, the WFD includes the guidelines that apply to define the groundwater bodies (GWB). Even in this case, some scale issues may arise when considering the definition of the GWB in mountain zones. By definition, the GWB are assumed to belong to a certain river basin. Despite of that, it is well known that groundwater basins, specially in mountain zones, may extend throughout several river basins (Struckmeier et al., 2006; Serianz et al., 2020). As a result, GWBs may include from several aquifers to only parts of them, as it happens in the PCM, whose discharge contributes to both the Ebro and the Llobregat rivers through GWB-44 and GWB-5, respectively. This is the reason why there are two different sets of NBL applying for the same aquifer (Table 1).

The WFD recognises the importance of having well defined NBLs. Given that these values are used to quantitatively assess whether or not anthropogenic pollution is taking place in the corresponding aquifer (Nieto et al., 2005), their characterization must be based on (1) a consistent and rigorous hydrochemical criteria, and (2) a sound hydrogeological conceptual model. The hydrogeological fingerprint of each aquifer belonging to the same GWB may be different. Therefore, the criterion of defining a single set of NBLs for the whole GWB may have no sense. Moreover, such criterium

may be counterproductive from a safety perspective, given that one may assume for the GWB some concentrations of species or chemical substances present in solution as normal, when actually those concentrations may be already indicating the existence of a polluting issue in some aquifers of the GWB. This is even worst when only one of these aquifers play a relevant role from a water resources perspective, as happens in the PCM. Here, the Lower Eocene karst aquifer generates an overall mean groundwater discharge that represents 15% of the mean annual water consumption in the city of Barcelona (Herms et al., 2019). Therefore, from a water resources management perspective, it might worth defining NBLs at the local scale for each aquifer. In this line, the methodology presented in this work to "complement" the sample pre-selection method is a useful tool to objectively reel off the NBL of the different high mountain aquifers belonging to a given GWB. Besides, the proposed methodology provides the GWBs managing authorities a full-sense hydrochemical criteria to better protect the high mountain pristine and strategic aquifers, while ensuring the good status of the associated high mountain river basins.

4.5 Conclusions

The PCM is a complex hydrogeological system composed by a main Eocene karst aquifer that drives the hydrodynamical discharge response of the massif. The PCM also includes small aquifers whose discharge present a different hydrochemical composition. The discrepancies between the official NBLs of the GWBs associated to the PCM reveal the disparities in the hydrochemical composition of groundwater from the different sampled springs belonging the GWBs. To estimate correctly the NBLs associated to one aquifer it is necessary to consider only samples from springs discharging groundwater from the aquifer of interest. In high complex hydrogeological settings, this selection is not easy and must be guided by a consistent and objective clustering method.

In the case of the PCM, four compositional groups have been identified by means of GMM clustering analysis. Most of the analysed springs are dominated by Ca–HCO_3 water type coming from the main aquifer of the area. There are some springs dominated by Ca–HCO_3, Ca–HCO_3–SO_4, Ca–SO_4-HCO_3, Ca–SO_4, Ca–HCO_3-Cl, Na–Cl water types derived from other small/local aquifers. Determination of NBLs values in the area must take into account the four groups defined in this study.

In complex aquifer systems, the proposed soft clustering approach, which is based on probabilistic Gaussian mixture models, provides the optimal number of clusters for the sampled springs only based upon the observed compositional data, while estimating the probability of belonging to everyone of these clusters for each spring. The presented clustering approach relies on multivariate statistics methods. In this framework, it is essential to transform the dataset using the CoDa analysis rules, specially when dealing with hydrochemical compositions. Otherwise, uninterpretable results will be likely obtained.

In the case of different existing aquifers with discrepant hydrochemical fingerprints in the same GWBs, it would be reasonable to evaluate the NBLs in all of them rather than having a single set of NBLs for the whole GWB. Otherwise, errors may appear when estimating the quality status of some of these aquifers, even if the overall assessed quality status of the GWB appears to be correct.

4.6 Acknowledgements

This research has been supported by Agencia Estatal de Investigación (AEI) from the Spanish Government and the European Regional Development Fund (FEDER) from EU through PACE-ISOTEC (CGL2017-87216-C4-1-R) projects, the EFA210/16/ PIRAGUA project which is co-founded by the European Regional Development Fund (ERDF) through the Interreg V Spain-France-Andorre Programme (POCTEFA 2014-2020) of the European Union, the Catalan Government projects to support consolidated research groups MAG (Mineralogia Aplicada, Geoquimica i Geomicrobiologia, 2017SGR-1733) from Universitat de Barcelona (UB) and GREM (Grup de Recerca de Minería Sostenible) from the Universidades Universitat Politècnica de Catalunya (UPC), the Ministerio de Ciencia, Innovación y through the METhods for COmpositional analysis of DAta (CODAMET) project (Ref: RTI2018-095518-B-C22, 2019-2021). We thank the Hydrogeology and Geothermics Unit Team of the Institut Cartogràfic i Geològic de Catalunya (ICGC) by their helpful collaboration. We acknowledge the Confederacion Hidrográfica del Ebro (CHE) and Agència Catalana de l'Aigua (ACA) for providing the official NBLs for WGB44 and WGB5, respectively. Meteorological data have been kindly provided by the Spanish Meteorological Agency (AEMET) and the Meteorological Service of Catalonia (SMC).

4.7 References

Aitchison, J., 1986. The Statistical Analysis of Compositional Data. Monographs on Statistics and Applied Probability Chapman and Hall, London, New York (416 pp.).

Aitchison, J., Greenacre, M., 2002. Biplots of compositional data. Journal of the Royal Statistical Society: Series C (Applied Statistics), 51(4), 375–392. https://doi.org/10.1111/1467-9876.00275

Appelo, C., Postma, D., 2005. Geochemistry, Groundwater and Pollution. 2nd edition. London: CRC Press, 683 pp. https://doi.org/10.1201/9781439833544

Ballesteros, D., Malard, A., Jeannin, P. Y., Jiménez-Sánchez, M., García-Sansegundo, J., Meléndez-Asensio, M., Sendra, G., 2015. KARSYS hydrogeological 3D modeling of alpine karst aquifers developed in geologically complex areas: Picos de Europa National Park (Spain). Environmental Earth Sciences, 74(12), 7699-7714. https://doi.org/10.1007/s12665-015-4712-0

Barbieri, M., Nigro, A., Petitta, M., 2017. Groundwater mixing in the discharge area of San Vittorino Plain (Central Italy): geochemical characterization and implication for drinking uses. Environmental Earth Sciences, 76(11), 393. https://doi.org/10.1007/s12665-017-6719-1

Biernacki, C., Govaert, Gérard., 1999. Choosing models in model-based clustering and discriminant analysis. J. Stat. Comput. Simul. 64, 49–71. https://doi.org/10.1080/00949659908811966

Blake, S., Henry, T., Murray, J., Flood, R., Muller, M.R., Jones, A.G., Rath, V., 2016. Compositional multivariate statistical analysis of thermal groundwater provenance: A hydrogeochemical case study from Ireland. Appl. Geochem. 75, 171–188. https://doi.org/10.1016/j.apgeochem.2016.05.008

Boeuf, B., Fritsch, O., 2016. Studying the implementation of the Water Framework Directive in Europe: a meta-analysis of 89 journal articles. Ecology and Society, 21(2):19. http://dx.doi.org/10.5751/ES-08411-210219

Bondu, R., Cloutier, V., Rosa, E., Roy, M., 2020. An exploratory data analysis approach for assessing the sources and distribution of naturally occurring contaminants (F, Ba, Mn, As) in

groundwater from southern Quebec (Canada). Appl. Geochem. 114, 104500. https://doi.org/10.1016/j.apgeochem.2019.104500

Bouveyron, C., Brunet-Saumard, C., 2014. Model-based clustering of high-dimensional data: A review. Comput. Stat. Data Anal. 71, 52–78. https://doi.org/10.1016/j.csda.2012.12.008

BRIDGE, 2007. Background cRiteria for the IDentification of Groundwater Thresholds. https://cordis.europa.eu/project/id/6538

Brock, G., Pihur, V., Datta, S., Datta, S., 2008. clValid: An R Package for Cluster Validation. Journal of Statistical Software 25(4). https://doi.org/10.18637/jss.v025.i04

Buccianti, A., Grunsky, E., 2014. Compositional data analysis in geochemistry: Are we sure to see what really occurs during natural processes? J. Geochem. Explor. 141, 1–5. https://doi.org/10.1016/j.gexplo.2014.03.022

Buccianti, A., Lima, A., Albanese, S., De Vivo, B., 2018. Measuring the change under compositional data analysis (CoDA): Insight on the dynamics of geochemical systems. J. Geochem. Explor. 189, 100–108. https://doi.org/10.1016/j.gexplo.2017.05.006

Carranza, E.J.M., 2011. Analysis and mapping of geochemical anomalies using logratio-transformed stream sediment data with censored values. J. Geochem. Explor. 110, 167–185. https://doi.org/10.1016/j.gexplo.2011.05.007

Charrad, M., Ghazzali, N., Boiteau, V., Niknafs, A., 2014. NbClust: an R package for determining the relevant number of clusters in data set. J Stat Soft.61:1–36.

Cloutier, V., Lefebvre, R., Therrien, R., Savard, M.M., 2008. Multivariate statistical analysis of geochemical data as indicative of the hydrogeochemical evolution of groundwater in a sedimentary rock aquifer system. J. Hydrol. 353, 294–313. https://doi.org/10.1016/j.jhydrol.2008.02.015

Coetsiers, M., Blaser, P., Martens, K., Walraevens, K., 2009. Natural background levels and threshold values for groundwater in fluvial Pleistocene and Tertiary marine aquifers in Flanders, Belgium. Environ. Geol. 57, 1155–1168. https://doi.org/10.1007/s00254-008-1412-z

Comas-Cufí, M., Thió-Henestrosa, S., 2011. CoDaPack 2.0: a stand-alone, multi-platform compositional software. In: Egozcue JJ, Tolosana-Delgado R, Ortego MI, eds. CoDaWork'11: 4th International Workshop on Compositional Data Analysis. Sant Feliu de Guíxols.

Custodio, E.; Nieto, P.; Manzano, M., 2007. Natural groundwater quality: policy considerations

and European opinion. The Natural Baseline Quality of Groundwater (eds. W.M. Edmunds & P. Shand). Blackwell Publ., Oxford. Chap. 8: 178–194. ISBN: 978–14051–5675–2. Dempster, A. P. , Laird, N. M.; Rubin, D. B. 1977. Maximum Likelihood from Incomplete Data via the EM Algorithm. Journal of the Royal Statistical Society. Series B (Methodological), Vol. 39, No. 1. pp. 1-38. https://doi.org/10.2307/2984875

Drew, D., Hötzl, H. (eds.), 1999. Karst Hydrogeology and Human Activities. Impacts, Consequences and Implications. – International Contributions to hydrogeology (IAH) 20, 322 p.

Ducci, D., Sellerino, M., 2012. Natural background levels for some ions in groundwater of the Campania region (southern Italy). Environ. Earth Sci. 67, 683–693. https://doi.org/10.1007/s12665-011-1516-8

Egozcue, J., Pawlowsky-Glahn, V., Mateu-Figueras, F., Barceló-Vidal, C., 2003. Isometric logratio transformations for compositional data analysis. Math Geol; 35:279–300.

Egozcue, J.J. Pawlowsky-Glahn, V., 2005. Groups of parts and their balances in compositional data analysis. Mathematical Geology, 37(7), 795-828.

Egozcue, J., Pawlowsky-Glahn V., 2006. Simplicial geometry for compositional data. In: Buccianti A, Mateu-Figueros G, Pawlowsky-Glahn V, editors. Compositional data analysis in the geosciences: from theory to practice. Bath, UK: Geological Society Publishing House; p. 67–77.

Engle, M.A., Rowan, E.L., 2013. Interpretation of Na–Cl–Br Systematics in Sedimentary Basin Brines: Comparison of Concentration, Element Ratio, and Isometric Log-ratio Approaches, Math Geosci (2013) 45:87-101 https://doi.org/10.1007/s11004-012-9436-z

Farnham, I.M., Sinh, A.k., Stetzenbach, K.J., Johannesson, K.H., 2002. Treatment of nondetects in multivariate analysis of groundwater geochemistry data. Chemometrics and Intelligent Laboratory Systems. Volume 60, Issues 1–2, 28 pp 265-281. https://doi.org/10.1016/S0169-7439(01)00201-5

Filzmoser, P., Steiger, B., 2009. StatDA: statistical analysis for environmantel data. R package version 1.1. http://cran.at.r-project.org/web/packages/StatDA/index.html

Filzmoser, P., Hron, K., Reimann, C., 2009b. Univariate statistical analysis of environmental (compositional) data: problems and possibilities. Sci Total Environ 407:6100–8. https://doi.org/10.1016/j.scitotenv.2009.08.008

Filzmoser, P., Hron, K., Templ, M., 2018. Applied Compositional Data Analysis. With Worked

Examples in R. Springer Series in Statistics. doi:10.1007/978-3-319-96422-5

Fraley, C., Raftery, A.E., 2002. Model-based clustering, discriminant analysis and density estimation, Journal of the American Statistical Association, 97/458, pp. 611-631

Fraley, C., Raftery, A.E., Murphy, T.B., Scrucca, L., 2012. mclust Version 4 for R: Normal Mixture Modeling for Model-Based Clustering, Classification, and Density Estimation. Technical Report No. 597, Department of Statistics, University of Washington

Gabriel, K.R., 1971. The biplot-graphic display of matrices with application to principal component analysis. Biometrika 58, 453e467.

Goldscheider, N., 2005. Fold structure and underground drainage pattern in the alpine karst system Hochifen-Gottesacker. Eclogae geol. Helv. 98, 1–17. https://doi.org/10.1007/s00015-005-1143-z

Güller, C., Thyne, G.D., 2004. Delineation of hydrochemical facies distribution in a regional groundwater system by means of fuzzy c-means clustering. Water Resour Res 40:W12503. https://doi.org/10.1029/2004WR003299

He Kim, S.H., Choi, B., Lee, G., Yun, S., Kim S., 2019. Compositional data analysis and geochemical modeling of CO2–water–rock interactions in three provinces of Korea. Environ Geochem Health 41, 357–380. https://doi.org/10.1007/s10653-017-0057-9

Herms, I., Jódar, J., Soler, A., Vadillo, I., Lambán, L. J., Martos-Rosillo, S., Núñez, J.A., Arnó, G., Jorge, J., 2019. Contribution of isotopic research techniques to characterize high-mountain-Mediterranean karst aquifers: The Port del Comte (Eastern Pyrenees) aquifer. Science of The Total Environment, 656, 209-230. https://doi.org/10.1016/j.scitotenv.2018.11.188

Hinsby, K., Condesso de Melo, M.T., Dahl, M., 2008. European case studies supporting the derivation of natural background levels and groundwater threshold values for the protection of dependent ecosystems and human health. Sci. Total Environ. 401, 1–20. https://doi.org/10.1016/j.scitotenv.2008.03.018

ICGC, 2007. Mapa Geològic Comarcal de Catalunya 1:50,000. Full Alt Urgell (BDGC50M). http://www.icgc.cat/ca/Administracio-i-empresa/Descarregues/Cartografia-geologica-i-geotematica/Cartografia-geologica/Mapa-geologic-comarcal-de-Catalunya-1-50.000/Mapa-geologic-comarcal-de-Catalunya-1-50.000

Kassambara, A., Mundt, F., 2016. Package 'factoextra': Extract and Visualize the Results of Multivariate Data Analyses, https://CRAN.R-project.org/package=factoextra, r package version 1.0.3

Kazakis, N., Chalikakis, K., Mazzilli, N., Ollivier, C., Manakos, A., Voudouris, K., 2018. Management and research strategies of karst aquifers in Greece: Literature overview and exemplification based on hydrodynamic modelling and vulnerability assessment of a strategic karst aquifer, Sci. Total Environ. 643, 592-609, https://doi.org/10.1016/j.scitotenv.2018.06.184

Kim, K.-H., Yun, S.-T., Park, S.-S., Joo, Y., Kim, T.-S., 2014. Model-based clustering of hydrochemical data to demarcate natural versus human impacts on bedrock groundwater quality in rural areas, South Korea. J. Hydrol. 519, 626–636. https://doi.org/10.1016/j.jhydrol.2014.07.055

Kim, K.-H., Yun, S.-T., Kim, H.-K., Kim, J.-W., 2015. Determination of natural backgrounds and thresholds of nitrate in South Korean groundwater using model-based statistical approaches. J. Geochem. Explor. 148, 196–205. https://doi.org/10.1016/j.gexplo.2014.10.001

Kresic, N., Stevanović, Z., 2010. Groundwater hydrology of springs: engineering, theory, management, and sustainability. Butterworth-Heinemann, Oxford

Kürzl, H., 1988. 'Exploratory data analysis: recent advances for the interpretation of geochemical data. Journal of Geochemical Exploration, 30(1-3), 309–322. https://doi.org/10.1016/0375-6742(88)90066-0

Lambán, L.J., Jódar, J., Custodio, E., Soler, A., Sapriza, G., Soto, R., 2015. Isotopic and hydrogeochemical characterization of high-altitude karst aquifers in complex geological settings. The Ordesa and Monte Perdido National Park (Northern Spain) case study. Science of the Total Environment, 506, 466-479. http://dx.doi.org/10.1016/j.scitotenv.2014.11.030

Luetscher, M., Perrin, J., 2005. The Aubonne karst aquifer (Swiss Jura). Eclogae Geologicae Helvetiae, 98(2), 237-248. https://doi.org/10.1007/s00015-005-1156-7

Marandi, A., Karro, E., 2008. Natural background levels and threshold values of monitored parameters in the Cambrian-Vendian groundwater body, Estonia. Environ. Geol. 54, 1217–1225. https://doi.org/10.1007/s00254-007-0904-6

Marín, A.I., Andreo, B., 2015. Vulnerability to Contamination of Karst Aquifers. In: Stevanović Z. (eds) Karst Aquifers—Characterization and Engineering. Professional Practice in Earth Sciences. Springer, Cham. https://doi.org/10.1007/978-3-319-12850-4_8

Martín-Fernández, J.A., Barceló-Vidal, C., Pawlowsky-Glahn, V., 2003. Dealing with zeros and missing values in compositional data sets using nonparametric imputation. Mathematical Geology 35 (3), 253–278.

Merchán, D., Auqué, L.F., Acero, P., Gimeno, M.J., Causapé, J., 2015. Geochemical processes controlling water salinization in an irrigated basin in Spain: Identification of natural and anthropogenic influence. Sci. Total Environ. 502, 330–343. https://doi.org/10.1016/j.scitotenv.2014.09.041

MHCASWS, 2003. Royal Decree 140/2003 of 7 February by which health criteria for the quality of water intended for human consumption are established. Ministry of Health, Consumer Affairs and Social Welfare, Spain

Moya, C.E., Raiber, M., Taulis, M., Cox, M.E., 2015. Hydrochemical evolution and groundwater flow processes in the Galilee and Eromanga basins, Great Artesian Basin, Australia: A multivariate statistical approach. Sci. Total Environ. 508, 411–426. https://doi.org/10.1016/j.scitotenv.2014.11.099

Müller, D., Blum, A., Hart, A., Hookey, J., Kunkel, R., Scheidleder, A., Tomlin, C., Wendland, F., 2006. Final proposal for a methodology to set up groundwater threshold values in Europe. In: Report to the EU project ‘‘BRIDGE’’, Deliverable D18.

Muñoz, J.A., Mencos, J., Roca, E., Carrera, N., Gratacós, A., Ferrer, O. Fernández, O., 2018. The structure of the South-Central-Pyrenean fold and thrust belt as constrained by subsurface data. Geologica Acta, Vol.16, No 4, 439-460 https://doi.org/10.1344/GeologicaActa2018.16.4.7

Nieto, P., Custodio, E., Manzano, M., 2005. Baseline groundwater quality: a European approach. Environmental Science & Policy, 8(4), 399-409. https://doi.org/10.1016/j.envsci.2005.04.004

Otero, N., Tolosana-Delgado, R., Soler, A., Pawlowsky-Glahn, V., Canals, A., 2005. Relative vs. absolute statistical analysis of compositions: A comparative study of surface waters of a Mediterranean river. Water Res. 39, 1404–1414. https://doi.org/10.1016/j.watres.2005.01.012

Owen, D.Des.R., Pawlowsky-Glahn, V., Egozcue, J.J., Buccianti, A., Bradd, J.M., 2016. Compositional data analysis as a robust tool to delineate hydrochemical facies within and between gas-bearing aquifers: COMPOSITIONAL DATA ANALYSIS TO DELINEATE WATER TYPES. Water Resour. Res. 52, 5771–5793. https://doi.org/10.1002/2015WR018386

Palarea-Albaladejo, J., Martin-Fernandez, J.A., Olea, R.A.,2014. A bootstrap estimation scheme for chemical compositional data with nondetects. Journal of Chemometrics, 28: 585-599. https://doi.org/10.1002/cem.2621

Palarea-Albaladejo, J., Martin-Fernandez, J.A., 2015. zCompositions — R package for multivariate imputation of left-censored data under a compositional approach. Chemometrics and Intelligent Laboratory Systems, Volume 143, pp 85-96, ISSN 0169-7439, https://doi.org/10.1016/j.chemolab.2015.02.019

Parkhurst, D.L., Appelo, C.A.J., 2013. Description of Input and Examples for PHREEQC Version 3—A Computer Program for Speciation, Batch-Reaction, One-Dimensional Transport, and Inverse Geochemical Calculations: U.S. Geological Survey Techniques and Methods, Book 6, Chap. A43: 1–497. (Available only at https://pubs.usgs.gov/tm/06/a43 Last access 28 August 2020).

Parrone, D., Ghergo, S., Preziosi, E., 2019. A multi-method approach for the assessment of natural background levels in groundwater. Sci. Total Environ. 659, 884–894. https://doi.org/10.1016/j.scitotenv.2018.12.350

Pawlowsky-Glahn, V., Egozcue, J.J., Tolosana-Delgado, R., 2015. Modeling and Analysis of Compositional Data. ed. John Wiley & Sons Ltd, The Atrium, Southern Gate, Chichester, West Sussex, PO19 8SQ, United Kingdom. 272 pages. ISBN: 9781118443064

Peel, M.C., Finlayson, B.L., McMahon, T.A., 2007. Updated world map of the Köppen– Geiger climate classification. Hydrol. Earth Syst. Sci. 11, 1633–1644. https://doi.org/10.5194/hess-11-1633-2007

Piña, A., Donado, L.D., Blake, S., Cramer, T., 2018. Compositional multivariate statistical analysis of the hydrogeochemical processes in a fractured massif: La Línea tunnel project, Colombia. Appl. Geochem. 95, 1–18. https://doi.org/10.1016/j.apgeochem.2018.05.012

Preziosi, E., Giuliano, G., Vivona, R., 2010. Natural background levels and threshold values derivation for naturally As, V and F rich groundwater bodies: a methodological case study in Central Italy. Environ. Earth Sci. 61, 885–897. https://doi.org/10.1007/s12665-009-0404-y

Puig, R., Tolosana-Delgado, R., Otero, N., Folch, A., 2011. Combining isotopic and compositional data: a discrimination of regions prone to nitrate pollution. In V. Pawlowsky-Glahn and A. Buccianti (Eds.), Compositional Data Analysis: Theory and Applications 390.

Raftery, AE., Scrucca, L., Brendan, T., Fop, M., 2020. Gaussian Mixture Modelling for Model-Based Clustering, Classification, and Density Estimation. Package 'mclust'. Version 5.4.6. https://mclust-org.github.io/mclust/

Reimann, C., Filzmoser, P., 2000. Normal and lognormal data distribution in geochemistry: death of a myth. Consequences for the statistical treatment of geochemical and environmental data.

Environmental Geology 39, 1001–1014. https://doi.org/10.1007/s002549900081

Reimann, C., Filzmoser, P., Garrett, R.G., Dutter, R., 2008. Statistical data analysis explained. Applied environmental statistics with R. Wiley, Chichester, UK, 362 pp. ISBN: 978-0-470-98581-6

Reimann, C., Filzmoser, P., Fabian, K., Hron, K., Birke, M., Demetriades, A., Dinelli, E., Ladenberger, A., 2012. The concept of compositional data analysis in practice — Total major element concentrations in agricultural and grazing land soils of Europe. Sci. Total Environ. 426, 196–210. https://doi.org/10.1016/j.scitotenv.2012.02.032

Sánchez, D., Antonio Barberá, J., Mudarra, M., Andreo, B., Martín, J.F., 2017. Hydrochemical and isotopic characterization of carbonate aquifers under natural flow conditions, Sierra Grazalema Natural Park, southern Spain. Geological Society, London, Special Publications, 466(1), 275–293. https://doi.org/10.1144/sp466.16

Scrucca, L., 2010. Dimension reduction for model-based clustering. Statistics and Computing, 20(4), pp. 471-484.

Scrucca, L., Fop, M., Murphy, T.B., Raftery, A.E., 2016. Mclust 5: clustering, classification and density estimation using Gaussian finite mixture models, The R Journal, 8/1, pp. 289-317.

Serianz, L., Cerar, S. Šraj, M., 2020. Hydrogeochemical characterization and determination of natural background levels (NBL) in groundwater within the main lithological units in Slovenia. Environ Earth Sci 79, 373. https://doi.org/10.1007/s12665-020-09112-1

Shelton, J.L., Engle, M.A., Buccianti, A., Blondes, M.S., 2018. The isometric log-ratio (ilr)-ion plot: A proposed alternative to the Piper diagram. J. Geochem. Explor. 190, 130–141. https://doi.org/10.1016/j.gexplo.2018.03.003

Stevanović, Z., 2019. Karst waters in potable water supply: a global scale overview. Environ Earth Sci 78, 662. https://doi.org/10.1007/s12665-019-8670-9

Struckmeier, W.F., Gilbrich, W.H., Gun, J.v.d., Maurer, S., Puri, S., Richts, A., Winter, P., Zaepke, M., 2006. WHYMAP and the groundwater resources map of the world at the scale of 1:50 000 000. Special edition for the 4th world water forum, Mexico City, March 2006. BGR Hannover/UNESCO, Paris.

Suk, H., Lee, K.K., 1999. Characterization of a groundwater hydrochemical system through multivariate analysis: clustering into groundwater zones. Groundwater v. 37, no. 3pp. 358-366.

Templ, M., Filzmoser, P., Reimann, C., 2008. Cluster analysis applied to regional geochemical

data: Problems and possibilities. Appl. Geochem. 23, 2198–2213. https://doi.org/10.1016/j.apgeochem.2008.03.004

Tolosana-Delgado, R., Otero, N., Soler, A., 2005. A compositional approach to stable isotope data analysis. Conference: CODAWORK'05

Van den Boogaart, K.G. Tolosana-Delgado, R., 2008 "Compositions": a unified R package to analyze Compositional Data, Computers & Geosciences. 34 (4), 320-338. https://doi.org/10.1016/j.cageo.2006.11.017

Vergés, J., 1999. Estudi geològic del vessant sud del Pirineu oriental i central. Evolució cinemàtica en 3D. PhD Thesis. University of Barcelona (UB), Faculty of Geology, 180 pp.

Viviroli, D., Kummu, M., Meybeck, M., Kallio, M., Wada, Y., 2020. Increasing dependence of lowland populations on mountain water resources. Nature Sustainability, 1-12. https://doi.org/10.1038/s41893-020-0559-9

Wendland, F., Blum, A., Coetsiers, M., Gorova, R., Griffioen, J., Grima, J., Hinsby, K., Kunkel, R., Marandi, A., Melo, T., Panagopoulos, A., Pauwels, H., Ruisi, M., Traversa, P., Vermooten, J.S.A., Walraevens, K., 2008. European aquifer typology: a practical framework for an overview of major groundwater composition at European scale. Environ. Geol. 55, 77–85. https://doi.org/10.1007/s00254-007-0966-5

WFD, 2000. Water Framework Directive, 2000. Directive 2000/60/CE of the European Parliament (ECOJ 22 December 2000). http://www.bygg.ntnu.no/borsanyi/eamn_web/documents/wfd-es.pdf.

Wu, X., Zheng, Y., Zhang, J., Wu, B., Wang, S., Tian, Y., Li, J., Meng, X., 2017. Investigating Hydrochemical Groundwater Processes in an Inland Agricultural Area with Limited Data: A Clustering Approach. Water 9, 723. https://doi.org/10.3390/w9090723

Yidana, S.M., 2010. Groundwater classification using multivariate statistical methods: Southern Ghana. Journal of African Earth Sciences 57(5):455-469 https://doi.org/10.1016/j.jafrearsci.2009.12.002

Yolcubal, İ., Gündüz, Ö.C.A., Kurtuluş, N., 2019. Origin of salinization and pollution sources and geochemical processes in urban coastal aquifer (Kocaeli, NW Turkey). Environmental Earth Sciences, 78(6), 181. https://doi.org/10.1007/s12665-019-8181-8

Zabala, M.E., Martínez, S., Manzano, M., Vives, L., 2016. Groundwater chemical baseline values to assess the Recovery Plan in the Matanza-Riachuelo River basin, Argentina. Sci. Total Environ. 541, 1516–1530. https://doi.org/10.1016/j.scitotenv.2015.10.006

Zwahlen, F. (ed.), 2004. Vulnerability and risk mapping for the protection of carbonate (karst) aquifers, final report COST Action 620. EUR 20912, European Commission, Brussels, 297 p.

J.Jódar, **I.Herms**, L.J. Lambán, S. Martos-Rosillo, C.Herrera-Lameli, J. Urrutia, A. Soler and E.Custodio.'Isotopic content in high mountain karst aquifers as a proxy for climate change impact in Mediterranean zones: The Port del Comte karst aquifer (SE Pyrenees, Catalonia, Spain). Science of the Total Environment Available online 29 May 2021, 148036 https://doi.org/10.1016/j.scitotenv.2021.148036

Science of The Total Environment
Volume 790, 10 October 2021, 148036

Isotopic content in high mountain karst aquifers as a proxy for climate change impact in Mediterranean zones: The Port del Comte karst aquifer (SE Pyrenees, Catalonia, Spain)

J. Jódar [a], I. Herms [b], L.J. Lambán [a], S. Martos-Rosillo [a], C. Herrera-Lameli [c], J. Urrutia [c, d], A. Soler [e], E. Custodio [f]

Show more

+ Add to Mendeley Share Cite

https://doi.org/10.1016/j.scitotenv.2021.148036

5 PAPER 3. ISOTOPIC CONTENT IN HIGH MOUNTAIN KARST AQUIFERS AS A PROXY FOR CLIMATE CHANGE IMPACT IN MEDITERRANEAN ZONES: THE PORT DEL COMTE KARST AQUIFER (SE PYRENEES, CATALONIA, SPAIN).

Authors: Jódar, J., **Herms. I**., Lambán, L.J., Martos-Rosillo, S., Herrera-Lameli, C., Urrutia, J., Soler, A., Custodio, E.

Abstract

The objective of this work is to characterize the impact of climate change in the karst aquifer of the Port del Comte Massif (PCM). Six regional climate models (RCMs) from CLYM'PY Project are used to analyse the magnitude and trends of changes on precipitation and temperature (RCP4.5 and RCP8.5 scenarios) and how these changes propagate through the hydrogeological system as groundwater resources availability and the associated water isotopic content. The study uses the RCMs climate change forcings as input data to a combination of (1) a semi-distributed hydrological model for simulating the hydrodynamical response of the aquifer, and (2) a lumped parameter model for simulating the isotopic content in groundwater at the outlet of the aquifer. A mean decrease of 2.6% and 1.9% in yearly precipitation and a mean increase of 1.9 and 3.1°C in average temperature is expected in PCM at the end of the 21st century in the RCP4.5 and RCP8.5 scenarios, respectively. This climate signal entering the hydrogeological system results in a mean decrease in recharge of 3.9% and 0.5% from rainfall and of 59.3% and 76.1% from snowmelt, and a decrease of 7.6% and 4.5% in total system discharge, but also generates an isotopic enrichment in groundwater discharge (δ18OGW) of 0.50‰ and 0.84‰, respectively. Moreover, from a long-term (2010-2100) perspective, the mean trend in δ18OGW is 0.7‰/100 yr and 1.2‰/100 yr for RCP4.5 and RCP8.5, respectively, resulting in easily measurable annual lapse rates with the current analytical methods.

Keywords: Environmental isotopes, Mountain aquifers, Climate change, Karst.

5.1 Introduction

High mountain zones are known as "water towers" because they generate the main water resources feeding the downstream depending ecosystems (Viviroli et al., 2007). When mountains constitute an aquifer, the recharged water remains longer in the basin, thus providing a strategic water resource in dry seasons, which is especially important in the drought-prone Mediterranean area (Hoerling et al., 2012; Vicente-Serrano et al., 2014), where water availability is scarce and greatly dependent on

runoff from headwater basins (De Jong et al., 2009). In this framework, it is essential to assess the impact of Climate Change (CC) on water resources availability in mountain areas (Chen et al., 2018). This will help to design the most appropriate adaptation measures to minimize adverse effects.

A plethora of climate models have been developed to investigate the extent of CC impact in the future. In their beginning, with no reference solutions available at that time, these models were generally tuned and evaluated against present day conditions. The intercomparison of models has become a mainstream method to assess the uncertainty and robustness of the different climate model predictions (Cess et al., 1989; Gates et al., 1999; Lambert and Boer, 2001; Taylor et al., 2012; Giorgetta et al., 2013; Eyring et al., 2016). A step ahead was done when climate models were used to reproduce the climate of the past, trying to simulate long complex climate scenarios based on proxy climate information (Braconnot et al., 2012; Lohmann et al., 2013; Pfeiffer and Lohmann, 2016). In this line and more recently, paleoclimate modelling studies have begun to adopt a new strategy by using fully coupled isotope-enabled global climate models (IGCM), allowing them to directly simulate paleoclimate proxies (Sjolte and Hoffmann, 2014; Holloway et al., 2016; Gierz et al., 2017; Cauquoin et al., 2019; Sjolte et al., 2020). Nevertheless, all these models require a direct validation using independent isotopic proxy data.

The stable H and O isotopes of water have become a relevant geochemical climate proxy. Their fractionation mechanisms along with their distribution throughout the hydro-climatic system make them a useful tool for reconstructing past climate situations (Dansgaard, 1964). In terms of climate model reliability, it is assumed that the better the model reproduce the paleoclimate evolution the better will perform the model for the future simulated scenarios. However, the paleoclimate reconstructions to be accounted by climate models rely on geochemical proxies to allow for the reconstruction of the climate state in the past, which is a method subject to potential errors and need calibration. For the reconstruction of past climate, a global database of speleothem carbon and oxygen isotope proxy records has been compiled recently, which include 455 records covering intervals within the last 21 ka (Atsawawaranunt et al., 2018, 2019). This information constitutes an “out-of-sample” test to evaluate the climate models against paleo-records for climate reconstruction (Schmidt et al., 2014). Additional information that is currently being used as climate proxy data is the oxygen and hydrogen isotopic content in water from the Global Networks of Isotopes in

Precipitation (GNIP) and Rivers (GNIR), which are managed by the International Atomic Energy Agency (IAEA) in cooperation with the World Meteorological Organization (WMO). To complement this, a global analysis, based on oxygen isotope content in modern cave drip water sampled in 163 drip sites, from 39 caves on five continents has been compiled recently (Baker et al., 2019). However, all this information is unevenly distributed, thus with large zones with scarce and even nil spatial coverage for precipitation isotope data, especially in mountain zones.

Carbonated karst aquifers may represent 15.2% of the land surface, of which 68.9% can be found globally in hills and mountain zones (Goldscheider et al., 2020). These aquifers have characteristics that make them quite different from other aquifers, such as high heterogeneity due to the endokarstic network (Bakalowicz, 2005), high velocities of groundwater flow in cavities, and short water residence times (Kiraly, 2003; Motyka, 1998). These hydrodynamic features allow a fast transmission of the recharge inflow signal, including the variation the environmental tracers entering the system with recharge, such as $\delta^{18}O$, to the outflow points draining aquifer. The hydrogeological system filters the high variability and dampens the seasonal variations of the input tracer signal (Jódar et al., 2014, 2016; Herms et al., 2019). This helps to identify in the output tracer signal the mean tracer content and any trend relative to the input tracer signal. Accordingly, the O and H isotopic content of groundwater discharge from karst aquifers can be used as climate proxy data for validating climate models, as those obtained by the GNIP and GNIR programs.

Lumped parameter models (LPMs) are useful to simulate the behaviour of complex mountain karst systems, even when their heterogeneity is poorly characterized (Hartmann et al., 2014). These models do not require a detailed hydrological knowledge of the physical system. Nevertheless, they allow reproducing the observed hydrodynamical response of such aquifers in terms of both, groundwater discharge and the associated tracer content for the corresponding measured input signals (Herms et al., 2019). Moreover, such models transform scenarios of CC into their hydrological results. In this sense, Custodio et al. (2018) analysed the effect on groundwater reserve and chloride and radiocarbon content of a wetter-than-present period, with enhanced recharge, on data collected from springs in arid lands. In this framework, the evolution in the isotopic content of groundwater for the different simulated scenarios may become a relevant source of isotopic data to be used by IGCMs for validating purposes, as they do currently with paleoclimate proxies such as $\delta^{18}O$ content in ice cores and speleothemes (Gierz et al., 2017; Cauquoin et al., 2019; Sjolte et al.,

2020). Surprisingly, there are no references in the scientific literature using either the O and H isotopic content in groundwater nor the expected evolution under CC scenarios as proxy data to validate IGCMs.

Understanding karst aquifer response to changing climate is critical from a water resources perspective, especially in the pan-Mediterranean zone, where water scarcity become a recurrent issue (Pedro-Monzonís et al., 2015). This work aims at characterizing the propagation of the CC impact in the Port del Comte Massif (PCM), a Mediterranean mountain karst aquifer located in the south-eastern sector of the Pyrenees, which plays a strategic role in providing water resources transferred to the metropolitan area of Barcelona. The analysis is focussed on the evolution of (1) the relevant hydrological variables controlling the mass water balance in the aquifer and their impact in the associated water resources, and (2) the isotopic content of the groundwater aquifer discharge, with the aim of identifying relevant trends to be used as CC impact proxies. Although the results of this work are specific for the PCM, the methods, proceedings and the general conclusions can be used in any other mountain karst aquifer.

5.2 Study area

The study area is located in the massif of Port del Comte (PCM), in the Eastern Pyrenees (**Figure 5. 1**). The area is thoroughly described in Herms et al. (2019, 2021). Only a summary describing the most important features is included here. The hydrological basin presents an abrupt topography. The elevation of the massif varies between 900 and 2387 m a.s.l. The PCM has an area of 130 km^2 and separates the Segre and Cardener river basins. The Segre River flows in the N part to the W and then turns to the S at the W side. The Cardener River, the main tributary to the Llobregat River, is at the E side and flows to the S.

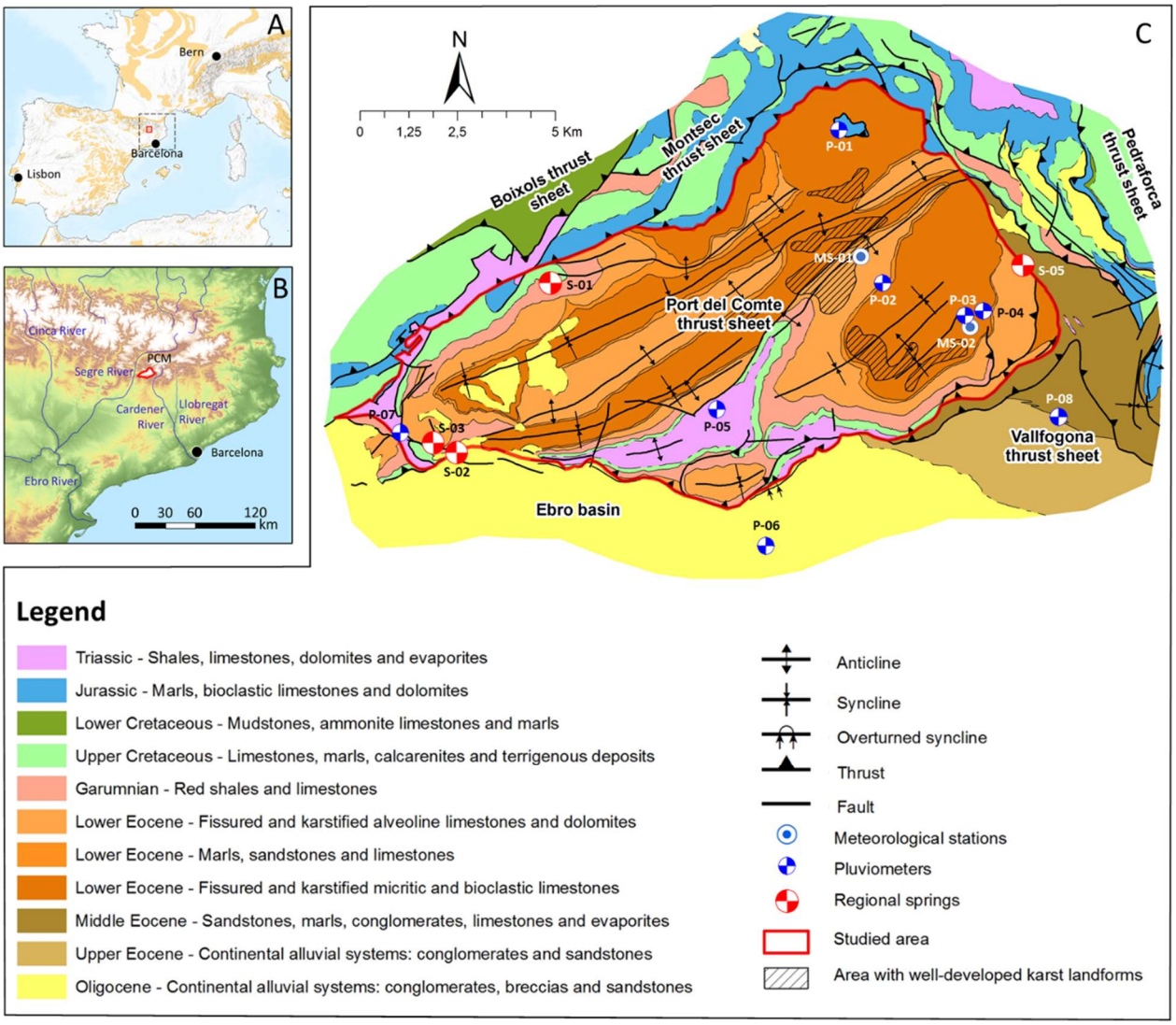

Figure 5. 1. (A) General map of southern west European continent where the brown shaded areas correspond to carbonate rock outcrops (map modified from the World Map of Carbonate Rock Outcrops v.3.0. (http://www.fos.auckland.ac.nz/our_research/karst). The shaded square shows the limits of the hydrological map shown in the inset below, while the small red square indicates the position of the Port del Comte Massif (PCM). (B) Hydrological setting of PCM (Digital elevation model from "Copernicus Land Monitoring Service", available from https://land.copernicus.eu/imagery-in-situ/eu-dem). (C) Geological map of PCM (modified from Herms et al., 2019).

From a climatic perspective, and according to the Köppen-Geiger classification, the study area presents a cold climate without a dry season and with cool summers. In the meteorological station MS-02, located at 2315 m a.s.l., precipitation (P), temperature (T) and potential evapotranspiration (PET, Hargreaves & Samani, 1982) show a seasonal variation (**Figure 5. 2**) with mean annual values

of 1047 mm/yr, 7.0 °C and 525 mm/yr for P, T and PET, respectively. The maximum of precipitation is in autumn, coinciding with the convective thunderstorms typical of the Mediterranean. Precipitation declines in winter to reach the minimum and then increases to reach a second peak in spring. In winter and spring, solid precipitation falls above 1800 m a.s.l.. The snow remains on the slopes and summits of the massif for 3 or 4 months before completely melting. In summer precipitation reaches a second marked minimum.

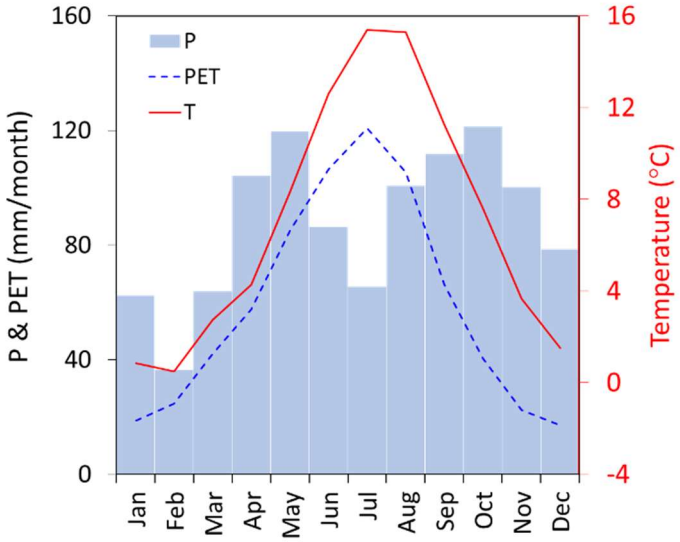

Figure 5. 2. Average seasonal variation of monthly precipitation (bars), potential evapotranspiration (dashed line) and temperature (line) measured at the meteorological station MS-02 (**Figure 5. 1**), located at 1800 m a.s.l., for the period Jan 1990–Sep 2016.

From a hydrogeological perspective, the carbonate karstified rocks of the Paleocene-Eocene formation hold the main aquifer of the PCM. The massif constitutes an independent structural and hydrogeological unit. Surface runoff is negligible, in agreement with the karstic nature of the massif. Aquifer recharge is produced by the infiltration of water from rainfall and snow melting. The aquifer discharges through a series of springs, of which only four (**Figure 5. 1**) have discharge rates greater than 1 L/s. The most important of them is Fonts del Cardener spring (S-05), which has a recharge area of 21.5 km^2, and produces a mean discharge of 7.5 hm^3/yr that tributes downstream into the Llobregat River and amounts 7% of the mean annual water use of Barcelona (Barcelona City Council, 2018).

The mean isotopic content of groundwater discharge in spring S-05 (δ_{GW}) is -9.7‰ and -63.3‰ for $\delta^{18}O$ and $\delta^{2}H$ respectively. These values coincide with the mean isotopic content of precipitation in the spring recharge zone. Moreover, the isotopic content of precipitation (δ_P) shows a seasonal variation, with heavier isotopic compositions in summer and lighter in autumn and winter (**Figure 5. 3**A), in agreement with the observed relationship between the isotopic fractionation and temperature (Clark and Fritz, 1997). δ_{GW} follows the sinusoidal variation of δ_P (**Figure 5. 3**B), thus indicating the short groundwater mean arrival time of 2.85 yr that has been estimated for this spring (Herms et al., 2019).

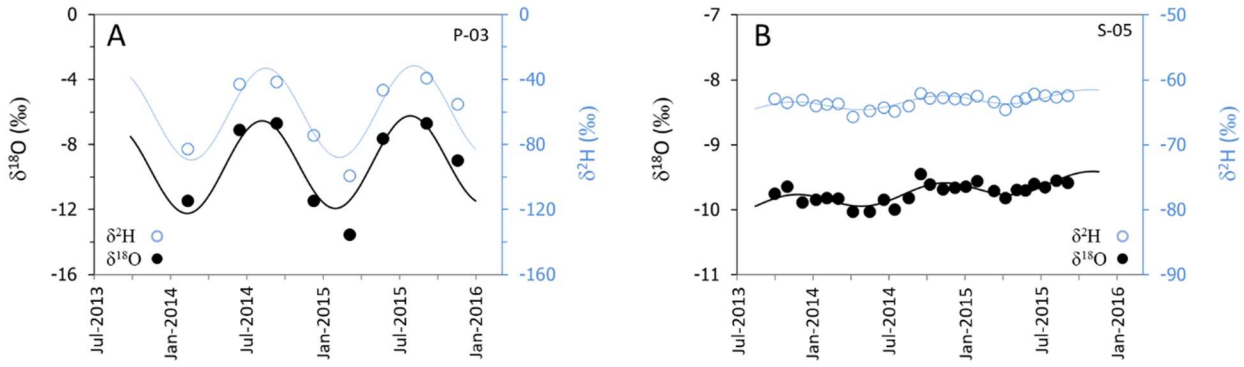

Figure 5. 3. Seasonal variation of O and H isotopic content. (A) δ_P in precipitation in pluviometer P-03. (B) δ_{GW} in spring S-05. In both cases $\delta^{18}O$ and $\delta^{2}H$ are indicated by solid and empty symbols, respectively. The sinusoidal lines in the figures correspond to the regression fit to the observed δ_P and δ_{GW} data (Jódar et al., 2016). These lines are thick and thin for $\delta^{18}O$ and $\delta^{2}H$, respectively. The identification codes P-03 and S-05 correspond to those of **Figure 5. 1**.

5.3 Methods and materials

The starting point is the combination of the hydrological and the environmental tracer transport models, known here as "hydrological model chain", to reproduce the observed hydrodynamic behaviour of both groundwater discharge and its O and H isotopic content in the PCM aquifer system (Herms et al., 2019).

Next, an ensemble of climate projections is used as input to the calibrated hydrological model to create an ensemble of future recharge values to the aquifer system. To this end, a delta change approach is used to calculate the CC signal between reference and future climate scenarios from precipitation and temperature. The CC signal is then used to modify the observed precipitation and temperature time series and therefore running the hydrological model chain. This allows evaluating the impact of CC on the groundwater system and its O and H isotopic content.

5.3.1 Hydrological model chain

Numerical lumped models of flow and transport calibrated by Herms et al. (2019) are used in this work to simulate the future hydrological behaviour of PCM.

The hydrodynamic behaviour of the aquifer is simulated in terms of spring discharge with the semi-distributed conceptual precipitation–runoff model HBV-Light (Seibert and Vis, 2012). This model is a standard tool for simulating high mountain snow-dominated hydrological systems (e.g., Konz and Seibert, 2010; Staudinger et al., 2017; Chen et al., 2018; Epting et al., 2018; Jódar et al., 2018; Herms et al., 2019). The HBV model solves a general water balance equation, requiring as input data hydroclimatic daily time series of P, T and PET, and some catchment information including (1) the vertical lapse rates of P and T, and (2) the relative weight with respect to the total catchment area of the different altitude and associated vegetation zones in the basin. For a given day, the model considers precipitation as rain or snow, depending on whether the corresponding daily temperature is above or below a threshold temperature. The snow accumulation and melting are computed according to a degree-day method by a snow routine. A two stacked linear reservoir is used to simulate the hydrological system dynamics. The upper reservoir is used to generate surface and subsurface runoff, and the lower reservoir generates groundwater runoff. As output, model HBV provides the daily basin discharge as the sum of surface and subsurface runoffs, but also provides the daily time series of aquifer recharge, which is afterwards used to simulate the hydrological system response to an environmental tracer input function that enters and migrates through the aquifer from the recharge zones to the discharge springs.

The isotopic content variation in groundwater is simulated with FlowPC (Małoszewski and Zuber, 1996, 2002). FlowPC is a lumped parameter model that requires only a few input parameters. It is useful in alpine catchment areas, where data are often scarce (Małoszewski et al., 1992; 2002; Müller et al., 2013; Lauber and Goldscheider, 2014; Jódar et al., 2016; Herms et al., 2019). The model solves numerically the convolution integral [Eq. (1)] to transform the isotopic input tracer signal $\delta_{in}(t)$ entering the hydrogeological system as recharge into the output tracer signal $\delta_{out}(t)$ leaving the system as spring discharge (**Figure 5. 4**).

$$\delta_{out}(t) = \int_{-\infty}^{t} \delta_{in}(t) g(t-\xi) d\xi \qquad (1)$$

where t is the time, ξ is the integration variable, g(τ) is a weighting function describing the transit time distribution (TTD) exit of tracer that entered the aquifer at different times in the past, and therefore implicitly includes hydraulic properties of the aquifer, and τ is the system transit time. FlowPC has already implemented four analytic g(τ) functions (Małoszewski and Zuber, 2002). In this work, the exponential piston flow (EPF) TTD is used, as did Herms et al. (2019) to reproduce the observed O and H isotopic content variation in groundwater for the PCM aquifer system. This distribution assumes that the system is composed of two parts in line, one of them with a volume V_{EM} and an exponential distribution of transit times, and the other one with a volume V_{PF} and a piston flow transit time distribution (Zuber, 1986). The parameter $\eta = (V_{EM} + V_{PF})/V_{EM}$, along with τ characterize the EPF-TTD of the system. For spring S-05, the values of η and τ are 1.02 and 2.88 yr, respectively (Herms et al., 2019).

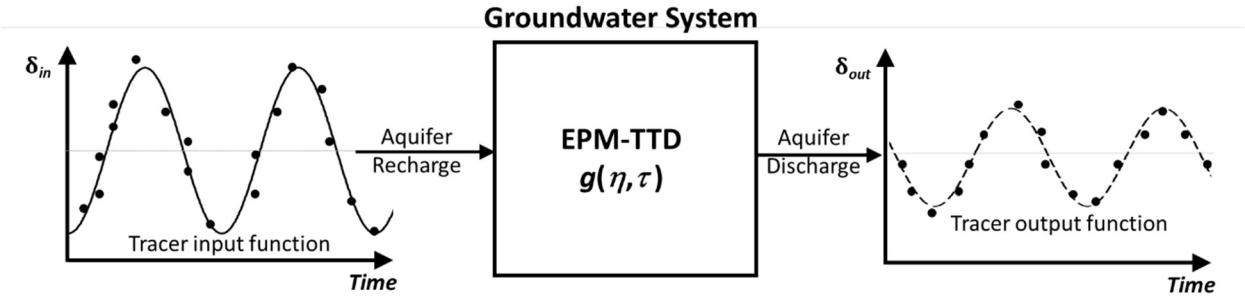

Figure 5. 4. Schematic representation of the groundwater system response to a hypothetical input tracer function (modified from Jódar et al., 2016).

The FlowPC model requires the time series of (1) monthly aquifer recharge, which is obtained by integrating monthly the daily recharge values from HBV, and (2) the monthly averaged isotopic content of recharge ($\widehat{\delta_R}$), which is assumed the same as the monthly averaged isotopic content of precipitation ($\widehat{\delta_P}$), given the karst nature of PCM. This assumption implicitly assumes that the correlation between δ_P and T (**Figure 5. 4**) also holds for δ_R and T.

The O and H isotopic signature of rainfall is linked strongly to changes in surface temperature (Dansgaard, 1964; Rozanski et al., 1992), especially in mid latitudinal to high latitudinal regions. This relationship has been used often as a paleothermometer and should be accounted if the climate community aims to better understand possible future warmer-than-present climate scenarios by examining past warm periods. Although this relationship may change in space and time (Gierz et al., 2017), it is known that the temporal slope of the δ_P-T relation has remained largely stable throughout the last 21,000 years over the middle and high latitudes of the globe. In the pan-Mediterranean zone, this temporal slope (m) is about 0.27‰/°C (Guan et al., 2016). The isotopic composition of recharge δ_R for the future scenarios is therefore estimated as

$$\delta_R(T) = m(T - \overline{T}) + T - \overline{\delta_R} \quad (2)$$

where $\overline{T}$ and $\overline{\delta_R}$ are the mean air temperature and isotopic composition recharge for the reference period. For the j-th month of the future climate projection scenario, $\widehat{\delta_{R_j}}$ is obtained by weighting the daily values of recharge isotopic composition $\delta_{R_{ij}}$ by the corresponding daily recharge rate $Q_{R_{ij}}$ as

$$\widehat{\delta_{R_j}} = \frac{\sum_{i=1}^{N} \delta_R(T_{ij}) \cdot Q_{R_{ij}}}{\sum_{i=1}^{N} Q_{R_{ij}}} \quad (3)$$

where N is the number of days of the j-th month.

5.3.2 Delta change approach

A delta change approach (Hay et al., 2000; Rätty et al 2014; Chen et al., 2018) is used to calculate the CC signal between reference and future climate. This signal has been produced specially for the Pyrenees in the framework of the CLYM'PY (Characterization of the evolution of climate and provision of information for adaptation in the Pyrenees) Project (Amblar-Francés et al., 2020), where high–resolution (5 km×5 km) climate projections for the 21st century have been generated using 24 downscaled general circulation models (GCMs) for several different emission scenarios. This work uses a subset of 6 climate models with the Representative Concentration Pathways (RCP) RCP4.5 and RCP8.5. The former corresponds to a "pathway" in which the radiative forcing stabilizes without overshooting 4.5 W/m^2 (~650 ppm CO_2- equivalent) in 2100, and the latter to the upper bound of the RCPs with a radiative forcing overpassing 8.5 W/m^2 (>1370 ppm CO_2-equivalent) in 2100. In this sense, the term "pathway" stresses that not only the long-term greenhouse gas concentration levels are of interest, but also the trajectory driven along time to reach that outcome (Moss et al., 2010; Van Vuuren et al., 2011).

According to their ability to reproduce the observed climate variability throughout Spain (CEDEX-MAPAMA, 2017), a subset of 6 climate models with the emission scenarios RCP4.5 and RCP8.5 (Table SM1, Chapter 9 Supplementary material, Part 9.3) were selected by the Spanish Minister of Agriculture, Fisheries, Food and Environment (MAPAMA) to evaluate the impact of CC on water resources in Spain. The subset includes the following climate models: bcc.csm1.1 (Wu et al., 2014), CNRM.CM5 (Voldoire et al., 2013), inmcm4 (Volodin et al., 2010), MIROC.ESM (Watanabe et al 2011), MPI.ESM.MR (Giorgetta et al., 2013) and MRI.CGCM3 (Yukimoto et al., 2012). This work adopts this subset as climate model ensemble to assess the impact of CC in the hydrogeological system of PC. In all cases, the temporal period associated to the reference period and future scenarios are 1975-2005 and 2005-2100, respectively.

To simulate the impact of CC in the behaviour of the hydrogeological system, the future model runs (RCM + HBV + FLOWPC) are used to capture the change signal, but not from the raw variables directly (P and T time series from RCMs). For the future period, a delta change approach is used. To this end, synthetic time series of precipitation (P_{sync}) and temperature (T_{sync}) are built based upon their corresponding observed time series (1981-2015), concatenating them in a row, as many times

as required, to equal the time interval length comprised in the future simulation scenarios (2005-2100). In this way, the observed seasonal and finer time variability of P and T, which are not captured by the RCMs (Figure SM1 in Suppl. Mat.), are preserved along with their corresponding frequency-magnitude relationships.

For every RCM, the simulations are used to calculate a multiplicative and an additive correction coefficient (delta change factor), for daily precipitation (P) and temperature (T), respectively, by comparing control and scenario climate model runs, as follows:

$$\alpha(t_i) = \frac{\widetilde{\mathrm{P}}(t_i)}{\mathrm{P_{ref}}} \quad (4)$$

$$\beta(t_i) = \widetilde{\mathrm{T}}(t_i) - \mathrm{T_{ref}} \quad (5)$$

where the tilde (~) over the variable stands for the 30 years backward daily mean of the variable for a given day (t_i), and the subscript "ref" stands for the variable averaged value for the last 30 years of the reference period (1975-2005). Once the delta change factors time series are obtained, they are applied to $\mathrm{P_{sync}}$ and $\mathrm{T_{sync}}$ (Eqs. 6 and 7, respectively; see Figure SM2, Chapter 9 Supplementary material, Part 9.3), thus including the CC signal in the input time series of the hydrological model chain.

$$\mathrm{P}(t_i) = \alpha(t_i) \cdot \mathrm{P_{sync}}(t_i) \quad (6)$$

$$\mathrm{T}(t_i) = \beta(t_i) + \mathrm{T_{sync}}(t_i) \quad (7)$$

5.3.3 Trend analysis of time series

Temporal trends in the isotopic composition are identified using the Mann–Kendall test (MKT). This is a robust test for trend detection, used widely in climatological, hydrological and environmental time series analysis. The test does not assume the data to be distributed according to any rule (e.g., it does not require data to be normally distributed). It is not affected by missing data in the time series other than the fact the number of sample points are reduced and hence might adversely affect the statistical significance. MKT is neither affected by irregular spacing of the time points of measurement nor by the length of the time series.

The MKT statistic S (Mann, 1945; Kendall, 1975) is obtained as

$$S = \sum_{i=1}^{N-1} \sum_{j=i+1}^{N} \operatorname{sgn}(x_i - x_j) \tag{8}$$

where N is the number of data points in the time series, x_i is the i-th data value in the time series, and sgn(x_i-x_j) is the indicator sign function defined by

$$\operatorname{sgn}(x_i - x_j) = \begin{cases} 1 & ; \ x_i - x_j > 0 \\ 0 & ; \ x_i - x_j = 0 \\ -1 & ; \ x_i - x_j < 0 \end{cases} \tag{9}$$

The variance associated with S is calculated as

$$\sigma_S^2 = \frac{1}{18}\left(N(N-1)(2N+5) - \sum_{k=1}^{h} n_k(n_k-1)\,(2n_k+5) \right) \tag{10}$$

where h is the total number of tied groups in the data, n_k is the number of ties of extent k. A tied group is a set of sample data having the same value.

For large sample sizes (N >10), S is approximated by the normal distributed statistic Z_S (Eq. 11), which is used by most statistical software. In this work, the trend analysis has been conducted using both the computer Program of Trend Test from the USGS (Helsel and Frans, 2006; Helsel et al., 2006), and the Real Statistics Resource Pack software (Zaiontz, 2020).

$$Z_S = \begin{cases} (S-1)/\sigma_S & ; \ S > 0 \\ 0 & ; \ S = 0 \\ (S+1)/\sigma_S & ; \ S < 0 \end{cases} \tag{11}$$

Positive and negative values of Z_S indicate increasing and decreasing trends, respectively. The trends are tested at a given significance level α. If $|Z_S| > |Z_{1-\alpha/2}|$, then the null hypothesis (i.e.,

there is no trend) is rejected and a significant trend is assumed in the time series. $Z_{1-\alpha/2}$ is the corresponding value of P = $\alpha/2$ for a standard normal distribution. In this work the significance level of 0.05 is considered. Therefore $Z_{1-\alpha/2}$ = 1.96. The slope of trend β in the time series is evaluated by the non-parametric procedure proposed by Sen (1968). It is calculated by

$$\beta = median\left(\frac{x_j - x_i}{j - i}\right) ;\ j > i \tag{12}$$

The confidence interval for the Sen's slope (β_L, β_U) can be computed as (Hollander and Wolfe, 1973; Gilbert, 1987)

$$\beta_L = \frac{1}{2}(N - C_\alpha) \tag{13}$$

$$\beta_U = \frac{1}{2}(N + C_\alpha) \tag{14}$$

$$C_\alpha = \sigma_S \cdot Z_{1-\alpha/2} \tag{15}$$

The MKT is indeed a robust test for trend detection. Nevertheless, it is not well suited for data with periodicities (i.e., seasonal effects) because the functional dependence of *S* (Eq. 8). To ensure the effectiveness of MKT for detecting trends, the seasonal effects are eliminated in this work by considering annual time series instead of monthly ones. To this end, the monthly time series of precipitation and aquifer recharge are annually integrated, whereas the monthly time series of temperature and isotopic content in water are annually averaged.

5.4 Results and discussion

5.4.1 Effect of climate projections on hydrology

The signal of CC enters the hydrological systems through variations in the terms conditioning the mass water balance in the system. **Figure 5. 5** shows the percentage of change associated to precipitation (P), temperature (T), actual evapotranspiration (AET), total runoff (Q_{tot}), rainfall recharge (Q_{rain}), snowmelt recharge (Q_{snow}) and total recharge (Q_{rec}), averaged for the 2011-2040,

2041-2070 and 2071-2100 intervals for the average ensemble of climate models. The interval length has been selected to ensure that the estimated values for the interval are not conditioned by the short-term patterns of temporal variability which often contain the climatic variables.

Precipitation seems to follow a slight downward trend for the different average intervals considered (**Figure 5. 5**), presenting maximum annual decreases of 29 and 30 mm for the RCP4.5 and RCP8.5 scenarios, respectively (Table SM2, Chapter 9 Supplementary material, Part 9.3). As can be shown, the variability in rainfall for the model ensemble is always greater in the case of the emission scenario RCP8.5. The precipitation signal, including the trend, propagates throughout the hydrological system. It is reflected almost homothetically in the obtained variations of Q_{rain}, Q_{rec} and Q_{tot}. Despite the variations shown for the selected multidecadal intervals, none of these variables present a statistically significant trend for the whole estimation period 2010-2100 (**Table 5. 1**).

Temperature shows a monotonous increasing trend for the three selected intervals, being the variation greater in every case for the RCP8.5 emission scenario. For the last interval (2071-2100), the average temperature with respect the reference period (1986-2015) is 1.9 and 3.1 °C for the scenarios RCP4.5 and RCP8.5, respectively. The temperature evolution signal propagates in a natural way to both AET and Q_{snw}, as it is well-known that both variables show a large dependence on T. Furthermore, for the whole period 2010-2100, the estimated trends for T, AET and Q_{snw} are statistically significant, increasing for T and AET and decreasing for Q_{snw}, as expectable for a warmer climate scenario. Such decreasing trends in Q_{snw} have been already observed in the Western Pyrenees and other mountain zones (López-Moreno et al., 2009; 2020; Matiu et al., 2021), and are expected to be more marked in the future, especially at low elevations, with more uncertain trends in observations and in future projections at higher elevations (Gobiet et al., 2014; Beniston et al., 2018; Hock et al., 2019; IPCC, 2019).

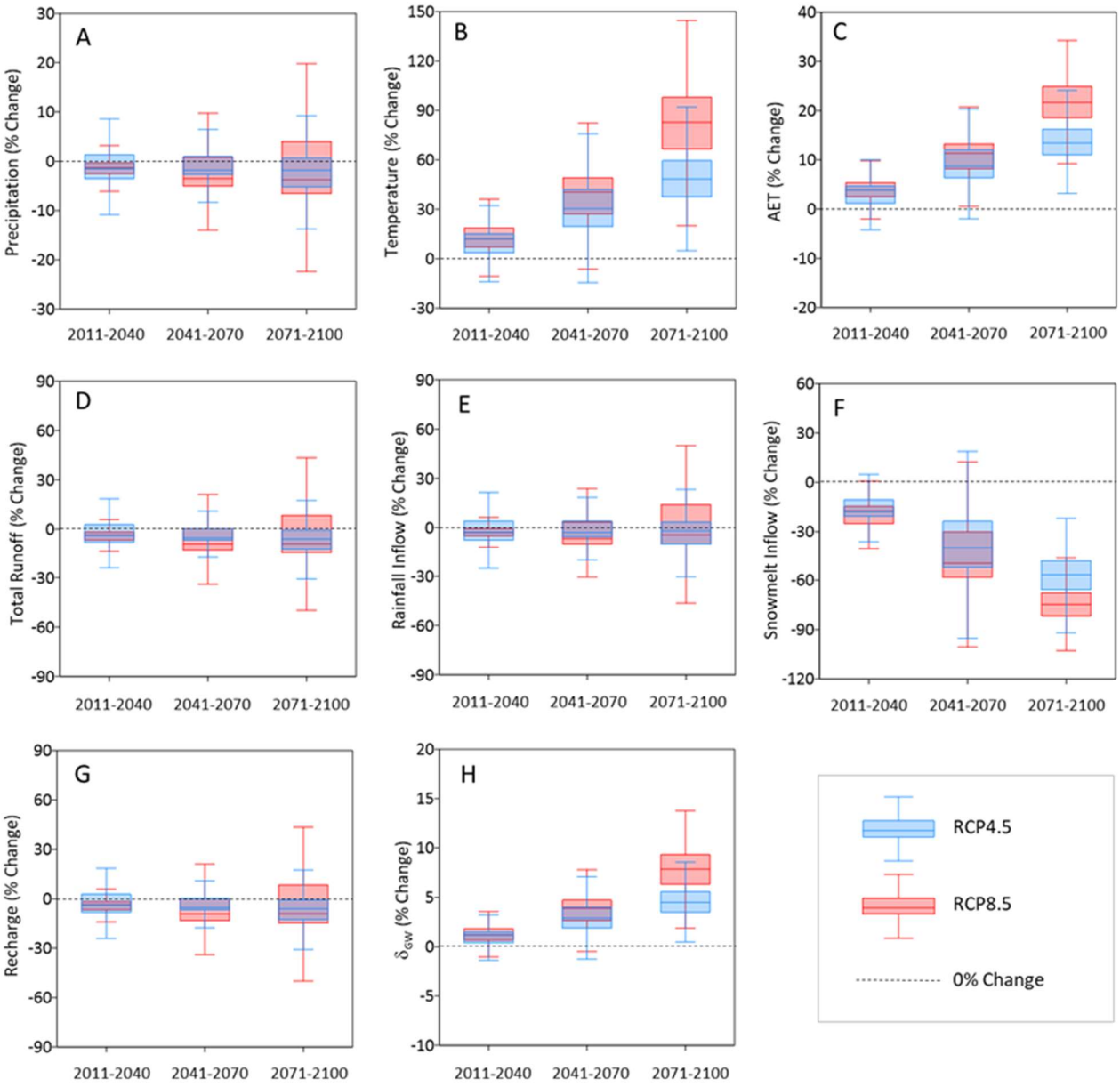

Figure 5. 5. Percentage of change of the hydrometeorological variables for the averaging periods 2011-2040, 2041-2070 and 2071-2100, obtained by the different climate models for the emission scenarios RCP4.5 and RCP8.5, with respect the corresponding averaged value of the variable obtained for the reference period (1998-2005). The dashed line indicates the null change position.

Table 5. 1 Estimated Sen's slopes for the hydrometeorological variables for the period 2010-2100, considering the different climate models and the two emission scenarios. The blue shaded values indicate statistically significant trends for the whole period.

RCP	GCM	β_P $\left(\frac{mm}{100\ yr}\right)$	β_T $\left(\frac{°C}{100\ yr}\right)$	β_{AET} $\left(\frac{mm}{100\ yr}\right)$	β_R $\left(\frac{mm}{100\ yr}\right)$	$\beta_{Q_{rain}}$ $\left(\frac{mm}{100\ yr}\right)$	$\beta_{Q_{snw}}$ $\left(\frac{mm}{100\ yr}\right)$	$\beta_{Q_{tot}}$ $\left(\frac{mm}{100\ yr}\right)$	$\beta_{\delta^{18}O_P}$ $\left(\frac{‰}{100\ yr}\right)$	$\beta_{\delta^{18}O_{GW}}$ $\left(\frac{‰}{100\ yr}\right)$
4.5	bcc.csm1.1	30.8	2.0	66.9	-2.8	15.4	-10.3	4.0	0.6	0.6
4.5	CNRM.CM5	51.7	1.8	61.3	10.0	31.2	-9.1	17.7	0.5	0.5
4.5	inmcm4	-1.3	1.6	57.3	-27.1	-5.2	-9.0	-19.2	0.5	0.4
4.5	MIROC.ESM	-48.7	4.0	122.3	-54.4	-22.1	-14.5	-46.7	1.1	1.2
4.5	MPI.ESM.MR	-3.2	2.3	76.2	-25.0	2.4	-12.1	-19.0	0.6	0.7
4.5	MRI.CGCM3	-11.6	1.9	68.4	-37.6	-9.7	-11.6	-30.8	0.5	0.5
4.5	*Average*	-9.4	2.3	74.3	-28.9	-3.5	-11.3	-20.8	0.6	0.7
8.5	bcc.csm1.1	-12.9	4.2	128.9	-21.3	5.6	-15.5	-13.9	1.2	1.1
8.5	CNRM.CM5	87.4	3.6	120.7	47.1	76.1	-15.2	54.1	1.0	1.0
8.5	inmcm4	-1.0	3.1	102.4	-28.6	-1.9	-15.1	-24.3	0.9	0.8
8.5	MIROC.ESM	-48.4	7.0	197.2	-46.3	-16.1	-18.0	-43.6	1.9	1.9
8.5	MPI.ESM.MR	-46.1	4.8	145.9	-48.3	-12.8	-17.9	-37.8	1.3	1.3
8.5	MRI.CGCM3	156.0	3.6	126.1	94.0	116.5	-16.2	100.5	1.0	1.0
8.5	*Average*	15.5	4.4	136.6	-2.8	26.6	-16.6	5.0	1.2	1.2

Previous works focusing on CC impacts in mountain zones indicate a generalized water resources decrease (Beniston and Stoffel, 2014; Beniston et al., 2018). This trend has already been observed in the Pyrenees (López-Moreno 2008b), highlighting the importance of this mountain range as an early warning system to mitigate the impact of CC, among other impacts, by implementing adaptation strategies before the impact arrival in the central and northern European zones. In the case of PCM, climate models predict a slight decrease in the total discharge flow Q_{tot}, with a not statistically significant long-term trend.

The evolution of Q_{tot} is highly controlled by the evolution of P. However, T also plays an important role in this regard, modifying not so much the magnitude of Q_{tot} but the associated seasonality, especially in basins where the dynamics of snow accumulation and melting processes are relevant. Snow melting is a process that maximizes the diffuse recharge of the aquifer, being able to play an

important role in the total aquifer recharge if the snow accumulation during the cold season is important, as occurs in the central zone of the Pyrenees (Jódar et al., 2020). Moreover, the snow accumulation and melting diffuse recharge may even condition the speleogenesis and development of karst (González-Ramón et al., 2020). In the study area, the aquifer recharge from snow melt represents only 7% of total recharge. Despite of that, it is enough to leave a clear fingerprint in terms of Q_{tot} response, as revealed when the hydrograph of the reference period is compared with that of the last considered period 2071-2100 (**Figure 5. 6**). The latter presents a discharge increase in the winter months (Nov-Feb). This discharge increment is generated by a decrease of snowfall and an increase of rainfall, driven by the warmer climate conditions obtained for the climate models for this period. Consequently, Q_{tot} presents a decrease in the thaw season (Mar-May), as in winter there is less accumulation of snow and therefore a lower snowmelt flow contributing to the total basin discharge in the spring season. In addition, the snow accumulation decrease will reduce the aquifer recharge, thus favoring an earlier low flow season. This effect has been already observed in some high mountain basins (López-Moreno et al., 2004, 2008a,b; Birsan et al., 2005; Bard et al., 2015; Mallucci et al., 2019).

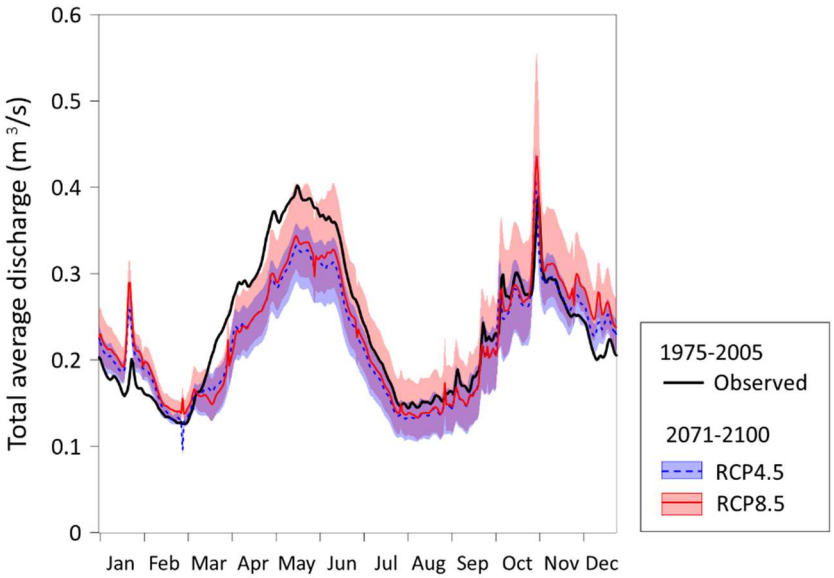

Figure 5. 6. Seasonal variation of the monthly averaged discharge for both the historical (1986-2015) and future (2071-2100) periods considering the climate projections RCP4.5 and RCP8.5. Black thick line shows Q_{tot} for the reference period. Red line and shaded area indicate mean Q_{tot} and the corresponding variation interval for RCP8.5, whereas blue dashed line and shaded area indicate the mean Q_{tot} and the associated variation interval for RCP4.5.

There is a net decrease in the mean annual spring discharge for the third period 2071-2100, of 0.6 and 0.4 hm^3/yr for the emission scenarios RCP4.5 and RCP8.5, respectively. These values may look not a huge decrease, but such variations may be critical downstream for the depending ecosystems (Goldscheider, 2019). These ecosystems are tacking with a structural water scarcity derived from the increased frequency and severity of the current Mediterranean droughts (Hoerling et al., 2012; Vicente-Serrano et al., 2014), and their expected increasing trend in the framework of CC (Cramer et al., 2018).

5.4.2 Effect of climate projections on the isotopic content of groundwater

Meteoric water recharging the aquifer introduces in the system not only the input signal in terms of inflows, but also enters the signal associated to the isotopic content of recharge water. This signal propagates downgradient from aquifer recharge to discharge areas, where regional springs drain the system. In the case of a trending input tracer signal, the trend will be transferred to the output tracer signal unless the tracer was not conservative (Jódar et al., 2014). Additionally, the aquifer filters the high-frequency variability of the input tracer signal, even damping the amplitude of the seasonal variation of δ_P (Figs. 3 and 4) (Herms et al 2019; Jodar et al., 2016, 2020). Such filtering makes it easier identifying trends in the δ_{GW} outflow signal because the "noise" associated to the high frequency variability of δ_P in the inflow signal hinders the trend detection (Figure SM3, Chapter 9 Supplementary material, Part 9.3). In this line, the PCM is an ideal system to evaluate how the signal of the impact of CC is propagated through a karst aquifer. The groundwater mean arrival time of 2.83 yr is long enough to eliminate the high-frequency variability signal of δ_P, but short enough to identify the most significant recharge events at the spring discharge from both the hydrodynamic and the isotopic perspective (Herms et al., 2019).

The evolution of δ_{GW} in spring S-05 shows a trend like that of T, becoming isotopically heavier in an increasing monotonic way for the three intervals considered (Figure 5). These variations are larger for scenario RCP8.5, regardless of the selected time interval. For the last analyzed period of the 21st century, the average annual increase in δ_{GW} for scenarios RCP4.5 and RCP8.5 is 0.50‰

and 0.84‰, respectively. From a long-term perspective (i.e., 2010-2100; **Figure 5. 7**), δ_{GW} shows statistically significant trends of 0.7‰/100 yr and 1.2‰/100 yr RCP4.5 and RCP8.5, respectively (Table 1).

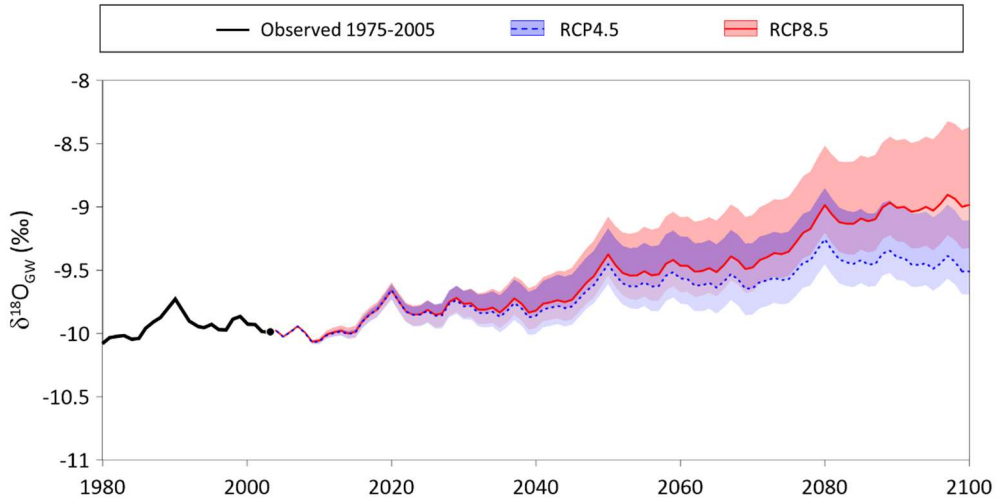

Figure 5. 7. Evolution of the isotopic ($\delta^{18}O$) content in groundwater discharge for spring S-05 considering the climate projections RCP4.5 and RCP8.5. Black thick line shows δ_{GW} for the reference period. The point marks the beginning of the RCP scenarios. The red line and shaded area indicate mean δ_{GW} and corresponding variation interval for scenario RCP8.5, whereas blue dashed line and shaded area indicate mean δ_{GW} and associated variation interval for scenario RCP4.5 (the violet colored strip is just the overlapping of red and blue)

Isotopic information from groundwater ultimately occurs from precipitation, but reflects the interplay between physical aspects of climate, meteorology and geo-hydrology at different spatial-temporal scales. Despite of that, the isotopic content of groundwater reveals as a useful source of information. The hydrogeological systems provide a response in terms of δ_{GW} that reflect faithfully not only the mean value of δ_P but also the associated trends. This behaviour makes the hydrogeological systems especially well-suited to be used as proxy data providers of δ_P for fully IGCM, which is a current promising research line (Yoshimura, 2015).

IGCMs provide the isotopic signal distribution of a particular time period along with the corresponding evolution of climate variables, which is particularly useful in paleoclimate and

paleo-altimetry studies (Rowley and Garzione, 2007; Bershaw et al., 2012; Gierz et al., 2017; Cauquoin et al., 2019). Besides, these models unravel the complex relationships between geochemical climate proxies (e.g., ice core $\delta^{18}O$, tree cellulose $\delta^{18}O$, and coral $\delta^{18}O$) and climate simulations (Okazaki and Yoshimura, 2019). To illustrate this, it could be considered to simulate the temperature evolution during interglacial $\delta^{18}O$-climate reconstructions while minimizing possible misinterpretations of isotope records used in such paleo-climatological studies. This is a focal topic given the growing concerns about future global CC. Nevertheless, there is still enough room for improving IGCMs (Gierz et al., 2017). In this regard, there is limited O and H water isotopic data regarding (1) the hydrological processes moving the water vapor in and out of clouds - this is being improved by applying laser spectroscopic isotopic measurement techniques (Wassenaar et al., 2018; Denisova et al., 2020) - and (2) terrestrial hydrological cycles at different scales, including the partitioning of total water transport as surface water, in transit recharge through the vadose zone and groundwater (Yoshimura, 2015). This point may be addressed by adding isotopic content data of both surface water and groundwater, which is crucial information to evaluate averages of precipitation O and H isotope contents at the corresponding aquifer recharge areas, especially in zones with nil spatial coverage of precipitation isotope data. As a result, more certain local and global budget of O and H isotopes could be obtained, especially for groundwater (Henderson-Sellers et al., 2004; Custodio and Jódar, 2016; Baker et al., 2019; Herms et al., 2019) to help validating IGCMs. In this line, the results obtained in this work will be useful to provide plausible scenarios to compare with, while making the IGCMs CC simulations more reliable. This is of paramount importance to develop CC adaptation strategies scaled to the expected impact in the hydrogeological systems.

Karst aquifers have been shown to be very vulnerable, especially to pollution, due to their high hydraulic conductivity and limited self-depuration capacity (Parise et al., 2015). Moreover, when the karst aquifers are unconfined, focused recharge through the most conductive karst features facilitates the widespread rapid incorporation and transport of pollutants to the groundwater (Hartmann et al., 2021). In this framework, and from the perspective of climate change impact, their vulnerability is even higher. In high mountain karst aquifers, the snow cover provides additional water storage for the hydrological system while protecting the aquifer from external pollutants. Besides, in the warm season, the generated snowmelt drives aquifer recharge as a spatially diffuse process driven by the snowmelt infiltration (Meeks and Hunkeler, 2015; Jódar et

al., 2020). The snowmelt flows diffusely through the snowpack while maintaining moderate drainage rates. This maximizes infiltration through the uppermost soil/epikarst layer along the slopes of the mountain (Custodio and Jódar, 2016). The warming trends obtained in this work impact directly in the snowpack cover formation and the corresponding snowmelt infiltration (Fig 5 and Table 1). As a result, the vulnerability of the karst system will be even increased, given that these mountain karst aquifers will be directly exposed longer to eventual contaminant surface spills. As shown, this stresses the interplay between vulnerability to pollutants and impact of climate change, given that they are not independent in high mountain aquifer karst systems.

5.5 Conclusions

Karst aquifers are particularly vulnerable to the impact of CC because they typically show short transit times that allow a fast propagation of the CC generated hydro- climatical signal through the hydrogeological system. This is the case of the PCM, in which the climate input signal variations propagate quickly through the hydrological system, as reflected in the hydrological variables that control the hydrodynamic functioning of the aquifer and impact the ecosystems dependent on groundwater discharge in a short time.

The estimated evolution of P and T for the last 30 years period of the 21st century shows a net decrease in P and an increase in T. These variations, which regardless of the climate model are bolded in the scenario RCP8.5, are primarily reflected in a decrease of snowfall and snow accumulation, which in turn have immediate consequences on the hydrological system, such as reducing both springtime high flows and aquifer recharge, and advancing the low flows period.

The temporal variability associated to the hydrological variables may hinder the fast detection of CC impact in hydrological systems. Nevertheless, the trend on the isotopic composition of groundwater may be used as a proxy of such impact. In the PCM, the isotopic composition of groundwater shows a clear enrichment trend, with mean rates of 0.7‰/100 yr and 1.2‰/100 yr for scenarios RCP4.5 and RCP8.5, respectively. These values are high enough to produce in the short-mean term an isotopic enrichment in groundwater that are easily detected by available analytical

methods. The methodology applied to obtain these values may be applied in other hydrogeological systems to provide valuable information for helping the validation of fully coupled isotope-enabled global climate models. Besides, measuring the evolution of the isotopic composition of groundwater in a regular scheme may serve as prognosis of the CC impact on the sampled aquifer if any isotopic enrichment trend is detected in the mean isotopic composition of the spring discharge.

5.6 Acknowledgments

This research was supported by the projects: PIRAGUA (EFA210/16/ PIRAGUA) funded by the European Union through the Interreg-POCTEFA territorial cooperation program; PACE-ISOTEC (CGL2017-87216-C4-1-R) funded by Agencia Estatal de Investigación (AEI) from the Spanish Government and the European Regional Development Fund (FEDER) from EU; and MAG (Mineralogia Aplicada, Geoquimica i Geomicrobiologia, 2017SGR-1733) of the Universitat de Barcelona (UB) funded by the Catalan Goverment (Generalitat de Catalunya). The Spanish Meteorological Agency (AEMET) and the Meteorological Service of Catalonia (SMC) have provided meteorological data. We would also like to thank the anonymous reviewers for their constructive comments and suggestions which led to a substantial improvement of the paper.

5.7 References

Amblar-Francés, M.P., Ramos-Calzado, P., Sanchis-Lladó, J., Hernanz-Lázaro, A., Peral-García, M. C., Navascués, B., Domínguez-Alonso, M., Pastor-Saavedra, M.A., and Rodríguez-Camino, E. (2020). High resolution climate change projections for the Pyrenees region. Advances in Science and Research, 17, 191-208. https://doi.org/10.5194/asr-17-191-2020

Atsawawaranunt, K., Comas-Bru, L., Amirnezhad Mozhdehi, S., Deininger, M., Harrison, S. P., Baker, A., Boyd, M., Kaushal, N., Ahmad, S. M., Ait Brahim, Y., Arienzo, M., Bajo, P., Braun, K., Burstyn, Y., Chawchai, S., Duan, W., Hatvani, I. G., Hu, J., Kern, Z., Labuhn, I., Lachniet, M., Lechleitner, F. A., Lorrey, A., Pérez-Mejías, C., Pickering, R., Scroxton, N.,

and SISAL Working Group Members (2018). The SISAL database: a global resource to document oxygen and carbon isotope records from speleothems, Earth Syst. Sci. Data, 10, 1687–1713, https://doi.org/10.5194/essd-10-1687-2018

Atsawawaranunt, K., Harrison, S. and Comas-Bru, L. (2019). SISAL (Speleothem Isotopes Synthesis and AnaLysis Working Group) database version 1b. University of Reading. Dataset. http://dx.doi.org/10.17864/1947.189

Bakalowicz, M. (2005). Karst groundwater: a challenge for new resources. Hydrogeology Journal 13, 148-160. https://doi.org/10.1007/s10040-004-0402-9

Baker, A., Hartmann, A., Duan, W., Hankin, S., Comas-Bru, L., Cuthbert, M. O., Treble, P.C., Banner, J., Genty, D., Baldini. L.M., Bartolomé, M., Moreno, A., Pérez-Mejías, C., and Werner, M. (2019). Global analysis reveals climatic controls on the oxygen isotope composition of cave drip water. Nature Communications, 10(1), 1-7. https://doi.org/10.1038/s41467-019-11027-w

Barcelona City Council, 2018. Evolution of Water Consumption in the City of Barcelona. https://www.bcn.cat/estadistica/angles/dades/economia/consum/evoconsum/coev04.htm . Accessed date: 20 March 2021.

Bard, A., Renard, B., Lang, M., Giuntoli, I., Korck, J., Koboltschnig, G., Janža, M., d- Amico, M., and Volken, D. (2015). Trends in the hydrologic regime of alpine rivers. J. Hydrol. 529, 1823–1837. http://dx.doi.org/10.1016/j.jhydrol.2015.07.052

Beniston, M. and Stoffel, M. (2014). Assessing the impacts of climatic change on mountain water resources, Sci. Total Environ., 493, 1129–1137, https://doi.org/10.1016/j.scitotenv.2013.11.122

Beniston, M., Farinotti, D., Stoffel, M., Andreassen, L.M., Coppola, E., Eckert, N., Fantini, A., Giacona, F., Hauck, C., Huss, M., Huwald, H., Lehning, M., López-Moreno, J.I., Magnusson, J., Marty, C., Morán-Tejéda, E., Morin, S., Naaim, M., Provenzale, A., Rabatel, A., Six, D., Stötter, J., Strasser, U., Terzago, S., and Vincent, C. (2018). The European mountain cryosphere: a review of its current state, trends, and future challenges, The Cryosphere, 12, 759–794, https://doi.org/10.5194/tc-12-759-2018

Bershaw, J., Penny, S.M., and Garzione, C.N. (2012). Stable isotopes of modern water across the Himalaya and eastern Tibetan Plateau: Implications for estimates of paleoelevation and paleoclimate. Journal of Geophysical Research: Atmospheres, 117(D2). https://doi.org/10.1029/2011JD016132

Birsan, M.V., Molnar, P., Burlando, P., and Pfaundler, M. (2005). Streamflow trends in Switzerland. J. Hydrol. 314 (1), 312–329. http://dx.doi.org/10.1016/j.jhydrol.2005.06.008.

Braconnot, P., Harrison, S.P., Kageyama, M., Bartlein, P.J., Masson-Delmotte, V., Abe-Ouchi, A., Otto-Bliesner, B.L., and Zhao, Y. (2012), Evaluation of climate models using palaeoclimatic data, Nat. Clim. Change, 2(6), 417–424, doi:10.1038/nclimate1456.

Cauquoin, A., Werner, M., and Lohmann, G. (2019). Water isotopes–climate relationships for the mid-Holocene and preindustrial period simulated with an isotope-enabled version of MPI-ESM. Climate of the Past, 15(6), 1913-1937. https://doi.org/10.5194/cp-2019-72.

CEDEX-MAPAMA (2017). Evaluación del impacto del cambio climático en los recursos hídricos y sequías en España. Informe Final. Clave CEDEX: 42-415-0-001. Madrid (https://www.miteco.gob.es/es/cambio-climatico/temas/impactos-vulnerabilidad-y-adaptacion/plan-nacional-adaptacion-cambio-climatico/rec_hidricos.aspx).

Cess, R. D., Potter, G.L., Blanchet, J.P., Boer, G.J., Ghan, S.J., Kiehl, J.T., Le Treut, H., Li, Z.X., Liang, X.Z., Mitchell J.F.B., Morcrette, J.J., Randall, D.A., Riches, M.R., Roeckner, E., Schlese, U., Slingo, A., Taylor, K.E., Washington, W.M., Wetherald, R.T., and Yagai, I. (1989). Interpretation of cloud-climate feedback as produced by atmospheric general circulation models, Science, 245, 513–516. https://doi.org/10.1126/science.245.4917.513.

Chen, Z., Hartmann, A., Wagener, T., and Goldscheider, N. (2018). Dynamics of water fluxes and storages in an Alpine karst catchment under current and potential future climate conditions. Hydrology and Earth System Sciences, 22(7), 3807-3823. https://doi.org/10.5194/hess-22-3807-2018.

Clark, I.D., Fritz, P., 1997. Environmental Isotopes in Hydrogeology. Lewis Publishers, New York.

Cramer, W., Guiot, J., Fader, M., Garrabou, J., Gattuso, J.P., Iglesias, A., Lange, M.A., Lionello, P., Llasat, M.C., Paz, S., Peñuelas, J., Snoussi, M., Toreti, A., Tsimplis, M.N., and Xoplaki, E. (2018). Climate change and interconnected risks to sustainable development in the Mediterranean. Nature Climate Change, 8(11), 972-980. https://doi.org/10.1038/s41558-018-0299-2 .

Custodio, E. and Jódar, J., (2016). Simple solutions for steady-state diffuse recharge evaluation in sloping homogeneous unconfined aquifers by means of atmospheric tracers. Journal of Hydrology. https://doi.org/10.1016/j.jhydrol.2016.06.035 .

Custodio, E., Jódar, J., Herrera, C., Custodio-Ayala, J., Medina, A. (2018). Changes in groundwater reserves and radiocarbon and chloride content due to a wet period intercalated in an arid

climate sequence in a large unconfined aquifer. Journal of Hydrology: 556: 427-437. https://doi.org/10.1016/j.jhydrol.2017.11.035 .

Dansgaard, W. (1964). Stable isotopes in precipitation, Tellus, 16(4), 436–468, https://doi.org/10.1111/j.2153-3490.1964.tb00181.x .

De Jong, C., Lawler, D., and Essery, R. (2009).Mountain hydroclimatology and snow seasonality and hydrological change in mountain environments. Hydrol. Process. 23, 955–961. https://doi.org/10.1002/hyp.7193 .

Denisova, N.Y., Gribanov, K.G. and Werner, M. (2020). Validation of ECHAM AGCMs Using Laser Spectrometer Data from Two Arctic Stations. Atmos Ocean Opt 33, 702–707 (2020). https://doi.org/10.1134/S1024856020060093 .

Epting, J.M., Page, R., Auckenthaler, A., Huggenberger, P. (2018). Process-based monitoring and modeling of Karst springs – linking intrinsic to specific vulnerability. Sci. Total Environ. 625, 403–415. https://doi.org/10.1016/j.scitotenv.2017.12.272 .

Eyring, V., Bony, S., Meehl, G. A., Senior, C. A., Stevens, B., Stouffer, R. J., & Taylor, K. E. (2016). Overview of the Coupled Model Intercomparison Project Phase 6 (CMIP6) experimental design and organization. Geoscientific Model Development, 9(5), 1937-1958. https://doi.org/10.5194/gmd-9-1937-2016 .

Gates, W.L., Boyle, J.S., Covey, C., Dease, C.G., Doutriaux, C.M., Drach, R.S., Fiorino, M., Gleckler, P.J., Hnilo, J.J., Marlais, S.M., Phillips, T.J., Potter, G.L., Santer, B.D., Sperber, K.R., Taylor, K.E., and Williams, D.N. (1999). An overview of the results of the Atmospheric Model Intercomparison Project (AMIP I). Bulletin of the American Meteorological Society, 80(1), 29-56. https://doi.org/10.1175/1520-0477(1999)080<0029:AOOTRO>2.0.CO;2.

Gierz, P., Werner, M., and Lohmann, G. (2017). Simulating climate and stable water isotopes during the Last Interglacial using a coupled climate-isotope model. Journal of Advances in Modeling Earth Systems, 9(5), 2027-2045. https://doi.org/10.1002/2017MS001056 .

Gilbert, R.O. (1987). Statistical Methods for Environmental Pollution Monitoring. John Wiley & Sons, New York.

Giorgetta,M.A., Jungclaus,J., Reick,C.H., Legutke,S., Bader,J., Böttinger,M., Brovkin,V., Crueger,T., Esch,M., Fieg,K., Glushak,K., Gayler,V., Haak,H., Hollweg,H.D., Ilyina,T., Kinne,S, Kornblueh,L., Matei,D., Mauritsen,T., Mikolajewicz,U., Mueller,W., Notz,D., Pithan,F., Raddatz,T., Rast,S., Redler,R., Roeckner, E., Schmidt, H., Schnur, R., Segschneider, J., Six,K.D., Stockhause,M., Timmreck,C., Wegner, J., Widmann, H.,

Wieners, K.H., Claussen,M., Marotzke,J., and Stevens,B. (2013). Climate and carbon cycle changes from 1850 to 2100 in MPI-ESM simulations for the Coupled Model Intercomparison Project phase 5, J. Adv. Model. Earth Syst., 5, 572–597. https://doi.org/10.1002/jame.20038.

Gobiet, A., Kotlarski, S., Beniston, M., Heinrich, G., Rajczak, J., and Stoffel, M. (2014). 21st century climate change in the European Alps—A review, Sci. Total Environ., 493, 1138–1151, https://doi.org/10.1016/j.scitotenv.2013.07.050 .

Goldscheider, N. (2019). A holistic approach to groundwater protection and ecosystem services in karst terrains. Carbonates and Evaporites, 1-9. https://doi.org/10.4409/Am-046-12-0047

Goldscheider, N., Chen, Z., Auler, A.S., Bakalowicz, M., Broda, S., Drew, D., Hartmann, H., Jiang, G., Moosdorf, N., Stevanovic, Z., and Veni, G. (2020). Global distribution of carbonate rocks and karst water resources. Hydrogeol. J. https://doi.org/10.1007/s10040-020-02139-5-

González-Ramón, A., Jódar, J., Samsó, J.M. Martos-Rosillo, S., Heredia, J., Zabaleta, A., Antigüedad, I., Custodio, E., and Lambán, L.J. (2020). Hydrometeorological factors determining the development of water table cave patterns in alpine zones. The Ordesa and Monte Perdido National Park, NE-Spain. International Journal of Speleology. https://doi.org/10.5038/1827-806X.49.3.2346.

Guan, J., Liu, Z., Wen, X., Brady, E., Noone, D., Zhu, J., and Han, J. (2016). Understanding the temporal slope of the temperature-water isotope relation during the deglaciation using isoCAM3: The slope equation. J. Geophys. Res. Atmos., 121, 10,342–10,354. https://doi.org/10.1002/2016JD024955.

Hargreaves, G.H., and Samani, Z.A. (1982). Estimating potential evapotranspiration. Journal of the irrigation and Drainage Division, 108(3), 225-230. https://doi.org/10.1061/JRCEA4.0001390 .

Hartmann, A., Goldscheider, N., Wagener, T., Lange, J., and Weiler, M. (2014). Karst water resources in a changing world: Review of hydrological modeling approaches. Reviews of Geophysics, 52(3), 218-242. https://doi.org/10.1002/2013RG000443.

Hartmann, A., Jasechko, S., Gleeson, T., Wada, Y., Andreo, B., Barberá, J.A., Briel-mann, H., Bouchaou, L., Charlier, J.B., Darling, W.G., Filippini, M., Garvelmann, J., Gold-scheider, N., Kralik, M., Kunstmann, H., Ladouche, B., Lange, J., Lucianetti, G., Martín, J.F., Mudarra, M., Sánchez, D., Stumpp, C., Zagana, E., Wagener, T. (2021). Risk of groundwater contamination widely underestimated because of fast flow into aquifers. Proceedings of the National Academy of Sciences, 118(20). https://doi.org/10.1073/pnas.2024492118.

Hay, L.E., Wilby, R.L., and Leavesley, G.H. (2000). A comparison of delta change and downscaled GCM scenarios for three mountainous basins in the United States 1. JAWRA J. Am. Water Resour. Assoc. 36 (2), 387–397. https://doi.org/10.1111/j.1752-1688.2000.tb04276.x.

Helsel, D.R., and Frans, L.M. (2006). Regional Kendall Test for trend. Environ. Sci. Technol. 40, 4066–4073. https://doi.org/10.1021/es051650b.

Helsel, D.R., Mueller, D.K., and Slack, J.R. (2006). Computer program for the Kendall family of trend tests: U.S. Geological Survey Scientific Investigations Report 2005–5275, 4 p.

Henderson-Sellers, A., McGuffie, K., Noone, D., and Irannejad, P. (2004). Using stable water isotopes to evaluate basin-scale simulations of surface water budgets. Journal of Hydrometeorology, 5(5), 805-822. https://doi.org/10.1175/1525-7541(2004)005<0805:USWITE>2.0.CO;2

Herms, I., Jódar, J., Soler, A., Lambán, L.J., Custodio, E., Núñez, J.A., Arnó, G., Ortego, M.I., Parcerisa, D., and Jorge, J. (2021). Evaluation of natural background levels of high mountain karst aquifers in complex hydrogeological settings. A Gaussian mixture model approach in the Port del Comte (SE, Pyrenees) case study. Science of the Total Environment, 756, 143864. https://doi.org/10.1016/j.scitotenv.2020.143864

Herms. I., Jódar, J., Soler, A., Vadillo, I, Lambán, L.J., Martos-Rosillo, S., Núñez, J.A., Arnó, G., and Jorge, J. (2019). Contribution of isotopic research techniques to characterize high-mountain-Mediterranean karst aquifers: The Port del Comte (Eastern Pyrenees) aquifer. Science of the Total Environment, Volume 656, 209-230. https://doi.org/10.1016/j.scitotenv.2018.11.188

Hock, R., Rasul, G., Adler, C., Cáceres, B., Gruber, S., Hirabayashi, Y., Jackson, M., Kääb, A., Kang, S., Kutuzov, S., Milner, Al., Molau, U., Morin, S., Orlove, B., and Steltzer, H. (2019). High Mountain Areas, in: IPCC Special Report on the Ocean and Cryosphere in a Changing Climate., edited by: Pörtner, H.O., Roberts, D.C., Masson-Delmotte, V., Zhai, P., Tignor, M., Poloczanska, E., Mintenbeck, K., Alegría, A., Nicolai, M., Okem, A., Petzold, J., Rama, B., and Weyer, N.M., Retrieved from http://urn.kb.se/resolve?urn=urn:nbn:se:uu:diva-414230 (Last access 1/04/2021)

Hoerling, M., Eischeid, J., Perlwitz, J., Quan, X., Zhang, T., and Pegion, P. (2012). On the increased frequency of Mediterranean drought. J. Clim. 25 (6), 2146–2161. https://doi.org/10.1175/JCLI-D-11-00296.1

Hollander, M., and Wolfe, D.A. (1973). Nonparametric Statistical Methods. John Wiley & Sons,

New York.

Holloway, M.D., Sime, L.C., Singarayer, J.S., Tindall, J.C., Bunch, P., and Valdes, P.J. (2016). Antarctic last interglacial isotope peak in response to sea ice retreat not ice-sheet collapse, Nat. Commun., 7, 12293. https://doi.org/doi:10.1038/ncomms12293

IPCC (2019). Summary for Policymakers, in: IPCC Special Report on the Ocean and Cryosphere in a Changing Climate, edited by: Pörtner, H.O., Roberts, D.C., Masson-Delmotte, V., Zhai, P., Tignor, M., Poloczanska, E., Mintenbeck, K., Alegría, A., Nicolai, M., Okem, A., Petzold, J., Rama, B., and Weyer, N.M., in press, 2019. Retrieved from http://urn.kb.se/resolve?urn=urn:nbn:se:uu:diva-414230 (Last access 1/04/2021)

Jódar, J., Carpintero, E., Martos-Rosillo, S., Ruiz-Constán, A., Marín-Lechado, C., Cabrera-Arrabal, J.A., Navarrete-Mazariegos, E., González-Ramón, A., Lambán, L.J., Herrera, C., and González-Dugo, M.P. (2018): Combination of lumped hydrological and remote-sensing models to evaluate water resources in a semi-arid high altitude ungauged watershed of Sierra Nevada (Southern Spain). Science of the Total Environment, 625, 285-300, https://doi.org/10.1016/j.scitotenv.2017.12.300

Jódar, J., Custodio, E., Lambán, J.L., Martos-Rosillo, S., Herrera, C., and Sapriza, G. (2016). Vertical variation in the amplitude of the seasonal isotopic content of rainfall as a tool to jointly estimate the groundwater recharge zone and transit times in the Ordesa and Monte Perdido National Park aquifer system, north-eastern Spain. Science of The Total Environment, https://doi.org/10.1016/j.scitotenv.2016.08.117

Jódar, J., González-Ramón, A., Martos-Rosillo, S., Heredia, J., Herrera, C., Urrutia, J., Caballero, Y., Zabaleta, A., Antigüedad, I., Custodio, E., and Lambán, L.J. (2020). Snowmelt as a determinant factor in the hydrogeological behaviour of high mountain karst aquifers: The Garcés karst system, Central Pyrenees (Spain). Science of The Total Environment, 748-141363. https://doi.org/10.1016/j.scitotenv.2020.141363

Jódar, J., Lambán, L.J., Medina, A., and Custodio, E., (2014). Exact analytical solution of the convolution integral for classical hydrogeological lumped-parameter models and typical input tracer functions in natural gradient systems. Journal of Hydrology, 519: pp 3275–3289. https://doi.org/10.1016/j.jhydrol.2014.10.027

Kendall, M.G. (1975). Rank Correlation Methods. Griffin, London, UK.

Kiraly, L. (2003). Karstification and groundwater flow. In: Gabrovsek, F. (ed.), Evolution of karst: from prekarst to cessation. Zalozba ZRC, Postojna-Ljbljana, pp. 155–190.

Konz, M., and Seibert, J. (2010). On the value of glacier mass balances for hydrological model calibration. J. Hydrol. 385 (1–4), 238–246. https://doi.org/10.1016/j.jhydrol.2010.02.025

Lambert, S.J., and Boer, G.J. (2001). CMIP1 evaluation and intercomparison of coupled climate models. Clim. Dyn., 17, 83–106. https://doi.org/10.1007/PL00013736

Lauber, U., and Goldscheider, N. (2014). Use of artificial and natural tracers to assess groundwater transit-time distribution and flow systems in a high-alpine karst system (Wetterstein Mountains, Germany). Hydrogeology Journal, 22(8), 1807-1824. https://doi.org/10.1007/s10040-014-1173-6

Lohmann, G., Pfeiffer, M., Laepple, T., Leduc, G., and Kim, J.H. (2013). A model–data comparison of the Holocene global sea surface temperature evolution, Clim. Past, 9(4), 1807–1839, https://doi.org/10.5194/cpd-8-1005-2012

López-Moreno, J.I., Goyette, S., and Beniston, M. (2008a). Climate change prediction over complex areas: spatial variability of uncertainties and predictions over the Pyrenees from a set of regional climate models. International Journal of Climatology: A Journal of the Royal Meteorological Society, 28(11), 1535-1550.

López-Moreno, J.I., Beniston, M., and García-Ruiz, J.M. (2008b). Environmental change and water management in the Pyrenees: Facts and future perspectives for Mediterranean mountains. Global and Planetary Change, 61(3-4), 300-312. https://doi.org/10.1016/j.gloplacha.2007.10.004

López-Moreno, J.I., and García-Ruiz, J.M. (2004). Influence of snow accumulation and snowmelt on streamflow in the Central Spanish Pyrenees. Hydrol. Sci. J. 49 (5), 787–802. https://doi.org/10.1623/hysj.49.5.787.55135

López-Moreno, J.I., Goyette, S., and Beniston, M. (2009). Impact of climate change on snowpack in the Pyrenees: Horizontal spatial variability and vertical gradients. Journal of Hydrology, 374(3-4), 384-396. https://doi.org/10.1016/j.jhydrol.2009.06.049

López-Moreno, J.I., Soubeyroux, J.M., Gascoin, S., Alonso-Gonzalez, E., Durán-Gómez, N., Lafaysse, M., Vernay, M., Carmagnola, C., and Morin, S. (2020). Long-term trends (1958–2017) in snow cover duration and depth in the Pyrenees, Int. J. Climatol., 40, 6122–6136, https://doi.org/10.1002/joc.6571

Mallucci, S., Majone, B., and Bellin, A. (2019). Detection and attribution of hydrological changes in a large Alpine river basin, J. Hydrol., 575, 1214–1229. https://doi.org/10.1016/j.jhydrol.2019.06.020

Małoszewski, P., Rauert, W., Trimborn, P., Herrmann, A., and Rau, R. (1992). Isotope hydrological study of mean transit times in an alpine basin (Wimbachtal, Germany). J Hydrol 140:343–360. https://doi.org/10.1016/0022-1694(92)90247-S

Małoszewski, P., Stichler, W., Zuber, A., and Rank, D. (2002). Identifying the flow systems in a karstic-fissured-porous aquifer, the Schneealpe, Austria, by modelling of environmental 18O and 3H isotopes. J. Hydrol. 256(1–2):48–59. https://doi.org/10.1016/S0022-1694(01)00526-1

Małoszewski, P., and Zuber, A. (1996). Lumped Parameter Models for the Interpretation of Environmental Tracer Data. Manual on Mathematical Models in Isotope Hydrology. IAEA-TECDOC 910. IAEA, Vienna (Austria).

Małoszewski, P., and Zuber, A. (2002). Manual on Lumped Parameter Models Used for the Interpretation of Environmental Tracer Data in Groundwaters (IAEA-UIAGS/CD-02-00131). International Atomic Energy Agency (IAEA) https://inis.iaea.org/search/search.aspx?orig_q=RN:33037906 (Last access 02/04/2021).

Mann, H.B. (1945). Nonparametric tests against trend. Econometrica ,Vol. 13, No. 3, 245-259. https://doi.org/10.2307/1907187

Matiu, M., Crespi, A., Bertoldi, G., Carmagnola, C.M., Marty, C., Morin, S., Schöner, W., Cat Berro, D., Chiogna, G., De Gregorio, L., Kotlarski, S., Majone, B., Resch, G., Terzago, S., Valt, M., Beozzo, W., Cianfarra, P., Gouttevin, I., Marcolini, G., Notarnicola, C., Petitta, M., Scherrer, S.C., Strasser, U., Winkler, M., Zebisch, M., Cicogna, A., Cremonini, R., Debernardi, A., Faletto, M., Gaddo, M., Giovannini, L., Mercalli, L., Soubeyroux, J.M., Sušnik, A., Trenti, A., Urbani, S., and Weilguni, V. (2021). Observed snow depth trends in the European Alps: 1971 to 2019. The Cryosphere, 15(3), 1343-1382. https://doi.org/10.5194/tc-15-1343-2021

Meeks, J., Hunkeler, D., (2015). Snowmelt infiltration and storage within a karstic environment, Vers Chez le Brandt, Switzerland. J. Hydrol. 529, 11–21. https://doi.org/10.1016/j.jhydrol.2015.06.040

Moss, R.H., Edmonds, J.A., Hibbard, K.A., Manning, M.R., Rose, S.K., Van Vuuren, D.P., Carter, T.R., Emori, S., Kainuma, M., Kram, T., Meehl, G.A., Mitchell, J.F.B., Nakicenovic, N., Riahi, K., Smith, S.J., Stouffer, R.J., Thomson, A.M., Weyant, J.P., Wilbanks, T.J. (2010). The next generation of scenarios for climate change research and assessment. Nature 463:747–756. https://10.1038/nature08823

Motyka, J.A. (1998). Conceptual model of hydraulic networks in carbonate rocks, illustrated by examples from Poland. Hydrogeology Journal 6, 469–482. https://doi.org/10.1007/s100400050169

Müller M.H., Weingartner, R., and Alewell, C. (2013). Importance of vegetation, topography and flow paths for water transit times of base flow in alpine headwater catchments. Hydrol Earth Syst Sci 17(4):1661–1679. https://doi.org/10.5194/hess-17-1661-2013

Okazaki, A., and Yoshimura, K. (2019). Global evaluation of proxy system models for stable water isotopes with realistic atmospheric forcing. Journal of Geophysical Research: Atmospheres, 124(16), 8972-8993. https://doi.org/10.1029/2018JD029463

Parise, M., Closson, D., Gutiérrez, F., and Stevanović, Z. (2015). Anticipating and managing engineering problems in the complex karst environment. Environ Earth Sci 74, 7823–7835 (2015). https://doi.org/10.1007/s12665-015-4647-5

Pedro-Monzonís, M., Solera, A., Ferrer, J., Estrela, T., and Paredes-Arquiola, J. (2015). A review of water scarcity and drought indexes in water resources planning and management. Journal of Hydrology, 527, 482-493. https://doi.org/10.1016/j.jhydrol.2015.05.003

Pfeiffer, M., and Lohmann, G. (2016). Greenland Ice Sheet influence on Last Interglacial climate: Global sensitivity studies performed with an atmosphere–ocean general circulation model, Clim. Past, 12(6), 1313–1338, doi:10.5194/cpd-11-933-2015

Räty, O., Räisänen, J., and Ylhäisi, J.S. (2014). Evaluation of delta change and bias correction methods for future daily precipitation: intermodel cross-validation using ENSEMBLES simulations. Climate Dynamics, 42(9-10), 2287-2303. https://doi.org/10.1007/s00382-014-2130-8

Rowley, D.B., and Garzione, C.N. (2007). Stable isotope-based paleoaltimetry. Annu. Rev. Earth Planet. Sci., 35, 463-508. https://doi.org/10.1146/annurev.earth.35.031306.140155

Rozanski, K., Araguas-Araguas, L., and Gonfiantini, R. (1992), Relation between long-term trends of oxygen-18 isotope composition of precipitation and climate. Science, 258(5084), 981–5. http://dx.doi.org/10.1126/science.258.5084.981

Schmidt, G. A., Annan, J. D., Bartlein, P. J., Cook, B. I., Guilyardi, E., Hargreaves, J. C., Harrison, S. P., Kageyama, M., LeGrande, A. N., Konecky, B., Lovejoy, S., Mann, M. E., Masson-Delmotte, V., Risi, C., Thompson, D., Timmermann, A., Tremblay, L.-B., and Yiou, P. (2014). Using palaeo-climate comparisons to constrain future projections in CMIP5, Clim. Past, 10, 221–250. https://doi.org/10.5194/cp-10-221-2014

Seibert, J., and Vis, M.J.P. (2012). Teaching hydrological modelling with a user-friendly catchment-runoff-model software package. Hydrol. Earth Syst. Sci. 16 (9), 3315–3325. https://doi.org/10.5194/hess-16-3315-2012, 102012

Sen, P.K. (1968). Estimates of the Regression Coefficient Based on Kendall's Tau, Journal of the American Statistical Association, 63:324, 1379-1389, https://doi.org/10.1080/01621459.1968.10480934

Sjolte, J., Adolphi, F., Vinther, B. M., Muscheler, R., Sturm, C., Werner, M., and Lohmann, G. (2020). Seasonal reconstructions coupling ice core data and an isotope-enabled climate model–methodological implications of seasonality, climate modes and selection of proxy data. Climate of the Past, 16(5), 1737-1758. https://doi.org/10.5194/cp-2019-72

Sjolte, J., and G. Hoffmann (2014). Modelling stable water isotopes in monsoon precipitation during the previous interglacial, Quat. Sci. Rev., 85, 119–135, https://doi.org/10.1016/j.quascirev.2013.12.006

Staudinger, M., Stoelzle, M., Seeger, S., Seibert, J., Weiler, M., and Stahl, K. (2017). Catchment water storage variation with elevation. Hydrol. Process. 31 (11), 2000–2015. https://doi.org/10.1002/hyp.11158

Taylor, K.E., Stouffer, R.J., and Meehl, G.A. (2012). An overview of CMIP5 and the experiment design, Bull. Am. Meteorol. Soc., 93, 485–498, https://doi.org/10.1175/BAMS-D-11–00094.1

Van Vuuren, D.P., Edmonds, J., Kainuma, M., Riahi, K., Thomson, A., Hibbard, K., Hurtt, G.C., Kram, T., Krey, V., Lamarque, J.F., Masui, T., Meinshausen, M., Nakicenovic, N., Smith, S.J.,Rose, S.K. (2011). The representative concentration pathways: an overview. Climatic change, 109(1), 5-31. https://doi.org/10.1007/s10584-011-0148-z

Vicente-Serrano, S.M., López-Moreno, J.I., Beguería, S., Lorenzo-Lacruz, J., Sanchez-Lorenzo, A., García-Ruiz, J.M., Azorin-Molina, C., Morán-Tejeda, E., Revuelto, J., Trigo, R., Coelho, F., and Espejo, F. (2014). Evidence of increasing drought severity caused by temperature rise in southern Europe. Environ. Res. Lett. 9 (4), 044001. https://doi.org/10.1088/1748-9326/9/4/044001

Viviroli, D., Dür, H.H., Messerli, B., Meybeck, M., and Weingartner, R. (2007). Mountains of the world, water towers for humanity: topology, mapping and global significance. Water Resources Research 43:W07447. https://doi.org/10.1029/2006WR005653

Voldoire, A., Sánchez-Gómez, E., Salas y Mélia, D., Decharme, B., Cassou, C., Sénési, S., Valcke,

S., Beau, I., Alias, A., Chevallier, M., Déqué, M., Deshayes, J., Douville, H., Fernández, E., Madec, G., Maisonnave, E., Moine, M.P., Planton, S., Saint-Martin, D., Szopa, S., Tyteca, S., Alkama, R., Belamari, S., Braun, A., Coquart, L., and Chauvin, F. (2013). The CNRM-CM5. 1 global climate model: description and basic evaluation. Climate dynamics, 40(9), 2091-2121. https://doi.org/10.1007/s00382-011-1259-y

Volodin, E.M., Dianskii, N.A., and Gusev, A.V. (2010). Simulating present-day climate with the INMCM4. 0 coupled model of the atmospheric and oceanic general circulations. Izvestiya, Atmospheric and Oceanic Physics, 46(4), 414-431. https://doi.org/10.1134/S000143381004002X

Wassenaar, L.I., Terzer-Wassmuth, S., Douence, C., Araguas-Araguas, L., Aggarwal, P. K., and Coplen, T.B. (2018). Seeking excellence: An evaluation of 235 international laboratories conducting water isotope analyses by isotope-ratio and laser-absorption spectrometry. Rapid Communications in Mass Spectrometry, 32(5), 393-406. https://doi.org/10.1002/rcm.6270

Watanabe, S., Hajima, T., Sudo, K., Nagashima, T., Takemura, T., Okajima, H., Nozawa, T., Kawase, H., Abe, M., Yokohata, T., Ise, T., Sato, H., Kato, E., Takata, K., Emori, S., Kawamiya, M. (2011). MIROC-ESM 2010: Model description and basic results of CMIP5-20c3m experiments. Geoscientific Model Development, 4(4), 845 https://doi.org/10.5194/gmd-4-845-2011

Wu, T., Song, L., Li, W., Wang, Z., Zhang, H., Xin, X., Zhang, Y., Zhang, L., Li, J., Wu, F., Liu, Y., Zhang, F., Shi, X., Chu, M., Zhang, J., Fang, Y., Wang, F., Lu, Y., Liu, X., Wei, M., Liu, Q., Zhou, W., Dong, M., Zhao, Q., Ji, J., Laurent, L., and Zhou, M. (2014). An overview of BCC climate system model development and application for climate change studies. Journal of Meteorological Research, 28(1), 34-56. https://doi.org/10.1007/s13351-014-3041-7

Yoshimura, K. (2015). Stable water isotopes in climatology, meteorology, and hydrology: A review. Journal of the Meteorological Society of Japan. Ser. II, 93(5), 513-533. https://doi.org/10.2151/jmsj.2015-036

Yukimoto, S., Adachi, Y., Hosaka, M., Sakami, T., Yoshimura H., Hirabara, M., Tanaka, T.Y., Shindo, E., Tsujino, H., Deushi, M., Mizuta, R., Yabu, S., Obata, A., Nakano, H., Koshiro, T., Ose, T., and Kitoh, A. (2012). A new global climate model of the Meteorological Research Institute: MRI-CGCM3—Model description and basic performance—. Journal of the Meteorological Society of Japan. Ser. II, 90, 23-64. https://doi.org/10.2151/jmsj.2012-A02

Zaiontz, C. (2020) Real Statistics Using Excel. www.real-statistics.com (Last access 01/01/2021)

Zuber, A. (1986). Mathematical models for the interpretation of environmental radioisotopes in groundwater systems. Handbook of environmental isotope geochemistry, terrestrial environment, pp. 1–59.

I.Herms, J. Jódar, A. Soler, L.J. Lambán, E. Custodio, J.A. Núñez, G. Arnó, D. Parcerisa, J. Jorge. Identification of Natural and Anthropogenic Geochemical Processes Determining the Groundwater Quality in Port del Comte High Mountain Karst Aquifer (SE, Pyrenees). Water 2021, 13, 2891. https://doi.org/10.3390/w13202891

Open Access Article

Identification of Natural and Anthropogenic Geochemical Processes Determining the Groundwater Quality in Port del Comte High Mountain Karst Aquifer (SE, Pyrenees)

by Ignasi Herms [1,2,*], Jorge Jódar [3], Albert Soler [4], Luis Javier Lambán [3], Emilio Custodio [5], Joan Agustí Núñez [1], Georgina Arnó [1], David Parcerisa [2] and Joan Jorge-Sánchez [2]

1 Àrea de Recursos Geològics, Institut Cartogràfic i Geològic de Catalunya (ICGC), 08038 Barcelona, Spain
2 Departament d'Enginyeria Minera, Industrial i TIC, Universitat Politècnica de Catalunya (UPC), 08240 Manresa, Spain
3 Instituto Geológico y Minero de España (IGME), 50006 Zaragoza, Spain
4 Grup MAiMA, SGR Mineralogia Aplicada, Geoquímica i Geomicrobiologia, Departament de Mineralogia, Petrologia i Geologia Aplicada, Facultat de Ciències de la Terra, Universitat de Barcelona (UB), 08028 Barcelona, Spain
5 Grupo de Hidrología Subterránea, Departament d'Enginyeria Civil i Ambiental, Real Academia de Ciencias, Universitat Politècnica de Catalunya (UPC), 08034 Barcelona, Spain
* Author to whom correspondence should be addressed.

Academic Editor: Kang-Kun Lee

Water **2021**, *13*(20), 2891; https://doi.org/10.3390/w13202891

Received: 6 September 2021 / Revised: 2 October 2021 / Accepted: 9 October 2021 / Published: 15 October 2021

(This article belongs to the Section Hydrogeology)

6 PAPER 4. IDENTIFICATION OF NATURAL AND ANTHROPOGENIC GEOCHEMICAL PROCESSES CONTROLLING GROUNDWATER QUALITY IN PORT DEL COMTE HIGH MOUNTAIN KARST AQUIFER (SE, PYRENEES)

Authors: **Ignasi Herms**, Jorge Jodar, Albert Soler, Luís J. Lambán, Emilio Custodio, Joan Agustí Nuñez, Georgina Arnó, David Parcerisa, Joan Jorge-Sánchez

Abstract

The Port del Comte Massif (SE, Pyrenees) contains one of the most important vulnerable and strategic karst aquifers for supplying freshwater to the city of Barcelona (Spain). It is a fragile system, whose possible environmental impact is highly conditioned by land use. To improve the hydrogeological knowledge of the system, between September 2013 and October 2015 a detailed fieldwork was carried out for the revision of the geological model, the inventory of water points, the in-situ physico-chemical characterization on major elements and isotopes of up to a total of 43 springs, as well as precipitation water. This paper focuses on the characterization of the geo-chemical processes that allow explaining the observed chemical variability of groundwater drained by the pristine aquifer system to determine the origin of salinity. The results show that the main process is the dissolution of calcite and dolomite, followed by gypsum and halite, and a minor cation exchange-like process. Sulfur and oxygen isotopes from dissolved sulfate in the studied springs points out a geogenic origin related to the dissolution of gypsum from Triassic and Tertiary materials, and that the contribution from anthropogenic sources, like fertilizers, are lower. Nitrate in groundwater is not an important issue, with a few localized cases related with agricultural activities. The multidisciplinary approach has allowed the development of a con-sistent hydrogeological conceptual model of the functioning of the aquifer system, which can be replicated in other places to understand the geogenic character of the hydrogeochemistry.

Keywords: high-mountain, karst system, Port del Comte Massif, water-rock interaction, geogenic and an-thropogenic contamination, stable isotopes, inverse modelling.

6.1 Introduction

High mountain karst aquifers are strategic freshwater reservoirs to maintain de-pendent ecosystems downstream, many of which are in semiarid zones. Globally, 68.9% of all the surface exposures of

carbonate rocks occur in hills and mountain areas. Roughly, 20–25% of the world's population depends directly or indirectly on water supplies from karst aquifers [1]. Given the relevance, it is essential to characterize such mountain karst aquifers and protect them to avoid undesirable quality issues in the stored water re-sources, because karst aquifers have been shown to be very vulnerable, especially to pollu-tion, given their inner structure, hydrogeological behavior, and limited self-depuration capacity [2]. This is true especially when these karst aquifers are unconfined and the fo-cused recharge flows through the most conductive karst features. This facilitates the widespread rapid incorporation and transport of pollutants to groundwater [3]. Such threating process might be even highlighted in the framework of climate change, mainly through the possible warming trends devised by the Intergovernmental Panel on Climate Change [4]. The expected increasing temperatures will reduce solid atmospheric precipi-tation and hence the snow cover duration in the mountain areas. This will drive the aqui-fer dominant recharge process to migrate from spatial diffuse to a focused one [5], while exposing longer the aquifer to eventual surface contamination by anthropogenic activities [6].

Mountain karst aquifers developed in carbonate materials are usually complex sys-tems that may show a distinctive hydrochemical response depending on the physico-chemical processes controlling the water-rock interactions. During the transit of ground-water (GW) from the recharge areas to the discharge zones, different hydrochemical pro-cesses may take place, including dissolution-precipitation reactions associated to car-bonate materials [7,8], dissolution processes often associated to evaporite lithologies (e.g., gypsum, anhydrite, halite) [9,10], and even cation release/retention processes associated to shales [11]. The existence and role of these hydrochemical processes depend strongly on the geological settings of the mountain range hosting the aquifer, which are typically complex due to the orogenic processes driving the range uplift. Such hydrochemical pro-cesses along with the heterogeneity in the inner karst structure make difficult characteriz-ing the behavior of the associated aquifer system. To this end, it is convenient to adopt a multidisciplinary approach [12], considering the hydrodynamic behavior and analyzing the physico-chemical and isotopic characteristics of groundwater (GW) throughout the aquifer [7,13–16], using both environmental and chemical tracers [17–19], applying data analysis techniques [20–22], conducting geophysical prospection [23], and/or applying hydrodynamic and hydrogeochemical and isotopic modeling tools [24–29].

The Port del Comte Massif (PCM) is a Mediterranean mountain karst aquifer located in the complex geotectonic zone of the south-eastern Pyrenean region **[30,31].** The aquifer discharges through a series of springs with typically low flow rates (< 1 L/s) **[29].** Never-theless, with a mean annual discharge of 7.5 hm3/yr, the spring Fonts del Cardener stands out. This spring tributes downstream to the Llobregat River and amounts 7% of the mean annual water use of Barcelona **[32].** Several authors have investigated the PCM karst aqui-fer from different perspectives, including the delineation of the catchment zone associated to the main springs of PCM by building a 3D geological model of the massif **[33],** the characterization of the hydrodynamic behavior of such springs and their associated GW transit time distributions **[29],** and the definition of natural background levels (NBLs) for NO3, SO4 and Cl in the aquifer, as NBLs are especially important to detect GW contamina-tion from anthropic activities in PCM, given that the aquifer system presents a high intrin-sic vulnerability **[34].**

Despite being the PCM a strategic freshwater resource, there is not a thorough hydro-geochemical characterization of the aquifer. There are only scarce attempts centered in the SW part of the massif **[35–37].** It is well known that mountain karst aquifers are vulnerable to climate change. The increasing warming trends impacts directly in the snowpack cover formation, the corresponding snowmelt infiltration and hence aquifer recharge. These ef-fects have been predicted in well-known high mountain karst systems, such as the Hochifen–Gottesacker system in the Northern Alps **[38]** and the aquifer system of Sierra de las Nieves **[39],** being the latter a privileged unparalleled observatory of the early im-pact of climate change in continental Europe since it is the southernmost high mountain karst system of the Iberian Peninsula. Moreover, **[6]** simulated the impact of climate change scenarios in the PCM at the end of the 21st century, considering an increase in temperature of up to +3.1 °C and a reduction of the snow cover of up to 76% respect to the current conditions. A decrease in the snow cover exposes longer the karst system to exter-nal pollutants, which is an issue, because the high hydraulic conductivity and limited self-depuration capacity of such aquifers make them especially vulnerable to pollution **[2].**

The aim of this work is to point out the geogenic origin of solutes as well as possible anthropogenic contributions driving the hydrogeochemical composition of GW in a pris-tine rural karst system to form a comprehensive picture of the hydrogeochemical behavior of this vulnerable type of aquifers

in order to prevent the effect of changes due to future scenarios for global change.

6.2 The study area

6.2.1 Geographical and Climatological Settings

The PCM is approximately 100 km north of Barcelona (Spain), in the south of the eastern Pyrenees (**Figure 6. 1**). The elevation of the mountainous massif ranges from 900 m a.s.l. to 2383 m a.s.l. at the 'Padró dels Quatre Batlles' peak. The study area covers an extension of about 110 km^2. The NW and SW part of the massif drain to the Segre River basin, whereas the eastern and southern parts drain to the Cardener river. The main source of this last river is the Fonts del Cardener spring (M-22, **Figure 6. 1**). The area is covered by forest (63.9%) and mountain meadows (21.1%), which include one Alpine ski resort and one cross-country (Nordic) ski resort, areas without soil and vegetation (11.5%), agricultural cultivation areas (1.5%) and the rest corresponding to residential zones (0.5 %) **[29]**. From a climatological point of view, and according to the Köppen-Geiger classification system **[40]**, the study area is characterized by a cold climate without a dry season and with a temperate summer. Within the study area, there are two meteorological stations located at 2315 m a.s.l. (SMC) and 1800 m a.s.l. (AEMET). For the period 2005 to 2019, the average annual precipitation, temperature and potential evapotranspiration (Hargreaves) measured at the SMC station are 1055 mm, 3.24 °C and 525 mm, respectively. During 3 to 4 months in the winter, depending on the year, the snow cover is above 1800 m a.s.l. The infiltration of the snowmelt during the spring season generates the main contribution to aquifer recharge in the PCM **[29]**. The massif presents a characteristic karst pattern in the upper part, which appears in the form of sinkholes and karren fields that allows a fast infiltration of the meteoric waters and prevent large surface runoff events.

6.2.2 Geology and Hydrogeology Setting

From the geological point of view, the PCM constitutes an independent thrust sheet limited by other

thrusts with complex structural relationships (**Figure 6. 1**). Internally, the massif presents a set of folds (anticlines and synclines) and some faults. The folds have a characteristic NE-SW direction parallel to the NW boundary of the thrust sheet [31]. Stratigraphically, the massif contains materials from the Triassic (Muschelkalk limestones and Keuper evaporites), the Cretaceous (limestones, calcarenites, shales), and the Paleogene from the Eocene to the Oligocene (karstified limestones with dolostones, sandstones and marls). The Jurassic carbonates only outcrops in the NW part of the study area. The massif has a total thickness exceeding 1300 m. From the geomorphological perspective, the PCM is characterized by presenting a rounded or flat relief in the highest part, where no vegetation cover is present and almost without any type of soil development exists. The rest of the massif is covered by mountain meadows and forests, with little thin soil. The area most affected by karstification becomes visible progressively, from 1950 m a.s.l. to the top.

Hydrogeologically, the PCM can be considered an independent unit and a multi-aquifer system. The Lower Eocene fissured and karstified limestones and dolostones form the main aquifer. It constitutes one of the most important high mountain karst aquifers (HMKA) of the Catalan Pyrenees. The other aquifers and aquitards in the study zone are related to the Cretaceous limestone formations, Triassic limestone and evaporites, other Paleogene conglomerates and sandstones, and small local quaternary aquifers (draining small areas) located at low or medium elevations. The Garumnian materials (Upper Cretaceous-Lower Paleogene), composed of shales, marls and multicolored clay deposits (geological unit 5 in **Figure 6. 1**), constitute a low permeability layer that acts as a lower impervious limit for both the Tertiary materials and the main karst aquifer. In addition, the geological structure of the system strongly influences the location and hydrodynamical behavior of the springs and their geochemical fingerprint.

Although many high mountain karst systems play a strategic role in terms of availability of underground water resources, such as the case of PCM [29], frequently they are not sufficiently known [44], because the conventional hydrogeological investigation techniques [45,46] are often difficult to be applied given the complicated access and harsh working conditions typically existing in high mountain zones [42,43].

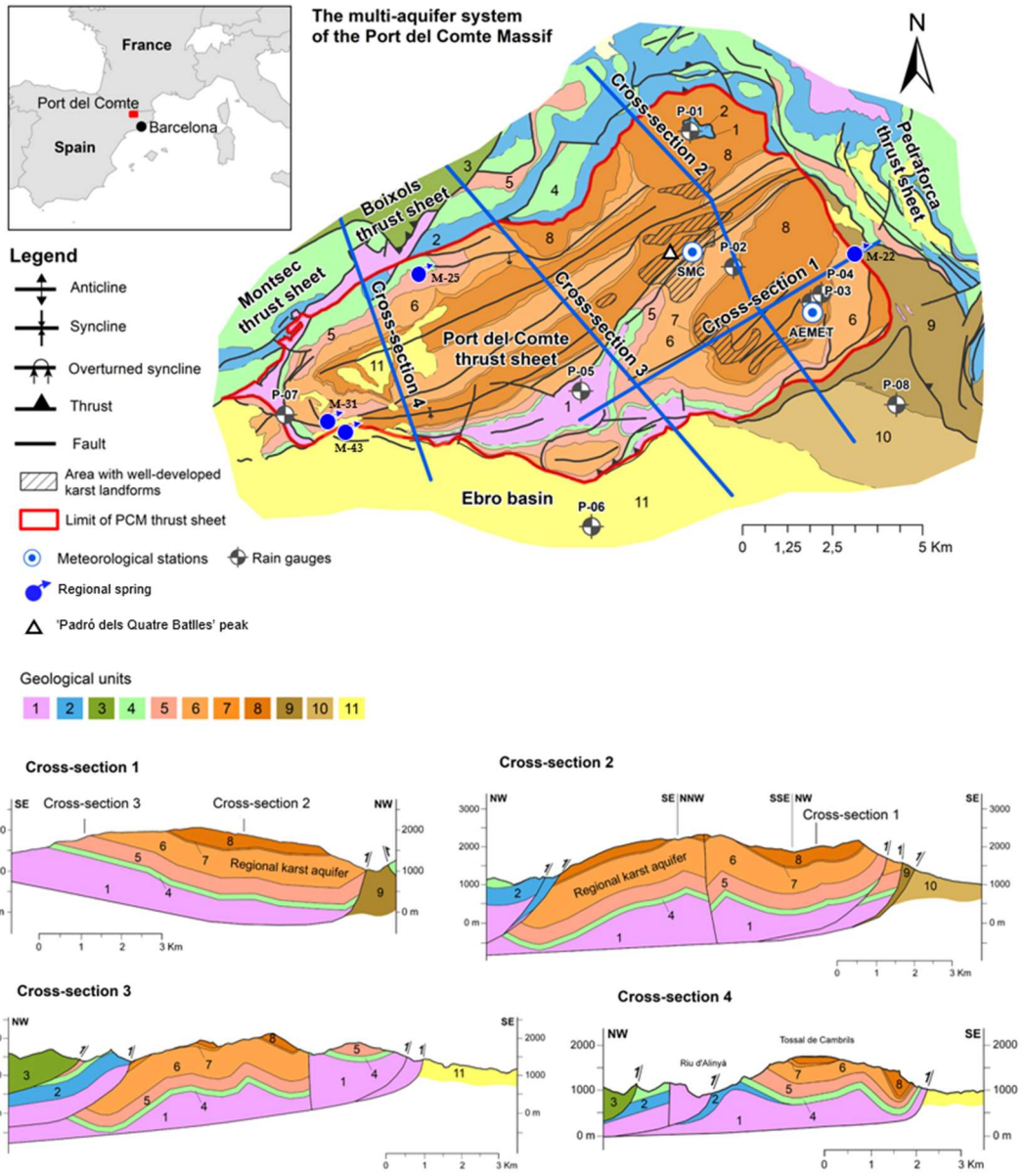

Figure 6. 1. Geological setting of the Port del Comte massif. 1) Triassic - Shales, limestones, dolomites and evaporites (Tk, Tm); 2) Jurassic - Marls, bioclastic limestones and dolomites (TJb, TJcd); 3) Lower Cretaceous - Micritic limestone-marl alternations; 4) Upper Cretaceous - limestone-marl alternations and calcarenites (Kat, KMca); 5) Garumnian (Upper Cretaceous-Lower Paleogene): shales, marls and limestone (Kgp), multicoloured 'redbed' facies clay deposits; 6) Lower Eocene - Fissured/karstified alveoline limestones and dolostones (PPEc), and includes colluvial Quaternary formations that partially overlap (Qpe, Qvl); 7) Lower Eocene - Marls, sandstones and limestones (PEci); 8) Lower Eocene - Fissured/karstified micritic and bioclastic limestones (PEcp1, PEcp2); 9) Middle Eocene - Sandstones, marls, conglomerates, limestones and evaporites (PEalb, PEm1, PEmb and PExb), including colluvial Quaternary deposits (Qcoo) and alluvium (Qoo) that partially overlap; 10) Upper Eocene - Alluvial systems: conglomerates and sandstones; and 11) Oligocene - Alluvial syst.: conglomerates and breccias deposits and sandstones (POcgs, POmlg). (Note: breccia deposits covering the Lower Eocene in the upper part of the massif are very thin). The epigraphs in parentheses correspond to the geological units [41] where the springs included in this work are located).

From a hydrological point of view, there are relevant processes, such as the aquifer recharge or the mean transit time, that need to be characterized to correctly manage the water resources generated in such alpine groundwater systems. Spring hydrograph analysis and the use of environmental tracer methods allow the characterization of aquifer recharge and discharge processes, assessing spring vulnerability, as well as estimating the available water resources **[47–50].** Rainfall-runoff hydrological models are useful to simulate the behavior of such complex mountain karst systems. Such models can be broadly categorized into lumped, semi-distributed, and fully-distributed models **[51]**. Semi-distributed and lumped parameter models (LPMs) are often used to simulate the behavior of high mountain aquifer systems, because they do not require a detailed hydrological knowledge of the physical system, and therefore, the are specially well suited when the hydrogeological systems are poorly characterized. Additionally, the stable isotopes of water ($\delta^{18}O$ and $\delta^{2}H$) in precipitation have proved to be good environmental tracers for investigating the dynamics of such hydrological systems karst systems **[52]**. These tracers enter the system as recharge, migrate downslope exploring the entire hydrological system, and leave the karst aquifer through the springs discharge. In the case of PCM, **[29]** presents a hydrogeological characterization of the aquifer system response that includes:

(1) the hydrodynamic behavior of the system, simulating the system response with a set of semi-distributed rainfall-runoff HBV models **[53,54]**, while taking into account the elevation dependences of both the hydrometeorological variables (e.g., precipitation and temperature) and the related processes (e.g. snow accumulation and ablation). The estimated groundwater storage capacity of the system is 35.2 hm^3, and the mean annual groundwater discharge is 15.4 hm^3, and
(2) the estimation of the mean transit times corresponding to the main springs draining the aquifer system. This is done by using a set of LPMs models **[55]** to simulate the environmental tracers content evolution in groundwater. The LPMs were implemented for the most important karst springs of the PCM systems, i.e., the four 'regional springs' named as M-22, M-25, M-31 and M-43 in Figure 1. The results indicate that the PCM karst system presents a relatively short mean transit time (~2.25 yr). This result is relevant if the hydrological high conductive features existing in the karst system are taken into account, which may favor a fast contaminant migration from the recharge to the discharge areas in the case of eventual surface spills of contaminants.

In the framework of the '*GeoERA Resources of groundwater harmonized at cross-border and pan-European scale (RESOURCE) Project'* (2018-2021) funded from the European Union's Horizon 2020 research and innovation programme, the PCM karst aquifer was incorporated as a pilot case study among other across Europe **[56]**. In this framework, it is applied a well-known hydrodynamic typology classification method proposed by Mangin (1975) **[57]**, which is based on a recession curve analysis of the spring hydrograph. The method describes the hydrodynamic behavior of a karst system as a function of two indices, *k* and *i*, defining the extent of the karst phreatic zone and characterizing the infiltration conditions, respectively. In the case of spring M-22, and for a diagram *k* vs *i* **[57]**, the indices lie in the $k < 0.5$ and $i > 0.5$ domain, thus indicating a complex, large karst system, made up of several sub-systems. This result is consistent with those obtained for other important karst springs in the Pyrenees, such as Fonts del Llobregat springs **[58],** which are one of the main groundwater resource for the Barcelona metropolitan area.

This manuscript presents the work did to characterize the PCM system from the hydrogeochemical point of view. In this sense, several geochemical fieldworks were carried out on 43 springs during the period Sep 2013 - Oct 2015. The 43 springs were grouped from a geochemical point of view **[59]** applying an approach based on a Gaussian Mixture Model (GMM) **[60]**, obtaining 4 groups (Figure 2). GMM is a 'soft' model-based clustering method that avoids the degree of subjectivity assumed by the classical 'hard' – or heuristic-based – algorithms (e.g., k-means, hierarchical clustering) **[61]** to determine the relevant number of clusters. Following **[59]**, the four spring clusters found in PCM can be summarized as:

- Cluster A: 27 springs characterized by low mineralization and dominated by slightly alkaline Ca–HCO_3 water type, which is associated to the Eocene carbonate materials conforming the main aquifer of PCM.
- Cluster B: 10 springs that include different types of water from Ca–HCO_3 to Ca–HCO_3–SO_4, Ca–SO_4–HCO_3 and Ca–SO_4, which are characterized by moderate mineralization. These springs are located both inside and outside the structural limits of the PCM trust sheet. The springs located inside the limits are mainly found in materials from the Cretaceous and Triassic (Keuper) that outcrop in the area. These materials underlie the main aquifer of the massif (the Eocene karst carbonate system). In the southeastern part of the study zone there are five springs related to sediments with a high content of tertiary gypsum from the Eocene-

Oligocene Beuda's gypsum Formation, pinched out within the South Pyrenees thrust fault in the front SE of the PCM.

- Cluster C: 4 springs with water types of Ca–HCO_3 and Ca–HCO_3–Cl. Three of these springs are located at the boundaries of the PCM sheet.
- Cluster D: corresponds to two salty springs with Na–Cl facies that are in the eastern and western limits of the PCM thrust sheet, respectively. They are characterized by remarkably high mineralization and are saturated relative to gypsum.

According to Herms et al. (2019) **[29]**, the recharge of the main aquifer of the PCM is produced by diffuse infiltration of precipitation-rainfall and snowmelt, but also it occurs concentrated through the well-developed karstic elements, mostly situated at the top of the massif. The infiltrated water flows vertically through the unsaturated zone, which may be thicker than 1000 m, towards the saturated zone of the aquifer. GW discharges through a large network of springs. In the framework of this work, more than 100 springs have been identified in the study zone. Most of them discharge local sub-surface waters with low flow rates ranging between <0.1 L/s and 10 L/s. There are four 'regional' springs (M-22, M-25, M-31, and M-43; **Figure 6. 1**) with mean flow rates from 1 L/s to 900 L/s, whose recharge areas are at medium to high elevation areas. Springs M-22 and M-25 discharge through Quaternary deposits overlying the Lower Eocene limestones, M-31 discharge directly through the limestone outcrops, and M-43 through well-developed karstic conduits affecting the conglomeratic materials of the Ebro Basin (the southern foreland basin of the Pyrenees), which are located just at the southern border of the PCM mantle. There are also some GW diffuse discharge zones, especially in the northern sector of the PCM. The regional water table main aquifer is located at elevations between 1000 and 1100 m a.s.l. **[29]**.

6.3 Materials and Methods

6.3.1 Field mesasurements, sampling and laboratory analysis

A total of 43 springs (**Figure 6. 2**A) were monitored in this research for the period between Sep 2013 – Oct 2015, in which the springs were sampled twice per year (i.e., before snowfall in October and after snowmelt in April). Additionally, springs M-04, M-20, M-22, M-25, M-31 and M-43 were

regularly sampled more frequently, every three to four weeks, along the same sampling period. In every case, the "in-situ" physico-chemical parameters (pH, EC, T, redox, alkalinity, TDS) were measured. A total of 288 GW samples were obtained. Table A1 in Appendix A summarizes the details of the GW sampling campaigns conducted in this work. Tables A21, A2, A3 in Appendix A provide the chemical characteristics of major constituents for the 43 water springs (median values for the whole campaigns carried out between Set 2013 - Oct 2015) and the rest of samples. Hereinafter, for simplicity, the different ions are indicated without the charge if this does not create confusion.

The hydrochemical composition of precipitation is obtained from an open (bulk) precipitation gauge **[62]** at the neighboring meteorological station of la Molina (42°20'30"N, 1°57'14"E, altitude 1704 m a.s.l.), which is located 30 km to the NW of PCM. The hydrochemical composition of recharge (**Figure 6. 2**B) is estimated from that of precipitation but applying an evapo-concentration process to simulate the effect of actual evapotranspiration in the PCM as estimated by **[29]**.

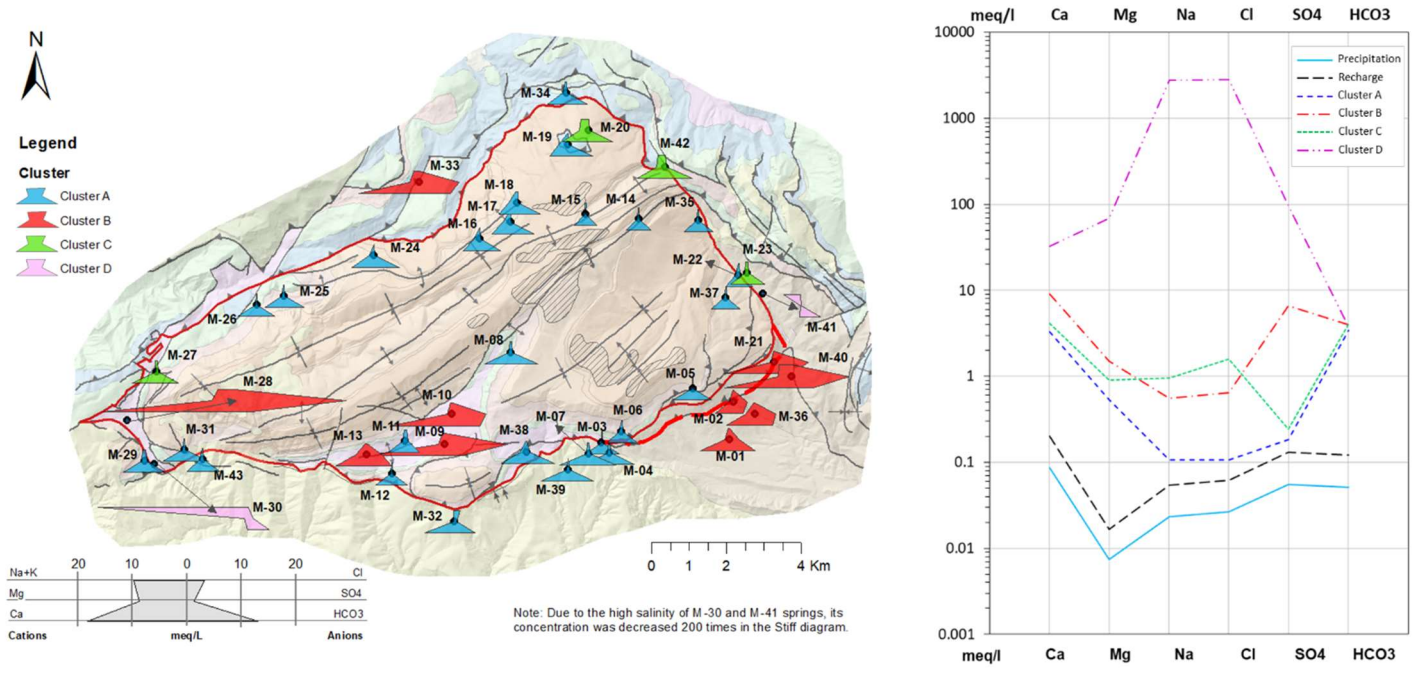

(**A**) (**B**)

Figure 6. 2. (A) Map of springs with the associated modified Stiff diagrams colored according with their corresponding cluster. For each spring, the different ionic content values (in meq/L) are obtained averaging the corresponding values for all the GW sampling campaigns during the period Sept 2013-Oct 2015.; **(B)**

Schoeller – Berkaloff diagram. Hydrochemical data corresponds to precipitation **[62]** calculated recharge with a concentration factor and GW as an average composition for the different clusters.

To estimate the impact of evapo-concentration in the meteoric water percolating through the soil, the modelling results obtained by Herms et al. (2019) **[29]** with the HBV model **[63]** for the springs M-25, M-43, M-31, M-22, and M-20 are used (springs in Figure 2). A regression line between the evaporation factor (Ef) and the recharge zone elevation of these 5 springs is obtained, thus allowing to estimate the associated Ef for the other 43 springs of the study zone. The average calculated value for the recharge chloride content is 2.2 mg/L, which is consistent with that obtained with the chloride mass balance method by **[64].** Figure 2B and Table A3 in Appendix A show the hydrochemical composition of precipitation **[62]** and the estimated average recharge evapo-concentrated water chemistry in the PMC applying a reduced concentration factor as estimated by Herms et al. (2019) **[29]**.

To characterize the temporal variation of the isotopic content of precipitation at the PCM, precipitation was sampled seasonally in 8 cumulative rain gauges installed at elevations between 896 and 1935 m a.s.l. A total of 71 precipitation water samples were taken, besides 10 snow samples (3 of them corresponding to artificial snow samples from a ski resort situated within the catchment area), and 2 surface water samples, from water ponds used for manufacturing artificial snow. In addition, rock samples containing gypsum were taken to characterize isotopically local sulfate. Figure A1 and Table A5 in Appendix A show the location of the sampling points and the results obtained.

All water samples were filtered in the field using a 0.45 µm membrane filter and stored in new 200-500 mL polyethylene bottles washed with diluted nitric acid and rinsed with the water to be sampled prior to sampling. Samples for cation analysis were acidified to pH < 2 with ultrapure HNO_3, to prevent precipitation, while samples for anion analysis were not acidified. Samples were preserved at 4 ºC until laboratory measurement. The physico-chemical parameters of GW (T, CE, pH, Eh and TDS) were measured in situ by a portable Hanna meter (Multiparameter Water Quality Meter HI9829). Total alkalinity was determined in-situ by using the titration method in the first four campaigns as well as with an Alkalinity Test Checker de (HI755) of Hanna Instruments.

The major ions, cations (Ca, Mg, Na, K, NH_4) and anions (Cl, NO_3, HCO_3, CO_3, SO_4 were measured in the Laboratori Ambiental d'Aigües de Terrassa: the cations were analysed by inductively coupled plasma atomic emission spectrometry – ICP-OES (Agilent 5100 DV), except ammonium that was determined by ultraviolet-visible (UV_VIS) spectrophotometer, and the anions by ion chromatography (Dionex, DX-120). Table A2.1 Appendix A summarize the median concentrations for the 8 major ions of the total 43 monitored springs.

The isotopic composition (δ^2H and $\delta^{18}O$) of the low salinity water samples was determined in the Center of Hydrogeology of the University of Málaga (CEHIUMA), with a Picarro® "L2130-I" cavity ring down-spectroscopy analyzer, which is based on cavity-enhanced, near-infrared laser absorption spectroscopy procedures, tuned on a narrow spectral region. The analytical uncertainties for δ^2H and $\delta^{18}O$ are ±0.2 ‰ and ±1.0 ‰, respectively. According to Coplen (2011) **[65]**, several international and laboratory standards have been interspersed for normalization of analyses. The standards used (WICO-13, WICO-14, WICO-15) were calibrated in an interlaboratory comparison exercise **[66]**. In the case of high salinity water samples, analysis of δ^2H and $\delta^{18}O$ for the GW brine samples (M-30 and M-41) were performed at the Centres Científics i Tecnològics of the Universitat de Barcelona (CCiT-UB). For the saline samples, δ^2H-H_2O was measured by pyrolysis using a Thermo-Quest high-temperature conversion analyzer (TC/EA) unit with a Finnigan MAT Delta XP IRMS. $\delta^{18}O$-H_2O was measured using the CO_2 equilibrium technique following the standard method **[67]** using a GasBench coupled to the MAT-253 IRMS. For GW samples with enough SO_4 and NO_3 concentration, also $\delta^{34}S_{SO4}$, $\delta^{18}O_{SO4}$, $\delta^{15}N_{NO3}$, $\delta^{18}O_{NO3}$ were determined.

The analysis of $\delta^{15}N_{NO_3}$ and $\delta^{18}O_{NO_3}$ was done with the method involving the chemical reduction of NO_3^- to NO_2^- using spongy cadmium **[68]**. Simultaneous $\delta^{15}N$ and $\delta^{18}O$ analyses of the produced N_2O were carried out using a Pre-Con (Thermo Scientific) coupled in continuous flow to a Finnigan MAT-253 Isotope Ratio Mass Spectrometer (IRMS, Thermo Scientific). The analysis of $\delta^{34}S_{SO_4}$ and $\delta^{18}O_{SO_4}$ was done adding $BaCl_2 \cdot 2H_2O$ to precipitate SO_4^{2-} as $BaSO_4$ after acidifying the sample with HCl and boiling it to prevent $BaCO_3$ precipitation according to standard methods **[69]**. Solid gypsum samples from Triassic and Tertiary evaporites were previously dissolved in water. The $\delta^{34}S$ was analysed in a Carlo Erba Elemental Analyser (EA) coupled in continuous flow to a Finnigan Delta XP IRMS. The $\delta^{18}O$ was analysed in duplicate with a Thermo Quest high-temperature conversion analyser (TC/EA) unit in continuous flow to a Finnigan Matt Delta XP

IRMS.

To check the accuracy of the analytical results, ionic balance errors were calculated using the USGS software PHREEQC® [70] using the phreeqc.dat database for all water springs, except for the brines from M-30 and M-41. Most of the samples have ionic balance errors below the recommended standard of ±5% [71]. Isotope ratios were calculated using both international and internal laboratory standards. Notation was expressed in terms of delta (δ)‰ relative to the international standards: V-SMOW for $\delta^{18}O$ and $\delta^{2}H$, atmospheric N_2 for $\delta^{15}N$ and V-CDT for $\delta^{34}S$. Precision of the analyses calculated from the reproducibility of standards interspersed in the analytical batches was ±0.3 ‰ for $\delta^{15}N$, ±0.2 ‰ for $\delta^{34}S$, and ±0.5 ‰ for $\delta^{18}O$ of SO_4 and NO_3.

6.3.2 Application of the dual-isotope approach for δ34S and δ15N

The existence of NO_3 and SO_4 in GW may pose in environmental risk in many mountains and rural areas with pristine waters. The use of stable isotopes of N and O of dissolved NO_3 and S and O of dissolved SO_4, together with the geochemical data, has proven to be a useful tool to evaluate the origin of solutes [7,20,72,73]. These tools help to improve the knowledge of the hydrogeological system, but also to understand both the natural and anthropogenic geochemical processes driving the GW quality in the aquifer system. In this research, stable isotopes of $\delta^{15}N_{NO_3}$ and $\delta^{18}O_{NO_3}$ as well as $\delta^{34}S_{SO_4}$ and $\delta^{18}O_{SO_4}$ were used to identify NO_3 and SO_4 sources in groundwater using the well-known dual isotope approach [74]. Ranges of NO_3 and SO_4 isotope compositions of the main potential sources were obtained from [73].

6.3.3 Determination of proportional contributions of NO3 and SO4 sources

To estimate the relative contribution of different sources, stable isotope mixing models have become a common tool in the environmental studies. Beyond the well-known limitations of the classical mass-balance mixing models - related to the restriction of taking at maximum n+1 sources for n isotopes [75] - nowadays the Bayesian isotope mixing models (BMM) [76,77] are being the

focus of attention a to determine the probable source apportionment. BMM are traditionally used to identify biogeochemical sources. They allow estimating the probability distribution for the relative contribution of each source considering the uncertainty associated within the sources themselves and their isotopic compositions. Since few years ago, these techniques have been used to assess the contribution of NO_3 pollution in general studies **[78–84].** They have been used also specifically in karst studies **[85,86],** and in very few cases for SO_4 studies **[87,88].** Different BMM codes for R and MATLAB has been reported, among them: SIAR, MixSIR, SIMMR and MixSIAR. In this research the Stable Isotope Mixing Model (SIMMR) package for R, an updated version of the Bayesian isotope mixing model named as SIAR **[76,77],** was used to determine the proportional contributions of natural and anthropogenic NO_3 and SO_4 sources into groundwater. The SIAR model (Stable Isotope Analysis in R) is an open-source software package for R. It uses a Markov chain Monte Carlo method to simulate plausible source proportions. The SIAR model is formulated according to equations (1) to (4).

$$X_{ij} = \sum_{k=1}^{K} p_k \cdot \left(S_{jk} + c_{jk}\right) + \varepsilon_{ij} \quad (1)$$

$$S_{jk} \sim N\left(\mu_{jk}, \omega_{kj}^2\right) \quad (2)$$

$$c_{jk} \sim N\left(\lambda_{jk}, \tau_{kj}^2\right) \quad (3)$$

$$\varepsilon_{ij} \sim N\left(0, \sigma_j^2\right) \quad (4)$$

where X_{ij} is the isotope value j of the mixture i, in which i = 1, 2, 3,…, N and j = 1, 2, 3,…, J; S_{jk} is the source value k on the isotope j (k = 1, 2, 3,…, K) and is normally distributed with mean μ_{jk} and standard deviation ω_{kj}^2; p_k is the proportion of source k, which is estimated by the SIAR model; c_{jk} is the fractionation factor for isotope j on source k and is normally distributed with mean λ_{jk} and standard deviation τ_{kj}^2; and finally ε_{ij} is the residual error representing the additional unquantified variation between individual mixtures and is assumed to be normally distributed with mean 0 and standard deviation σ_j^2.

6.3.4 Delineation of the main Recharge-Discharge Pathways

The stable isotopes of water δ^2H_{H20} and $\delta^{18}O_{H20}$ values were used by **[29]** to study the response of

the hydrologic system to the seasonal variation of the isotope content in the recharge waters, estimating the Local Meteoric Water Line (LWML) and the local Isotopic Altitudinal Lines (IALs) for $\delta^{2}H_{H20}$ and $\delta^{18}O_{H20}$. In this work, the IAL is used to support the building of the hydrogeochemical conceptual model. To this end, the main Recharge-Discharge Pathways (RDP) of the system are delineated based on (1) the estimated centroid of the recharge zone elevation associated to every spring, and (2) the geological structure of the PCM.

6.3.5 Inverse hydrogeochemical modeling for the quantification of chemical processes

Using the PHREEQC code **[70]**, mass-balance inverse geochemical models are applied to analyze the chemical changes that occur from the recharging areas to the discharge points, and to validate the conceptual hydrogeochemical model of the PCM. Inverse modelling is based on a geochemical mole-balance model, which calculates the transfer of moles of minerals and gases that must enter or leave a solution, while accounting for the differences in an initial and a final water composition along a hypothetic GW flow line. In this work, the study is focused on 14 springs that are considered representative of the main Recharge-Discharge Pathways (RDP) of the system, which were previously defined based on the recharge elevations inferred by means of the IALs. The differences in hydrogeochemical composition between the springs are assumed due exclusively to reactions between GW and the minerals within the PCM. The selection of the solid phase reactants is based on the geological knowledge of the main lithologies, which comprise calcite, dolomite, gypsum and halite. In addition, it is also considered soil gas CO_2. The existence of marl and clay materials in the limits of the PCM as in the Cretaceous and Triassic materials, suggests that ionic exchange-like processes between cations Ca, Mg, Na, and K and an exchanger X might occur. As all water samples are undersaturated according to the calculated saturation index, the inverse modeling was constrained so that dolomite, gypsum and halite only dissolve whereas calcite is allowed to both dissolving and precipitating. In summary, the expected reactions responsible of the groundwater composition can be defined as:

- Dissolution of carbonate minerals such as calcite and dolomite and precipitation of calcite according to equation (5) and (6) **[89]**. Equation (7) is obtained as the sum of equations (5) and (6), and it shows that the molar ratio Ca^{2+}/Mg^{2+} is 3:1.

$$2CaCO_3 + 2CO_2(g) + 2H_2O \leftrightarrow 2Ca^{2+} + 4HCO_3^- \quad (5)$$

$$2CaMg(CO_3)_2 + 4CO_2(g) + 4H_2O \leftrightarrow Ca^{2+} + Mg^{2+} + 8HCO_3^- \quad (6)$$

$$2CaCO_3 + 2CaMg(CO_3)_2 + 6CO_2(g) + 6H_2O \leftrightarrow 3Ca^{2+} + Mg^{2+} + 12HCO_3^- \quad (7)$$

- Dissolution of evaporite minerals such as gypsum and halite, according to equations (8) and (9).

$$CaSO_4 \cdot 2H_2O \leftrightarrow Ca^{2+} + SO_4^{2-} + 2H_2O \quad (8)$$

$$NaCl \leftrightarrow Na^+ + Cl^- \quad (9)$$

- Dedolomitization processes according to equation (10) [71], which causes an increment of Ca^{2+} due to gypsum dissolution (as indicated in equation 8) and precipitation of calcite.

$$CaMg(CO_3)_2 + CaSO_4 \cdot 2H_2O \leftrightarrow 2CaCO_3 + Mg^{2+} + SO_4^{2-} + 2H_2O \quad (10)$$

- Ion exchange reactions due to weathering reactions in marls, shales and clays associated to Triassic and Cretaceous layers, according to the following equations (11-14).

$$2NaX + Ca^{2+} \leftrightarrow 2Na^+ + CaX_2 \quad (11)$$

$$2NaX + Mg^{2+} \leftrightarrow 2\,Na^+ + MgX_2 \quad (12)$$

$$2KX + Ca^{2+} \leftrightarrow 2K^+ + CaX_2 \quad (13)$$

$$2KX + Mg^{2+} \leftrightarrow 2K^+ + MgX_2 \quad (14)$$

Silicate minerals in the aquifer were generated in the marine environment in which the carbonates were deposited, and this affects the sorbed cation composition. Dispersed silicates in the carbonate rock matrix may progressively contribute Na^+ as carbonates are dissolved, as well as a fraction of the K^+, at the time that HCO_3 increases This is a minor process. Marl and clay layers may contain evaporitic minerals that slowly diffuse out, contributing Cl^-, SO_4^{2-} and cations that correspond approximately to halite and gypsum dissolution, although with a modified cation composition. All these processes can be assumed steady in a hydrogeological system under natural conditions, so cation exchange is minor and not significant. However, the silicate weathering and porewater diffusion in clays produce similar results as cation exchange, and therefore they are considered as such for general treatment and called cation exchange-like process.

There are no data on soil CO_2 partial pressure and therefore this value and the carbon isotopic

composition must be assumed. Then, the CO_2 dissolved in the meteoric water recharging the aquifer is assumed to be (1) in equilibrium with atmospheric CO_2 partial pressure for elevations above 1900 m a.s.l. and equal to $\log(PCO_2) = -3.2$ (no vegetation), and (2) equilibrated with the soil CO_2 for elevations below 1900 m a.s.l., with the CO_2 content estimated by the following equation **[71]** to consider the existence of decaying vegetation and root respiration:

$$\log(PCO_2) = -3.47 + 2.09(1 - e^{-0.00172 \cdot ETP}) \quad (15)$$

where PCO_2 corresponds to the mean growing-season soil CO_2 partial pressure and ETP is the mean potential evapotranspiration. The mean ETP in the PCM is 525 mm/yr **[90]** and the obtained $\log(PCO_2)$ is -2.23.

Considering the geological structure of the PCM along with the estimated average recharge altitude associated to every sampled spring, a total of fourteen representative Recharge-Discharge Pathways, named as RDPs 1 to 14 (**Figure 6. 3**) have been considered for inverse hydrochemical modeling with PHREEQC.

Every RDP tries to recreate the GW flow line integrating all the processes driving the hydrochemical composition of the corresponding spring discharge, from which the RDP adopts the cluster type. Therefore, the RDPs are classified in clusters as:

- RDP - Cluster A: RDP-1 to RDP-4 correspond to the four regionals springs (M-22, M-43, M-31 and M-25). RDP-05 is related to the springs located in the upper part of the PCM (M-16, M-17, M-18 and M-19) that discharge to the north and are oversaturated with respect to dolomite. On the contrary, RDP-06 refers to the other two springs located in the upper part of the PCM (M-14 and M-15) draining to the south, which are under-saturated with respect to dolomite. RDP-07 is related to the five local springs M-06, M-03, M-04, M-07 and M-39 of Cluster A that drain the southern part of the PCM through fractures that affect the PPEc unit or contact the underlying Kgp unit.
- RDP - Cluster B: RDP-08 represents the flow line associated with the four springs M-01, M-02, M-36 and M-21 that drain through the southeast part of the PCM while being affected by the presence of the Eocene-Oligocene Beuda's gypsum Formation. RDP-09 and RDP-10

are associated with the local springs M-10 and M-09 respectively. According to the recharge elevation zone associated to these springs, the meteoric water enters the system through the Kgp unit. Then GW flows downstream through the Kat and KMca units and finally discharges through the Tk unit. RDP-11 is associated with M-28 spring whose recharge zone is in the PPEc unit. Then GW flows through the Cretaceous and discharges through the Tk unit.

- RDP - Cluster C: RDP-12 and RDP-13 correspond to local RDPs running through the Tk unit that contains halite. These two RDPs are located at the NW and W of the PCM, respectively. Finally, RDP-14 is a flow path out of the PCM boundaries and associated to spring M-23, a spring with a water-type like that of the neighboring spring M-22 (**Figure 6. 2**A).

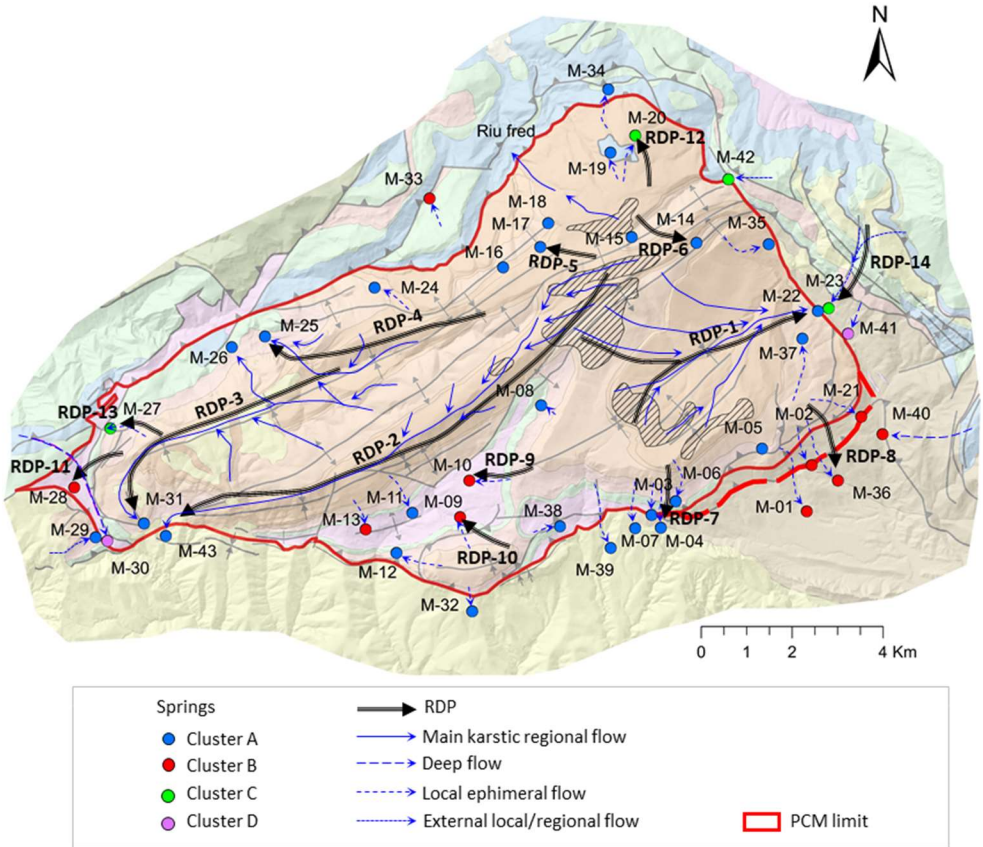

Figure 6. 3. Recharge-Discharge Pathways (RDP) considered on the geological map (**Figure 6. 1**), to be analyzed with PHREEQC. The cluster associated to every RDP coincides with that of the corresponding

6.4 Results and discussion

The hydrochemical and isotope data of GW corresponding to the different sampling campaigns conducted in this work are reported in Tables A1 to A5, Appendix A.

6.4.1 Saturation indexes

The saturation indexes (SI) were calculated using PHREEQC® **[70]**. The SI relative to calcite for all the dataset ranges from 0 to 0.82 indicating calcite saturation to oversaturation throughout the PCM (**Figure 6. 4**A). The SI relative to dolomite ranges from -1.32 to 0.61, except for a 2.3 value corresponding to the deep flow brine spring M-30 (**Figure 6. 4**B). The SI relative to gypsum ranges from -3.26 to 0.27 (the highest value in M-30), between under-saturated to almost equilibrium conditions within the Triassic (Keuper) window and the Tertiary window (Eocene-Oligocene Beuda's gypsum Formation which is pinched out within the South Pyrenees thrust fault in the front SE of the PCM) affecting the springs M-21, M-40, M-01, M-02 and M-36 (**Figure 6. 4**C).

Figure A4 shows the relationship between SI relative to calcite, dolomite, gypsum, and halite with respect to TDS [mg/L], besides SI of gypsum with respect to SI of halite, and SI of calcite with respect to SI of gypsum. In all cases, it is possible to observe a clear separation between all the clusters A, B, C and D. In addition, a trend of increasing TDS can be observed from clusters A, C towards cluster B and later to the extreme D.

In general, the springs of Cluster A have lower TDS than those of Cluster B. Figure 5A shows that despite being all the samples in equilibrium or slightly supersaturated with respect to calcite, Cluster A shows much less TDS content than Cluster B. Additionally, Figure 5B indicates that most of the samples are subsaturated relative to dolomite, except in four samples from Cluster A (springs M-16, M-17, M-18 and M-19 located in the northern part of the PCM that discharge the PPEc unit in contact with the PEci unit), four samples from Cluster B (M-28, M-36, M-09, M-13), and one sample from Cluster C (M-20) that is close to the equilibrium relative to dolomite. Figure 5C shows how all the springs but one (M-30 from Cluster D) are under-saturated with respect to gypsum. Moreover, here the separation between Clusters A and C with respect to B and D can be clearly

observed, indicating that the samples of Cluster B are influenced by Triassic (Keuper) and Tertiary (Beuda Formation) formations that contain gypsum. Furthermore, the clusters separation is even clearer when looking at the relationship between SI relative to halite and TDS (Figure 5D), SI of gypsum and SI of halite (Figure 5E) and less evident for SI of calcite and SI gypsum (Figure 5F).

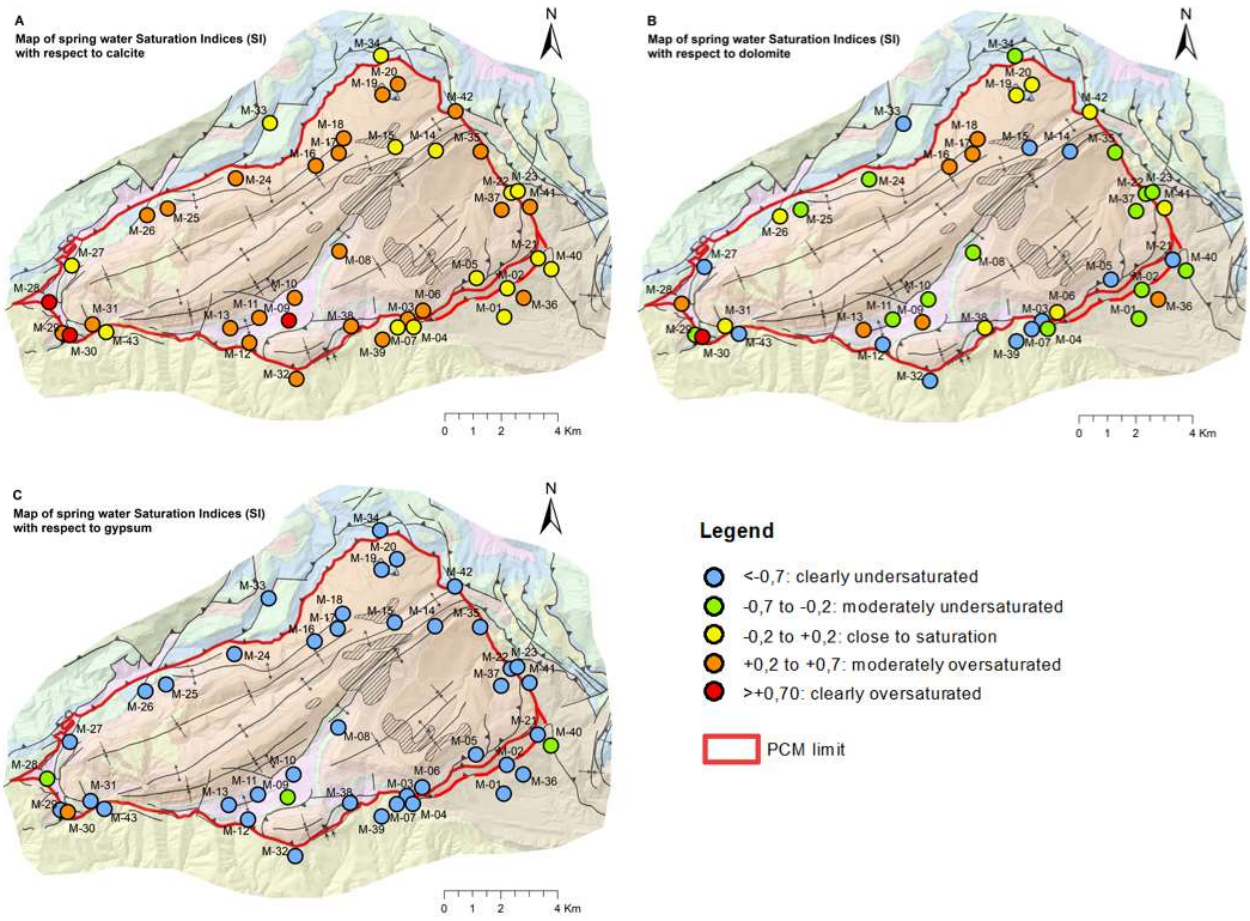

Figure 6. 4. Saturation index maps relative to calcite **(A)**, dolomite **(B)** and gypsum **(C)** in GW for the sampled springs.

6.4.2 Identification of hydrogeochemical processes explaining the spring clusters

To determine the main rock-water interactions within the PCM system driving the hydrogeochemical composition of GW, it is necessary to focus on the relationships between major

cations and anions. This will help to decipher the main hydrogeochemical processes conditioning the cluster definition presented by **[59]**. The data presented in this analysis for every spring corresponds to average content values for the monitored period Sept 2013-Oct 2015 (Table A2.1 Appendix A).

The relationship between Ca and SO_4 is depicted in **Figure 6. 5A**. The samples of Cluster B follow the line of slope 1:1, thus indicating most probably the dissolution of gypsum as the origin of sulfate in Cluster B, while Cluster A and C are not clearly related with this process. This suggests that calcite and dolomite are not the primary sources of Ca for Cluster B, but they might be for Cluster A and C.

The relative contribution of calcite and dolomite in the carbonate weathering processes can be approached by looking at the molar ratio rCa/rMg (r = concentration in meq/L) (**Figure 6. 5B**). A molar ratio of 1 (1:1 slope line) indicates pure dolomite contribution (equation 6, ratio values between 1 and 3 indicate a dominance of dolomite dissolution with some calcite contribution, rCa/rMg = 3 indicates dissolution of both calcite and dolomite according to equation (7). Larger ratio values mean a predominance of calcite dissolution plus certain dolomite contribution, and finally, rCa/rMg = 10 represents a total contribution of calcite, beyond the evident contribution of sulphate dissolution in Cluster B, as indicated in **Figure 6. 5A**. As can be shown, all the GW samples have rCa/rMg >1. Almost 50% of the molar ratio values range between 3 and 10, and 16% between 1 and 3. Cluster A shows twelve springs with rCa/rMg >10, eleven springs with 3 < rCa/rMg < 10, four springs with rCa/rMg < 3. The four springs of this latter case (M-16, M-17, M-18, and M-19) also show saturation indices (SI) relative to dolomite >1. Dolomite is present in the recharge area within the PPEc unit. Cluster B contains two springs (M-10 and M-21) with rCa/rMg >10, seven springs with 3 < rCa/rMg < 10, and one spring (M-36) with rCa/rMg < 3. Cluster C shows one spring (M-27) with rCa/rMg >10, two springs (M-23 and M-42) springs with 3 < rCa/rMg < 10, one spring with rCa/rMg < 3. The two springs of Cluster D show rCa/rMg values equal to 0.18 (M-30) and 4.32 (M-41). These results suggest that, except for the 4 cited samples from Cluster A that drain the upper part of the PCM, where the materials associated with the PPEc unit are richer in dolomite, the contribution of dolomite increases as the discharge altitude decreases.

The influence of calcite dissolution on Cluster A can be observed looking at the ratio $rCa/rHCO_3$ in **Figure 6. 5C**. Here, the samples of Cluster A plot aligned along the line of slope 1:1 representing the stoichiometric ratio of calcite dissolution. To evaluate the influences of the combined dissolution of calcite and dolomite on karst groundwater chemistry, **Figure 6. 5D** shows the ratio between rCa+rMg respect $rHCO_3$. The plot shows that one part of the data for Cluster A fits the 3: 1 slope line, suggesting that both dissolution of calcite and dolomite contributes defining groundwater chemistry, whereas the remainder seems to be concentrated at the base of the 10: 1 slope indicating exclusive contribution from calcite. In the case of Cluster C, the four springs plot displaced above while maintaining the slope 1:1, which might be related to ion exchange-like processes adding Ca into dissolution according to equation 11. The samples of Cluster B are clearly scattered relative to the 1:1 slope line, thus confirming that they have other Ca sources than calcite and/or dolomite dissolution.

To confirm that dissolution of carbonates (calcite and dolomite) and evaporites (gypsum and halite) are the dominant processes affecting the hydrochemical features of the different clusters, and that ion exchange is a minor process driving the hydrogeological composition of GW, the relationship between (rCa + rMg) and ($rHCO_3$ + rSO_4) is presented in **Figure 6. 5E**. Most of the springs match the line 1:1 with just very small shifts for Clusters B and C, thus suggesting the existence of a very small ion exchange-like process adding Ca and/or Mg into dissolution (equations 11 and 12). **Figure 6. 5F** shows the scatterplot of rNa content versus rCl. In general, the gravity center of all the clusters is below the line of 1:1 slope, reflecting a chloride excess that principally comes from the atmospheric chloride deposition, although a minor part, especially in the case of samples from Cluster B and C, might be attributed to silicate weathering and ion exchange-like reactions in marls, shales and clays associated with the Triassic and Cretaceous layers through which the groundwater of these springs interacts.

In this regard, and to get more information about the possible contribution of such exchange-like process, Schoeller (1965) **[91]** propose using the chloro-alkaline indices indexes, CAI_1 and CAI_2, of common use in hydrogeochemical studies, which are defined as:

$$CAI\_1 = \big(rCl - (rNa + rK)\big)/rCl \quad (16)$$

$$CAI\_2 = \big(rCl - (rNa + rK)\big)/(rHCO_3 + rSO_4 + rCO_3 + rNO_3) \quad (17)$$

Values >0 of both indexes indicate ion exchange and ion exchange-like processes in which dissolved Na and/or K are retained while Ca and/or Mg are released, or Ca-rich brines are incorporated. Values <0 point to a reverse ion exchange prevalent process [91] or weathering of alkaline ion-rich silicates. In this line, most of the samples does not show a clear sensitivity of CAI_2 with respect CAI_1 (Figure 6A). Nevertheless, the samples of Cluster C are clearly located in the first quadrant where both CAI_1 and CAI_2 are >0.

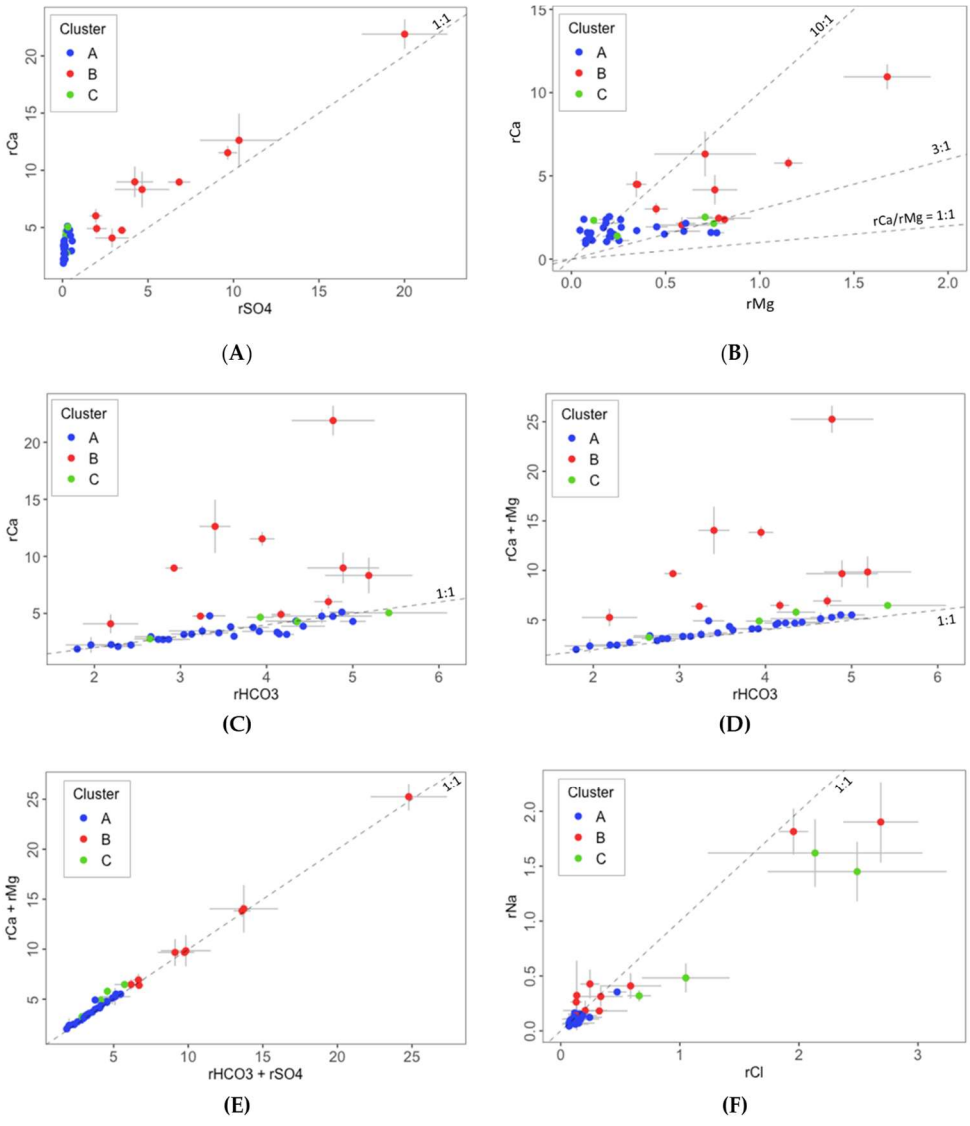

Figure 6. 5. Bivariate relationship graphs of major ions in spring water samples **(A)** rCa/rSO_4; **(B)** rMg/rCa; **(C)** $rHCO_3/rCa$; **(D)** $(rMg+rCa)/rHCO_3$; **(E)** (rCa + rMg) and $(rHCO_3 + rSO_4)$; **(F)** rNa vs. rCl), where 'r'

means that the concentration is given in meq/L.

The **Figure 6. 6A** shows the plot of (rCa + rMg) – (rSO_4 + $rHCO_3$) versus (rNa + rK - rCl). The dependent variable represents the increment of Ca and Mg that are attributed to processes that exclude weathering by carbonates and evaporites (dissolution of calcite, dolomite and gypsum) while the independent variable gives information of the increment of Na generated by processes other than halite dissolution. A linear relation between these two variables with a slope equal to -1 indicates the significance of ion exchange-like processes as an important factor controlling the groundwater chemistry and its evolution. In the case of the samples of the PCM, the slope of the regression line between (rCa + rMg) – (rSO_4 + $rHCO_3$) and (rNa + rK - rCl) is -0.90 (**Figure 6. 6B**). Such relationship is basically conditioned by the samples of cluster B and C, which would suggest that there may be indeed ion exchange-like processes between the monovalent ions Na and K, and the bivalent Ca and Mg. Moreover, values of (rCa + rMg) – (rSO_4 + $rHCO_3$) > 0 indicate adsorption of Na and release of Ca [92].

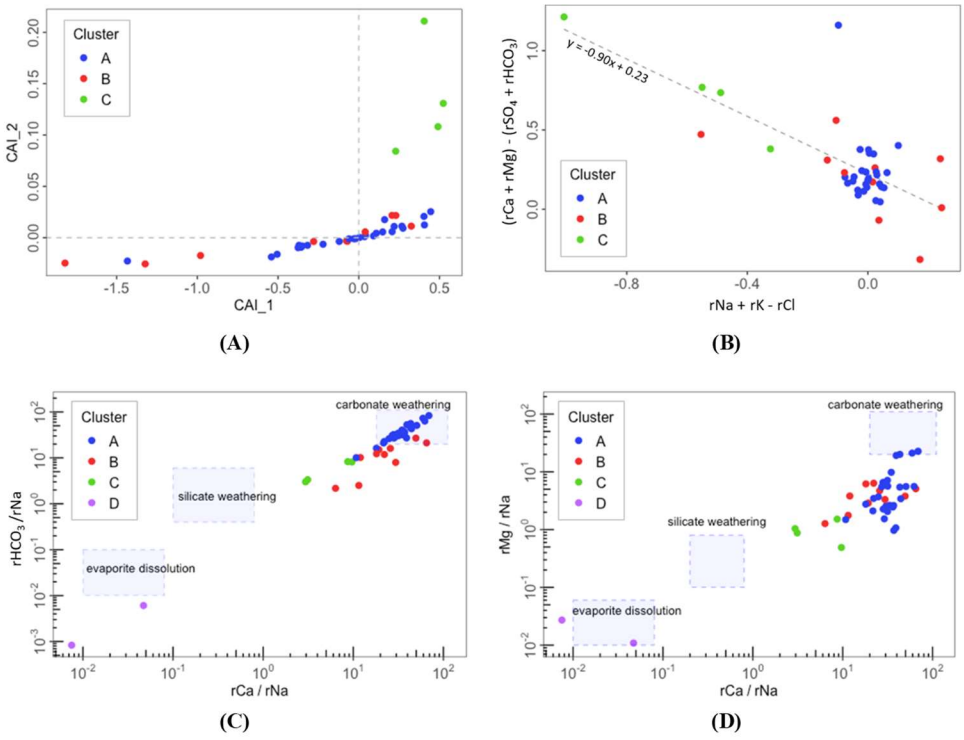

Figure 6. 6. (**A**) Chloro-Alkaline Indexes (CAI_1 and CAI_2) relationship; (**B**) (rCa + rMg) - (rSO_4 + $rHCO_3$) vs. (rNa + rK - rCl); (**C**) bivariate mixing diagrams of Na-normalized HCO_3 vs. Ca; and (**D**) Na-normalized Mg vs. Ca; where 'r' means that the concentration is in meq/L.

The relationship between both HCO_3/rNa and rMg/rNa vs. rCa/rNa, in **Figure 6. 6C** and **Figure 6. 6D** respectively, can be used to check the main geochemical process in the system [15, 61–63]. In these figures, it can be shown how the origin of HCO_3 for the samples of Cluster A is carbonate dissolution. Cluster C and some samples of Cluster B tend to the silicate weathering zone, which also would be related to sodium-calcium ion exchange-like in the weathering of shales. Besides, the two samples of Cluster D, corresponding to the deep flow brines, fit in the evaporite window domain.

6.4.3 Aquifer recharge altitude based on δ^2H and δ^{18}O in precipitation and GW.

The estimation of the recharge elevation associated to the springs sampled during this study is conducted by projecting the mean isotopic content of δ^2H and δ^{18}O associated to every spring discharge to the corresponding IAL obtained by **[33],** which are shown in **Figure 6. 7**. Table 1 shows the mean recharge elevation intervals for each cluster. The slope of the isotopic altitudinal line for precipitation ($\nabla_z\delta_P = \Delta\delta_P/\Delta z$) is -1.9 and –12.1 ‰/km for δ^{18}O and δ^2H, respectively. The overall isotopic altitudinal line for GW (IAL_{GW}) shows a slope ($\nabla_z\delta_{GW} = \Delta\delta_{GW}/\Delta z$) of -1.4 and 9.5 ‰/km for δ^{18}O and δ^2H, respectively. The slope values are larger than those corresponding to the isotopic altitudinal line of precipitation (IAL_P), indicating the existence of aquifer recharge along the mountain slope and mixing at the sampling point, a process also known as slope effect **[96]**.

Table 6. 1 and **Figure 6. 7**. show the values and graphs of slope of IAL_{GW} for the different clusters. Table A2.2 in Appendix A summarize the isotope data for each spring, Figure A3 shows the IAL_{GW} graphs for all water samples, including snow water and water ponds, and Figure A4 shows the location of the sampling points for the 10 snow samples and water ponds. As can be shown in **Figure 6. 7**., the steepest gradient, and therefore the highest role played by slope recharge, corresponds to Cluster A, whose springs show typically a Ca-HCO_3 water composition that is related to the Tertiary karst aquifer, which presents a well-developed epikarst zone, thus favoring the infiltration along the mountain slopes where this Tertiary formation crops out.

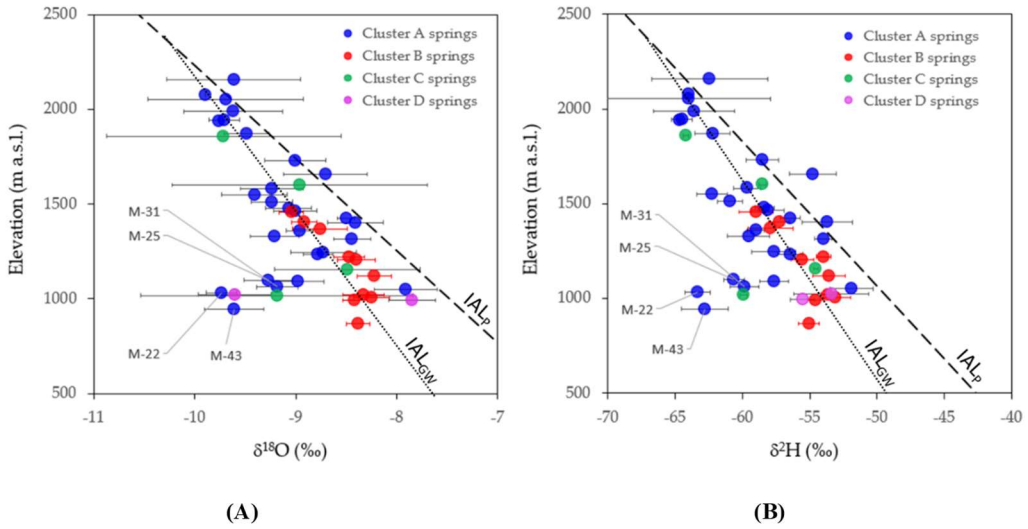

Figure 6. 7. Relationship between elevation the isotopic content in GW and the isotopic altitudinal line defined by Herms et al. (2019) **[29].** The dashed and dotted lines correspond to the isotopic altitudinal lines of precipitation (IAL_P) and groundwater (IAL_{GW}), respectively. **(A)** $\delta^{18}O$, and **(B)** $\delta^{2}H$.

Table 6. 1 Recharge elevation associated to GW clusters in the PCM.

	Recharge elevation (m a.s.l.)			$\nabla_z\delta_{GW}$ (‰/km)	
	Average	Min	Max	$\delta^{18}O$	$\delta^{2}H$
Cluster A	1823	1259	2228	-1.53	-9.76
Cluster B	1541	1409	1758	-1.46	-9.65
Cluster C	1776	1557	2010	-1.21	-7.95
Cluster D	1193	1061	1324	-1.16	-9.27

6.4.4 Quantification of hydrogeochemical processes along the recharge-discharge pathways.

The principal results obtained with the application of PHREEQC are depicted in **Figure 6. 8**, which shows the contribution of the different species to all the 14 RDPs considered in the inverse modelling exercise that has been conducted. **Table 6. 2** summarises the complete results for clusters A, B and C. Additionally, Table A7 Appendix A provides the complete data set of results.

The predominant geochemical process in Cluster A is the dissolution of carbonates, mainly calcite (37% of dissolved species), followed by dolomite (9.9%) with a bit part of gypsum (1.1%), halite (2.2%) and a residual part corresponding to ion exchange-like processes (0.8%), which agrees with the observations obtained in the scatterplots of ions. The predominance process in Cluster B is dissolution of gypsum (52.3%), followed by dolomite (12.1%), halite (9.9%) and calcite (4%), and a small contribution of ion exchange-like processes (3.2%). In this case, this highlights the great range of gypsum dissolution, with values of 1.64E-03 mol/L (M-36 in RDP-08 with Ca-SO_4-HCO_3 water type), 5.23E-03 mol/L (M-10 in RDP-09 with Ca-SO_4-HCO_3 water type), 2.11E-03 mol/L (M-09 in RDP-10 with Ca-SO_4 water type) and 9.94E-02 mol/L (in the M-28 in RDP-11 with Ca-SO_4), which are highly conditioned to the typology and extension of Keuper outcrops with gypsum (Tk) and Tertiary with gypsum (PExb), as well as the transit time of groundwater through these materials. The presence of calcite precipitation with dolomite and gypsum dissolution also stands out, which is an indication of de-dolomitization processes in RDP-08 and RDP-11. This process may be especially important in sample M-28 from RDP-11, which shows SI values of 0.70 respect to calcite, 0.55 respect to dolomite and -0.24 respect to gypsum **[71]**.

Table 6. 2 Summary of the results obtained by the inverse modeling using PHREEQC. For every RDP cluster, the results are given in terms of the average of the total mass of dissolved species in GW, and the corresponding percentage of mass of the dissolved species.

Cluster	Total mass dissolved (mol/L)	Calcite (%)	Dolomite (%)	$CO_{2(g)}$ (%)	Gypsum (%)	Halite (%)	Ca X_2 (%)	Mg X_2 (%)	Na X (%)	K X (%)
RDP-A [(a)]	3.25E-03	37.02	9.87	48.25	1.11	2.20	-	0.75	-	0.81
RDP-B [(b)]	9.73E-03	4.00	12.15	17.12	52.23	9.89	-	3.21	0.56	0.83
RDP-C [(c)]	4.61E-03	24.81	7.61	32.03	1.20	25.16	6.18	2.99	-	0.02

(a) DRP-01, DRP-02, DRP-03, DRP-04, DRP-05, DRP-06, DRP-07; (b) DRP-08, DRP-09, DRP-10, DRP-11; (c) DRP-12, DRP-13, DRP-14

Although it has not been modeled, it is worth noting that, according to Municio (2017) **[97],** feldspar is encountered in the Cretaceous layers (Kat, KMca units), so a small contribution of feldspar dissolution in the weathering processes might be also possible, to explain the contribution of Na

and K [98]. In the case of Cluster C, the predominant geochemical process is the dissolution of halite (25.2%), but with a similar contribution of calcite dissolution (24.8%), followed by dolomite (7.6%), with a bit part of gypsum (1.2%) and reverse ion exchange-like process in the weathering of shales, where the Ca (6.2%) and Mg (3%) ions in the aquifer matrix replace Na in solution that comes probably from halite dissolution.

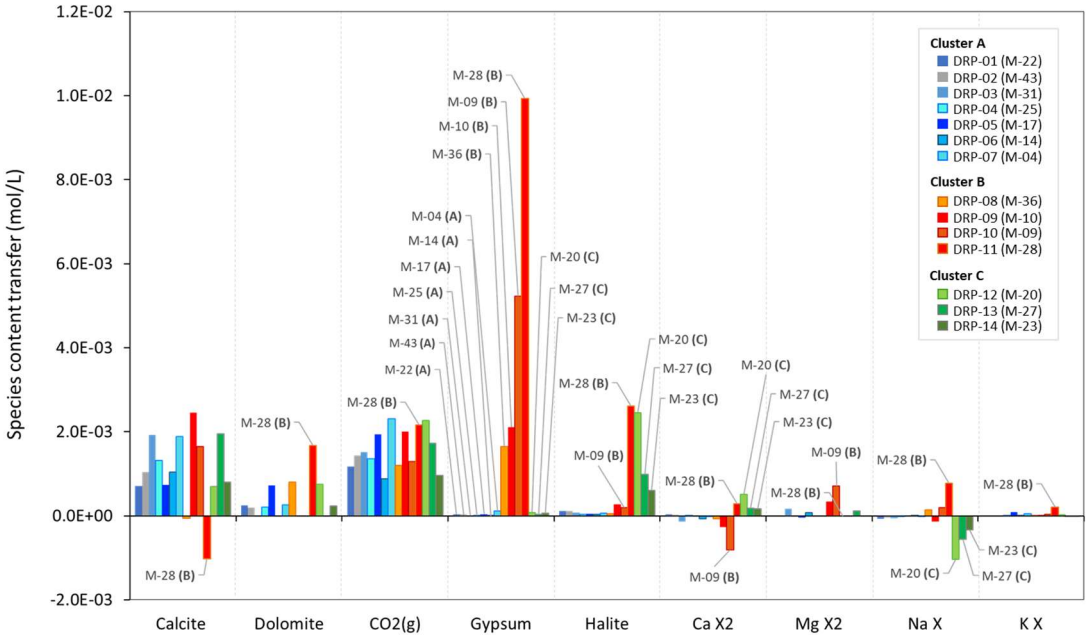

Figure 6. 8. Graph of the inverse geochemical results using PHREEQC for the different RDPs (recharge-discharge-pathways) and their associated reference spring. Results in moles per liter of H_2O. Positive and negative values indicate species dissolution and precipitation, respectively.

6.4.5 Identification of SO_4 in GW based on stable isotopes.

To infer the origin of SO_4 in GW, the relationship between $\delta^{34}S_{SO_4}$ and $\delta^{18}O_{SO_4}$ is considered for the different groundwater samples. In this analysis it is included the isotopic content obtained for the eight gypsum rock samples collected in the PCM area (**Figure 6. 9**). The overall mean $\delta^{34}S_{SO_4}$ and mean $\delta^{18}O_{SO_4}$ in GW are +6.5‰ and +9.5‰, respectively, with a large variation throughout the study area, between -17.5 and +20.4‰, and between +3.4 and +14.3‰, respectively. Based on

the geological context, and supported by all available isotopic groundwater compositions, eight possible sources of SO_4 are considered: (1) Atmospheric deposition of SO_4 (Satm); (2) SO_4 derived from fertilizers (F); (3) SO_4 derived from sewage (Sew); (4) SO_4 derived manure (M); (5) SO_4 derived from soil (S); (6) SO_4 derived from weathering (oxidation) of sulfide minerals mainly related to Cretaceous carbonate rocks (SO); (7) dissolution of SO_4 from evaporites in the Triassic sequence (Tri), and (8) dissolution of SO_4 from evaporites in the Tertiary sequence (Ter).

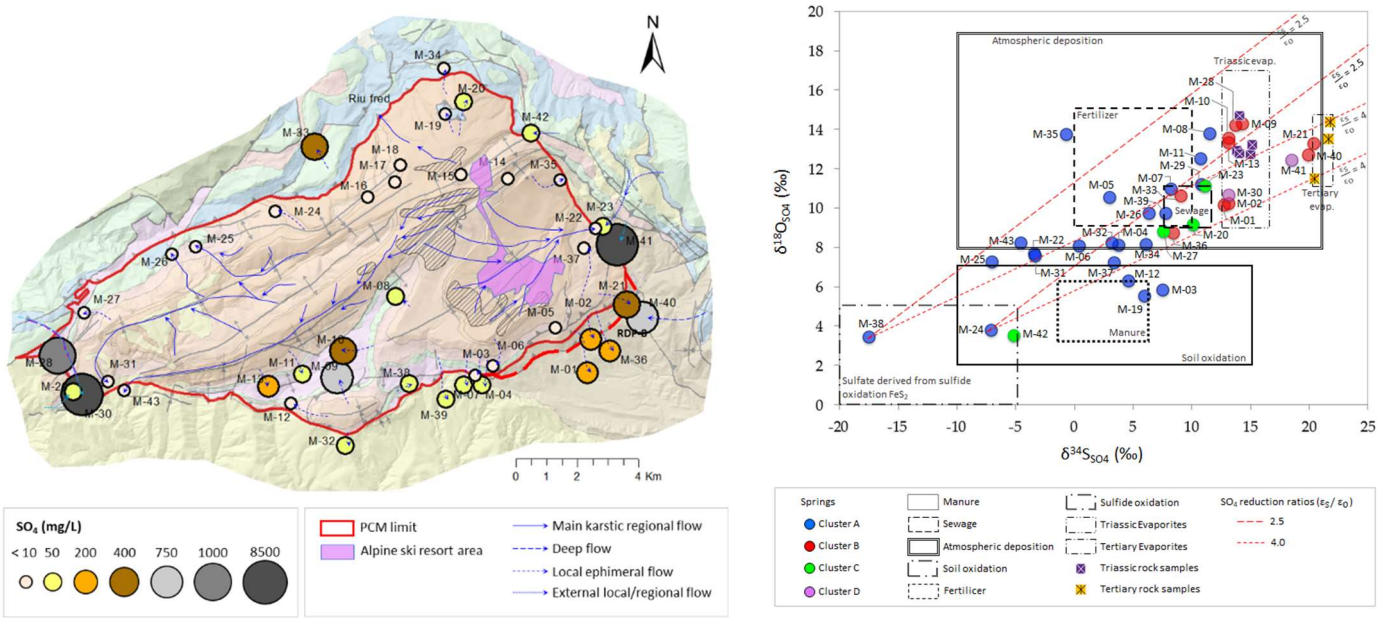

(A) **(B)**

Figure 6. 9. (A) Map of sulfate dissolved in GW. The values correspond to averaged concentration for all the GW sampling campaigns conducted during the period Sep 2013 – Oct 2015. **(B)** Dual isotope scatterplot using $\delta^{18}O_{SO_4}$ and $\delta^{34}S_{SO_4}$. The areas of sulfates are derived from (1) sulfide oxidation **[99]**; (2) manure **[100]**; (3) soil **[101]**; (4) atmospheric deposition **[102];** (5) fertilizers **[103]**; (6) sewage **[104]**; (7) Triassic evaporites **[105]** and (8) Tertiary evaporites **[106]**. The long and short dashed red lines define the isotopic fractionation range ($\varepsilon^{34}S/\varepsilon^{18}O_{SO4}$) in SO_4 reduction reactions, varying between 2.5 and 4, respectively **[107]**.

Table 6. 3 Mean $\delta^{34}S_{SO_4}$, $\delta^{18}O_{SO_4}$, $\delta^{15}N_{NO_3}$ and $\delta^{18}O_{NO_3}$ isotopic content along with the sulfate and nitrate concentrations associated to the four GW clusters defined in the PCM.

	Cluster A	Cluster B	Cluster C	Cluster D
$\delta^{34}S_{SO_4}$(‰)	3.65	13.21	8.93	15.89
$\delta^{18}O_{SO_4}$(‰)	8.07	12.95	8.93	11.51
SO_4 (mg/L)	6.9	213.3	11.5	4701
$\delta^{15}N_{NO_3}$(‰)	3.27	3.80	3.91	8.65
$\delta^{18}O_{NO_3}$(‰)	2.88	2.55	1.40	3.90
NO_3 (mg/L)	10.1	16.8	10.4	5.6

Table 6. 3 shows the mean isotopic content by clusters. Table A4 and A5 Appendix A provide the average values for $\delta^{34}S_{SO4}$ and $\delta^{18}O_{SO4}$ of samples available of all springs and the corresponding average SO_4 concentration and the data for the rock samples collected for the characterization of sulfate isotopes content in Triassic and Tertiary gypsum in the PCM study area.

The results suggest that the main source of SO_4 for Cluster A might be related to all the factors, from pyrite oxidation to Beuda gypsum dissolution. Due to their intermediate isotopic composition, the role of atmospheric deposition, fertilizers and sewage cannot be determined. Fertilizers has high sulphate contents **[103,108]** and cannot be discarded because they are applied in Alpine ski resort areas to help the grass on the slopes reaching a maximum growth, and those applied in the agricultural soils, which are planted with potato in some areas of the PCM. The sample with the lowest $\delta^{34}S_{SO_4}$ content (-17.5‰, in M-38 of Cluster A) is assumed to be, according to Municio (2017) **[97]**, the result of sulfide mineral weathering. The spring M-38 is in the upper limit of the 'sulphide oxidation field' as defined by Van Stempvoort and Krouse (1994) **[99]**. Here, the sulfide minerals correspond to pyrites from marls with lignite materials, such as those appearing in the Upper Cretaceous - limestone-marl alternations and calcarenites (Kat, KMca) formations of the PCM.

The GW samples from Cluster B show a clear relationship with the Triassic (Keuper) window (M-09, M-10, M-28) and Tertiary window (Eocene-Oligocene Beuda's gypsum Formation pinched out

within the South Pyrenees thrust fault in the front SE of the PCM) (M-40, M-21), and partially mixed with soil inputs and atmospheric deposition (M-36 and M-33). Samples M-01 and M-02 are geologically affected by Tertiary gypsum. This has been observed directly in the field, so their position in the graph could be explained as a mixture of this source with soil sulfate.

The samples of Cluster C are mostly related to Triassic evaporites but mixed with other sources. In the case of M-20 (Cluster C), the isotopic content is consistent with the existence of a klippe of Triassic with Keuper outcropping, which affects the spring catchment, and with some contributions of fertilizers related to the cross-country (Nordic) ski resort, which is close to the spring. The isotopic composition of springs M-23 and M-42 suggests an origin in the soil. Nevertheless, in the case of M-42 there is an additional contribution of sulfate from atmospheric deposition.

The origin of the isotopic composition of the springs belonging to Cluster D is related with the Triassic materials. The deep flow brine in spring M-30 match perfectly inside the Triassic window, whereas the deep flow brine in spring M-41 falls between the Triassic and the Tertiary window, suggesting that the isotopic composition of this spring it is affected by SO_4 contributions from these two origins. This is consistent with the structural geological context in which the spring M-41 is located, where the PCM and the Pedraforca thrust sheets coexist and are related to the ductile materials of the Keuper. As a result, the isotopic fingerprint of the Tertiary gypsum is added to that of the Triassic materials into the GW sampled in this spring.

6.4.6 Proportional contribution of SO4 sources in GW in the PCM

To enhance the existing knowledge regarding the sources of sulfate in groundwater, and to better explain the sources contribution, a Bayesian isotope mixing model was prepared using the SIMMR package for R (an updated version of the SIAR model **[76,77]. Figure 6. 10** presents the corresponding outputs aggregated for the four cluster A, B, C and D with a horizontal boxplot showing the probabilistic contributions for each SO_4 source.

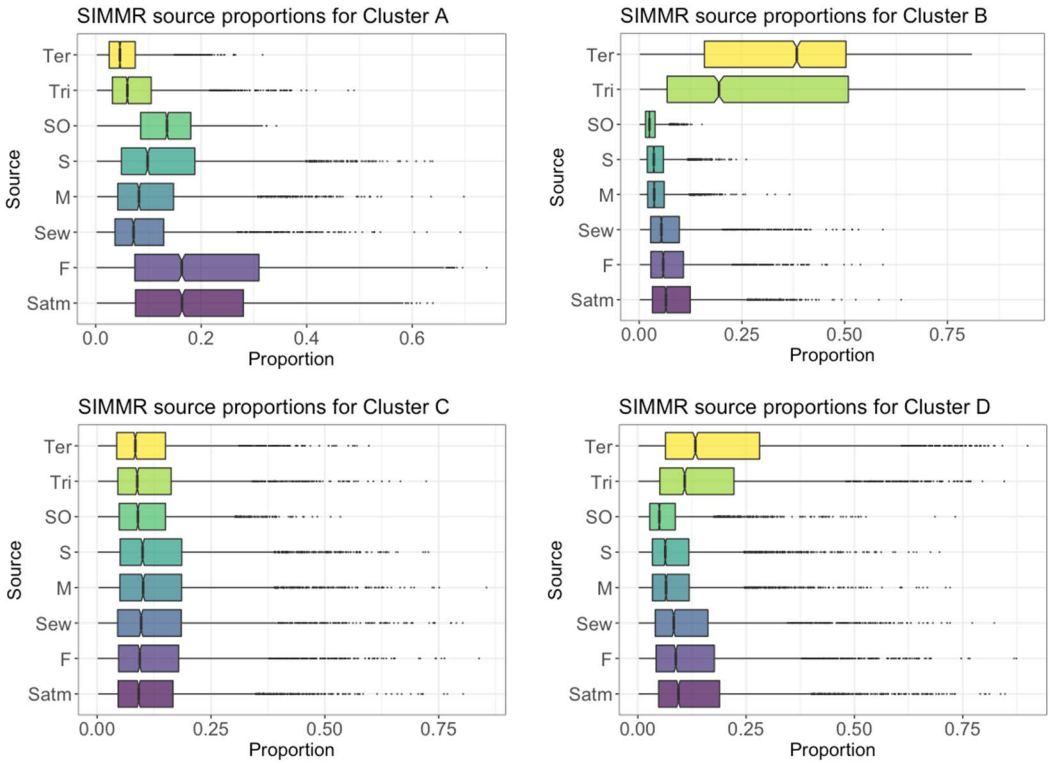

Figure 6. 10. Bayesian isotope mixing model corresponding to sulfate for clusters A, B, C and D. The considered sources are the same of the biplots (**Figure 6. 9**): (SO) sulfide oxidation; (M) manure; (S) soil; (Satm) atmosphere deposition (F) fertilizers; (S) sewage; (Tri) Triassic evapo-rites and (Ter) Tertiary evaporites.

The results of the model indicate that the greatest contribution to springs associated with cluster A, which are mostly recharged in areas with little development of soil cover, comes from fertilizers (proportion ~ 20.4%). They are probably related to their use in (1) the "Port del Comte" alpine ski resort, which is located near the top of the massif (**Figure 6. 11**), an area that is drained by the four regional spring M-22, M-25, M-31 and M-43, and also other local springs, and (2) in the potato fields that exist scattered throughout the massif. The atmospheric deposition also contributes (~ 18.9%), and finally sulfate from sulphide oxidation (~ 13.4%). For cluster B, the results confirm the clear effect of geogenic sulfate pollution, normally exceeding the drinking water limits >250 mg/L, of groundwater springs principally located at the lowest parts of the PCM. This is due to dissolution of Tertiary evaporites, mainly in the eastern part, with a mean proportion of ~ 34.4% respect the total sulfate contributions, and Triassic evaporites (~ 29.2%). In cluster C, the model

shows a generalized mix of all eight sulfate sources considered, ranging all of them between 10.8% and 13.7%. Regarding cluster D, which is composed of springs M-31 and M-41, the model also confirms that the origin of sulfate is mainly geogenic, related to Triassic and Tertiary evaporites with contributions between 16 and 19.6%. Figure A5, Appendix A, presents the model output for every spring. In relation to Cluster A, the results obtained for the spring M-38 suggest that the contribution due to sulfide oxidation (64%) is consistent with the biplot shown in **Figure 6. 9B**, and it is consistent with the field inspections, where the oxidation of sulphides associated with the Cretaceous limestones located in its drainage basin is observed. Another group of outstanding results from the Bayesian model are those associated with the springs belonging to cluster B, which are located at the eastern end of the PCM, an area where Tertiary gypsum outcrop. This is the case of springs M-21, M-41 and M-40 that present a clear contribution, almost exclusive, from this source, with contributions of 85.2%, 78,1% and 89% respectively.

6.4.7 Identification of NO_3 in GW and perspectives on aquifer vulnerability in PCM.

The most important N cycling reactions in lands are nitrification, mineralization-immobilization-turnover (MIT), plant uptake, denitrification and NH_4 volatilization **[109–111].** MIT refers to the recycling of NO_3 via immobilization as organic N, subsequent mineralization to NH_4 via organic matter degradation and a turnover back to NO_3 via nitrification **[111].** Immobilization, together with plant uptake, are two N assimilation pathways, which involve the production of organic N from inorganic compounds such as NO_3, NO_2 or NH_4 **[112].**

The GW sampling campaigns revealed the existence of nitrate in some of the springs of the study area (**Figure 6. 11**). With a median and a mean value of 3.83 and 7.13 mg/L, respectively, the nitrate content in GW does not seems a water quality issue in the PCM. Nevertheless, the spatial distribution of nitrate shows that the sources of nitrate may play a role locally. This is important when recharge is produced in a concentrated way, given that focused recharge facilitates the widespread, rapid incorporation and transport of pollutants to groundwater **[3]**.

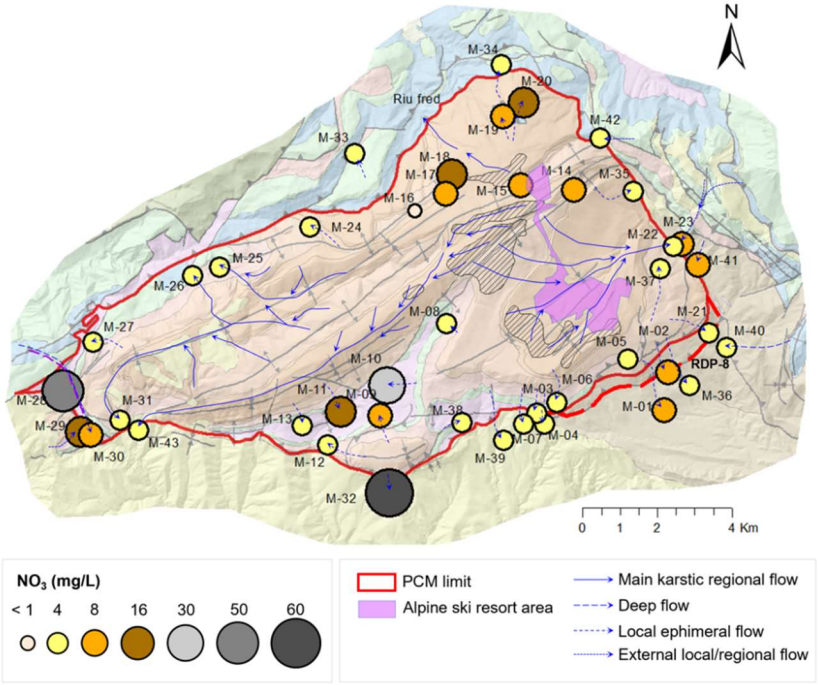

Figure 6. 11. Map of nitrate dissolved in GW. The values correspond averaged concentration obtained for all the GW sampling campaigns conducted during the period Sep 2013 – Oct 2015.

From the total 43 sampled springs, only 20 of them show high enough nitrate concentrations in the GW samples to allow determining the corresponding isotopic ($\delta^{15}N_{NO_3}$ and $\delta^{18}O_{NO_3}$) content (Figure 12A). The isotope content in GW ranges between -0.9‰ and +10.7‰ for $\delta^{15}N_{NO_3}$, and between -0.0‰ and +8.2‰ for $\delta^{18}O_{NO_3}$, with overall mean isotopic contents of +3.5‰ and +2.6‰ for $\delta^{15}N_{NO_3}$ and $\delta^{18}O_{NO_3}$, respectively. **Table 6. 3** shows both the mean nitrate and isotopic content by clusters.

Table A6 Appendix A provide the average values for $\delta^{15}N_{NO_3}$ and $\delta^{18}O_{NO_3}$ of samples available of all springs and the corresponding average NO_3 concentration. The nitrate in GW seems to be unlinked to nitrate fertilizers, as the values of $\delta^{18}O_{NO_3}$ and $\delta^{15}N_{NO_3}$ in GW are far from the values of nitrate fertilizers (**Figure 6. 12**), although some mixing is not discarded. Nevertheless, NO_3 in GW appears to be originated from soil organic nitrogen compounds, NH_4 fertilizers, sewage/manure sources or even from a mixing of them. The highest NO_3 content value is 57.3 mg/L in spring M-

32 (Cluster A; **Figure 6. 11**). This spring is located close to a potato crop field, where fertilizers are applied. This is consistent with the results obtained for $\delta^{18}O_{SO_4}$ and $\delta^{34}S_{SO_4}$, which suggest the origin of SO_4 to be a mixture of soil and fertilizers sulfate sources contributing to GW (**Figure 6. 9** and Figure A5, Appendix A for M-32). There is only one spring, M-28, whose H and O water isotopic composition presents the fingerprint of manure and sewage. In fact, this spring is in the neighboring of a cattle farm where manure stocks are managed.

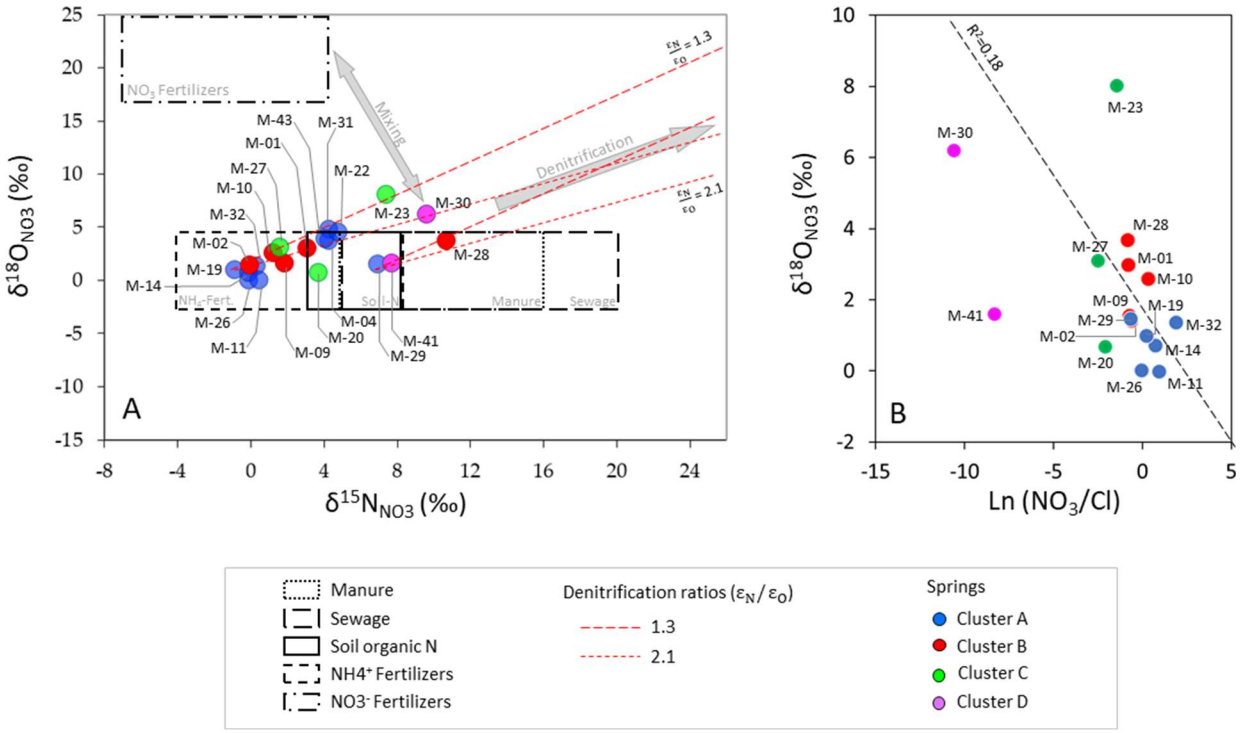

(A) **(B)**

Figure 6. 12. (A) Dual isotope scatterplot using $\delta^{18}O_{NO_3}$ and $\delta^{15}N_{NO_3}$. The area of nitrates is derived from (1) NO_3-fertilizers and (2) NH_4-fertilizers **[103]**; (3) Soil organic N **[116]**; (4) Manure **[103]**; (5) Sewage **[116]**. The long and short dashed red lines define the isotopic fractionation range ($\varepsilon^{15}S/\varepsilon^{18}O_{NO3}$) in denitrification reactions, varying between 1.3 **[117]** and 2.1 **[118],** respectively. **(B)** scatterplot of $\delta^{18}O_{NO_3}$ values against ln(NO_3/Cl).

Concerning the $\delta^{18}O_{NO3}$ in the NO_3 from GW, its value depend on the $\delta^{18}O$ of NO_3^- in water (-11,1‰, SD = 5.08‰) and on the isotopic effect produced during nitrification, which is in turn

influenced by the +23.5‰ $\delta^{18}O$ of dissolved atmospheric O_2 **[113]** and that of H_2O. The limited variation of $\delta^{18}O_{NO3}$ values along the study seems to indicate a negligible isotopic effect from plant uptake. Also, it pointed that denitrification processes were not significant along the studied area. Most of the samples seem to align following a straight-line relationship between the $\delta^{15}N$ and $\delta^{18}O$, with a factor between 1.3 and 2.1, which is consistent with natural denitrification **[114]** but with a slight variation. The natural denitrification process would be supported by the negative linear correlation between $\delta^{18}O_{NO_3}$ and ln (NO_3/Cl) for the GW samples **[115]** (**Figure 6. 12**B). Nevertheless, in the case of PCM, there is almost no correlation indicating that such process, if they exist, is not significant.

The contamination of groundwater by nitrates in the PCM is mostly related with anthropic activities conducted in aquifer recharge areas. Here, the highest nitrate contents in GW are related to agricultural practices. Other relevant anthropic activities in the study area are restricted to those linked with the "Port del Comte" alpine ski resort. It is located near the top of the massif (**Figure 6. 11**) in an area drained by the regional spring M-22, which is the most important resource of the PCM. Given the high karstification degree of the highest parts of the PCM, a hypothetical contamination coming from the ski resort would reach the aquifer feeding the spring M-22. Despite of that, the impact of the sky resort in M-22 is not relevant at all, at least from the perspective of the NO_3 content in GW. This result stresses the good practices of the ski resort managers in terms of adopting measures to minimize the impact of such activity in the environment.

The dual-isotope diagram $\delta^{15}N_{NO_3}$ vs. $\delta^{34}S_{SO_4}$ representing the isotopic composition of atmospheric deposition, soil, fertilizers and sewage (Figure A7, Appendix A) for the water samples with both data available (i.e., $\delta^{15}N_{NO_3}$ and $\delta^{34}S_{SO_4}$; a total of 19 springs) confirms that the main sources of groundwater pollution for springs belonging to Cluster A, which are those discharging close to main recharge areas at the top of the PCM, are mainly the atmospheric deposition and fertilizers, and less the mineralization of soil organic matter. Nevertheless, in the case of the regional springs M-22, M-32 and M-43 (**Figure 6. 1**) the oxidation of sulfides or organogenic sulfur appear to be an additional polluting source as pointed out by the BBM model. Besides, in the case of springs belonging to cluster B there must be another contribution of sulfate, along with the atmospheric deposition, to explain their isotope content. According to the results of BMM, this

source might be the sulfate of geogenic origin, due to the dissolution of Triassic and / or Tertiary gypsum.

6.4.8 Proportional contribution of NO3 sources in GW in PCM

A Bayesian isotope mixing model was prepared using the SIMMR package for R and was run to estimate proportional contributions of NO_3 source for the 20 spring groundwater samples The considered sources are the same of the biplots (Figure 12A) plus atmospheric deposition: (NHF) NO_3^- derived from NH_4^+ in chemical fertilizers and precipitation; (NF) NO_3 in chemical fertilizer; (SN) Soil organic nitrogen; (S) soil; (M) manure; and (Natm) atmospheric deposition. Figure A6, Appendix A, presents the corresponding outputs separated for each water spring. The result of the model confirms that, in general, the greatest contribution of nitrates comes from pollution related to anthropic activities carried out in the aquifer recharge areas, mainly the use of fertilizers (NHF), except in a specific case with a notable proportion of manure (M) and sewage (S). Most springs have nitrate concentrations below current standards for drinking water. The only spring that exceeds the reference levels established at 50 ppm is the M-32 spring (with 57.3 ppm). This spring is located downstream of an area of field potato crops. The model indicates that it has a NHF proportion of 32%. The rest of the springs present similar or slightly higher NHF contributions although with always-lower nitrate concentrations. The second spring with the highest nitrate concentration corresponds to spring M-28 (38.6 ppm). In this case, the origin is clearly influenced by the livestock activity located upstream, presenting a proportion of 39.2% coming from manure and 31.7% coming from sewage.

6.4.9 Conceptual model for hydrogeochemical evolution of GW in the PCM

From the combined analysis of the geological and hydrogeological context and chemical and isotopic data, global hydrogeological and hydrogeochemical conceptual models have been interpreted based on the four cross-sections indicated in **Figure 6. 1**.

The PCM is a high mountain karst aquifer, built upon several thrust sheets of carbonate materials. Precipitation is usually as snow in the highest part of the massif, where bare land abounds, along with the most developed karst forms in the epikarst (**Figure 6. 13** and **Figure 6. 14**). The meteoric water from snowmelt and rainfall infiltrates and recharges the aquifer, mostly as Ca-Cl-HCO_3 type water. Recharged water flows in all directions and discharge through multiple significant springs. The main aquifer of the system is the one associated with the karstified limestones and dolostones of the Tertiary PPEc unit (**Figure 6. 1**., **Figure 6. 13** and **Figure 6. 14**), which underlies the PEcp1 and PEcp2 units.

The four most important springs in the system - named in decreasing discharge rate – are the M-22 (in **Figure 6. 13A**), M-25 and M-31 (in **Figure 6. 14B**) and M-43 (see **Figure 6. 1**.). These springs drain the Tertiary karst aquifer along the syncline axes and were classified into the Cluster A by Herms et al. (2021) **[59]**. According to both their recharge elevation zones obtained with the H and O water isotopic content and the 3D geological structure, these four springs present recharge-discharge pathways, several km long, while presenting a Ca-HCO_3 water types with low TDS (from 122 to 182 mg/L). These characteristics are interpreted as an indicator of high karstification degree affecting the geological PPEc, PEcp1 and PEcp2 units, which favors large flow rates in both the percolating meteoric water through the unsaturated zone and the GW flow in the saturated zone. The hydrochemical signature of the GW flowing through the karst aquifer is obtained quickly, during the percolation and the first stages of the GW flow phases, as supported by the inverse modeling analysis done with the help of PHREEQC.

To illustrate this, **Figure 6. 13A** shows the conceptual long RDP associated to the regional karst spring M-22. It includes a thick unsaturated zone and a regional water table level at elevations between 1000 and 1100 m a.s.l. Additionally, small and local springs, such as M-08 and M-05 (in **Figure 6. 13A**), M-15 (in **Figure 6. 13B**), or M-24 (in **Figure 6. 14A**), drain the same karst aquifer and get a Ca-HCO_3 hydrochemical water type, with TDS mostly between 99 to 255 mg/L, and SO_4 coming from soil and atmospheric deposition, a composition which is similar to that of the regional springs. Additionally, the local springs may be affected by NH_4 fertilizers and/or manure. The discharge of springs located in the SE part of the study zone, which crosses the limits of the South

Pyrenees thrust fault in the front SE of the PCM (right side of the **Figure 6. 13B**) may be affected by Tertiary gypsum (PExb unit), generating from Ca-SO_4-HCO_3 to Ca-SO_4 water types.

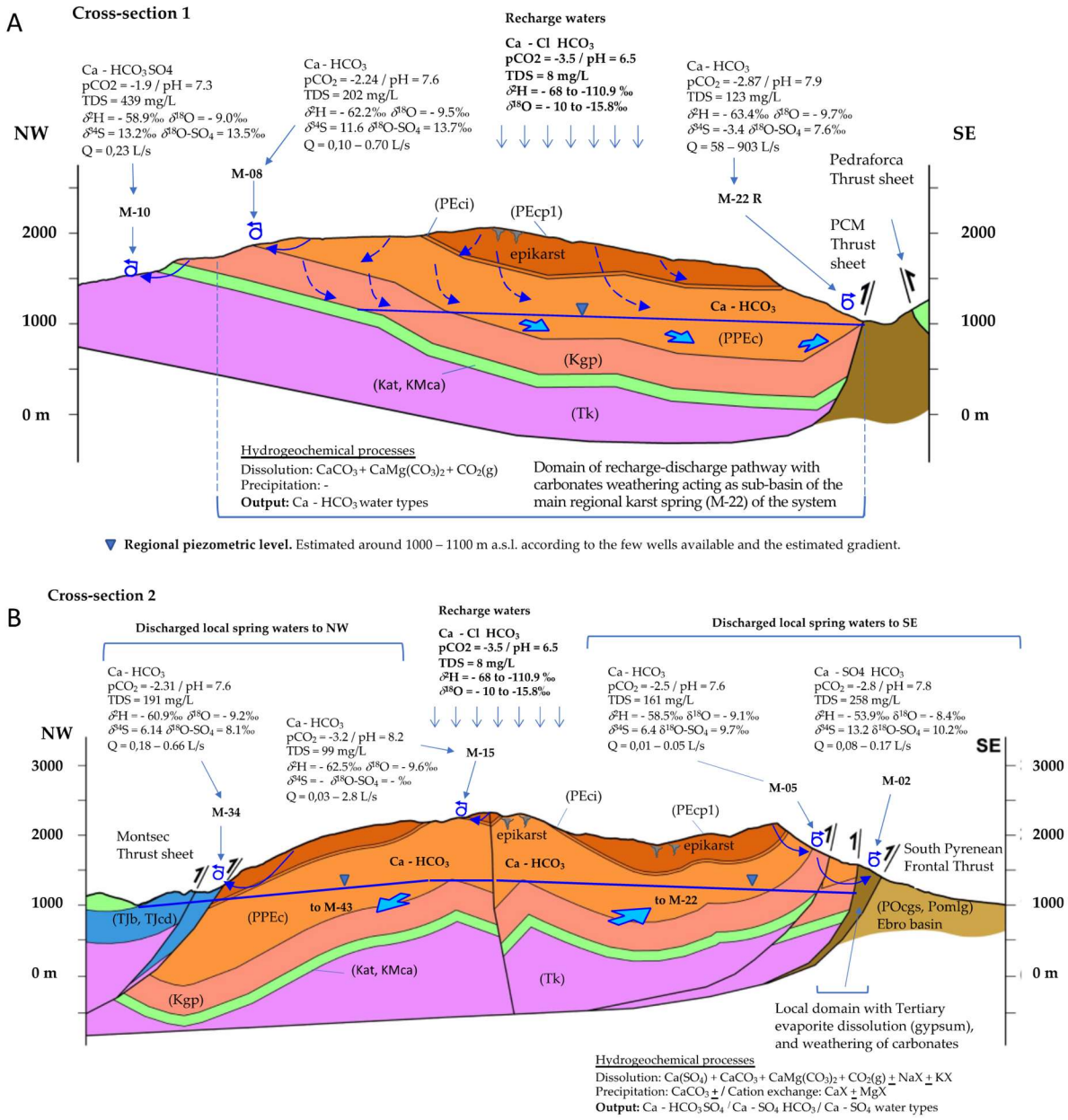

Figure 6. 13. Hydrogeological-hydrogeochemical conceptual models of **(A)** cross-section 1 and **(B)** cross-section 2. The sketch includes different water springs projected close to the cross-section. The situation of the cross-sections is shown in **Figure 6. 1**.

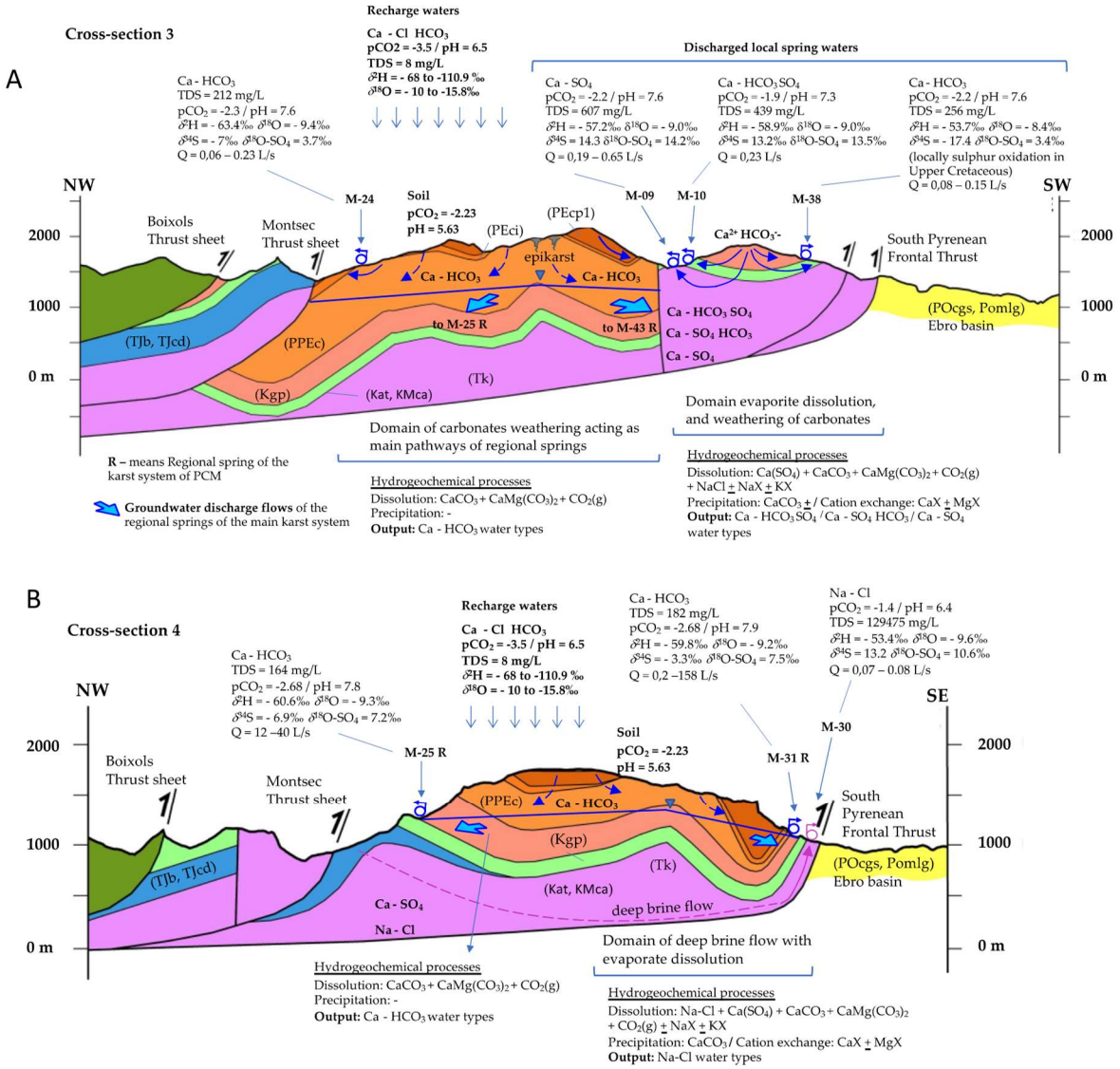

Figure 6. 14. Hydrogeological-hydrogeochemical conceptual models corresponding to the cross-section 3 **(A)** and 4 **(B)**. The sketch shows the closest springs, projected in the cross-section.

Below the Tertiary limestone layers, the Garumnian Kgp unit act as an aquitard, while the Upper Cretaceous Kat, KMca units, the Keuper Tk unit, and the Muschelkalk Tm unit (Triassic) act as local aquifers. These aquifer units drain through small local springs that may have been recharged through the overlying Tertiary carbonate units. The incoming recharge presents an initial Ca-HCO_3 signature, but it changes along the GW flow line by incorporating other solutes from the most soluble evaporite minerals in such local aquifers. There are some springs whose discharge present some hydrochemical special characteristics. Spring M-38 in Cluster A (**Figure 6. 14A**) interacts with lignite bearing marls (KMca unit), incorporating sulfate from sulfide minerals (disseminated

pyrites) or coal organic sulfur weathering, as is supported by the SO_4 isotope composition in groundwater; spring M-20 in Cluster C incorporates Cl by dissolution of halite from the outcropping Keuper materials in the NE part of the massif (**Figure 6. 1**). Additionally, Ca is dissolved by a reverse ion exchange-like process in weathering of shales, in which Na in dissolution replaces Ca in the terrain matrix. The springs that interact with the Keuper (Tk) unit, which are recharged either in the outcrops of this TK unit or through the geological units overlying it (e.g., Kgp, Kat, KMca), incorporate significant amounts of sulfate by dissolution of gypsum, as happens in springs M-10 (in Figure 13A and **Figure 6. 14A**) and M-09 (**Figure 6. 14A**). Both the S and O from dissolved sulfate isotope composition and the inverse modeling with PHREEQC support this. Additionally, GW discharge may experience local de-dolomitization, as in case of M-28 (see **Figure 6. 8**) which presents the highest content of sulfate (**Figure 6. 9**), thus inducing the precipitation of calcite, while those with deeper flow lines, such as springs M-30 (**Figure 6. 14B**) and M-41 (see **Figure 6. 1**) of Cluster D, incorporate Cl and Na by dissolution of halite as well.

6.5 Conclusions

The Port del Comte Massif (PCM) contains one of the most important karst aquifers of the in the South-Eastern part of the Pyrenees. In this work, hydrochemical and multi-isotope data along with hydrogeological framework information have been coupled to characterize the hydrochemical processes driving the hydrogeochemical behavior of this complex hydrogeological system.

In general, the groundwater is dominantly of the calcium bicarbonate and calcium–magnesium bicarbonate type, suggesting a dominant calcite dissolution process in agreement with the lithology associated to the Eocene carbonate materials conforming the main aquifer of PCM. The main source of sulfate in GW is the dissolution of geogenic origin from gypsum dissolution from the Eocene-Oligocene Beuda Formation and from Triassic evaporites. Some influence of sulfate from sulfide mineral or coal organic sulfur weathering also has been point out. From the anthropogenic point of view, sulphate from fertilizers seems to play a role in some places around the ski resort. Due to their intermediate values, the role of soil sulphate and sulphate from atmospheric deposition cannot be discarded. Isotope data have shown that the source of recharge is precipitation that enters the

system along the mountain slopes, favored by the high karstification of the carbonate materials that abundantly crop out in the area. Isotopes also show that dissolved NO_3 in groundwater mainly comes from mineral fertilizers, soil organic nitrogen and pig manure application to the fields, with at most minor contributions from sewage. As the other high mountain karst systems, the PCM is very vulnerable to pollution. Here, nitrates from agricultural practices represent the main threat to the pristine waters of the aquifer system despite its low significance. Fortunately, the dissolved nitrate concentration in GW is generally low.

The carbonate karstic aquifer of the PCM is a very complex hydrological system developed in a high mountain environment. The multidisciplinary approach has allowed developing a hydrogeological conceptual model of aquifer system functioning, which is coherent with the available information from previous studies, but which is also consistent with the processes driving the hydrogeochemical and isotopic fingerprint of groundwater in this aquifer system.

6.6 Refereneces

1. Goldscheider, N.; Chen, Z.; Auler, A.S.; Bakalowicz, M.; Broda, S.; Drew, D.; Hartmann, J.; Jiang, G.; Moosdorf, N.; Stevanovic, Z.; et al. Global Distribution of Carbonate Rocks and Karst Water Resources. Hydrogeol. J. 2020, 28, 1661–1677, doi:10.1007/s10040-020-02139-5.
2. Parise, M.; Closson, D.; Gutiérrez, F.; Stevanović, Z. Anticipating and Managing Engineering Problems in the Complex Karst Environment. Environ. Earth Sci. 2015, 74, 7823–7835, doi:10.1007/s12665-015-4647-5.
3. Hartmann, A.; Jasechko, S.; Gleeson, T.; Wada, Y.; Andreo, B.; Barberá, J.A.; Brielmann, H.; Bouchaou, L.; Charlier, J.-B.; Darling, W.G.; et al. Risk of Groundwater Contamination Widely Underestimated Because of Fast Flow into Aquifers. Proc. Natl. Acad. Sci. 2021, 118, e2024492118, doi:10.1073/pnas.2024492118.
4. Hock, R., G. Rasul, C. Adler, B. Cáceres, S. Gruber, Y. Hirabayashi, M. Jackson, A. Kääb, S. Kang, S. Kutuzov, A. Milner, U. Molau, S. Morin, B. Orlove, and H. Steltzer, 2019: High Mountain Areas. In: IPCC Special Report on the Ocean and Cryosphere in a Changing

Climate [H.-O. Pörtner, D.C. Roberts, V. Masson-Delmotte, P. Zhai, M. Tignor, E. Poloczanska, K. Mintenbeck, A. Alegría, M. Nicolai, A. Okem, J. Petzold, B. Rama, N.M. Weyer IPCC Special Report on the Ocean and Cryosphere in a Changing Climate, edited by: Pörtner, H.O., Roberts, D.C., Masson-Delmotte, V., Zhai, P., Tignor, M., Poloczanska, E., Mintenbeck, K., Alegría, A., Ni-colai, M., Okem, A., Petzold, J., Rama, B., and Weyer, N.M. Retrieved from http://urn.kb.se/resolve?urn=urn:nbn:se:uu:diva-414230. (Last access 01/06/2021). In; IPCC, 2019.

5. Jódar, J.; Lambán, L.J.; González, A.; Martos, S.; Custodio, E. High Mountain Karst Aquifer Vulnerability to Climate Change and Groundwater Transit Times; oral, 2020;
6. Jódar, J.; Herms, I.; Lambán, L.J.; Martos-Rosillo, S.; Herrera-Lameli, C.; Urrutia, J.; Soler, A.; Custodio, E. Isotopic Content in High Mountain Karst Aquifers as a Proxy for Climate Change Impact in Mediterranean Zones: The Port Del Comte Karst Aquifer (SE Pyrenees, Catalonia, Spain). Sci. Total Environ. 2021, 790, 148036, doi:10.1016/j.scitotenv.2021.148036.
7. Lambán, L.J.; Jódar, J.; Custodio, E.; Soler, A.; Sapriza, G.; Soto, R. Isotopic and Hydrogeochemical Characterization of High-Altitude Karst Aquifers in Complex Geological Settings. The Ordesa and Monte Perdido National Park (Northern Spain) Case Study. Sci. Total Environ. 2015, 506–507, 466–479, doi:10.1016/j.scitotenv.2014.11.030.
8. Sheikhy Narany, T.; Bittner, D.; Disse, M.; Chiogna, G. Spatial and Temporal Variability in Hydrochemistry of a Small-Scale Dolomite Karst Environment. Environ. Earth Sci. 2019, 78, 273, doi:10.1007/s12665-019-8276-2.
9. Mudarra, M.; Andreo, B.; Mudry, J. Monitoring Groundwater in the Discharge Area of a Complex Karst Aquifer to Assess the Role of the Saturated and Unsaturated Zones. Environ. Earth Sci. 2012, 65, 2321–2336, doi:10.1007/s12665-011-1032-x.
10. Montalván, F.J.; Heredia, J.; Ruiz, J.M.; Pardo-Igúzquiza, E.; García de Domingo, A.; Elorza, F.J. Hydrochemical and Isotopes Studies in a Hypersaline Wetland to Define the Hydrogeological Conceptual Model: Fuente de Piedra Lake (Malaga, Spain). Sci. Total Environ. 2017, 576, 335–346, doi:10.1016/j.scitotenv.2016.10.048.
11. Apollaro, C.; Fuoco, I.; Bloise, L.; Calabrese, E.; Marini, L.; Vespasiano, G.; Muto, F. Geochemical Modeling of Water-Rock Interaction Processes in the Pollino National Park. Geofluids 2021, 2021, 1–17, doi:10.1155/2021/6655711.
12. Goldscheider, N. Overview of Methods Applied in Karst Hydrogeology. In Karst Aquifers—

Characterization and Engineering; Stevanović, Z., Ed.; Professional Practice in Earth Sciences; Springer International Publishing: Cham, 2015; pp. 127–145 ISBN 978-3-319-12849-8.

13. Simsek, C.; Elci, A.; Gunduz, O.; Erdogan, B. Hydrogeological and Hydrogeochemical Characterization of a Karstic Mountain Region. Environ. Geol. 2008, 54, 291–308, doi:10.1007/s00254-007-0817-4.
14. Mustafa, O.; Merkel, B.; Weise, S. Assessment of Hydrogeochemistry and Environmental Isotopes in Karst Springs of Makook Anticline, Kurdistan Region, Iraq. Hydrology 2015, 2, 48–68, doi:10.3390/hydrology2020048.
15. Guo, Y.; Zhang, C.; Xiao, Q.; Bu, H. Hydrogeochemical Characteristics of a Closed Karst Groundwater Basin in North China. J. Radioanal. Nucl. Chem. 2020, 325, 365–379, doi:10.1007/s10967-020-07247-w.
16. De la Torre, B.; Mudarra, M.; Andreo, B. Investigating Karst Aquifers in Tectonically Complex Alpine Areas Coupling Geological and Hydrogeological Methods. J. Hydrol. X 2020, 6, 100047, doi:10.1016/j.hydroa.2019.100047.
17. Farlin, J.; Małoszewski, P. On Using Lumped Parameter Models and Temperature Cycles in Heterogeneous Aquifers. Groundwater 2018, 56, 969–977, doi:10.1111/gwat.12651.
18. Jódar, J.; Custodio, E.; Lambán, L.J.; Martos-Rosillo, S.; Herrera-Lameli, C.; Sapriza-Azuri, G. Vertical Variation in the Amplitude of the Seasonal Isotopic Content of Rainfall as a Tool to Jointly Estimate the Groundwater Recharge Zone and Transit Times in the Ordesa and Monte Perdido National Park Aquifer System, North-Eastern Spain. Sci. Total Environ. 2016, 573, 505–517, doi:10.1016/j.scitotenv.2016.08.117.
19. Jódar, J.; González-Ramón, A.; Martos-Rosillo, S.; Heredia, J.; Herrera, C.; Urrutia, J.; Caballero, Y.; Zabaleta, A.; Antigüedad, I.; Custodio, E.; et al. Snowmelt as a Determinant Factor in the Hydrogeological Behaviour of High Mountain Karst Aquifers: The Garcés Karst System, Central Pyrenees (Spain). Sci. Total Environ. 2020, 748, 141363, doi:10.1016/j.scitotenv.2020.141363.
20. Díaz-Puga, M.A.; Vallejos, A.; Sola, F.; Daniele, L.; Molina, L.; Pulido-Bosch, A. Groundwater Flow and Residence Time in a Karst Aquifer Using Ion and Isotope Characterization. Int. J. Environ. Sci. Technol. 2016, 13, 2579–2596, doi:10.1007/s13762-016-1094-0.
21. Gao, Z.; Liu, J.; Xu, X.; Wang, Q.; Wang, M.; Feng, J.; Fu, T. Temporal Variations of Spring

Water in Karst Areas: A Case Study of Jinan Spring Area, Northern China. Water 2020, 12, 1009, doi:10.3390/w12041009.

22. Safari, M.; Hezarkhani, A.; Mashhadi, S.R. Hydrogeochemical Characteristics and Water Quality of Aji-Chay River, Eastern Catchment of Lake Urmia, Iran. J. Earth Syst. Sci. 2020, 129, 199, doi:10.1007/s12040-020-01469-y.
23. Chalikakis, K.; Plagnes, V.; Guerin, R.; Valois, R.; Bosch, F.P. Contribution of Geophysical Methods to Karst-System Exploration: An Overview. Hydrogeol. J. 2011, 19, 1169–1180, doi:10.1007/s10040-011-0746-x.
24. Jia, Z.; Zang, H.; Hobbs, P.; Zheng, X.; Xu, Y.; Wang, K. Application of Inverse Modeling in a Study of the Hydrogeochemical Evolution of Karst Groundwater in the Jinci Spring Region, Northern China. Environ. Earth Sci. 2017, 76, 312, doi:10.1007/s12665-017-6631-8.
25. Moran-Ramírez, J.; Ramos-Leal, J.A.; Mahlknecht, J.; Santacruz-DeLeón, G.; Martín-Romero, F.; Fuentes Rivas, R.; Mora, A. Modeling of Groundwater Processes in a Karstic Aquifer of Sierra Madre Oriental, Mexico. Appl. Geochem. 2018, 95, 97–109, doi:10.1016/j.apgeochem.2018.05.011.
26. Zheng, X.; Zang, H.; Zhang, Y.; Chen, J.; Zhang, F.; Shen, Y. A Study of Hydrogeochemical Processes on Karst Groundwater Using a Mass Balance Model in the Liulin Spring Area, North China. Water 2018, 10, 903, doi:10.3390/w10070903.
27. Pérez-Ceballos, R.; Canul-Macario, C.; Pacheco-Castro, R.; Pacheco-Ávila, J.; Euán-Ávila, J.; Merino-Ibarra, M. Regional Hydrogeochemical Evolution of Groundwater in the Ring of Cenotes, Yucatán (Mexico): An Inverse Modelling Approach. Water 2021, 13, 614, doi:10.3390/w13050614.
28. Chen, Z.; Goldscheider, N. Modeling Spatially and Temporally Varied Hydraulic Behavior of a Folded Karst System with Dominant Conduit Drainage at Catchment Scale, Hochifen–Gottesacker, Alps. J. Hydrol. 2014, 514, 41–52, doi:10.1016/j.jhydrol.2014.04.005.
29. Herms, I.; Jódar, J.; Soler, A.; Vadillo, I.; Lambán, L.J.; Martos-Rosillo, S.; Núñez, J.A.; Arnó, G.; Jorge, J. Contribution of Isotopic Research Techniques to Characterize High-Mountain-Mediterranean Karst Aquifers: The Port Del Comte (Eastern Pyrenees) Aquifer. Sci. Total Environ. 2019, 656, 209–230, doi:10.1016/j.scitotenv.2018.11.188.
30. Betzler, C. A Carbonate Complex in an Active Foreland Basin: The Paleogene of the Sierra de Port Del Comte and the Sierra Del Cadi (Southern Pyrenees). Geodin. Acta 1989, 3, 207–

220, doi:10.1080/09853111.1989.11105187.

31. Vergès i Masip, J. Estudi geològic del vessant sud del Pirineu oriental i central. Evolució cinemàtica en 3D, Universitat de Barcelona UB: Barcelona, 1993.
32. Barcelona City Council Evolution of Water Consumption in the City of Barcelona; 2008;
33. Herms, I. 3D Geological Modelling as a Tool for Supporting Spring Catchment Delineation in High-Mountain Karst Aquifers: The Case Study of the Port Del Comte (Eastern Pyrenees) Aquifer. In Proceedings of the "5th European Meeting on 3D Geological Modelling"; Bern, Switzerland, 2019.
34. Arnó, G.; Conesa, A.; Carreras, X.; Camps, V.; Fraile, J.; Herms, I.; Iglesias, M. Mapa de Vulnerabilitat Intrínseca a la contaminació dels Aqüífers de Catalunya (MVIAC) 2020.
35. DARP, G. Proyecto de Prospección e Investigación Hidrogeológica (Solsonès– Lleida).; DARP (Departament d'Agricultura, Ramaderia i Pesca, Generalitat de Catalunya: Barcelona, 1990; pp. 117, 20 and 58;.
36. Gil, R.; Núñez, I. Estudio hidrogeológico de la sierra de Odén – Port del Comte (Solsonès–Lleida).; CIHS: Barcelona, 2003; p. 85;.
37. Núñez, I.; Gil, R.; Vázquez, E. Estudio hidrogeológico de la cabecera de la Ribera Salada, (Lleida). In Proceedings of the VIII Simposio de Hidrogeología; AIH-IGME: Zaragoza, 2004; pp. 107–120.
38. Chen, Z.; Hartmann, A.; Wagener, T.; Goldscheider, N. Dynamics of Water Fluxes and Storages in an Alpine Karst Catchment under Current and Potential Future Climate Conditions. Hydrol. Earth Syst. Sci. 2018, 22, 3807–3823, doi:10.5194/hess-22-3807-2018.
39. Pardo-Igúzquiza, E.; Collados-Lara, A.J.; Pulido-Velazquez, D. Potential Future Impact of Climate Change on Recharge in the Sierra de Las Nieves (Southern Spain) High-Relief Karst Aquifer Using Regional Climate Models and Statistical Corrections. Environ. Earth Sci. 2019, 78, 598, doi:10.1007/s12665-019-8594-4.
40. Peel, M.C.; Finlayson, B.L.; McMahon, T.A. Updated World Map of the Köppen-Geiger Climate Classification. Hydrol Earth Syst Sci 2007, 12.
41. ICGC. Full Alt Urgell. Mapa Geològic Comarcal de Catalunya 1:50.000. 2007.
42. Lauber, U.; Kotyla, P.; Morche, D.; Goldscheider, N. Hydrogeology of an Alpine Rockfall Aquifer System and Its Role in Flood Attenuation and Maintaining Baseflow. Hydrol. Earth Syst. Sci. 2014, 18, 4437–4452, doi:10.5194/hess-18-4437-2014.
43. Hood, J.L.; Hayashi, M. Assessing the Application of a Laser Rangefinder for Determining

Snow Depth in Inaccessible Alpine Terrain. Hydrol. Earth Syst. Sci. 2010, 14, 901–910, doi:10.5194/hess-14-901-2010.

44. Goldscheider, N. Alpine Hydrogeologie. Grundwasser 2011, 16, 1–1, doi:10.1007/s00767-010-0157-2.
45. Bakalowicz, M. Karst Groundwater: A Challenge for New Resources. Hydrogeol. J. 2005, 13, 148–160, doi:10.1007/s10040-004-0402-9.
46. Goldscheider, N.; Drew, D. Methods in Karst Hydrogeology.; International Contributions to Hydrogeology 26.; Taylor&Francis.; London, 2007; ISBN 978-0-415-42873-6.
47. Wetzel, K.-F. On the Hydrology of the Partnach Area in the Wetterstein Mountains (Bavarian Alps). Erdkunde 2004, 58, 172–186, doi:https://www.jstor.org/stable/25647659.
48. Malard, A.; Sinreich, M.; Jeannin, P.-Y. A Novel Approach for Estimating Karst Groundwater Recharge in Mountainous Regions and Its Application in Switzerland: Karst Groundwater Recharge: Approach and Application. Hydrol. Process. 2016, 30, 2153–2166, doi:10.1002/hyp.10765.
49. Epting, J.; Page, R.M.; Auckenthaler, A.; Huggenberger, P. Process-Based Monitoring and Modeling of Karst Springs – Linking Intrinsic to Specific Vulnerability. Sci. Total Environ. 2018, 625, 403–415, doi:10.1016/j.scitotenv.2017.12.272.
50. Jódar, J.; Custodio, E.; Liotta, M.; Lambán, L.J.; Herrera, C.; Martos-Rosillo, S.; Sapriza, G.; Rigo, T. Correlation of the Seasonal Isotopic Amplitude of Precipitation with Annual Evaporation and Altitude in Alpine Regions. Sci. Total Environ. 2016, 550, 27–37, doi:10.1016/j.scitotenv.2015.12.034.
51. Beven, K.J. Rainfall-Runoff Modelling, The Primer, 2nd Edition; Wiley-Blackwell.; Chichester, 2012; ISBN ISBN: 978-0-470-71459-1.
52. Andreo, B.; Liñán, C.; Carrasco, F.; Jiménez de Cisneros, C.; Caballero, F.; Mudry, J. Influence of Rainfall Quantity on the Isotopic Composition (18O and 2H) of Water in Mountainous Areas. Application for Groundwater Research in the Yunquera-Nieves Karst Aquifers (S Spain). Appl. Geochem. 2004, 19, 561–574, doi:10.1016/j.apgeochem.2003.08.002.
53. Bergström, S. Development and Application of a Conceptual Runoff Model For Scandinavian Catchments, SMHI.; Norrköping, 1976; p. 134;.
54. Seibert, J. HBV Light Version 2. User's Manual.; Stockholm University: Uppsala, Sweden., 2005;

55. Małoszewski, P.; Zuber, A. Lumped Parameter Models for the Interpretation of Environmental Tracer Data. Manual on Mathematical Models in Isotope Hydrology.; IAEA, Vienna (Austria), 1996;
56. Maréchal, JC.; Bailly-Comte, V.; Hickey, C.; Maurice, L.; Stroj, A.; Bunting, S.Y.; Charlier, JB.; Elster, D.; Hakoun, V.; Herms, I.; et al. GeoERA Resources of Groundwater Harmonized at Cross-Border and Pan-European Scale (RE-SOURCE) Project'. Deliverable 5.3 Karst and Chalk Aquifers Classification and Management Recommendations; BRGM: Toulousse, France, 2021; p. 114;.
57. Mangin, A. Contribution à l'étude Hydrodynamique Des Aquifères Karstiques, Université de Dijon: Dijon, France, 1975.
58. Freixes, A. Els aqüífers càrstics dels Pirineus de Catalunya. Interès estratègic i sostenibilitat, Universitat de Barcelona UB: Barcelona, 2014.
59. Herms, I.; Jódar, J.; Soler, A.; Lambán, L.J.; Custodio, E.; Núñez, J.A.; Arnó, G.; Ortego, M.I.; Parcerisa, D.; Jorge, J. Evaluation of Natural Background Levels of High Mountain Karst Aquifers in Complex Hydrogeological Settings. A Gaussian Mixture Model Approach in the Port Del Comte (SE, Pyrenees) Case Study. Sci. Total Environ. 2021, 756, 143864, doi:10.1016/j.scitotenv.2020.143864.
60. Fraley, C.; Raftery, A.E. Model-Based Clustering, Discriminant Analysis, and Density Estimation. J. Am. Stat. Assoc. 2002, 97, 611–631, doi:10.1198/016214502760047131.
61. Bouveyron, C.; Brunet-Saumard, C. Model-Based Clustering of High-Dimensional Data: A Review. Comput. Stat. Data Anal. 2014, 71, 52–78, doi:10.1016/j.csda.2012.12.008.
62. Camarero, L.; Catalan, J. Chemistry of Bulk Precipitation in the Central and Eastern Pyrenees, Northeast Spain. Atmospheric Environ. Part Gen. Top. 1993, 27, 83–94, doi:10.1016/0960-1686(93)90073-8.
63. Bergström, S. The HBV Model – Its Structure and Applications; Reports Hydrology; SMHI: Norrkoping, Sweden, 1992;
64. Alcalá, F.J.; Custodio, E. Atmospheric Chloride Deposition in Continental Spain. Hydrol. Process. 2008, 22, 3636–3650, doi:10.1002/hyp.6965.
65. Coplen, T.B. Guidelines and Recommended Terms for Expression of Stable-Isotope-Ratio and Gas-Ratio Measurement Results: Guidelines and Recommended Terms for Expressing Stable Isotope Results. Rapid Commun. Mass Spectrom. 2011, 25, 2538–2560, doi:10.1002/rcm.5129.

66. Wassenaar, L.I.; Ahmad, M.; Aggarwal, P.; Duren, M.; Pöltenstein, L.; Araguas, L.; Kurttas, T. Worldwide Proficiency Test for Routine Analysis of Δ2H and Δ18O in Water by Isotope-Ratio Mass Spectrometry and Laser Absorption Spectroscopy: Proficiency Test for Δ2H and Δ18O in Natural Waters. Rapid Commun. Mass Spectrom. 2012, 26, 1641–1648, doi:10.1002/rcm.6270.
67. Epstein, S.; Mayeda, T. Variation of O18 Content of Waters from Natural Sources. Geochim. Cosmochim. Acta 1953, 4, 213–224, doi:https://doi.org/10.1016/0016-7037(53)90051-9.
68. McIlvin, M.R.; Altabet, M.A. Chemical Conversion of Nitrate and Nitrite to Nitrous Oxide for Nitrogen and Oxygen Isotopic Analysis in Freshwater and Seawater. Anal. Chem. 2005, 77, 5589–5595, doi:10.1021/ac050528s.
69. Dogramaci, S.S.; Herczeg, A.L.; Schi, S.L.; Bone, Y. Controls on D34S and D18O of Dissolved Sulfate in Aquifers of the Murray Basin, Australia and Their Use as Indicators of ¯ow Processes. Appl. Geochem. 2001, 14.
70. Parkhurst, D.L.; Appelo, C.A.J. Description of Input and Examples for PHREEQC Version 3—A Computer Program for Speciation, Batch-Reaction, One-Dimensional Transport, and Inverse Geochemical Calculations; Techniques and Methods, book 6, chap. A43; U.S. Geological Survey, 2013; p. 497;.
71. Appelo, C.A.J.; Postma, D. Geochemistry, Groundwater and Pollution; 2nd edition.; CRC Press: London, 2005;
72. Puig, R.; Folch, A.; Menció, A.; Soler, A.; Mas-Pla, J. Multi-Isotopic Study (15N, 34S, 18O, 13C) to Identify Processes Affecting Nitrate and Sulfate in Response to Local and Regional Groundwater Mixing in a Large-Scale Flow System. Appl. Geochem. 2013, 32, 129–141, doi:10.1016/j.apgeochem.2012.10.014.
73. Puig, R.; Soler, A.; Widory, D.; Mas-Pla, J.; Domènech, C.; Otero, N. Characterizing Sources and Natural Attenuation of Nitrate Contamination in the Baix Ter Aquifer System (NE Spain) Using a Multi-Isotope Approach. Sci. Total Environ. 2017, 580, 518–532, doi:10.1016/j.scitotenv.2016.11.206.
74. Kendall, C. Kendall, C. (1998). Tracing Nitrogen Sources and Cycling in Catchments. Isotope Tracers in Catchment Hydrology, 519–576. 1998, doi:doi:10.1016/b978-0-444-81546-0.50023-9.
75. Xue, D.; De Baets, B.; Van Cleemput, O.; Hennessy, C.; Berglund, M.; Boeckx, P. Use of a Bayesian Isotope Mixing Model to Estimate Proportional Contributions of Multiple Nitrate

Sources in Surface Water. Environ. Pollut. 2012, 161, 43–49, doi:10.1016/j.envpol.2011.09.033.

76. Parnell, A.C.; Phillips, D.L.; Bearhop, S.; Semmens, B.X.; Ward, E.J.; Moore, J.W.; Jackson, A.L.; Grey, J.; Kelly, D.J.; Inger, R. Bayesian Stable Isotope Mixing Models. Environmetrics 2013, n/a-n/a, doi:10.1002/env.2221.
77. Parnell, A.C.; Inger, R.; Bearhop, S.; Jackson, A.L. Source Partitioning Using Stable Isotopes: Coping with Too Much Variation. PLoS ONE 2010, 5, e9672, doi:10.1371/journal.pone.0009672.
78. Kazakis, N.; Matiatos, I.; Ntona, M.-M.; Bannenberg, M.; Kalaitzidou, K.; Kaprara, E.; Mitrakas, M.; Ioannidou, A.; Vargemezis, G.; Voudouris, K. Origin, Implications and Management Strategies for Nitrate Pollution in Surface and Ground Waters of Anthemountas Basin Based on a d15N-NO3− and d18O-NO3− Isotope Approach. Sci. Total Environ. 2020, 724, 138211, doi:10.1016/j.scitotenv.2020.138211.
79. Kim, K.-H.; Yun, S.-T.; Mayer, B.; Lee, J.-H.; Kim, T.-S.; Kim, H.-K. Quantification of Nitrate Sources in Groundwater Using Hydrochemical and Dual Isotopic Data Combined with a Bayesian Mixing Model. Agric. Ecosyst. Environ. 2015, 199, 369–381, doi:https://doi.org/10.1016/j.agee.2014.10.014.
80. Matiatos, I. Nitrate Source Identification in Groundwater of Multiple Land-Use Areas by Combining Isotopes and Multivariate Statistical Analysis: A Case Study of Asopos Basin (Central Greece). Sci. Total Environ. 2016, 541, 802–814, doi:10.1016/j.scitotenv.2015.09.134.
81. Wang, M.; Lu, B.; Wang, J.; Zhang, H.; Guo, L.; Lin, H. Using Dual Isotopes and a Bayesian Isotope Mixing Model to Evaluate Nitrate Sources of Surface Water in a Drinking Water Source Watershed, East China. Water 2016, 8, 355, doi:10.3390/w8080355.
82. Xu, W.; Xu, W.; Cai, Y.; Tan, Q.; Xu, Y. Estimating the Proportional Contributions of Multiple Nitrate Sources in Shallow Groundwater with a Bayesian Isotope Mixing Model. Int. J. Environ. Sci. Dev. 2016, 7, 581–585, doi:10.18178/ijesd.2016.7.8.843.
83. Yu, L.; Zheng, T.; Zheng, X.; Hao, Y.; Yuan, R. Nitrate Source Apportionment in Groundwater Using Bayesian Isotope Mixing Model Based on Nitrogen Isotope Fractionation. Sci. Total Environ. 2020, 718, 137242, doi:10.1016/j.scitotenv.2020.137242.
84. Paredes, I. Agricultural and Urban Delivered Nitrate Pollution Input to Mediterranean Temporary Freshwaters. 2020, 12.

85. El Gaouzi, F.-Z.J.; Sebilo, M.; Ribstein, P.; Plagnes, V.; Boeckx, P.; Xue, D.; Derenne, S.; Zakeossian, M. Using d15N and d18O Values to Identify Sources of Nitrate in Karstic Springs in the Paris Basin (France). Appl. Geochem. 2013, 35, 230–243, doi:10.1016/j.apgeochem.2013.04.015.
86. Ming, X.; Groves, C.; Wu, X.; Chang, L.; Zheng, Y.; Yang, P. Nitrate Migration and Transformations in Groundwater Quantified by Dual Nitrate Isotopes and Hydrochemistry in a Karst World Heritage Site. Sci. Total Environ. 2020, 735, 138907, doi:10.1016/j.scitotenv.2020.138907.
87. Samborska, K.; Halas, S.; Bottrell, S.H. Sources and Impact of Sulphate on Groundwaters of Triassic Carbonate Aquifers, Upper Silesia, Poland. J. Hydrol. 2013, 486, 136–150, doi:10.1016/j.jhydrol.2013.01.017.
88. Torres-Martínez, J.A.; Mora, A.; Knappett, P.S.K.; Ornelas-Soto, N.; Mahlknecht, J. Tracking Nitrate and Sulfate Sources in Groundwater of an Urbanized Valley Using a Multi-Tracer Approach Combined with a Bayesian Isotope Mixing Model. Water Res. 2020, 182, 115962, doi:10.1016/j.watres.2020.115962.
89. Szramek, K.; Walter, L.M.; Kanduč, T.; Ogrinc, N. Dolomite Versus Calcite Weathering in Hydrogeochemically Diverse Watersheds Established on Bedded Carbonates (Sava and Soča Rivers, Slovenia). Aquat. Geochem. 2011, 17, 357–396, doi:10.1007/s10498-011-9125-4.
90. Brook, G.A.; Folkoff, M.E.; Box, E.O. A World Model of Soil Carbon Dioxide. Earth Surf. Process. Landf. 1983, 8, 79–88, doi:10.1002/esp.3290080108.
91. Schoeller, H. Qualitative Evaluation of Groundwater Resources. In Methods and Techniques of Groundwater Investigations and Developemnt; Water Resource Series; Paris, 1963; pp. 54–83.
92. Kumar, P.; Mahajan, A.K.; Kumar, A. Groundwater Geochemical Facie: Implications of Rock-Water Interaction at the Chamba City (HP), Northwest Himalaya, India. Environ. Sci. Pollut. Res. 2020, 27, 9012–9026, doi:10.1007/s11356-019-07078-7.
93. Gaillardet, J.; Dupré, B.; Louvat, P.; Allègre, C.J. Global Silicate Weathering and CO2 Consumption Rates Deduced from the Chemistry of Large Rivers. Chem. Geol. 1999, 159, 3–30, doi:10.1016/S0009-2541(99)00031-5.
94. Wang, J.; Lu, N.; Fu, B. Inter-Comparison of Stable Isotope Mixing Models for Determining Plant Water Source Partitioning. Sci. Total Environ. 2019, 666, 685–693, doi:10.1016/j.scitotenv.2019.02.262.

95. Talib, M.; Tang, Z.; Shahab, A.; Siddique, J.; Faheem, M.; Fatima, M. Hydrogeochemical Characterization and Suitability Assessment of Groundwater: A Case Study in Central Sindh, Pakistan. Int. J. Environ. Res. Public. Health 2019, 16, 886, doi:10.3390/ijerph16050886.
96. Custodio, E.; Jódar, J. Simple Solutions for Steady–State Diffuse Recharge Evaluation in Sloping Homogeneous Unconfined Aquifers by Means of Atmospheric Tracers. J. Hydrol. 2016, 540, 287–305, doi:10.1016/j.jhydrol.2016.06.035.
97. Municio, G. Estudi geològic del marge meridional de la làmina del Port del Comte (Pirineu Oriental): desxifrant-ne l'estructura i estratigrafía. BSc. Thesis in Geology., Universitat Autònoma de Barcelona: Catalonia, Spain, 2017.
98. Blum, A.E.; Stillings, L.L. Chapter 7. FELDSPAR DISSOLUTION KINETICS. In Chemical Weathering Rates of Silicate Minerals; White, A.F., Brantley, S.L., Eds.; De Gruyter: Berlin, Boston, 1995; pp. 291–352 ISBN 978-1-5015-0965-0.
99. Van Stempvoort, D.R.; Krouse, H.R. Controls of δ 18 O in Sulfate: Review of Experimental Data and Application to Specific Environments. In Environmental Geochemistry of Sulfide Oxidation; Alpers, C.N., Blowes, D.W., Eds.; ACS Symposium Series; American Chemical Society: Washington, DC, 1993; Vol. 550, pp. 446–480 ISBN 978-0-8412-2772-9.
100. Cravotta, C.A. Use of Stable Isotopes of Carbon, Nitrogen, and Sulfur to Identify Sources of Nitrogen in Surface Waters in the Lower Susquehanna River Basin, Pennsylvania; Water-Supply Paper; U.S. Geological Survey: Pennsylvania, 1997;
101. Krouse, H.R.; Mayer, B. Sulphur and Oxygen Isotopes in Sulphate. In Environmental Tracers in Subsurface Hydrology; Cook, P.G., Herczeg, A.L., Eds.; Springer US: Boston, MA, 2000; pp. 195–231 ISBN 978-1-4613-7057-4.
102. Mayer, B. Assessing Sources and Transformations of Sulphate and Nitrate in the Hydrosphere Using Isotope Techniques. In Isotopes in the Water Cycle; Aggarwal, P.K., Gat, J.R., Froehlich, K.F.O., Eds.; Springer-Verlag: Berlin/Heidelberg, 2005; pp. 67–89 ISBN 978-1-4020-3010-9.
103. Vitòria, L.; Otero, N.; Soler, A.; Canals, À. Fertilizer Characterization: Isotopic Data (N, S, O, C, and Sr). Environ. Sci. Technol. 2004, 38, 3254–3262, doi:10.1021/es0348187.
104. Otero, N.; Soler, A.; Canals, À. Controls of d34S and d18O in Dissolved Sulphate: Learning from a Detailed Survey in the Llobregat River (Spain). Appl. Geochem. 2008, 23, 1166–1185, doi:10.1016/j.apgeochem.2007.11.009.
105. Ortí, F.; Pérez-López, A.; García-Veigas, J.; Rosell, L.; Cendón, D.I.; Pérez-Valera, F.

SULFATE ISOTOPE COMPOSITIONS d34S, d18O) AND STRONTIUM ISOTOPIC RATIOS (87Sr/86Sr) OF TRIASSIC EVAPORITES IN THE BETIC CORDILLERA (SE SPAIN). 2014, 13.

106. Utrilla, R.; Pierre, C.; Orti, F.; Pueyo, J.J. Oxygen and Sulphur Isotope Compositions as Indicators of the Origin of Mesozoic and Cenozoic Evaporites from Spain. Chem. Geol. 1992, 102, 229–244, doi:10.1016/0009-2541(92)90158-2.
107. Mizutani, Y.; Rafter, T.A. Isotopic Behaviour of Sulphate Oxygen in the Bacterial Reduction of Sulphate. Geochem. J. 1973, 6, 183–191, doi:https://doi.org/10.2343/geochemj.6.183.
108. Otero, N.; Vitòria, L.; Soler, A.; Canals, A. Fertiliser Characterisation: Major, Trace and Rare Earth Elements. Appl. Geochem. 2005, 20, 1473–1488, doi:10.1016/j.apgeochem.2005.04.002.
109. Craine, J.M.; Brookshire, E.N.J.; Cramer, M.D.; Hasselquist, N.J.; Koba, K.; Marin-Spiotta, E.; Wang, L. Ecological Interpretations of Nitrogen Isotope Ratios of Terrestrial Plants and Soils. Plant Soil 2015, 396, 1–26, doi:10.1007/s11104-015-2542-1.
110. Kelley, C.J.; Keller, C.K.; Evans, R.D.; Orr, C.H.; Smith, J.L.; Harlow, B.A. Nitrate–Nitrogen and Oxygen Isotope Ratios for Identification of Nitrate Sources and Dominant Nitrogen Cycle Processes in a Tile-Drained Dryland Agricultural Field. Soil Biol. Biochem. 2013, 57, 731–738, doi:10.1016/j.soilbio.2012.10.017.
111. Mengis, M.; Walther, U.; Bernasconi, S.M.; Wehrli, B. Limitations of Using δ 18 O for the Source Identification of Nitrate in Agricultural Soils. Environ. Sci. Technol. 2001, 35, 1840–1844, doi:10.1021/es0001815.
112. Cabello, P.; Roldán, M.D.; Moreno-Vivián, C. Nitrate Reduction and the Nitrogen Cycle in Archaea. Microbiology 2004, 150, 3527–3546, doi:10.1099/mic.0.27303-0.
113. Kroopnick, P.; Craig, H. Atmospheric Oxygen: Isotopic Composition and Solubility Fractionation. Science 1972, 175, 54–55, doi:10.1126/science.175.4017.54.
114. Kendall, C.; Elliott, E.M.; Wankel, S.D. Tracing Anthropogenic Inputs of Nitrogen to Ecosystems. In Stable Isotopes in Ecology and Environmental Science; Michener, R., Lajtha, K., Eds.; Blackwell Publishing Ltd: Oxford, UK, 2007; pp. 375–449 ISBN 978-0-470-69185-4.
115. Vitòria, L.; Soler, A.; Canals, À.; Otero, N. Environmental Isotopes (N, S, C, O, D) to Determine Natural Attenuation Processes in Nitrate Contaminated Waters: Example of Osona (NE Spain). Appl. Geochem. 2008, 23, 3597–3611, doi:10.1016/j.apgeochem.2008.07.018.

116. Aravena, R.; Mayer, B. Isotopes and processes in the nitrogen and sulfur cycles. In Environmental isotopes in biodegradation and bioremediation; Aelion, C.M., Höhener, P., Hunkeler, D., Aravena, R., Eds.; CRC Press: Boca Raton, 2010; pp. 203–246 ISBN 978-1-56670-661-2.
117. Fukada, T.; Hiscock, K.M.; Dennis, P.F.; Grischek, T. A Dual Isotope Approach to Identify Denitrification in Groundwater at a River-Bank Infiltration Site. Water Res. 2003, 37, 3070–3078, doi:10.1016/S0043-1354(03)00176-3.
118. Böttcher, J.; Strebel, O.; Voerkelius, S.; Schmidt, H.-L. Using Isotope Fractionation of Nitrate-Nitrogen and Nitrate-Oxygen for Evaluation of Microbial Denitrification in a Sandy Aquifer. J. Hydrol. 1990, 114, 413–424, doi:10.1016/0022-1694(90)90068-9.

7 CONTRIBUTION TO THE EUROPEAN GEOERA RESOURCE PROJECT

In the framework of the GeoERA (Establishing the European Geological Surveys Research Area to deliver a Geological Service for Europe, 731166) H2020 Era-Net, the "Resources of groundwater harmonized at cross-border and pan- European scale (RESOURCE)" co-financed project was approved. Its work package 7 (WP7), called CHAlk and KArst Aquifer (CHAKA), focused on Typology of karst aquifers in Europe and the development of new easy-to-use technical topological classification systems oriented to karstic aquifers for the categorization of available resources and their vulnerability. That project was executed between 2018 and 2021.

During the course of the thesis, I have contributed within the WP7 CHAKA as a member of the Hydrogeology team of the Geological Survey of Catalonia (Institut Cartogràfic i Geologic de Catalunya) leading the work of the "**Port del Comte karst aquifer pilot area**". This chapter presents the overall work carried out and the results obtained. The work done must be considered as a complement to the specific objectives of the thesis by compendium of articles.

7.1 Objectives

To date, numerous authors have used methods to classify springs, and specifically, karst springs, based on geological and hydrogeological observations and using their expert knowledge for the establishment of a conceptual theoretical hydrogeological model of functioning (Ford and Williams, 1989, 2007), or on classified metrics such as flow rates and water chemistry either from specific data, or based on hydrographs and hydro-chemograms and their respective statistics (Mangin, 1970, 1975 and 1984; Kresic and Stevanović, 2010; Omed and Broder, 2015, among other). Other authors propose methods for the identification of the karst functioning system based on numerical models. (Hartmann et al., 2013). In deliverable D.1 of the CHAKA project (Hakoun et al., 2020), the state of the art on methods is collected and analysed in greater depth.

In any case, the reality is that, in Europe, although karst aquifers represent a widespread groundwater resource, there is no unified classification and therefore each country usually adopts his own typology, taking into account the characteristics of their own karst aquifers.

The main objective of the CHAKA (CHAlk and KArst) work package, part of the GeoERA RESOURCE project (http://geoera.eu/projects/resource9/), was to achieve a joint classification typology based on metrics that should be applicable to a large spectrum of karstic environments, availability of data and to associate it to recommendations regarding aquifer management (aquifer protection, monitoring strategies, exploitation, etc.) and can be integrated not only into the research carried out by European geological surveys organizations in the framework of EuroGeosurveys, but also by water and environmental agencies, researchers and professionals.

7.2 Methods

In the framework of CHAKA work, an Excel based data treatment tool was developed by the geological survey of French (BRGM) and rest of the partners of the project (inclusive ICGC in which myself I was integrated and lead) in order to compute the necessary parameters for the application of the different methodologies. Among them, includes the "Methodology of the functional approach" developed by the Laboratoire Souterrain du CNRS à Moulis thanks to Dr. Alain Mangin as ex-Director or research (nowadays converted to CNRS Moulis Station d'Écologie Théorique et Expérimentale), who implemented the methodology of recession flow curve analysis, discharge flow frequency analysis and time series analysis from different perspectives in karst hydrogeology. All these was already applied in Catalonia in some specific springs by Freixes (2014) as is being cited hereafter. Th new Excel tool is called "XLKarst", and it is an open access application ready to be downloaded (link) based on MS Excel for the hydrodynamic characterization of karst Systems (BRGM, 2021).

7.2.1 Classification based on recession flow analysis. The Mangin method (1975)

One of the most used method in the world to classify karst aquifers up to now was developed by Mangin (1970, 1975). It provides information on infiltration processes in the vadose zone of the karst aquifer and groundwater flow into the saturated zone. This has been commonly applied among others mainly in France, Croatia, Spain, Belgium and Greece (Mudarra et al., 2012; Freixes, 2014; Rosas et al., 2016; Paiva and Cunha, 2020; among many other). Specifically, in the territory of Catalonia, Freixes (2014) applied this method in several of the most important and well-known

karst springs (see chapter 1.1.6). The basis of the approach is to model the spring discharge curve after a flood peak (Mangin, 1970). The method is based on the decomposition of the recession curve (that is, the part of the hydrograph between the peak of any flood event to the beginning of the next flood) in two parts: the first corresponds to the 'decrease part' and the second to 'recession part'. The decreasing and recession of the spring discharge are modelled as a sum of function ψ_t and an exponential function $\phi_{(t)}$ as indicated following:

$$Q_{(t)} = \psi_{(t)} + \phi_{(t)}; \quad \text{where}$$

$$\psi_{(t)} = q_0 \cdot \frac{1-\eta}{1+\epsilon\, t}; \quad \text{and} \quad \phi_{(t)} = Q_{Ro} \cdot e^{-\alpha t}; \quad \text{Maillet's law}$$

where:

- $\boldsymbol{\eta}$ – is the infiltration speed coefficient, which represents the speed with which the effect of a given recharge is transmitted to the spring and can be expressed as $\eta = \frac{1}{t_i}$ (days^{-1}). Its value expresses whether the infiltration is fast or slow.
- $\boldsymbol{\epsilon}$ – is the non-dimensional coefficient of "heterogeneity" that characterizes the concavity of the decrease curve, that is, describe the flood recession dynamics still influenced by the recharge event, i.e. for 0<t<ti; and can be expressed as $\epsilon = \frac{1}{t} - 2\eta$; where t is the time that must elapse for q=q_0/2, and q_0 is the flow contributed by the saturated zone at the peak of the flood. is the non-dimensional coefficient of "heterogeneity" used in the homographic function that is chosen by Mangin (1970, 1975) to describe the flood recession dynamics still influenced by the recharge event, i.e. for 0<t<ti.
- **Q_{R0}** (m^3/s) is the value of the modeled discharge using the Maillet's law at *t=0*. It is a fictive discharge that theoretically represents the discharge coming from storage at the beginning of the recession. It is used to compute the infiltration rate q_0.
  q_0 (m^3/s) is the initial infiltration rate, computed as the difference between Q_0 and Q_{R0}.
- **q_i** (m^3/s) is the discharge at $t=t^i$, i.e. when recharge of the phreatic zone is supposed to stop and the Maillet's law applies.
- **t_i** (d) represents the duration of the infiltration after which the baseflow can be modeled by the Maillet's law.
- **α** (d^{-1}) is the recession coefficient used in the Maillet's law.

- **V_d** (m^3) is the dynamical storage volume, which represents the volume of water coming from the phreatic zone that flows to the spring. It is assessed by integration over time of the Maillet's law. Mangin (1975) recommends starting its computation at *t=ti*, considering that the discharge evolution coming from the phreatic zone is unknown from *t=0* to *t=ti*. The calculation of *Vd* by the XLKarst tool (BRGM, 2021) gives $V_d = 86400 \frac{Q'_0}{\alpha}$, with V_d in m^3, Q'_0 in m^3/s and α in d^{-1}.

The function $\psi_{(t)}$is fitted to the decreasing part while the latter function $\phi_{(t)}$is fitted to the recession part (see **Figure 7. 1**):

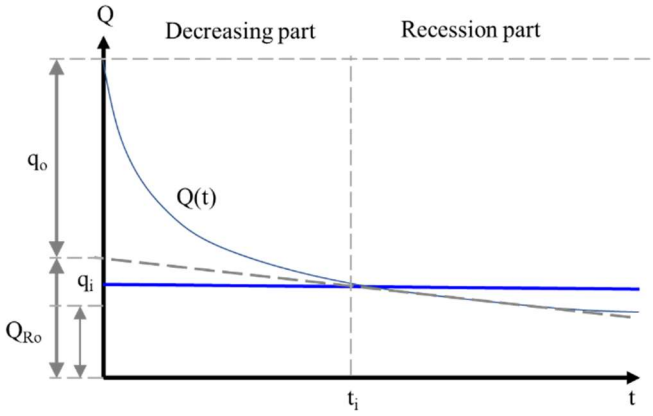

Figure 7. 1. Decomposition of the recession curve, according to Mangin (1970, 1975)

The determination of η and ϵ allows to define the function "y" that represents the way in which the input function (precipitation) has been laminated to its input into the system. The "y" function is expressed as:

$$y = \frac{\psi_{(t)}}{q_0} = \frac{1-\eta}{1+\epsilon\, t}$$

Mangin's classification (Mangin, 1970, 1975) es bases in two indices: "*i*" and "*k*", which describe an infiltration delay and how the aquifer system regulates flow respectively.

- The "i" represents the infiltration delay, and ranges between 0 and 1. It is estimated of the 'y' function when time t = 2 days. High *i* values (i → 1) relates to complex infiltration

processes, conversely small values relate to fast transfers to the saturated zone. Values of i between 0.5 and 1 are related to complex and large-scale infiltration and circulation karstic systems, while values less than 0.25 are systems with a very well-developed karstic conduit system.

- The "k" represents the regulating capacity (Mangin, 1975). It is computed as the ratio of the largest value of '*dynamic volume'* (V_D) respect to the '*transit volume'* or mean discharge computed over the annual hydrological cycles. k was proposed by Mangin (1975) as a non-dimensional parameter lower than 1 for karst systems, but El Hakim and Bakalowicz (2007) consider it as a proxy for the mean residence time (MRT) of water in the phreatic zone, allowing k to be higher than one in their classification to account for karst systems with very large regulating power. In addition, the classification proposed by El-Hakim and Bakalowicz (2007) expresses k in a logarithmic scale. In addition, this last proposed the classification proposed expresses k in a logarithmic scale.

Finally, following the 5 categories proposed by Mangin (1975), and updating it according El-Hakim and Bakalowicz (2007) (**Figure 7. 2**):

- Group (1): ($k < 0.5$; $i > 0.5$): domain of complex systems.
- Group (2): ($k < 0.5$; $0.25 < i < 0.5$): more karstified system upstream than downstream with delay in feeding as a result of non-karstic terrain.
- Group (3): ($k < 0.1$; $i < 0.5$): highly karstified downstream system, very developed.
- Group (4): ($0.1 < k < 0.5$; $i > 0.5$): well-developed speleological network that downstream connects with an important flooded karst.
- Group (5) domain of non-karstic or scarcely karstified systems (aquifers porous and fissured carbonates) according Mangin (1975), and karst systems with very large regulating capacity or for deep confined karst aquifers according to El-Hakim and Bakalowicz (2007)

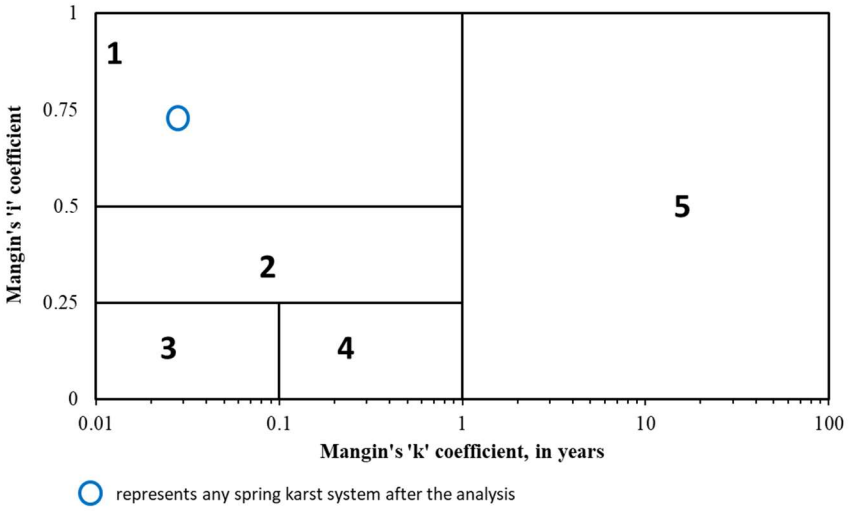

Figure 7. 2. Plot for the classification of karst aquifers systems. Based on Mangin (1975) and after modified for high *k (>1)* by El-Hakim and Bakalowicz (2007).

The k index is the ratio between the dynamic storage volume and the mean annual volume flowing through the phreatic zone. The *dynamic volume* (V_D) is given by:

$$V_{Dr} = \int_0 q_i . e^{-at} = \frac{q_i}{\alpha} . c$$

in which qi is the flow rate at the beginning of the recession period (see Figure 7. 1**Error! No s'ha trobat l'origen de la referència.**). Thus, V_{Dr} can be calculated from the quantitative analysis of the recession period with Maillet's law (see above).

It is important to emphasize that apart from the fact that through the recession curves it is possible to calculate a volume V_{Dr} and infer the MRT, as indicated by El-Hakim and Bakalowicz (2007), the mean time can also be calculated by means of environmental tracers (referred as mean transit time or MTT according to with what was presented in chapter 3). In this respect, Zuber (1986) and Farlin and Maloszewski (2013) highlight a very important key point to be taken into account when analysis the results as far as both values MRT and MTT and the respective V_{Dr} and V_{De} (that here refers the mean time in the saturated zone calculated from a 'hydraulic recession' and the mean time calculated from 'environmental tracer transport', and their 'dynamic volume') will be approximately equal if only two assumptions are met:

a) Zones of stagnant volume 'Vs' of water are negligible or must be inactive: Stagnant zones can be present in double porous aquifers with active diffusion into the matrix.
b) The geometric bottom of the aquifer should not be convex, i.e. the basis of the aquifer must be sloping continuously towards the outlet or be at most horizontal. If not, some flowlines can plunge below the heigh of the aquifer outlet (the spring point) in a part of groundwater reservoir referred to by Zuber (1986), the called 'minimum volume Vm', that does not influence the discharge rate because it is situated deeper than the discharging point. In that case, the MRT based on recession only inform on the dynamic volume, i.e. the outflow rate (the volume of water stored above the height of the discharging point), whereas MTT based on tracer consider the sum of the dynamic and that 'minimum volume'.

Therefore, two assumptions must be checked in order to be able to compare the volume and transit times estimated by recession and by environmental tracers. In case when these not happen, the comparison between MRT calculated from recession and MTT estimated from traces allow to estimate the ratio matrix porosity to total porosity.

7.2.2 Classification based on correlation analysis

Another common classification system used mostly by the French school is through the correlative (time) and spectral analysis (frequencies) of time-series. The mathematical development was formulated by Box and Jenkins (1974) and after his adaptation by Mangin, A. (1981a, 1981b, 1985) for karst hydrogeology, it has been applied extensively in many papers (Larocque, et al 1998; Antigüedad, I. 1998; Jiménez-Gavilán and Andreo, 2012; Mudarra et al., 2012; Freixes, 2014, Pavlic and Parlov, 2019; Tamburini et al., 2020; Denic-Jukic, et al., 2020; Çağdaş et al., 2020) among many other). It can be applied to the series of rainfall (P – precipitation) over the aquifers (input signal) and flows (Q – flow rates) from the discharge points – springs - (output signal) in a simple way, but above all crosswise, it provides information on the behaviour of the aquifer, that is, of the modulating effect produced by it on rainfall and, consequently, on the structure and functioning of the investigated aquifer. More detailed explanations and the complete mathematical development can be found at Larocque et al. (1998) and Padilla and Pulido-Bosch (1995).

Auto-correlation and simple spectral analysis

Some karst springs exhibit a certain degree of high or low dependence of past events. This reflects the memory of the system and is expressed as the called 'Memory effect - ME". This can be estimated by simple correlation analysis which quantifies the linear dependency of successive values over a time period. The defined '**auto-correlation function' r_k,** quantifies the lineal dependency of successive values over a period of time. If an event has a long-term influence on the time series, the slope of the r(k), decreases slowly

$$r_k = \frac{\frac{1}{n-k}\sum_{i=1}^{n-k}(x_i - x_{av})(x_{i+k} - x_{av})}{\frac{1}{n}\sum_{i=1}^{n}(x_i - x_{av})^2}$$

The numerator is the called C(k) autovariance or just covariance, and the denominator is the variance of the time series, where

n - is the total number of data in the sample

k – is the time lag (k = 0 to m), where m is the truncation point, which accordingly to Mangin (1984) must be taken 1/3 of the length of the whole dataset

x_i – is the value of the variable (spring discharge) at time t = i

x_{i+k} – is the value of the variable (spring discharge) at time t = i+k

x_{av} – is the average value of the data in the sample.

Auto-correlation function' r_k, describes the time series' persistence, which is the tendency for the magnitude of an event to be dependent on the magnitude of the previous event. Therefore, persistence is present if data in the time series are dependent on each other, describing a **'Memory Effect' ME** of a system (Schuler et al., 2020). The ME attributed to the karst system represents the way the system modulates the input, i.e. the precipitation in form of effective recharge, either in the short, medium or long term, which is linked strongly to its internal degree of organization, i.e., karstification, its water storage capacity and its hydrodynamic properties (Mathevet et al., 2004). The ME value (Mangin, 1984) is computed graphically as the time lag that is reached as the

autocorrelation function of the Q flow discharge time series falls below the value of $r_k = 0.2$. It somehow expresses the resilience of the karst system after a rain event and is used to compare the response time between karst systems. According to the author, high memory suggests a poorly developed karst network with large groundwater reserves (storage), whereas a low memory value is understood to reflect low storage capacity and highly karstified aquifer. Nevertheless, it also must be considered that the shape of the resulting correlogram depends also on other aspects beyond the internal karst structure such the frequency of precipitation events, wet and dry periods, etc (Eisenlohr, R, 1997). Therefore, the auto-correlogram should be considered as a more simply indicative tool when developing conceptual models of karst springs.

The simple spectral analysis is complementary to the auto-correlation analysis. The '**spectral density function**' $\boldsymbol{S(f)}$ corresponds to a change from a time mode to a frequency mode through a Fourier transformation of the auto-correlation function. The interpretation of $S(f)$ through the identification of the different peaks representing periodical phenomena in the output series, leads to the characterization of the system:

$$S(f) = 2 \cdot \left[1 + 2 \sum_{k=1}^{m} D(k) \cdot r(k) \cdot cos(2\pi f k)\right]$$

$$D(k) = \frac{\left(1 + \cos \pi \frac{k}{m}\right)}{2}$$

where:

f = k/2m; j=1 to m, f – is the frequency and

$D(k)$ – is a filter proposed to ensure that the $S(f)$ values are not biased

The 'spectral density function' $S(f)$ of the flow discharge Q time series allows determines the '**regulation time**' $\mathbf{T_{reg}} = \frac{S(f=0)}{2}$; i.e. the value of the spectral density function when frequency = 0 divided by 2. It defines the duration of the influence of the input signal to the output and gives an indication of the length of the impulse response of the system (Larocque et al., 1998). Other key aspect is the called '**cut-off frequency**' **Fc** (Mangin, 1981a, 1981b and 1984) that is the time lag when the S(f) of flow discharge data gets the values lower than 1 and gets negligible. Mangin (1984) established a system for classifying the functioning of karst aquifers based on the parameters **ME**, $\mathbf{T_{reg}}$ and **Fc** obtained from the correlogram analysis. The method compares them with four well-

known karst aquifers taken as reference ("Aliou spring": corresponding to system highly karstified and evolved and well drained with 'Reduced' **ME:** 5 days; $\mathbf{T_{reg}}$:10-15 days; **Fc:** 0.30; "Baget spring" corresponding to medium karstified system, but well drained: 'Low' **ME:** 10-15 days; $\mathbf{T_{reg}}$: 20-30 days; **Fc:** 0.20; "Fontestorbes spring" corresponding to moderately karstified system with imperfect drainage: 'high' **ME:** 50-60 days; $\mathbf{T_{reg}}$: 50 days; **Fc:** 0.10; "Torcal spring": corresponding to poorly drained and with very high inertia or 'considerable or very high' **ME:** 70 days; $\mathbf{T_{reg}}$: 70 days; **Fc:** 0.05) used for many authors (Ibarra-Lozano et al., 1987; Jiménez-Gavilán and Andreo, 2012, among many others).

Cross-correlation and simple spectral analysis

By contrast, the '**cross-correlation function**' $\boldsymbol{r_{xy}(k)}$ quantifies the strength of the linear relationship between two time series (input-output) of a karst aquifer (Larocque et al., 1998). Let consider x representing the input time series, i.e. precipitation P(t) and y represent the resulting output time series, i.e. the flow discharge Q(t) from a karst hydrological system. The cross-covariance function between series x and y, $C_{xy}(k)$ both of length n, is defined by:

$$C_{xy}(k) = \begin{cases} \frac{1}{n} \cdot \sum_{t=1}^{n-k} (x_t - \bar{x}) \cdot (y_{t+k} - \bar{y}), k = 0, 1, 2, \ldots. \\ \frac{1}{n} \cdot \sum_{t=1}^{n-k} (y_t - \bar{y}) \cdot (x_{t-k} - \bar{x}), k = 0, -1, -2, \ldots. \end{cases}$$

Where, $\bar{x}$ and $\bar{y}$ are the average values of time-series of x and y (i.e., P(t) and Q(t) available for the karst spring), respectively. Therefore, the '**cross correlation function' $\mathbf{r_{xy}(k)}$** at lag k is estimated by the following equation:

$$r_{xy}(k) = \frac{C_{xy}(k)}{\sigma_x \cdot \sigma_y}, k = 0, \pm 1, \pm 2, \ldots.$$

where, σ_X and σ_y are the standard deviations of the time series x and y, respectively.

The '**cross-spectral density function' $\boldsymbol{S_{xy}(f)}$** represents the Fourier transformation of the $r_{xy}(k)$. In polar coordinates, the cross spectrum $S_{xy}(f)$ can be expressed as: by the following equation:

$$S_{xy}(f) = \left| S_{xy}(f) \right| e^{-i\theta_{xy}(f)}$$

where: f- frequency; $\left| \boldsymbol{S_{xy}(f)} \right|$ represents the '**cross-amplitude function'** and $\boldsymbol{\theta_{xy(f)}}$ represents the '**phase function'** for the frequency *f*, which represents the travel time of the information, are defined as:

$$\theta_{xy}(f) = arctan \frac{\Lambda_{xy}(f)}{\psi_{xy}(f)}$$

$$\left| S_{xy}(f) \right| = \sqrt{h_{xy}^2(f) + \lambda_{xy}^2(f)}$$

$$\Lambda_{xy}(f) = 2\left[\sum_{k=1}^{m}\left[r_{xy}(k) - r_{yx}(k)\right]\right] \cdot D(k)\sin(2\pi f k)$$

$$\psi_{xy}(f) = 2\left[r_{xy}(0) + \sum_{k=1}^{m}\left[r_{xy}(k) - r_{yx}(k)\right] \cdot D(k)\cos(2\pi f k)\right]$$

where, according to Padilla and Pulido (1995):

$\Lambda_{xy}(f)$ – is the called 'quadrature-spectrum', and

$\psi_{xy}(f)$ – is the called 'co-spectrum', and

$D(k)$ – is the same filter proposed to ensure that the $S(f)$ values are not biased

Finally, with the cross-amplitude function, two other functions can be defined: The called '**coherence function'** CO_{xy} which represents the linearity of the input/output relationship and the called '**gain function'** $g_{xy}(f)$ which expresses the amplification (>1) or attenuation (<1) of the output signal in comparison to the input signal for the different frequencies. These are defined as:

$$CO_{xy} = \frac{\left| S_{xy}(f) \right|}{\sqrt{S_x(f) \cdot S_y(f)}}$$

$$g_{xy}(f) = \frac{|S_{xy}(f)|}{\sqrt{S_x(f)}}$$

where $S_x(f)$ and $S_y(f)$ are the simple spectral functions; whereas $|S_{xy}(f)|$ is the cross spectral density function. CO_{xy} should be ~1 when a change in the input (precipitation) implies a proportional change of the output (discharge). The '**phase function'** can be used complementarily to the **cross-correlation function' r_{xy}(k)** analysis in term of calculating the mean delay time, concerning different frequencies. According to Padilla and Pulido (1995), the mean delay 'd' in '**phase function'** can be obtained by the slope of the line of best fit to $\theta_{xy}(f) = 2\pi df$.

7.2.3 Cumulative frequency analysis of flow discharge duration

Flow rates and their frequency using semi-normal probability plots on a logarithmic scale can be ranked according to Mangin (1971, 1975). The curve of cumulative frequency of flows of a spring represents the percentage of days of the period considered in which the flow has a value equal to or less than a given one. It informs about the regularity or irregularity of the flows of a spring, that is, the frequency with which a certain flow occurs. For each flow, the relative frequency (absolute frequency divided by the number of days of the considered period), can be represented cumulatively. According to Mangin, (1971), the distribution of relative frequencies of the flows can be assimilated to the positive part of a normal Gaussian distribution. The relative percentage of the occurrence of a discharge is defined by a probability law of the Laplace (Mangin, 1971):

$$F(x) = Prob(X < x) = \frac{2}{\sqrt{2}} \int_0^x e^{\frac{-u^2}{2}} \cdot du$$

where us is the variable of the probability function and $F(x)$ is the probability that X<x. The representation of the cumulative probability $Prob(X < x)$ on the Y axis and the flow classes Q/Q_L on a logarithmic scale on the X axis (where Q is a given discharge and Q_L the lowest observed discharge flow) is different depending on the karstic system being considered will result in a set of points aligned in one or several sections. The "XLKarst" tool developed by BRGM (2021) allows

to generate it automatically from the available Q time-series. Thus, in homogeneous aquifer the relationship or response is approximately linear, with slope 'a'. The deviation from that linearity can be identified in changes in the slope of the straight line for a given range of discharge. Numerous authors have applied this methodology (among the most recent Mudarra et al., 2012; Rosas et al., 2015; Dubois, et al, 2020). The resulted graph can be interpreted following the hydrodynamic supported models proposed by Dörfliger et al., 2010 and the guide presented by Hakoun et al., 2020 (modified after Crochet and Marsaud (1997) and Mangin (1971).

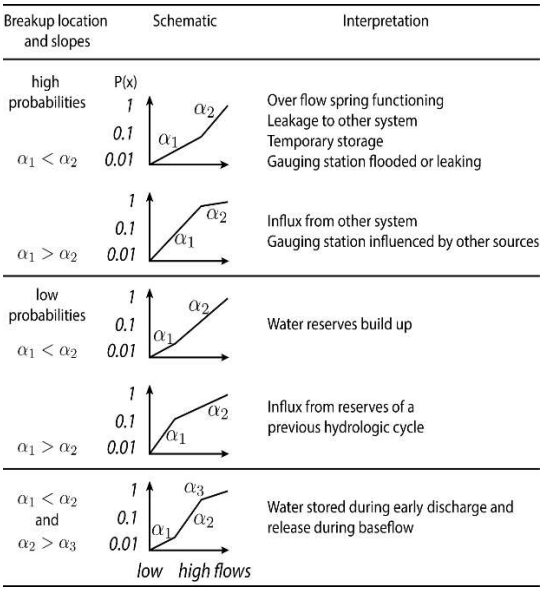

Figure 7. 3. Interpretation of the slope trap sequences of cumulative frequencies with respect to the logarithm of flow classes (source: XLKarts tool, (BRGM, 2021).

According to Mangin (1971), changes in the slope of the straight line defined between different sections reflect variations in the rate of growth or decrease in flows. Thus, an "**increase"** in slope means that the spring drains certain flows for a longer time, that is, the variations are slower. In times of *flooding* it represents a temporary leakage of reserve to other systems or the overflow functioning of the spring or activation of "trop-pleins". In times of *recession* it would indicate a draining of a pre-existing reserve. On the other hand, a "**decrease**" in the slope indicates a lower frequency, that is, a faster growth or decrease in the flow of the spring. In times of *flooding* it represents the contribution of a reserve from other system while, in times of *recession*, it would indicate the formation of a reserve that could be restored in a subsequent cycle or the existence of water losses in a drainage karst network other than the one which usually drains the spring.

7.2.4 CHAKA classification methods

The hydrodynamic typology applied using the recession analysis as well as the correlation and spectral analysis is usually applied by karst researchers to compare karst springs but is not generally used by water operators and management authorities. From the perspective of water providers and policymakers, the main interest is the capability of an aquifer to provide good quality of water in large quantities and at long term. This implies questions about the volume of water stored into the aquifer, but also above all the vulnerability of this aquifer to pollution. The objective of the CHAKA WP5- GeoERA RESOURCE project in which I have fully involved participating leading the pilot area of 'The Port del Comte high-mountain karst aquifer', was to provide water providers and regulators with a classification method which uses indicators that are important for groundwater resource management and provision. The two main classical management issues in relation with aquifer characteristics have been identified:

- the quantity of water that the aquifer is able to store and provide
- the quality of water that the aquifer can supply which is dependent on the vulnerability of this aquifer to pollution.

In this sense, 3 approaches have been proposed with different degrees of necessary information.

- **Method 1: Classification of karst aquifer intrinsic vulnerability to pollution**. It uses information on the catchment coupled with indicators measured on spring in order to assess the intrinsic vulnerability of the aquifer to pollution.
- **Method 2: Mixed classification system V-KGWRAI.** It uses the method 1 plus the the Karst Groundwater Resource Availability Index (KGWRAI) parameter obtained with from the discharge time series analysis.
- **Method 3: V-RC classification system**: It is a quantitative classification based on monitoring data - discharge and other time series.

These three methods are described and applied to the case studies below. The three methods have

been principally developed in the framework of the CHAKA WP5- RESOURCE project (Maréchal et al., 2021) in which the " Cardener spring" located in the 'high mountain karstic aquifer of Port del Comte' was one of the 16 pilot cases in karstic springs throughout EU (**Figure 7. 4**) included as case studies in the project and in which the methods of classification. More Information about the case studies can be found in Maréchal et al. (2021a) and the RESOURCE project website.

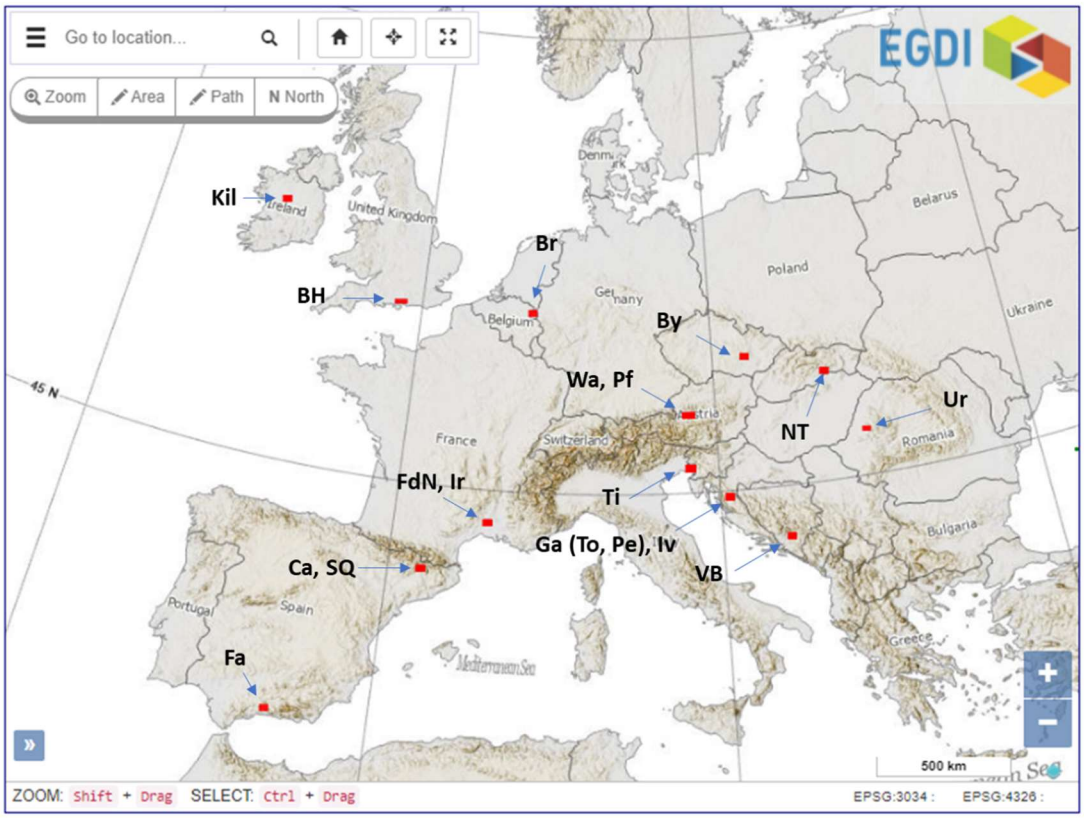

Figure 7. 4. Location of karst springs tested within the CHAKAWP5- GeoERA RESOURCE project. The point identified as "Ca" corresponds to the "Cardener Spring" located in the 'Port del Comte high-mountain karst aquifer'(modified, from the RESOURCE map viewer – EGDI EuroGeoSurveys' European Geological Data Infrastructure https://geoera.eu/projects/resource9/resource-map-viewer/)

Method 1: Classification of karst aquifer intrinsic vulnerability to pollution based on catchment information

The aim of this method is to use multiple criteria to assess the intrinsic vulnerability of a spring in a karst aquifer to pollution. In this case, by intrinsic vulnerability we mean the vulnerability of the

spring that arises due to the karstic nature of the aquifer which enables rapid groundwater flow through connected networks of solutional fissures, conduits and caves, whatever the nature of the pollutant. Focused recharge in karst is demonstrated to be a key feature of risk of contamination (Hartmann et al., 2014). Intrinsic vulnerability does not consider the risk of pollution of a spring due to long-term land use practices within the catchment. Karst networks may provide varying degrees of attenuation via dispersion into smaller voids and the intrinsic vulnerability depends on how much flow occurs rapidly through connected networks of larger voids or the rate at which water and contaminants can enter these voids. This classification uses parameters which are indicative of this vulnerability and it can be applied to any spring regardless of the amount of data available, including those springs with no time series data. Therefore, this method has to be considered as the most general classification level and as a first approximation. Where time series data are available, the outputs from this method are combined with discharge time series data in Method 2, to provide a more comprehensive assessment of karst aquifers including both intrinsic vulnerability and reserve assessments.

Method 1 considers 6 parameters (for springs) which are indicative of vulnerability: 1) Surface Karst Features (SKF); 2) Cave Development (CD); 3) Water Quality Indicators (WQI) of rapid groundwater flow; 4) Presence of Coliforms (CF); 5) Tracer Velocity from tracer test (TV) indicating rapid groundwater flow; 6) Spring Discharge Response (SDR).

The surface karst features (SKF) Surface karst features result in high vulnerability as they are indicative of connected karstic flowpaths through the unsaturated zone, and enable pollutants to travel rapidly from the surface to the saturated zone, and their scores are:

- *SKF with direct water input present in catchment = high vulnerability, Score 3*
- *SKF with no obvious water input present in catchment = moderate vulnerability, Score 2*
- *No SKF present in catchment = low vulnerability, score 1*

For the assessment of the “Cave development” (CD) criteria, it is assumed that the more extensive the cave development is, the more vulnerable the aquifer will be. Therefore, an assessment of the degree of cave development (i.e. conduits that are large enough for humans to enter and are therefore indicative of a greater degree of conduit development) is used for assessing the aquifer vulnerability. The cave Development (CD) scores are:

- *Caves > 1 km in length present in the catchment = high vulnerability, score 3*
- *Caves < 1 km in length present in the catchment = moderate vulnerability, score 2*
- *No caves present in the catchment = low vulnerability, score 1.*

The "water quality" parameter assumes that evidence from chemical, physicochemical, or ecological measurements that is indicative of rapid groundwater flows can be used as a proxy of vulnerability of groundwater to pollution due to the presence of karstic flowpaths enabling the rapid groundwater flow. Water Quality Indicators (WQI) include (but are not limited to) for example: turbidity, salinity, etc. The concept is to see how many WQI are observed in the spring water. More explanation of the criteria to apply the method can be found in (Maréchal et al., 2021b).

- *More than one indicator of rapid flow present at the spring = High vulnerability, Score 3*
- *One indicator of rapid flow present at the spring, = moderate vulnerability, Score 2*
- *No indicators of rapid flow present at the spring, but monitoring conducted = Low vulnerability, Score 1.*

The "Coliforms" parameter assumes that the more coliforms that are present in groundwater, the higher the intrinsic vulnerability of the aquifer Coliforms (CF) scores are:

- *Maximum coliform counts > 1000 cfu/100 mls = high vulnerability, score 3*
- *Maximum coliform counts 10 to 1000 cfu/100 mls, = moderate vulnerability, score 2*
- *Maximum coliform counts < 10 cfu/100 mls = low vulnerability, score 1, if sufficient sampling coverage following rainfall events*

The Tracer tests are extremely useful for assessing vulnerability as they provide direct evidence for rapid groundwater flow impacting a spring. Their scores, are assed according with the estimated velocity obtained with the results and are:

- *Tracer velocity of > 500 m/day; or velocities of 10-500 m/day combined with tracer recoveries > 5 % = high vulnerability, score 3*
- *Tracer velocity of 10 to 500 m/day with no tracer recovery data, or with tracer recovery < 5 % = moderate vulnerability, score 2*
- *Tracer tests with no tracer recovery from all stream sinks in the catchment or from at least 3 different injection points if no stream sinks present = low vulnerability, score =1*

The spring discharge response (SDR) scores are:

- *Rapid response of spring observed within 24 hours of rainfall = high vulnerability, score 3*
- *Response of spring observed within more than 24 hours = moderate vulnerability score 2*
- *No discernible short-term responses to rainfall = low vulnerability, score 1*

For each parameter a score of 1 (low vulnerability), 2 (moderate vulnerability), or 3 (high vulnerability) is assigned. For each spring or borehole abstraction, the average score from all parameters is used as an overall indicator of the vulnerability. Sites with average scores ≥ 2.5 are considered to have high vulnerability, those with scores 1.5 to 2.49 are considered moderately vulnerable, and those with scores < 1.5 are considered low vulnerability. More explanation of the criteria to apply the method can be found at (Maréchal et al., 2021b).

Method 2: Mixed classification system V-KGWRAI

Method 2 assumed that a long-term discharge time series is available, whatever the time step of this time series, and aims at classifying karst aquifers using a biplot related to the following two parameters:

- the Vulnerability of the spring to pollution, for which the results of method 1 is used,
- the responsiveness of the karst spring, which will be used to characterize either the hydrodynamics of the karst system or the GW resource availability according to the objectives of the classification.

The analysis of the possible parameters to consider in the method are tested and evaluated in Maréchal et al. (2021b). The final approach considered assume that the groundwater availability increases with both the mean flow discharge (**Qavg**) and the Memory Effect (**ME**) (Mangin, 1984). The results are expressed in two different plots. In the first plot the Y axis represent the mean flow discharge (**Qavg**). The X axis represents the Memory Effect (**ME**)/125. Then, crossing the information given by the **Qavg** and the **ME** is used to assess a new Karst Groundwater Resource Availability Index (**KGWRAI**): This is done by subdividing the Y axis representing the **Qavg** in 4 classes in a log scale from 0.01 m^3/s to 100 m^3/s in order to distinguish karst systems that show various mean discharge capacities. This new scale allows to compute an index linearly varying from 0 (0.01 m^3/s) to 1 (100 m^3/s), following a log scale as follow, with **Qavg** in m^3/s.

$$\boldsymbol{Y = \frac{2 + logQ_{avg}}{4}}$$

For instance, a mean discharge of 1 m^3/s will give an index Y of [2+log(1)]/4 = 0.5 = 50%. Then the product of this Y index with the value of the **ME** (divided by 125) is shown on **Figure 7. 5** (a) with the different hyperbolas. Each hyperbola refers to the square roots of this product which ranges between 0 and 1. The result is used as a proxy for the assessment of the karst groundwater availability resource, by means of the KGWRAI index.

$$\boldsymbol{KGWRAI = \sqrt{Y \cdot \frac{ME}{125}} = \sqrt{\frac{2+logQ_{avg}}{4} \cdot \frac{ME}{125}}}$$

This index is then used for the classification combining the vulnerability assessment from the method 1 with the karst GW resource availability index (**Figure 7. 7** b). The result of combining the vulnerability assessment 'V' (from Method 1) with the KGWRAI, leads to different range of classified with the colour scale showed at **Figure 7. 6**.

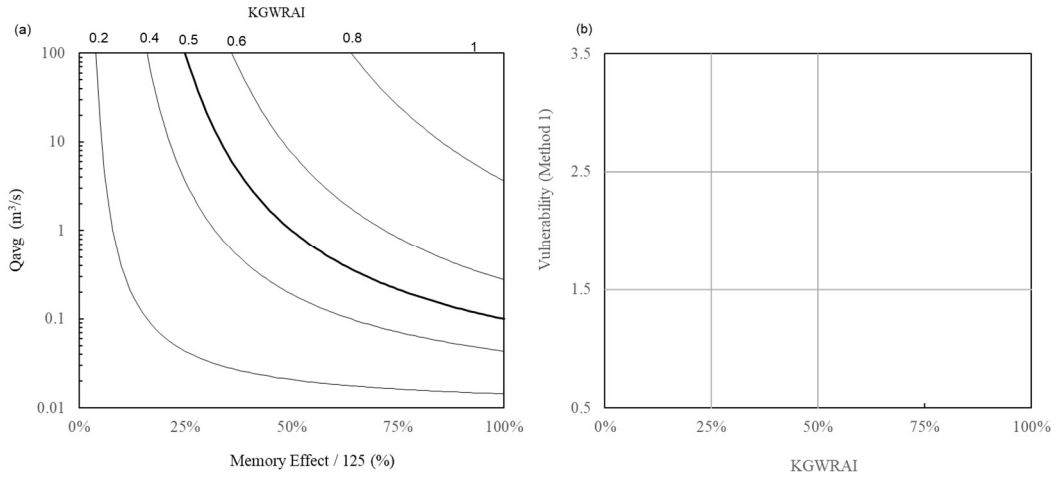

Figure 7. 5. Plots 1 (a) and 2 (b) for the Method 3 RC-V (modified from Maréchal et al., (2021b).

KGWRAI / Vulnerability	Low (KGWRAI <25%)	Medium (25%<KGWRAI <50%)	High (KGWRAI >50%)
High			
Medium			
Low			

Figure 7. 6. Categorization of the mixed classification system IV-KGWRAI. (Maréchal et al., 2021)

Method 3: V-RC classification system

V-RC classification (Maréchal et al., 2021b) is aimed principally at aquifer and environmental management as a basis for effective drinking water source protection measures, draught management among other objectives. The classification separates two source characteristics that are most important for management: 1) '**regulation capacity**' (**RC**), addressing spring discharge dynamics, and 2) '**Intrinsic Vulnerability**' to pollution (**V**). Average discharge (Qavg) is also considered as an additional parameter, which serves as a basis for system size classification. RC in combination with Qav describes available water reserves, especially during draught periods when water shortages are typically present in many karst areas. The classification is based only on quantitative water source monitoring data. The main characteristics of the V-RC classification method are:

- RC **estimation** is based only in discharge monitoring data, while V estimation is based on available monitoring data of various (optional) physio-chemical parameters. In this way, RC and V estimations are mutually separated.

- Input **data** (time series) can have various measuring frequencies and timespan: from occasional or monthly measurements to high frequency long-term continuous (i.e. hourly) measurements. However, resulting reliability level is specified, based on available input data.

- All **incorporated** methods are relatively simple to apply in order to be easily applicable in different countries, on various datasets. The discharge analysis can be performed automatically in the excel XLKarst tool (BRGM, 2021).

- **Classification** results are finally represented using a biplot diagram: Y axis represents Vulnerability, X axis Regulation Capacity. The symbol size is related to system size and symbol color represents estimation reliability level. In that way the representation diagram

provides complete information on the classified source and the basis (available data) on which the classification was made.

The **Figure 7. 7** shows the schematic representation of the combination of possible outcomes in Method 3: V-RC Classification System. The results (circles) are separated in three categories in respect to vulnerability V and regulation capacity RC (9 possible combinations in total). Circles are placed based on their V-RC estimation scores (in decimal number) which allows distinction of different positions within the same category. Additionally, the size of the circles represents system sizes based on their average discharge (5 categories, **Figure 7. 7**), while the color of the circles represents reliability level of the final V score (red=low, yellow=medium, green=high). Wells (classified for V only) and springs lacking data for V estimation (classified for RC only) are not represented on the diagram.

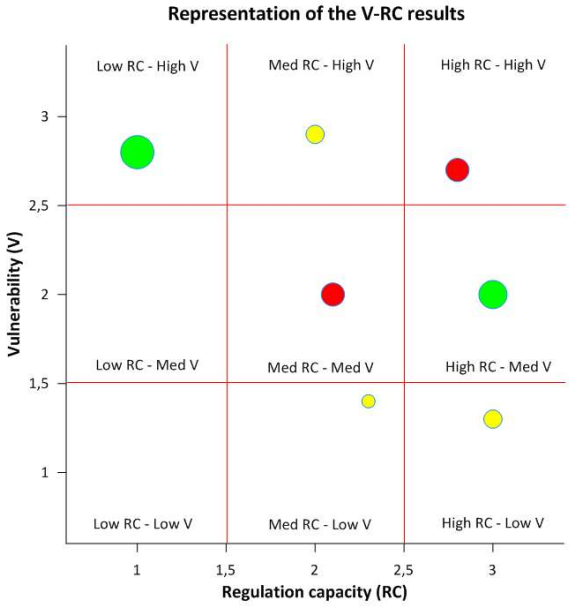

Figure 7. 7. Representation scheme of the Method 3: V-RC classification system (Maréchal et al., 2021)

Regulation Capacity assessment (**RC**)

The evaluation of the **regulation capacity' (RC)**, is based on four parameters: a) the relation between $\mathbf{Q_{max}/Q_{baseflow}}$; b) the **recession coefficient** α; c) the calculation of the '**Memory Effect' (ME)** taken from the Auto-correlation function' r_k analysis (value when r_k= 0.2) of the flow

discharge time-series which can be done using the XLKarst tool (BRGM, 2021); and d) the '**spring variability coefficient' (SVC)**, (Flora, S. P. , 2004; Springer et al., 2004) expressed as:

$$SVC = \frac{Q_{10}}{Q_{90}}$$

where Q_{10} corresponds to the discharge that is exceeded 10% of the time, and Q_{90} is the rate that is exceeded 90% of the time. The final RC score is calculated as a mean value of their results. In that way RC represents aggregate indicator of spring dynamics regarding both flow variability and system inertia. **ME** is mostly applicable for continuous (daily) time series data only while SVC is applicable for both non-continuous (e.g. monthly) and continuous data. If continuous (daily) data is not available, **SVC** still can be used for preliminary RC estimation of the spring, but with low reliability level of the result. Additionally, the average spring discharge value is used for a categorization of a spring size **Table 7. 1**

Table 7. 1. Spring size categories (from **Maréchal et al., 2021**)

$Q_{average}$	Categories
<0.01 m^3/s	v. small (1)
0.01-0.1 m^3/s	small (2)
0.1-0.5 m^3/s	medium (3)
0.5-1 m^3/s	large (4)
>1 m^3/s	v. large (5)

Threshold values for categorizing RC based on '**Memory Effect' (ME)** and the '**spring variability coefficient' (SVC)**, are specified in following **Table 7. 2.**

Table 7. 2. Parameters, corresponding methods and their threshold values for determination of RC and V score (modified from **Maréchal et al., 2021**)

Parameter	Method for estimation	Low (1)	Med (2)	High (3)	Variable
Discharge Q (m^3/s)	SVC (Q_{10}/Q_{90})	>10	3-10	<3	**RC**
	Memory effect (days)	<40	40-80	>80	

	Exp. rec. coef. (α, 1/day)	>0.01	0.005-0.01	<0.005	
	Q_{max}/Q_b	>6	3-6	<3	
SEC (µS/cm)	Min. to mod diff. (10 µS hist.)**	<20	20-50	>50	**V**
	Max. drop in 1 day**	<10	10-30	>30	
Temp. (°C)	Extreme to mod diff. (0.1 °C hist.)**	<0.5	0.5-1.5	>1.5	
	Max. diff. in 1 day**	<0.15	0.15-0.5	>0.5	
TOC (mg/l)	Max. observed value	<0.4	0.4-0.8	>0.8	
Turbidity (NTU)	Max. observed value	<4	4-10	>10	
Colif. (cfu/100 ml)	Max. observed value	<5	5-100	>100	
Isotope ^{18}O (‰)	Amplitude (spring)/amplitude (prec.)	<0.01	0.05-0.1	>0.1	

Final V & RC value = average based on all considered parameters, weighted by respective reliability levels (reliability levels are determined by available input data, **Figure 7. 8**).

*average result of both methods is used,

**only one method is used based on available data.

Intrinsic Vulnerability assessment (**V**)

In the V-RC classification system, the intrinsic vulnerability V assessment is based on a possible six physio-chemical indicators of the existence of rapid water transport processes from the surface through the aquifer to a specific spring: a) Specific Electrical Conductivity (SEC); b) Temperature (T); c) Total Organic Carbon (TOC); d) Turbidity; e) Total coliforms; f) Isotope ^{18}O (‰). Indicators used in the process are chosen according to the monitoring data availability at the analysed spring. Therefore, all available indicators are used for assessment, and final score is computed as average score of the considered parameters, weighted by quality of their input data. Threshold values for categorizing V are specified in **Table 7. 2.**

The final score for RC and V estimation is calculated as a mean value of scores based on both proposed and used methods. Final reliability level of RC-V score depends on the quantity of the input data. Corresponding reliability levels to available input data are specified in **Table 7. 3**. The

entire process of calculating the final values of the V and RC parameters, assigning their reliability levels and final classification can be done in an automated way with an MS Excel spreadsheet. (**Figure 7. 8**)

Table 7. 3. Reliability levels corresponding to available data for rc and v assessments (from **Maréchal, et al, 2021**)

Discharge (Q)		**Final RC rel.**
Irreg. or monthly 10-60; Weekly 1-3 y.; Daily 0.5-1 y.		**Low (1)**
Daily 1-3y.; Weekly >3 y.; Monthly >5 y.;		**Med (2)**
Daily >3 y.		**High (3)**
SEC; Temp.	**V rel.**	**Final V rel.**
Irreg. or monthly >10 in >12 months per.	Low (1)	
Daily 3-6 months; weekly 6-12 months		
Daily 6-12 months; weekly ≥12 months	Med (2)	
Daily ≥13 months	High (3)	
TOC; Turb.; Colif.; ^{18}O		
Irreg. or monthly >10 in >12 months per.	Low (1)	
Monthly >36 months; weekly 12-24 months	Med (2)	
Daily >12 months; weekly >24 months	High (3)	
Summed V rel. (all available parameters)	<4	**Low (1)**
	4-7	**Med (2)**
	≥7	**High (3)**

PARAMETER	METHOD			RESULT	RC	V	RC reliability	V reliability	V weighting
Discharge (Q, m3/s)	SVC (Q10/Q90)	Q10	Q90						
	Acf to 0.2 (days)	Daily data							
	Exp. rec. coeff. (α)	Daily data							
	Qmax/Qbaseflow	Qmax	Qb						
SEC (µS/cm)	Min. to mod diff. (10 µS hist.)	Irreg/monthly data							
	Max. drop in 1 day	Daily/hourly data							
T (°C)	Extreme to mod diff. (0.1 °C hist.)	Irreg/monthly data							
	Max. diff. in 1 day	Daily/hourly data							
TOC (mg/l)	Max. value (mg/l)								
Turb. (NTU)	Max. value (mg/l)								
Coliforms (cfu/100 ml)	Max. value (mg/l)								
Isotope ^{18}O (‰)	Max. diff. spring/prec.	dSpring (‰)	dPrec. (‰)						
				Final Values:					

Figure 7. 8. Automated excel sheet for RC-V score calculation tool. Fields marked with yellow are left to be filled according to available data and results of the applied methods. Final scores are then automatically

calculated. (Maréchal et al., 2021)

7.3 Results

7.3.1 Results of recession curve analysis for the Cardener spring and its classification using the modified Mangin plot.

The XLKarst tool (BRGM, 2021) implemented in the framework of the CHAKAWP5- GeoERA RESOURCE project was used to carry out a first classification of karstic System based on the analysis of recession curves. In the case of Port del Comte, only the Cardener spring could be considered since it is the only one that had a historical time series with daily data, from the permanent gauging station officially named "EA087 La Coma i La Pedra" equipped with an analogue limnograph. In an advanced phase of this thesis, it was possible to compile the available flow discharge Q time series of that gauging station, operated years ago by the ACA (Catalan Water Agency). At the beginning of the thesis this station was no longer operational. The flow data period compiled covers from 02/27/1985 to 12/01/2010, although the time series is discontinuous and presents multiple gaps of more or less duration. In total, 9 periods with continuous availability of Q data have been identified. In contrast, the precipitation data available from AEMET station 0127O do not cover the first period between 1985 and 1990. After data inspection, in total 28 recession curves have been analysed. Fitting the $Q_{(t)} = \psi_{(t)} + \phi_{(t)}$ recession curve was carried out numerically. To evaluate the performance and efficiency of the adjustments the tool uses the Nash-Sutcliffe efficiency (NSE) as quality criteria, which is one of the most used performance indicators in hydrological modeling.

$$NSE = 1 - \frac{\sum_{i=1}^{n}\left(Q_{sim,i} - Q_{obs,i}\right)^2}{\sum_{i=1}^{n}\left(Q_{obs,i} - \overline{Q_{obs,i}}\right)^2}$$

where

$Q_{sim,i}$ - is the simulated discharged flow (m^3/s),

$Q_{obs,i}$ - is the observed simulated flow (m^3/s),

$\overline{Q_{obs,i}}$ - is the average observed flow (m^3/s),

n - is the total number of observed flow data,

i – is the time step

For the calculation of the Mangin parameters: "k" (describing the mean hydraulic residence time of groundwater in the phreatic zone, above the point of discharge) and "i" (describing the infiltration conditions within the system, i.e., slow vs. fast), some authors used the called MCR or 'Master Recession Curve analysis' approach (Gregor and Malík, 2012). This is an integrated recession curve derived from a series of single-event recession curves over a wider flow range, and thus providing an average characterization of baseflow response. Nevertheless, this approach has been criticized for its inability to adequately represent the whole variability (Kovacs, 2021). On the contrary, individual or single-event hydrograph analysis (SERC), event by event, it is more informative for better understanding of the system's dynamic, and to quantify parameters uncertainty. In this thesis, and in the CHAKA project, an individual analysis or SERC has been followed. Then the k and i parameters have been calculated for each of the 28 curves. The **Figure 7. 9.** show the whole Q- time-series data available in which the 28 calibrated / modeled recession curves (in orange) are indicated. The results achieved are listed in **Table 7. 4.**

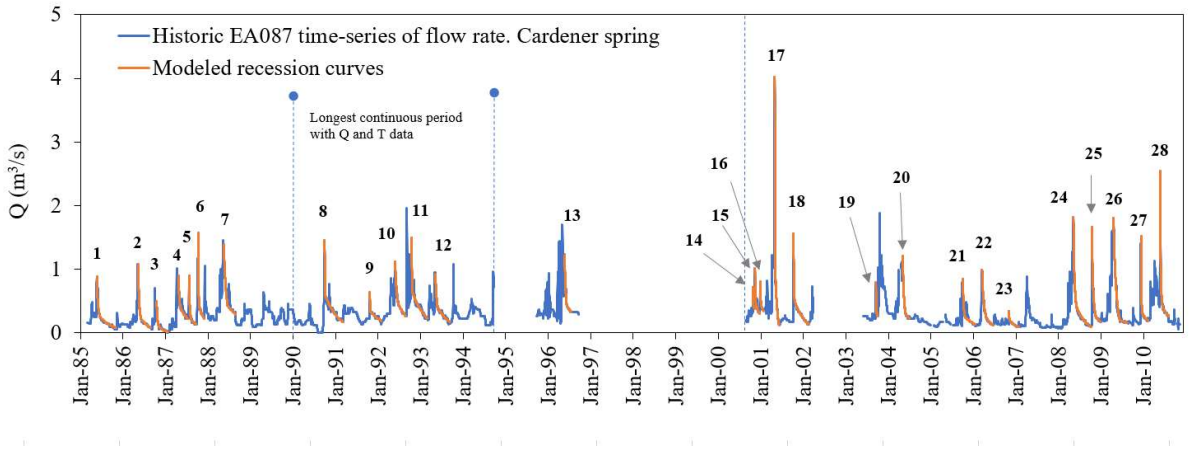

Figure 7. 9. Historical recovered data of "EA087. La Coma i La Pedra" gauging station. Cardener spring flow discharge Q. In it the 28 analysed recession curves are highlighted in orange colour.

Table 7. 4. Results of the single event recession analysis by means of the XLKarst tool for Cardener Spring

SERC	Date peak	Date end	Qend (m^3/s)	T_d (d)	Q_0 (m^3/s)	QR_0 (m^3/s)	q_0 (m^3/s)	Q'_0 (m^3/s)	t_i (d)	α (d^{-1})	ε [-]	V_{Dr} (m^3)	NSE	i [-]	k (year)
1	22/05/85	07/11/85	0.06	169	0.88	0.31	0.57	0.25	25	0.008	0.11	2.71E+06	94%	0.76	0.27
2	13/05/86	30/08/86	0.08	109	1.08	0.30	0.78	0.23	22	0.012	0.15	1.64E+06	98%	0.70	0.16

3	19/10/86	22/01/87	0.01	95	0.50	0.17	0.33	0.12	15	0.024	0.21	4.28E+05	90%	0.61	0.04
4	24/04/87	12/07/87	0.23	79	0.90	0.46	0.44	0.39	17	0.009	0.12	3.70E+06	80%	0.71	0.36
5	25/07/87	21/09/87	0.14	58	0.90	0.23	0.67	0.19	21	0.008	0.25	1.99E+06	97%	0.60	0.20
6	11/10/87	28/11/87	0.23	48	1.57	0.48	1.09	0.43	7	0.015	0.16	2.43E+06	98%	0.54	0.24
7	18/05/88	28/08/88	0.17	102	1.39	0.51	0.88	0.43	33	0.005	0.04	6.91E+06	83%	0.87	0.68
8	02/10/90	11/03/91	0.17	160	1.45	0.62	0.83	0.59	7	0.008	0.05	6.27E+06	89%	0.65	0.61
9	27/10/91	30/01/92	0.17	95	0.64	0.34	0.30	0.33	6	0.006	0.18	4.73E+06	86%	0.49	0.46
10	02/06/92	01/09/92	0.26	91	1.12	0.57	0.55	0.46	25	0.009	0.07	4.60E+06	98%	0.80	0.45
11	20/10/92	07/03/93	0.23	138	1.49	0.68	0.81	0.64	8	0.008	0.10	7.02E+06	90%	0.63	0.69
12	14/05/93	16/09/93	0.17	125	0.93	0.47	0.46	0.41	17	0.008	0.05	4.35E+06	93%	0.81	0.43
13	31/05/96	28/07/96	0.33	58	1.22	0.48	0.74	0.43	17	0.006	0.10	5.75E+06	97%	0.74	0.56
14	07/11/00	22/11/00	0.38	15	0.72	0.44	0.28	0.42	4	0.009	0.66	3.99E+06	74%	0.22	0.39
15	24/11/00	03/01/01	0.30	40	1.01	0.48	0.53	0.43	9	0.012	0.25	3.20E+06	91%	0.52	0.31
16	07/01/01	04/02/01	0.37	28	0.81	0.48	0.33	0.43	9	0.012	0.30	3.21E+06	98%	0.49	0.32
17	13/05/01	21/06/01	0.12	39	4.02	1.33	2.69	0.92	6	0.062	0.13	1.29E+06	99%	0.53	0.13
18	21/10/01	01/03/02	0.14	131	1.56	0.56	1.00	0.50	10	0.011	0.09	4.11E+06	99%	0.68	0.40
19	01/10/03	16/10/03	0.26	15	0.80	0.39	0.41	0.33	6	0.026	0.40	1.08E+06	98%	0.37	0.11
20	19/05/04	15/07/04	0.23	57	1.21	0.36	0.85	0.30	23	0.008	0.09	3.32E+06	99%	0.78	0.33
21	19/10/05	02/02/06	0.11	101	0.85	0.28	0.57	0.25	18	0.007	0.19	3.05E+06	62%	0.64	0.30
22	02/04/06	08/07/06	0.12	83	0.99	0.37	0.62	0.25	33	0.011	0.06	1.88E+06	99%	0.83	0.18
23	17/11/06	09/02/07	0.09	144	0.34	0.22	0.12	0.20	8	0.011	0.43	1.64E+06	97%	0.40	0.16
24	27/05/08	25/10/08	0.10	141	1.82	0.56	1.26	0.41	27	0.011	0.14	3.11E+06	98%	0.72	0.31
25	03/11/08	11/01/09	0.18	69	1.66	0.34	1.32	0.25	34	0.009	0.15	2.30E+06	97%	0.73	0.23
26	07/05/09	03/09/09	0.16	119	1.80	0.24	1.56	0.20	53	0.003	0.04	5.11E+06	96%	0.89	0.50
27	30/12/09	27/02/10	0.19	59	1.52	0.34	1.18	0.30	13	0.010	0.67	2.61E+06	97%	0.36	0.26
28	14/06/10	24/08/10	0.27	71	2.54	0.44	2.10	0.38	22	0.007	0.47	4.71E+06	98%	0.47	0.46

NSE - Nash–Sutcliffe model efficiency coefficient

SERC - Single-Event Recession Curve

The results obtained from the SERC analysis for the Cardener spring are represented in the **Figure 7. 10,** which corresponds to the modified version of the Mangin (1975) plot according to the by El-Hakim and Bakalowicz (2007)**.** In this plot, the springs analysed by Freixes (2014) in the southeast Pyrenees (Uelhs deth Joeau; Font de Lastoar, Bastareny System; Fonts Térme-Pilar; Fonts Llobregat, Font del Bor) have been also added, as well as the French springs characterized by Mangin (1975) (see **Table 7. 5**; where it is also included among other values, the CV is spring coefficient of variation, SVC is the spring variability coefficient (Flora, 2004), the Base Flow Index (BFI) computed as the ratio, in volume, of the baseflow to the total flow based on the Lyne and Hollick (1979) filter following the standard approach of Ladson et al., (2013), the memory effect ME (Mangin, 1984), the regulation time R_T (Mangin, 1984) and the parameter σ250/σ (%). The

Figure 7. 11 shows, using the same modified Mangin plot, the results of the analysis of the SERC of the Cardener spring for the period 2000-2010 (point S-1c) together with the results obtained for the rest of the springs considered in the CHAKA project, and in the **Table 7. 6.** the results obtained. The location of the springs of the project are shown in **Figure 7. 4**.

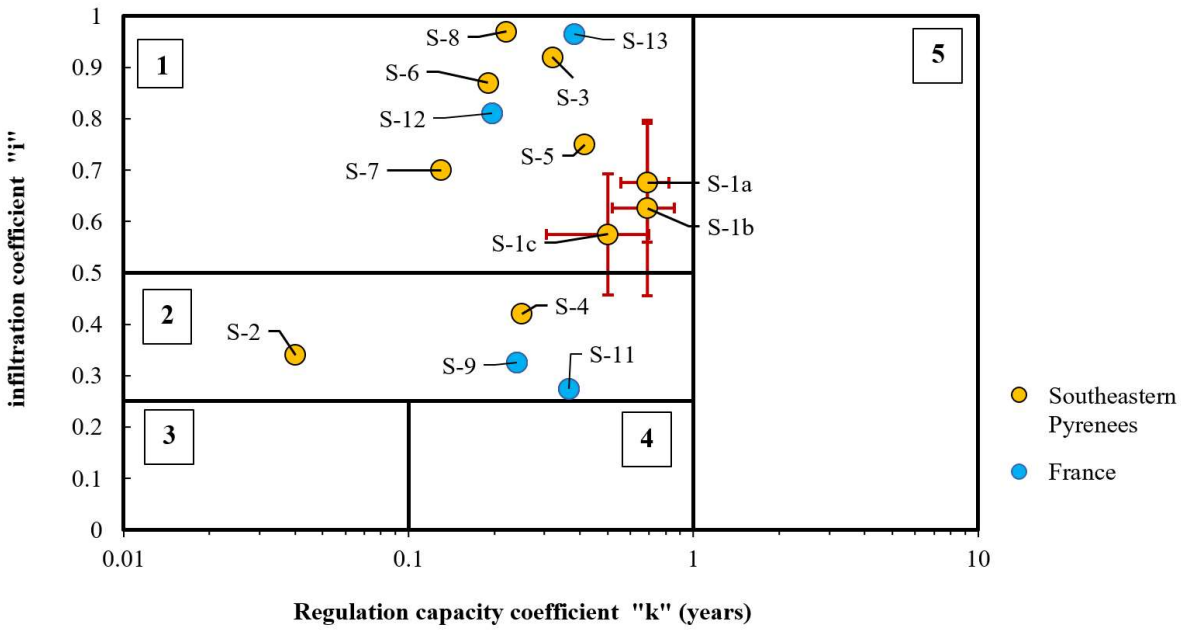

Figure 7. 10. Mangin's plot (modified by El-Hakim and Bakalowicz, 2007) with the SERC results obtained for the different Cardener Spring selected periods of data (S-1a, S-1b, S-1c) in **Table 7. 5**.

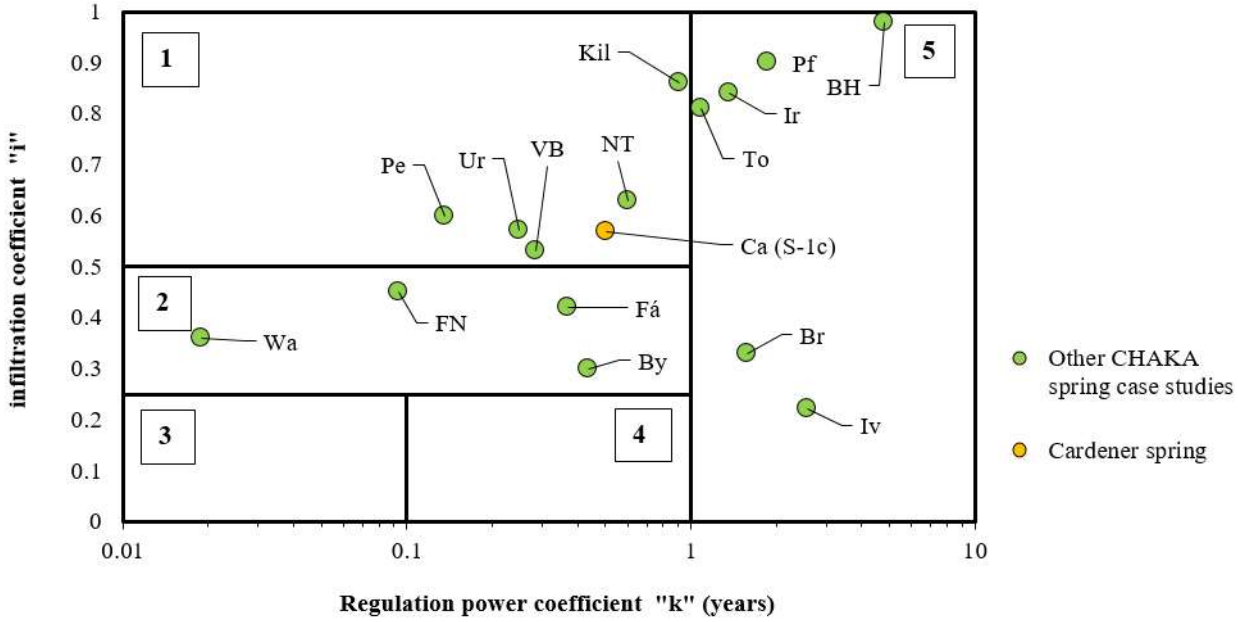

Figure 7. 11. Mangin's plot (modified by El-Hakim and Bakalowicz, 2007) with the SERC results S-1c obtained for "CA" 'Cardener Spring' with the rest of the CHAKA springs pilot cases (Maréchal et al 2021b)

Table 7. 5. Results of the single event recession analysis by means of the XLKarst tool for "CA" 'Cardener Spring'

Name	'Cardener spring'	'Cardener spring'	'Cardener spring'	'Uelhs deth Joeu' spring	'Font de Lastoar' spring	'Bastareny system' springs	'Font Aigüeira' spring	'Font de Tèrme-Pila' spring	'Fonts del Llobregat' spring	'Font del Bor' spring	Baget spring	Aliou spring	Fontestorbes spring	Fne de Vaucluse sping	Fne l'Evèque spring
Identifier	S-1a	S-1b	S-1c	S-2	S-3	S-4	S-5	S-6	S-7	S-8	S-9	S-10	S-11	S-12	S-13
Ref	Herms (2022)	Herms (2022)	Herms (2022)	Freixes (2014)	Freixes (2014)	Freixes (2014)	Freixes (2014)	Freixes (2014)	Freixes (2014)	Freixes (2014)	Mangin (1975)	Mangin (1975)	Mangin (1975)	Mangin (1975)	Mangin (1975)
Country	(Catalonia, Spain)										France				
number of data	1734	7019	3150	-											
From	Jan-90	May-85	Sep-00	Mar-96	Oct-88	Oct-95	Sep-95	Oct-88	Apr-97		-	-	-	-	-
To	Sep-94	Aug-10	Aug-10	Mar-97	Apr-91	Dec-98	Feb-00	Apr-91	Aug-98		-	-	-	-	-
Mean	0.32	0.31	0.30	1.59	0.17	1465.00	0.26	0.38	0.90	0.18	0.48	0.459	2.301	17.5	1.019
Median	0.30	0.23	0.20	-	-	-	-	-			-	-	-	-	-
σ	0.20	0.25	0.27	-	-	-	-	-			-	-	-	-	-
Min	0.01	0.01	0.06	0.25	0.04	0.31	0.13	0.03	0.14	0.05	-	-	-	-	-
Max	1.96	4.02	2.54	9.50	0.55	8.78	0.85	2.20	8.00	5.00	-	-	-	-	-
Min/Max	5.1E-03	2.5E-03	2.0E-02	2.6E-02	7.3E-02	3.6E-02	1.5E-01	1.4E-02	1.8E-02		-	-	-	-	-
SVC Q10/Q90	3.93	4.83	2.70	-	-	-	-	-			-	-	-	-	-
Q25/Q50	1.50	1.44	1.33	-	-	-	-	-			-	-	-	-	-
Coeff. of variation	0.61	0.82	1.24	-	-	-	-	-			-	-	-	-	-
Memory effect (d)	49	-	-	53-57	-	33	50-75	-	30		-	-	-	-	-
Regulation time (d)	44			49-50	-	32.00	40-75	-	22.00		-	-	-	-	-
σ250/σ (%)	57%	-	-	-	-	-	-	-	-		-	-	-	-	-
BFI	0.81	-	-	-	-	-	-	-	-		-	-	-	-	-
Vd (m3)	7.02E+06	7.02E+06	5.11E+06	1E+6 / 3E+6	1.00E+06	1.14E+07	3E+6 / 4E+6	4.00E+06	3.70E+06	1.30E+06	-	-	-	-	-
Vtot(m3/an)	1.02E+07	9.78E+06	9.46E+06	5E+7 / 6E+7	5.30E+06	4.62E+07	8.30E+06	1.47E+07	2.83E+07	5.80E+06	-	-	-	-	-
α(d-1)	4.86E-01	1.20E-02	1.39E-02	-	-	9.80E-03	4.70E-03	-	1.43E-02	5.10E-03	-	-	-	-	-
k	0.69	0.69	0.50	0.04	0.32	0.25	0.42	0.19	0.13	0.22	0.24	0.01	0.37	0.20	0.38
i	0.68	0.63	0.57	0.34	0.92	0.42	0.75	0.87	0.70	0.97	0.33	0.03	0.27	0.81	0.96
dk	0.13	0.17	0.20	-	-	-	0.03	-	-	-	-	-	-	-	-
di	0.12	0.17	0.12	-	-	-	-	-	-	-	-	-	-	-	-

Table 7. 6. Results of the single event recession analysis by means of the XLKarst tool for the whole CHAKA project.

Name	Killeglan	Nagy-Tohonya	Vrelo Bune	Bytčí skála (Bull Rock)	Grota Ursului	Waldbachursprung	Fontaine de Nîmes	St Brigida	La Fájara	Ivanscica	Tonkovic (Gacka river)	Pecina (Gacka river)	Bedhampton	Ironselle	Pfannbauernquelle
Identifier	Kil	NT	VB	By	Ur	Wa	FN	Br	Fá	Iv	To	Pe	BH	Ir	Pf
Ref	Maréchal, JC et al 2021. Deliverabe D.5.3 CHACKA WP6. Resource GeoERA project														
Country	Ireland	Hungary	B & H	Czech R	Romania	Austria	France	NL	SPAIN	Croatia	Croatia	Croatia	UK	France	Austria
number of data	3165	10958	2191	3652	365	1420	6309	2133	866	735	7305	7305	2884	1030	1342
From	Jan-10	Jan-64	Jan-10	Jan-09	Oct-97	Nov-12	Dec-00	Jun-94	May-15	Mar-19	Jan-97	Jan-97	Jan-61	Jan-17	Jan-14
To	Aug-18	Dec-93	Dec-15	Dec-18	Sep-98	Sep-16	Apr-18	Apr-00	Sep-17	Mar-21	Dec-16	Dec-16	Apr-16	Oct-19	Sep-17
Mean	1.02	0.11	24.26	0.29	0.06	3.00	0.55	0.01	0.12	0.05	3.66	1.55	1.11	0.14	0.29
Median	0.93	0.06	16.05	0.17	0.04	1.94	0.09	0.01	0.05	0.05	3.28	0.97	1.06	0.13	0.29
σ	0.58	0.13	23.95	0.39	0.06	3.28	1.32	0.01	0.16	0.00	1.62	1.58	0.26	0.05	0.02
Min	0.22	0.02	3.44	0.05	0.01	0.08	0.00	0.00	0.01	0.04	0.74	0.00	0.61	0.07	0.23
Max	4.50	1.14	133.90	7.65	0.64	14.24	16.50	0.06	2.24	0.06	13.70	10.60	1.96	0.34	0.34
Min/Max	0.05	0.01	0.03	0.01	0.02	0.01	0.00	0.00	0.01	0.71	0.05	0.00	0.31	0.21	0.69
SVC Q10/Q90	4.13	8.66	12.31	7.58	4.80	55.94	190.94	494.47	20.31	1.21	2.95	27.11	1.83	2.95	1.24
Q25/Q50	0.63	0.62	0.51	0.66	0.74	0.13	0.52	0.39	0.40	1.05	0.77	0.39	0.84	0.81	0.95
Coeff. of variation	0.57	1.24	0.99	1.37	1.11	1.09	2.41	0.86	1.38	0.07	0.44	1.02	0.24	0.37	0.08
Memory effect (d)	73.00	85.00	57.00	32.00	14.00	66.00	13.00	125.00	35.00	76.00	82.00	53.00	98.00	73.00	87.00
Regulation time (d)	77.86	51.42	46.96	29.85	5.02	56.10	20.06	116.44	32.57	78.32	59.80	47.42		66.54	82.16
σ250/σ (%)	0.75	0.63	0.60	0.50	0.16	0.63	0.38	0.95	0.47	0.78	0.68	0.60	0.85	0.71	0.78
Class	3	3	3	3	3	3	4	1	3	1	3	3	3	2	2
k	0.907	0.599	0.284	0.436	0.249	0.019	0.093	1.578	0.368	2.576	1.092	0.136	4.780	1.360	1.870
Qmax/Qbaseflow	11.85	5.05	5.85	19.15	5.79	17.52	550.33	1.25	7.47	1.13	1.88	6.00	1.00	1.70	1.08

The results of the Cardener spring (‘Ca’ in the table) are indicated with three points listed as "S-1a" (includes SERCs from January 1990 to September 1994 which is the longest continuous period available with Q and P data where the correlation analyses will be performed), "S-1b" (all 28 identified SERCs from the period May 1985 to August 2010) and "S1-c" (includes the SERCs from the period September 2000 to August 2010 which has been the considered it in the Chaka project) adding their respective standard deviations with an error bar. In all three cases, the Cardener Spring falls within the Mangin class “1” where in this updated plot: $k < 1$ and $i > 0.5$ corresponding to a domain of ‘complex karst systems’, largely extended with several sub-systems and/or thick infiltration zone, as in fact it was already expected, since the Cardener spring, as it has been presented in previous chapters, presents approximately 1000m of thickness of unsaturated zone.

Figure 7. 12. Correlation between a) SVC vs ME; b) CV bs ME; c) BFI vs ME and RT vs ME for the 16 pilot cases. On point which outlies (in graph ‘a’) is the St Brigida spring (Br, NL). It shows a high SVC Q_{10}/Q_{90} value which can be explained due to its discharge is very low for a long time as a response of low recharge during several years, while its memory effect is very high (>125 days). In that particular case, the SVC can bring another important information that is really not only covered by the memory effect. Besides CV given by the discharge time series of “Br” spring. (Br, CV=0.86) is close to the one from the “Ca” Cardener spring, (Ca, CV=0.93), while in reality they give very distinct memory effects (47 days and 125 days respectively, the latter in fact being underestimated for a maximum correlation length of 125 days). But the corresponding Q time series shape demonstrate that the responsiveness of the Cardener Spring is higher than the one of the St Brigida Spring. Therefore, one must keep in mind that although CV its common use in karst hydrology, it can lead to misleading interpretations when most of the discharge variations are due

to long term fluctuations (annual or higher period). Therefore, in the application of the classification methods, this Br spring must be considered a special case.

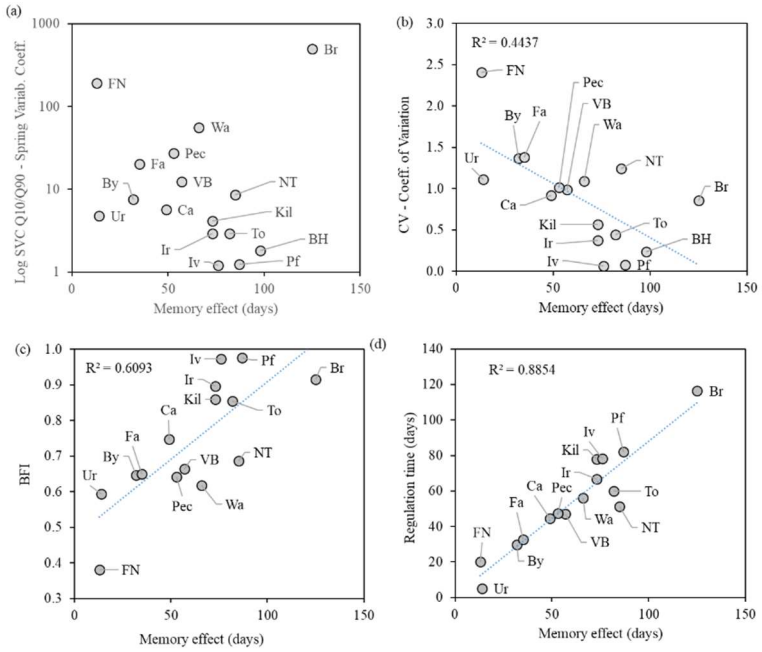

Figure 7. 12. Correlation between a) SVC vs ME; b) CV bs ME; c) BFI vs ME and RT vs ME for the 16 pilot cases (modified from Maréchal et al. (2021b). The "Ca" corresponds to the 'Cardener spring' of the Port del Comte high-mountain karst aquifer.

7.3.2 Cumulative probability of flow rates and their classification in Cardener spring

The analysis of flow discharge frequencies from the time-series of Cardener spring for the period 2005-2010 (Qmin = 0.06 m^3/s; Qmax = 2.54 m^3/s and Qavg= 0.3 m^3/s) can be used to improve a bit more the understanding of the aquifer hydrodynamics. The cumulative probability plot in **Figure 7. 13** can be divided into four different behaviours based on the slopes of the cumulative probability curve respect Q.

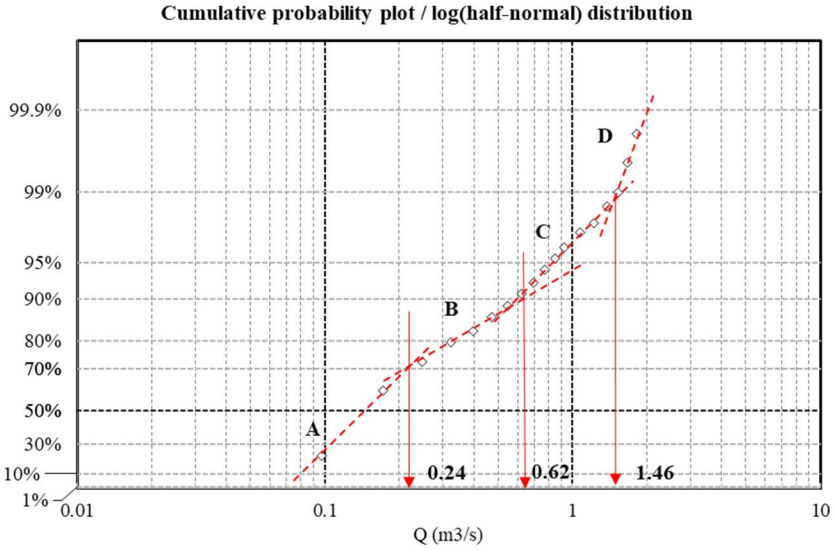

Figure 7. 13. Cumulative probability of flow rates vs. log(half-normal Distribution) in Cardener spring for the 2005–2010

The flow rate frequencies indicate that 70% of the time the spring drained flows lower than 0.24 m^3/s, while the upper three sections above this flow, corresponding to 30% of the remaining time that is when flood situations occur at different stages (20% section B, 9.9% section C and less than 0.1% section D). The first section A with flow rates of less than 0.24 m^3/s (break in the slope between A and B in the plots) correspond to the general spring depletion of the aquifer reserves. water that is slowly released from the aquifer from reserves of a previous hydrologic cycle. The section B (between 0.24 and 0.6 m^3/s) with a "**decrease**" in the slope would possibly indicate the times of *recession* of large events (sections C and D). The following increasingly steep slope sections (C, D, which accumulate 9,9%+0,1% = in total 10% of time) may indicate in times of *flooding* that the system is not capable of draining the entire volume of water that reaches the main discharge point and according to Mangin (1971) "trop-pleins" may begin to function. In the particular case of the Cardener spring, during the field work carried out, e.g. it was observed that in the flood event of April 2014 (with a peak of 0.93 m^3/s), the discharge point begins to be located upstream, going up almost 13m from the usual discharge point, water appearing with more and more energy in the stream that is normally almost or completely dry. The break in slope between C and D (1.46 m^3/s) may be indicative then that the system reaches another overflowed stage for flow rates above. Flows greater than 1.46 m^3/s, steeper (slower decrease in flows), corresponding to the most important but occasional floods of the spring in the period analysed (less than 0.1% of

the time). The flow rates corresponding to slopes B (between 0.24 and 0.6 m^3/s) and C (between 0.62 and 1.46 m^3/s, covering 29.9% of the time) can be interpreted as the presence of two slightly distinct temporary storages within the aquifer.

In summary, it can be interpreted that the flow rates are related to a single aquifer with two interacting base flow reservoirs corresponding to a capacitive and conductive function, or slow (section A) and fast flows (B and C, with section D the most extreme). It general, shows that flow rate variations occur slowly (almost 70% in time), which leads to an inertial behaviour of the aquifer system.

7.3.3 Correlation and spectral analysis results

To perform the correlation and spectral analysis, the same XLKarst tool (BRGM, 2021) was used. The period considered for the analysis is the longest continuous period with available Q and T data, which corresponds between January 1990 and October 1994. (The SERC analysis carried out in said period is the one represented as S-1a in **Figure 7. 10**). A step of 1 day and a truncation point of 125 days are considered for short term auto-correlation analysis. The '**auto-correlation function' r_k,** (**Figure 7. 14, a**) of the rainfall time series shows a very quick loss in its memory to below the 0.15 in a lag of 1 day and below the 0.05 significance level in 2 days indicating randomness. The discharge time series gives information about the **'Memory Effect' ME** and the storage of the karst aquifer for the whole period with a value of 49 days (i.e. when $r_x = 0.2$).

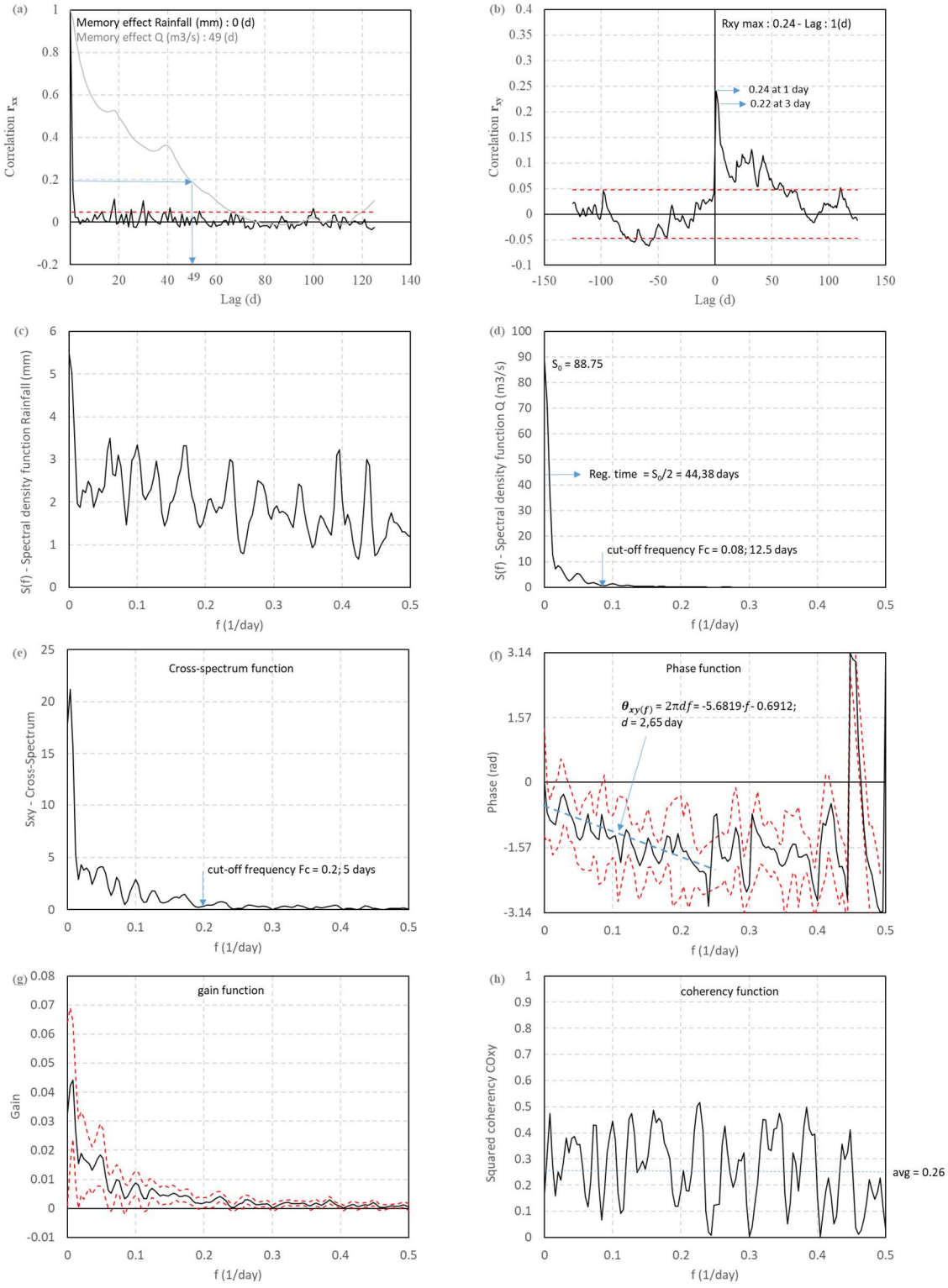

Figure 7. 14. Correlogram and spectral analysis for 'Cardener Spring' in Port del Comte massif (for period 1990-1994). (a) Auto-correlogram functions r_{xx} for rainfall and flow discharge; (b) Cross-correlation r_{xy}; (c,d) Simple spectral density functions for daily precipitation and flow discharge; (e) Cross-spectrum S_{xy} function (f) phase function; (g) gain function and (h) coherency function.

The simple '**spectral density function**' $\boldsymbol{S(f)}$ (**Figure 7. 14,** c and d) allowed to determine how the variance is distributed over the different frequencies. The aquifer seems to exhibit a relatively large filtering effect of the random rainfall input. In $\boldsymbol{S(f)}$ for the flow discharge (**Figure 7. 14,** d) in the Cardener spring no peaks are clearly intuited that coincide with those observed peaks in the simple rainfall spectrum (periods 4 (f=0.24), 6 (f =0.172), 8 (f =0.128), 10 (f =0.1), 17 (f =0.06) days, indicating the annual and seasonal precipitation pattern characteristics) (**Figure 7. 14,** c), which therefore means that the system dilutes the information contained in the rainy episodes, that is, the system considerably filters part of the input signal.

The estimated '**regulation time**' $\mathbf{T_{reg}}$ ($S_0/2$) is 44.38 days which indicates that the regulatory capacity of the system is significantly important. The '**cut-off frequency**' **Fc** is 0.08 which suggests that the signal of the rain that falls beyond 12.5 days is filtered by the karstic aquifer system, and therefore, the effects later related to these rain events in the discharge cannot be detected. Taking the classification system based on the parameters **ME**, $\mathbf{T_{reg}}$ and **Fc** obtained from the correlogram analysis (Mangin, 1981a, 1981b and 1984), the Cardener spring it is more similar than Fontestorbes springs equivalent to moderately karstified system with imperfect drainage.

The behaviour and response function of the karst system can also be characterized by the '**cross correlation function' $\mathbf{r_{xy}(k)}$** (**Figure 7. 14,** b) and '**cross-spectral density function**' $\mathbf{S_{xy}(k)}$ (**Figure 7. 14,** e) analysis between input (precipitation) and output (discharge) time series. The $\mathbf{r_{xy}(k)}$ shows a rapid response with a peak of 0.24 at a delay of 1day followed by change in the slope at 0.2 at a delay of 3 days with very rapid decrease for finally a slower decrease. The result suggests that the first part of the curve demonstrates a good response of the system to rainfall due to a well-developed endokarst that facilitates drainage corresponding to the rapid flow component, while the second and the most main part characterizes an inertial effect or effect of inertia capacity of the system, that is, the component of base flow that contributes the late response.

The $\mathbf{S_{xy}(k)}$ (**Figure 7. 14,** e) shows a cut-off frequency of about 5 days (f=0.2), suggesting that the input-output relationship is nonlinear at a shorter timescale, but linear on a long timescale. This suggest that the karst system has a medium inertial behaviour.

The '**phase function' $\boldsymbol{\theta_{xy(f)}}$** (**Figure 7. 14,** f), which represents the travel time of the response,

shows a more or less steady behaviour at low to mid-term frequencies which might indicate the general predominance of the base flow in the Cardener spring outflow function, although it is observable a high distortion for high frequencies, short time, representing probably the quickflow. The mean delay 'd' calculated by means of the expression proves to be 2.5 days which are consistent with the delay observed in the first peak of the **r_{xy}(k).**

The '**gain function'** $g_{xy}(f)$ (**Figure 7. 14,** g) shows that the system strongly attenuates the input signal ($g_{xy}(f)$ is <1) from mid-term that characterizes a system with medium to large storage capacity, although at low frequencies it is slightly lower, possible reflecting late infiltration through the non-saturated zone in the Cardener basin which is really thick (~1000m).

The '**coherence function'** CO_{xy}, (**Figure 7. 14,** h) which indicates the degree of linearity of the response of the karst system, it shows a high oscillation with values between 0.05 and 0.5 with an average of 0.26, suggesting a poor linearity of the response, also probably affected by the snowpack that decrease its degree. L8. Low coherence means the non-linearity for the input-output system, and non-linearity might indicate a sign of poor karstification.

7.3.4 Results of the new CHAKA Method 1: Classification of karst aquifer intrinsic vulnerability to pollution for the Cardener and Sant Quintí Springs

The results obtained from the application of Method 1 in the pilot karst springs in the CHAKAWP5-GeoERA RESOURCE project are shown in **Table 7. 7**. In the specific case of the "Ca" spring corresponding to the Cardener del Port del Comte spring, the value of class V of intrinsic vulnerability was made using four of the six criteria that the method contemplates: 'Surface karstic characteristics', 'Caves' ,'Discharge' and WQI considering the Specific Electrical conductance (SEC) measurements identified pattern where there is a decrease in SEC during the turbidity event such could be abrupt recharge, as this decrease in SEC indicates transport of fresher surface water (see **Figure 2. 30** Chemograph and hydrographs of the Sant Quintí and Cardener karst springs). In this case neither 'Tracer test' data nor 'Coliform' data nor 'Turbidity' data for the WQI were available. The resulted 2.3 score based on the available information was that it should be classified with a 'moderate' intrinsic vulnerability 'V' (although close to "High" class between 2.5 to 3). Most of

the rest of the CHAKA project karst springs case studies have higher scores being classified mainly with "high" vulnerabilities, of which 4 springs obtain the highest possible vulnerability assessment with a score of 3 considering all available parameters (the FdN and Wa springs) and only one of the rest of the springs evaluated (the Grota Ursului, in Romania) obtained the same average score of 2.3, although in this last case information was available to assess the 6 parameters of the method. This left the doubt or the 'open door' for the cases in which all the information was not available to consider the six parameters (e.g. Tracer tests which provide an important additional line of evidence for vulnerability in these types of karst aquifer) as in the cases of "Fa, "pf" and "Ca" among others, about the possible modification of the final score, and in the last case of "Ca", if it could signify reaching the upper class.

Table 7. 7. Results of method 1 for the CHAKA case study springs. "Low" between 1 to 1.99, "Moderate" between 2 to 2.49. "High between 2.5 to 3.

Country/Region	ID	Site name	Surface karst	Caves	Water quality	Coliforms	Tracer tests	Discharge	Average score	Vulnerability Class
France	FdN	Fontaine de Nimes	3	3	3	-	3	3	3	High
Austria	Wa	Waldbachursprung	3	3	3	-	3	3	3	High
Hungary	NT	Naga-Tohonya	3	3	-	-	3	-	3	High
Bosnia and Herzogovina	VB	Vrelo Bune	3	3	-	-	3	3	3	High
Croatia	Ga	Gacka Pecina spring	3	2	3	-	3	3	2.8	High
UK	BH	Bedhampton and Havant	3	1	3	3	3	2	2.5	High
Croatia	Ga	Gacka Tonkovic spring	3	2	2	2	3	3	2.5	High
Czech Republic	By	Bull Rock	3	3	2	1	3	3	2.5	High
Ireland	Kil	Killeglan	3	1	3	3	3	2	2.5	High
Spain	Fa	La Farara	2	2	3	-	-	3	2.5	High
France	Ir	Ironselle	2	3	2		3	2	2.4	moderate
Catalonia	Ca	Cardener	2	2	2	-	-	3	2.3	moderate
Romania	Ur	Grota Ursului	3	3	2	1	2	3	2.3	moderate
Austria	Pf	Pfannbauernquelle	2	2	-	-	-	2	2	moderate
Croatia	Iv	Ivanscica springs	1	1	2	1		2	1.4	low
Netherlands	Br	St Brigida	1	1	1	-	-	1	1	low

7.3.5 Results of the new CHAKA Method 2: Mixed classification using the method 1 plus a discharge time series for the Port del Comte Massif 'Cardener spring'

The results of the application of method 2 based on the combination of mean flow discharge (**Qavg),** Memory Effect (**ME**) and the calculated Karst Groundwater Resource Availability Index (**KGWRAI**) for all springs (see values in **Table 7. 8**) is shown in **Figure 7. 15** a) and b). The results of classification shows that **"Ca" corresponds to the 'Cardener spring' of the Port del Comte high-**

mountain karst aquifer with (V=2.30, KGWRAI=0.38) is characterized by a medium-to-high vulnerability with a medium karst GW resource availability for water supply management. Other such as for instance that the Fontaine de Nîmes karst spring in France is characterized by a high vulnerability with a low karst GW resource availability (V=3, KGWRAI=0. 0.21) which gives poor characteristics for water supply management, whereas the Tonkovic karsts spring (Gacka river) in Croatia shows the most elevated value KGWRAI but with higher vulnerability too (V=2.50, KGWRAI=0.65). On the contrary there is no karst system that shows low vulnerability with high KGWRAI. The best compromise between these two factors is exemplified by the Pfannbauernquelle case study (Pf, AU), which shows a high KGWRAI but a moderate vulnerability.

Table 7. 8. Results of the single event recession analysis by means of the XLKarst tool for the whole CHAKA project.

Number	1	2	3	4	5	6	7	8	9	10	11	12	13	14	15	16
Name	Cardener Spring	Killeglan spring	Nagy-Tohonya spring	Vrelo-Brune spring	Byčí skála (Bull Rock) spring	Grota Ursului spring	Waldbachursprung spring	Fontaine de Nîmes spring	St Brigida spring	La Fájara spring	Tonkovic spring (Gacka riv)	Pecina spring (Gacka riv)	Bed-Hampton	Ironselle spring	Pfannbauernquelle spring	Ivanscica springs
Short-name	Ca	Kil	NT	VB	By	Ur	Wa	FN	Br	Fa	To	Pec	BH	Ir	Pf	Iv
Situation	Catalonia, Spain	Ireland	Hungary	Bosn&Herz	Czech Republic	Romania	Austria	France	Netherlands	Spain	Croatia	Croatia	Uk	France	Austria	Croatia
Data	2729	3165	10958	2191	3652	365	1420	6309	2133	866	7305	7305	2884	1030	1342	735
From	13/6/03	1/1/10	1/1/64	1/1/10	1/1/09	1/10/97	7/11/12	25/12/00	22/6/94	19/5/15	1/1/97	1/1/97	2/1/61	4/1/17	1/1/14	1/3/19
To	1/12/10	31/8/18	31/12/93	31/12/15	31/12/18	30/9/98	26/9/16	3/4/18	23/4/00	30/9/17	31/12/16	31/12/16	4/4/16	30/10/19	3/9/17	4/3/21
Mean	0.3	1.02	0.11	24.26	0.29	0.06	3	0.55	0.01	0.12	3.66	1.55	1.11	0.14	0.29	0.05
Median	0.2	0.93	0.06	16.05	0.17	0.04	1.94	0.09	0.01	0.05	3.28	0.97	1.06	0.13	0.29	0.05
σ	0.27	0.58	0.13	23.95	0.39	0.06	3.28	1.32	0.01	0.16	1.62	1.58	0.26	0.05	0.02	0
Min	0.06	0.22	0.02	3.44	0.05	0.01	0.08	0	0	0.01	0.74	0	0.61	0.07	0.23	0.04
Max	2.54	4.5	1.14	133.9	7.65	0.64	14.24	16.5	0.06	2.24	13.7	10.6	1.96	0.34	0.34	0.06
Min/Max	0.02	0.05	0.01	0.03	0.01	0.02	0.01	0	0	0.01	0.05	0	0.31	0.21	0.69	0.71
SVC Q10/Q90	5.7	4.13	8.66	12.31	7.58	4.8	55.94	190.94	494.47	20.31	2.95	27.11	1.83	2.95	1.24	1.21
Q25/Q50	1.33	0.63	0.62	0.51	0.66	0.74	0.13	0.52	0.39	0.4	0.77	0.39	0.84	0.81	0.95	1.05
CV	0.92	0.57	1.24	0.99	1.37	1.11	1.09	2.41	0.86	1.38	0.44	1.02	0.24	0.37	0.08	0.07
ME (d)	49	73	85	57	32	14	66	13	125	35	82	53	98	73	87	76
RT (d)	44.38	77.86	51.42	46.96	29.85	5.02	56.1	20.06	116.44	32.57	59.8	47.42	*	66.54	82.16	78.32
α250/σ (%)	0.54	0.75	0.63	0.6	0.5	0.16	0.63	0.38	0.95	0.47	0.68	0.6	0.85	0.71	0.78	0.78
BFI	0.75	0.86	0.69	0.66	0.65	0.59	0.62	0.38	0.92	0.65	0.86	0.64	*	0.9	0.98	0.97
RT (d) α250/σ	43	71	49	46	31	3	50	18	113	27	57	45	90	64	76	76
V - Method 1	2.3	2.5	3	3	2.5	2.3	3	3	1	2.5	2.5	2.8	2.5	2.4	2	1.4
Y=(2+log(Q))/4	0.37	0.50	0.26	0.85	0.37	0.19	0.62	0.44	0.00	0.27	0.64	0.55	0.51	0.29	0.37	0.17
Relat ME (%)	0.39	0.58	0.68	0.46	0.26	0.11	0.53	0.10	1.00	0.28	0.66	0.42	0.78	0.58	0.70	0.61
KGWRAI	0.38	0.54	0.42	0.62	0.31	0.15	0.57	0.21	0.19	0.27	0.65	0.48	0.63	0.41	0.51	0.33

In Plot 1 (**Figure 7. 15** a), springs are grouped / coloured according to the following rules:

- Green points: Low vulnerability and high memory effect (>50%)
- Red points: High vulnerability and low memory effect (<25%)

- Orange points: Other cases with low memory effect or high vulnerability
- Yellow points: All the other cases

In Plot 2 (**Figure 7. 15** b) the 9 possible groups within the graph are classified with the colours according to the rules defined in **Figure 7. 6**.

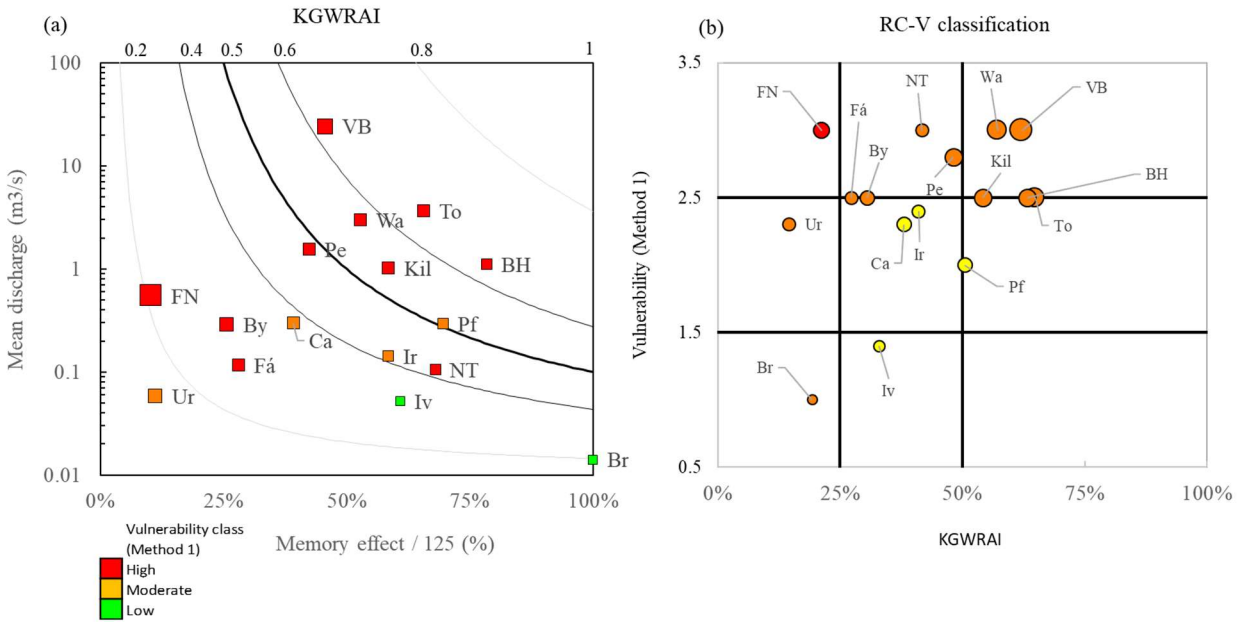

Figure 7. 15. Plots 1 (a) and 2 (b) for the Method 3 RC-V with the results obtained for the 16 pilot cases (modified from Maréchal et al. (2021b). The "Ca" corresponds to the 'Cardener spring' of the Port del Comte high-mountain karst aquifer.

7.3.6 Results of the new CHAKA Method 3: Method 3 (V-RC classification): quantitative classification based on monitoring data - discharge and other time series for the Port del Comte Massif Cardener and Sant Quintí springs

V-RC classification (Method 3) was applied on all CHAKA pilot sites indicated in the map of the **Figure 7. 4**. Sufficient data was available for computing both V and RC scores for 14 out of 16 included spring sites. For the springs numbered as 4 (VB, Bosn.&Herz.) and 5 (BY, Cz) have only discharge data available, so they are not included hereafter. The results obtained are summarized in **Table 7. 9.** Additionally, the St. Quintí (SQ) karst spring of the Port del Comte, was also

considered using the fortnightly field campaigns carried out during the fieldwork period of this thesis (Set 2013 - Oct 2015). In this regard the Q flow discharge data was used to determine the RC value in it as well as the SEC (Specific Electrical Conductivity) and temperature (T) to determine the V value. As no daily based time series data was available in this, it was not possible to analyse the hydrograph according to Mangin, and therefore neither determine the regression coefficient, nor carry out the autocorrelation analysis to obtain the Memory Effect (ME). Therefore, the difference between Cardener and Sant Quintí regarding the application of the RC-V method 3 is that the reliability of their Information is completely different, as is indicated in the **Table 7. 9.** Considering the rules defined in **Table 7. 3**.

Table 7. 9. Results of V-RC classification (method 3) for the 16 CHAKA pilot sites springs (V score <1.5 is low, 1.5-2.4 medium and ≥2.5 high; spring sizes vary from 1 = very small to 5 = very large). The RC and V reliability levels accordingly to **Table 7. 3**

Site	Short name	ID	RC	V	RC rel	V rel	Size
1	**Card Cat**	Ca	**2.0**	**2.7**	3	1	3
extra	**St. Quintí Ca**	SQ	**2.0**	**2.7**	1	1	3
2	**Kill Ir**	Kill	2.0	3.0	3	3	4
3	**NT Hu**	NT	2.5	2.0	3	2	2
4	**VB B&H**	-	-	-	-	-	-
5	**BY Cz**	-	-	-	-	-	-
6	**GU Ro**	Ur	1.5	2.4	1	2	2
7	**Wald Au**	Wa	1.5	2.4	3	3	4
8	**FdN Fr**	FdN	1.0	2.8	3	3	4
9	**StB Neth**	Br	2.0	1.5	3	1	2
10	**Fa Esp**	Fa	1.5	2.8	2	2	3
11	**Ton Cro**	To	3.0	1.1	3	3	5
12	**Pec Cro**	Pec	1.5	3.0	3	3	4
13	**BHS UK**	BH	3.0	3.0	3	3	4
14	**Iron Fr**	Ir	2.5	1.6	3	3	3
15	**Pfann Au**	Pf	3.0	1.0	3	2	3
16	**Iva Cro**	Iv	3.0	1.0	2	2	2

The results suggest are plotted **Figure 7. 16.** As indicated in **Table 7. 9.,** the same values of RC and V are obtained either for Sant Quintí and Cardener springs (2.0, 2.7). Therefore, the circle lies in the same position. The red colour of Sant Quintí, related to the estimated V reliability is overlapping to the cercle of Cardener Spring (which is green). In any case, what it suggests is that both springs, the largest in the Port del Comte Karst System, have the same characteristics, a similar vulnerability (both areas are recharged at the same heights and in the same karstified area) and have hydrological behaviours in general very similar terms (as can be seen in the chemograph presented in chapter 2, **Figure 2. 30**.).

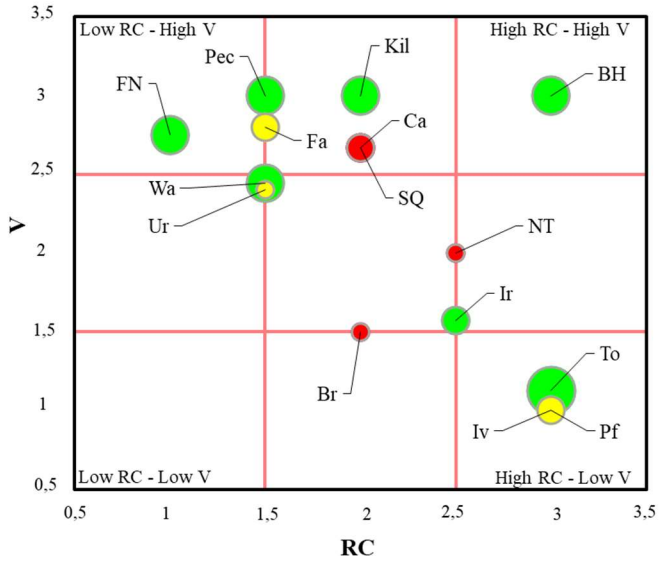

Figure 7. 16. Results of Method 3 for the CHAKA pilot sites (where both V and RC estimation was possible) on proposed V-RC representation diagram (circle position according to V and RC scores, circle color based on estimated V reliability and circle radius on spring size (mean discharge; some circles are overlapping due to similar V-RC scores) (modified from Maréchal et al. (2021b). The "Ca" corresponds to the 'Cardener spring' of the Port del Comte high-mountain karst aquifer.

7.4 Discussion

The three classification methods use different information to assess two main characteristics of karst springs: as far as the "Intrinsic Vulnerability": For methods 1 and 2 the same system (method 1) is used for assessing the intrinsic vulnerability. For these methods, the intrinsic vulnerability is assessed using a combination of the karstic characteristics of the catchment (Surface karst and the extent of cave development) coupled with parameters measured at springs which are indicative of vulnerability: rapid flow demonstrated by tracer tests, water quality indicators of rapid flow, maximum coliform counts, and timing of discharge response to precipitation. In method 3 intrinsic vulnerability is assessed directly from monitoring data (time-series) of physio-chemical parameters: Temperature variability, SEC (maximum drop in one day or minimum to modal difference), TOC (maximum), ^{18}O isotope (ratios between site and precipitation), turbidity (maximum), coliforms (maximum). Then Method 2 use the same Intrinsic Vulnerability V index jointly with the Memory Effect ME considered to be the best represent of the storage of the system which must be obtained by the correlation analysis of daily time-series combined with the mean flow discharge to provide the water resource availability index named KGWRAI, whereas the Method 3 averages two criteria

(the memory effect and SVC) from time series analysis to infer the 'Regulation Capacity' of the System.

Figure 7. 17 a) compares the vulnerability levels estimated using for method 1 vs method 3. Method 1 uses the catchment characteristics and water quality indicators of rapid groundwater flow and the implications this has for ease with which potential pollutants may enter the aquifer and method 3 measures vulnerability using evidence of rapid flow from water quality parameters at the outlet of the karst system including time series data where available. Both methods have strengths and weakness for assessing the overall vulnerability of the system and it should must consider that Method 1 is the first level of assessment. Taking this in mind, what it can be observed at a first glance is that vulnerability scores are slightly different for some sites using the two different methods. For example, the To and IR karst springs have much higher scores with Method 1 than Method 3, and NT and Wa springs have slightly higher vulnerability with Method 1 than Method 3. In contrast, BH, Kil and Br have slightly lower vulnerability with method 1 compared to Method 3. However, the general patterns in vulnerability appear fairly similar with both methods. In both methods the average of the available parameters is used to produce an overall vulnerability score. In the particular case of the "Ca" Cardener spring, in both methods a medium-to high vulnerability was been assessed which agrees to the previous information. In method 1 resulted 2.3 score based on the available information and classified with a 'moderate' intrinsic vulnerability 'V' (although close to "High" class between 2.5 to 3). In method 3 the V resulted in 2.7 score based on the available information and classified with a 'high' intrinsic vulnerability 'V' (between 2.5 to 3). The differences may reflect the different data available at different sites and particularly the different data used in the two methods. Therefore the result of the classification obtained does not disagree, but it is in reality quite consistent with the assessment of the intrinsic vulnerability mapped of outcropping carbonated and karstifiable materials and that is valued at a regional scale with the "Map of intrinsic vulnerability of Catalonia at 25:000 scale in the area of the Port del Comte massif (Arnó et al., 2020, ICGC) applying the COP method (Zwalhen, 2003; Vias et al., 2006) which indicates that the two first predominate vulnerability classes of five that consider the method in total covering the whole massif are the 'High vulnerability class' with a 55.8% and then the 'Moderate vulnerability" class 18%. The most in-depth analysis for the rest of springs can be consulted in Maréchal et al. (2021b).

Regarding the comparison of the parameters considered in method 2 and 3 to contemplate the management capacity of the aquifer, expressed as KGWRAI (considering the Memory effect and the discharge), and the RC factor of regulation capacity, **Figure 7. 17 b)** shows the comparison between the Memory Effect/125 criteria for method 2 vs RC Method 3 on proposed V-RC representation diagram, whereas **Figure 7. 17 c)** shows the comparison between KGWRAI method 2 vs RC method 3 on proposed V-RC representation diagram.

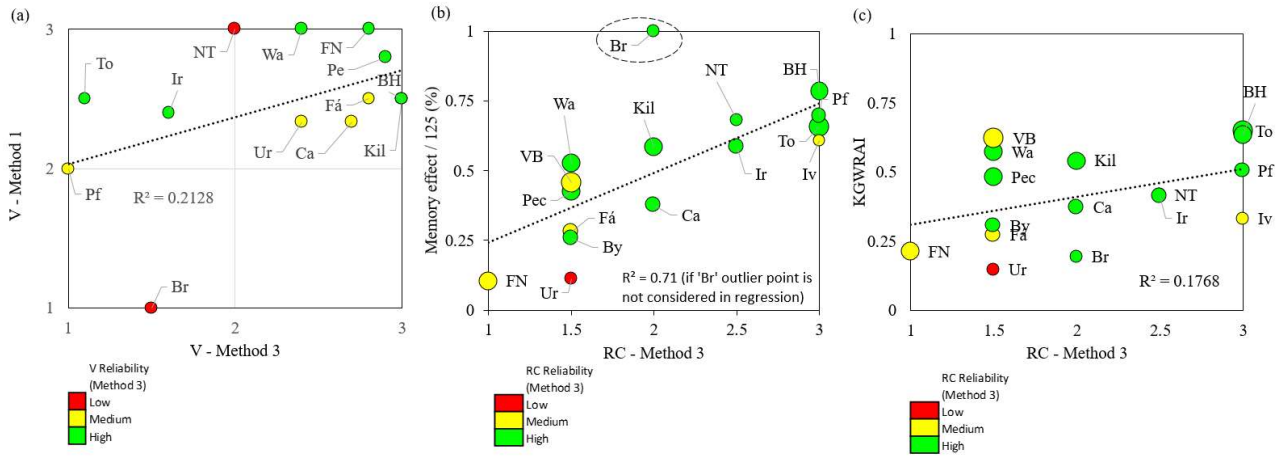

Figure 7. 17. (a) Comparation of vulnerability inferred for method 1 vs method 3; (b) the memory effect/125 criteria for method 2 vs RC Method 3; (c) KGWRAI method 2 vs RC method 3 on proposed V-RC representation diagram (modified from Maréchal, et al, (2021b). The "Ca" corresponds to the 'Cardener spring' of the Port del Comte high-mountain karst aquifer.

In **Figure 7. 17 b)** the correlation is relatively poor, even if a positive trend can be identified. This can partly be explained by the use of thresholds in the RC assessment. One point stands out clearly in this relationship: The St Brigida Sp. (Br, NT) has a medium RC while its memory effect is very high. Going back to **Figure 7. 12**, the St Brigida spring point. (Br, NL) shows different behaviour in SVC and CV respect to ME. As has been said, the CV can lead to misleading interpretations when most of the discharge variations are due to long term fluctuations (annual or higher period).Thus, the RC assessment using both the SVC and the memory effect ends up for this case study with a mean value that is different from the one given by the memory effect alone. Removing this point, it rises the correlation to R^2=0.71.

In **Figure 7. 17 c)** the comparison between the KGWRAI and the regulation capacity is illustrated.

The correlation is positive, with higher values of the KGWRAI for case studies with a higher mean discharge (larger circles). This is explained by the fact that the KGWRAI contains information on the mean discharge of the system. In the particular case of the "Ca" Cardener spring, in both methods KGWRAI and RC suggests the same medium behaviour.

7.5 Conclusions

The work carried out in the framework of the participation in the CHAKAWP5- GeoERA RESOURCE project, has allowed expanding the characterization and hydrogeological analysis of the Port del Comte karstic massif beyond the objectives initially set by the thesis specifically for the Cardener karst spring, which is the one with more available information. The results obtained have allowed the application of classical methods of classification of karstic media such as the Mangin (1975) method with other European aquifers and with the previous works of Freixes (2014) in Catalonia, as well as contributing to the implementation and testing of the new classification methodology Method 1, Method 2 and Method 3 presented.

The application of Mangin's method for the recession curve analysis in Cardener spring, provided a mean value of the infiltration "i" function of 0.63 for the period May 1985 to August 2010, and 0.50 for the period September 2000 to August 2010, and also a regulation "k" parameter of 0.63 and 0.57 respectively which reveals the large storage capacity of the saturated zone of the karst aquifer. Therefore, both parameters suggest that the springs is in the domain of complex karst systems (Mangin, 1984), similar to the behaviour for the for the Font Lastaour, Font Aigüeira, Font Térme-Pila (Vielha valley System, NO Catalonia) and Fonts Llobregat, Fonts Bor (Alt Llobregat and Alt Segre System, N, Catalonia) estimated by Freixes (2014). The relatively high values of i and k obtained in Cardener spring may suggest favourable conditions for their groundwater resource exploitation. A high value of 'i' means that the decrease of the discharge is relatively small 2 days after the flood peak, which mean that the infiltration is somehow delayed through the infiltration zone and towards the un-saturated zone, while the relatively high value of k means that there is a high baseflow component with a high proportion of the discharge derived from long term storage as opposed to rapid infiltration. These characteristics provide the aquifer with some degree of resilience to precipitation variability and drought, although certain vulnerability at long-term

climate change effects.

With the aim to evaluate the karstification level and to analyse the hydrodynamic properties of the aquifer, correlation and spectral analyses were applied to the data of precipitation (taken from 127O AEMET weather station) and the flow discharge from the period January 1990 to September 1994. following the Mangin (1910, 1984a,b) approaches. According to his classification system based on the parameters ME, Treg and Fc obtained from the correlogram analysis, the Cardener spring it is equivalent to a high inertia karst aquifer system, with a medium to large regulatory capacity of the system and significant memory effect. The results obtained in the analysis of time series in relation to the fact that the 'Cardener karst spring' system shows a medium to large inertia, is consistent with the volumetric capacity that can be intuited in the geological cross-sections (chapter 2), and with the estimated MTT of 2.85 years - using environmental tracers - and the corresponding volume (Vm) stored in the aquifer of 19.4 Hm^3 (chapter 3).

In this section of Methods, the 3 new classifications methods of karst aquifers proposed in the framework for the CHAKAWP5- GeoERA RESOURCE project in order to help water operators and hydrogeologists to prioritize prospection and exploitation of well suited aquifers approaches have been presented and applied into the Cardener spring in Port del Comte and 15 more karst springs located throughout EU. All these needs different degrees of necessary information.

Method 1 is a classification of vulnerability only. It combines the use of catchment data that are indicative of vulnerability and are generally always available (the degree of cave development; surface karst) with indicators of rapid groundwater flow (tracer tests, water quality indicators of rapid flow, coliform counts, and a rapid discharge response to rainfall). Beyond the limitations and advantages of the method, the vulnerability class obtained from its application to the particular case of the "Ca" Cardener karstic spring (and also to the rest according to Maréchal, et al, (2021a, 2021b) is consistent with the hydrogeological conceptual model of functioning.

Method 2 provides an assessment of the water resource availability based on discharge time series analysis which is combined with the vulnerability assessment of Method 1 to enable consideration of both these factors that are important for water resource management. In Method 2 a groundwater resource availability index called KGWRAI is proposed which is based upon the memory effect

time series analysis method combined with the Qavg (mean spring discharge). The memory effect provides an evaluation of the proportion of rapid groundwater flow, and the amount of storage in the system thereby providing useful information on the resilience of the system to precipitation variability, which when combined with the mean spring discharge gives an indication of the overall resource availability. The obtained results of classification for “Ca” Cardener karst spring of the Port del Comte high-mountain karst aquifer with (V=2.30, KGWRAI=0.38) characterizing it by a medium-to-high vulnerability with a medium karst GW resource availability for water supply management it is in agreement of what was expected according with the rest of available Information.

Method 3 provides an alternative to method 2 for combining an evaluation of intrinsic vulnerability with an evaluation of the regulation capacity of a spring. For the vulnerability assessment, it uses mostly different parameters to Method 1 and is focused entirely on physico-chemical parameters measured at the spring that can be indicative of vulnerability. The method highlights these parameters as useful indicators of high vulnerability in karst aquifers. For the regulation capacity assessment, Method 3 uses two times series analysis methods: It combines the memory effect (also used in Method 2) to characterize the response time, with the SVC parameter which characterizes the discharge variation at different time scales. The assessment of groundwater availability, which is important information for potential end users for a sustainable management of the resource, requires consideration of average flow discharge, which is used as a third piece of information to set point sizes in the output graph. This method has as a point in favor that it allows considering in its final representation, the reliability of the results, based on the starting data that have been considered. The method has been applied to both the “Ca” Cardener and “SQ” Sant Quintí karst springs in of the Port del Comte high-mountain karst aquifer. The results obtained suggest that both have moderately RC regulation capacity, although the reliability of the results is different since in the second management there are no daily data series available. In any case, the result is consistent with the rest of the analyses carried out (see chapter 2, chemographs, chapter 3 hydrological modeling, and chapter 6, the conceptual model of hydrological behaviour of both springs).

The use of these methods could be extended and applied to the rest of the karst springs in the Pyrenees in order to have a comparative overview of their behavior and general vulnerability.

7.6 References

Antigüedad Auzmendi, I. (1998). Estudio de los acuíferos kársticos a partir de sus respuestas naturales. Aplicación a dos sistemes del País Vasco. Rev. Soc. Geol. España, 1, (1-2)

Arnó, G.; Conesa, A.; Carreras, X.; Camps, V.; Fraile, J.; Herms, I.; Iglesias, M. (2020) Mapa de Vulnerabilitat Intrínseca a la contaminació dels Aqüífers de Catalunya (MVIAC) 2020.Institut Cartogràfic i Geològic de Catalunya (ICGC)

Box, G.E.P. i Jenkins, G.M. (1974) Time Series Analysis: Forecasting and Control. Holden-Day, San Francisco, Califòrnia. Pp 575

BRGM (2021). Deliverable D5.6 Karst data time series treatment tool, an excel code for data time series treatment in karst aquifers (Downloadable from https://www.brgm.fr/fr/logiciel/xlkarst-application-excel-caracterisation-hydrodynamique-systemes-karstiques)

Çağdaş,S.,; Kurtuluş, B., Razack, M.. (2020). "Hydrodynamic Characterization of Mugla Karst Aquifer Using Correlation and Spectral Analyses on the Rainfall and Springs Water-Level Time Series" Water 12, no. 1: 85. https://doi.org/10.3390/w12010085

Crochet, P. and Marsaud, B (1997). Approaces conceptualles de l'Aquifère karstique. Problèmes méthodologiques et d'exploitation. Hydrogéologie, nº3, pp. 3-18, 12.

Dörfliger, N., Crochet, Ph., Guerrin, R., Jozja, N., Marsaud, B., Mondain, P. H., Muet, P.,Plagnes, V. (2010): Guide méthodologique – Les outils de l'hydrogéologie karstique pour la caractérisation de la structure et du fonctionnement des systèmes karstiques et l'évaluation de leur ressource, BRGM, Orléans, France.

Dubois, E., Doummar, J., Pistre, S., and Larocque, M. (2020): Calibration of a lumped karst system model and application to the Qachqouch karst spring (Lebanon) under climate change conditions, Hydrol. Earth Syst. Sci., 24, 4275–4290, https://doi.org/10.5194/hess-24-4275-2020

El-Hakim, M., Bakalowicz, M., (2007). Significance and origin of very large regulating power of some karst aquifers in the Middle East. Implication on karst aquifer classification. J. Hydrol. 333 329–339. https://doi.org/10.1016/j.jhydrol.2006.09.003

Farlin, J. and Maloszewski, P. (2013). On the use of spring baseflow recession for a more accurate parameterization of aquifer transit time distribution functions, Hydrol. Earth Syst. Sci., 17, 1825–1831, https://doi.org/10.5194/hess-17-1825-2013.

Flora, S. P. (2004). Hydrogeological Characterization and Discharge Variability of Springs in the

Middle Verde River Watershed, Central Arizona. PhD thesis, Northern Arizona University. (accessed from http://watersheddev.nau.edu/Research/Flora/springs.html)

Ford, D.C. and Williams, P.W. (1989) Karst Geomorphology and Hydrology. Chapman and Hall, London, 601 pp. https://doi.org/10.1177/030913339001400209

Ford, D.C. and Williams, P. (2007) Karst Hydrogeology and Geomorphology. John Wiley, Chichester, 562pp. https://doi.org/10.1002/9781118684986

Hakoun, V.; Bailly-Comte V; Charlier JB.; **Herms I.**; Hickey C.; Pardo-Igúzquiza E.; Stroj A.; Van Vliet M. (TNO), Vernes R.; Maréchal, JC. (2020). Deliverable D5.1 Karst typology in Europe: state of the art. (Downloadable from https://repository.europe-geology.eu/egdidocs/resource/geoera+resource+chaka+deliverable+51+state+of+the.pdf)

Hartmann, A., Wagener, T., Rimmer, A., Lange, J., Brielmann, H., Weiler, M., (2013). Testing the realism of model structures to identify karst system processes using water quality and quantity signatures. Water Resour. Res. 49, 3345–3358. https://doi.org/10.1002/wrcr.20229

Hartmann, A., N. Goldscheider, T. Wagener, J. Lange, and M. Weiler (2014). Karst water resources in a changing world: Review of hydrological modeling approaches. Reviews of Geophysics 52 (3), 218–242. https://doi.org/10.1002/2013RG000443

Jiménez Gavilán, P. and Andreo, B. (2012). Estudio comparativo de la respuesta hidrodinámica de varios acuíferos carbonáticos del Sur de España a partir del análisis correlatorio y espectral. Gaceta, 52.

Kovács, A. (2021) Quantitative classification of carbonate aquifers based on hydrodynamic behaviour. Hydrogeol J 29, 33–52. https://doi.org/10.1007/s10040-020-02285-w

Kresic, N., Stevanović, Z., (2010). Groundwater hydrology of springs: engineering, theory, management, and sustainability. Butterworth-Heinemann, Oxford. Pp 567. ISBN 978-1-85617-502-9

Ladson, A.R., Brown, R., Neal, B., Nathan, R. (2013) "A standard approach to baseflow separation using the Lyne and Hollick filter." Australian Journal of Water Resources, vol. 17, no. 1, Apr. 2013, pp. 25. https://doi.org/10.7158/W12-028.2013.17.1.

Larocque, M., Mangin, A., Razack, M., Banton, O. (1998). Contribution of correlation and spectral analyses to the regional study of a large karst aquifer (Charente, France). Journal of Hydrology 205 (1998) 217-231. https://doi.org/10.1016/S0022-1694(97)00155-8

Lyne, V. and Hollick, M. (1979) Stochastic Time-Variable Rainfall-Runoff Modeling. Institute of Engineers Australia National Conference, 89-93.

Mangin, A. (1970): Contribution à l'étude des aquifères karstiques à partir de l'analyse des courbes de décrue et tarissement. Annales Spéléologie, 25(3): 581-610.

Mangin, A. (1971) Etude des débits classés d'exutoires karstiques portant sur un cycle hydrologique, Annales de spéléologie, t 26, 2, pp 283,329.

Mangin, A. (1975) Contribution à l'étude hydrodynamique des aquifères karstiques, PhD thesis, Université de Dijon, Dijon, France, 1975. https://hal.archives-ouvertes.fr/tel-01575806

Mangin, A. (1981a): Utilisation des analyses corrélatoire et spectrale dans l'approche des systèmes hydrologiques. C. R. Acad. Sci. Paris, Sciences de la terre et des planètes, 293: 401-404.

Mangin, A. (1981b): Apports des analyses correlatoire et spectrale dans l'approche des systèmes hydrologiques. C. R. Acad. Sci. Paris, Sciences de la terre et des planètes, 293: 1011-1014.

Mangin, A. (1984). Pour une meilleure connaissance des systèmes hydrologiques à partir des analyses corrélatoire et spectrale. J. Hydrol. 67, 25–43. https://doi.org/10.1016/0022-1694(84)90230-0

Maréchal, JC.; Stroj A.; Bailly-Comte V.; Bunting, S.Y.; Elster D.; **Herms I.**; Hickey C.; Kovács A.; Krystofova E.; Maurice, L.; Pardo-Igúzquiza E.; Persa D.; Skopljak F.; Szucs A.; Urbanc, J.; Van Vliet M.E.; Vernes R.W. (2021a). Deliverable D5.2 Detailed conceptual hydrogeological models for pilot areas and case studies. (Downloadable from https://repository.europe-geology.eu/egdidocs/resource/geoera+resource+chaka+deliverable+52+detailed+con.pdf)

Maréchal, JC.;, Bailly-Comte V.; Hickey C.; Maurice, L; Stroj A.; Bunting, S.Y.; Charlier JB.; Hakoun V.; **Herms I**.; Krystofova E.; Pardo-Igúzquiza E.; Persa D.; Schubert G.; Skopljak F.; Szucs A.; Urbanc, J. Van Vliet M.E.; Vernes R.W. (2021b). Deliverable D5.3 Karst aquifer typology tool. (Downloadable from https://repository.europe-geology.eu/egdidocs/resource/geoera+resource+chaka+deliverable+53+karst+typolo.pdf)

Maréchal JC.; Hickey C.; Bailly-Comte V.; Maurice; Stroj A.; Bunting, S.Y.; Charlier JB.; Hakoun V.; **Herms I.**; Krystofova E.; Pardo-Igúzquiza E.; Persa D.; Schubert G.; Skopljak F.; Szucs A.; Urbanc, J.; Van Vliet M.E.; Vernes R.W. (2021c). Deliverable D5.4 Groundwater management recommendations for karst and chalk aquifers. Accessed https://repository.europe-geology.eu/egdidocs/resource/geoera+resource+chaka+deliverable+54+groundwater.pdf

Maréchal, Jean-Christophe and CHAKA Team (*) (2021d). Deliverable D5.5 Data set which contains time series of precipitation and discharge of springs in the CHAKA pilot areas (last

accessed https://zenodo.org/record/5668387#.Yg_8wOqZOUm).
DOI:10.5281/zenodo.5668387 ; Where (*) the CHAKA Team were formed by: Maréchal, Jean-Christoph; Bailly-Comte, Vincent; Hickey, Caoimhe; Maurice, Lou; Stroj, Andrej; Bunting, Sarah; Charlier, Jean-Baptiste; Ladouche, Bernard; **Herms, Ignasi**; Krystofova, Eva; Pardo- Igúzquiza, Eulogia; Persa, Diana; Schubert, Gerhard; Skopljak, Ferid; Szucs, Andrea; Urbanc, Janko; Van Vliet, Mariëlle; Vernes, Ronald; Elster, Daniel; Jasmika, Nikolic; Fleury, Perrine; Kovacs, Attila; Hunter-Williams, Taly; Macovei, Monica; Bartolome, Andreo; Arno, Georgina; Camps, Victor; Hans Peter Broers.

Mathevet, T., Lepiller, M. l., and Mangin, A. (2004): Application of time-series analyses to the hydrological functioning of an Alpine karstic system: the case of Bange-L'Eau-Morte, Hydrol. Earth Syst. Sci., 8, 1051–1064, https://doi.org/10.5194/hess-8-1051-2004

Mudarra, M., Jiménez-Gavilán, Andreo, B. (2012). Respuesta hidrodinámica del manantial de Villanueva del Rosario (acuífero de las Sierras de Camarolos y del Jobo, provincia de Málaga) bajo diferentes condiciones climáticas. SIAGA 2012,

Omed, M.; Broder, M. (2015). Classification of karst springs based on discharge and water chemistry in Makook karst System, Kurdistan Region, Iraq. Freiberg Online Geoscience Vol 39, 2015. 1-25 pp. FOG special volume: Regional Hydrogeology in Asia and the Middle East. 130pp.

Padilla A, Pulido-Bosch A. 1995. Study of hydrographs of karstic aquifers by means of correlation and cross-spectral analysis. Journal of Hydrology, 168, 73–89. https://doi.org/10.1016/0022-1694(94)02648-U

Paiva, I., Cunha, L. (2020). Characterization of the hydrodynamic functioning of the Degracias-Sicó Karst Aquifer, Portugal. Hydrogeol J 28, 2613–2629. https://doi.org/10.1007/s10040-020-02201-2

Pavlić, Krešimir, and Jelena Parlov. (2019). "Cross-Correlation and Cross-Spectral Analysis of the Hydrographs in the Northern Part of the Dinaric Karst of Croatia" Geosciences 9, no. 2: 86. https://doi.org/10.3390/geosciences9020086

Rosas, P. Sanz, E & Menéndez-Pidal, I. (2016). Hidrogeología del Karst de Pico Frentes (Cordillera Ibérica, España). Estudios Geológicos 72(1): e047. http://dx.doi.org/10.3989/egeol.42132.375.

Schuler, P., Duran, L., Johnston, P., & Gill, L. (2020). Quantifying and numerically representing recharge and flow components in a karstified carbonate aquifer. Water Resources Research,

56, e2020WR027717. https://doi.org/10.1029/2020WR027717

Springer, A. E., Stevens, L. E., Anderson, D. E., Parnell, R. A., Kreamer, D. K., Levin, L., and Flora, S. P. (2004). Chapter 4. A comprehensive springs classification system: integrating geomorphic, hydrogeochemical, and ecological criteria. page 31.

Tamburini, Andrea, and Marco Menichetti. (2020). "Groundwater Circulation in Fractured and Karstic Aquifers of the Umbria-Marche Apennine" Water 12, no. 4: 1039. https://doi.org/10.3390/w12041039

Vías, J.M.; Andreo, B.; Perles, M.J.; Carrasco, F.; Vadillo, I.; Jiménez, P. (2006) Proposed method for groundwater vulnerability mapping in carbonate (karstic) aquifers: The COP method. Hydrogeol., 14, 912–925. https://doi.org/10.1007/s10040-006-0023-6

Zuber, A. (1986). On the interpretation of tracer data in variable flow systems, J. Hydrol., 86, 45–57. https://doi.org/10.1016/0022-1694(86)90005-3

Zwalhen (2003). COST Action 620. Vulnerability and Risk Mapping for the Protection of Carbonate (Karst) Aquifers. Final Report (link).

8 GENERAL DISCUSSION AND CONCLUSIONS

8.1 Discussion

The objective of this section is to carry out a cross general discussion of all the work carried out in the thesis, from the point of view of the methodologies used, the results obtained in the 4 articles presented (chapter 3, 4, 5 and 6) published in Science of the Total Environment (Elsevier) and WATER (MDPI) together with the complements presented in chapters 2 and 7.

The importance of high-mountain karst aquifers: High mountain karst aquifers are associated with "water towers" because they generate the main water resources that feed the downstream waters and this is especially true in the Catalan Pyrenees, as for instance in the Alt Llobregat-Alt Segre system and the Aran Valley system (Freixes, 2014). These perform a very important regulation function since the water recharged in their carbonate aquifers remains longer in the basin in winter in form of snow cover or inside the aquifer itself, thus providing a strategic water resource in dry seasons, which is especially important in the Mediterranean areas prone to drought, especially important ahead of the foreseeable effects of climate change in Catalonia. These are stored resources for future That is probably the main reason why its characterization and knowledge is key both for the management of the resource in these future scenarios but also for its protection.

The challenge of facing the hydrogeological characterization of the HMKA: The main difficulties when addressing a hydrogeological research of a high mountain complex karstic systems undoubtedly lies in the lack of previous data (Dubois et al., 2020) and therefore in the obligatory need to generate new data through the planning and execution of new field campaigns. And that must be done within a geographic context that normally presents complicated accessibility not only because of the distances, but also because of the permits, the impossibility to implement fixed gauging stations, also because of the abrupt and irregular topography that forces the use of off road vehicles, and the weather itself that makes it difficult to access and execute sampling campaigns in winter periods. Notwithstanding all of this, the use of orderly and guided planning of the fieldwork, the use of adequate equipment and methods adapted to the ground, and the important logistic support of local agents can make possible, to achieve the objectives and obtain valuable information with which to obtain various novel conclusions on new hydrogeological knowledge.

The doctoral thesis presented has used a multidisciplinary approach to study the hydrogeological functioning of the Port del Comte Massif (PCM) one of the most important karst aquifer system of the in the South-Eastern part of the Pyrenees. The results obtained have meant an important global advance in the improvement of the knowledge of its conceptual model of functioning. The methodologies used to interpret and analyse data have included the: 1) 3D surface-based geological modeling of the main layers and structures, 2) the distributed rainfall-runoff hydrological modeling of the recharge and discharge pattern of the main karstic springs, inferring the Mean Transit Time inside the system using the stable isotopes of precipitation as environmental tracers; 3) the hydrogeochemical characterization of its groundwater based on field campaigns carried out over 2 years, identifying the different facies, grouping them and distinguishing them according to their characteristics through multivariate statistics taking into account the compositional data analysis approach, explaining their anthropogenic origin or geogenic (taking into account the geological variability of the massif) based on a multi-isotopic modeling study, and determining the natural background geochemical levels of the main pollutants in this type of environment, such as nitrate, chloride and sulfate 4) as well as establishing, testing and validating a karstic spring-based classification system that considers their vulnerability and their regulation capacity as function on various hydrological and geochemical parameters. All of this combined has allowed establishing a general and global view of the hydrogeological conceptual model of the massif. Therefore, the use of a multi-focus methodology has made it possible to generate a solid geoscientific knowledge base that will allow a more rigorous approach to the planning and management of water resources within the framework of groundwater masses, taking into account their vulnerability and the necessary adaptation to the foreseeable effects of climate change.

The geological framework: The Port del Comte Massif constitutes an independent geological and hydrogeological unit that forms an ‘aquifer system’, i.e. a collection of aquifers and aquitards which together constitute the environment of groundwater - "communicating vessels" that are filled or can be filled with water, according to the terms defined in the hydrogeological data model in the European Directive INSPIRE, Directive 2007/2/CE, Infrastructure for Spatial Information in Europe, for data specifications on Geology (INSPIRE Thematic Working Group Geology, 2013). In this context, the principal aquifer corresponds to the named Lower Eocene - Fissured/karstified aquifer of alveoline limestones and dolostones of the ‘PPEc’ geological unit of the 1:50,000

geological database of the ICGC (2007), which is the one that has been analysed in greater detail. This aquifer in the highest parts of the massif present 1000 m thick unsaturated zone and also a very developed field of karstic landforms such as karren fields and sinkholes manly distributed between 2050 and 2300 m a.s.l.

Hydrological functioning of the system: One of the necessary steps to study the functioning of a hydrogeological system is from its modeling which should allow calculating the recharge and discharges. However, one of the most common problems with high mountain karstic aquifers is that usually the scarcity of data with no direct information on the hydraulic characteristics and the position of the regional piezometric level. Besides these aquifers have characteristics that make them quite different from other aquifers, such as high heterogeneity due to the endokarst network which make it difficult to model. Lumped parameter models (LPMs) are useful to simulate the behaviour of such complex mountain karst systems, even when their heterogeneity is poorly characterized. In the case of the Port del Comte massif, the main aquifer of the system (PPEc Tertiary unit) is essentially discharged through 4 springs, which in order of importance are: the 'Cardener spring', 'Sant Quintí', 'Aiguaneix' and 'Can Sala'. To study them in the frame of this thesis, a semi-distributed rainfall-runoff hydrological approach for each spring was followed using the HBV model. This allows to consider land use distribution for catchments and at different altitudes and the effect of snow accumulation and its melting. In order to model the system, we have started from the capacity data taken over two years of monitoring in the 4 springs. The fortnightly gauging monitoring campaigns during two complete and continuous years using the slug injection using salt in dilution in the four regional karst springs (Cardener, Sant Quintí, Can Sala and Aiguaneix) have allowed to characterize the hydrodynamics of the main aquifer. Although it is true that the information obtained does not have the detail that a time series on a daily scale could have, it has allowed us to have the best approximation of the water balance that has been had to date, which allowed afterwards to quantify such important factors as the effective recharge rate and the infiltration rate and how it is influenced depending on the ground cover. Apart from the two four most important springs, two additional local springs representative of smaller points have been modelled. The results have allowed us to conclude that the aquifer infiltration capacity (i.e., the ratio between the effective recharge of the aquifer, and precipitation at the spring recharge zone) ranges as the yearly average ranges from 28,3% to almost 62% in the highest parts of the massif, which is precisely where there is less ground cover and where the karst development is more evident

and spectacular. A regression model has shown that the altitude is the most important predictor controlling the aquifer infiltration capacity. These rates are consistent with other modeled karst systems (see chapter 3). Besides the recharge is almost concentrated in spring thanks the rainfall and the snowmelt with almost 46% of total.

The research has also been supported by the isotopic characterization of the inputs (precipitation) based on data from 8 rain gauges installed expressly for this research. This has made it possible to determine the local water meteoric water line (LMWL) of Port del Comte, as $\delta^2H = 8{,}05 \cdot \delta^{18}O + 12{,}74$. The annual isotopic content of the precipitation in autumn and winter presents a greater variability while the isotopic content in groundwater changes much less seasonally. The modeling of the isotopic response in the discharge made possible to calculate the Mean Transit Time of water within the system applying both analytical approach using the sine-wave method (in the four regional most important karst springs plus 13 local minor springs) and numerical approach using the FlowPC model. The analytical approach showed that MTT varied between 0,5 to almost 6 years. The study has shown how the MTT values obtained by this numerical approach considering recharge time-series calculated by means of the HBV model in 6 of the springs (the 4 regional plus 2 local) are 1,9 times shorter than the MTT values using the classical analytical approach, which could be crucial if this is considered a vulnerability assessment indicator for karst-fissure aquifers. The results indicates that there is a relatively significant mixing process inside the aquifer (i.e. between infiltrated water with old water inside the aquifer) giving values between 1,69 yr (Sant Quintí spring) and 2,85 yr (Cardener spring), and volumetric capacities of 11.54 Hm^3 (Sant Quintí spring) and 19.4 hm^3 (Cardener spring). These volumes are consistent according with the analysis obtained with the time series analysis (correlation analysis, in chapter 7) for the Cardener spring (the one that only has time-series of Q daily flow discharge data available), indicating the system present moderate to high memory effect and a considerably filter of the input signal. The relatively apparent large average MTTs of 2,3 yr effectively points to groundwater mixing as a natural attenuation/dilution process inside the aquifer system. However, it should be noted that the presence of well-developed hidden endokarst in the unsaturated zone may favor the rapid migration of contaminants from recharge areas to groundwater. (e.g. when periods of rapid snowmelt occur due to sudden increases in temperature, concentrating the infiltration in short periods of time), hypothesis that is consistent classifying the springs of Cardener and Sant Quintí with a ‘high’ vulnerability as well as with ‘moderately regulation capacity’. It is worth be noted that such

classification is the result of applying the RC-V System, which was developed, tested, and validated in Port del Comte and other HMKS in the EU, within the framework of the CHAKA GeoERA Resource project (see chapter 7).

Simulated future responses to climate changes: In the current context of Climate Change (CC), and particularly in the Pyrenees, understanding the response to climate change of high-mountain karst aquifers at a local scale is essential from the perspective of future water resources availability. This is key to help design the most appropriate adaptation measures, to minimize adverse effects, especially in this pan-Mediterranean area, where water scarcity becomes an environmental recurrent issue, and the concern about the impact of a possible significant reduction in snow cover on economic activities (such as alpine skiing) is not negligible. In this sense, the calibrated semi-distributed rainfall-runoff hydrological models were used to simulate the impacts of climate change based on a delta change approach to calculate Climate Change signals between reference and future climate produced specially for the Pyrenees in the framework of the CLYM'PY (Characterization of the evolution of climate and provision of information for adaptation in the Pyrenees) Project where high–resolution (5 km×5 km) climate projections for the 21st century were generated using 24 downscaled general circulation models (GCMs) for several different Representative Concentration Pathways (RCP) emission scenarios. It was used the RCP4.5 (the radiative forcing stabilizes without overshooting 4.5 W/m^2 (~650 ppm CO_2- equivalent) in 2100) and the RCP8.5 (radiative forcing overpassing 8.5 W/m^2 (>1370 ppm CO_2- equivalent) in 2100) adopted by the Intergovernmental Group of Experts on Climate Change (IPCC) from a subset of 6 well-known global climate models. In this these simulated scenarios the evolution in the isotopic content of groundwater were considered with the aim of identifying relevant trends to be used as CC impact proxies and also because they may become a relevant source of isotopic data to be used by isotope-enabled global climate models (IGCM) for validating purposes of future paleoclimate modeling studies. Although the results of this work are specific for the Port del Comte Massif, the methodology used, and the general conclusions obtained can be used in any other mountain karst aquifer. The results were expressed as a percentage of change associated with precipitation (P), temperature (T), actual evapotranspiration (AET), total runoff (Q_{tot}), rainfall recharge (Q_{rain}), snowmelt recharge (Q_{snow}) and total recharge (Q_{rec}), averaged for the 2011-2040, 2041-2070 and 2071-2100 intervals. The results achieved highlights that precipitation seems to follow a slight downward trend for the different average intervals considered presenting maximum annual

decreases of 29 and 30 mm for the RCP4.5 and RCP8.5 scenarios respectively. The latter climate scenario shows more variability, whereas Q_{rain}, Q_{rec} and Q_{tot} does not present a statistically significant trend for the whole estimation period 2010-2100. But a significant change is observed with a monotonous increasing trend in temperature, with its average variation compared to the reference period (1986-2015) for the last interval (2071-2100) of up to 1.9 and 3.1 ºC for the RCP4 and RCP8.5 scenarios respectively, which impact both in AET and Q_{snw} producing a rapid reduction of the number of days with snow cover and it thickness. These decreasing trends in Q_{snw} are already being observed in the Western Pyrenees and it is expected that in the future, especially at low altitudes, it will be even more marked.

Figure 8. 1 highlights the expected CC impact on snow cover of the Port del Comte massif. On average between the two emission scenarios considered (RCP4.5 and RCP8.5) respect the reference period (1986–2015), and taking into account the range of variability of the results, the temperature in a horizon of 35 years could increase up to+1.3 ºC, the extent of snow cover could be reduced in the most extreme case up to almost 50%, and the average height of the mantle goes up to about 300m in height. By the middle of the second part of the 21st century, and in the worst of the climate change scenarios and in the most extreme case, the rise in temperature could reach +3.1 ºC, the cover could decrease by up to 76% and the average height could go up to 500m in height respectively.

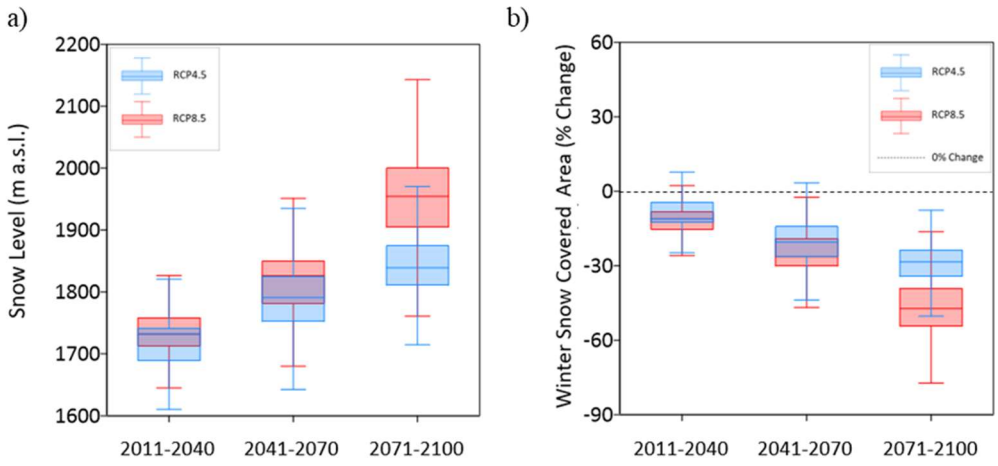

Figure 8. 1. Estimated variation of the average height of the snow cover (a) and winter snow cover area, in % (b) for the averaging periods 2011-2040, 2041-2070 and 2071-2100, obtained by the different climate models for the emission scenarios RCP4.5 and RCP8.5, with respect the corresponding averaged value of the variable obtained for the reference period (1998-2005). The dashed line indicates the null change position.

OPCC-CTP (2018) concludes that Climate Change could be decisive in the determination of the necessary conditions for the practice of certain tourist activities in the Pyrenees. In particular, the greater variability in thickness and duration of snow cover could be a challenge for alpine ski resorts, which will have to be adapted to keep the stations operational and ensure the sustainability of its activity, and in this regard, the Port del Comte sk resort, the most southern in Catalonia will probably suffer more. Although, in total terms, there is not a very significant trend in the reduction of total precipitation, a net decrease in the average annual spring flow is expected for the third period 2071-2100, of 0.6 and 0.4 hm^3/yr for the RCP4 and RCP8.5 scenarios respectively. These values may seem insignificant, but these variations may be critical downstream for dependent ecosystems due to the increase in temperature, and as a result of the alteration of the discharge regime to the basin due to less precipitation in the form of snow (which could be retained as a cover) reducing the flow in the spring due to melting, but on the contrary there will be more precipitation in the winter slightly increasing the discharge flow during this period. The same effects of a reduction in spring flow rates under the equivalent climate change scenarios have been predicted in similar complex alpine karst springs (Dubois, et al, 2020).

Hydrogeochemical aspects: The research has made it possible to characterize the families of groundwater existing in the system in 43 monitoring springs. The results were somewhat surprising in the sense that up to 6 types or variants of different water facies were identified, and this is explained by the lithological variability present in the study area. The most relevant thing is that springs that are located in the same geological unit can present different facies, and springs that are located in different geological units can also present the same facies. Therefore, the geological unit where the spring is located is not a good predictor neither a conclusive aspect to be able to explain the origin of groundwaters. In this line, the well-known Piper diagram can not be considered directly conclusive. Therefore, the approach was to analyze the variability from statistical point of view using the compositional data approach, which is crucial in this type of data to avoid spurious and unrealistic associations or conclusions or making results uninterpretable (Otero et al., 2005, Blake et al., 2016) for instance when using the classical standardization approach (or z-score normalization) as it has been demonstrated in detail in Chapter 3 (Paper 1). A univariate first EDA analysis quickly showed that different clusters were probably superimposed. Then a multivariate clustering process was followed to identify groups with hydrogeological sense. In this type of

complex settings, there are certainly mixtures of groundwaters, and this entails a challenge when it comes to classifying them in a deterministic way and unequivocally to one or another cluster. For this reason, first a PCA was addressed which allowed visualizing in the clr-biplots several subgroups of waters with clear similarities likely these associated with changes in terms of bedrock lithology. To aggregate water with a statistical, but also with a hydrogeological sense, a clustering process was followed. 'Hard' clustering methods are not the most suitable, even more so when there is a certain variability of criteria to determine the appropriate number of clusters. In the research it was used the 'soft' model-based clustering method Gaussian Mixture Model (GMM) that assume finite mixtures of multivariate-normal or Gaussian distributions, so a probability-based approach. Therefore, the obtained partition can be interpreted from a statistical point of view, unlike the classical 'hard' - or heuristic-based - algorithms (k-means, hierarchical clustering, etc.) The results separated 4 clusters: a **Cluster A** characterized by low mineralization and dominated by slightly alkaline Ca–HCO3 water type, mostly associated with the main HMKA of the Port del Comte; a **Cluster B** encompasses water types from Ca–HCO3 to Ca–HCO3–SO4, Ca–SO4-HCO3 and Ca–SO4, which are characterized by slightly alkaline moderate mineralization mostly in Cretaceous and Triassic (Keuper) materials outcropping in the area; **Cluster C** including water types from Ca–HCO3 and Ca–HCO3-Cl water types related with groundwater flow through areas with the presence of relict halite or salty water in closed pores in the Keuper materials; and **Cluster D** with the most evident and special waters corresponding to Na–Cl type facies discharging from Keuper confined bedrocks and interpreted as the contribution of deep groundwater flow with elevated transit times that allows a significant solute diffusion.

The separation of groundwaters using MSA supported by the CoDa approach has been crucial for determining robust Natural Background Levels associated with the main karst aquifer of the Port del Comte Aquifer, which corresponds to the named Lower Eocene - Fissured/karstified aquifer of alveoline limestones and dolostones of the 'PPEc' geological unit of the 1:50,000 geological database of the ICGC (2007). These were determined just applying the PS-method developed in the framework of the EU "BRIDGE" (2007) project (Müller et al., 2006). Although the whole PCM massif belongs to the same geomorphological structure, the SE sector has been assigned to GWB-5 ('Conca Alta del Cardener i Llobregat'), whereas the rest of the PCM was assigned to GWB-44 ('Cadí Port del Comte'). Their corresponding official NBLs followed the same method but took a few points from different aquifers inside. The resulting NBLs values are assigned to the entire

GWBs, and therefore are understood as representative of all units / aquifers included in these bodies. In the current Spanish regulation for drinking water (MHCASWS, 2003) the limit of potability for sulfate is 250 mg/L of SO_4. According to this value, the whole GWB 5 and 44 with NBL of 485 and 609 mg/L would be exceeding the regulatory limit, when groundwater from the Lower Eocene - Fissured/karstified aquifer is being used safely for drinking downstream. The results of the research have demonstrated that Cluster A (associated with that aquifer) NVBL for sulfate is just 14.33 mg/L. Therefore, assigning a global NBL value when the GWB integrates several aquifers with different hydrochemical signatures can lead to completely wrong conclusions.

To go in-depth identifying the natural and anthropogenic geochemical processes controlling groundwater quality in Port del Comte aquifer system, and finally stablish a conceptual model, the variability of hydrogeochemical classes detected in the 4 clusters were studied using bivariate analysis through the most important stoichiometric relationships between the main anions and cations in carbonate media and with evaporites. The dissolution of carbonates (calcite and dolomite) and evaporites (gypsum and halite) are the dominant processes affecting the hydrochemical features of the different clusters, and that ion exchange is a minor process driving the hydrogeological composition of groundwater. The estimation of the recharge elevation associated with the springs sampled during this study was conducted by projecting the mean water isotopic content of δ^2H and $\delta^{18}O$ associated with every spring discharge to the corresponding altitudinal isotopic water line obtained in the isotope characterization of the precipitation. Results confirms that, e.g. Cluster A waters recharges mainly in the highest part of the massif which is consistent with the hydrologic model. The quantification of the hydrogeochemical processes along the recharge-discharge pathways was studied using inverse geochemical modeling. Results suggested e.g. that the predominant geochemical process in Cluster A is the dissolution of carbonates, mainly calcite (37% of dissolved species), followed by dolomite (9.9%) which is consistent with the geological mapping description with the presence of calcite but also dolomite in the highest part of the massif where mainly occur the recharge according to the isotope and the hydrologic model. On the opposite side, the predominance process in Cluster B is the dissolution of gypsum (52.3%), followed by dolomite (12.1%), halite (9.9%) and calcite (4%), and a small contribution of ion exchange-like processes (3.2%). This evidences the need to separate both clusters, that is, those springs that may be influenced by Triassic and Tertiary materials with gypsum to adequately estimate the NBL of the main karstic carbonate aquifer at a regional scale.

In order to determine the origin of $SO_4^{=}$ in groundwater, the relationship between $\delta^{34}S_{SO_4}$ and $\delta^{18}O_{SO_4}$ from dissolved sulphate was considered for the different groundwater samples firstly through the classical dual-isotope approach and secondly using Bayesian isotope mixing models (BMM) to determine the probable source apportionment. The study was supported by gypsum rock samples collected in the Port del Comte area. The results suggested that the main source of the very low $SO_4^{=}$ for Cluster A might be related to all the factors (sulfide oxidation; manure; soil; atmospheric deposition; fertilizers; sewage; Triassic evaporites and Tertiary evaporites), but the BMM specifically indicated that the greatest contribution, comes from fertilizers (proportion ~ 20.4%), which suggested probably related to their use in the "Port del Comte" alpine ski resort, although their impact is not affecting the groundwater quality, whereas groundwater samples from Cluster B showed a very clear relationship with the geogenic origin (from Triassic-Keuper and Tertiary-Eocene-Oligocene Beuda's gypsum Formation pinched out within the South Pyrenees thrust fault in the front SE of the Port del Comte Massif), the samples of Cluster C are mostly related to Triassic evaporites but mixed with other sources and in the Cluster D is related with the Triassic but also Tertiary materials. Regarding the origin of dissolved NO_3^- in groundwater, the relationship between $\delta^{15}N_{NO_3}$ and $\delta^{18}O_{NO_3}$ using either the dual-isotope approach and the BMMs suggested. In general NO_3^- appears to be originated from soil organic nitrogen compounds, NH_4^+ fertilizers, sewage/manure sources or even from a mixing of them. No polluted points were detected except a local spring exceeding the limit of 50 mg/L of NO_3^- (57 mg/L) close to a potato crop field where fertilizers are applied, and another with 42 mg/L of NO_3^- whose isotopic composition presents the fingerprint of manure and sewage, which is in the neighbouring of a cattle farm where manure stocks are managed. Although only these two affected springs with a relatively moderate to high nitrate concentration have been detected within the investigated area, they can indeed be considered a typical example that agricultural activities and branches can easily be a source of nitrate contamination in areas of mountain and this in an environment as vulnerable as a karst aquifer, it is important to keep it under control.

Hydrogeological-geochemical conceptual model: From the combined analysis of all collected and elaborated data, a global hydrogeological and hydrogeochemical conceptual models were interpreted based on four cross-sections derived from the 3D geological model. The PCM is a high mountain karst aquifer, built upon several thrust sheets of carbonate materials. Precipitation is

usually as snow in the highest part of the massif, where bare land abounds, along with the most developed karst forms in the epikarst. The meteoric water from snowmelt and rainfall infiltrates and recharges the aquifer, mostly as Ca-Cl-HCO3 type water. Recharged water flows in all directions and discharge through multiple significant springs. The main aquifer of the system is the one associated with the karstified limestones and dolostones of the Tertiary PPEc unit which underlies the PEcp1 and PEcp2 units. The four most important springs in the system which in order of importance are: the 'Cardener spring', 'Sant Quintí', 'Aiguaneix' and 'Can Sala', springs drain the Tertiary karst aquifer along the syncline axes and were classified into the Cluster A. These characteristics are interpreted as an indicator of high but also complex karstification degree affecting the geological PPEc, PEcp1 and PEcp2 units, which is also what the recession analysis in particular for Cardener spring indicated. Below the Tertiary limestone layers, the Garumnian Kgp unit act as an aquitard, while the Upper Cretaceous Kat, KMca units, the Keuper Tk unit, and the Muschelkalk Tm unit (Triassic) act as local aquifers. These aquifer units drain through small local springs that may have been recharged through the overlying Tertiary carbonate units. The incoming recharge presents an initial Ca-HCO_3 signature, but it changes along the GW flow line by incorporating other solutes from the most soluble evaporite minerals in such local aquifers. The whole system acts then as a "Aquifer System" in terms of the INSPIRE Directive data specifications on Geology as it is said.

Hydrogeological comparison between Can Sala spring and Sant Quintí spring: Gil & Núñez (2003), and (Núñez et al., 2004) suggested an hypothesis about the relationship between both springs which are just separated 542m each other, the former located at 1062 m. a.s.l, and the last at 944 m a.s.l.. At the first glance is very difficult to explain the reliably hydrological difference between neighbouring karst springs, such as 'Can Sala spring' and 'Sant Quintí spring', without extensive hydrogeological research. The results of the current thesis showed that geologically, their discharge point location correspond to different geological units (from the limestones of the PPEc unit in Can Sala spring, and through a karst conduit developed in the conglomerates of the POcgs unit in the case of Sant Quintí spring). But beyond the discharge point, the 3D geological model also showed that its flow path has different travel distances, the geometric volume of their reservoirs in capacity are different, would be disconnected - at least according to the 3D geological model - for hydraulic gradients less than 1-2% and their hydrodynamic responses observed in the chemograms show different patterns with respect for precipitation (chapter 2). Isotopically they

also present differences: The Can Sala average values of δ^2H = 59.9 ‰ and $\delta^{18}O$ = -9.2 ‰ while Sant Quintí presents δ^2H = 62.8 ‰ and $\delta^{18}O$ = -9.6 ‰, which indicates that both are recharged from different altitudes: Can Sala from 1300 to 1900m a.s.l. and Sant Quintí from 2100 m a.s.l. and 2300 m a.sl. Their MTT also differs (chapter 3), from 2,3 yr for Can Sala to 1,7 yr for Sant Quintí. About their hydrogeochemistry, they show slightly different average EC (n=25): Can Sala with 353 microS/cm whereas Sant Quintí 283 microS/cm, although both are classified in Cluster A as Ca–HCO_3 water type waters.

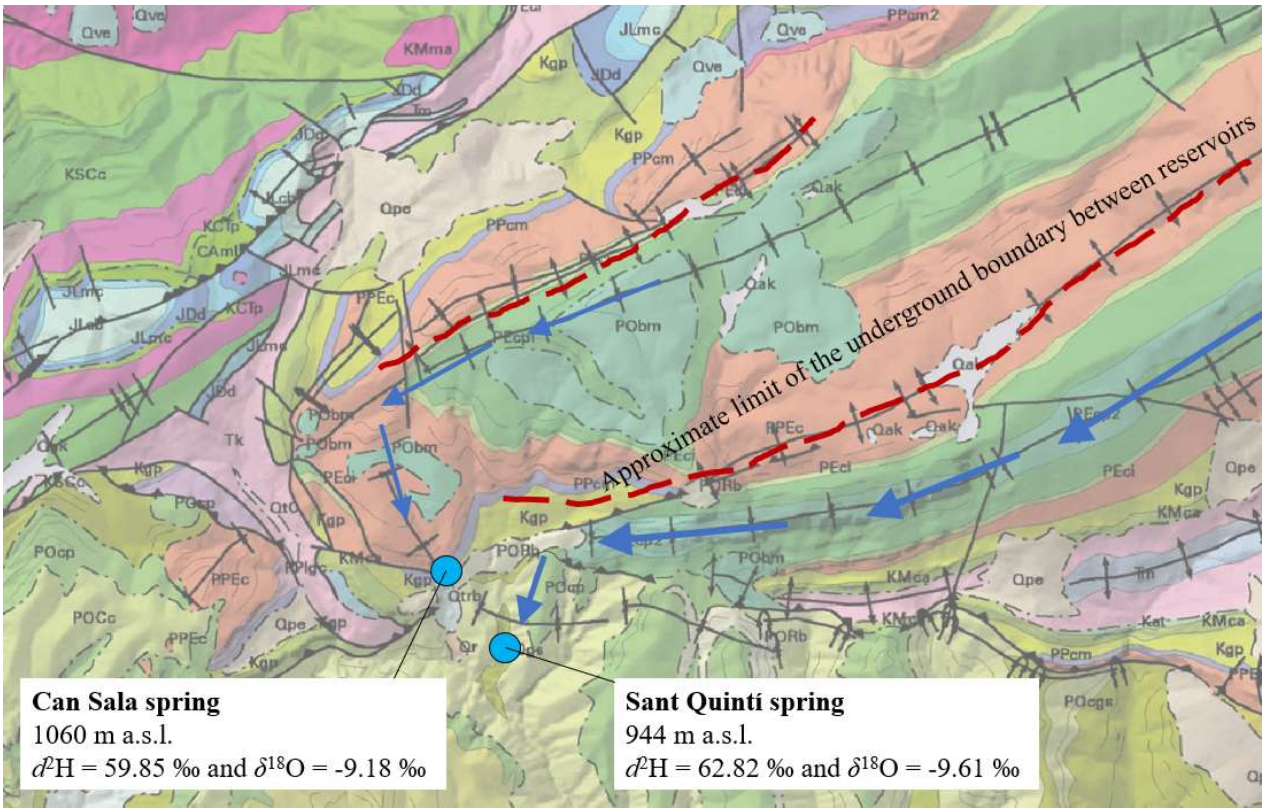

Figure 8. 2. Interpretation of local flowpath between Can Sala spring and Sant Quintí spring. (source: geological map ICGC, 2007)

In summary, it can be concluded that both springs can be assumed that effectively recharge and flow for the most part through the same PPEc geological unit, although from different parts probably hydraulically disconnected, being explained simply by the disposition of the main geological structures already mapped. The Sant Quintí spring collects waters recharged at higher altitudes from the eastern part in a much more karstified area and has longer flowpath, while the

waters of the Cal Sala spring have a shorter path and much less volumetric and regulation capacity. Respect the fault suggested by the authors, this has not been observed in the field. In any case, based on the interpretation of the 3D geological model, it can be argued that it would not be geologically necessary that fault to explain such a disconnection. It is interpreted simply as different parts or reservoirs of the same aquifer, (**Figure 8. 2**), and in which, in the case of the flowpath towards the Sant Quintí source, the reservoir has developed a direct karstic connection with the POrb unit of breccias in contact with the geological thrust front of the Port del Comte mantle and the PPEC unit and then towards then the conglomerates of the POcgs unit located afterwards from which in reality discharges.

8.2 Conclusions

The main general conclusions of the Ph.D. thesis are outlined below:

- This research aimed at improving the hydrogeological knowledge of the Port del Comte Massif (PCM), a Mediterranean mountain karst aquifer system located in the south-eastern sector of the Pyrenees, which plays a strategic role in providing water resources transferred to the both Llobregat and Segre river basins.

- The ‘Port del Comte unit’ is a geological and hydrogeological independent ‘Aquifer System’ in which the main aquifer corresponds to the Lower Eocene - Fissured/karstified aquifer of alveoline limestones and dolostones of the ‘PPEc’ geological unit according to the 1:50,000 geological database of the ICGC (2007). This constitute the main high-mountain karst aquifer (cited simply as ‘HMKA’) of Port del Comte and can be classified as karstic aquifer of strategic pristine waters. The Upper Cretaceous “Garumnian facies” (also called “Garumnian Red Beds of the Pre-Pyrenees”) act as an aquitard and lower boundary of the HMKA. Apart from very minor levels of Quaternary deposits, the overlying upper-Eocene-Oligocene and the underlying Cretaceous and Triassic materials constitute minor local aquifers but they are very important in terms of their potential ability to contribute pollution of natural origin due to the presence of evaporites facies.

- More than 100 springs have been inventoried in the area plus 2 supply water wells in operation that pump water from the HMKA but with a residual extraction rate compared to the whole HMKA capacity. Of the springs 4 correspond to the main discharge points of the system, which in order of importance are: Cardener, Sant Quintí, Aiguaneix and Can Sala. There is also a diffuse groundwater flow to the north towards the La Vansa river basin.

- The hydrologic modeling has allowed estimating aquifer infiltration capacities of the HMKA (i.e., the ratio between the effective recharge of the aquifer, and precipitation at the spring recharge zone) from 28,3% to almost 62% in the highest parts of the massif where the more karstified features are developed. In spring periods, recharge reach almost 46% of total thanks the rainfall and the snowmelt events.

- The implementation of a network of 8 precipitation collectors and the monitoring campaign during 2 complete years made it possible to determine the Local Water Meteoric Water Line (LMWL) of Port del Comte massif, as $\delta^2H = 8{,}05 \cdot \delta^{18}O + 12{,}74$. The Mediterranean as the most important source of precipitation in the PCM..

- The coupled use of distributed rainfall-runoff modelling and lumped parameter models simulating the hydrological system response using exponential piston flow behaviour to an environmental tracer input function that enters and migrates through the aquifer from the recharge zones to the discharge springs allowed to estimate the mean transit times (MTT) of groundwater on the 4 main karst springs with an average of 2.4 years, (2.9 yr for Cardener spring; 1.7 yr for Sant Quintí; 2.6 yr for Aiguaneix; and 2.3 yr for Can Sala).

- The estimation of mean residence time (MRT) and 'dynamic volumes' (V_{Dr}) available in the aquifer during the depletion flow of a karst spring obtained through the classical recession curves analysis provides only partial information for aquifers in which their geometric bottom is convex or can have important stagnant waters inside. In contrast, when data from environmental tracers, such as H and O isotopic composition of water, are used to infer the mean transit time (MTT) and V_{De}, the results are closer to the actual water volume stored in the saturated zone, in short, the actual aquifer volume, including here the aquifer volume located below the discharge level where some flowlines can plunge below the height of the aquifer outlet. This effect can be observed in the results obtained at the

Cardener spring (MRT ~ k = 0.5 yr; MTT = 2.85 yr; V_{Dr} = 5-7 Hm^3; V_{De} = 19 Hm^3). Thanks to 3D geological modeling, it can be verified that the volumetric capacity of the aquifer is actually extended considerably below the discharge level. On the other hand, the MTT estimated by numerical modeling of environmental tracer datasets considering the recharge time series as input is much more robust and provides a better approximation than the MTT estimated using the classical simple sine-wave analytical approach.

- The recession and correlation analysis (chapter 7) did in the available historic Cardener spring's flow time-series, revealed that the system has a moderate to high regulatory function, with moderate to considerable storage capacity providing stable flow (with minimum of 0.01 m^3/s during the dry season and up to 4 m^3/s during the wet season), with an average of 0.3 m^3/s (annual discharge is 9.5 Hm^3/yr as the average for the 1985-2010 period; equivalent to the 9.34 Hm^3/yr reported in IGME (1985), based on 6 gauging for one year. It presents high inertia with memory effect (49 days) and provided a mean value of the infiltration "i" function of 0.63 (period May 1985 to August 2010), and 0.50 (period September 2000 to August 2010), and also a regulation "k" parameter of 0.63 and 0.57 respectively which reveals the large storage capacity of the saturated zone of the karst aquifer, suggesting the springs is in the domain of "complex karst systems" similar to the behaviour for instance of Font Aigüeira (Vielha valley System, NO Catalonia) and Fonts Llobregat, Fonts Bor (Alt Llobregat and Alt Segre System, N, Catalonia). Taking the classification system based on the parameters ME, T_{reg} and Fc obtained from the correlogram analysis, Cardener spring it is more similar than Fontestorbes springs of Mangin's classification equivalent to moderately karstified system with imperfect drainage.

- The novel management-oriented KGWRAI-V and RC-V classification systems (Chapter 7) developed within the CHAKAWP5-GeoERA RESOURCE project -applied in the pilot demonstration case of Port del Comte- show that the Cardener and Sant Quintí springs (the latter with lower reliability) can be classified as 'medium to high vulnerability springs' and 'moderate regulatory capacity'

- According to the simulated RCP4.5 and RCP8.5 climate change scenarios (in Cardener spring) (Chapter 6), a net decrease in the average annual spring flow is expected for the

third period 2071-2100, of 0.6 and 0.4 hm^3/yr respectively, increase in temperature, with its average variation compared to the reference period (1986-2015) for the last interval (2071-2100) of up to 1.9 and 3.1º C, and on average between the two emissions scenarios considered, the mantle could shrink by almost 50%, while in the middle of the 21st century, and in the worst of the scenarios of climate change, could reach 76% respectively. Therefore, the climate crisis will lead to a decrease in the storage of this resource in winter. There will be a decrease in the thickness and duration of the snow cover, which will represent a problem for the alpine ski resort of Port del Comte, which will have to adapt to keep the resort operational and ensure the sustainability of its activity.

- In general, from the hydrogeochemical point of view (Chapters 4 and 6), the groundwater is dominantly of the calcium bicarbonate and calcium–magnesium bicarbonate type, suggesting a dominant calcite dissolution process in agreement with the lithology associated with the Eocene carbonate materials conforming the main aquifer of PCM.

- The main source of sulfate in GW is the dissolution of geogenic origin from gypsum dissolution from the Eocene-Oligocene Beuda Formation and Triassic evaporites. Some influence of sulfate from sulfide mineral or coal organic sulfur weathering also has been pointed out. From the anthropogenic point of view, sulfate from fertilizers seems to play a role in some places around the ski resort.

- Dissolved NO_3 in groundwater mainly comes from mineral fertilizers, soil organic nitrogen and pig manure application to the fields, with at most minor contributions from sewage. Like the other high mountain karst systems, the PCM is very vulnerable to pollution. Here, nitrates from agricultural practices represent the main threat to the pristine waters of the aquifer system despite its low significance. Fortunately, the dissolved nitrate concentration in GW is generally low.

- The multidisciplinary approach (the 4 pillars suggested in Chapter 1, part 1.1.5) has allowed developing a hydrogeological conceptual model of aquifer system functioning, which is coherent with the available information from previous studies, but which is also consistent with the processes driving the hydrogeochemical and isotopic fingerprint of groundwater in this aquifer system.

8.3 Outlook

According to the conclusions, the lines of study that are considered important to be able to develop in future research are listed below:

The alpine carbonated karstic aquifers (and specifically in the Pyrenees) are very complex and vulnerable hydrological that are highly strategic. In the context of climate change, it is necessary to improve the knowledge of its hydrogeological functioning at a local scale to model and predict the possible impacts on its resources. The existing knowledge particularized by aquifers is scarce and is limited, in Catalonia, to the Freixes Ph.D. thesis (2014) and to the result of the current research in Port del Comte, beyond the more regional studies of the 80's.

A necessary line of research should be precisely to replicate the methodology proposed in this thesis in the rest of the strategic karst aquifers of the Pyrenees, starting with the 3D geological modeling of all of them to estimate their volumetric capacities for then modeling the hydrologic response and simulate CC scenarios.

Without this, all the water balances at a global level that usually appear in technical reports from the administration, and the estimates of the impact of CC at a regional scale that are made, are precisely that, global estimates at a regional scale based on results without greater precision.

8.4 References

Botsyun, S. and Ehlers, T.A. (2021). How Can Climate Models Be Used in Paleoelevation Reconstructions?. Front. Earth Sci. 9:624542. doi: 10.3389/feart.2021.624542

Bühler, J. C., Roesch, C., Kirschner, M., Sime, L., Holloway, M. D., and Rehfeld, K.: Comparison of the oxygen isotope signatures in speleothem records and iHadCM3 model simulations for the last millennium, Climate of the Past, 17, 985–1004, 2021a.

Bühler, J. C., Axelsson, J. M., Lechleitner, F. A., Fohlmeister, J., LeGrande, A. N., Midhun, M.,

Sjolte, J., Werner, M., Yoshimura, K., and Rehfeld, K.: Investigating oxygen and carbon isotopic relationships in speleothem records over the last millennium using multiple isotope-enabled climate models, Clim. Past Discuss. [preprint], https://doi.org/10.5194/cp-2021-152, in review, 2021b.

Dubois, E., Doummar, J., Pistre, S., and Larocque, M. (2020): Calibration of a lumped karst system model and application to the Qachqouch karst spring (Lebanon) under climate change conditions, Hydrol. Earth Syst. Sci., 24, 4275–4290, https://doi.org/10.5194/hess-24-4275-2020.

ICGC (2007). Mapa geològic comarcal de Catalunya 1:50 000. Full Alt Urgell (BDGC50M). http://www.icgc.cat/ca/Administracio-i-empresa/Descarregues/Cartografia-geologica-i-geotematica/Cartografia-geologica/Mapa-geologic-comarcal-de-Catalunya-1-50.000/Mapa-geologic-comarcal-de-Catalunya-1-50.000

INSPIRE Thematic Working Group Geology. (2013). D2.8.II.4 INSPIRE Data Specification on Geology – Technical Guidelines. Directive 2007/2/EC of the European Parliament and of the Council of 14 March 2007 establishing an Infrastructure for Spatial Information in the European Community (INSPIRE)

OPCC-CTP (2018). El canvi climàtic als Pirineus: impactes, vulnerabilitats i adaptació. 150pp ISBN: 978-84-09-06268-3

9 SUPPLEMENTARY MATERIAL. APPENDIXES OF DATA

9.1 CHAPTER 2- FIELD WORK

Table 9.1.1. dip/azimuth measures collected on the field. Geological fieldworfk

ID	X	Y	Z (m. a.s.l.)	Azimuth/dip	Polarity	Date	Unit	Lithology
1	380053	4665336	1355	101/05	Normal	Jul-13	POcgs	Conglomerates
2	379869	4665736	1430	210/20	Normal	Jul-13	POcgs	Conglomerates, sandstones and clays
3	379193	4666113	1464	123/73	Normal	Jul-13	POcgs	Vertical conglomerates
4	379195	4666120	1464	139/80	Normal	Jul-13	POcgs	Vertical conglomerates
5	380168	4665637	1485	278/10	Normal	Jul-13	POmlg	Conglomerates
6	380101	4665653	1475	245/37	Normal	Jul-13	POmlg	Conglomerates
7	380098	4665704	1475	211/48	Normal	Jul-13	POmlg	Conglomerates
8	380110	4665741	1472	222/62	Normal	Jul-13	POmlg	Conglomerates
9	378919	4666406	1578	348/74	Normal	Jul-13	PEalb	Bioturbated gray and brown sandstones with cross-stratification
10	379596	4666567	1531	061/24	Normal	Jul-13	KSCat	Alternation of sandstones and marls
11	379740	4666634	1542	349/52	Normal	Jul-13	KCMca	Bioturbated gray sandstones
12	379732	4666745	1644	334/47	Normal	Jul-13	KMgp	Gray limestones (Garumnian)
13	379535	4666787	1671	017/53	Normal	Jul-13	KMgp	Gray limestones (Garumnian)
14	383192	4666823	981	111/76	Invertit	Jul-13	PEm1	Turbidite sandstone
15	377758	4671091	2323	110/49	Normal	Jul-13	PEcp2	Limestones with alveolins
16	377692	4670994	2315	107/52	Normal	Jul-13	PEcp2	Limestone bar with nummulites and asilines
17	378594	4672710	2144	187/37	Normal	Jul-13	PPEc	Ocher-colored limestones and dolomites with flint nodules
18	378143	4674445	1944	019/51	Normal	Jul-13	TJcd	Gray micritic limestones and dolomites, often brecciated and laminated
19	378727	4674349	1942	240/79	Normal	Jul-13	PEcp2	Ocher-colored limestones and dolomites with flint nodules
20	378798	4674310	1935	233/88	Normal	Jul-13	PEcp2	Ocher-colored limestones and dolomites with flint nodules
21	380991	4670390	1667	003/15	Normal	Jul-13	PEcp2	Ocher limestones with alveolins and others
22	381390	4672514	1488	153/35	Normal	Jul-13	PEcp1	Ocher micritic limestones with some alveolins
23	380155	4674054	1704	061/40	Normal	Jul-13	JLcm	Ocher marls and limestones
24	380193	4674050	1703	108/70	Normal	Jul-13	JLcm	Ocher marls and limestones
25	380132	4674114	1701	014/29	Normal	Jul-13	PEcp2	Sandstones and calcarenites of bluish gray color, with nummulites and asilines and marls

ID	X	Y	Z (m. a.s.l.)	Azimuth/dip	Polarity	Date	Unit	Lithology
26	379531	4674358	1771	006/09	Normal	Jul-13	PEcp2	Sandstones and calcarenites of bluish gray color, with nummulites and asilines and marls
27	378871	4669119	2048	069/22	Normal	Jul-13	PEcp1	Ocher-colored limestones and dolomites with some fossils
28	378595	4668678	2062	338/17	Normal	Jul-13	PEcp1	Ocher-colored limestones and dolomites with some fossils
29	378298	4668596	2073	122/20	Normal	Jul-13	PEcp1	Ocher-colored limestones and dolomites with alveolins and flint nodules
30	381681	4668813	1847	269/45	Normal	Jul-13	PPEc	Bioclastic ocher limestones with alveolins
31	381565	4667871	1717	349/52	Normal	Jul-13	PPcm	Dark gray brecciated marly limestones
32	381776	4668250	1826	273/78	Normal	Jul-13	PPcm	Dark gray brecciated marly limestones
33	382592	4666321	1017	204/66	Normal	Jul-13	PEm1	Alternation of gray-ocher sandstones and shales
34	380899	4666738	1341	301/62	Normal	Jul-13	PEcgm1	Sandstones, conglomerates and red shales
35	382231	4671892	1145	345/65	Normal	Jul-13	PEOcmg	Monogenic conglomerates, with red matrix
36	373325	4665578	1228	061/57	Invertit	Jul-13	KMgp	Limestones near the thrust sheet overhang front
37	373239	4665563	1219	046/33	Invertit	Jul-13	PPcm	Micritic dark gray to ocher limestones (Garumnian)
38	374826	4666440	1413	000/00	Horitzontal	Jul-13	Tk	Gypsum and gray shales (Keuper)
39	376156	4666854	1760	092/20	Normal	Jul-13	KMgp	Gray wackestones with fossils
40	376020	4666585	1718	271/24	Normal	Jul-13	KCMca	Ocher gray calcarenites
41	374807	4666925	1437	317/66	Normal	Jul-13	Tm	Tabulated limestones alternating with light beige marls (Muschelkalk)
42	367915	4667815	1502	208/12	Normal	Jul-13	PEcp1	Limestones with alveolins
43	372652	4666520	1380	006/38	Normal	Jul-13	KMgp	Micritic and nodular ocher limestones and red and gray shales (Garumnian)
44	366203	4667602	1238	228/42	Normal	Jul-13	JDd	Dolomites and karstified ocher and gray limestones
45	367792	4666270	1078	064/44	Normal	Jul-13	PPEc	Eocene limestones - left flank of the syncline of the Can Sala karst spring
46	367957	4666295	1072	339/56	Normal	Jul-13	PPcm	Eocene limestones - right flank of the syncline of the Can Sala karst spring
47	376627	4667470	1919	014/15	Normal	Oct-13	PPcm	Gray micritic limestones (Garumnian)
48	377391	4667729	1970	040/25	Normal	Oct-13	PPEc	Limestones with alveolins
49	375148	4665773	1836	166/35	Normal	Oct-13	PPEc	Limestones with alveolins
50	375581	4665301	1836	341/26	Normal	Oct-13	PPEc	Limestones with alveolins

ID	X	Y	Z (m. a.s.l.)	Azimuth/dip	Polarity	Date	Unit	Lithology
51	375524	4666698	1580	322/60	Normal	Oct-13	Tk	Coarse ocher sandstones - very coarse
52	375176	4666158	1617	157/31	Normal	Oct-13	KMgp	Gray massive limestones
53	374058	4666536	1219	193/31	Normal	Oct-13	Tm	Tabulated gray limestones
54	376428	4664943	1311	255/05	Normal	Oct-13	POmlg	Alternation of red-grained lutites and fine-grained sandstones
55	381444	4667597	1599	074/22	Normal	Oct-13	PPEc	Gray limestones
56	382395	4667063	1204	272/41	Normal	Oct-13	PEcgm1	Alternation of fine sandstones with reddish-brown shales
57	381482	4666279	1140	347/36	Normal	Oct-13	PEm1	Gray-blue nodular bioclastic sandstones
58	382977	4671165	1046	114/39	Normal	Oct-13	PEcgc2	Micritic gray limestones
59	382433	4670930	1147	006/37	Normal	Oct-13	PPEc	Limestones with alveolins (possible displaced block)
60	382213	4670914	1263	206/30	Normal	Oct-13	PPEc	Limestones with alveolins
61	381410	4670242	1683	145/23	Normal	Oct-13	PEcp2	Sandstones with carbonates
62	379731	4670751	1936	124/26	Normal	Oct-13	PEcp1	Bioclastic sandstones
63	380765	4669894	1757	325/21	Normal	Oct-13	PECp1	Limestones with bioclastic sandstones
64	380402	4669962	1769	153/21	Normal	Oct-13	PECp1	Limestones with asilines
65	377827	4673675	2013	006/16	Normal	Oct-13	PEcp2	Limestones, sandstones and conglomerates
66	378352	4672918	2178	318/36	Normal	Oct-13	PEcp1	Bioclastic limestones
67	376894	4674646	1511	088/40	Normal	Oct-13	PEcp2	Gray limestones
68	375768	4675452	1048	344/30	Normal	Oct-13	TJcd	Limestones
69	375761	4675432	1052	253/27	Normal	Oct-13	TJcd	Limestones
70	376250	4675079	1171	318/37	Normal	Oct-13	KSCat	Alternation of red sandstones and shales
71	375097	4664819	1539	270/17	Normal	Aug-14	KMgp	Bluish micritic limestones
72	375341	4664270	1331	271/15	Normal	Aug-14	POmlg	Limestone and shale
73	374073	4666490	1224	215/17	Normal	Aug-14	Tm	Limestones, dolomites with marl intercalations
74	373991	4666412	1228	183/39	Normal	Aug-14	Tm	Limestones, dolomites with marl intercalations
75	374451	4667281	1333	194/19	Normal	Aug-14	KMgp	Limestones
76	374674	4666180	1506	143/52	Normal	Aug-14	KCMca	Limestone (outcrop on the front part of the thrust. Subvertical layers)
77	374694	4666147	1539	193/63	Normal	Aug-14	KMgp	Limestones and marl-limestones (outcrop on the front part of the thrust. Subvertical layers)
78	372616	4666491	1377	357/50	Normal	Aug-14	KMgp	Limestones
79	375063	4665645	1816	199/51	Normal	Aug-14	PPEc	Limestones with alveolins
80	376648	4667476	1919	034/20	Normal	Aug-14	PPcm	Maastrichtian blue micritic limestones
81	376509	4667557	1911	322/21	Normal	Aug-14	PPcm	Maastrichtian blue micritic limestones

ID	X	Y	Z (m. a.s.l.)	Azimuth/dip	Polarity	Date	Unit	Lithology
82	376025	4666689	1732	234/27	Normal	Aug-14	KMgp	Gray wackestones with fossils
83	379065	4671950	2280	293/44	Normal	Aug-14	PEcp1	Pink micritic limestones. Penya Terrades Formation
84	370167	4670527	1223	261/57	Normal	Aug-15	KMgp	Limestones within the Garumnian. Maastrichtian
85	370834	4670378	1200	334/32	Normal	Aug-15	PPcm	Garumnian limestones
86	368746	4669959	1080	319/56	Normal	Aug-15	KMgp	bioclastic limestones. Garumnian - Maastrichtian
87	367273	4667621	1371	100/38	Normal	Aug-15	PPcm	micritic limestones
88	367727	4667711	1433	099/09	Normal	Aug-15	PEcp1	Limestones with alveolins
89	367146	4668194	1283	321/45	Normal	Aug-15	PPcm	Limestones
90	371530	4669633	1513	199/38	Normal	Aug-15	PEcp1	Limestones with nummulites and asilines
91	371718	4668791	1721	344/48	Normal	Aug-15	PEcp1	Limestones with nummulites and asilines
92	372233	4668508	1765	331/26	Normal	Aug-15	PPEc	bioclastic limestones
93	372211	4667215	1798	325/14	Normal	Aug-15	PEcp1	micritic limestones
94	372867	4667174	1714	304/46	Normal	Aug-15	PEcp1	bioclastic limestones -nummulites and asylines-
95	373228	4667117	1566	327/48	Normal	Aug-15	PPEc	limestones with alveolins
96	366646	4668157	1260	205/54	Normal	Nov-17	KSCc	Nodular limestones and marly limestones
97	367256	4667641	1371	115/33	Normal	Nov-17	PPcm	limestones. Garumnian
98	367740	4667700	1438	65/04	Normal	Nov-17	PEcp1	Limestones with alveolins
99	367894	4667945	1531	351/25	Normal	Nov-17	PEci	Green sandstones and marls
100	368149	4668195	1590	322/45	Normal	Nov-17	PPEc	Micritic limestones
101	372627	4668722	1758	358/19	Normal	Nov-17	PPEc	Limestones with alveolins
102	372764	4668888	1745	313/21	Normal	Nov-17	PPEc	Limestones with alveolins
103	373139	4669401	1825	313/42	Normal	Nov-17	PPEc	Limestones with alveolins
104	369405	4668585	1687	116/45	Normal	Nov-17	PEcp1	Micritic limestones
105	377946	4673671	2004	311/12	Normal	Nov-17	PEcp2	Micritic limestones
106	376846	4673197	1965	341/25	Normal	Nov-17	PEcp2	Micritic limestones
107	376757	4673065	1954	330/41	Normal	Nov-17	PEcp2	Micritic limestones
108	379799	4674558	1614	356/16	Normal	Nov-17	PEcp2	Micritic limestones

Table 9.1.2. Results of δ18O and δ2H stable isotope analysis in the 70 samples collected from precipitation in the 9 installed rain gauges from December 2013 to December 2015

ID pluviometer	Sample and period	Year	δ18O ‰	δ2H ‰
P-01	Sample Winter 13-13	2013-2013	-12,16	-88,7
P-01	Sample Winter 13-14	2013-2014	-8,23	-44,6
P-01	Sample Spring 14	2014	-7,07	-44,3

ID pluviometer	Sample and period	Year	δ18O ‰	δ2H ‰
P-01	Sample Summer 14	2014	-6,91	-43,2
P-01	Sample Autumn 14	2014	-12,01	-78,0
P-01	Sample Winter 15-15	2014-2015	-	
P-01	Sample Spring 15	2015	-6,44	-38,8
P-01	Sample Summer 15	2015	-6,82	-40,8
P-01	Sample Autumn 15	2015	-10,11	-63,2
P-02	Sample Winter 13-13	2013-2013	-11,76	-84,7
P-02	Sample Winter 13-14	2013-2014	-8,27	-47,4
P-02	Sample Spring 14	2014	-7,31	-46,0
P-02	Sample Summer 14	2014	-7,03	-45,4
P-02	Sample Autumn 14	2014	-11,59	-75,9
P-02	Sample Winter 15-15	2014-2015	-11,91	-83,1
P-02	Sample Spring 15	2015	-7,48	-44,6
P-02	Sample Summer 15	2015	-7,46	-44,3
P-02	Sample Autumn 15	2015	-9,63	-59,5
P-02	Sample Winter 13-13	2013-2013	-11,45	-82,7
P-03	Sample Winter 13-14	2013-2014	-8,87	-57,9
P-03	Sample Spring 14	2014	-7,08	-42,8
P-03	Sample Summer 14	2014	-6,69	-41,2
P-03	Sample Autumn 14	2014	-11,45	-74,3
P-03	Sample Winter 15-15	2014-2015	-13,55	-99,2
P-03	Sample Spring 15	2015	-7,62	-46,4
P-03	Sample Summer 15	2015	-6,68	-38,9
P-03	Sample Autumn 15	2015	-8,96	-55,3
P-04	Sample Winter 13-13	2013-2013	-10,75	-79,3
P-04	Sample Winter 13-14	2013-2014	-7,39	-43,6
P-04	Sample Spring 14	2014	-7,06	-41,1
P-04	Sample Summer 14	2014	-6,40	-39,4
P-04	Sample Autumn 14	2014	-12,05	-80,8
P-04	Sample Winter 15-15	2014-2015	-12,19	-89,7
P-04	Sample Spring 15	2015	-7,29	-44,2
P-04	Sample Summer 15	2015	-6,48	-39,9
P-04	Sample Autumn 15	2015	-8,90	-54,2
P-05	Sample Winter 13-13	2013-2013	-11,19	-75,7
P-05	Sample Winter 13-14	2013-2014	-8,23	-53,9
P-05	Sample Spring 14	2014	-6,94	-42,9
P-05	Sample Summer 14	2014	-6,73	-42,6

ID pluviometer	Sample and period	Year	δ18O ‰	δ2H ‰
P-05	Sample Autumn 14	2014	-11,92	-82,0
P-05	Sample Winter 15-15	2014-2015	-11,50	-81,2
P-05	Sample Spring 15	2015	-7,31	-45,6
P-05	Sample Summer 15	2015	-6,10	-36,5
P-05	Sample Autumn 15	2015	-9,52	-57,6
P-06	Sample Winter 13-13	2013-2013	-10,37	-70,9
P-06	Sample Winter 13-14	2013-2014	-5,96	-37,2
P-06	Sample Spring 14	2014	-6,63	-42,0
P-06	Sample Summer 14	2014	-3,48	-23,3
P-06	Sample Autumn 14	2014	-10,94	-76,6
P-06	Sample Winter 15-15	2014-2015	-10,49	-81,3
P-06	Sample Spring 15	2015	-6,66	-40,9
P-06	Sample Summer 15	2015	-5,84	-34,4
P-06	Sample Autumn 15	2015	-8,56	-54,2
P-07	Sample Winter 13-13	2013-2013	-10,48	-73,6
P-07	Sample Winter 13-14	2013-2014	-5,10	-31,5
P-07	Sample Spring 14	2014	-5,56	-34,5
P-07	Sample Summer 14	2014	-5,57	-34,9
P-07	Sample Autumn 14	2014	-10,16	-68,9
P-07	Sample Winter 15-15	2014-2015	-9,01	-65,3
P-07	Sample Spring 15	2015	-7,05	-44,6
P-07	Sample Summer 15	2015	-5,64	-33,3
P-07	Sample Autumn 15	2015	-8,34	-51,8
P-08	Sample Winter 13-13	2013-2013	-9,67	-67,4
P-08	Sample Winter 13-14	2013-2014	-7,48	-49,2
P-08	Sample Spring 14	2014	-5,38	-35,4
P-08	Sample Summer 14	2014	-5,63	-37,4
P-08	Sample Autumn 14	2014	-10,55	-72,8
P-08	Sample Winter 15-15	2014-2015	-10,78	-80,7
P-08	Sample Spring 15	2015	-6,04	-37,0
P-08	Sample Summer 15	2015	-5,54	-33,6
P-08	Sample Autumn 15	2015	-7,26	-45,3
		Max	-3,48	-23,28
		Min	-13,55	-99,23

Table 9.1.3. ID coordinates and name of water point samples used in the thesis (M-XX) and rest of inventoried on the field. (*) Number associated with the initial inventory

N (*)	Name	ID	Sampling type	Type	X (UTM)	Y (UTM)	Z m a.s.l.	Date of visit	Q (L/s)	pH	T (ºC)	EC (uS/cm)
1	Font de la Mata_Puigarnau-Canalda	-		Spring	378501	4665328	1272	Jun-13	0,15	-	-	-
2	Font del Teixo	-		Spring	379721	4665286	1306	Jul-13	0,07	6,6	17,4	768
3	Font Fenerals	-		Spring	380094	4665332	1357	Jul-13	0,13	8,0	12,0	472
4	Font Coll de Jou	M-04	monthly	Spring	379240	4666210	1464	Jul-13	0,19	7,3	11,9	474
5	Font del Codó	-		Spring	380125	4665644	1472	Jul-13	0,04	7,8	19,0	404
6	Font de les Costes	M-03	biannually	Spring	379036	4666490	1582	Jul-13	0,14	-	13,1	309
7	Font de la Garganta	M-06	biannually	Spring	379567	4666793	1657	Jul-13	0,11	7,3	6,2	263
8	Font dels Llebadors	M-36	biannually	Spring	383136	4667247	1005	Jul-13	0,29	7,6	11,4	632
9	Pou de Cal Terrerol	-		Dug well	382016	4672640	1315	Jul-13	0,57	7,6	12,7	643
10	Font Estivella	M-14	biannually	Spring	380025	4672470	2053	Jul-13	0,11	7,9	5,6	382
11	Font del Duc	-		Spring	378609	4671522	2270	Jul-13	0,01	7,9	8,1	411
12	Font Arderic	M-15	biannually	Spring	378598	4672595	2158	Jul-13	0,07	7,7	6,2	231
13	Font del Casalí	M-16	biannually	Spring	375770	4671930	2077	Jul-13	0,003	8,0	9,6	461
14	Font del Diumenge	M-17	biannually	Spring	376589	4672378	1989	Jul-13	0,01	7,9	6,7	352
15	Font barraca Sangonella	M-18	biannually	Spring	376761	4672902	1940	Jul-13	0,03	8,2	9,4	411
16	Font del Refugi de l'Arp	M-19	biannually	Spring	378133	4674452	1944	Jul-13	0,13	8,1	7,3	416
17	Font carretera Refugi Arp	M-20	monthly	Spring	378679	4674828	1858	Jul-13	0,62	8,0	6,7	607
18	Font Ginebret - despla. crta-	M-42	biannually	Spring	380725	4673866	1601	Jul-13	0,02	7,3	10,4	690
19	Font riera de l'Arp	-		Spring	378550	4674373	1937	Jul-13	not measurable	7,7	6,1	364
20	Font Esquerrana	M-23	biannually	Spring	382933	4671032	1017	Jul-13	0,44	8,2	9,2	344
21	Font pla de Bacies	-		Spring	378313	4668477	2035	Jul-13	not measurable	7,7	10,2	320
22	Font de la Rata	-		Spring	381620	4668869	1857	Jul-13	lost	-	-	-
23	Font de Querol	-		Spring	381751	4668060	1789	Jul-13	lost	-	-	-
24	Font del Ginebró	M-05	biannually	Spring	381469	4667947	1730	Jul-13	not measurable	8,3	12,2	237
25	Font Cap Rec	M-01	biannually	Spring	382506	4665923	970	Jul-13	1,75	7,5	12,4	598
26	Font Casserra	-		Spring	382421	4666371	1078	Jul-13	0,05	7,3	13,7	475
27	Font Aberades	-	-	Spring	380878	4666901	1392	Jul-13	not measurable	7,5	19,8	331
28	Font de la Canaleta - de la rasa-	M-02	biannually	Spring	382560	4667585	1220	Jul-13	0,13	7,9	11,2	547
29	Font la Puda	M-40	biannually	Spring	384119	4668266	867	Jul-13	4,00	7,3	12,7	1312
30	Pou Joan Batlle	-		Dug well	381965	4672440	1268	Jul-13	not measurable	7,6	17,4	670
31	Pou Cal Bep	-		Dug well	381918	4672242	1295	Jul-13	not measurable	-	-	-
32	Font Ca l'Arreplegant	M-35	biannually	Spring	381614	4672438	1330	Jul-13	-	7,9	17,1	261
33	Pou Cal Tet	-		Dug well	382387	4672291	1297	Jul-13	not measurable	7,6	14,8	307

34	Font Cal Cameta	-		Spring	382231	4671664	1116	Jul-13	-	7,5	12,2	613
35	Font dels Pasqüests	M-21	biannually	Spring	383652	4668648	970	Jul-13	1,00	7,5	16,5	647
36	Font de Sant Joan dels Regats	M-39	biannually	Spring	378140	4665788	1078	Jul-13	0,60	7,7	12,4	497
37	Font Borda	M-32	biannually	Spring	375089	4664373	1392	Jul-13	0,25	-	12,5	490
38	Font del Vermell	M-12	biannually	Spring	373469	4665658	867	Jul-13	0,41	7,8	11,2	255
39	Font Torelló	M-11	biannually	Spring	373773	4666536	1268	Jul-13	0,73	7,8	11,1	309
40	Font dels Regats	M-09	biannually	Spring	374823	4666442	1330	Jul-13	1,50	8,0	10,5	1178
41	Riera de Cal Ton Riu	-		Spring	382216	4671776	1116	Jul-13	0,33	-	11,3	703
42	Fonts torrent Cal Tafaret	-		Spring	375215	4666846	1525	Jul-13	0,25	-	10,3	464
43	Font del Beralet	-		Spring	375524	4666649	1567	Jul-13	lost	-	-	-
44	Font dels Prats	-		Spring	376110	4666907	1745	Jul-13	dry	-	-	-
45	Font Margarida	-		Spring	375970	4667048	1757	Jul-13	0,032	7,8	11,4	302
46	Font Orris	-		Spring	375883	4667468	1722	Jul-13	lost	-	-	-
47	Font Mosquera	M-29	biannually	Spring	366802	4665999	1050	Jul-13	0,63	7,7	10,7	468
48	Font salada de Cambrils	M-30	biannually	Spring	367061	4665923	1023	Jul-13	0,072	7,2	19,0	244000
49	Font del Pi	-		Spring	366688	4666088	1135	Jul-13	0,024	7,9	12,1	895
50	Font del Prat de Cordes	-		Spring	367909	4667858	1464	Jul-13	not measurable	8,5	18,7	985
51	Estany font del Borrisol	-	-	Spring	370423	4668253	1619	Jul-13	lost	-	-	-
52	Font del Pouet	-		Spring	371132	4667288	1705	Jul-13	lost	-	-	-
53	Font del Port	-		Spring	374710	4669234	2018	Jul-13	lost	-	-	-
54	Font toll Roca d'Esquers	-		Spring	372676	4666507	1410	Jul-13	stagnant	8,1	11,4	1912
55	Font rasa lateral riu Oden	-		Spring	375621	4667947	1547	Jul-13	0,17	-	9,0	372
56	Font Orris 01	-		Spring	376699	4669192	1882	Jul-13	0,025	8,6	18,8	212
57	Font Orris 02	M-08	biannually	Spring	376608	4668898	1871	Jul-13	0,23	8,0	6,3	420
58	Font Berauda	-		Spring	376358	4668364	1806	Jul-13	dry	-	-	-
59	Font de Cal Obac	-		Spring	366159	4667582	1247	Jul-13	-	7,3	12,7	986
60	Font de la Gorga de ca l'Agustí	M-28	biannually	Spring	366332	4667093	1119	Jul-13	4,00	8,1	12,0	1722
61	Font Querol - dalt-	-		Spring	367343	4668582	1197	Jul-13	1,00	8,0	9,2	307
62	Font Querol - baix-	M-27	biannually	Spring	367129	4668391	1156	Jul-13	0,35	7,5	9,3	461
63	Font Petera	-		Spring	367818	4669038	1247	Jul-13	0,005	8,2	17,9	390
64	Font de la Sort	-		Spring	369656	4670497	990	Jul-13	0,05	8,2	17,3	337
65	Font de San Joan	M-07	biannually	Spring	378675	4666199	1478	Jul-13	-	7,5	13,7	456
66	Font de Les Preses	-		Spring	378577	4665758	1357	Jul-13	-	7,5	11,8	944
67	Font Aiguaneix - Font Val-Longa	M-25	monthly	Spring	370529	4670411	1098	Jul-13	47,80	8,2	8,2	337
68	Font dels Acens	M-24	biannually	Spring	372940	4671484	1550	Jul-13	0,30	7,7	9,1	416
69	Font Jordanera	-		Spring	374353	4671968	1740	Jul-13	dry	-	-	-
70	Font Negre sobreixidor Alzina	-		Spring	371676	4672173	1431	Jul-13	not measurable	7,9	14,2	424
71	Font del Jardi - de les Mates-	M-26	biannually	Spring	369800	4670173	1091	Jul-13	3,07	8,4	10,1	311
72	Pou Cambrils	-		Well	368414	4666525	1099	Jul-13	not measurable	8,4	14,8	517

73	Pou Llinars	-		Well	366028	4667660	1284	Jul-13	not measurable	7,1	12,8	743
74	Font de l'Alzinera - desviada- cámping	-		Spring	366742	4666498	1064	Jul-13	2,23	8,2	12,0	914
75	Font 1 Roc Falcon SL	-	-	Spring	375552	4664801	1439	Jul-13	no accessible	-	-	-
76	Font dels Corralets	-		Spring	375929	4665174	1563	Jul-13	lost	-	-	-
77	Font - est- de Canalda	-	-	Spring	376737	4666480	1530	Jul-13	1,00	7,8	8,7	342
78	Pou sondeig 01 Port del Comte	-		Well	382307	4670338	1348	Jul-13	not measurable	8,1	11,2	298
79	Font La Part	M-37	biannually	Spring	382356	4670365	1315	Jul-13	1,14	8,2	10,2	278
80	Pou sondeig 02 Port del Comte	-		Borehole	382123	4670645	1325	Jul-13	sealed	-	-	-
81	Pou sondeig Ca l'Andal	-		Borehole	382398	4670192	1375	Jul-13	sealed	-	-	-
82	Pou sondeig Rasa de la bòfia	-		Borehole	379732	4669850	1832	Jul-13	dry	-	-	-
83	Font de Padrinás	-		Spring	375888	4674736	1105	Jul-13	lost	-	-	-
84	Font tres fonts	-		Spring	374644	4674517	1246	Jul-13	not measurable	8,2	13,9	657
85	Font captació Ossera	M-33	biannually	Spring	374151	4673445	1369	Jul-13	0,23	-	9,0	923
86	Font Freda - riu Fred	-		Spring	375660	4675651	1003	Jul-13	0,02	8,4	9,8	385
87	Font Tirapeus	M-34	biannually	Spring	378084	4675841	1511	Jul-13	0,02	7,8	9,6	357
88	Font El salí La Coma - surgència secundaria-	-		Spring	383359	4670473	993	Jul-13	1,60	8,2	13,3	51010
89	Font El salí La Coma - surgència principal-	M-41	biannually	Spring	383325	4670462	992	Jul-13	1,00	8,2	12,5	8528
90	Fonts del Cardener	M-22	monthly	Spring	382697	4670971	1032	Aug-13	146,00	8,3	7,6	255
91	Font Can Sala	M-31	monthly	Spring	367887	4666301	1063	Aug-13	23,00	8,0	8,5	367
92	Font Sant Quintí	M-43	monthly	Spring	368347	4666032	944	Aug-13	153,00	8,0	9,1	291
93	Font Ramonet	M-10	biannually	Spring	375027	4667246	1456	Sep-13	-	-	-	0
94	Font del Torrentó	M-13	biannually	Spring	372744	4666173	1205	Sep-13	0,04	7,8	11,9	668
95	Font de Pellerols	M-38	biannually	Spring	377276	4666261	1402	Oct-13	0,15	7,7	9,3	492
96	Sondeig inv. Cinglera Urbanitzacó| JAC 1987	-		Borehole	381896	4669881	1636	dry	-	-	-	-
97	Sondeig inv. Aj.Cambrils (2n) 1990	-		Borehole	366621	4665770	1148	lost	-	-	-	-
98	Sondeig inv. Aj.Cambrils (1r) 1990	-		Borehole	366571	4665913	1158	lost	-	-	-	-
99	Sondeig inv. Cal Sala TEYGE GGCC 1992	-		Borehole	366665	4665914	1141	lost	-	-	-	-
100	Sondeig inv. Cambrils IV (2n) TEYGE-GGCC 1992	-		Borehole	366629	4665774	1145	lost	-	-	-	-

9.2 CHAPTER 3- PAPER 1.

CONTRIBUTION OF ISOTOPIC RESEARCH TECHNIQUES TO CHARACTERIZE HIGH-MOUNTAIN-MEDITERRANEAN KARST AQUIFERS: THE PORT DEL COMTE (EASTERN PYRENEES) AQUIFER

Appendix A: Groundwater catchment areas for the springs S-01 to S-06.

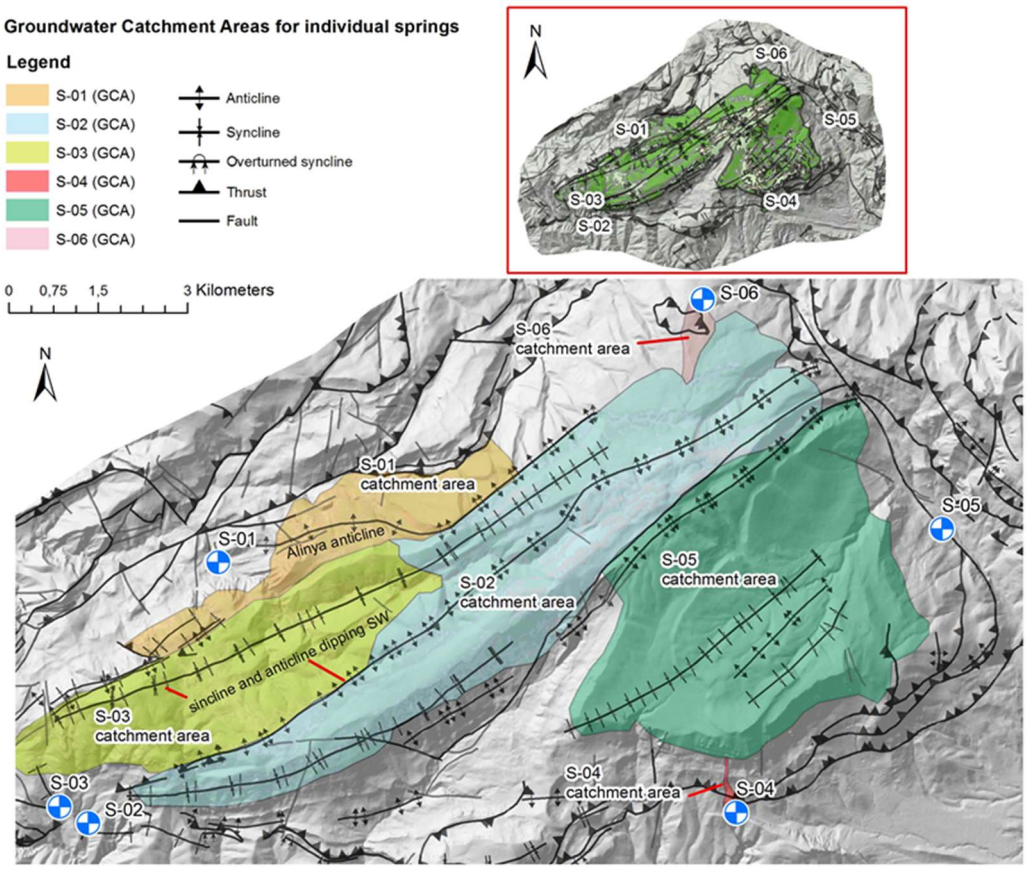

Figure A1. Groundwater catchment areas for the springs S-01 to S-06.

Table A1. Distribution of geographical and elevation zones considered into the HBV semi-distributed rainfall-runoff model into the groundwater catchment zones. The areas of the different vegetation zones (VZs) are provided, considering the three different elevation zones into which every GWC is divided.

GWC		Elevation Zones			Vegetation Zone Areas			Percentage Areas		
Index	Associated Spring	Z_{min} (m a.s.l.)	Z_{max} (m a.s.l.)	EZ_{ij}[a] (ha)	VZ_1[b] (ha)	VZ_2[c] (ha)	VZ_3[d] (ha)	VZ_1/EZ_{ij} (%)	VZ_2/EZ_{ij} (%)	VZ_3/EZ_{ij} (%)
1	S-01	1334	1600	204,0	41,8	56,8	105,5	20,5	27,8	51,7
		1601	1851	219,1	19,0	67,7	132,4	8,7	30,9	60,4
		1851	2141	122,8	4,8	6,8	111,1	3,9	5,5	90,5
2	S-02	1122	1543	106,9	8,2	26,0	72,7	7,7	24,3	68,0
		1544	1965	756,5	32,2	210,3	514,0	4,3	27,8	67,9
		1966	2385	1389,5	183,8	443,5	762,2	13,2	31,9	54,9
3	S-03	1201	1443	102,3	1,7	36,9	63,7	1,7	36,1	62,3
		1444	1686	561,2	19,5	178,9	362,8	3,5	31,9	64,6
		1687	1927	522,6	12,6	119,4	390,6	2,4	22,8	74,7
4	S-04	1468	1710	9,1	0,1	2,8	6,2	1,1	30,8	68,1
		1711	1847	0,9	0,1	0,5	0,3	11,1	55,6	33,3
		1848	1875	0,1	0,0	0,1	0,0	0,0	100,0	0,0
5	S-05	1421	1663	234,3	8,1	24,4	201,8	3,5	10,4	86,1
		1664	1973	635,5	45,4	126,0	464,1	7,1	19,8	73,0
		1974	2348	1278,4	215,5	495,0	568,0	16,9	38,7	44,4
6	S-06	1838	1926	11,9	0,7	0,7	10,5	5,9	5,9	88,2
		1927	2014	20,7	0,1	1,8	18,8	0,5	8,7	90,8
		2015	2101	13,4	0,0	2,3	11,2	0,0	17,2	83,6

(a) For a given elevation zone EZ_{ij} the subscripts "i" (from 1 to 6) and "j" refer to the corresponding groundwater catchment zone and elevation zone number, respectively; (b) VZ_1 corresponds to open areas; (c) VZ_2 corresponds to mountain meadows; (d) VZ_3 corresponds to forest zones

Appendix B: Sinusoidal functions fitting the measuring the isotopic content ($\delta^{18}O$ and $\delta^{2}H$) variation in precipitation and spring discharges.

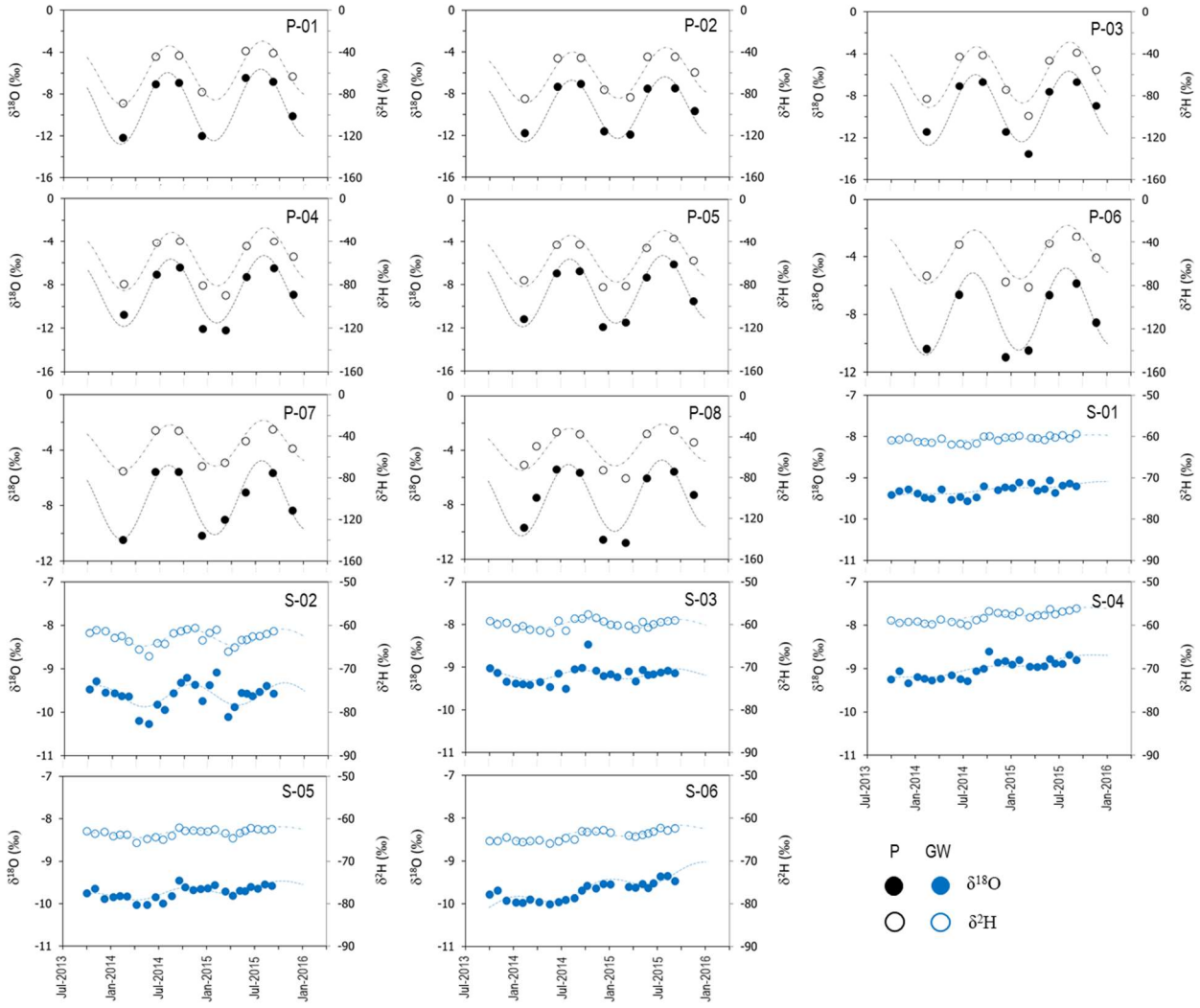

Figure B1. Isotopic content of precipitation (P; black symbols) and spring discharge (GW; blue symbols). $\delta^{18}O$ and $\delta^{2}H$ are indicated by solid and empty symbols, respectively The dashed lines indicate the fitted sinusoidal function [Eq.1]. The identification codes correspond to those in Table 1.

Appendix C: HBV hydrological modeling

Table C1. List of abbreviations for the vegetation zone parameters of HBV (Seibert, 2005)

Parameter	Units	Valid range	Description
TT	°C	(-inf,inf)	Threshold temperature to produce accumulation of precipitation as snow. Melt of snow starts if temperatures are above TT calculated with a simple degree-day (degree-Δt in case of a non-daily time step) method
CFMAX	mm/Δt/°C	[0,inf)	Degree-Δt factor - CFMAX varies normally between 1.5 and 4 mm oC-1 day-1 (in Sweden), with lower values for forested areas. As approximation the values 2 and 3.5 can be used for CFMAX in forested and open landscape respectively.
SFCF	-	[0,inf)	Snowfall correction factor
CFR	-	[0,inf)	Refreezing coefficient
CWH	-	[0,inf)	Water holding capacity, according to: refreezing meltwater = CFR·CFMAX(TT-T)'
FC	mm	(0,inf)	Maximum soil moisture storage
LP	-	[0,1)	Soil moisture value above which AET reaches PET
BETA	-		Parameter that determines the relative contribution to runoff from rain or snowmelt

Table C2. List of abbreviations for the catchment parameters of HBV (Seibert, 2005)

Parameter	Units	Valid range	Description
PERC	mm/Δt	[0,inf)	Threshold parameter
UZL	mm	[0,inf)	Threshold parameter
K0	1/Δt	[0,1)	Storage (or recession) coefficient 0
K1	1/Δt	[0,1)	Storage (or recession) coefficient 1
K2	1/Δt	[0,1)	Storage (or recession) coefficient 2

MAXBAS	Δt	[1,100]	Length of triangular weighting function

Table C3. Objective functions for the calibration of the HBV hydrologic model, where Q_{obs_i} and Q_{sim_i} are the measured and computed of spring discharge values, respectively, $\overline{Q_{obs}}$ is the arithmetic mean of the observed spring discharge values, and $\overline{Q_{sim}}$ is the arithmetic mean of the computed spring discharge values.

Objective function	Observations
$R_{eff} = 1 - \frac{\sum_{i=1}^{N}(Q_{sim_i} - Q_{obs_i})^2}{\sum_{i=1}^{N}(Q_{obs_i} - \overline{Q_{obs}})^2}$	R_{eff} = 1 means perfect fit R_{eff} = 0, indicates that the model fits the observed data no better than a horizontal line through $\overline{Q_{obs}}$ R_{eff} < 0 means very poor fit
$R^2 = \frac{(\sum_{i=1}^{N}(Q_{obs_i} - \overline{Q_{obs}}) * (Q_{sim_i} - \overline{Q_{sim}}))^2}{\sum_{i=1}^{N}(Q_{obs_i} - \overline{Q_{obs}})^2 * \sum_{i=1}^{N}(Q_{sim_i} - \overline{Q_{sim}})^2}$	R^2 is the determination coefficient. The higher the R^2 value the better the model performance

Table C4. Calibrated values of the parameters in the HBV-light model

Catchment Parameters	Units	S-01	S-02	S-03	S-04	S-05	S-06
Snow Routine (VZ_1)							
TT	°C	-0,2	-4,52	-1,6	-1,1	-1	-1,1
CFMAX	mm/d/°C	1,9	2,4	2	1,7	2,8	1,2
SFCF	-	1	2,38	0,5	1	1,2	1,5
CFR	-	1	2,5	0,7	0,5	0,6	0,6
CWH	-	0,5	2	2	1	0,8	0,8
Snow Routine (VZ_2)							
TT	°C	-0,2	-4,39	-1,6	-0,5	-3	-0,46

CFMAX	mm/d/°C	1,9	1	2	1,6	1	2,1
SFCF	-	1	2,6	0,7	1	1,2	1,16
CFR	-	1	2,5	0,7	0,3	1	1
CWH	-	1	2	1	1	0,2	0,2
Snow Routine (VZ_3)							
TT	°C	4	6	6	0	5,5	6,5
CFMAX	mm/d/°C	1,5	1	1,5	1,5	1	4
SFCF	-	0,001	0,001	0,001	0,01	0,001	0,001
CFR	-	0,7	1	0,7	0,2	0,4	0,4
CWH	-	2	2	3	1	1	1
Soil Moisture Routine (VZ_1)							
FC	mm	95	75	80	75	50	80
LP	-	0,07	0,01	0,02	0,02	0,01	0,01
BETA	-	0,60	0,40	1,54	1,70	0,30	2,5
Soil Moisture Routine (VZ_2)							
FC	mm	180	120	150	125	139	150
LP	-	0,07	0,01	0,06	0,01	0,01	0,01
BETA	-	0,60	2,20	3,90	3,45	1,80	2,7
Soil Moisture Routine (VZ_3)							
FC	mm	750	550	490	750	660	700
LP	-	0,00	0,01	0,01	0,01	0,01	0,01
BETA	-	6,00	3,00	5,70	6,00	3,50	4,00
Response Routine							
PERC	mm/d	5	20,0	2,2	1,1	25,0	1,7
UZL	mm	100	80	100	110	100	100

K0	1/d	0,20	0,50	0,20	0,20	0,20	0,40
K1	1/d	0,07	0,11	0,13	0,17	0,20	0,20
K2	1/d	0,01	0,02	0,04	0,04	0,05	0,05
Routing Routine							
MAXBAS	d	1,7	6,2	2	2,45	4,3	4,22

Table C5. Goodness of the result of the HBV calibrations for each spring model

HBV model	R_{eff} (-)	R^2 (-)
S-01	0,55	0,55
S-02	0,66	0,67
S-03	0,73	0,78
S-04	0,57	0,73
S-05	0,77	0,80
S-06	0,62	0,66

Appendix D: FlowPC modeling

Table D1. Fitted parameters of the exponential-piston flow model (EPM) for the estimated mean transit times (τ) with FlowPC model and $\delta^{18}O$ data

Parameters	S-01	S-02	S-03	S-04	S-05	S-06
β (%)[a]	0	0	0	0	0	0
δ_β (‰)[b]	0	0	0	0	0	0
η (-)[c]	1,02	1,02	1,00	1,01	1,02	1,02
τ (yr)	2,25	1,42	2,25	2,33	2,88	2,58
RMSE (‰)	0,03	0,04	0,03	0,03	0,02	0,03

(a) A constant discharge component as a fraction (usually older) of the total spring volumetric discharge flow rate. (b) Constant isotopic content of β. (c) η is the ratio of the total volume to the volume with exponential distribution transit time (TTD). η = 1 means the Exponential model (EM) and η>1 for Exponential-piston flow model (EPM)

Table D2. Fitted parameters of the exponential-piston flow model (EPM) for the estimated mean transit times (τ) with FlowPC model and $\delta^{2}H$ data

Parameters	S-01	S-02	S-03	S-04	S-05	S-06
β (%)[a]	0	0	0	0	0	0
δ_β (‰)[b]	0	0	0	0	0	0
η (-)[c]	1,01	1,00	1,01	1,00	1,01	1,02
τ (yr)	3,00	1,92	2,33	2,67	2,83	2,75
RMSE (‰)	0,19	0,21	0,17	0,22	0,18	0,20

(a) A constant discharge component as a fraction (usually older) of the total spring volumetric discharge flow rate. (b) Constant isotopic content of β. (c) η is the ratio of the total volume to the volume with exponential distribution transit time (TTD). η = 1 means the Exponential model (EM) and η>1 for Exponential-piston flow model (EPM)

9.3 CHAPTER 4- PAPER 2.

EVALUATION OF NATURAL BACKGROUND LEVELS OF HIGH MOUNTAIN KARST AQUIFERS IN COMPLEX HYDROGEOLOGICAL SETTINGS. A GAUSSIAN MIXTURE MODEL APPROACH IN THE PORT DEL COMTE (SE, PYRENEES) CASE STUDY'

Supplementary Material

Subset 1: Hydrochemistry

Table SM.1. Summary of the major ions content (median values of time series of the 43 monitored springs for the period September 2013 – October 2015).

Spring	GU	water-type	Cluster	Cluster Probability (%)	CE (mS/cm)	pH (-)	T (°C)	Ca (meq/L)	Mg (meq/L)	Na (meq/L)	K (meq/L)	HCO_3 (meq/L)	Cl (meq/L)	NO_3 (meq/L)	SO_4 (meq/L)
M-01	PEm1	Ca-HCO_3	B	91.10	640.5	7.3	12.2	120.5	10.5	7.6	1.8	288.7	8.9	5.3	88.9
M-02	PEmb	Ca-SO_4-HCO_3	B	100.00	493.0	7.8	10.7	78.0	13.5	4.6	1.3	141.7	4.0	3.5	133.7
M-03	PEalb	Ca-HCO_3	A	100.00	306.3	7.8	11.4	61.0	2.0	2.9	1.9	184.1	2.7	2.5	4.4
M-04	POcgs	Ca-HCO_3	A	100.00	470.0	7.4	10.2	95.0	6.3	2.1	2.6	289.0	3.3	3.6	15.4
M-05	Qpe	Ca-HCO_3	A	100.00	307.0	7.7	10.1	66.0	1.1	2.4	0.5	190.7	2.5	2.0	3.1
M-06	Kgp	Ca-HCO_3	A	100.00	251.0	8.1	7.3	54.0	5.3	3.0	0.9	166.5	3.3	2.2	9.0
M-07	POcgs	Ca-HCO_3	A	100.00	461.5	7.3	9.7	101.5	4.7	3.5	0.9	296.9	3.2	2.0	12.7
M-08	Kgp	Ca-HCO_3	A	100.00	384.3	7.6	5.5	87.0	4.1	3.3	1.0	269.6	3.0	1.9	9.6
M-09	Tk	Ca-SO_4	B	100.00	$1.2 \cdot 10^3$	7.9	9.0	242.0	14.5	8.5	2.2	212.2	7.8	4.2	488.3
M-10	Tk	Ca-HCO_3-SO_4	B	100.00	829.5	7.3	9.6	173.0	8.3	4.2	1.3	292.4	7.4	17.8	174.0
M-11	KMca	Ca-HCO_3	A	99.93	312.0	8.0	10.7	59.5	5.6	3.7	0.7	157.5	4.2	10.9	25.3
M-12	Kgp	Ca-HCO_3	A	99.99	252.0	7.9	8.5	53.5	2.3	1.7	0.6	167.3	4.3	1.9	4.1
M-13	Tm	Ca-HCO_3	B	96.88	574.0	7.7	11.2	96.5	19.0	9.0	1.7	253.9	20.9	1.8	97.7
M-14	PPEc	Ca-HCO_3	A	100.00	190.8	8.0	5.8	39.5	1.9	1.4	0.5	118.7	2.5	3.7	2.8
M-15	PEci	Ca-HCO_3	A	100.00	186.6	8.2	6.0	38.0	1.9	1.6	0.6	112.0	2.5	5.9	2.6
M-16	PEci	Ca-HCO_3	A	100.00	306.0	8.0	13.4	60.0	12.0	1.0	0.8	221.0	2.5	0.0	6.3
M-17	PEci	Ca-HCO_3	A	100.00	361.5	8.0	7.0	67.0	14.5	1.3	1.0	251.5	2.8	7.0	3.3
M-18	PEci	Ca-HCO_3	A	100.00	385.0	7.9	11.9	64.0	18.0	1.7	3.8	253.0	2.5	8.3	6.4
M-19	TJcd	Ca-HCO_3	A	100.00	392.0	7.8	7.4	62.5	18.5	1.7	0.7	256.4	3.4	5.7	4.7

M-20	PEcp2	Ca-HCO_3-Cl	C	100.00	701.6	7.7	6.2	86.0	18.0	33.0	1.1	266.9	80.9	9.1	10.7
M-21	Qcoo	Ca-SO_4	B	100.00	867.3	7.4	11.8	179.5	8.6	3.3	1.2	180.4	3.8	2.0	329.7
M-22	Qvl	Ca-HCO_3	A	100.00	241.0	7.9	7.4	45.0	6.2	1.6	0.4	147.4	3.6	2.7	6.5
M-23	Qt0	Ca-HCO_3	C	99.92	332.0	7.8	8.3	54.0	5.8	6.7	0.6	159.0	24.4	4.5	10.9
M-24	PPEc	Ca-HCO_3	A	100.00	402.5	7.6	8.2	76.0	10.5	2.8	1.2	266.1	3.7	1.8	5.5
M-25	Kgp	Ca-HCO_3	A	100.00	323.8	7.8	8.0	66.0	4.9	1.5	0.5	209.8	2.5	1.8	5.9
M-26	KMca	Ca-HCO_3	A	100.00	296.3	8.1	10.5	61.0	2.4	2.6	0.5	183.5	2.7	3.0	4.9
M-27	KMca	Ca-HCO_3	C	100.00	492.3	7.5	9.3	90.5	2.9	11.0	0.7	241.2	39.0	3.1	9.7
M-28	Tk	Ca-SO_4	B	100.00	$2.1 \cdot 10^3$	7.5	12.9	445.0	40.0	42.5	8.8	298.5	94.5	40.9	989.0
M-29	Qpe	Ca-HCO_3	A	99.79	436.0	7.7	10.2	76.0	6.5	8.1	1.7	218.0	15.6	9.0	23.4
M-30	Tk	Na-Cl	D	100.00	$2.5 \cdot 10^5$	6.4	15.4	754.5	$1.6 \cdot 10^3$	$1.2 \cdot 10^5$	$3 \cdot 10^3$	249.8	$1.8 \cdot 10^5$	4.4	$8 \cdot 10^3$
M-31	PPEc	Ca-HCO_3	A	100.00	353.8	7.9	8.6	75.0	4.1	1.2	0.4	234.0	2.5	2.4	4.6
M-32	POmlg	Ca-HCO_3	A	100.00	461.8	7.6	10.9	94.5	1.7	3.0	0.9	201.5	6.8	60.9	20.0
M-33	Tk	Ca-HCO_3-SO_4	B	100.00	851.0	7.1	7.8	158.5	18.5	3.8	2.2	328.8	4.6	1.7	205.9
M-34	TJb	Ca-HCO_3	A	100.00	331.8	7.6	7.6	68.5	8.4	2.8	0.7	237.0	3.5	0.9	7.3
M-35	PEcp1	Ca-HCO_3	A	100.00	232.0	8.1	12.6	39.5	4.6	1.5	0.4	133.7	3.2	2.9	4.1
M-36	PEmb	Ca-SO_4-HCO_3	B	100.00	601.3	7.9	11.0	96.5	20.0	5.7	1.2	197.5	4.0	1.6	168.6
M-37	Qvl	Ca-HCO_3	A	99.99	223.8	8.1	8.2	45.5	2.4	2.6	0.4	133.5	4.1	3.1	4.1
M-38	Kat	Ca-HCO_3	A	99.99	486.5	7.6	8.8	86.5	15.0	2.4	0.8	303.0	3.7	0.6	22.7
M-39	POmlg	Ca-HCO_3	A	100.00	472.3	7.5	11.2	94.5	4.2	2.4	0.5	284.5	3.0	0.6	12.8
M-40	Tk	Ca-SO_4	B	100.00	$1.2 \cdot 10^3$	7.2	12.3	229.5	28.0	39.5	2.4	241.0	71.2	2.1	468.9
M-41	Tk	Na-Cl	D	100.00	$5.7 \cdot 10^4$	7.3	12.3	550.0	76.5	$1.3 \cdot 10^4$	124.5	210.0	$2.1 \cdot 10^4$	4.9	$1 \cdot 10^3$
M-42	KMca	Ca-HCO_3	C	100.00	747.0	7.5	10.6	101.5	17.5	38.0	1.0	315.3	82.3	2.2	15.3
M-43	POcgs	Ca-HCO_3	A	100.00	283.8	7.74	9.0	54.0	4.7	2.3	0.4	177.0	4.0	2.6	6.2

Table SM.2. Average, standard deviation, and coefficient of variation for the time series of solute (CL, NO_3 and SO_4) concentration in groundwater for the high frequency sampled springs. Besides the same statistics are presented for the spatial distributions of solute concentrations considering the ensemble of the low frequency sampled springs.

Spring Time Series	Num. Samples	Cl^-		NO_3^-		$SO_4^=$	
		Value[d]	CV	Value[d]	CV	Value[d]	CV
M-04[a]	25	4.32±2.43	0.56	3.88±1.53	0.40	16.13±2.53	0.16
M-22[a]	25	5.35±4.72	0.88	3.19±2.22	0.69	7.14±1.90	0.27
M-25[a]	25	3.36±1.29	0.38	2.54±1.54	0.61	5.87±0.78	0.13
M-31[a]	25	4.34±4.00	0.92	3.03±1.33	0.44	4.55±0.60	0.13
Spring Time Series Avg[b]		4.34±3.11	0.69	3.16±1.66	0.53	8.42±1.45	0.17
Spatial.Avg[c]		4.71±2.17	0.42	6.28±1.80	0.41	9.10±1.47	0.14

(a) High frequency sampled spring
(b) Average for the high frequency sampled springs
(c) Spatial average from the low high frequency sampled springs M-03, M-05, M-06, M-07, M-08, M-11, M-12, M-14, M-15, M-16, M-17, M-18, M-19, M-24, M-26, M-29, M-32, M-34, M-35, M-37, M-38, M-39
(d) Average ± Std.Dev

Subset 2: Exploratory analysis of the original dada

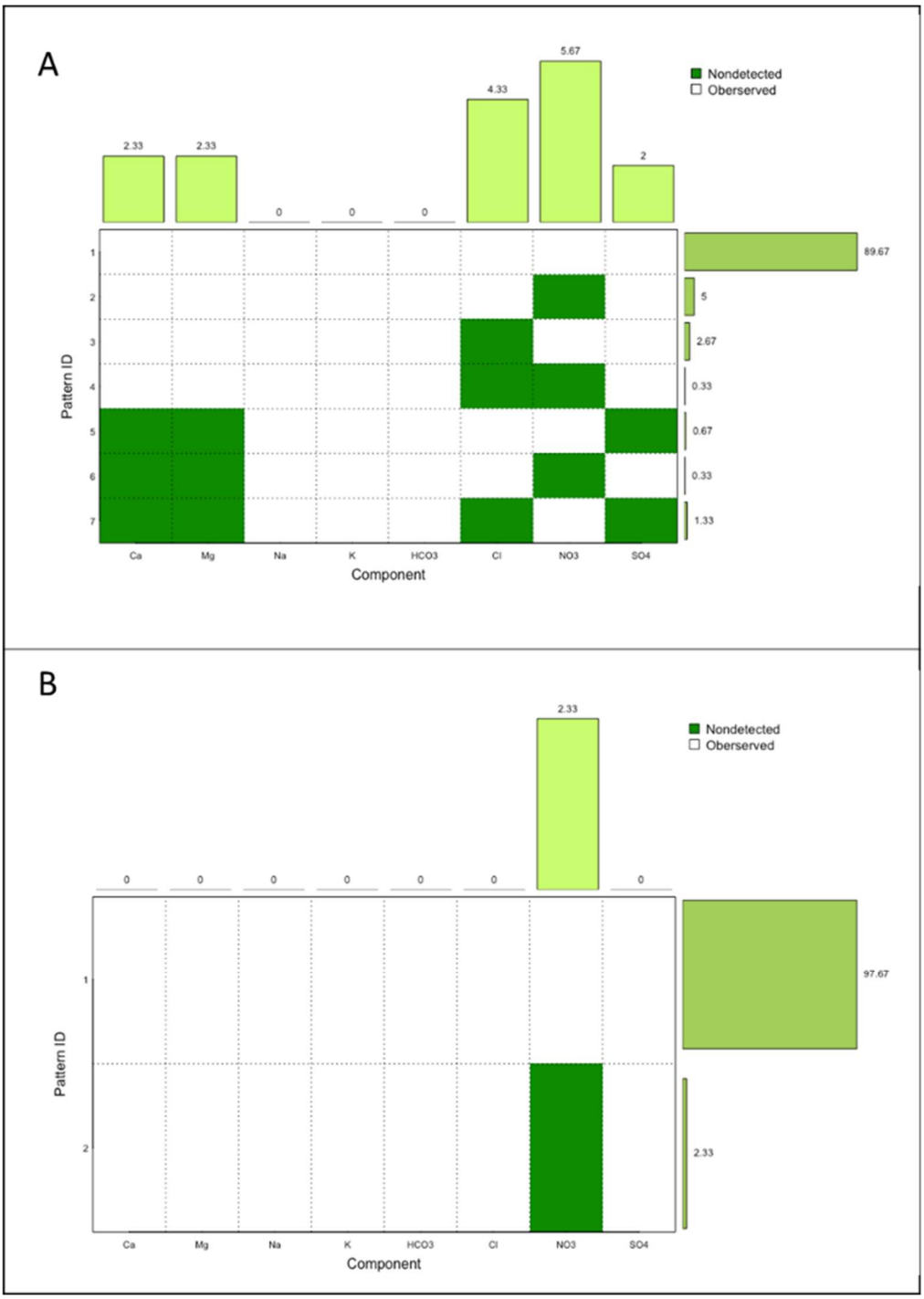

Figure SM.2.1. Pattern diagram of data. The 'zPatterns' function of {zCompositions} package was used for visual exploratory issues and inspecting zero patterns for the data matrix. (A) Data matrix 300 x 8. In this case there are censored values in Cl, NO3, SO4, Ca and Mg ions, most of them related to the 10 snow

samples. In total 89,67% of samples have complete value sets. Missing values have been imputed with the 'lrDA' (log ratio Data Argumentation) function (B) Data matrix 43 x 8 (median values).

- **Univariate analysis: Matrix 300 x 8 variables**

Edaplot (combination of histogram, density trace, one-dimensional scattergram and Boxplot in one plot) were calculated for each ion.

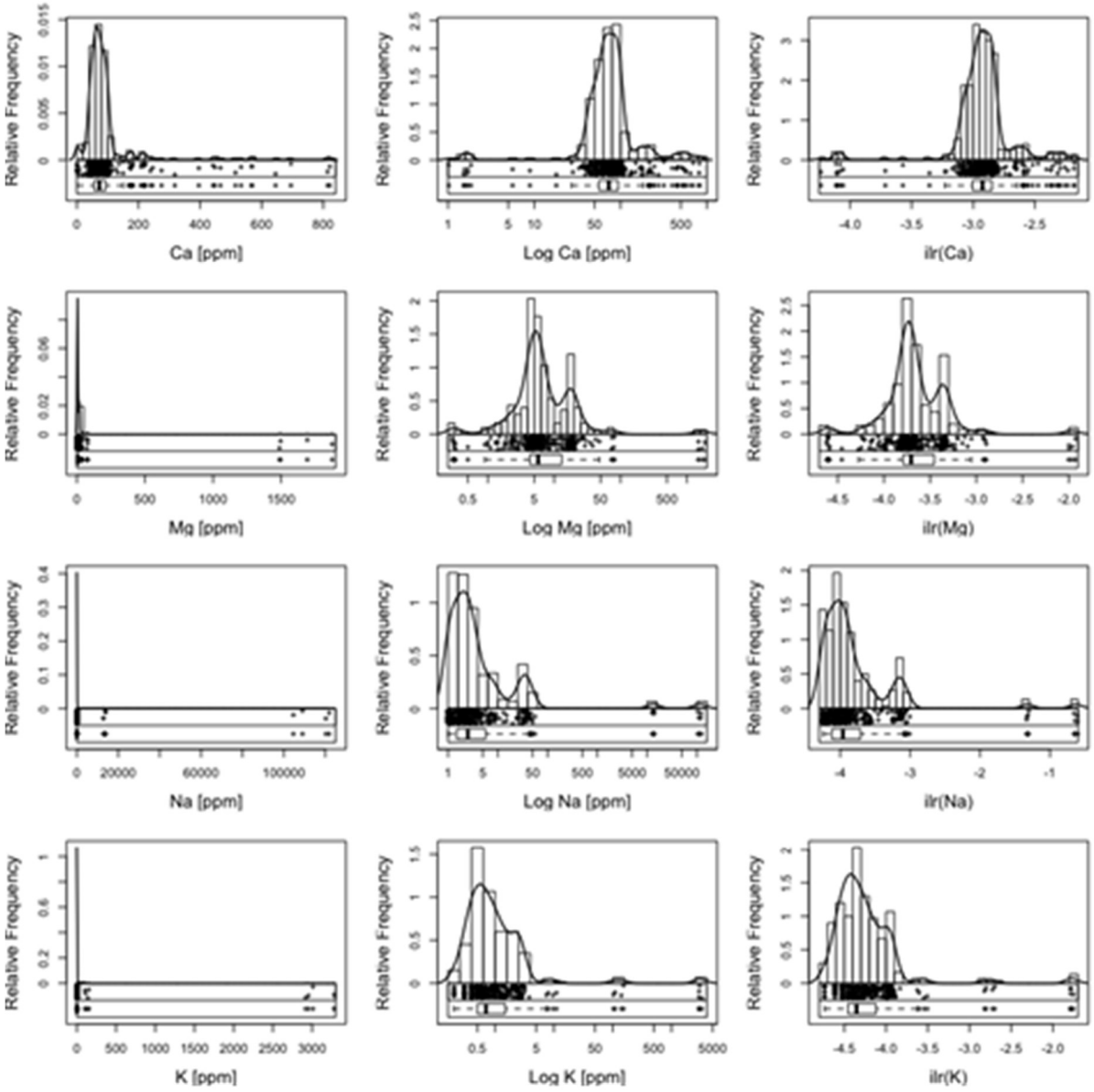

Figure SM.2.2. (a) EDA plot for the eight ions (matrix 300x8), for Ca, Mg, Na, K

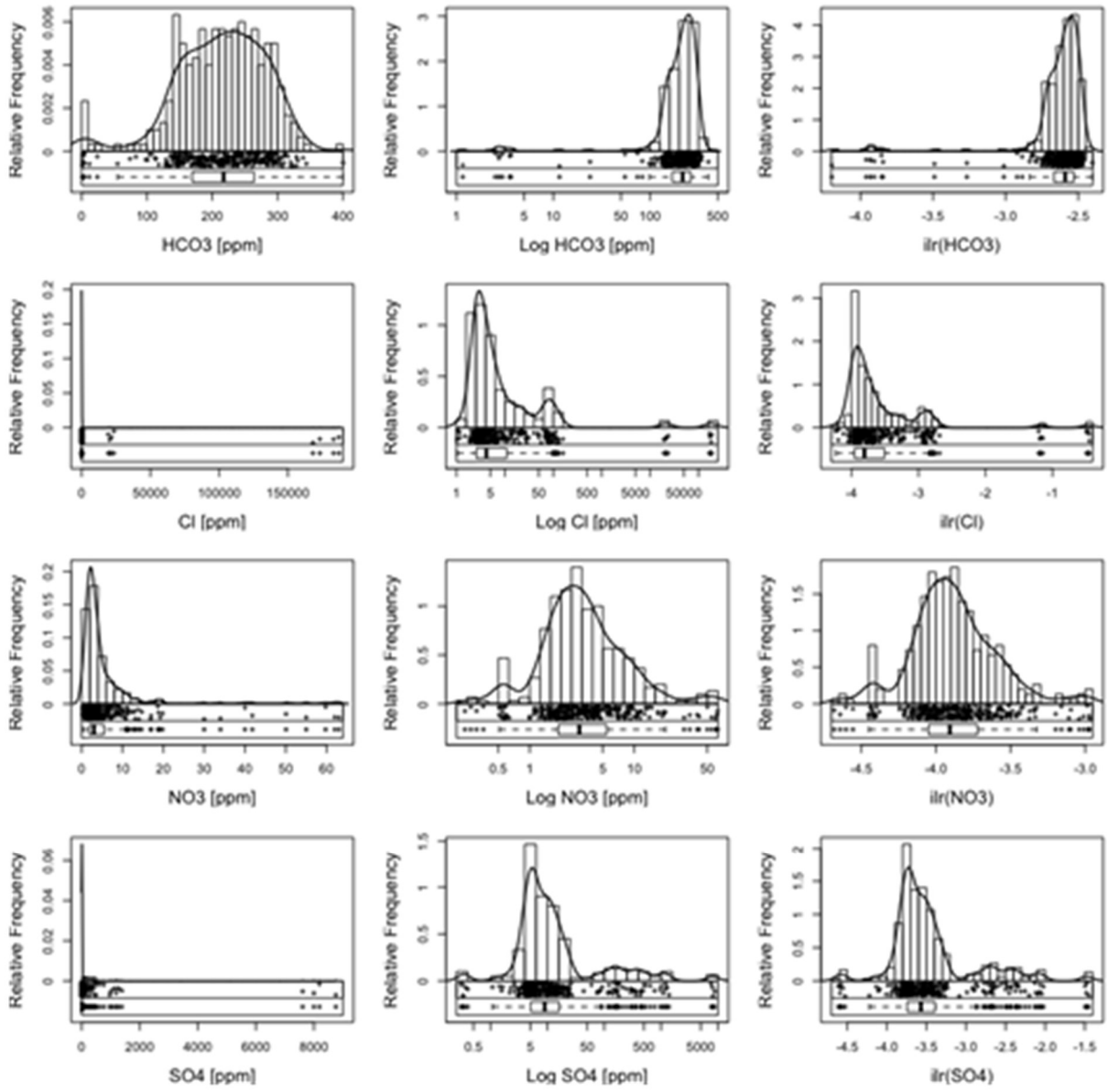

Figure SM.2.2. (a) EDA plot for the eight ions (matrix 300x8), for HCO_3^-, Cl^-, NO_3^-, $SO_4^=$

Subset 3: Principal Component Analysis

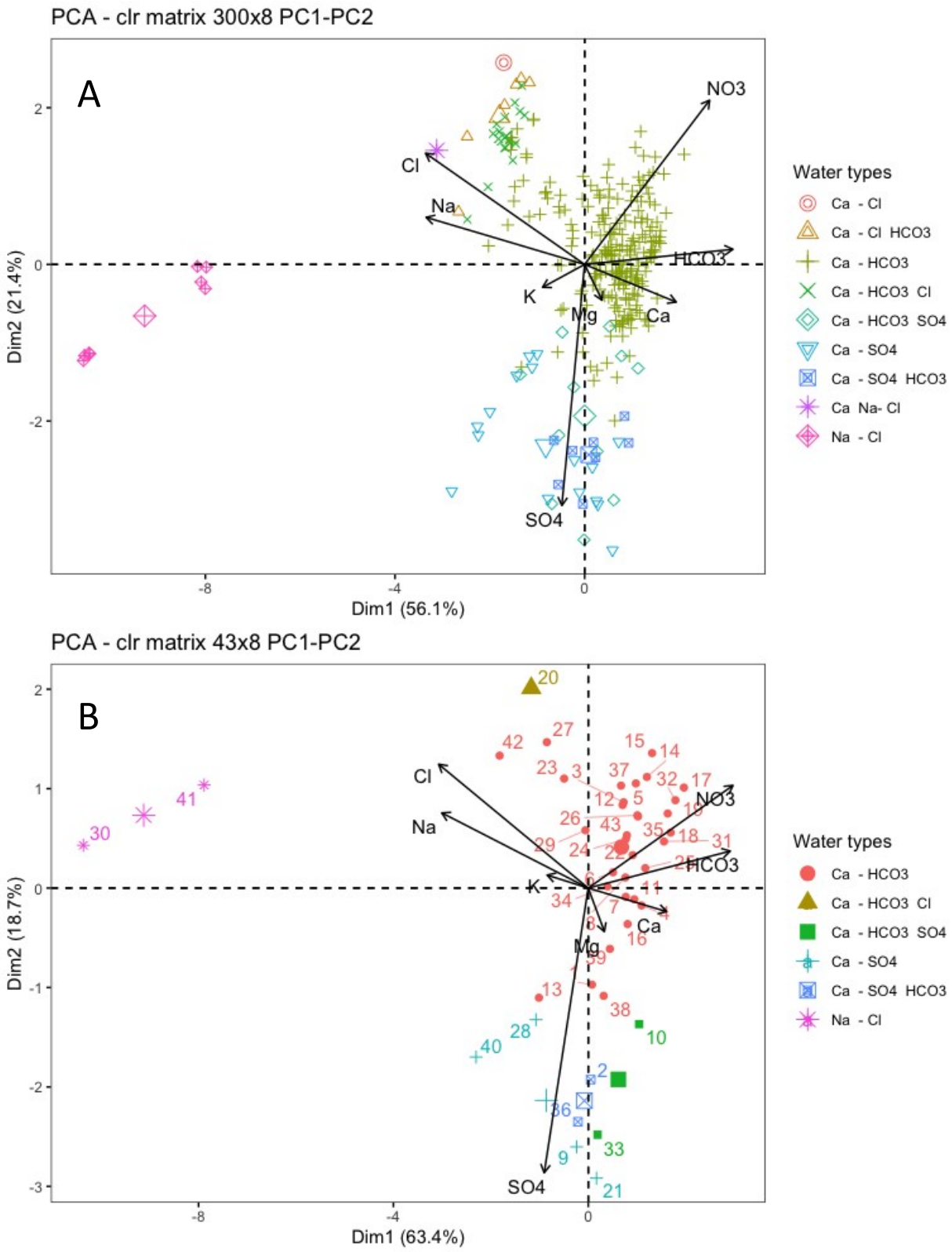

Figure SM.3.1. Biplots clr-transformed, PC1-PC2 with the links interpreted for the data Matrix 300x8 (A)

and the data Matrix 43x8 (B)

Table SM.3.1 Parameters 'included' and 'excluded' for the MSA.

Parameters 'included'	
Major ions	Ca, Mg, Na, K, HCO3, Cl, NO3, SO4
(8 variables)	Existence of left-censored values in the Compositional Data set (no missing values):
Matrix 300x8 and Matrix 43x8	Ca: 2% samples < LOQ (samples of snow) [<2ppm])
	Mg: 2% samples < LOQ (samples of snow) [<0,4ppm])
	SO4: 2% samples < LOQ (samples of snow) [<0,7ppm])
	Cl: 3% (springs samples) + 1,3% (snow samples) < LOQ [<2,5ppm])
	NO3: 1 sample with a value below LOQ [<1ppm]) (spring sample)
Parameters 'excluded'	
EC, TDS, pH, Eh	Parameters with additive characteristics.
	Non-compositional data
T°	Physical parameter. Non-compositional data
F-; CO3-;	>90% samples < LOQ - (*) severe degree of censored data
DOC	>28% samples < LOQ
NH4	>67% samples < LOQ - (*) high degree of censored data
Isotopes	Not considered although there are some references (Tolosana-Delgado, 2005; Puig et al 2011)
Total alkalinity	Parameter linked to HCO3 concentration
DUR (water hardness)	Parameter linked to Ca and Mg concentration

Subset 4: Model-based clustering results

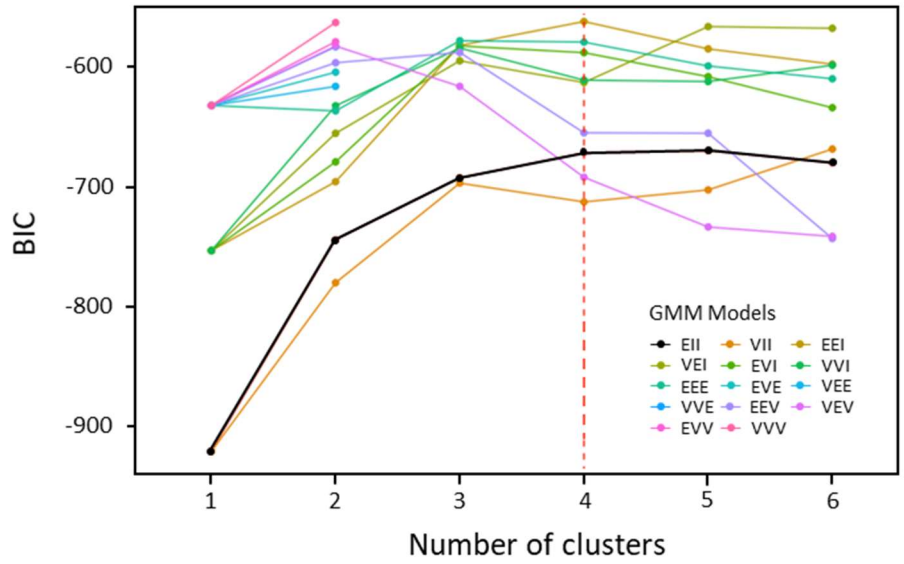

Figure SM.4.1. Graphic of the BIC criteria for the considered 14 GMM models. The lowest BIC value can be observed considering the 'EEI' model and 4 clusters. (See Scrucca et al., 2016; for the corresponding geometric characteristics of the EEI model)

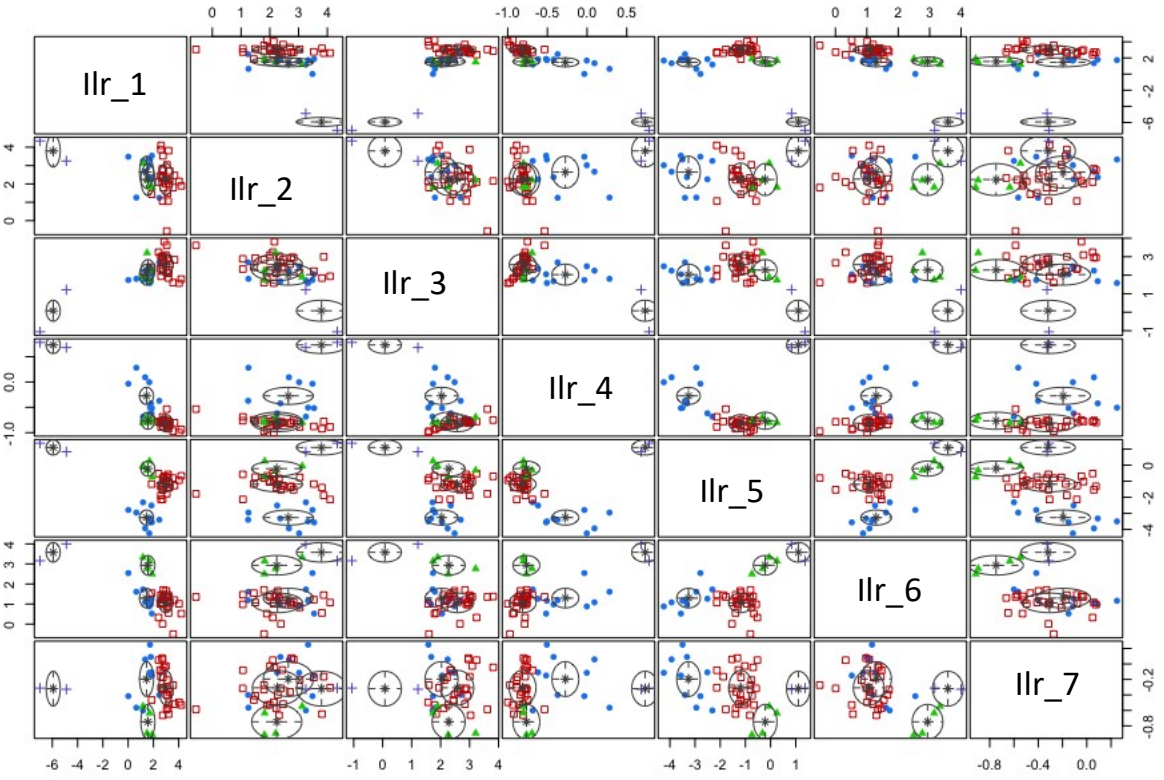

Figure SM.4.2. Scatterplot matrix obtained with the model-based clustering process using the dataset Matrix (43x8) and seven ilr balances (D-1, being D the dimension of the matrix)

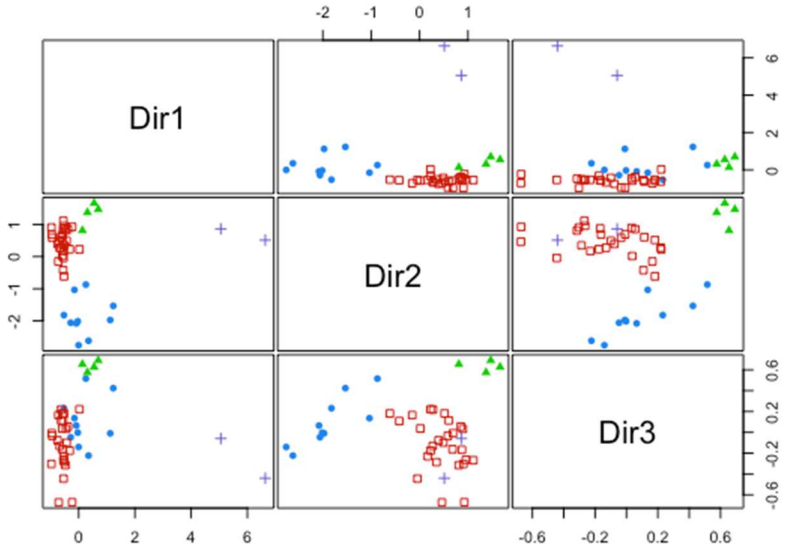

Figure SM.4.3. scatterplot of the reduced ilr-matrix

Table. SM.4.1. Calculated principal dimension of the reduced ilr-matrix.

	Dir1	**Dir2**	**Dir3**
ilr_1	-0.456	0.166	-0.075
ilr_2	0.007	0.094	-0.062
ilr_3	-0.183	0.197	-0.028
ilr_4	**0.836**	-0.252	-0.802
ilr_5	0.242	**0.913**	-0.231
ilr_6	0.013	0.145	0.387
ilr_7	0.037	-0.083	-0.378

Table SM.4.2. Mean groundwater chemistry of the spring water groups determined from the model-based clustering with GMM (model 'EEI' and k=4 clusters)

	Cluster A			Cluster B			Cluster C			Cluster D		
	Avg.	Max.	Min.	Avg.	Max.	Min.	Avg.	Max.	Min.	Avg.	Max.	Min.
CE (mS/cm)	337	486	186	875	2102	493	568	747	332	152135	247100	57170
pH (-)	7.8	8.2	7.3	7.5	7.9	7.1	7.6	7.8	7.5	6.9	7.3	6.4
T (°C)	9.1	13.0	5.5	10.9	12.9	7.8	8.6	10.6	6.2	13.9	15.4	12.3
Ca^{2+} (mg/L)	66.3	101.5	38.0	181.9	445.0	78.0	83.0	101.5	54.0	652.3	754.5	550.0
Ca^{2+} (mg/L)	6.4	18.5	1.1	18.1	40.0	8.3	11.1	18.0	2.9	835.3	1594.0	76.5
Mg^{2+} (mg/L)	2.4	8.1	1.0	12.9	42.5	3.3	22.1	38.0	6.7	63938.8	114650.0	13227.5
Na+ (mg/L)	0.9	3.8	0.4	2.4	8.8	1.2	0.8	1.1	0.6	1553.5	2982.5	124.5
K^{+} (mg/L)	209.7	303.0	112.0	243.5	328.8	141.7	245.6	315.3	159.0	229.9	249.8	210.0
HCO_3^- (mg/L)	3.8	15.6	2.5	22.7	94.5	3.8	56.7	82.3	24.4	99596.0	178185.5	21006.4
NO_3^- (mg/L)	5.5	60.9	0.6	8.1	40.9	1.6	4.7	9.1	2.2	4.6	4.9	4.4
$SO_4^{=}$ (mg/L)	8.8	25.3	2.6	314.5	989.0	88.9	11.6	15.3	9.7	4667.8	8093	1242.6

Table SM.4.3. Conditional probabilities (P) of belonging to a certain cluster obtained in the model-based clustering analysis using a GMM ('EEI' model, k = 4). The springs belonging to an unique cluster (i.e. P=1) are highlighted in blue

	Probability of belonging to a certain cluster								
Spring	Cluster-A	Cluster-B	Cluster-C	Cluster-D	**Spring**	Cluster-A	Cluster-B	Cluster-C	Cluster-D
M-01	0.089	0.911	0	0	M-23	0.001	0	0.999	0
M-02	0	**1**	0	0	M-24	**1**	0	0	0
M-03	**1**	0	0	0	M-25	**1**	0	0	0
M-04	**1**	0	0	0	M-26	**1**	0	0	0
M-05	**1**	0	0	0	M-27	0	0	**1**	0
M-06	**1**	0	0	0	M-28	0	**1**	0	0
M-07	**1**	0	0	0	M-29	0.998	0	0.002	0
M-08	**1**	0	0	0	M-30	0	0	0	1
M-09	0	**1**	0	0	M-31	**1**	0	0	0
M-10	0	**1**	0	0	M-32	**1**	0	0	0
M-11	0.999	0.001	0	0	M-33	0	**1**	**1**	0
M-12	**1**	0	0	0	M-34	**1**	0	0	0
M-13	0.031	0.9687	0.0003	0	M-35	**1**	0	0	0
M-14	**1**	0	0	0	M-36	0	**1**	0	0
M-15	**1**	0	0	0	M-37	0.9999	0	0.0001	0
M-16	**1**	0	0	0	M-38	0.9999	0.0001	0	0
M-17	**1**	0	0	0	M-39	**1**	0	0	0
M-18	**1**	0	0	0	M-40	0	**1**	0	0
M-19	**1**	0	0	0	M-41	0	0	0	**1**
M-20	0	0	**1**	0	M-42	0	0	**1**	0
M-21	0	**1**	0	0	M-43	**1**	0	0	0
M-22	**1**	0	0	0					

Subset 5: CoDa approach vs classical standardization (z-score method)

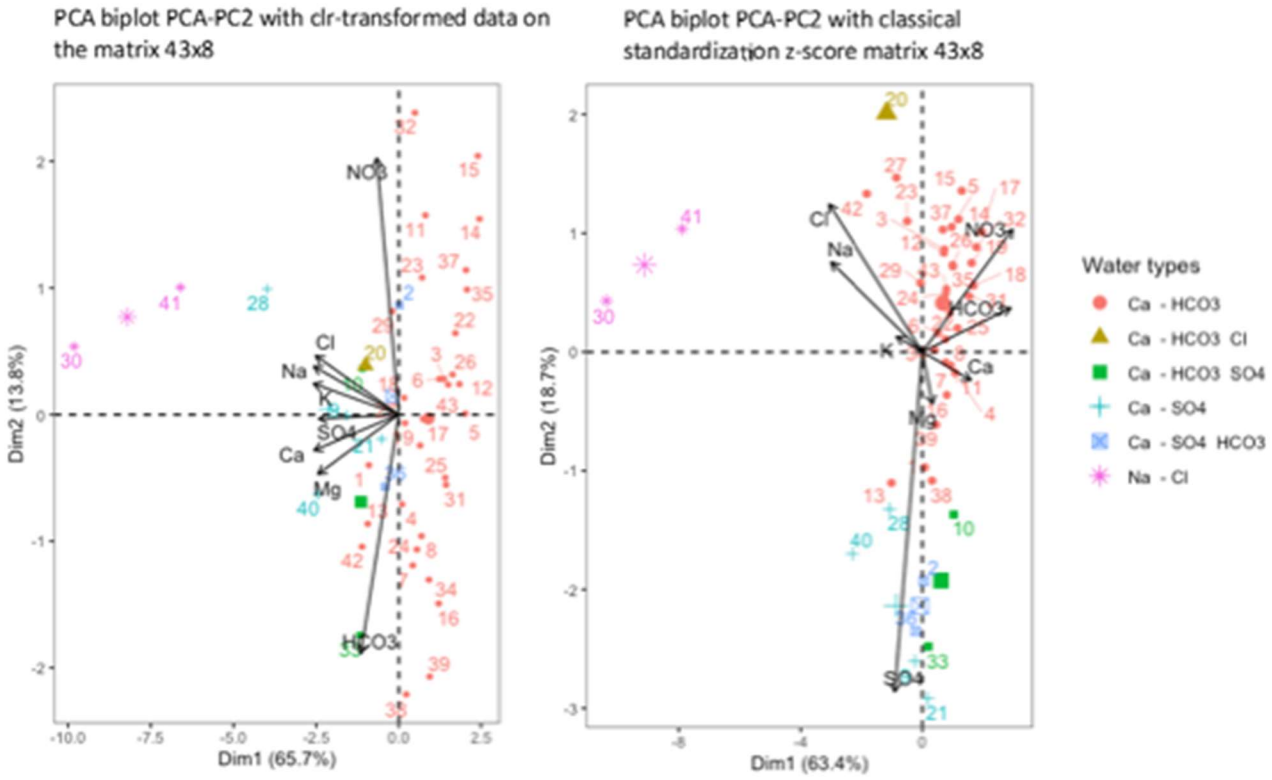

Figure SM.5.1. Biplot considering the classical standardization z-score approach (A) vs. considering the CoDA approach (B) on the dataset Matrix (43x8). As can be shown, considering the effect of the closed nature of geochemical data (CoDA approach) has a critical effect on the variable loading's distribution into the biplot, and no sense variable loading results are obtained when the classical standardization z-score approach is assumed.

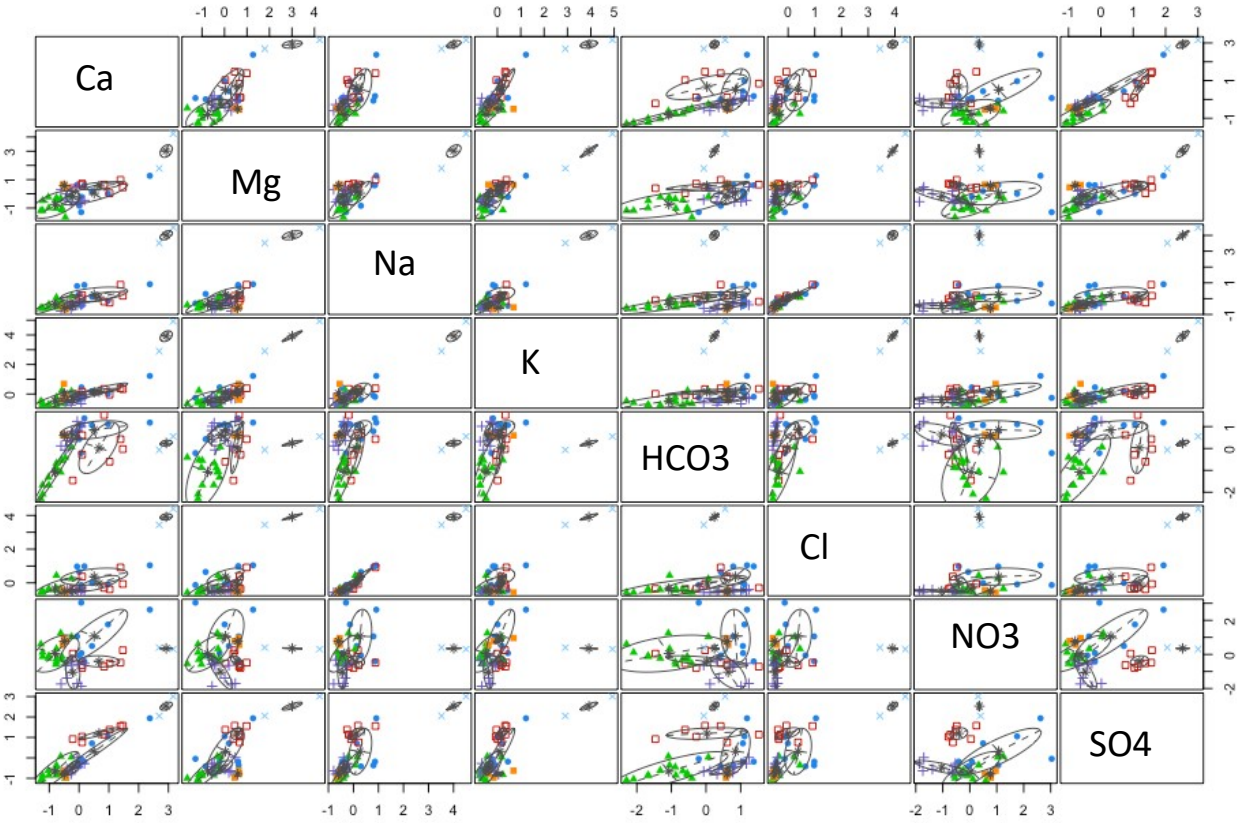

Figure SM.5.2. Scatterplot matrix obtained with the model-based clustering process using transformed data form the dataset matrix (43x8) and using the classical standardization z-score approach.

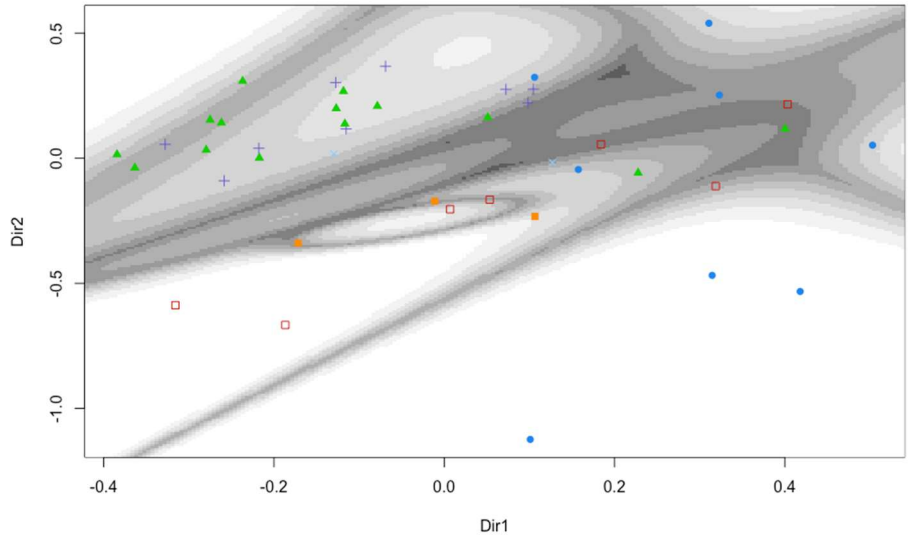

Figure A.5.3. Density biplot for PC1 vs PC2 components obtained from GMM for the Matrix (43x8) of data z-score transformed after dimension reduction.

Subset 6: Preliminary clustering analysis considering 'hard' clustering methods

Clustering is an unsupervised classification method widely used in hydrogeological research studies. There are multiple and variate "hard" clustering (where each data point can only belong to exactly one cluster; as e.g. the agglomerative hierarchical clustering HCA; and the partitional methods such as the k-means, k-medoids, among others) and criteria to take into account. The hierarchical clustering is a set of nested clusters that are organized as a tree (dendogram). The partitional clustering look for a division of the set of data objects into non-overlapping subsets (clusters) such that each data object is in exactly one subset. The selection of the method for clustering, the assumed number of clusters (to be used as initial centroids in case of the partitional methods), and the dissimilarity and linkage method selected have a strong impact on the clustering results obtained. Therefore, their use relies heavily on the analyst's knowledge to classify the clusters in a meaningful way. In practice it's important to test different methods, test the different indexes that allows found the best one, but finally take a look for the one with the most hydrogeological sense and the most useful or interpretable solution.

The clValid() function of the {clValid} R package (Brock et al. 2008), calculates validation measures for a given set of clustering algorithms and number of clusters. Available options are "hierarchical", "kmeans", "diana", "fanny", "som", "model", "sota", "pam", "clara", and "agnes", with multiple choices allowed. The internal measures include the connectivity, the silhouette coefficient and the Dunn index.

The fviz_nbclust() function of the {factoextra}R package (Kassambara and Mundt, 2016) determines and visualize the optimal number of clusters using computing the three different methods [elbow, silhouette and gap statistic]. Allowed methods include: partitional clustering "kmeans", "k-medoids" (pam, clara), "funny" (fuzzy clustering methods), etc.

The NbClust() function of the {NbClust} R package (Charrad et al. 2014) provides 30 indices for determining the relevant number of clusters and proposes to users the best clustering scheme from the different results obtained by varying all combinations of number of clusters, distance measures, and clustering methods. The results can be visualized in a summary graph.

In order to inspect the suitability of considering 'hard' clustering methods to determine the optimal number of clusters (k), a first and preliminary analysis was performed using the clValid(), fviz_nbclust() and NbClust() functions using ilr coordinates with the Matrix 43x8. The clustering

models may account for different linkage methods (i.e., '*complete*', '*average*', 'single' and '*ward*') and dissimilarity metrics ('*Euclidean*' and '*Manhattan*', among others). Results are presented in Figure A.6.1., Figure A.6.2. Figure A.6.3.

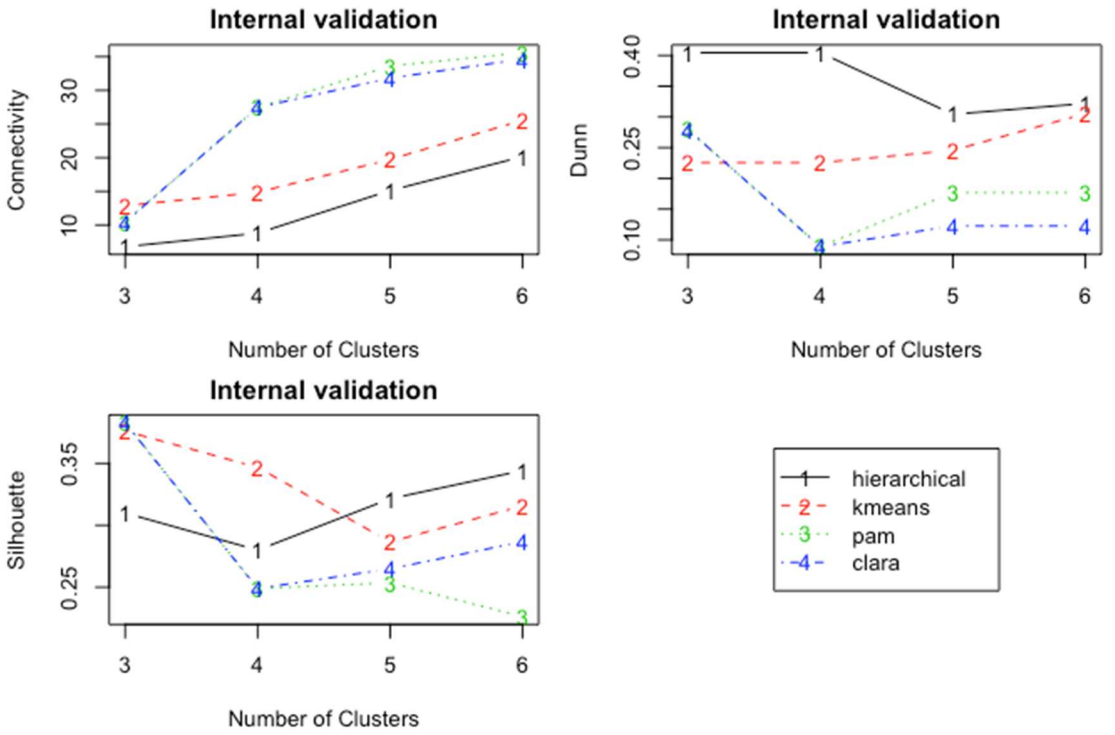

Figure A.6.1. Measures of connectivity, the silhouette coefficient and the Dunn indexes obtained using the function clValid()

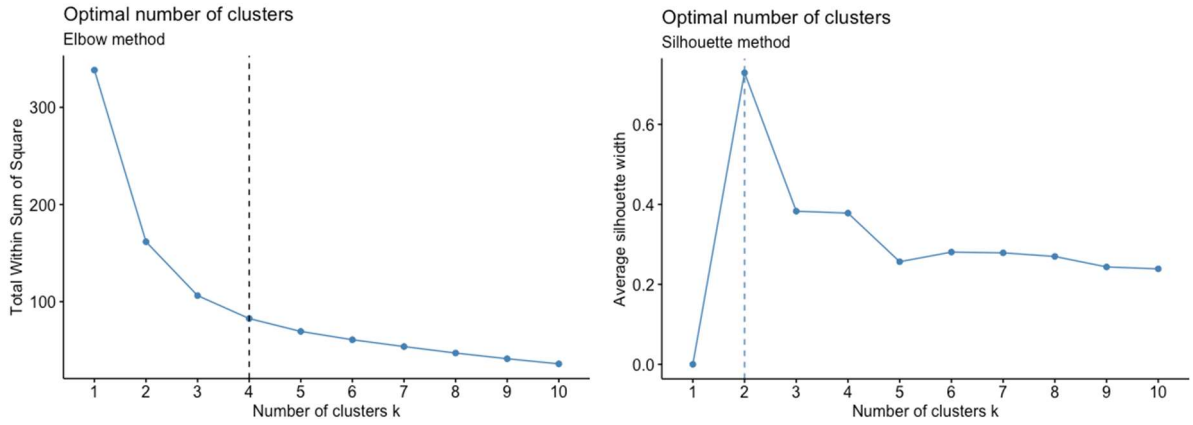

Figure A.6.2. Results of the Elbow and Silhouette methods using the fviz_nbclust() function

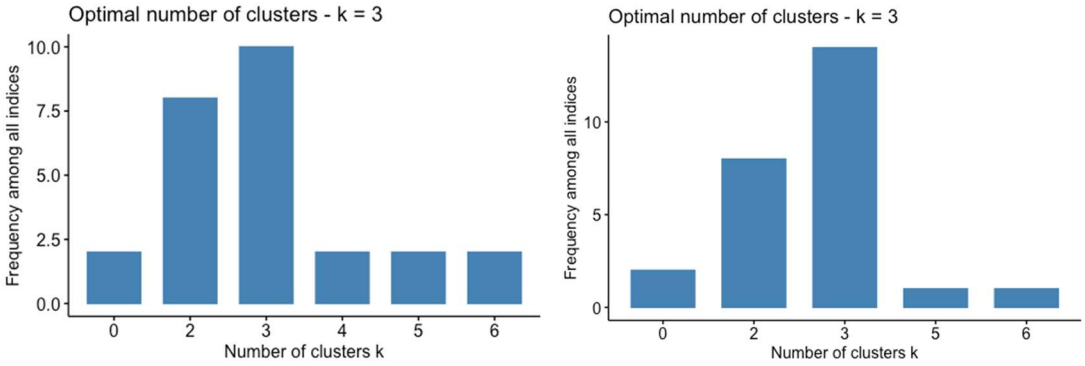

Figure A.6.3. Results obtained using NbClust() function for different cluster agglomeration methods: linkage 'ward.D' and 'complete'; distance = "euclidean".

The results obtained with the function clValid() suggest that the best number of cluster k is 3 but with no clear clustering method prevailing to the others. The results obtained with the Elbow method using the fviz_nbclust() function shows suggests that the best k value would be 4, whereas in the Silhouette method using the same function suggest that the best k value would be 4. The results obtained using NbClust() function for different cluster agglomeration methods: linkage 'ward.D' and 'complete' suggest that the best number is 3.

In summary, the results obtained indicates that good models would be obtained using *hierarchical* and *k-medoids* methods and for k clusters between 2 and 4. So there is no definitive and clear answer to the question about what which would be best method and the best number of k. Therefore it is concluded that the optimal number of clusters is somehow subjective and depends on the method used for measuring similarities and the parameters used for partitioning but also the criteria used to selected them, which cause that it is not evident to determine which could be the best grouping model for the available data using 'hard' clustering methods.

9.4 CHAPTER 5- PAPER 3.

ISOTOPIC CONTENT IN HIGH MOUNTAIN KARST AQUIFERS AS A PROXY FOR CLIMATE CHANGE IMPACT IN MEDITERRANEAN ZONES: THE PORT DEL COMTE KARST AQUIFER (SE PYRENEES, CATALONIA, SPAIN).

Supplementary Material

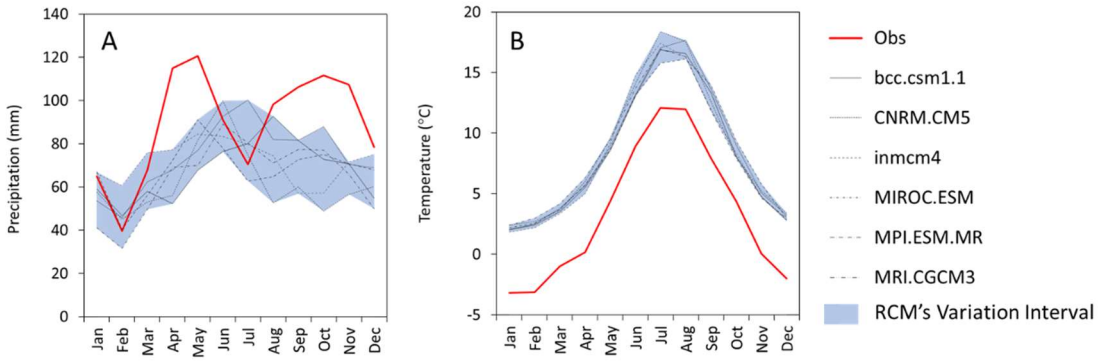

FigureSM1. Mean monthly precipitation (A) and temperature (B) at the basin for the period 1990–2020. Thick red lines are observed values. Thin black lines are RCMs values for the reference period. The blue shaded area reflects the maximum and minimum values among all the RCMs as a glimpse of their variability.

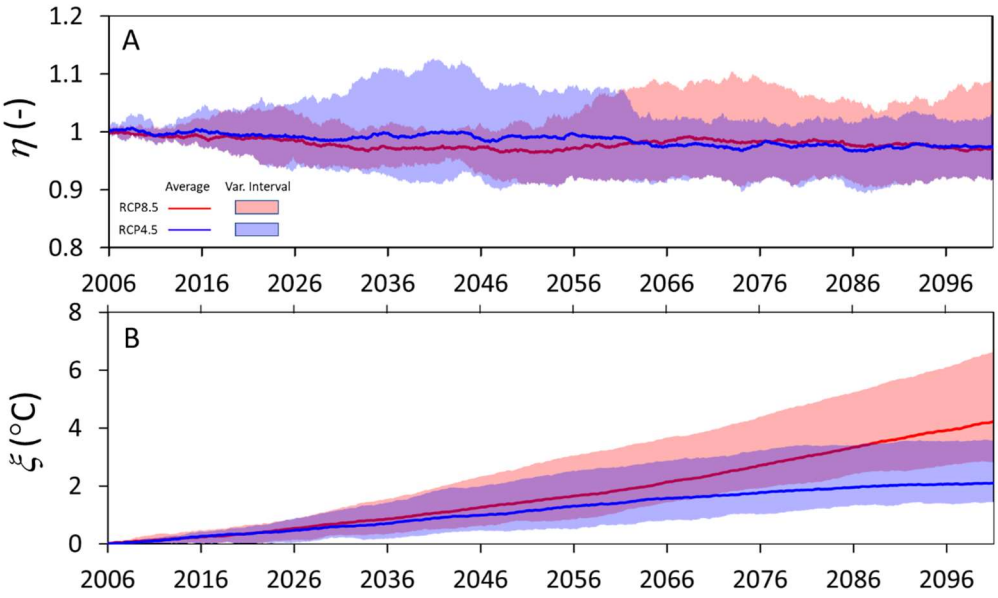

Figure SM2. Correction coefficients η and ξ for (A) daily precipitation and (B) temperature. Red line and shaded area indicate the mean coefficient value and the corresponding variation interval for RCP8.5. Blue line and shaded area indicate the mean coefficient value and the associated variation interval for RCP4.5

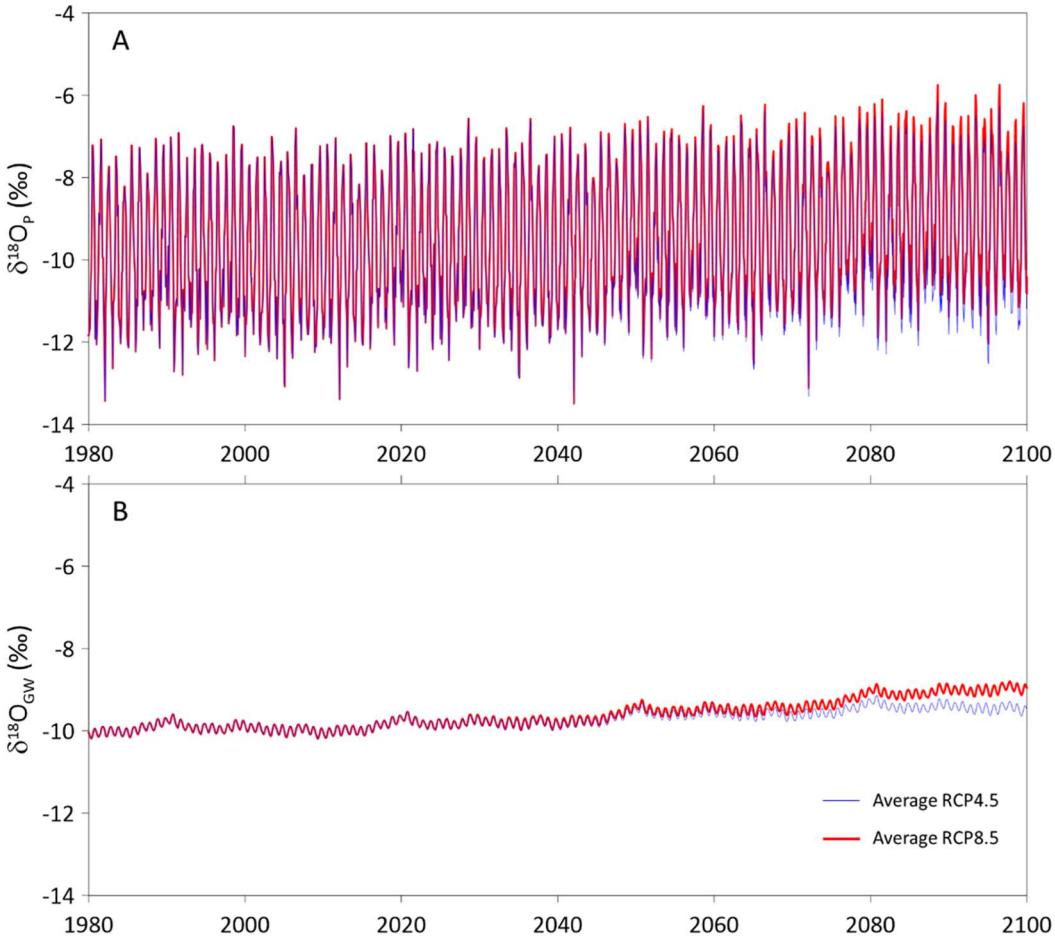

Figure SM3. Simulated monthly values of isotopic content in (A) precipitation and (B) groundwater as they would be obtained if these variables were sampled following the monthly sampling scheme assumed in the GNIP and GNIR networks.

Table SM1: Climate models used in this work.

Climate Model	Data Producer	Reference[a]
bcc.csm1.1	Beijing Climate Center (China)	Wu et al., 2014
CNRM.CM5	National Center for Meteorological Research (France)	Voldoire et al., 2013
inmcm4	Institute of Numerical Mathematics (Russia)	Volodin et al., 2010
MIROC.ESM	Agency for Marine-Earth Science and Technology (Japan)	Watanabe et al 2011
MPI.ESM.MR	Max Planck Institut (Germany)	Giorgetta et al., 2013
MRI.CGCM3	Meteorological Research Institute (Japan)	Yukimoto et al., 2012

(a) References are included in the reference section of the manuscript

Table SM2: Averaged values of the hydrometeorological variables for the historical period 1985-2015, and their corresponding increments obtained by considering the different climate models and the two emission scenarios RCP4.5 and RCP8.5 for the averaging intervals 2011-2040, 2041-2070 and 2071-2100.

Variable	Averaged value 1985/2015	Increments RCP4.5 2011/2040	Increments RCP4.5 2041/2070	Increments RCP4.5 2071/2100	Increments RCP8.5 2011/2040	Increments RCP8.5 2041/2070	Increments RCP8.5 2071/2100
P (mm/yr)	1082	-7	-12	-29	-16	-30	-21
AET (mm/yr)	425	14	41	62	16	50	97
Q_{Tot} (mm/yr)	350	-7	-13	-26	-14	-27	-16
Q_{rain} (mm/yr)	327	-4	-3	-13	-10	-15	2
Q_{snw} (mm/yr)	23	-4	-11	-18	-4	-11	-18
Q_{Rec} (mm/yr)	350	-7	-13	-26	-14	-27	-16
T (°C)	3.4	0.4	1.2	1.9	0.4	1.5	3.1
δ_{GW} (‰)[a]	-9.73	0.11	0.32	0.50	0.12	0.41	0.84

(a) δ_{GW} means $\delta^{18}O$ in the groundwater discharge of spring S-05

Table SM3: Estimated Sen's slopes and associated p-value (significance level 0.05) for the hydrometeorological variables in the period 2010-2100 and considering the different climate models and the two emission scenarios RCP4.5 and RCP8.5.

	β_P	β_T	β_{AET}	β_R	$\beta_{Q_{rain}}$	$\beta_{Q_{snw}}$	$\beta_{Q_{tot}}$	$\beta_{\delta^{18}O_P}$	$\beta_{\delta^{18}O_{GW}}$
	p-value	*p-value*	*p-value*	*p-value*	*p-value*	*p-value*	*p-value*	*p-value*	*p-value*
bcc.csm1.1-	-5.2	1.2	42.4	-21.0	-5.4	-9.9	-15.5	0.6	0.6
RCP4.5	*0.96*	*9.9e-7*	*6.2e-6*	*0.61*	*0.86*	*4.3e-3*	*0.67*	*6.4e-11*	*7.2E-23*
CNRM.CM5-	19.6	1.1	40.7	3.6	19.0	-8.9	7.9	0.5	0.5
RCP4.5	*0.73*	*4.3e-6*	*1.1e-5*	*0.89*	*0.53*	*8.5e-3*	*0.79*	*2.9E-09*	*3.7E-21*
inmcm4-RCP4.5	-38.8	0.5	18.7	-28.8	-15.0	-5.0	-21.2	0.5	0.4
	0.60	*2.1e-2*	*2.1e-2*	*0.48*	*0.64*	*0.13*	*0.55*	*9.9E-09*	*7.3E-20*
MIROC.ESM-	-86.1	2.4	80.4	-66.9	-50.6	-16.7	-68.7	1.1	1.2
RCP4.5	*0.20*	*4.7e-14*	*1.2e-12*	*7.7e-2*	*0.16*	*6.7e-6*	*8.5e-2*	*1.1E-20*	*1.3E-31*
MPI.ESM.MR-	-20.3	1.6	58.7	26.5	41.1	-12.7	29.1	0.6	0.7
RCP4.5	*0.73*	*1.0e-9*	*6.7e-9*	*0.47*	*0.23*	*6.3e-4*	*0.43*	*1.8E-10*	*4.8E-25*
MRI.CGCM3-	-12.4	0.5	23.0	108.1	109.6	-2.6	107.3	0.5	0.5
RCP4.5	*0.86*	*1.4e-2*	*7.4e-3*	*1.9e-2*	*6.3e-03*	*0.49*	*1.3e-2*	*8.5E-13*	*2.1E-21*
Average-RCP4.5	**-12.4**	**1.2**	**44.7**	**-0.5**	**13.7**	**-9.2**	**6.1**	**0.6**	**0.7**
	0.86	***4.1E-07***	***3.2E-06***	***0.99***	***0.66***	***8.3E-03***	***0.88***	***6.1E-22***	***1.8E-24***
bcc.csm1.1-	-47.0	1.8	63.9	-43.4	-26.7	-14.1	-43.6	1.2	1.1
RCP8.5	*0.49*	*1.2e-11*	*6.4e-10*	*0.27*	*0.42*	*1.1e-4*	*0.32*	*6.1E-22*	*5.0E-33*
CNRM.CM5-	60.6	1.1	42.7	12.2	29.4	-9.2	17.7	1.0	1.0
RCP8.5	*0.29*	*2.2e-6*	*5.7e-6*	*0.70*	*0.40*	*9.1e-3*	*0.62*	*1.4E-19*	*1.8E-30*
inmcm4-RCP8.5	-31.2	0.8	29.5	-13.2	-2.5	-7.1	-8.1	0.9	0.8
	0.61	*7.2e-4*	*9.0e-4*	*0.71*	*0.92*	*3.9e-2*	*0.76*	*3.4E-17*	*4.0E-27*
MIROC.ESM-	-87.1	2.7	90.3	-49.2	-30.3	-17.8	-49.0	1.9	1.9
RCP8.5	*0.26*	*1.5e-14*	*1.0e-13*	*0.20*	*0.43*	*1.7e-6*	*0.22*	*1.0E-29*	*1.7E-39*
MPI.ESM.MR-	-62.7	1.8	63.0	-11	1.0	-13.8	-8.8	1.3	1.3
RCP8.5	*0.35*	*6.0e-11*	*2.5e-9*	*0.79*	*0.97*	*2.4e-4*	*0.77*	*1.1E-23*	*2.0E-34*
MRI.CGCM3-	119.5	0.8	29.3	5.3	16.2	-6.1	9.2	1.0	1.0
RCP8.5	*0.14*	*4.5e-4*	*7.6e-4*	*0.87*	*0.61*	*7.5e-2*	*0.76*	*1.3E-19*	*1.1E-29*
Average-RCP8.5	**-11**	**1.5**	**53.8**	**-20.6**	**-4.7**	**-11.3**	**-14.1**	**1.2**	**1.2**
	0.81	***4.1E-09***	***6.5E-08***	***0.60***	***0.87***	***2.1E-03***	***0.64***	***1.5E-22***	***1.9E-33***

$\beta_P, \beta_{AET}, \beta_R, \beta_{Q_{rain}}, \beta_{Q_{snw}}$ and $\beta_{Q_{tot}}$ are expressed in $\left(\frac{mm}{100\ yr}\right)$, β_T in $\left(\frac{°C}{100\ yr}\right)$, and $\beta_{\delta^{18}O_P}$ and $\beta_{\delta^{18}O_{GW}}$ in $\left(\frac{‰}{100\ yr}\right)$

Table SM4: Estimated Sen's slope upper limit for the hydrometeorological variables in the period 2010-2100 and considering the different climate models and the two emission scenarios RCP4.5 and RCP8.5..

	β_P	β_T	β_{AET}	β_R	$\beta_{Q_{rain}}$	$\beta_{Q_{snw}}$	$\beta_{Q_{tot}}$	$\beta_{\delta^{18}O_P}$	$\beta_{\delta^{18}O_{GW}}$
bcc.csm1.1-RCP4.5	206.3	2.5	83.7	86.5	101.3	-4.3	89.2	0.7	0.7
CNRM.CM5-RCP4.5	226.7	2.2	78.2	100.5	118.4	-2.9	108.4	0.6	0.6
inmcm4-RCP4.5	171.8	2.1	74.3	57.6	70.5	-2.3	64.0	0.6	0.5
MIROC.ESM-RCP4.5	108.6	4.5	140.3	28.9	51.4	-9.6	32.0	1.3	1.2
MPI.ESM.MR-RCP4.5	175.1	2.8	92.2	61.7	87.0	-6.3	67.3	0.8	0.7
MRI.CGCM3-RCP4.5	184.9	2.4	86.2	59.8	83.7	-4.8	62.1	0.7	0.6
Average-RCP4.5	**175.5**	**2.7**	**91.8**	**57.4**	**84.9**	**-5.3**	**66.9**	**0.8**	**0.7**
bcc.csm1.1-RCP8.5	158.2	4.7	144.6	59.4	84.3	-10.7	66.2	1.3	1.2
CNRM.CM5-RCP8.5	271.4	4.1	138.2	138.8	167.6	-10.1	150.6	1.1	1.0
inmcm4-RCP8.5	168.1	3.6	119.1	53.9	85.5	-9.3	66.6	1.0	0.9
MIROC.ESM-RCP8.5	102.5	7.4	212.0	42.4	71.9	-13.8	44.5	2.0	1.9
MPI.ESM.MR-RCP8.5	134.8	5.2	161.5	46.5	76.8	-13.2	52.2	1.5	1.3
MRI.CGCM3-RCP8.5	339.3	4.1	143.2	191.8	217.4	-10.1	194.5	1.2	1.0
Average-RCP8.5	**194.0**	**4.9**	**153.6**	**84.5**	**115.7**	**-11.8**	**94.8**	**1.3**	**1.2**

$\beta_P, \beta_{AET}, \beta_R, \beta_{Q_{rain}}, \beta_{Q_{snw}}, and\ \beta_{Q_{tot}}$ *are expressed in* $\left(\frac{mm}{100\ yr}\right)$, β_T in $\left(\frac{^{\circ}C}{100\ yr}\right)$, *and* $\beta_{\delta^{18}O_P}$ *and* $\beta_{\delta^{18}O_{GW}}$ in $\left(\frac{‰}{100\ yr}\right)$

Table SM5: Estimated Sen's slope lower limit for the hydrometeorological variables in the period 2010-2100 and considering the different climate models and the two emission scenarios RCP4.5 and RCP8.5.

	β_P	β_T	β_{AET}	β_R	$\beta_{Q_{rain}}$	$\beta_{Q_{snw}}$	$\beta_{Q_{tot}}$	$\beta_{\delta^{18}O_P}$	$\beta_{\delta^{18}O_{GW}}$
bcc.csm1.1-RCP4.5	-117.0	1.5	50.3	-78.6	-59.6	-15.9	-78.6	0.4	0.5
CNRM.CM5-RCP4.5	-110.9	1.3	45.4	-71.9	-49.6	-15.4	-69.6	0.4	0.5
inmcm4-RCP4.5	-158.7	1.1	40.8	-99.9	-79.6	-16.5	-101.8	0.3	0.4
MIROC.ESM-RCP4.5	-193.0	3.5	104.5	-134.6	-103.9	-19.3	-131.6	0.9	1.1
MPI.ESM.MR-RCP4.5	-163.1	1.8	58.7	-116.6	-76.5	-17.8	-104.5	0.5	0.6
MRI.CGCM3-RCP4.5	-192.8	1.4	51.6	-134.3	-104.0	-19.6	-131.2	0.4	0.5
Average-RCP4.5	**-145.3**	**1.8**	**58.5**	**-95.3**	**-74.0**	**-17.3**	**-99.4**	**0.5**	**0.6**
bcc.csm1.1-RCP8.5	-164.3	3.7	113.4	-105.2	-77.3	-20.3	-101.1	1.0	1.1
CNRM.CM5-RCP8.5	-63.7	3.1	103.8	-43.6	-7.6	-20.6	-33.3	0.9	0.9
inmcm4-RCP8.5	-152.9	2.6	85.2	-106.1	-77.3	-21.2	-99.7	0.7	0.7
MIROC.ESM-RCP8.5	-199.1	6.5	183.3	-134.6	-96.0	-21.9	-129.8	1.8	1.8
MPI.ESM.MR-RCP8.5	-212.9	4.2	128.1	-138.5	-99.2	-22.5	-130.9	1.2	1.2
MRI.CGCM3-RCP8.5	-18.0	3.1	109.4	-7.6	30.5	-22.5	2.7	0.9	0.9
Average-RCP8.5	**-127.2**	**3.8**	**121.3**	**-89.0**	**-52.8**	**-21.4**	**-72.5**	**1.1**	**1.1**

$\beta_P, \beta_{AET}, \beta_R, \beta_{Q_{rain}}, \beta_{Q_{snw}}, and\ \beta_{Q_{tot}}$ *are expressed in* $\left(\frac{mm}{100\ yr}\right)$, β_T in $\left(\frac{^{\circ}C}{100\ yr}\right)$, *and* $\beta_{\delta^{18}O_P}$ *and* $\beta_{\delta^{18}O_{GW}}$ in $\left(\frac{‰}{100\ yr}\right)$

9.5 CHAPTER 6- PAPER 4.

IDENTIFICATION OF NATURAL AND ANTHROPOGENIC GEOCHEMICAL PROCESSES CONTROLLING GROUNDWATER QUALITY IN PORT DEL COMTE HIGH MOUNTAIN KARST AQUIFER (SE, PYRENEES)

Appendix A

Table A1. Summary of water sample types and analysis done in the research project

Type of sample	number of control points	Total field campaigns	Total number of samples	Number of analysis with major ions	Number of analysis with trace metals	Total number analysis stable isotopes of δ^2H_{H2O}, $\delta^{18}O$	Total number analysis stable isotopes of $\delta^{34}S$, $\delta^{18}O_{SO42-}$	Total number analysis stable isotopes of $\delta^{15}N$, $\delta^{18}O_{NO3-}$
Pluviometers (quarterly)	8	9	71	-	-	71	-	-
Spring samples	-	-	288	**288**	**285**	**283**	**209**	**72**
Springs (biannually)	40 / 43	4	-	138	136	134	88	42
Spring (monthly)	6	25	-	150	149	149	121	30
Snow samples			10	**10**	**10**	**10**	**1**	**-**
Natural snow	10	-	-	7	7	7	-	-
Artificial snow	3	-	-	3	3	3	1	-
Water ponds (artificial snow production)	2	-	2	2	2	-	-	-
		TOTAL	**371**					

Table A2.1. Chemical characteristics of major constituents for the 43 water springs (median values for the whole campaigns carried out between Set 2013 - Oct 2015).

ID	Num. Samples	Water type	Cluster	GU_(BG50M)	EC [µS/cm]	TDS [ppm]	pH	T [ºC]	Ca [ppm]	Mg [ppm]	Na [ppm]	K [ppm]	HCO_3 [ppm]	Cl [ppm]	NO_3 [ppm]	SO_4 [ppm]
M-03	4	Ca - HCO3	A	PEalb	306.25	161.00	7.8	11.4	63.75	2.05	2.53	1.93	190.96	3.75	3.83	4.38
M-04	25	Ca - HCO3	A	POcgs	470.04	241.68	7.4	10.2	94.84	6.35	2.16	2.60	291.00	4.32	3.88	16.13
M-05	4	Ca - HCO3	A	Qpe	307.00	160.75	7.7	10.1	69.25	1.10	2.15	0.50	198.48	2.80	3.92	3.14
M-06	4	Ca - HCO3	A	KMgp	251.00	132.25	8.1	7.8	54.25	5.18	2.83	1.18	170.68	5.67	3.36	8.82
M-07	4	Ca - HCO3	A	POcgs	461.50	241.75	7.3	9.7	102.25	4.90	3.53	0.88	297.37	5.56	2.20	14.10
M-08	4	Ca - HCO3	A	KMgp	384.25	202.50	7.6	5.5	86.50	4.45	3.28	0.85	264.86	4.24	2.01	10.03
M-11	4	Ca - HCO3	A	KMca	312.75	164.00	8.0	10.7	59.25	5.50	3.78	0.65	162.11	4.16	10.84	25.35
M-12	4	Ca - HCO3	A	KMgp	252.00	132.25	7.9	8.5	54.50	2.35	1.70	0.58	167.31	4.29	1.88	4.19
M-14	4	Ca - HCO3	A	PPEc	190.75	100.25	8.0	5.8	44.75	1.85	1.43	0.48	119.61	2.55	5.48	2.62
M-15	3	Ca - HCO3	A	PEci	186.67	99.67	8.2	6.0	37.67	1.83	1.53	0.53	109.90	2.87	7.35	2.49
M-16	1	Ca - HCO3	A	PEci	306.00	184.00	8.0	13.4	60.00	12.00	1.00	0.80	221.00	2.50	0.50	6.30
M-17	2	Ca - HCO3	A	PEci	361.50	198.50	8.0	7.0	67.00	14.50	1.30	1.00	251.50	2.75	6.99	3.29
M-18	1	Ca - HCO3	A	PEci	385.00	231.00	7.9	11.9	64.00	18.00	1.70	3.80	253.00	2.50	8.30	6.40
M-19	4	Ca - HCO3	A	TJcd	392.00	206.00	7.8	7.4	63.25	18.75	1.85	0.73	258.30	4.43	5.62	4.60
M-22	**25**	**Ca - HCO3**	**A**	**Qvl**	**241.04**	**122.71**	**7.9**	**7.4**	**44.64**	**6.14**	**1.63**	**0.49**	**147.94**	**5.35**	**3.19**	**7.14**
M-24	4	Ca - HCO3	A	PPEc	402.50	211.50	7.6	8.2	77.50	11.00	3.18	1.08	269.94	6.59	3.00	5.45
M-25	**25**	**Ca - HCO3**	**A**	**KMgp**	**323.76**	**164.32**	**7.8**	**8.0**	**65.84**	**5.03**	**1.75**	**0.59**	**210.24**	**3.36**	**2.54**	**5.87**
M-26	3	Ca - HCO3	A	KMca	296.33	158.00	8.1	10.5	63.00	2.50	2.30	0.53	185.50	2.97	2.90	4.76
M-29	4	Ca - HCO3	A	Qpe	436.00	228.25	7.7	10.2	76.50	6.43	8.15	1.70	218.59	16.82	8.86	27.32
M-31	**25**	**Ca - HCO3**	**A**	**PPEc**	**353.80**	**182.12**	**7.9**	**8.6**	**75.52**	**4.12**	**1.40**	**0.46**	**234.54**	**4.34**	**3.03**	**4.55**
M-32	4	Ca - HCO3	A	POmlg	461.75	242.50	7.6	10.9	95.75	1.60	2.83	0.85	203.77	8.61	58.70	20.12
M-34	4	Ca - HCO3	A	TJb	331.75	191.00	7.6	7.6	68.50	8.43	2.90	0.75	238.90	4.22	1.94	7.15
M-35	4	Ca - HCO3	A	PEcp1	232.00	123.00	8.1	12.6	42.00	4.55	1.53	0.48	138.85	3.27	3.48	4.12
M-37	4	Ca - HCO3	A	Qvl	223.75	117.25	8.1	8.2	45.25	2.68	2.40	0.40	133.98	3.99	3.81	4.43
M-38	4	Ca - HCO3	A	KSCat	486.50	255.50	7.6	8.8	86.00	14.75	2.85	1.08	305.16	3.92	1.65	22.39
M-39	4	Ca - HCO3	A	POmlg	472.25	247.50	7.5	11.2	95.25	4.48	2.48	0.55	283.15	5.95	1.78	13.75
M-43	**25**	**Ca - HCO3**	**A**	**POcgs**	**283.76**	**144.36**	**7.7**	**9.0**	**54.48**	**4.90**	**2.51**	**0.43**	**174.64**	**5.47**	**2.88**	**6.95**
M-01	4	Ca - HCO3	B	PEm1	640.50	336.50	7.3	12.2	120.50	10.93	7.20	1.83	287.83	11.93	5.48	93.48
M-02	4	Ca - SO4 HCO3	B	PEmb	493.00	257.50	7.8	10.7	81.75	14.25	4.25	1.43	133.56	7.30	4.02	139.26
M-09	4	Ca - SO4	B	Tk	1155.50	606.75	7.9	9.0	252.50	17.25	9.83	2.28	207.56	8.70	4.29	495.92
M-10	4	Ca - SO4 HCO3	B	Tk	829.50	438.50	7.3	9.6	179.75	8.38	4.18	1.45	298.25	11.51	16.36	203.08
M-13	4	Ca - HCO3 SO4	B	Tm	574.25	320.75	7.7	11.2	98.25	19.00	9.43	1.65	254.25	20.83	1.94	96.03
M-21	4	Ca - SO4	B	Qcoo	867.25	453.25	7.4	11.8	179.50	8.55	3.18	1.13	178.47	4.63	3.43	327.72
M-28	4	Ca - SO4	B	Tk	2102.75	1102.75	7.5	12.9	438.00	40.75	43.75	9.03	291.14	95.40	42.70	961.12
M-33	4	Ca - SO4 HCO3	B	Tk	851.00	450.25	7.1	7.8	166.50	18.50	7.43	2.20	316.42	4.77	1.88	223.46
M-36	4	Ca - SO4 HCO3	B	PEmb	601.25	316.00	7.9	11.0	95.25	19.75	6.05	1.58	197.18	4.64	1.97	166.82
M-40	4	Ca - SO4	B	Tk	1234.13	644.88	7.2	12.3	230.75	28.00	41.75	2.40	240.88	69.38	2.72	464.13
M-20	25	Ca - HCO3 Cl	C	PEcp2	701.56	356.56	7.7	6.2	85.64	18.36	33.36	1.19	265.67	88.37	10.95	10.88
M-23	4	Ca - HCO3	C	Qt0	332.25	174.25	7.8	8.3	55.50	5.90	7.35	0.63	161.46	23.39	5.37	11.25
M-27	4	Ca - HCO3	C	KMca	492.25	257.25	7.5	9.3	93.25	2.88	11.10	0.70	239.60	37.29	3.06	9.78
M-42	4	Ca - HCO3	C	KMca	747.00	390.25	7.5	10.6	101.00	17.25	37.25	1.08	330.65	75.82	2.43	15.16
M-30	4	Na - Cl	D	Tk	247100	129475	6.4	15.4	743.75	1637.50	113946	3040.25	251.83	177879	4.35	8138.20
M-41	4	Na - Cl	D	Tk	57170	29855	7.3	12.3	546.00	76.75	13347	126.25	215.27	21196	5.11	1264.67

Table A2.2. Average values of saturation indices (SI) relative to calcite, dolomite, gypsum and halite, values of pCO_2, and δ^2H_{H2O}, $\delta^{18}O_{H2O}$ for the 43 water springs (median values for the whole campaigns carry out between Set 2013 - Oct 2015). pCO_2 is $-\log PCO_2$, the partial pressure of CO_2 in the gas in atm.

ID	Num. Samples	Water type	Cluster	Ca / Mg [mmol/L]	Si calcite	SI dolomite	SI gypsum	SI halite	SI pCO_2g	ZR_mean (m a.s.l.)	Zd (m a.s.l.)	ZR-Zd (m)	δ^2H_{H20} (‰)	$\delta^{18}O_{H20}$ (‰)
M-03	4	Ca - HCO3	A	18.9	0.3	-0.8	-2.9	-9.8	-2.6	1865.1	1582.0	283.1	-59.6	-9.2
M-04	25	Ca - HCO3	A	9.1	0.2	-0.7	-2.2	-9.7	-2.1	1770.6	1464.0	306.6	-58.1	-9.0
M-05	4	Ca - HCO3	A	38.2	0.2	-1.3	-3.0	-9.8	-2.5	1751.8	1730.0	21.8	-58.5	-9.0
M-06	4	Ca - HCO3	A	6.4	0.4	-0.2	-2.6	-9.5	-3.0	1698.8	1657.0	41.8	-54.7	-8.7
M-07	4	Ca - HCO3	A	12.7	0.1	-1.0	-2.3	-9.4	-1.9	1803.0	1478.0	325.0	-58.4	-9.1
M-08	4	Ca - HCO3	A	11.8	0.3	-0.7	-2.4	-9.5	-2.2	1935.2	1871.0	64.2	-62.2	-9.5
M-11	4	Ca - HCO3	A	6.5	0.3	-0.3	-2.2	-9.4	-2.8	1590.1	1245.0	345.1	-57.7	-8.7
M-12	4	Ca - HCO3	A	14.1	0.2	-0.8	-2.9	-9.7	-2.8	1679.6	1234.0	445.6	-56.4	-8.8
M-14	4	Ca - HCO3	A	14.7	0.0	-1.3	-3.2	-10.1	-3.0	2108.4	2053.0	55.4	-64.0	-9.7
M-15	3	Ca - HCO3	A	12.5	0.1	-1.1	-3.3	-10.1	-3.2	2228.4	2158.0	70.4	-62.5	-9.6
M-16	1	Ca - HCO3	A	3.0	0.5	0.5	-2.8	-11.8	-2.7	2149.4	2077.0	72.4	-64.0	-9.9
M-17	2	Ca - HCO3	A	**2.8**	0.5	0.4	-3.0	-10.0	-2.7	2074.0	1989.0	85.0	-63.6	-9.6
M-18	1	Ca - HCO3	A	**2.2**	0.5	0.5	-2.8	-10.0	-2.6	2027.8	1940.0	87.8	-64.6	-9.8
M-19	4	Ca - HCO3	A	**2.0**	0.3	0.2	-2.9	-9.7	-2.5	1995.6	1944.0	51.6	-64.5	-9.7
M-22	25	Ca - HCO3	A	4.4	0.1	-0.6	-2.8	-9.7	-2.9	2061.2	1032.0	1029.2	-63.4	-9.7
M-24	4	Ca - HCO3	A	4.3	0.3	-0.3	-2.7	-9.5	-2.3	1878.2	1550.0	328.2	-62.3	-9.4
M-25	25	Ca - HCO3	A	7.9	0.3	-0.5	-2.7	-9.8	-2.6	1850.6	1098.0	752.6	-60.6	-9.3
M-26	3	Ca - HCO3	A	15.3	0.6	-0.2	-2.8	-9.8	-3.0	1769.5	1091.0	678.5	-57.7	-9.0
M-29	4	Ca - HCO3	A	7.2	0.2	-0.5	-2.1	-8.4	-2.4	1259.7	1050.0	209.7	-51.9	-7.9
M-31	25	Ca - HCO3	A	11.1	0.5	-0.2	-2.8	-9.9	-2.7	1820.0	1062.0	758.0	-59.9	-9.2
M-32	4	Ca - HCO3	A	36.4	0.2	-1.2	-2.1	-9.2	-2.4	1483.7	1425.0	58.7	-56.4	-8.5
M-34	4	Ca - HCO3	A	4.9	0.1	-0.6	-2.7	-9.5	-2.3	1813.8	1511.0	302.8	-60.9	-9.2
M-35	4	Ca - HCO3	A	5.6	0.3	-0.3	-3.0	-10.0	-3.0	1852.1	1330.0	522.1	-57.0	-8.9
M-37	4	Ca - HCO3	A	10.3	0.2	-0.7	-3.0	-9.6	-3.1	1544.7	1315.0	229.7	-54.0	-8.4
M-38	4	Ca - HCO3	A	3.5	0.3	-0.1	-2.1	-9.6	-2.2	1534.2	1402.0	132.2	-53.7	-8.4
M-39	4	Ca - HCO3	A	12.9	0.2	-0.7	-2.3	-9.5	-2.1	1697.2	1360.0	337.2	-59.0	-9.0
M-43	25	Ca - HCO3	A	6.7	0.1	-0.8	-2.7	-9.5	-2.6	1996.2	944.0	1052.2	-62.8	-9.6
M-01	4	Ca - HCO3	B	6.7	0.2	-0.5	-1.4	-8.7	-2.0	1478.0	970.0	508.0	-53.7	-8.3
M-02	4	Ca - SO4 HCO3	B	3.5	0.1	-0.4	-1.4	-9.4	-2.8	1567.3	1220.0	347.3	-54.0	-8.5
M-09	4	Ca - SO4	B	8.9	0.8	0.6	-0.6	-8.7	-2.7	1742.7	1404.0	338.7	-57.3	-8.9
M-10	4	Ca - SO4 HCO3	B	13.0	0.3	-0.7	-1.0	-9.0	-2.0	1758.8	1456.0	302.8	-59.0	-9.0
M-13	4	Ca - HCO3 SO4	B	3.1	0.4	0.2	-1.5	-8.3	-2.4	1449.6	1205.0	244.6	-55.5	-8.4
M-21	4	Ca - SO4	B	12.8	0.1	-0.9	-0.8	-9.5	-2.3	1501.8	992.0	509.8	-54.6	-8.4
M-28	4	Ca - SO4	B	6.5	0.7	0.5	-0.2	-7.0	-2.2	1409.4	1119.0	290.4	-53.6	-8.2
M-33	4	Ca - SO4 HCO3	B	5.5	0.0	-0.9	-1.0	-9.2	-1.7	1603.1	1369.0	234.1	-57.9	-8.8
M-36	4	Ca - SO4 HCO3	B	2.9	0.5	0.4	-1.3	-9.2	-2.7	1446.2	1005.0	441.2	-53.1	-8.2
M-40	4	Ca - SO4	B	5.0	0.2	-0.5	-0.7	-7.1	-2.0	1456.0	867.0	589.0	-55.1	-8.4
M-20	25	Ca - HCO3 Cl	C	2.8	0.3	-0.1	-2.5	-7.1	-2.4	2010.3	1858.0	152.3	-64.2	-9.7
M-23	4	Ca - HCO3	C	5.7	0.1	-0.7	-2.5	-8.3	-2.7	1817.5	1017.0	800.5	-59.9	-9.2
M-27	4	Ca - HCO3	C	19.7	0.2	-1.0	-2.4	-8.0	-2.3	1557.6	1156.0	401.6	-54.5	-8.5
M-42	4	Ca - HCO3	C	3.6	0.3	0.1	-2.3	-7.2	-2.1	1721.0	1601.0	120.0	-58.5	-9.0
M-30	4	Na - Cl	D	0.3	0.8	2.5	0.3	0.3	-1.8	1324.2	1023.0	301.2	-53.4	-9.6
M-41	4	Na - Cl	D	4.3	0.1	-0.4	-0.7	-2.2	-2.3	1061.7	993.0	68.7	-55.5	-7.8

Table A2.3. Chemical characteristics of major constituents for the 10 snow samples (7 natural and 3 artificial) and 2 water ponds. (Samples type T-1 correspond to artificial snow (snow gun); T-2 natural snow (inside sky trail); T-3 natural snow (outside sky trail); and T-4 water ponds for artificial snow production.

ID	Date	Water type	Sample type	EC [µS/cm]	TDS [ppm]	pH	T [ºCl]	Ca [ppm]	Mg [ppm]	Na [ppm]	K [ppm]	HCO_3 [ppm]	CO_3 [ppm]	Cl [ppm]	NO_3 [ppm]	SO_4 [ppm]	δ^2H_{H20} (‰)	$\delta^{18}O_{H20}$ (‰)
M-09as	09/12/2013	Ca - HCO3 Cl	T-1	49.00	24.00	10.3	-	5.60	0.50	1.30	1.20	11.59	2.86	4.86	1.58	1.56	-59.6	-9.2
M-120	07/12/2014	Ca-HCO3	T-1	142.00	71.00	10.0	-	18.00	4.00	6.30	1.20	55.00	12.00	9.32	1.27	5.00	-58.1	-9.0
M-100	07/12/2014	Ca-HCO3	T-1	51.00	26.00	9.6	-	8.90	1.00	1.20	0.20	24.00	<2,4	2.50	<1	1.08	-58.5	-9.0
M-08ps	09/12/2013	Ca Na- Cl	T-2	25.00	13.00	7.0	-	<2	<0,4	1.40	1.30	3.00	<2,4	3.98	0.24	<0,7	-54.7	-8.7
Ms-11	09/03/2014	Ca - Cl HCO3	T-2	21.00	11.00	6.7	-	<2	<0,4	1.00	0.90	3.54	<2,4	<2,5	2.90	<0,7	-58.4	-9.1
Ms-09	09/03/2014	Ca - Cl HCO3	T-2	16.00	8.00	6.2	-	<2	<0,4	1.00	0.40	2.75	<2,4	<2,5	2.25	<0,7	-62.2	-9.5
Ms-08	09/03/2014	Ca - Cl	T-2	21.00	10.00	5.6	-	<2	<0,4	1.00	0.70	1.16	<2,4	<2,5	3.45	<0,7	-57.7	-8.7
Ms-12	09/03/2014	Ca - Cl HCO3	T-2	13.00	6.00	5.7	-	<2	<0,4	1.00	0.40	2.50	<2,4	<2,5	1.93	<0,7	-56.4	-8.8
M-07ps	07/12/2013	Ca - Cl HCO3	T-3	5.00	2.00	6.7	--	<2	<0,4	1.00	0.30	2.75	<2,4	2.50	0.31	<0,7	-64.0	-9.7
M-10ps	12/01/2014	Ca - Cl HCO3	T-3	20.00	9.00	5.5	-	<2	<0,4	1.00	0.20	3.66	<2,4	4.23	<1	1.43	-62.5	-9.6
M-80	23/10/2014	Ca-HCO3	T-4	142.00	71.00	8.3	10.6	28.00	1.80	1.60	0.70	83.00	<2,4	4.18	<1	3.27	-64.0	-9.9
M-70	23/10/2014	Ca-HCO3	T-4	177.00	88.00	8.2	10.2	27.00	3.50	4.80	1.00	74.00	<2,4	19.92	1.66	5.34	-63.6	-9.6

Table A3. Hydrochemical composition of precipitation [62] and the estimated average recharge evapo-concentrated water chemistry in the PMC applying a concentration factor as estimated by Herms et al. (2019) [29].

Precipitation and recharge water chemistry	HCO_3 [ppm]	Ca [ppm]	Cl [ppm]	K [ppm]	Mg [ppm]	Na [ppm]	SO_4 [ppm]	NO_3 [ppm]
Precipitation water from the metereological station of La Molina (42º20'30"N, 1º57'14"E, altitude 1704 m a.s.l.)	3.14	1.73	0.94	0.35	0.09	0.54	2.66	1.31
Estimated average recharge (evapo-concentrated water chemistry in the PMC applying a reduced concentration factor).	7.35	4.06	2.19	0.82	0.20	1.25	6.23	3.07

Table A4. Average values for $\delta^{34}S_{SO4}$ and $\delta^{18}O_{SO4}$ of samples available of all springs and the corresponding average SO_4 concentration

Spring	Cluster	Num. Samples	GU (BG50M)	SO_4 [ppm]	water-type	$\delta^{34}S_{SO4}$ (‰)	$\delta^{18}O_{SO4}$ (‰)
M-03	A	2	PEalb	4.44	Ca -HCO3	7.6	5.8
M-04	A	21	POcgs	16.29	Ca -HCO3	3.9	8.1
M-05	A	1	Qpe	3.39	Ca -HCO3	6.4	9.7
M-06	A	2	Kgp	9.82	Ca -HCO3	0.4	8.0
M-07	A	3	POcgs	14.14	Ca -HCO3	8.3	10.9
M-08	A	2	Kgp	8.72	Ca -HCO3	11.6	13.7
M-11	A	3	KMca	25.13	Ca -HCO3	10.8	12.5
M-12	A	1	Kgp	4.03	Ca -HCO3	4.7	6.3
M-19	A	2	TJcd	4.52	Ca -HCO3	6.0	5.5
M-22	A	21	Qvl	7.07	Ca -HCO3	-3.3	7.6
M-24	A	2	PPEc	5.44	Ca -HCO3	-7.0	3.7
M-25	A	20	Kgp	Kgp	Ca -HCO3	-7.0	7.2
M-26	A	1	KMca	4.94	Ca -HCO3	3.1	10.5
M-29	A	3	Qpe	28.42	Ca -HCO3	10.9	11.1
M-31	A	19	PPEc	4.45	Ca -HCO3	-3.3	7.5
M-32	A	2	POmlg	19.72	Ca -HCO3	3.2	8.2
M-34	A	3	TJb	6.93	Ca -HCO3	6.1	8.1
M-35	A	1	PEcp1	4.49	Ca -HCO3	-0.6	13.7
M-37	A	2	Qvl	3.89	Ca -HCO3	3.5	7.2
M-38	A	3	Kat	21.52	Ca -HCO3	-17.5	3.4
M-39	A	2	POmlg	14.69	Ca -HCO3	7.8	9.7
M-43	A	21	POcgs	6.66	Ca -HCO3	-4.5	8.2
M-01	B	2	PEm1	106.52	Ca - HCO3	12.8	10.1
M-02	B	4	PEmb	139.26	Ca - SO4 HCO3	13.2	10.2
M-09	B	4	Tk	495.92	Ca - SO4	14.4	14.2
M-10	B	4	Tk	203.08	Ca - SO4 HCO3	13.2	13.5
M-13	B	4	Tm	96.03	Ca - HCO3 SO4	13.2	13.3
M-21	B	4	Qcoo	327.72	Ca - SO4	20.4	13.2
M-28	B	4	Tk	961.12	Ca - SO4	13.8	14.1
M-33	B	4	Tk	223.46	Ca - SO4 HCO3	9.1	10.6
M-36	B	4	PEmb	166.82	Ca - SO4 HCO3	8.5	8.7
M-40	B	4	Tk	464.13	Ca - SO4	20.0	12.7
M-20	C	22	PEcp2	10.8	Ca - HCO3 Cl	10.2	9.1
M-23	C	2	Qt0	12.2	Ca - HCO3	11.2	11.1
M-27	C	2	KMca	9.7	Ca - HCO3	7.7	8.8
M-42	C	3	KMca	14.9	Ca - HCO3	-5.1	3.5
M-30	D	4	Tk	8138.20	Na - Cl	13.2	10.6
M-41	D	4	Tk	1264.67	Na - Cl	18.6	12.4

Table A5. Rock samples collected for the characterization of S and O isotopic composition of from sulfate in Triassic and Tertiary gypsum in the PCM study area.

Rock sample ID	Lithology	Geology	Geological Unit (BG50M)	$\delta^{34}S_{SO4}$ (‰)	$\delta^{18}O_{SO4}$ (‰)
RS-01	massive nodular gypsum with shales	Keuper (Upper Triassic)	Tk	14.2	14.8
RS-02	massive nodular gypsum with shales	Keuper (Upper Triassic)	Tk	14.3	12.9
RS-03	massive nodular gypsum with shales	Keuper (Upper Triassic)	Tk	14.1	13.0
RS-04	massive nodular gypsum with shales	Keuper (Upper Triassic)	Tk	15.3	13.3
RS-05	massive nodular gypsum with shales	Keuper (Upper Triassic)	Tk	15.1	12.8
RS-06	laminated gypsum and marls	Beuda Fm. Eocene (Paleogene)	Pexb	22.0	14.5
RS-07	laminated gypsum and marls	Beuda Fm. Eocene (Paleogene)	Pexb	20.7	11.6
RS-08	laminated gypsum and marls	Beuda Fm. Eocene (Paleogene)	Pexb	21.9	13.6

Table A6. Average values for $\delta^{15}N_{NO3}$, $\delta^{18}O_{NO3}$, of samples available of all springs and the corresponding average NO_3 concentration.

Spring	Cluster	Num. Samples	GU (BG50M)	NO_3 [ppm]	water-type	$\delta^{15}N_{NO3}$ (‰)	$\delta^{18}O_{NO3}$ (‰)
M-04	A	11	POcgs	4.15	Ca -HCO3	4.3	3.7
M-11	A	2	KMca	10.76	Ca -HCO3	0.5	0.0
M-14	A	1	PPEc	11.69	Ca -HCO3	-0.1	0.7
M-19	A	3	TJcd	6.06	Ca -HCO3	-0.9	1.0
M-22	A	4	Qvl	5.62	Ca -HCO3	4.8	4.5
M-26	A	1	KMca	2.54	Ca -HCO3	-0.1	0.0
M-29	A	3	Qpe	8.78	Ca -HCO3	7.0	1.5
M-31	A	4	PPEc	3.73	Ca -HCO3	4.3	4.8
M-32	A	3	POmlg	57.27	Ca -HCO3	0.3	1.4
M-43	A	2	POcgs	3.64	Ca -HCO3	4.1	3.9
M-01	B	2	PEm1	6.16	Ca-HCO3	3.1	3.0
M-02	B	2	PEmb	4.58	Ca - SO4 HCO3	-0.1	1.4
M-09	B	2	Tk	4.90	Ca - SO4	1.9	1.5
M-10	B	3	Tk	18.14	Ca - SO4 HCO3	1.2	2.6
M-28	B	3	Tk	38.60	Ca - SO4	10.7	3.7
M-20	C	21	PEcp2	11.3	Ca - HCO3 Cl	3.7	0.7
M-23	C	2	Qt0	4.4	Ca - HCO3	7.4	8.0
M-27	C	1	KMca	2.1	Ca - HCO3	1.6	3.1
M-30	D	1	Tk	4.49	Na - Cl	9.6	6.2
M-41	D	1	Tk	6.75	Na - Cl	7.7	1.6

Table A7. Results of inverse geochemical reaction Recharge-Discharge Pathway Modelling using PHREEQC.

Springs	water-type	Cluster	RDP-1	n models	Selected models	Ca/Mg molar ratio	Calcite	Dolomite	$CO_2(g)$	Gypsum	Halite	Ca X_2	Mg X_2	Na X	K X
M-22R	Ca - HCO3	A	RDP-01	8	Model 4	4.41	7.10E-04	2.48E-04	1.17E-03	3.59E-05	1.13E-04	3.80E-05	-	-7.60E-05	-
					Model 6		7.86E-04	2.10E-04	1.17E-03	3.59E-05	1.13E-04	-	3.80E-05	-7.60E-05	-
M-43R	Ca - HCO3	A	RDP-02	4	Model 2	6.75	1.03E-03	1.96E-04	1.44E-03	2.93E-05	1.11E-04	2.15E-05	-	-4.00E-05	-3.00E-06
					Model 3		1.08E-03	1.75E-04	1.44E-03	2.93E-05	1.11E-04	-	2.15E-05	-4.00E-05	-3.00E-06
M-31R	Ca - HCO3	A	RDP-03	8	Model 7	11.14	1.93E-03	-	1.51E-03	2.31E-06	7.70E-05	-1.35E-04	1.64E-04	-5.60E-05	-3.00E-06
					-		-	-	-	-	-	-	-	-	-
M-25R	Ca - HCO3	A	RDP-04	4	Model 2	7.95	1.31E-03	2.03E-04	1.36E-03	6.69E-06	3.86E-05	2.66E-06	-	-7.00E-06	1.67E-06
					Model 3		1.32E-03	2.00E-04	1.36E-03	6.69E-06	3.86E-05	-	2.66E-06	-7.00E-06	1.67E-06
M-17	Ca - HCO3	A	RDP-05	8	Model 5	2.81	7.33E-04	7.26E-04	1.93E-03	3.41E-05	4.40E-05	-	-4.35E-05	9.99E-07	8.60E-05
					Model 6		7.33E-04	7.26E-04	1.93E-03	3.41E-05	4.50E-05	-	-4.30E-05	-	8.60E-05
M-14	Ca - HCO3	A	RDP-06	18	Model 8	14.69	1.04E-03	-	8.75E-04	4.00E-09	3.70E-05	-6.99E-05	6.74E-05	2.00E-06	3.00E-06
					-		-	-	-	-	-	-	-	-	-
M-04	Ca - HCO3	A	RDP-07	4	Model 2	9.08	1.88E-03	2.53E-04	2.31E-03	1.08E-04	6.50E-05	-1.20E-05	-	-2.30E-05	4.70E-05
					Model 3		1.86E-03	2.65E-04	2.31E-03	1.08E-04	6.50E-05	-	-1.20E-05	-2.30E-05	4.70E-05
M-36	Ca - SO4 HCO3	B	RDP-08	4	Model 2	2.93	-6.42E-05	8.02E-04	1.20E-03	1.64E-03	5.13E-05	-7.64E-05	-	1.40E-04	1.30E-05
					Model 3		-2.17E-04	8.79E-04	1.20E-03	1.64E-03	5.13E-05	-	-7.64E-05	1.40E-04	1.30E-05
M-10	Ca - SO4 HCO3	B	RDP-09	4	Model 4	13.04	2.45E-03	-	2.01E-03	2.11E-03	2.67E-04	-2.74E-04	3.35E-04	-1.38E-04	1.64E-05
					-		-	-	-	-	-	-	-	-	-
M-09	Ca - SO4	B	RDP-10	5	Model 5	8.89	1.65E-03	-	1.29E-03	5.23E-03	1.86E-04	-8.15E-04	7.03E-04	1.86E-04	3.76E-05
					-		-	-	-	-	-	-	-	-	-
M-28	Ca - SO4	B	RDP-11	4	Model 2	6.53	-1.03E-03	1.67E-03	2.16E-03	9.94E-03	2.61E-03	2.88E-04	-	7.80E-04	2.03E-04
					Model 3		-4.50E-04	1.38E-03	2.16E-03	9.94E-03	2.61E-03	-	2.88E-04	-7.80E-04	2.03E-04
M-20	Ca - HCO3 Cl	C	RDP-12	4	Model 2	2.83	6.92E-04	7.50E-04	2.27E-03	7.06E-05	2.45E-03	5.09E-04	-	-1.04E-03	1.70E-05
					-		-	-	-	-	-	-	-	-	-
M-27	Ca - HCO3	C	RDP-13	3	Model 3	19.7	1.94E-03	-	1.72E-03	2.77E-05	9.82E-04	1.77E-04	1.08E-04	-5.64E-04	-7.00E-06
					-		-	-	-	-	-	-	-	-	-
M-23	Ca - HCO3	C	RDP-14	4	Model 2	5.71	8.01E-04	2.35E-04	9.55E-04	6.11E-05	6.04E-04	1.68E-04	-	-3.33E-04	-3.00E-06
					Model 3		1.14E-03	6.70E-05	9.55E-04	6.11E-05	6.04E-04	-	1.68E-04	-3.33E-04	-3.00E-06

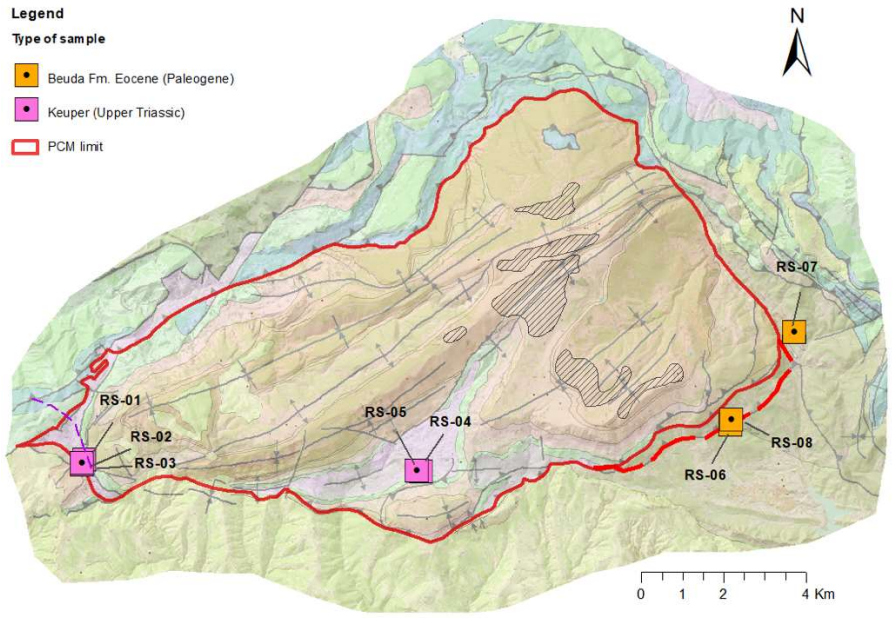

Figure A1. Map of rock samples collected for the characterization of S and O isotopes from sulfate content in Triassic and Tertiary gypsum in the PCM.

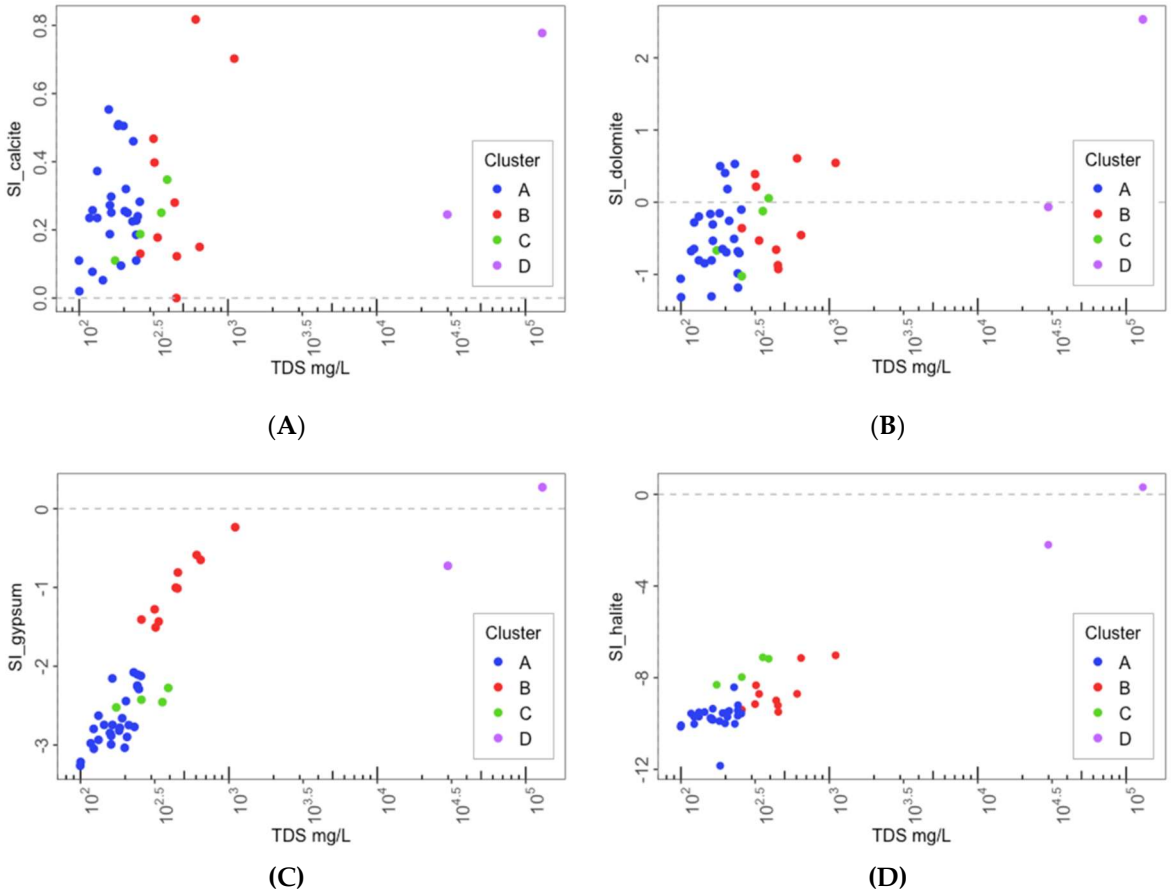

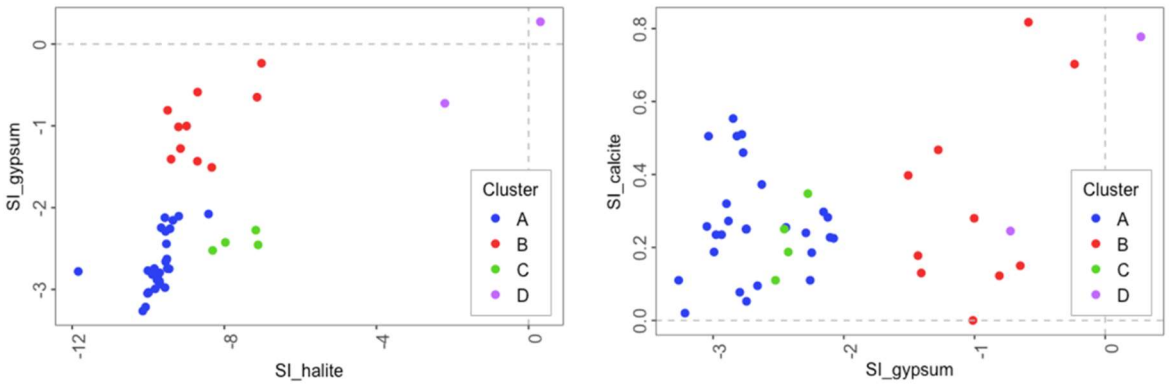

Figure A2. Bivariate relationship graphs. **(A)** SI calcite vs. TDS (mg/L); **(B)** SI dolomite vs. TDS (mg/L); **(C)** SI gypsum vs. TDS (mg/L); **(D)** SI halite vs. TDS (mg/L); **(E)** SI gypsum vs. SI halite and **(F)** SI calcite vs. SI gypsum

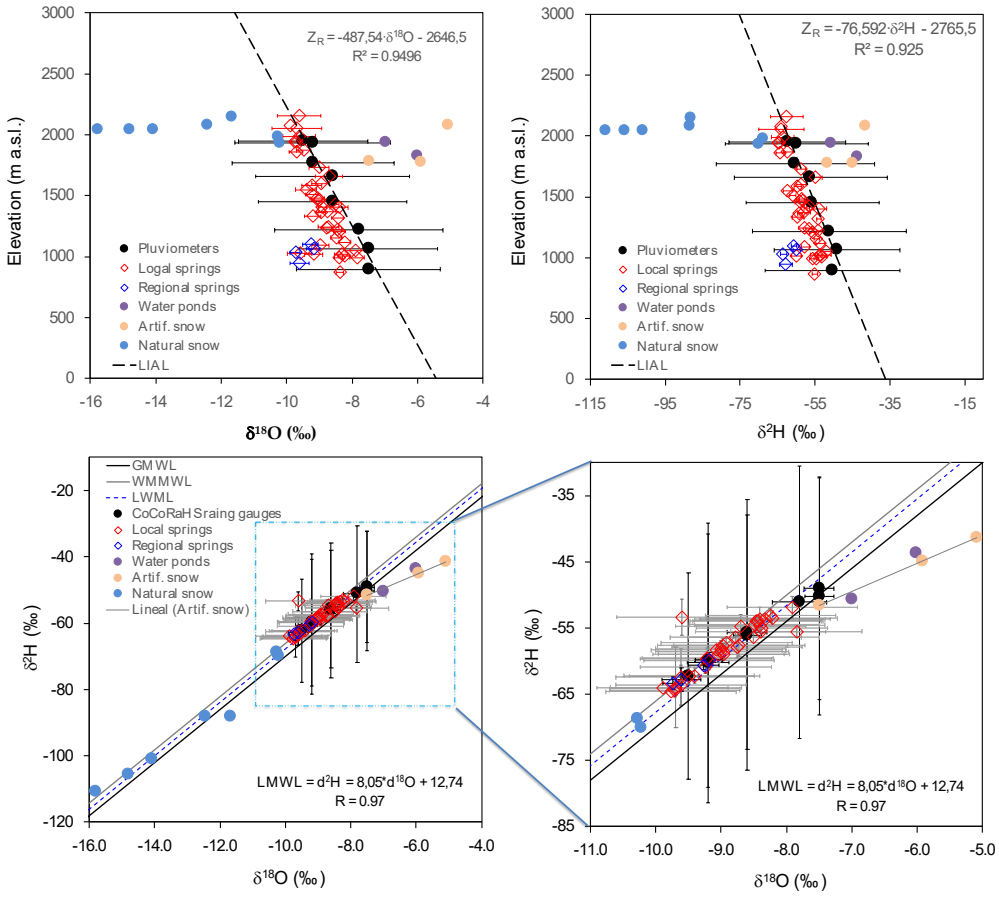

Figure A3 (A) H and O stable isotope composition water lines derived in [29] used to infer recharge altitudes for the whole dataset. (A) Relationship between elevation and $\delta^{18}O$ content, where LIAL is the Local isotope altitudinal line; (B) Relationship between elevation and $\delta^{2}H$ content; (C) Relationship between $\delta^{2}H$ vs. $\delta^{18}O$ content and (D), zoom in the graph $\delta^{2}H$ vs. $\delta^{18}O$. GWML is the Global Water Meteoric Line WMMWL is West Mediterranean Meteoric Line and LWML is Local Water Meteoric Line.

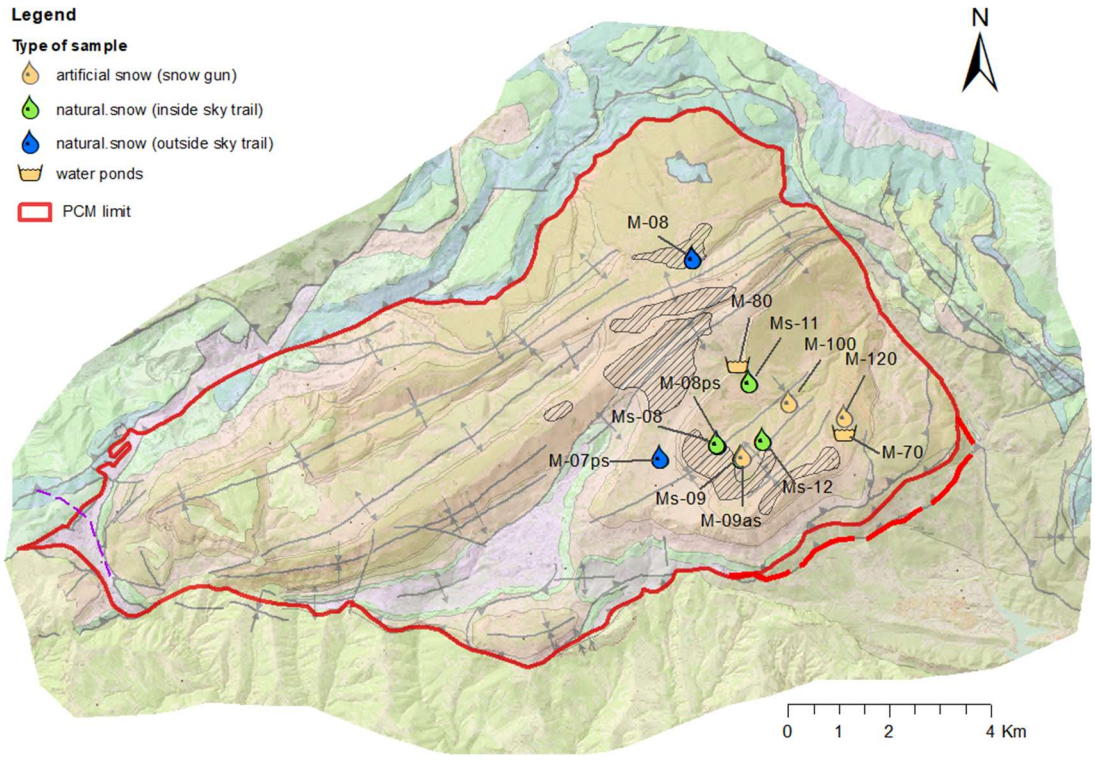

Figure A4. Map of sampling point for the 10 snow samples (7 natural and 3 artificial) and 2 water ponds.

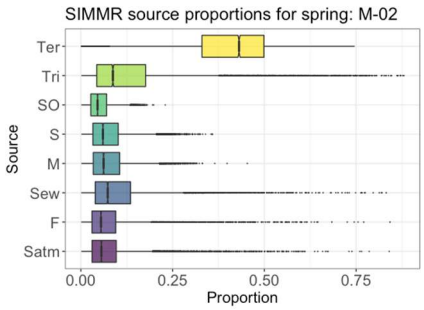

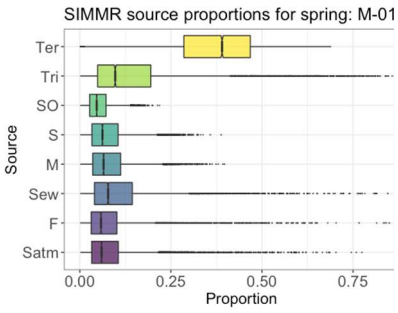
SIMMR source proportions for spring: M-01
Source
Ter
Tri
SO
S
M
Sew
F
Satm
0.00
0.25
0.50
0.75
Proportion

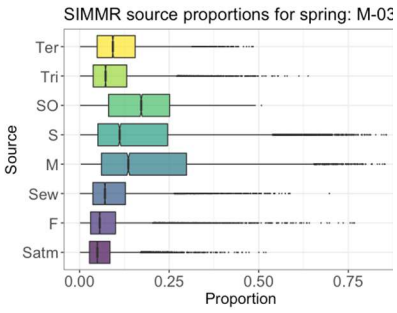
SIMMR source proportions for spring: M-03
Source
Ter
Tri
SO
S
M
Sew
F
Satm
0.00
0.25
0.50
0.75
Proportion

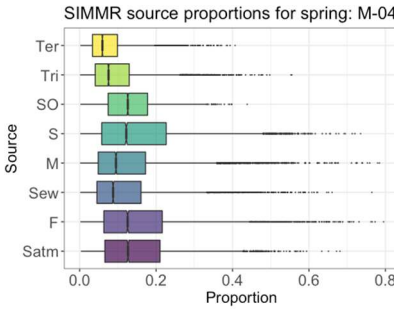
SIMMR source proportions for spring: M-04
Source
Ter
Tri
SO
S
M
Sew
F
Satm
0.0
0.2
0.4
0.6
0.8
Proportion

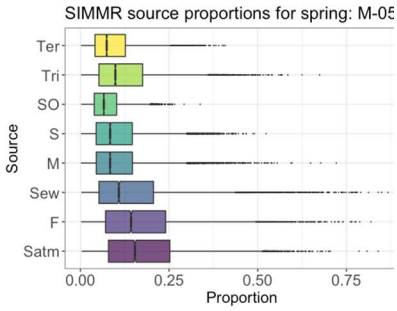
SIMMR source proportions for spring: M-05
Source
Ter
Tri
SO
S
M
Sew
F
Satm
0.00
0.25
0.50
0.75
Proportion

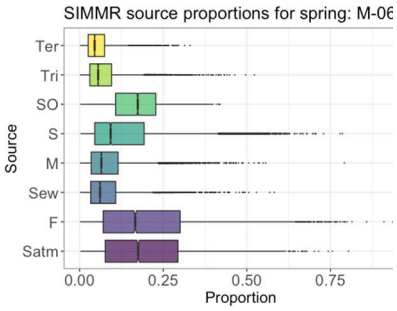
SIMMR source proportions for spring: M-06
Source
Ter
Tri
SO
S
M
Sew
F
Satm
0.00
0.25
0.50
0.75
Proportion

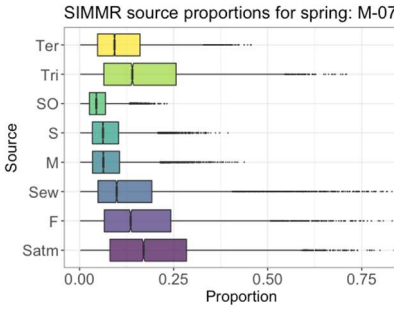
SIMMR source proportions for spring: M-07
Source
Ter
Tri
SO
S
M
Sew
F
Satm
0.00
0.25
0.50
0.75
Proportion

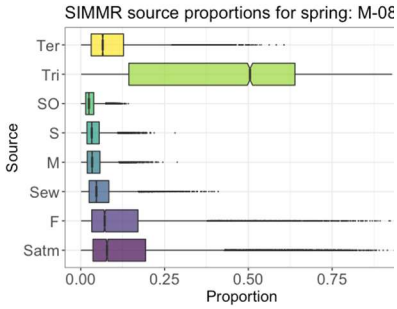
SIMMR source proportions for spring: M-08
Source
Ter
Tri
SO
S
M
Sew
F
Satm
0.00
0.25
0.50
0.75
Proportion

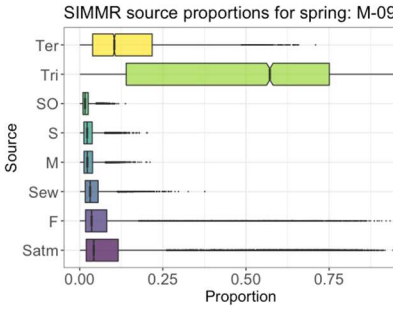
SIMMR source proportions for spring: M-09
Source
Ter
Tri
SO
S
M
Sew
F
Satm
0.00
0.25
0.50
0.75
Proportion

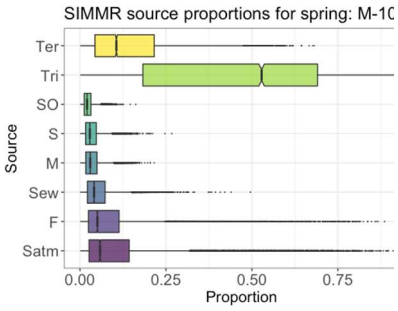
SIMMR source proportions for spring: M-10
Source
Ter
Tri
SO
S
M
Sew
F
Satm
0.00
0.25
0.50
0.75
Proportion

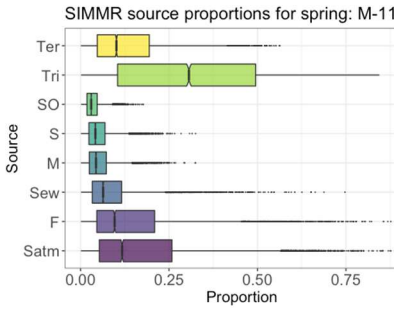
SIMMR source proportions for spring: M-11
Source
Ter
Tri
SO
S
M
Sew
F
Satm
0.00
0.25
0.50
0.75
Proportion

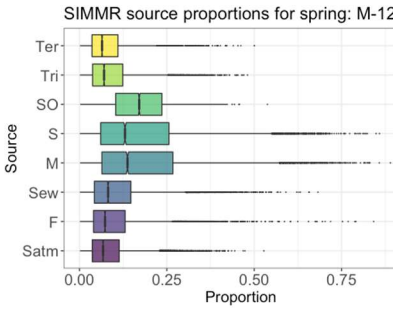
SIMMR source proportions for spring: M-12
Source
Ter
Tri
SO
S
M
Sew
F
Satm
0.00
0.25
0.50
0.75
Proportion

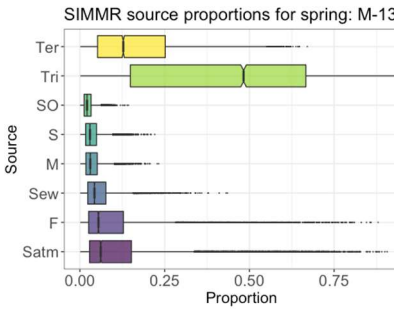
SIMMR source proportions for spring: M-13
Source
Ter
Tri
SO
S
M
Sew
F
Satm
0.00
0.25
0.50
0.75
Proportion

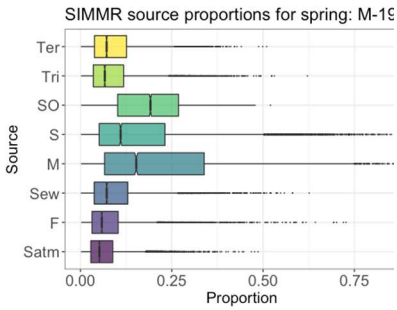
SIMMR source proportions for spring: M-19
Source
Ter
Tri
SO
S
M
Sew
F
Satm
0.00
0.25
0.50
0.75
Proportion

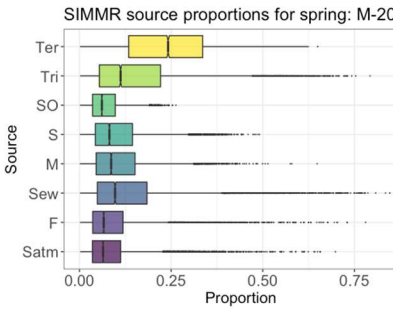
SIMMR source proportions for spring: M-20
Source
Ter
Tri
SO
S
M
Sew
F
Satm
0.00
0.25
0.50
0.75
Proportion

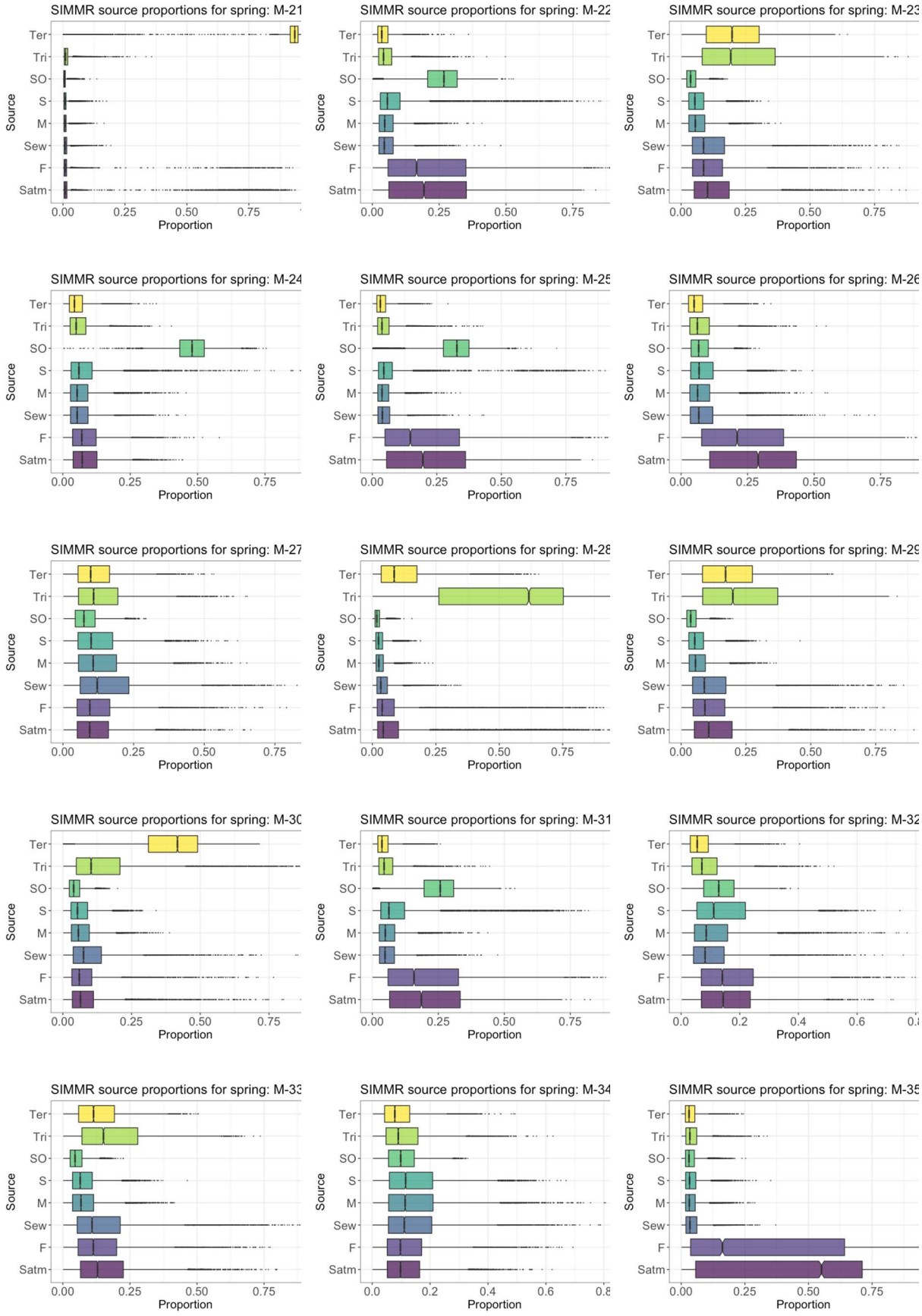
SIMMR source proportions for spring: M-21
SIMMR source proportions for spring: M-22
SIMMR source proportions for spring: M-23
SIMMR source proportions for spring: M-24
SIMMR source proportions for spring: M-25
SIMMR source proportions for spring: M-26
SIMMR source proportions for spring: M-27
SIMMR source proportions for spring: M-28
SIMMR source proportions for spring: M-29
SIMMR source proportions for spring: M-30
SIMMR source proportions for spring: M-31
SIMMR source proportions for spring: M-32
SIMMR source proportions for spring: M-33
SIMMR source proportions for spring: M-34
SIMMR source proportions for spring: M-35
Source
Ter
Tri
SO
S
M
Sew
F
Satm
Proportion
0.00
0.25
0.50
0.75
0.0
0.2
0.4
0.6

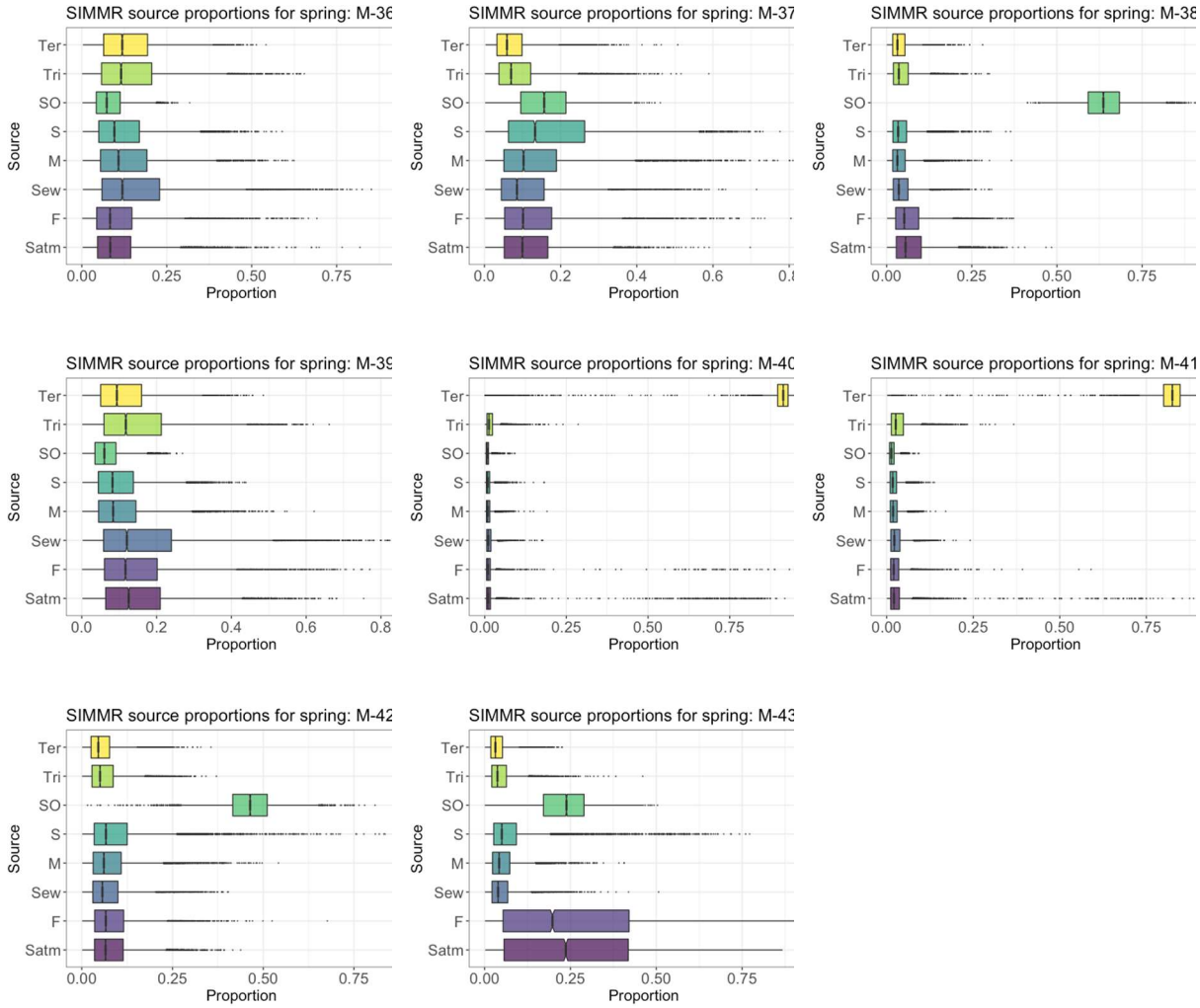

Figure A5. Bayesian isotope mixing model outputs for S and O from SO_4 for all 38 springs. The considered sources are the same of the biplots (Figure 9): (SO) sulfide oxidation; (M) manure; (S) soil; (Satm) atmosphere deposition (F) fertilizers; (S) sewage; (Tri) Triassic evaporites and (Ter) Tertiary evaporites. In total 209 samples that were averaged from 38 springs were available of the 43 springs in total. No samples could be prepared for the remaining 5 springs (M-14, M-15, M-16, M-17 and M-18) corresponding to those with lower concentrations of sulfate and situated at the highest part of the massif and associated to Cluster A

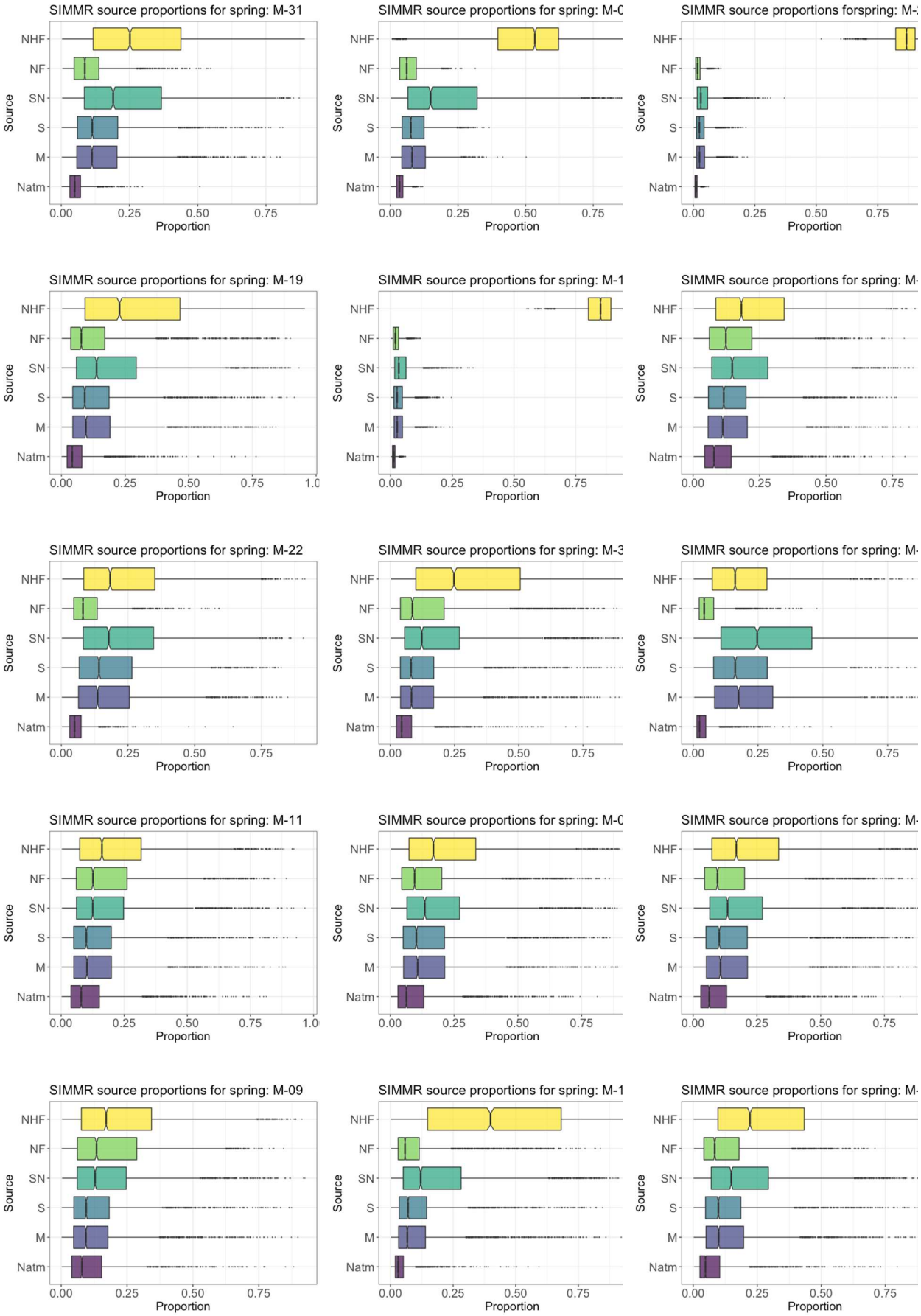
SIMMR source proportions for spring: M-31
SIMMR source proportions for spring: M-0
SIMMR source proportions forspring: M-
SIMMR source proportions for spring: M-19
SIMMR source proportions for spring: M-1
SIMMR source proportions for spring: M-
SIMMR source proportions for spring: M-22
SIMMR source proportions for spring: M-3
SIMMR source proportions for spring: M-
SIMMR source proportions for spring: M-11
SIMMR source proportions for spring: M-0
SIMMR source proportions for spring: M-
SIMMR source proportions for spring: M-09
SIMMR source proportions for spring: M-1
SIMMR source proportions for spring: M-
NHF
NF
SN
S
M
Natm
Source
Proportion
0.00
0.25
0.50
0.75
1.0

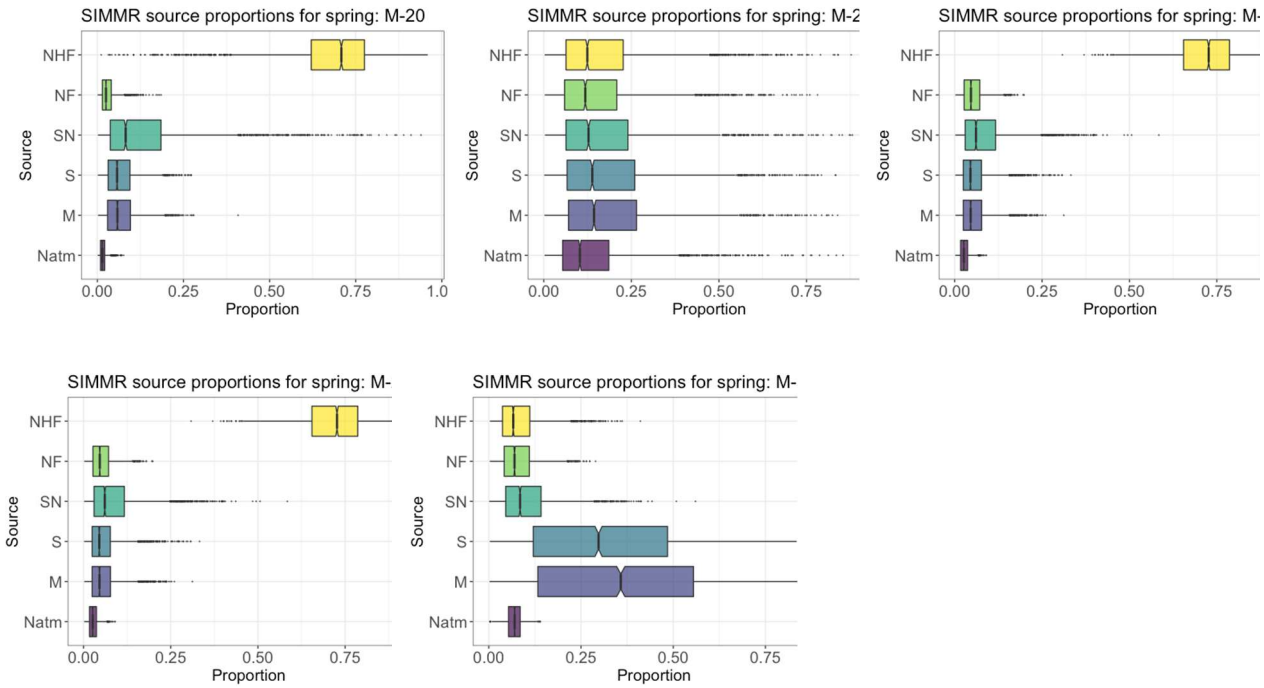

Figure A6 Bayesian isotope mixing model outputs for NO3 for all 20 springs. The considered sources are the same of the biplots (Figure 12A) plus atmospheric deposition: (NHF) NO3- derived from NH4+ in chemical Fertilizer and Precipitation; (NF) NO3 in chemical fertilizer; (SN) Soil organic nitrogen; (S) soil; (M) manure; (Natm) atmospheric deposition. In total 72 samples that were averaged from 20 springs were available of the 43 springs in total. No samples could be prepared for the remaining 23 springs corresponding to those with lower concentrations of nitrate.

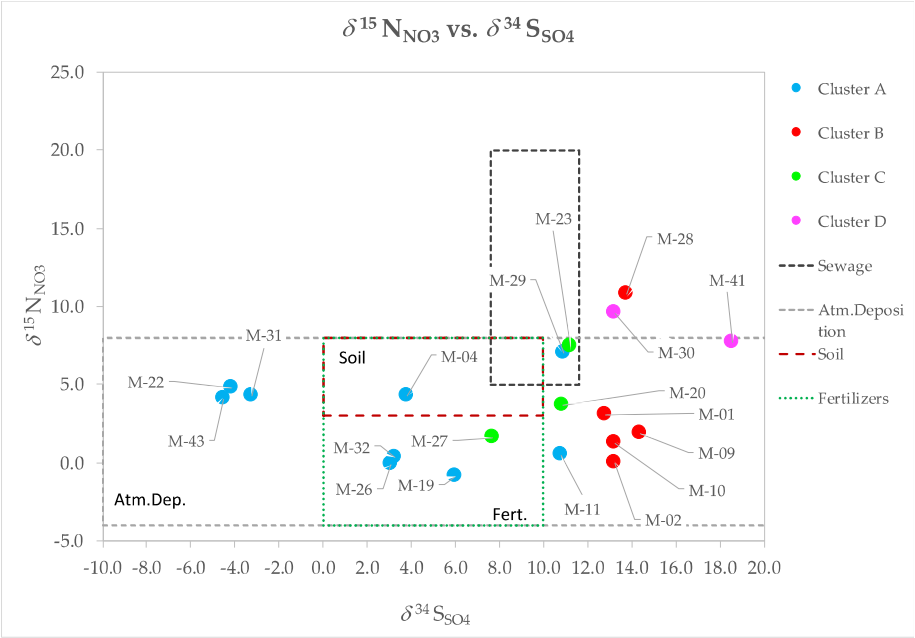

Figure A7 Dual-isotope diagram $\delta^{15}N_{NO_3}$ versus $\delta^{34}S_{SO_4}$ representing the isotopic composition boxes of atmospheric deposition, soil, fertilizers, and sewage. with the water samples collected in the study area with both data available (in total 19 springs).